Numerical Modelling for the Hydrothermal Activity & Habitability of Mars

Evangelos Christou

BSc. (Honours), MSc., Universität Bremen

Submitted in Fulfilment of the Requirements of the Degree of

Doctor of Philosophy

School of Geographical & Earth Sciences,

College of Science & Engineering

University of Glasgow

February 2023

University of Glasgow

VIA VERITAS VITA

ABSTRACT

Modern space and planetary explorations are enthusiastically searching for extraterrestrial biosignatures, and even intelligence in our cosmic neighbourhood. Mars is the epicentre of planetary research and astrobiology, as during ancient geological periods, the Red Planet should have had a thicker atmosphere, and exhibits evidence for ancient aqueous, volcanic and hydrothermal activity. Such physical processes that persist on a planetary body through geological time increase the probability of the emergence and evolution of antediluvian microbial species. However, present-day Mars is a cold and arid desert. So, could the Red Planet host evidence of extinct or/and even extant microbial life? To contribute towards deciphering this mystery, this PhD research focuses on determining the thermodynamic and hydrological evolution, and subsequent habitability of ancient hydrous environments on Mars.

Martian habitability, especially during the planet's ancient geological history, has not been decisively established yet. Moreover, quantitative analyses and models for the ancient or present bioenergetic potential on Mars are scarce. Water – rock interactions enduring in long-lived hydrothermal settings on Earth yield appreciable quantities of chemical nutrients that support microbial species under hydrothermal conditions. Through this perspective, the habitability of simulated Martian hydrothermal systems deserves to be computed and analysed. This PhD research explores simulated volcanogenic and impact-induced hydrodynamics on Mars, and the astrobiological potential of such ancient or more recent Martian aqueous environments via computational scenarios.

High-resolution numerical simulations for the aqueous circulation and thermodynamics in a variety of putative Martian hydrothermal systems have been constructed and interpreted. Rock permeability, porosity, temperature, pressure, enthalpy, heat capacity, and thermal conductivity comprise governing physical parameters for the duration and mechanics of the hydrothermal cycle in each simulation. Therefore, the presented thermodynamic simulations explore thoroughly the evolution and duration of putative impact-induced or magmatic-induced hydrological systems on Mars from the pre-Noachian to the late Amazonian. The thermodynamic results of these models are then used as input conditions in further computations for Martian water – basaltic rock reaction pathways and their subsequent bioenergetic yield (habitability). Eventually, quantitative habitability assessments are

conducted based on the energy – chemical nutrient availability and on the thermal constraints that cumulatively render these environments habitable or uninhabitable for hypothetical lithotrophic microbial species in the Martian subsurface.

In parallel, NWA 8159 (shergottite) and Lafayette (nakhlite) Martian meteorite samples were examined through Scanning Electron Microscopy (SEM) analysis to identify their Martian mineralogies, and detect alteration phases – fluid compositions that have affected these basaltic rocks on Mars, or on Earth due to weathering processes after their fall. Petrological analyses provided additional insights into the geochemical composition and evolution of these Martian rocks. Furthermore, image processing on acquired SEM-BSE montage maps of the NWA 8159 and Lafayette samples revealed the porosity of these Martian rocks, and subsequently constrained and enhanced the hydromechanic and habitability models of this PhD research.

The hydrothermal and habitability simulations indicate that the Martian basaltic subsurface could have supported hydrogenotrophic microbial life for periods ranging from 0.1 Myr to 3 Myr under preserved hydrothermal conditions. The modelling results additionally suggest that deeper basaltic domains (subsurface depth $\geq$ 1.5 km) in large impact craters (100-, 200-km diameters) or intrusive volcanic rock settings, could comprise the most promising sites for astrobiological research. The ideal habitable thermal range in which nutrients, and specifically H_2, are released in appreciable amounts through ongoing water – rock reactions is from 50 °C to 121 °C. Under such hydrothermal conditions, the Martian subsurface is modelled able to support the survival and growth criteria of hydrogenotrophic life. However, aqueous circulation and geochemical reactions should endure for an average minimum period of 120 Kyr to support microbial growth, and conceivably, the microbial colonization of the Martian subsurface.

The numerical simulations of this research support that cold aqueous flows and short-in-duration hydrological systems on Mars are unable to support the survival of potential microbial species for a period $\geq$ 2 Kyr. Finally, even in the most optimistic thermodynamic scenarios for Martian habitability, microbial species in the deep Martian subsurface cannot be supported for a period longer than 1 – 2 Myr, after hydrothermal activity has halted. This indicates that any potentially inhabited environments on Mars could have supported microbial life only for an average maximum period of 3 – 4 Myr. Conclusively, planetary environments beyond Earth that may have been hosting hydrothermal or aqueous activity continuously for Myr or even

Gyr (i.e.: the Jovian and Kronian moons, beneath their icy crusts) comprise the most habitable extraterrestrial niches of the Solar System, and promising sites for astrobiological findings.

ACKNOWLEDGEMENTS

First and foremost, I express my sincere gratitude to my principal supervisor Dr. Lydia Hallis, who entrusted me with conducting planetary research as a member of the Planetary Science group at the University of Glasgow (UoG), and who cordially welcomed me in the most friendly, supportive, and simultaneously innovative research environment that a PhD student could ask for. Dr. Lydia Hallis has been a genuine inspiration and role model for my own career in research and academia. I am hugely grateful to you for assigning me to the PhD researcher's position in your awarded Leverhulme Research Project Grant 2018 – 298, for your limitless support, scientific insights, encouragement and problem-solving skills. Thank you for the flexibility that you demonstrated as a supervisor in adjusting this research project as required; especially, when the pandemic constrained significantly, and even critically at some point, our lab-based research at the UoG and abroad. My PhD research and this doctoral dissertation could have not been completed without you.

In parallel, I am grateful to Professor Dr. Martin Lee (second supervisor), Dr. Luke Daly, Dr. Annemarie Pickersgill and Professor Dr. Caroline Smith for including me in their own wonderful research projects and for assigning me side-PhD research roles that resulted in fascinating scientific contributions, activities and conferences around the world. Thank you for all your support, recommendations and advice, when my circumstances were requiring me to ask or even shout for help. Thank you for always being there for me, and for allowing me to explore the mysteries of Solar System objects and planetary processes with you (e.g.: Itokawa asteroid, Mars, impact processes on terrestrial planetary bodies). Additionally, I am vastly thankful to Dr. Leanne Staddon and Dr. Joshua Franz Einsle, the examiners of my PhD thesis, for their extraordinarily insightful and constructive comments towards enhancing the final version, and for all their time, interest and energy dedicated in this PhD research. You are both excellent and admirable scientists and academics!

A huge thank you to Dr. Sammy Griffin, Dr. Aine O'Brien and Dr. Nicola Mari for sharing their scientific ideas and expertise on Martian geochemistry, and their own geochemical datasets from Martian meteorite analyses that enhanced my own computational research and meteoritical understanding too. Merci beaucoup Pierre-Etienne Martin, Laura Jenkins and Cameron Floyd; vous êtes unique en votre genre! For my time as a tutor and lab leader at the UoG, I am grateful to Dr. Hannah Mathers, Dr. Cristina Persano, and Dr. Kimberly Wilder-Davis for helping me develop through my academic teaching role and achieve a RET status at the College of Science and Engineering. I am also thankful to Dr. Eamon McKenna and Isobel Stemp who collaborated significantly with me during my time as a GTA. Thank you for being so collegial, supportive and exceptional friends inside and outside of work. The Planetary Science team at the UoG, with which I shared 4 years of my research and PhD life, comprises my most unique alma mater, and the most wonderful academic and working environment that I have ever experienced. Thank you to Leenah Khan, Aileen Quinn and Dawn Bradshaw for supporting me as an employee and PhD student of the UoG through their administrative positions.

I thank Dr. Ingrid McCarroll, Dr. Limei Jang, Dr. Magnus Garbrecht and Professor Dr. Julie Cairney for hosting Lydia, Luke and myself as visiting researchers at the University of Sydney (UoS) and for supervising the successful performance of APT and TEM analyses of Martian meteorites at the Australian Centre for Microscopy and Microanalysis of the UoS. EPMA of Martian meteorite samples were performed at the Grant Institute (School of Geosciences) of the University of Edinburgh (UoE) thanks to Dr. Chris Hayward. I am honestly grateful to you Chris for your hospitality during my research visits at the UoE and for all your invaluable and hard work toward unveiling the volatile composition of aqueous minerals and alteration phases in our Martian meteorite samples. Thank you for being such a good friend and research colleague. I thank Dr. Liene Spruzeniece and Peter Chung, for all their great help in analysing Martian rocks via SEM and Raman Spectroscopy at the ISAAC of the UoG. My PhD and all analytical investigations of Martian meteorites were funded by the Leverhulme Trust, to which I am extremely grateful. I am also thankful to the Royal Astronomical Society, NASA, LPI, ESA, Europlanet Society and to the Meteoritical Society for awarding me travel grants to attend international conferences during the last 3 – 4 years, and for funding collaborative research projects to which I have also contributed. A great thank you to the USGS and to the developing teams of the publicly available HYDROTHERM and PHREEQC codes. I am thankful to Dr.

Tori Hoehler (NASA) for his insightful and innovative biogeochemical – astrobiological models that have been made available through distinguished research publications.

I am grateful to my postgraduate classmates and friends, Nestor Gaviria and Amr Elshafei, for the wonderful collaboration during our time at the University of Bremen (Germany). A huge thank you to my best friends from the undergraduate programme of the Aristotle University of Thessaloniki: Christos, Dimitris, Giannos, Irene, and Nikolas (your names are in alphabetical order to prevent conflict!). I am so fortunate to have you as friends! You are friends for life, and I am very grateful to you and your families for being there during some of my most difficult and wonderful times.

I am vastly grateful to my sister, Irene – Niovi, who has been my soulmate since childhood and one of the brightest stars in my sky thanks to her personality, creativity, values and virtues. Thank you Irene – Niovi for all your love, sisterly affection and encouragement during the last 30 years! You will always be my home in Greece. I am hugely grateful to my mother (Katerina), my aunt (Mary), my grandmother (Maria) and my grandfather ((Ev)Angelos) for all their love and support during my childhood and studies. Thank you for all your love, affection, devotion and personal sacrifices to create a better future for me and my sister in Greece, and for the education and ethos that you have provided to us. I am grateful to my father (Vasilis) and his family (Christalle and Alexandra). Thank you dad for continuously encouraging my philosophical engagement with science and research since childhood, and I know that you might be the only person to thoroughly read this PhD dissertation. I dearly miss my grandparents from my father's side (Evangelos and Irene) who have also emphasized to me during my childhood the importance of education and ethical behaviour in a person's life.

My interest in nature and natural sciences was sparked during my childhood, as my grandfather from my mother's side, Angelos (also named Evangelos), was getting me to explore the natural environment with him almost daily, by going fishing out to sea, or by accompanying him in his agricultural activities at his allotment. He and my grandmother (Maria) were explaining to me useful things about the soil compositions, plants, sediments, weather, ocean currents, etc., that were relevant to their daily activities in the beautiful seaside village of Preveza (Greece). Therefore, such experiences of mine, together with presents from my family and their friends such as astronomy, seismology and volcanology books, and a telescope, excited my curiosity and inspired me to study geophysical and planetary sciences. My grandpa, who I hugely miss

as he passed just a few months before I began my PhD, has been the most inspirational and admirable figure in my life, and he has shaped the character and moral values that I have today.

I am hugely grateful to my in-laws: Aphrodite, Spyros, Hercules, Helen, Nickos, grandmother Helene, and grandfather Leonidas (grandpa Leonidas, you are dearly missed but you always live in our memories). I could have not asked for a more caring and supportive in-law family. Thank you for all your love and immense support through my and Katia's continuous endeavours in four different countries in the last 8 years. My dearest childhood friends from Preveza: Petros, Vasilis, Giorgos, Elias…thanks to you….life is a never-ending comedy. I love you all! Finally, I thank my 33 houseplant friends that managed to survive within a Glaswegian home, under Scottish climatic conditions for almost 4 years now, and that have been continuously refreshing my oxygen during very long writing, computing and studying days. I am so proud that you are still alive and that you have now seen this PhD dissertation completed.

Although I consider my PhD thesis to be an original piece of work, it finds itself lying on your desk today solely due to the incredible and yet somehow almost exhausted patience of my wife. It is a miracle that she is still here with me and that she has never left…! Katia has been an angelic figure of limitless patience, encouragement, support, calmness and affection during this PhD research, and throughout my entire postgraduate and undergraduate life. I have persevered through these 13 years of continuous undergraduate and postgraduate studies, adventures, and research, thanks to you! I promise that I will not study medicine or join another postgraduate or training programme after this PhD. Katia, you mean the Universe to me, and I dedicate my PhD dissertation to you with all the love in the Cosmos!

" So we can swim forever "

AUTHOR'S DECLARATION

I declare that this PhD dissertation is original, the product of my own research and writing, and has not been submitted for any other degree at the University of Glasgow or any other institution. Any work by other researchers has been explicitly referenced in the text. No editor or editing software has been used for the writing or drafting of this PhD dissertation.

Evangelos Christou

21 January 2023

TABLE OF CONTENTS

LIST OF ACRONYMS

ADP	Adenosine Diphosphate
ALH	Allan Hills (ALH 84001 meteorite)
APT	Atom Probe Tomography
ATP	Adenosine Triphosphate
AU	Astronomical Unit: Earth – Sun distance = 150 Mkm
BEQ	Biological Energy Quantum
BSE	Backscatter Electron
CHZ	Circumstellar Habitable Zone
CRISM	Compact Reconnaissance Imaging Spectrometer for Mars
CTX	Context Camera (on board the Mars Reconnaissance Orbiter)
D	Diameter
d	depth
Ea	Activation Energy
EDS	Energy-Dispersive X-ray Spectroscopy
EELS	Electron Energy Loss Spectroscopy
EF	Energy-Filtered
EOS	Equations of State
EPMA	Electron Probe Micro-Analysis
ESA	European Space Agency
FIB	Focused Ion Beam
GMRES	Generalized Minimal RESidual Method
GWB	Geochemist's Workbench
HiRISE	High Resolution Imaging Science Experiment
HST	Hubble Space Telescope
HT (3)	HYDROTHERM (3)
HTI	HYDROTHERM Interactive (software)
HZ	Habitable Zone
iSALE	impact - Simplified Arbitrary Lagrangian Eulerian
JUICE	JUpiter ICy moons Explorer
JWST	James Webb Space Telescope
k	permeability

KST	Kepler Space Telescope
LREE	Light Rare Earth Elements
m	mass
MARSIS	Mars Advanced Radar for Subsurface & Ionosphere Sounding
ME	Maintenance Energy
MIL	Miller Range (e.g.: MIL 03346 meteorite, MIL 090136 meteorite)
MOLA	Mars Orbiter Laser Altimeter
MRO	Mars Reconnaissance Orbiter
NASA	National Aeronautics & Space Administration
NASA ADS	NASA Astrophysics Data System
NWA	Northwest Africa (e.g.: NWA 8159 meteorite)
p	pressure
PHREEQC	PH (pH), RE (redox), EQ (equilibrium), C (program written in C)
r	radius
RAS	Royal Astronomical Society
ROI	Regions of Interest
RSL	Recurring Slope Lineae
SE	Secondary Electron
SEM	Scanning Electron Microscope
SHARAD	Shallow Radar (on board the Mars Reconnaissance Orbiter)
SIMS	Secondary Ion Mass Spectrometry
SNC	Shergottites – Nakhlites – Chassignites (Group of Martian Meteorites)
T	Temperature
TEM	Transmission Electron Microscopy
TESS	Transiting Exoplanet Survey Satellite
THEMIS-IR	Thermal Emission Imaging System - Daytime InfraRed (Mars Odyssey)
UoE	University of Edinburgh
UoG	University of Glasgow
UoS	University of Sydney
V	volume
WMF	Water Mass Flux
yr	years (e.g.: Gyr, Myr, Kyr); (y)a: (Ga, Ma, Ka) = years ago
$\Delta_r G$	Free Gibbs Energy
$\Delta_r G_{rxn}$	Gibbs Free Energy Yield under ambient conditions

ρ	Density
Φ	porosity
$\oplus$	Earth
$\male$	Mars

§1 INTRODUCTION & LITERATURE REVIEW

1.1 Habitable Worlds Beyond Earth

Life beyond Earth has comprised a philosophical quest of human civilization since antiquity (Coustenis and Encrenaz, 2013; Roush, 2020). Notably, Anaxagoras, the ancient Greek philosopher (circa 500 BC – 428 BC), who had accurately described the cause of eclipses, had speculated that the Moon is a "great rock" and that the Moon or similar "rocky worlds" might be inhabited (Curd, 2007). Democritus (460 BC – 370 BC) also believed that, as there is an infinite number of atoms in our ‘’world’’ (meaning the Earth), there must also exist an infinite number of worlds (Dick, 1984; Warren, 2004). The existence of other potentially inhabited worlds concerned several philosophers, including Epicurus (341 BC – 270 BC), who once wrote to the historian Herodotus (484 BC - 425 BC) that “there is an unlimited number of cosmoi, and some are similar to this one and some are dissimilar.” Epicurus’ belief influenced the Roman poet Lucretius (99 BC – 55 BC) who later wrote: “nothing in the universe is unique and alone, and therefore, in other regions there must be other Earths inhabited by different tribes of men and breeds of beasts’’ (Warren, 2004; Curd, 2007; Roush, 2020).

The evolution of scientific philosophy throughout the last 2 millennia led to the recent advancements in science and technology that have unveiled many mysteries of our cosmos. Solar System and exoplanetary exploration have detected potentially habitable environments in places we would have never expected (e.g., potential liquid oceans on outer solar system bodies, exoplanets with a high probability of retaining water on their terrestrial surfaces). Our Solar System hosts the only proof of life in the Universe until now, solely constrained on planet Earth. Water and organics are the building blocks for life on Earth and based on this axiom, planets and moons with a considerable presence of these elements are assumed favorable habitats for microbial life.

Establishing the habitability of planetary bodies has been a major focus of planetary research while exploring our Solar System. For decades, space organizations have been exploring geological environments beyond Earth and searching passionately for habitable conditions and biosignatures on Mars (e.g.: Mars 2020 Perseverance rover

mission (NASA), Curiosity rover mission (NASA), after Berger et al., 2022; Cardenas et al., 2022; Bedford et al., 2022; Van Bommel et al., 2023) and on the icy moons of Jupiter (Galileo mission: Kivelson et al., 2000; upcoming JUICE mission: Grasset et al., 2013; Coustenis et al., 2021) and Saturn (Cassini – Huygens mission, NASA – ESA; Iess et al., 2014; Waite et al., 2017; Solomonidou et al., 2018). Space missions that explore beyond the Solar System via the Hubble Space Telescope (HST;), Kepler Space Telescope (KST;), Transiting Exoplanet Survey Satellite (TESS) and James Webb Space Telescope (JWST) are revealing thousands of planets orbiting other stars, some of which have already been identified as Earth-like and potentially habitable (via HST: de Wit et al., 2018; via KST: Gilbert et al., 2020; via TESS: Palle et al., 2023; via JWST: Ahrer et al., 2022; Ahrer et al., 2023; and references therein).

Determining the Circumstellar Habitable Zone (CHZ) or Habitable Zone (HZ) of such planetary systems is a key research aim, so that we are soon capable of detecting Earth-like planets, extraterrestrial life and perhaps, even intelligence. The CHZ or HZ of a planetary system is defined as the circumstellar region in which a terrestrial mass planet ($0.1 \leq M \leq 10\ M\oplus$, where $\oplus$ = Earth's Mass) can sustain liquid water on its surface under sufficient atmospheric pressure (Dole, 1964; Kasting et al., 1993; Kaltenegger & Sasselov, 2011; Kopparapu et al., 2013; Abe et al., 2013). This theory is using our Solar System and Earth as a prototype and has recently concluded that just our galaxy may be hosting approximately 40 billion Earth-sized planets orbiting within the HZ of Sun-like stars and red dwarfs (Petigura et al., 2013).

Nevertheless, in our Solar System, we have discovered several planetary bodies that are far beyond the habitable zone (Jovian and Kronian moons) which host liquid oceans beneath their icy crust (e.g., Europa, Enceladus, Ganymede) or lakes of liquid methane and other organics mixed with ice on their surface (i.e.: Titan). In environments where water-rock and organics interactions may be taking place, the habitability potential increases significantly. For example, beneath Enceladus' icy crust, the liquid ocean is probably reacting with its rocky core, triggering the serpentinization of olivine in the chondritic core and releasing appreciable amounts of CH_4 and H_2, as detected by NASA's Cassini probe while flying through Enceladus' south polar plume (Waite et al., 2017; Taubner et al., 2018). Such findings strongly imply that our perception of extraterrestrial habitability has been too conservatively defined, as it has so far been

based on a star's mass and radiation flux, and on an orbiting planetary body's distance from its host star. Therefore, the broader thesis of extraterrestrial habitability should be enriched by considering subterranean environments as potential habitats for microbial life.

Searching for life beyond Earth is one of the most challenging scientific endeavors. To fully decipher the habitability of extrasolar planets and moons, the thorough investigation of planets and moons in our Solar System is paramount. This PhD research focuses on the habitability of Mars; the Red Planet orbiting at the outer edge of the Solar system's habitable zone. To understand Mars' significance for astrobiological research, we should firstly consider its place and evolution history in the Solar System.

1.2 The Formation & Evolution of Mars

1.2.1 The Formation and Evolution of the Protoplanetary Disk

In our galactic province, 4.6 billion years ago and within a massive interstellar cloud of hydrogen, helium and dust, a nearby star burns its fuel rapidly, and is triggered into runaway thermonuclear fusion (Montmerle et al., 2006). Consequently, the star collapses through a colossal explosion, called a supernova. This astronomic event causes the gravitational destabilization of our interstellar nebula, and within a 100Kyr to 1Myr period, the resulting gravity and angular momentum form our presolar nebula (Montmerle et al., 2006; Adams, 2010; and references therein). In a "geologic" blink of an eye (within circa 100Ky), our presolar nebula is furthermore flattened into a swirling disk of a 200 AU diameter (Pfalzner et al., 2015). In its centre, where molecular masses condensate tightest, the Protostar (or Proto-Sun) is formed under extreme temperatures and pressures.

Pb-Pb chronological dating of the most primitive minerals in the Solar System revealed that the first rocks of the protoplanetary disk formed at around 4,568.22 ± 0.17 Ma

(Bouvier and Wadhwa, 2010; Connelly et al., 2012). As it is hotter near the sun, only elements that solidify at high temperatures (more refractory elements) can condense in the inner Solar System and the chemical composition of the solids in this astronomical province relates to metals and silicates. Farther from the Sun, at a 2.7 AU distance, volatile compounds such as CO^-, H_2O, HCN, C_2H_2, CO_2 and HCO^+ condense into icy grains. The inner border of this circumstellar domain, where volatile ice compounds and gases are found, is defined as the snow line of the Solar System. During the early evolutionary stages of the protoplanetary disc, the snow line may have been located at circa 2.7 AU (Martin and Livio, 2012), but the current snow line of the Solar System is approximately at 5 AU. A logical explanation is that during the formation of the Solar System, the Proto-Sun was less energetic, more opaque, and hence, temperatures were lower closer to the star. As the solar nebula evolved, the Sun started being thermonuclearly much more active, the temperature within the circumstellar disk increased, and this process caused the migration of the snow line at the current astronomical distance of 5 AU (Sasselov and Lecar, 2000).

Within a few million years after the formation of the protoplanetary disk, dust and ice particles gravitationally attract each other and coalesce to form the first planetesimals (Stevenson and Lunine, 1988; Arny and Schneider, 2019; fig. 1.1). Jupiter and Saturn are the first planets to form within 10 My in the icy and gaseous neighborhood of the protoplanetary disk, beyond the frost line (Walsh et al., 2011). The volatile compounds and ices are far more abundant in the protoplanetary disk than the metallic and silicic amalgam, allowing the gas giants (Jupiter, Saturn, Uranus, Neptune) to accrete first (Morbidelli et al., 2010). Additionally, the abundance of volatiles beyond the frost line allowed the gas giants to evolve vast atmospheres of hydrogen and helium, the lightest and most abundant elements of the Solar System. Jupiter should have formed at 3.5 AU and then migrated inward to 1.5 AU due to gravitational interference with Sun, within 0.1 My (Walsh et al., 2011; Johnson et al., 2016). Because Jupiter captured the newly formed Saturn in an orbital resonance, the planet eventually reversed its trajectory, migrated outward, and halted near its current orbit at 5.2 AU (Bitsch et al., 2015a;b; Levison et al., 2015). Both gas giants have undergone a gas-driven inward and then outward migration of their orbits, described by the Grand Tack hypothesis, and only after their migration was over, the terrestrial planets formed (Tsiganis et al., 2005; Morbidelli et al., 2010; Walsh et al., 2011; Brasser et al., 2016; 2020; Mojzsis et al.,

2019; Woo et al., 2018; 2022). The migration event of Jupiter and Saturn early in the Solar System (Grand Tack Hypothesis) was revealed and confirmed via N-body simulations (Tsiganis et al., 2005; Morbidelli et al., 2010; Walsh et al., 2011). Volatile-poor asteroids (S-type asteroids: silica-rich) are predominant in the inner asteroid belt and hence, S-type planetesimals should have been initially located between 0.3 and 3.0 AU in the protoplanetary disk.

Volatile-rich asteroids (C-type: carbon-rich) are mainly observed in the outer belt and thus, C-type planetesimals should have been initially between 8.0 and 13.0 AU (Walsh et al., 2011; and references therein). The inward migration of the giant planets scattered much of the S-type planetesimals, doubling the mass of the inner protoplanetary disk through resonant trapping, eccentricity excitation and gas drag (Tsiganis et al., 2005; Morbidelli et al., 2010). Walsh et al (2011) reproduced through dynamical simulations the formation of the terrestrial planets (Mercury, Venus, Earth and Mars), and showed that this was initiated via planetesimal collisions and huge impact events. They also showed that only a small mass of S-type remnants should have scattered outward and beyond 3 AU.

Afterwards, Jupiter and Saturn migrated outward and encounter the population of C-type planetesimals, a part of which was also shepherded into the asteroid belt (Walsh et al., 2011; Johnson et al., 2016). This narrative explains efficiently the compositional differences between the asteroids orbiting in the asteroid belt. The asteroid belt is chemically an inhomogeneous territory comprised by more than just S- and C-type asteroidal bodies (Mothe´-Diniz et al., 2003).

However, S-type objects dominate in the inner asteroid belt and C-type objects in the outer belt (Morbidelli et al., 2000). Computational studies (Gomes et al., 2005; Tsiganis et al. 2005; Morbidelli et al., 2005; O'Brien et al., 2006; 2018) have shown that C-type planetesimals and asteroids from beyond 8 AU were implanted in the outer asteroid belt and ended up on highly eccentrical orbits (with perihelion $q < 1.5$ AU). Consequently, these volatile-rich asteroids entered the inner protoplanetary disk region, where the terrestrial planets were still forming. Since C-type planetesimals contain 10 % water by mass (Kerridge, 1985; Alexander et al., 2017; Raymond and Izidoro, 2017), and having already proven that these were placed onto orbits crossing the terrestrial planetary

neighborhood, this astrodynamic theory implies that the main source of water for the terrestrial planets, and specifically for Earth and Mars, should have been the C-type asteroids.

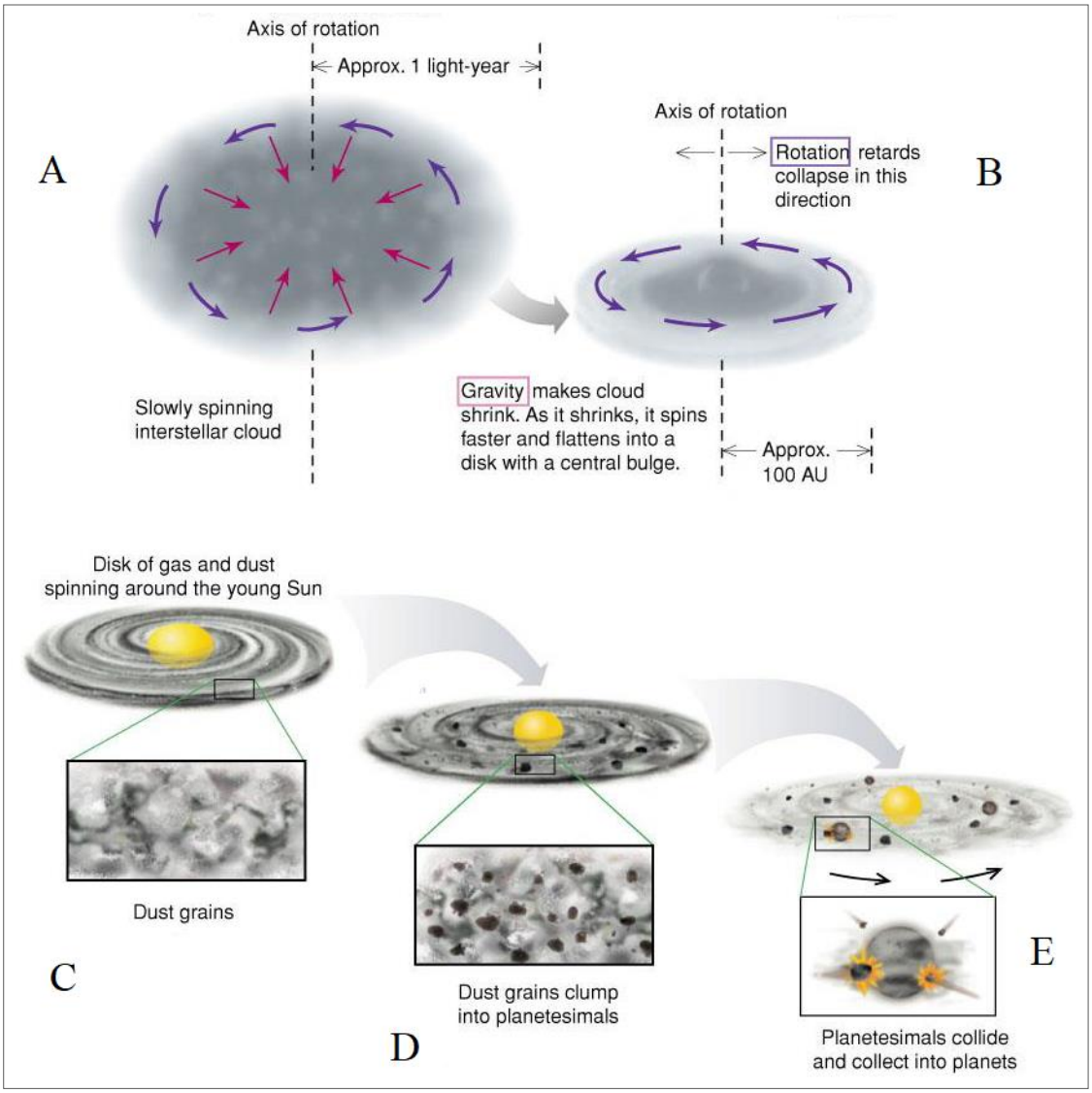

Fig. 1.1. Schematic model of the proto-Solar disk formation and evolution of the early Solar System (revised after Arny and Schneider (2019); © The McGraw-Hill Companies). The diagram shows the initial phase of a slowly spinning interstellar cloud (A) that collapses due to gravity, and its subsequent increase in spinning results to a flattened disk. The collapse of the cloud is much slower on the axis of rotation, and since rotation decelerates the gravitational collapse at the center a central bulge is formed (B). This central bulge will later evolve to the Proto-Sun (C) and the circumstellar regions of disk consist of dust grains (ices and volatiles) at this stage. As the Proto-Solar disk evolves to a protoplanetary disk, dust grains clump into planetesimals (D); metals and silicates condense in the inner regions of the protoplanetary disk (distance ≤ 2.5 AU) and at a distance ≥ 2.7 AU, volatile compounds condense into icy grains (Connelly et al., 2012). Eventually, planetesimals collide and form protoplanets (E).

Nevertheless, the detected low D/H ratio of Earth's interior composition (Robert et al., 2000; McKeegan and Leshin, 2001; Clog et al., 2013; Hallis et al., 2015) concurs to the hypothesis that Earth's oceans could not originate solely from a C-type asteroid water supply. On top of that, E-type (enstatite-rich) planetesimals, asteroids and comets that should have hammered proto-Earth and proto-Mars during their accretion. E-type asteroids may have even delivered about 0.5 oceans of water to Earth (1 Earth's ocean = 1.4×10^{21} kg; Dauphas, 2017). Conclusively, the origin of water on planets and moons in the Solar System is very complex, as revealed by contradicting hypotheses between dynamical models and cosmochemical analyses.

1.2.2 The Formation & Evolution of the Terrestrial Planets

Earlier within the inner protosolar disk, hundreds or even thousands of rocky planetesimals (≥ 100 km in diameter) have formed by accretion (as shown in N-body simulations; Walsh et al., 2011). The main mass of the asteroid belt claims its orbital stability though, only after the giant planets finish their migration (at circa 600 Kyr, after Jupiter's formation; fig. 1.2). Until then, the majority of rocky planetesimals has been destroyed via planetesimal collisions, merging, and intense impact bombardment of asteroids and comets, dynamically triggered by the Grand Tack of Jupiter (Mojzsis et al., 2019). After the giant planets conclude their Grand Tack, the terrestrial planets still require circa 30 My to complete their accretion (Walsh et al., 2011). That should have been due to the migration of Jupiter which resulted to the formation of a truncated inner disk (Hansen, 2009; Morbidelli et al., 2012).

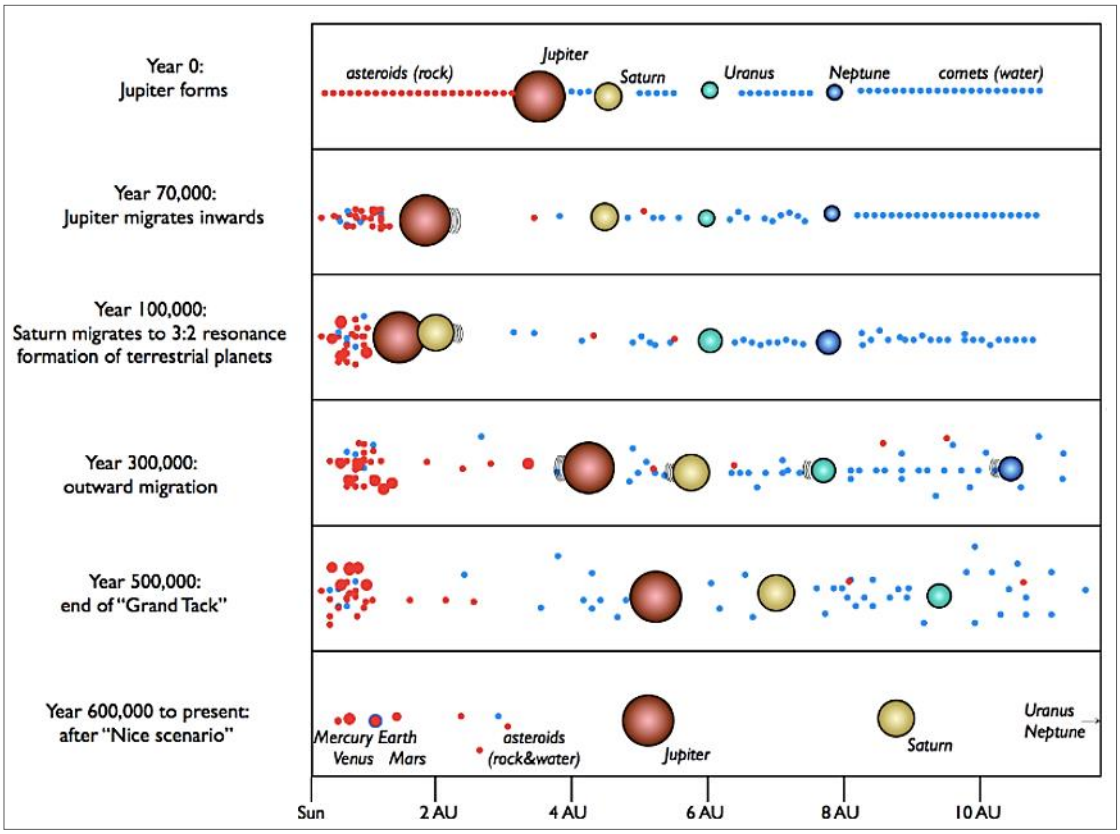

Fig. 1.2. Illustration of the Grand Tack hypothesis and Nice scenario, as provided by Tsiganis et al. (2005) and Walsh et al. (2011). Small blue objects are composed of ice and volatiles. Red small objects are rocky and of higher density. Jupiter's migration is initiated earlier than Saturn's. Then the migration of Saturn follows and the two gas giants catch up later. Jupiter has migrated inward and stopped at 1.5 A.U., where it comes into resonance with Saturn later. Dust gaps overlap and the torques on Jupiter and Saturn change, resulting to Jupiter's and Saturn's outward migration. Rocky planetary embryos form near the Sun after Jupiter starts its outward migration. Mars is low in mass (11% of Earth mass), because Jupiter absorbs and scatters a significant amount of protoplanetary disk material and planetesimals away. The asteroid belt gets depleted and reformed by a mixture of objects from both the inner and outer Solar System.

Eventually, Mercury, Venus and Earth formed after having accreted most of the truncated disk's mass, at 0.39, 0.72 and 1.0 AU, respectively (fig. 1.2). Nevertheless, dynamical models suggest Mars to have accreted by planetary embryos that were scattered out beyond the outer periphery of the truncated inner circumstellar disk, at circa 1.52 AU (Walsh et al., 2011; Tait and Day, 2018). This could mean that Mars may have received the major proportion of its water content from C-type asteroids, planetesimals and comets (Alexander et al., 2017; Raymond and Izidoro, 2017; Morbidelli, 2018; Tait and Day, 2018). Petrological models by Wade et al. (2017) report that hydrous mineral species could have composed more than 9% volume of the early

Martian mantle, when compared to a 4% volume in the Earth's mantle. Therefore, we can assume that the early Martian mantle and crust could have been more hydrated than Earth's (Wade et al., 2017; Barnes et al., 2020; Dong et al., 2022). In general, the geological dates and hypotheses for the origin and aqueous history of Mars are continuously modified, as new evidence is collected via remote sensing, in-situ rover observations, new Martian meteorite analyses, and updated computational models.

Johansen et al. (2015) suggest that the growth of planetesimals results from gas drag-assisted accretion of chondrules, based on their numerical simulations. Conclusively, the primitive materials that formed planetesimals, planetary embryos, protoplanets and eventually, the terrestrial planets of the Solar System should be chondrules (Johansen and Lambrechts, 2017; Lammer et al., 2021). Furthermore, Lammer et al. (2020; 2021) modelled the accretion and evolution of Venus, Earth and Mars as time-dependent processes, and demonstrated that the speed of accretion generates two distinctive scenarios for the formation and evolution of the terrestrial planets: the "slow accretion", and the "fast accretion" scenarios (fig. 1.3). Both scenarios explain how accreting pebbles and planetesimals grow to planetary embryos and consequently, to terrestrial planets, and provide insights into the physical and chemical evolution of the Solar System's terrestrial planets. They (Lammer et al., 2021; fig. 1.3) proposed five main stages for the accretion and evolution of Venus, Earth and Mars, which are the following:

I) Dust settling and pebble accretion
II) Formation of planetesimals through pebbles' collisions
III) Formation of planetary embryos through planetesimals' collisions
IV) Accretion of protoplanets that later evolve to terrestrial planets via planetary collisions and giant impacts (e.g.: the Moon-forming giant impact event)
V) After the magma oceans of the terrestrial planets solidify, the planets outgas their primordial atmospheres. Then, secondary atmospheres' formation is initiated due to volcanic outgassing and tectonic activity.

In the "slow accretion" scenario (fig. 1.3), terrestrial planets' mass accretion follows the dissipation of the protoplanetary nebula (after $\approx 3.3 - 4.5$ Myr; Bollard et al., 2017). On the other hand, the "fast accretion" scenario shows that protoplanets accrete much faster and capture primordial atmospheres from the protoplanetary nebula (illustrated

as blue envelopes in fig. 1.3). In the "fast accretion" scenario the primordial atmospheres are gradually lost as the protoplanets grow their mass and their magma oceans solidify (Lammer et al., 2020; 2021).

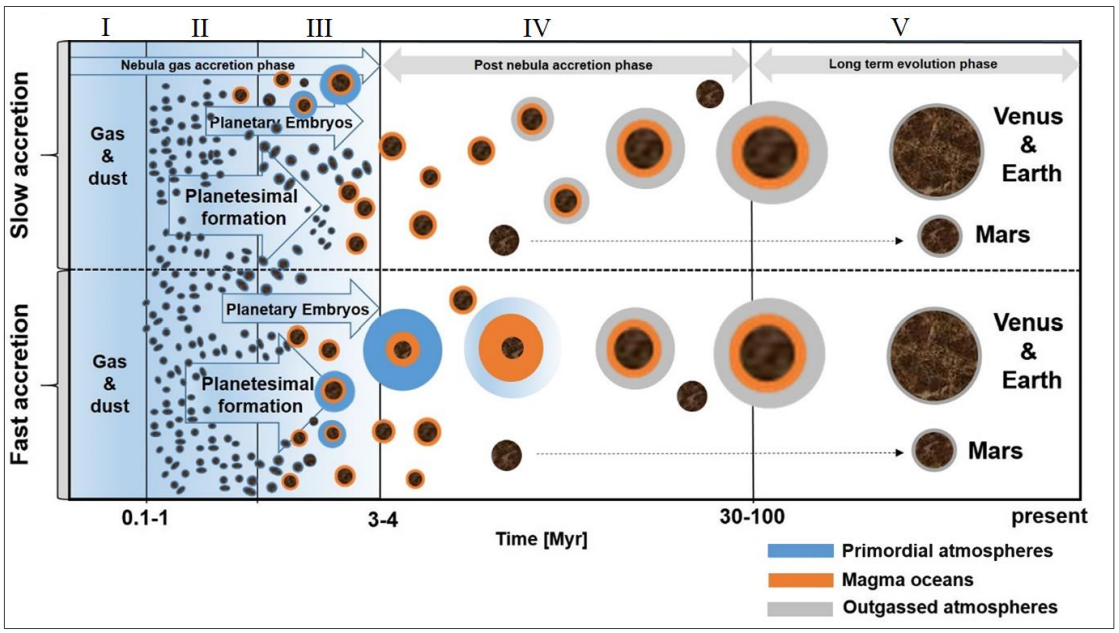

Fig. 1.3. Schematic representation of the five stages (I-V) of terrestrial planets' formation and evolution (Lammer et al., 2021), with the slow accretion scenario being shown above the horizontal dashed line, and the fast accretion scenario below the horizontal dashed line.

So far, geochronological dating investigations show that the age of the Earth is 4.543 ± 0.05 Gy (Dalrymple, 2004; and references therein). Rock samples returned from the Moon by the Apollo missions have been recently re-dated, with formation ages up to 4.48 ± 0.05 Gy, and with Lu-Hf model ages up to 4.51 ± 0.01 Gy (Nemchin et al., 2009; Barboni et al., 2017); these findings indicate that the Moon is indeed a product of a planetary collision between the Earth and a Mars-sized protoplanet (referred as ″Theia″). Moreover, zircon grains within Martian meteorite NWA (Northwest Africa) 7034 have recently been dated via U-Pb techniques to 4.42 ± 0.07 Ga (Bouvier et al., 2018; Cassatta et al., 2018). In addition, the primitive host-rock environment of NWA 7034 experienced impact-related metamorphism 100-150 My after Mars' formation, providing new thermodynamic constraints for the nature, extent and duration of the surficial metamorphism and aqueous alteration on early Mars (Agee et al., 2013; Wade et al., 2017; Barnes et al., 2020; Dong et al., 2022).

1.2.3 Terrestrial Planets' Evolution via Impact Cratering

1.2.3.1 Impact Cratering in the Solar System

Impact cratering is a ubiquitous physical process in the Solar System and has had serious implications for the origin and evolution of primitive life on Earth or even on other planetary bodies (Shoemaker, 1977, pp. 1-10; Mojzsis et al., 2001; Abramov and Mojzsis, 2009; Zahnle et al., 2020; Kenkmann, 2021). Impact craters comprise the predominant geomorphological feature on most terrestrial planetary bodies of the Solar System, except for Earth and Venus, where active tectonics and resurfacing processes have eroded and overprinted a significant amount of impact structures, respectively (French, 1998). For Earth, hypervelocity impacts have been considered agents of mass extinctions and global climatic changes throughout the planet's geological history from the Hadean until present, but simultaneously, life on Hadean Earth may have emerged from impact-induced hydrothermal environments (Mojzsis et al., 1996; Cockell, 2006).

Impact craters are categorized into simple or complex according to their geomorphological features that depend on the scale of their formation process (small-scale impact events versus large-scale impact events, respectively: fig. 1.4; French, 1998; Osinski et al., 2011). For example, the presence of a central uplift in an impact crater is unique to impact structures that are commonly larger than 15 km in diameter (Melosh, 1989; Osinski et al., 2011). Impact craters provide insights into planetary evolution processes, as they reveal the subsurface materials of planetary bodies due to impact-generated excavation (Melosh, 1989; French, 1998). In addition, large scale impact cratering processes on planetary bodies with abundant water-ice or other volatile-aqueous deposits at or close to the impact site, can generate hydrothermal systems which can durate for thousands to even millions of years (Rathbun and Squyres, 2002; Abramov and Kring, 2004; 2005; 2007). Such impact-generated hydrological systems are of great astrobiological significance for planets such as Mars, and for the Jovian and Kronian icy moons. Therefore, improving our understanding on impact cratering as a geological process and researching further its physicochemical effects on planetary crusts and even interior structures (e.g.: planetary mantles and cores, during large scale impact events) will assist considerably future space missions that will return samples from the Moon, Mars and asteroids within this and upcoming decades.

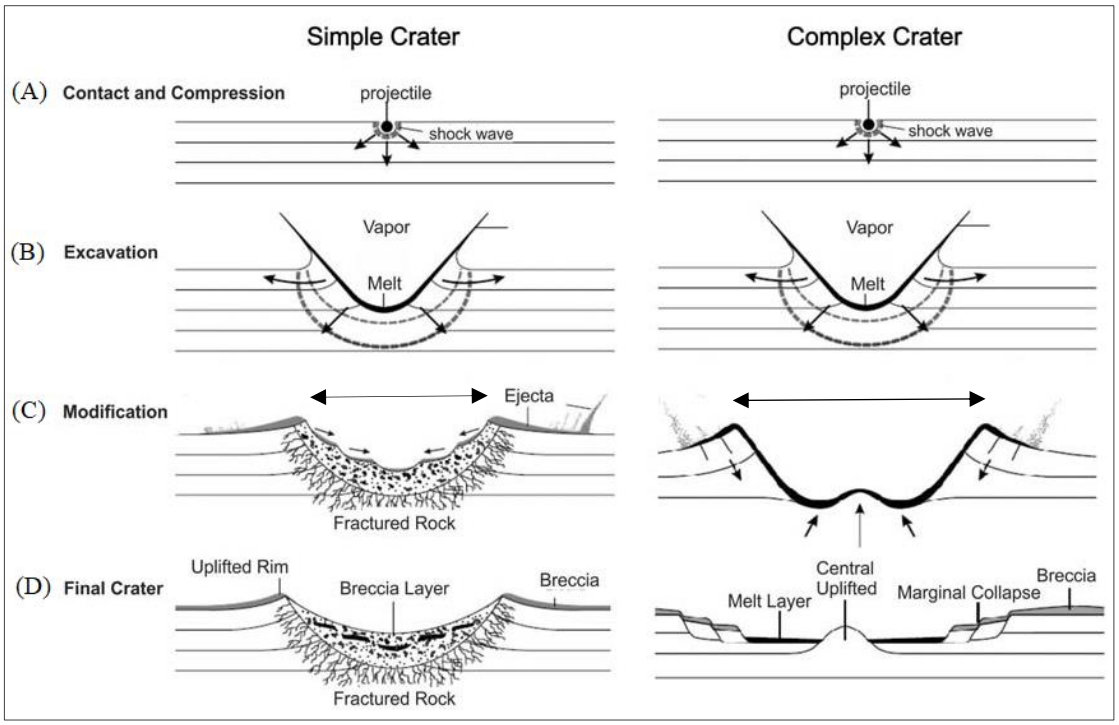

Fig. 1.4. Schematic model of the impact cratering process resulting to the formation of a simple and a complex crater along with the different stages of impact crater formation (A-D; modified after French, 1998, pp. 21 – 26; and simplified by W.S. Kiefer, © LPI). Two types of craters can form after an impact event: simple and complex. Simple craters are bowl-shaped depressions and are the typical structure forming during smaller-scale impact events, and when rim diameters are less than 10 km (black arrows shown in stage C for the two craters). Craters with rim diameters larger than 10-15 km are more complex structures and exhibit more flat floors, central uplifts, listric and extensional faults, and terraces on the inner slope of the crater rim (Osinski et al., 2011).

1.2.3.2 The Evolution of Mars via Impact Cratering

After its formation and for a period of almost 800 My, Mars may have been a habitable planet as it hosted abundant water and fluids on its surface, and a much thicker atmosphere (Ehlmann et al., 2011). Nowadays, Mars orbits slightly outside of the outer edge of the habitable zone, since it is much colder and drier than it used to be from 4.5 to 3.7 Ga. Additionally, the habitable zone may have gradually decreased in extent due to Solar flux fluctuations through geological time, based on hypotheses about the Sun's evolution (Claire et al., 2012; Tu et al., 2015). Mars lost its atmosphere and became colder at the surface, but the mechanism via which this planet-scale environmental change occurred remains controversial.

Mars was severely hammered by asteroids, comets and possibly by remaining planetesimals during the Noachian period and such evidence concurs to the hypothesis of the Late Heavy Bombardment (Abramov and Mojzsis, 2016; Bottke and Norman 2017). Nevertheless, impact events during the Noachian should have heated the Martian crust and generated widespread hydrothermalism, with long-lived hydrous and hydrothermal flows present in larger impact structures. The abundant geomorphological features associated with fluvial activity on the Red Planet (Carr, 1999) together with evidence of ancient water-rock interactions on the Martian surface (Ehlmann et al., 2009; 2011) indicate that Mars was a hydrologically active environment from 4.6 Ga to 3.7 Ga (Carr, 2012; Abramov and Mojzsis, 2016). Thus, the heating of the Martian surface and subsurface due to impact cratering, and to a lesser extent due to volcanism (Kring, 2000), combined with active hydrological cycles during the first 800 Myr, suggest a habitable early Mars (Abramov and Kring, 2005; Abramov and Mojzsis, 2016).

The abrupt decrease of Martian habitability that followed, however, may be also linked to a giant impact event which probably occurred by the beginning of the Hesperian geological period on Mars (Marinova et al., 2008; Andrews-Hanna et al., 2008). Recent studies suggest that a Ceres-mass protoplanet could have impacted on Mars' northern hemisphere and that the evidence for this huge impact event is revealed by the Martian hemispheric dichotomy (Wilhelms and Squyres, 1984; Andrews-Hanna et al., 2008; Marinova et al., 2008; Brasser and Mojzsis, 2017); videlicet, the dramatic difference in elevation, crustal thickness and cratering density between the southern highlands and northern lowlands of Mars (fig. 1.5; Andrews-Hanna et al., 2008).

Nevertheless, the origin of the dichotomy may be associated with a hemispheric-scale mantle upwelling that resulted to the thermal thinning or volcanic thickening of the Martian crust at the northern hemisphere (Zhong and Zuber, 2001; Roberts and Zhong, 2006; Keller and Tackley, 2009). In parallel, Elkins-Tanton et al. (2005) suggest that the solidification process of a global magma ocean on Mars could have preceded, and even triggered, a synchronous overturn of a buoyantly unstable cumulate mantle, leading to the Martian crustal dichotomy (a hypothesis that has been later supported also by: Keller and Tackley, 2009; Irwin and Watters, 2010).

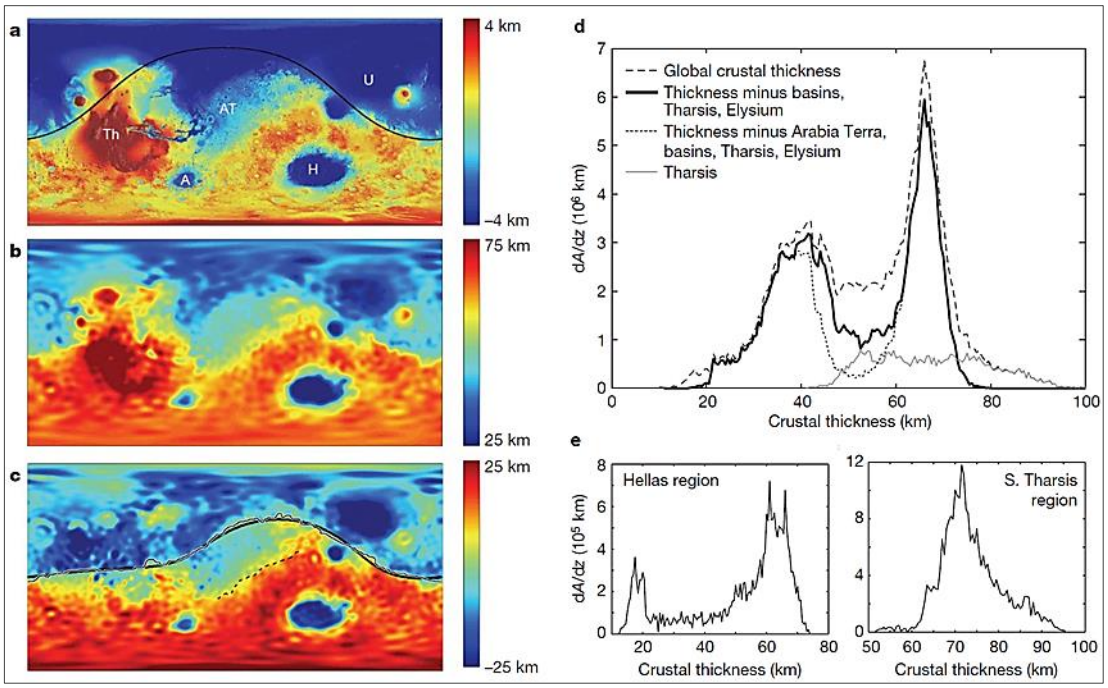

Fig. 1.5. Topography (a), crustal thickness (b) and isostatic root (c) of Mars; modified after Andrews-Hanna et al. (2008). Borealis basin outline (a-c; solid black line) was incorporated after Wilhelms and Squyres (1984). Features: Tharsis (Th), Arabia Terra (AT), Hellas (H), Argyre (A), and Utopia (U) basins; (d) and (e): radial profiles of Borealis, Hellas and S. Tharsis basins.

1.2.3.3 The Astrobiological Significance of Hydrothermal Activity

Hydrothermal systems could have comprised cradles for the emergence and evolution of primitive life forms on Earth, and potentially, even on Mars (Abramov and Kring, 2004; 2005; 2007; Osinski et al., 2013). The provision of abundant thermal energy and liquid H_2O in hydrothermal environments boosts water-rock interactions for extended periods of time (ranging from a few Hyr to Myr). Thus, hydrothermal activity can support the habitability of host lithologies through the release of mineral substrates and chemical nutrients after water-rock reactions, for potential lithotrophic microorganisms to harvest (Kring, 2000; Hoehler, 2004; Cockell, 2006).

The most primitive thermophilic (metabolic growth at $T \geq 50$ °C) or hyper-thermophilic (metabolic growth at $T \geq 80$ °C) microorganisms observed on Earth may have originated from hydrothermal environments, and especially from impact-generated

ones, as these were more ubiquitous than volcanogenic hydrothermal systems during Earth's earliest geological periods (Mojzsis et al., 1996; Kring et al., 2000; Cockell and Lee, 2002; Cockell, 2006). Research on evidencing microbial activity in post-impact hydrothermal systems on Earth has been, nevertheless, limited and constrained to impact structures that have been preserved, e.g.: the Chicxulub crater (Cockell et al., 2019; Kring et al., 2021). The most reliable biological findings originate from the Chicxulub crater's site M0077 samples (retrieved drilled core after the joined IODP-ICPD 364 expedition; Morgan et al., 2017; Gulick et al., 2017), where Cockell et al. (2019) identified different species of microbial life within the site M0077 impactites (impactites = impact-generated rocks; Stöffler and Grieve, 2007) via DNA extraction techniques. Cockell et al (2019) support that these microbial communities may have colonized the Chicxulub target lithologies during the period of impact-induced hydrothermal activity. Additionally, Kring et al. (2021) indicated that evidence for sulfate reduction in the impact-induced hydrothermal mineral assemblages of the M0077 site is most probably of biotic origin; and that sulfate reduction due to biologic fractionation (rather than inorganic fractionation) should have been synchronous with the period of post-impact hydrothermal circulation.

Other researchers have reported biomorphs hosted in post-impact hydrothermally precipitated mineral assemblages (e.g.: Ries impact structure: Glamoclija, 2007; Dellen impact structure: Lindgren et al., 2010; Haughton impact structure: Parnell et al., 2010; for more details please see Osinski et al. (2013)). Nevertheless, all the aforementioned impact craters on Earth formed during geological periods where life had already been thriving in the pre-impact environments. Hence, prudence and a more conservative perspective are required when assessing the potential of impact-induced hydrothermal systems to boost microbial activity (Osinski et al., 2013; Kring et al., 2021).

Through this prism, the potential of microbial activity in hydrous and hydrothermal systems ((cryo-)volcanogenic and impact-generated) of other planetary bodies such as Mars or the icy moons of Jupiter and Saturn, should be far more limited due to the extremely low temperatures and low energy availability that describe such planetary environments (Hoehler, 2004; Schwenzer et al., 2012; Hoehler and Jørgensen, 2013; Hoehler et al., 2018; Tauber et al., 2018; Hoehler, 2022). Ice melting and the production of hydrous/hydrothermal flows induced by impact events on the cryosphere of Mars, or

on the icy crusts of the Jovian and Kronian moons are of great astrobiological significance (Barnhart et al., 2010; Ivanov and Pierazzo, 2011; Schwenzer et al., 2012). However, the duration of such hydrological/hydrothermal systems, which comprises an important factor for providing stable thermodynamic conditions for the potential synthesis and evolution of biotic molecules (Hoehler and Jørgensen, 2013; Hoehler, 2022) and their subsequent habitability, remain understudied.

This PhD research explores the duration and thermodynamics of putative hydrothermal (impact-induced and volcanogenic) systems on Mars through numerical simulations and focuses on quantifying the habitability of such aqueous environments. Eventually, the results and implications of this PhD research should broaden and enhance the applicability of such computational methods in quantifying and determining the astrobiological potential of aqueous and hydrothermal systems in our planetary neighborhood and other exoplanetary systems.

1.3 The Circumstellar Habitable Zone of the Solar System

In our planetary backyard, the terrestrial planets share a common accretional history regarding the formation and differentiation of their core, mantle, and crust. Moreover, the evolution of their atmospheres is related mostly to the astronomical distance of the inner-planets from the Sun and to the outgassing processes that followed their cooling-down and the solidification of their newly formed crust. The atmospheric dynamics of each terrestrial planet has been a significant factor in allowing the presence of water and liquids on their surface, and the formation of the first prebiotic molecules and subsequent evolution of life.

Apart from Mercury due to its proximity to the Sun, Earth, Venus and Mars may have all experienced outgassing processes during their early geological time that resulted in the formation of their hot and dense primitive atmospheres (Lammer et al., 2021). The planets cooled down gradually, and as the atmospheric and surface temperatures

decreased, the first masses of water accumulated onto their surfaces by precipitation (Lammer et al., 2018; Odert et al., 2018). However, due to distinctive planetary differentiation processes, the geological activity of these three terrestrial planets diverged and is nowadays unique for each planetary body. Volcanic eruptions, active tectonics, and the deep-planetary dynamics (core-mantle thermodynamics and mechanics) responsible for the generation of the magnetosphere that protects the surface from Solar radiation, resulted in Earth being the most geologically active planet since its formation, in comparison with Venus and Mars. Asteroidal and cometary fluxes delivered essential amounts of water, gas and organic chemistry on the planetary surfaces, and so the delivered volatile substances could only be preserved under discrete atmospheric conditions (Kasting and Harman, 2013). Due to its astronomical distance from the Sun, the Earth could support the highest amount of water on its surface and formed oceans. In combination with the active-plate tectonics, the global ocean which covers about 70% of the Earth's surface is the most significant thermodynamic catalyst, as it absorbs and preserves most of the heat via the circulation of currents (Rahmstorf, 2002). The subduction of the tectonic plates into the mantle heats up the crustal rocks that contain water and volatiles. Water and gases are then released within the asthenosphere and return to the Earth's oceanic and continental crust, hydrosphere and atmosphere via volcanic intrusions, eruptions, and hydrothermal venting. This continuous 4.5 Gy process known as the geodynamic cycle is critical to the sustainability of a favorable thermodynamic equilibrium for the evolution and preservation of life on Earth (Bach, 2016; Hoehler et al., 2022; and references therein).

The quantification of those physical factors that govern the habitability in our stellar system is encapsulated via the Circum-Solar Habitable Zone (CHZ). The CHZ is the range of astronomical orbits around a star in which a planetary surface can sustain liquid water under favorable atmospheric pressure (Kasting et al., 1993; Kaltenegger and Sasselov, 2011; Kopparapu et al., 2013, Abe et al., 2013). Our Solar System has been much more thoroughly explored (e.g. Venus and Mars were mentioned previously) in comparison with other distant exoplanetary systems from which in-depth knowledge for their planetary surfaces and atmospheres is so far too difficult to obtain. Thus, for our Solar System, we have much more robustly determined several other physical parameters and phenomena that furtherly dictate the habitability of our planetary province.

The additional significant variables on which our Solar System's habitability is also highly dependent, are illustrated in fig. 1.6 and regard:

I. The ″Moist Greenhouse″ limit within which water is lost by photodissociation and hydrogen escape, as a planet's stratosphere becomes wetter (Kasting et al., 1993; Kopparapu et al., 2013; Leconte et al. 2013).

II. The ″Runaway Greenhouse″ limit where all surface water evaporates (Kasting et al., 1993; Kasting and Harmann, 2013; Yang et al., 2013; 2019).

III. The ″Recent Venus″ curve, estimating that Venus may have lost its water about 1 Ga, when the Sun was by 8% less bright than today (Kasting et al., 1993; Kopparapu et al., 2013; Goldblatt et al., 2015).

IV. The ″Maximum Greenhouse″ limit, a model that predicts the sustainability of a much colder CO_2–H_2O planetary atmosphere (Kasting et al., 1993; Kasting and Harman, 2013).

V. The ″Early Mars″ curve, based on the theory that Mars may have been habitable 3.8 Ga, when the Sun was by 25% less bright than today (Kasting et al., 1993; Kopparapu et al., 2013).

This new and revised model for the habitability within stellar systems, that was introduced by Kasting and Harman (2013; fig. 1.6), has acutely incorporated all generic functions and principles for exoplanetary habitability and on top of that, all five limitations for our Circum-Solar Habitable Zone. Finally, Kasting and Harman (2013) presume that all stellar objects emit much of their radiation at long wavelengths. Hence, this results to the planets' albedos being lower and explains why the CHZ curves move towards lower stellar flux at lower stellar surface temperatures in fig. 1.6.

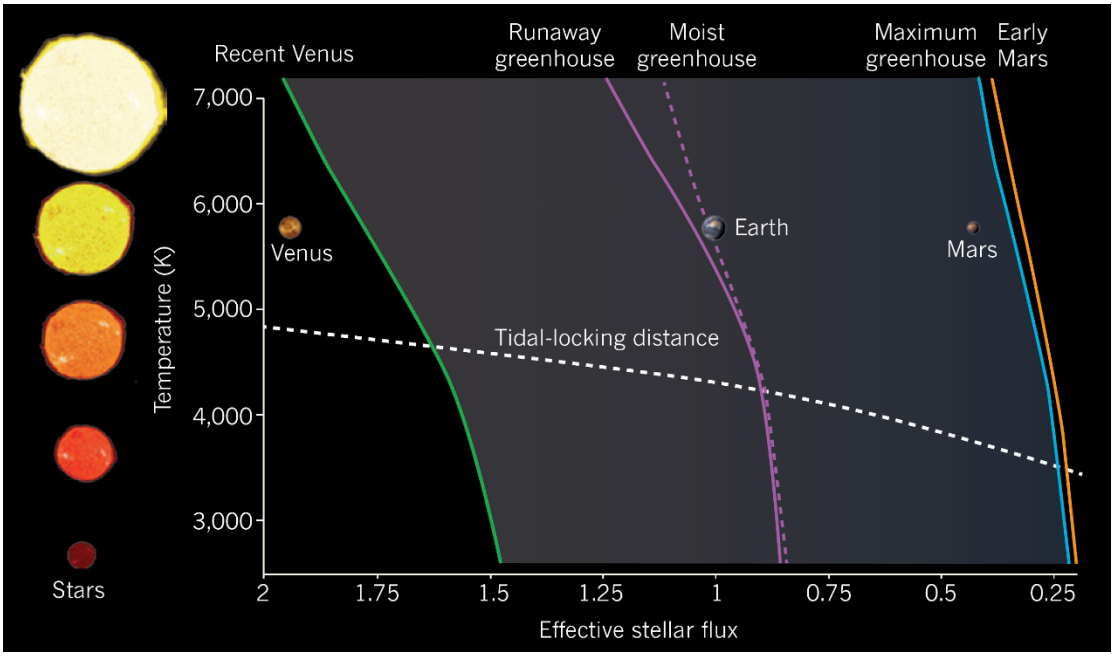

Fig. 1.6. Schematic model depicting the habitable zone borders of our Solar System (Venus, Earth and Mars) and how these borders are affected per star type (modified after Kasting and Harman, 2013). 3D climate models for planetary habitability from Leconte et al. (2013) and Yang et al. (2013) were also implemented to calculate the critical curves (Recent Venus, runaway greenhouse, moist greenhouse, maximum greenhouse, early Mars) of our Solar System's habitable zone. The white dashed curve (defined by Edson et al., 2011) corresponds to the orbital distance in which an Earth-like planet with an initial rotational period of 13.5 hours would become tidally locked (synchronous rotation) within 4.5 Gyr (e.g.: Earth and Moon dynamical system). The horizontal axis represents the effective stellar flux at a planet's orbit, using as a reference the Solar flux at Earth's orbit.

1.4 The Habitability of Mars: An Introduction

At a 1.5 AU distance lies a quite enigmatic planet of our Solar System; Mars. The Red Planet is much smaller than Earth ($M_{♂} = 0.107\ M_{⊕}$; where ♂: Mars, ⊕: Earth), cooled off more quickly than Earth and Venus due its small size and distance from the Sun, and exhibits weak tectonic activity that is quite different from Earth-like geodynamics. Due to the loss of Mars' geomagnetic field during the Hesperian (perhaps, due to a giant impact event (Marinova et al., 2008; Andrews-Hanna et al., 2008), or due to the thickening of the Martian crust by heat loss (Ruiz, 2014), or both), the planet's volcanic activity started to fade, and around the early-mid Amazonian it

almost ceased. The geological timescale of Mars is summarized via fig. 1.7 (Catling, 2014, p. 357). Hence, since the late Hesperian - early Amazonian, the planet could not replenish its atmosphere and consequently lost it to space, with a total atmospheric volume today less than 1% of Earth's (Franz et al., 2017). Thus, an essentially weaker greenhouse effect is taking place on Mars from the early Amazonian up to present due to the insufficient abundance of greenhouse gases. The models for the climatic evolution of Mars (Kasting and Harman, 2013; Lammer et al., 2018; 2020; 2021) have further helped in determining the amount of greenhouse gases required for a cold terrestrial planet to sustain water on its surface. Therefore, Mars serves as an ideal case study for exoplanetary exploration in assessing the habitability of "colder" planetary bodies that orbit at the outer edge of the CHZ.

We know that Mars once had a much thicker CO_2 atmosphere that permitted an appreciable greenhouse effect (Catling, 2014, pp. 343 - 357; Ehlmann et al., 2016). Simultaneously, the reflectivity of the thick CO_2 atmosphere increases as it experiences the Rayleigh scattering effect. This means that beyond a certain concentration of CO_2 and other greenhouse gases within a planetary atmosphere, the Rayleigh scattering increase dominates over the increase and enhancement of the greenhouse effect, initiating global cooling (Meadows et al., 2020). This threshold represents the maximum concentration of greenhouse gases that can be sustained within a planetary atmosphere, so that the planetary body can avoid global cooling and ensure its habitability. In relation to the margins of the habitable zone around G-type main sequence stars, this limitation is defined as the ″ Maximum Greenhouse ″ limit (Kasting and Harman, 2013). Early Mars should have been very close to this limit from 4.5 Ga to 3.7 Ga and can be therefore, optimistically characterized as habitable during its most ancient geological times.

Volcanism is mainly absent on present-day Mars, as indicated by explorations of the largest Martian volcanic provinces (Tharsis Rise and Elysium Planitia) via the Mars Global Surveyor Thermal Emission Spectrometer (TES; Christensen et al., 2001), Mars Odyssey Thermal Imaging system (THEMIS; Christensen et al., 2004), Compact Reconnaissance Imaging Spectrometer for Mars (CRISM; Murchie et al., 2007) and MSL/Curiosity (Wiens et al., 2012; Achilles et al., 2017). Although InSight did find a warm source region which implies magmatic activity at depths of 30–50 km in Cerberus

Fossae (Stähler et al., 2022), the presence of appreciably active volcanogenic or impact-induced hydrous/hydrothermal systems in the shallow subsurface of Mars is highly unlikely, as the effects of such geothermal activity should have been detected by orbital and rover exploration missions.

Some local-scale volcanic events and heterogeneities in the composition of the lavas persisted through the Amazonian period, but it is evident that the planet is far less volcanically active after the Hesperian period (Tanaka et al., 2005; Rampey and Harvey, 2012; Daly et al., 2019a;b; Whelley et al., 2021; Griffin et al., 2022). Despite that, the planet still boasts the largest volcano in the entire Solar System, the 25 km in altitude Olympus Mons, formed during the Hesperian to early Amazonian period (Williams et al., 2007; 2008) by continuous vertical building of the crust from plumes rising from below; such vertical formation processes of geological units on Mars are mainly due to the lack of plate movement (Cohen et al., 2017).

Moreover, Mars has been the arid and cold desert that we observe today for most of the Amazonian period (Catling, 2014, pp. 343 – 357; Ehlmann et al., 2016). The latest appreciable aqueous flows may have occurred during the late Hesperian – early Amazonian, as evidenced by high-resolution infrared spectroscopy analyses of large-scale chloride deposits and their accessory minerals (carbonate, phyllosilicate and sulfate; Ye and Glotch, 2019; Ye et al., 2019; Leask and Ehlmann, 2021; 2022).

This combination of volcanic and hydrothermal quiescence, together with the presence of a very thin atmosphere and the absence of hydrological activity on Mars from the early Amazonian until present, implies that the astrobiological potential of the Red Planet during the Amazonian period is low. Nevertheless, this qualitative approach on Martian habitability cannot establish alone the hypothesis of an uninhabitable Mars, as on top of that, it ignores the probability for Martian microbial activity during the Hesperian and more importantly, during the Noachian period. Therefore, quantifying the habitability of the Red Planet during its entire geological history (fig. 1.7) and coupling it with rover and remote sensing observations, should lead to determining rigidly the ancient or/and recent astrobiological potential of Mars.

1.5 The Geological History of Mars

1.5.1 Martian Accretion & Differentiation

The so-called ″ Mars problem ″ refers to the small mass of Mars and the inability of recent astrophysical simulations and observations to accurately reproduce it and explain it, respectively. In other observed exoplanetary systems, planets that orbit close to the snow line, are on average by a few factors more massive than Mars (Brasser, 2013). This problem was solved after Hansen (2009) suggested the formation of the terrestrial planets from a narrow annulus of material between 0.7 and 1 AU, and successfully reproduced the masses of Mars and Mercury through numerical modelling (fig. 1.7). Walsh et al. (2011) and Brasser (2013) confirmed this hypothesis, solving the problem of Mars' mass. In particular, according to Hansen (2009), Mars finished growing within 10 My, and recent Th/Tu and Th/Hf ratio analyses of Martian meteorites (SNC: shergottite–nakhlite–chassignites) and ordinary chondrites (CHUR: chondritic uniform reservoir) additionally support that Mars probably accreted half of its mass within less than 2 My (Dauphas and Pourmand, 2011). The accretional process of Mars was completed much more rapidly than the accretion of Earth ($T_{\oplus accretional} > 50$ My; Kleine et al., 2009). The explanation for that was also provided through N-body simulations (Hansen, 2009; Walsh et al., 2011; Brasser et al., 2013) proving that Mars was a protoplanet that formed within the outer edge annulus of the inner-protoplanetary disk that experienced severe truncation due to the migration of Jupiter, and as a result, proto-Mars had insufficient material to grow more than 0.107 $M_{\oplus}$ at 1.5 AU. (at circa 1.5 AU) due to Jupiter's migration.

In addition to astrodynamic simulations, geochemical models for the accretion and differentiation of Mars that were generated after high-precision analyses of SNC meteorites and ordinary chondrites also confirm that water-rich material from the outer Solar System merged with the water-poor material from the inner Solar System during its early evolutionary stages (Dauphas and Pourmand, 2011; Dauphas, 2017; Tait and Day, 2018; Jin and Bose, 2019). Further coupling of astrophysical and geochemical theories implies that Mars should have hosted a magma ocean during accretionary

impacts with other planetesimals and protoplanets. The metal-silicate differentiation of the proto-Martian core and mantle most probably occurred simultaneously with its magma ocean formation, as more protoplanetary material was assimilated through impact fluxes. After the accretion of Mars is completed and the impact fluxes decrease by a factor of 30 from 4.4 Ga to 4.1 Ga (based on the Bottke and Norman (2017) model for impact fluxes during the late heavy bombardment), magma ocean crystallization takes place. The crystallization of the magma ocean is the thermodynamic process that determines the physicochemical conditions of the newly formed crust. Presuming that Mars finished accreting closer to the snow line (richer in H_2O-ice annulus) of the protoplanetary disk, then the Red Planet should have been much more H_2O-enriched than the other terrestrial planets, and should have contained appreciable amounts of water, even up to 0.2 % by mass (Morbidelli et al., 2000; Brasser, 2013).

The geological periods of Mars are determined after their relationship to geodynamic processes (e.g.: impact processes, volcanic events, flooding etc.) that formed major geological features on the planet's crust (since 4.5 Ga), predominant mineral phases, and events that have affected the Martian atmosphere (Catling, 2014, pp. 343 - 357). Other researchers have defined the geological periods of Mars by using mainly the distinctive impact-cratering rate for each period (Soderblom et al., 1974; Scott and Tanaka, 1986; Hartmann and Neukum, 2001; Ivanov, 2001; Carr and Head, 2010). In this research, the Catling (2014, p. 357) model is preferred, as it incorporates a spectrum of several geological phenomena that have affected the Martian crust from its accretion until present. These geological periods and their associated geological processes are illustrated through fig. 1.7 and are the following:

(1) Pre-Noachian period, from the planetary accretion at 4.5 Ga to 4.1 Ga.
(2) Noachian period, from the formation of the Hellas Basin at circa 4.1 to 3.7 Ga.
(3) Hesperian period, from 3.7 to 3.0 Ga, related to the formation of Olympus Mons.
(4) Amazonian period, from 3.0 Ga to present, named after the Amazonis Planitia plain.

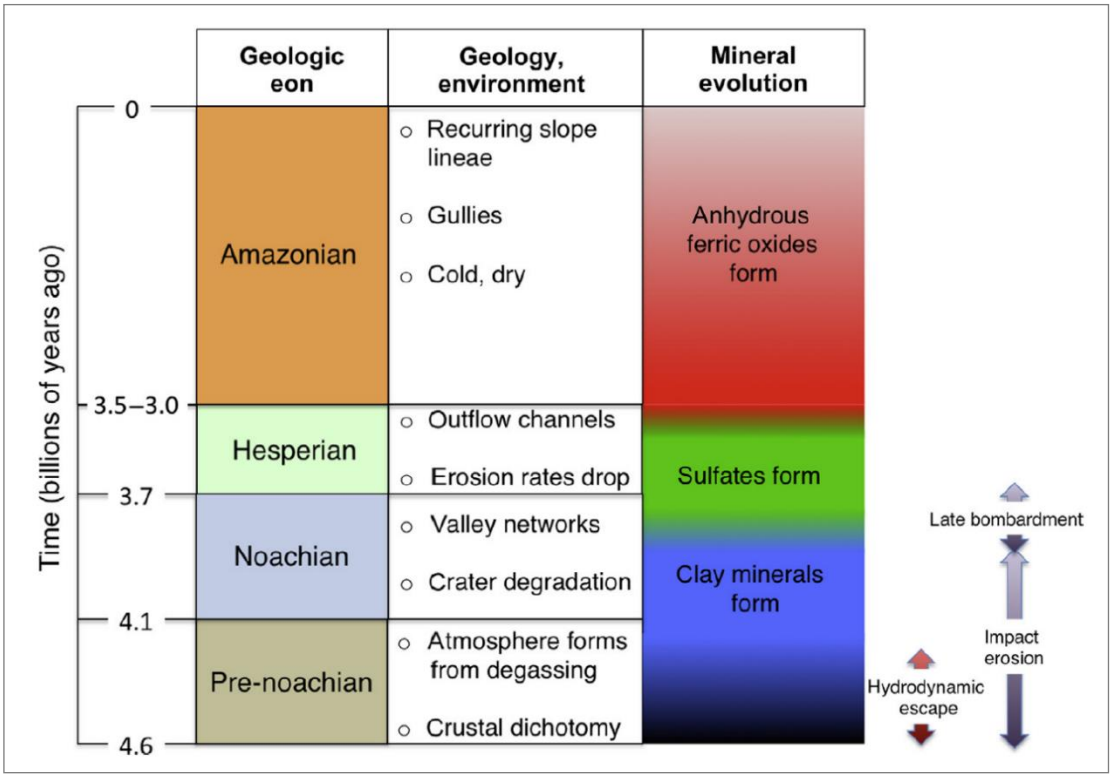

Fig. 1.7. The Martian geologic timescale related to geological processes, inferred mineralogies and atmospheric conditions per each geological period (Catling, 2014, p. 357).

1.5.2 The Pre - Noachian Period

The pre-Noachian is the geological period in which major impacts of asteroids, comets and planetesimals should have taken place. The impact cratering events of the pre-Noachian (at 4.6 - 4.47 Ga) should have entirely re-crystallized and modified the crust and deep interior of Mars (Marinova et al., 2008; Andrews-Hanna et al., 2008; Abramov and Mojzsis, 2016; Bottke and Andrews-Hanna, 2017). The formation of Hellas, Isidis and Argyre basins (at circa 3.9 - 4.1 Ga,) represents the boundary between the pre-Noachian and Noachian period (Carr and Head, 2010; Robbins et al., 2013), as the distribution and preservation of impact basins from 4.47 Ga to 4.10 Ga indicates a decrease in impact flux during that period (Werner, 2008; Bottke and Andrews-Hanna, 2017), when compared to the Late Heave Bombardment (4.1 – 3.9 Ga; Ryder, 2002; Bottke et al., 2010). This hypothesis is, nevertheless, substantiated only via astrodynamic simulations and crater-count chronology for the distribution of planetary impact events during the pre-Noachian period, and within the annular regions of the

terrestrial planets and the asteroid belt. But so far, there is no further meteoritical/geochemical evidence confirming that the impact flux was lower during the pre-Noachian period.

Climatologically, Mars should have been a much wetter and warmer world during the pre-Noachian due to volcanogenic and impact-induced outgassing processes that should have jointly contributed to generating the planet's greenhouse gases and atmosphere. Moreover, late veneer impacts of chondritic and cometary material delivered significant amounts of water to the planet, and together with the precipitation from the newly formed atmosphere, fluvial valley networks, lakes, and even sedimentation were initiated early in the pre-Noachian (Catling, 2014, pp. 343 – 357). Unfortunately, the pre-Noachian evidence of sedimentary processes would later be destroyed by the increased impact flux rate that characterizes the early Noachian period (Bottke and Andrews-Hanna, 2017; Werner et al., 2019), or/and by the widespread volcanism and catastrophic flooding of the Hesperian (Werner, 2009).

1.5.3 The Noachian Period

The Noachian Period is characterized by high rates of impacts, craters' degradation, erosion, valley networks, volcanic activity, and weathering of surface rocks, resulting in ubiquitous abundances of phyllosilicates (clay-mineral) on a global scale (Carr and Head, 2010; Catling, 2014, pp. 343 – 357; Ehlmann et al., 2016). Furthermore, the strong presence of olivine in Noachian-aged rocks, which is a mineral that weathers to phyllosilicates when exposed to water, implies that the Noachian period was characterized by a humid climate with a few episodic warm intervals (T_{μ} ranging from +3 °C to -15 °C; Ramirez et al., 2014; Wordsworth et al., 2017; Kling et al., 2020). Spectrally and stratigraphically explored outcrops (via the OMEGA instrument on the Mars Express orbiter) of early-Noachian rock units in regions such as the Nili Fossae and Mawrth Vallis, that were affected by impacts and erosion, also exhibit high abundances of the clay minerals smectite, kaolinite and illite; after Ehlmann et al., 2011; Bristow et al., 2018; Tu et al., 2021 and confirm that during the early-Noachian, aqueous activity and weathering substantially affected the surface of Mars (Bibring et

al., 2006; Carr and Head, 2010; Catling, 2014, pp. 343 – 357; Ehlmann et al., 2016; Brown et al., 2020).

Increased in frequency impact events during the Noachian hammered the Martian crust, produced a megaregolith zone of fractured basalts and breccias, and deposited ejecta of an average 300m thickness at a global scale (Ivanov, 2001; Segura et al., 2002). Huge impact events of the Noachian may have also been responsible for the excavation and ejection of significant masses of magnetized crustal segments (and even of mantle material, as excavation depth may have reached values of circa 50 km), and for a subsequent 60% decrease in magnetic field strength within 400 My, leading to the demagnetization of Mars by the collapse of its core convection and dynamo after 3.7 Ga (Langlais and Thébault, 2011; Mittelholz et al., 2018). Physical parameters that must have played an important role in the Martian convection and its evolution during and after impact bombardment are also the planet's small size and the thermodynamic state of its interior, which is mainly associated with the solid state rather than the liquid (Mittelholz et al., 2018; 2020). This also means that the permeability and porosity of the Martian crust were significantly increased due to impact cratering processes, and thus, groundwater was able to penetrate to far greater depths.

In addition, surface water runoff patterns were affected by impact structures, resulting in sediment deposition commonly within crater floors. Such drainage processes are evident by deltas and fans that cross-cut crater rims and pond in the lower topographical terrains of the central regions of the crater (e.g.: in the central breccia-lens region or around the central uplift, if the crater is simple or complex, respectively). Thus, draining through valley networks has formed large lakes within craters, as over 200 Noachian lakes (some similar to the size of Lake Baikal or the Caspian Sea) have been identified in the southern highlands of the planet (Fassett and Head, 2008). Furthermore, most Noachian impact structures have allowed appreciable amounts of water to accumulate therein and reach a sufficiently high level, so that they would later erode the opposing crater rim (Melosh, 1989). Such spectacular crater examples are the Eberswalde, Holden, and Jezero Crater - the latter being the chosen landing site for NASA's Mars 2021 Perseverance rover mission (fig. 1.8).

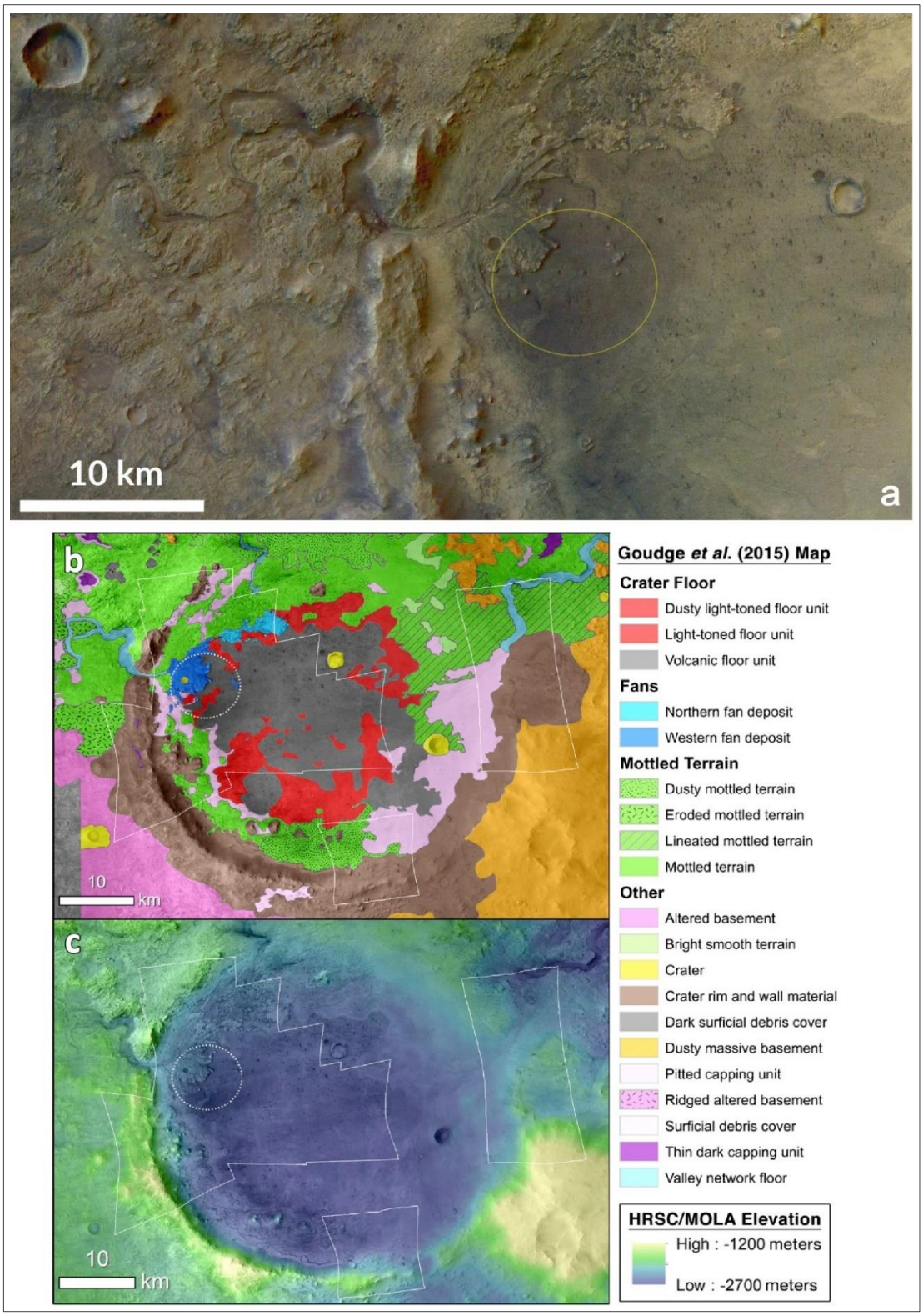

Fig. 1.8. Overview of the landing location (a: circled area; © NASA), geological map (b) and topography (c) of the Jezero Crater, that the Perseverance Rover is currently exploring (modified after Goudge et al., 2015). Jezero Crater exhibits deltaic - alluvial deposits that reveal the aqueous history of Mars. After the crater's formation (3.98 – 3.82 Ga; Werner, 2008; Mandon et al., 2020), river channels should have formed a lake in the crater. A plethora of sedimentary units of Noachian age and of volcanic lithologies (including an olivine cumulate outcrop) have already been identified (Liu et al., 2022).

Moreover, Steele et al. (2022) proved via investigations of the Allan Hills 84001 (ALH 84001) Martian meteorite which formed during the Noachian period (with an igneous crystallization age of 4.09 Ga, according to Mittlefehldt, 1994; Borg et al., 1999; Lapen et al., 2010) that the magnetite, Fe-, Mg-, and Ca-rich carbonate phases, amorphous silica, and talc-like phases observed within altered ALH 84001 orthopyroxene consist chemical products of serpentinization or/and mineral carbonation reactions that took place on Mars during the Noachian period. Similar alteration processes have been observed in rocks from Earth. The implications for the habitability of similar terrestrial environments, where serpentinization and mineral carbonation occur and chemolithotrophic microbial communities can thrive by harvesting the H_2 and CH_4 produced from the serpentinization reactions, have been thoroughly explored (Kelley et al., 2001; Cardace and Hoehler, 2009; McCollom and Seewald, 2013; Greenberger et al., 2015). So, the production of carbonates through CO_2 sequestration, as a result of the serpentinization of peridotitic and basaltic rocks, should have comprised a significant sink for the CO_2 in the early Martian atmosphere, and a contributing mechanism in the geochemical composition evolution of the Martian subsurface crust (Tomkinson et al., 2013; Blamey et al., 2015; Edwards and Ehlmann, 2015). Conclusively, aqueous alteration of mafic igneous rocks on Mars seems to have occurred consistently during the Noachian period and should have resulted to the release and accumulation of organics and carbonate species in its atmosphere, subsurface and on the planet's surface, as well as to the mineralogical diversity of its upper crust (Holm and Neubeck, 2009; Viviano et al., 2013; 2019).

The Noachian Period temporarily coincides with the Hadean and early Archean eons here on Earth, when the first lifeforms likely arose in hydrothermal environments (Mojzsis et al, 1996; Pace, 1997; Mojzsis et al., 2001). Recent evidence supports that the most primitive microbial communities in our Solar System could be genetically characterized as hyperthermophiles; and that mesophilic or thermophilic microbial life could have emerged under impact-induced hydrous or hydrothermal conditions on Mars (Cockell, 2006; Schwenzer et al., 2012; Osinski et al., 2013). Therefore, impact craters are considered as the cradles of the most ancient biomolecules (Abramov and Kring, 2004; Abramov and Kring, 2005; Abramov and Kring, 2007; Abramov and Mojzsis, 2009; 2016). Theoretically, craters that formed during the Noachian period on Mars, and that show evidence of drainage and sedimentary processes, are presumed as the

most promising environments for evidence of past life (Bibring, 2006; McMahon et al., 2018; Beaty et al., 2019 (International Mars Sample Return Objectives and Samples Team (iMOST); Brown et al., 2020; Lapôtre and Ielpi, 2020).

1.5.4 The Hesperian Period

Declining impact cratering and erosional rates, intense and frequent volcanism, catastrophic flooding, and a transition from the wet and warm world of the Noachian to a colder (T_{μ} = -25 °C) and relatively dryer world, are the geological signatures of the Hesperian period (3.7 to 3.0 Ga; Catling, 2014; Ramirez et al., 2014; Wordsworth et al., 2017, Kling et al., 2020). By the end of the Hesperian, the impact rate began to resemble the current impact flux and the maximum greenhouse effect was initiated, causing a global cooling. The earliest evidence of glacial activity on Mars is dated within the Hesperian, as the planet cooled dramatically during that time and a thick cryosphere covered the northern hemisphere. Liquid water reservoirs during the Hesperian should have become more localized and concerned mainly aquifers stored within the regolith, or some water masses that flowed to the topographically lower terrains of the northern hemisphere. Ice caps may have overlaid and assimilated transient flows of the Martian surface and could have been the main cause for the equatorial canyon system of Valles Marineris.

In fact, geodetic and morphological observations of glacial activity on the equatorial regions of Mars via the Mars Orbiter Laser Altimeter (MOLA) (De Blasio, 2011; Mège and Bourgeois, 2011; Gourronc et al., 2014) have revealed that the Valles Marineris landforms (2000 km in length) were entirely covered by a glaciated valley network from the late Noachian to Hesperian times (fig. 1.9). Presumably, Valley Marineris may contain huge volumes of water-ice deposits in the subsurface, as indicated by Mitrofanov et al. (2022), who detected unusually high hydrogen abundances in the central part of Valles Marineris by analyzing data from the FREND (Fine Resolution Epithermal Neutron Detector) telescope onboard the ExoMars Trace Gas Orbiter (fig. 1.10). Hence, these water-ice deposits of Valley Marineris, that are well-hidden from

remote sensing exploration satellites, may be originating from this ancient period of global glaciation that the Red Planet once hosted.

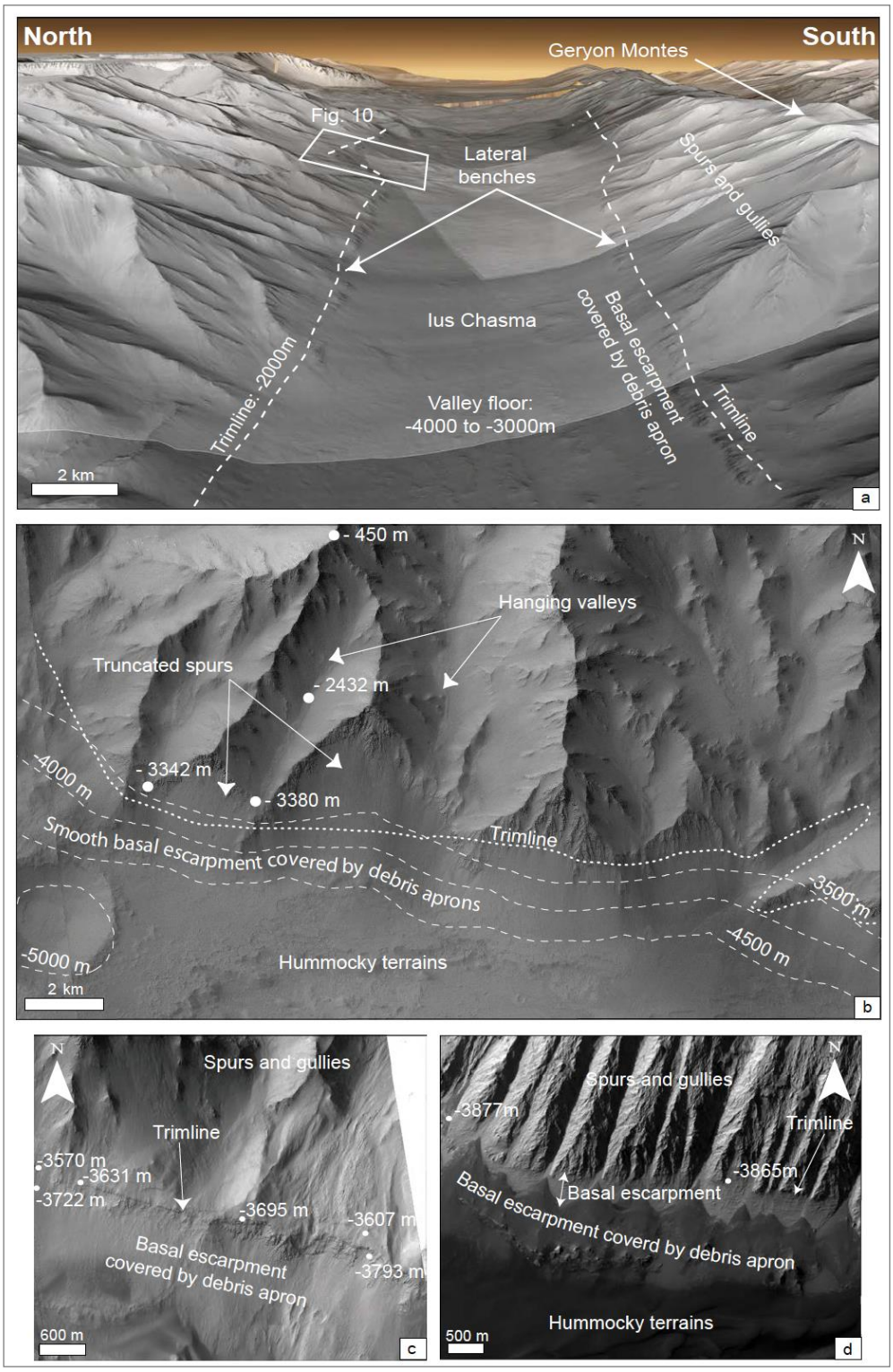

Fig. 1.9. Mars Orbiter Laser Altimeter (MOLA) observations along the Valles Marineris; (a): Ius Chasma, (b-d): Coprates Chasma, and (c): Candor Chasma, identifying glacial landforms and processes of the early Hesperian (modified after Gourronc et al. (2014), and references therein).

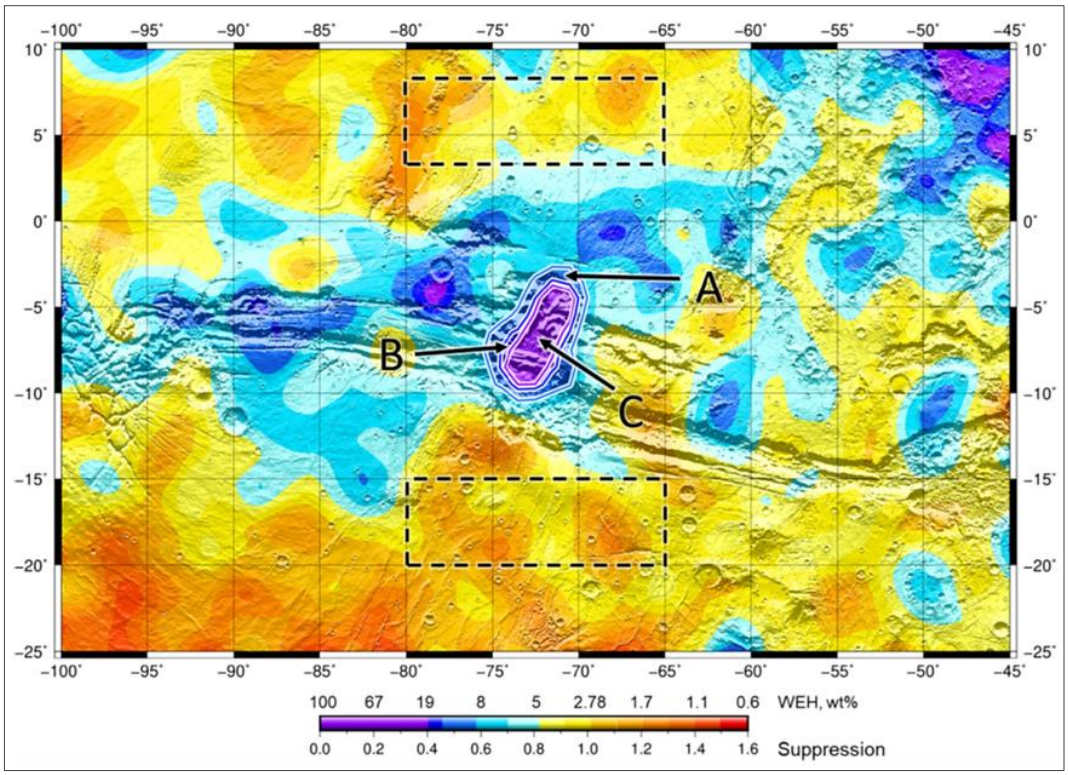

Fig. 1.10. Fine Resolution Epithermal Neutron Detector (FREND) measurements for the epithermal neutron suppression (NS) around Valles Marineris along with the derived water content (WEH: Water Equivalent Hydrogen scale; legend values above the colour scale) in this region. The boundary of the Local Area of Neutron Suppression (LANS) is shown as 7◦ - smoothed NS = 0.58 isoline. NS isolines are indicated as LANS-A, LANS-B and LANS-C sub-regional boundaries (blue, dark blue and magenta, respectively). The local reference areas (LRAs) are shown as black dashed lines. The Mars Orbiter Laser Altimeter (MOLA) relief (Smith et al., 2001) in fig. 1.9 (Gourronc et al., 2014) is shown by grey shading.

Besides the extremely cold Martian surface during the Hesperian, volcanism was the primary geological process around that time, producing flood basalts and forming all major volcanic landforms (Martian shield volcanoes, e.g., the 22 km in altitude Olympus Mons). Volcanic and tectonic activity should have thus occasionally fractured the Martian cryosphere, melted significant volumes of ice and released appreciable quantities of ground- and surface runoff water. Much of this water should have subsequently flowed into the lowland basins and renewed the hydro- and cryo-sphere of the northern hemisphere (Carr and Head, 2010; Gourronc et al., 2014; Kling et al., 2020). Extrusive volcanic events released large amounts of SO_2 and H_2S into the atmosphere, temporarily increasing the temperature, but amplifying the maximum greenhouse effect in the long run and hence, gradually decreasing the global

temperature. Sulfiric-acid precipitation initiated intense weathering of the surface and caused the transition from the predominant phyllosilicate mineralogies of the Noachian to the abundance of sulfate minerals during the Hesperian. By the end of the Hesperian period at circa 3 Ga, cold and arid climatic conditions prevailed globally, and the planet's geological activity has been since then dramatically decreased (Carr and Head, 2010; Mittelholz et al., 2018; 2020).

1.5.5 The Amazonian Period & Present-Day Mars

The Amazonian period of Mars began at about 3.0 Ga and continues to present day (Tanaka, 1986; Carr and Head, 2010). The less active glacial dynamics, essentially weaker volcanic and erosional activity, and the further decrease of impact fluxes close to present-day rates are the characteristics of the Amazonian period that clearly distinguish this geological period of Mars from the older and more geologically active periods (Golombek et al., 2006).

Volcanism of the Amazonian period is restricted within the Tharsis and Elysium volcanic regions, and only rarely a few volcanic events occurred due to magma ascent in feeder dikes along trough-bounding normal faults (Neukum et al., 2007; Werner, 2009; Broz et al., 2015; 2017; 2021). Most of the Amazonian volcanic units have been observed and identified through HiRISE, CRISM and CTX and are considered as lava flows mainly of basaltic composition. Dacite and granite have been supposedly detected on the Martian surface from the Mars Reconnaissance Orbiter (MRO – NASA) in the borders between Syrtis Major Planum and Isidis Planitia (Christensen et al., 2005). Nevertheless, considering that these plutonic rocks are chemically more evolved and differentiated than basalts, and that the Martian mantle and crust have been too inactive for such magmatic compositions to evolve and crystallize, dacite and granite should be seen as very rare rocks for Mars. The central area of Syrtis Major Planum is of Hesperian age, but its northern borders are transiting to early Amazonian ages and lithologies (Isidis Palanitia; Christensen et al., 2005). Such findings imply that many mysteries remain unsolved in regard to the evolution and geochemical differentiation of the Martian crust and mantle.

Generally, volcanic events during the Amazonian are linked to the localized shield volcanism of the Olympus Mons and Tharsis Montes, and to magma ascent through feeder dikes parallel to normal faulting – graben formation in the Valles Marineris (Andrews-Hanna, 2012a; 2012b; Brustel et al., 2017). The successive flows of highly fluid lava and leveed lava channels associated with the shield volcanoes of Amazonis Planitia, comprise the most tangible evidence of active volcanism during the Amazonian on Mars. Martian volcanic activity today though is ambiguous, with observations confirming that the most recent volcanic events have occurred within the period from 25 to 40 Ma (Basilevsky et al., 2006). Moreover, due to the excavation and ejection of considerable amounts of the Martian crust and mantle because of vast impacts from 4.6 Ga to 3.7 Ga, convection within the core and mantle ceased around the early Amazonian, causing the collapse of the planet's magnetosphere (Mittelholz et al., 2018; Mittelholz et al., 2020). The Martian core nowadays could therefore be considered fully or partially liquid.

Hydrological activity during the Amazonian was dramatically reduced, limited to a few outflow channels and gullies, resulting in the formation of Recurring Slope Lineae (e.g., Ojha et al., 2015). Salinity lowers the freezing point of water to sustain a liquid flow, and salt deposits on Mars are abundant. Thus, periodical peak surface temperatures from −23 °C to 27 °C close to the equator produce liquid brines, even under current Martian conditions. Outflow events during the Amazonian were also generated via small impact events and faulting. The brines produced are composed of high concentrations of magnesium perchlorate ($Mg(ClO_4)_2$), magnesium chloride ($MgCl_2(H_2O)_x$) and sodium perchlorate ($NaClO_4$) in aqueous solutions (Ojha et al., 2015). Recurring Slope Lineae have been observed in the broader Elysium Planitia region and Hale Crater (Carr and Head, 2010; Ojha et al., 2015; Schmidt et al., 2017).

Liquid water that flows transiently on the Martian surface today is only related to moisture from the atmosphere or brine fluids from the Recurring Slope Lineae. All recent surficial water reservoirs on Mars appear in the form of ice caps and are observable mainly in the North and South poles of Mars. The North and South Pole ice caps have an average thickness of about 3-4 km (Tanaka et al., 2005; Carr and Head, 2010) and are surrounded by evaporitic deposits of gypsum, kieserite and phyllosilicates (kaolinite and montmorillonite; Squyres et al., 2008), probably induced

after water-ice and basalt interactions. Appreciable amounts of liquid water may be preserved at shallow depths of the Martian crust, as subglacial liquid water was discovered at a depth of 1.5 km beneath the surface of the South Pole, after analyses on datasets obtained from the MARSIS (Mars Advanced Radar for Subsurface and Ionosphere Sounding) instrument that was deployed on the Mars Express Orbiter (fig. 1.11, Orosei et al., 2018).

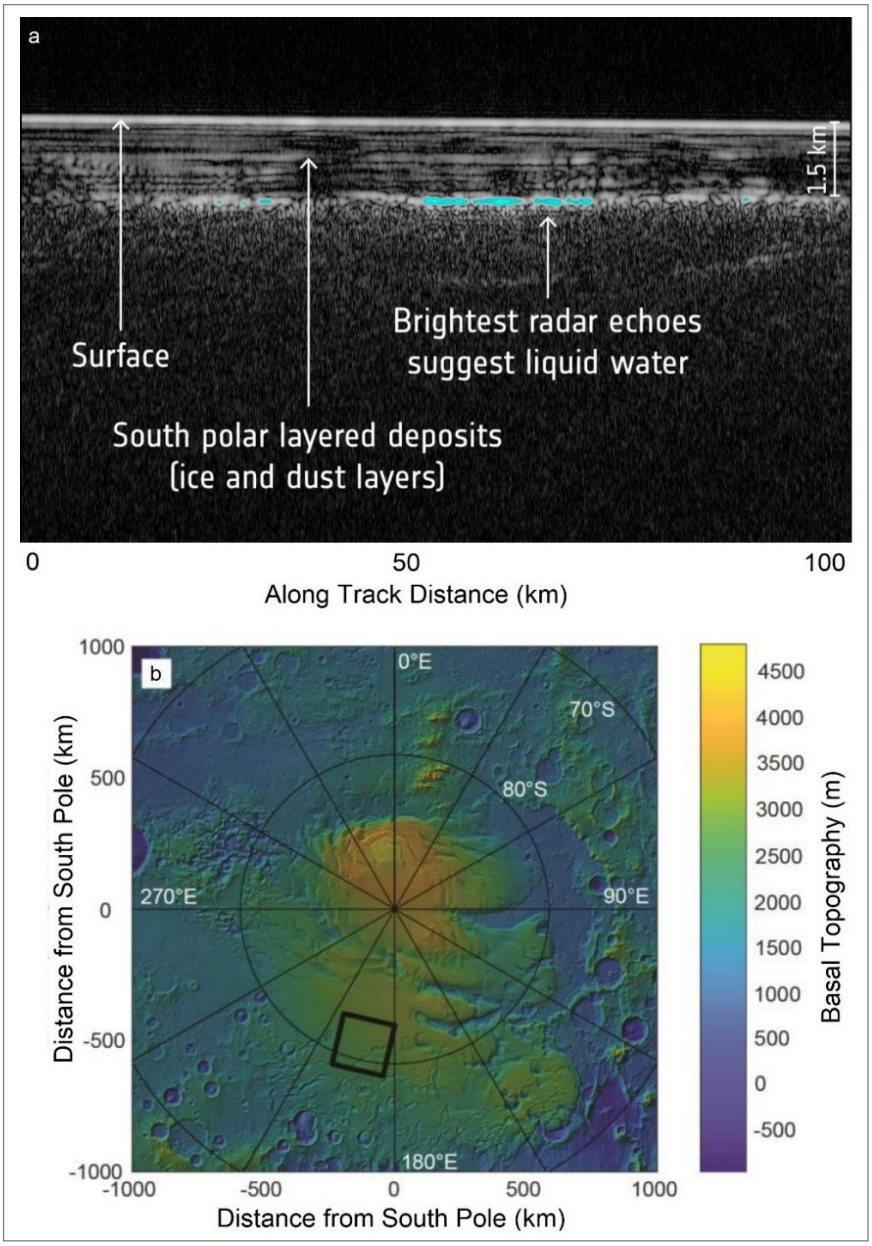

Fig. 1.11. Detection of subglacial liquid water on Mars beneath the South Pole deposit, via the MARSIS instrument (modified after Orosei et al. (2018)); (a): ground-penetrating radar echo reflections revealing liquid water deposits as brightest radar echoes; (b): MARSIS topography of the broader location where Mars Express detected evidence of water below the south polar region (indicated with a black box).

1.6 The Astrobiological Potential of Mars: A Review

1.6.1 Previous Models for the Habitability of early Earth & Mars

The most habitable conditions on Mars should have prevailed from 4.4 Ga to 3.7 Ga (pre-Noachian and Noachian; Schwenzer et al., 2012; Abramov and Mojzsis, 2016). During these geological periods, the abundance of liquid water, ice reservoirs and greenhouse gases, the predominance of phyllosilicate minerals on the planet's surface (Phyllosian era; see Bibring et al., 2006; Catling, 2014, p. 357), and the highest estimated rate of impact fluxes, reciprocally attribute the highest habitability rate to the most ancient Martian crust (Abramov and Mojzsis, 2016; Mojzsis et al., 2019; Moser et al., 2019). Remarkably, impact-induced hydrothermal systems on Hadean Earth, and possibly on pre-Noachian and Noachian Mars, have been presumed to coincide with the emergence of the most primitive life forms at 4.28 Ga (Dodd et al., 2017) or even at 4.5 Ga (Betts et al., 2018). Therefore, impact craters could have comprised cradles for the most ancient life on early Earth, and perhaps even on Mars.

Rathbun and Squyres (2002), and Abramov and Kring (2005) provided computational models for the duration and magnitude of aqueous flows generated in target lithologies after impacts on early Mars. Furthermore, Pierazzo et al. (2005) constrained the initial conditions and requirements for the generation of impact-induced hydrothermal systems on Mars via hydrocode simulations. These studies investigated the dynamics and duration of impact-induced flows in simple and complex craters with varying diameters (e.g.: 30, 100, 180 km) and identified the physical factors that govern impact-induced hydrothermal activity. Further simulations by Abramov and Mojzsis (2009; 2016) explored the crustal heating induced via impact bombardments on Hadean Earth (fig. 1.12) and pre-Noachian and Noachian Mars (fig. 1.13), respectively. Moreover, they computed the volume of molten crust in each of their scenarios and calculated the crustal habitable volume (20 °C ≤ T ≤ 110 °C; fig. 1.12 and 1.13). More contributions also modelled the response of the Martian cryosphere after large-scale impact events (Barnhart et al., 2010; Ivanov and Pierazzo, 2011; Schwenzer et al., 2012). Particularly, after simulations for impact processes on a putative thick (2 – 6 km) cryosphere on late Noachian Mars, Schwenzer et al. (2012) concluded that small impactors (D ≈ 0.6 – 1.8

km) could result in the formation of large craters (D = 10 – 26 km) in subglacial basaltic targets, large-scale impact-generated ice melting, and long-lived (1 – 10 Myr) hydrous and hydrothermal systems beneath the Martian cryosphere.

Nonetheless, previous contributions have not proceeded with modelling potential bioenergetics under hydrothermal/hydrous conditions in the Martian crust, and may have also underestimated the thermal distribution in their scenarios (e.g.: use of a 13 °C / km geothermal gradient; Abramov and Kring, 2005; Schwenzer et al., 2012; Abramov and Mojzsis, 2016). This PhD research will focus on re-exploring via thermodynamic simulations these Martian hydrothermal systems, and on computing the bioenergetics (habitability) induced by water – rock reactions in the Martian crust.

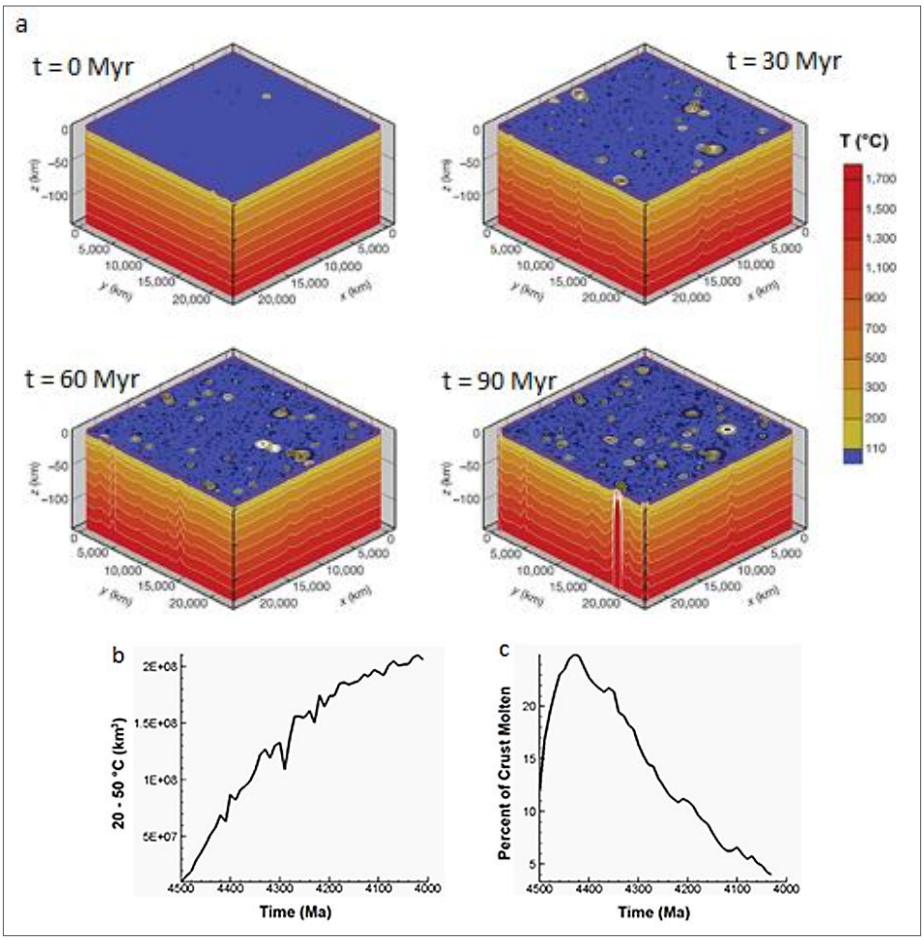

Fig. 1.12. (a): 3D thermal model for Earth's Hadean lithosphere at various times (0 – 90 Myr) from the initiation until the end of the Late Heavy Bombardment (LHB); only regions affected by post-impact temperatures below 110 °C can be considered as habitable (blue regions), and thermal distributions within the range of 110 °C - 1700 °C (yellow to red regions) illustrate the sterilized lithosphere; (b) and (c): computations for the habitable volume of the terrestrial lithosphere (20-50 °C/km^3) during the first 0.5 Gy of Earth's history under impact-induced thermodynamics; and calculations for the evolution of the molten crust due to impact cratering, respectively (modified after Abramov and Mojzsis, 2009).

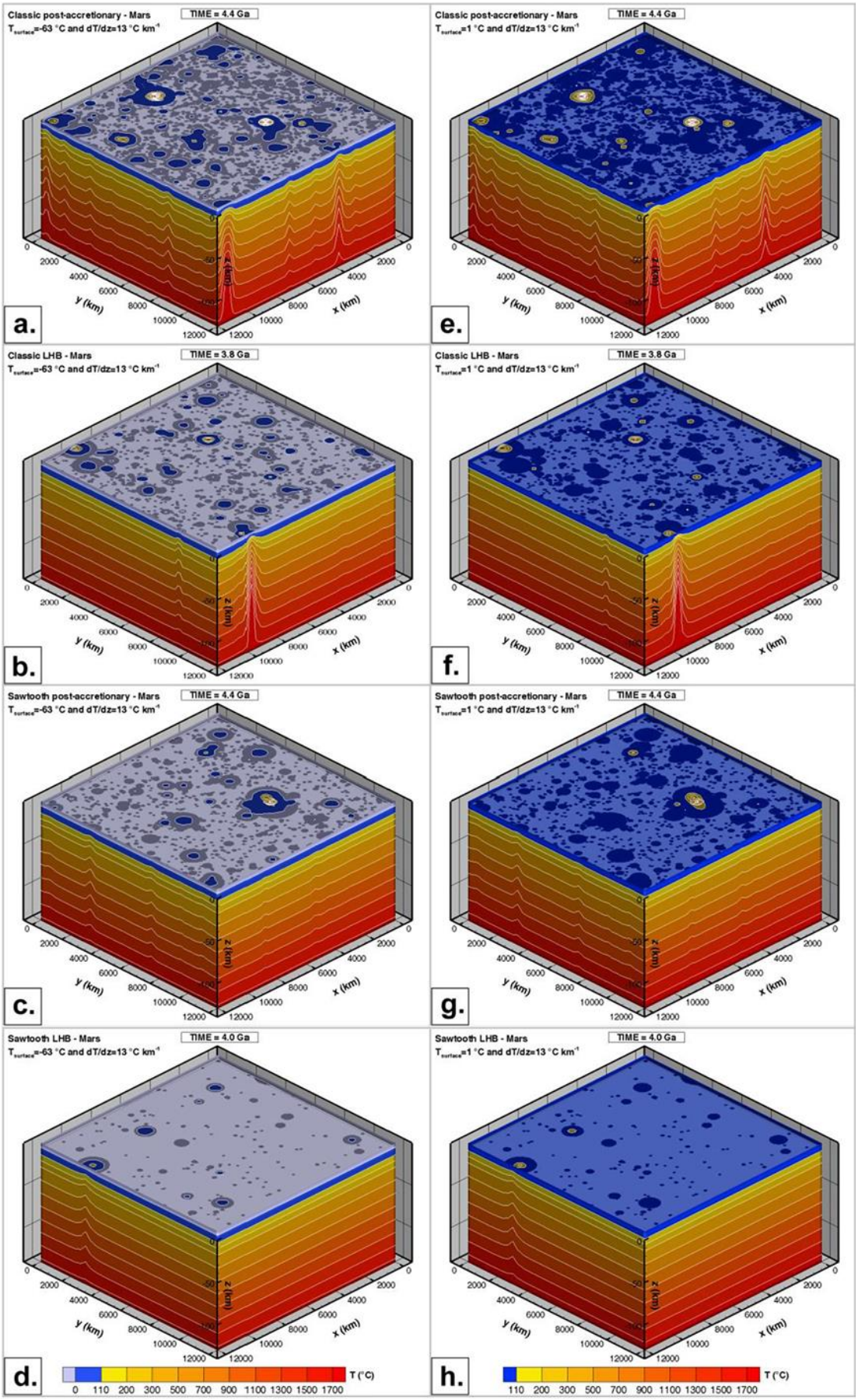

(**Fig. 1.13**: continued to the next page)

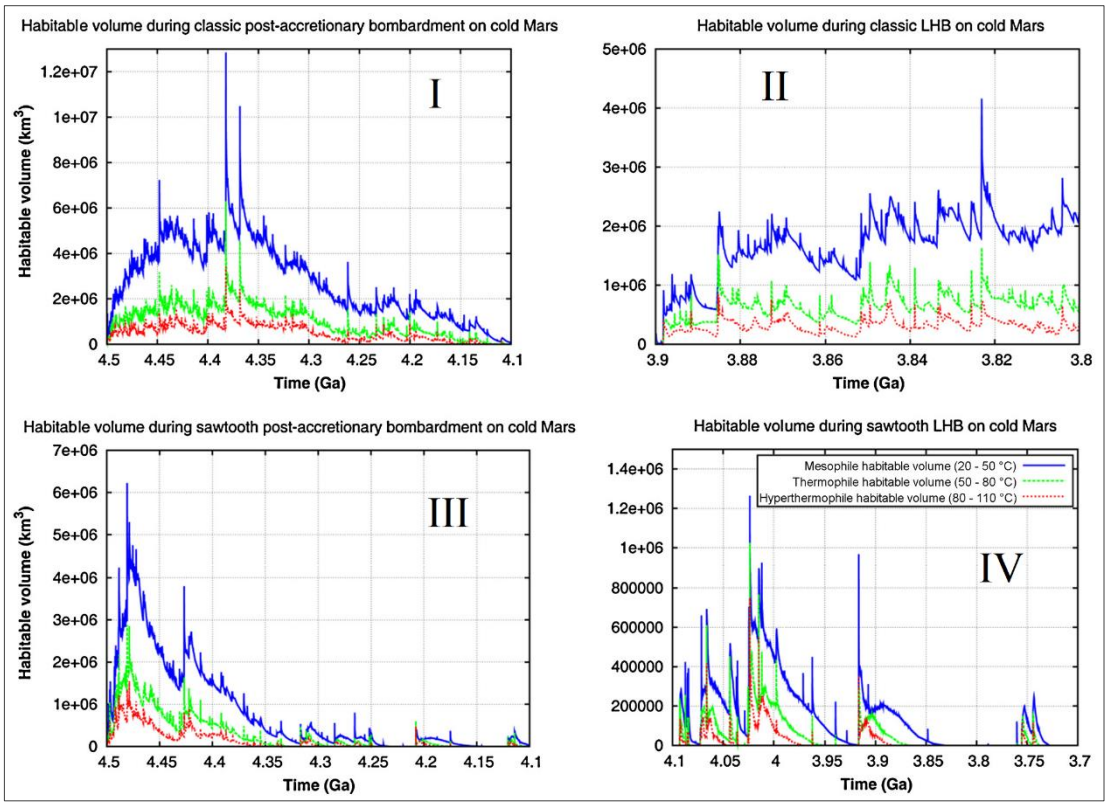

Fig. 1.13. (a - h): 3D thermal models for the upper 140 km of Mars, and for the 100 Myr period into the bombardment. Surface temperature in these simulations was adjusted to either – 63 °C or 1 °C, and all impactors were larger than 2.5 km in diameter. Impact cratering events and formed craters are shown as circular features. Light greyish-blueish areas illustrate the modelled cryosphere (a – d). Dark blue areas represent the habitable domains of the Martian subsurface (a – h). The upper layer of the simulative grid shows temperatures from 0 to 4 km depth. (a): Classical post-accretionary hypothesis (Ivanov et al., 2002), (b): classical LHB (Tera et al., 1974; Ryder, 1990; 2002), (c): Sawtooth post-accretionary (Morbidelli et al., 2012; Marchi et al., 2014), and (d): Sawtooth LHB scenario (Hopkins and Mojzsis, 2015). Scenarios a – d used a surface temperature of – 63 ◦C and a geothermal gradient of 13 °C / km. (e): Classical post-accretionary scenario, (f): classical LHB scenario, (g): Sawtooth post-accretionary scenario, (h): Sawtooth LHB scenario. Scenarios e – h used a surface temperature of 1 °C, and a geothermal gradient of 13 °C / km. (I – IV): Computations for the habitable volumes of the upper 4 km of the Martian crust, under impact bombardment, for mesophiles (20 – 50 °C, blue plots), thermophiles (50 – 80 °C, green plots) and hyperthermophiles (80 – 110 °C, red plots), and under cold surface conditions (Abramov and Mojzsis, 2016). The habitable volume plots derived from the 3D transient thermal models. (I): Habitable volumes during the classical post-accretionary scenario. (II): Habitable volumes during the classical LHB scenario. (III): Habitable volumes during the Sawtooth post-accretionary scenario. (IV): Habitable volumes during the Sawtooth LHB.

1.6.2 Life under Extreme Conditions on Earth

Within the last decades, the discovery of life under extreme energy limitations in the great depths of Earth's oceans (e.g., in hydrothermal vents of mid-ocean ridges or within sediments at 2km beneath the ocean floor; Hinrichs et al., 1999; 2006; Kelley et al., 2001; 2005) have altered our perspective of habitability. The magnificent ability of hyperthermophiles and extremophiles not only to preserve their biomass, but even to grow under anaerobic, non-photosynthetic, and low-energetic conditions of extreme pressures and temperatures (Hoehler, 2004) proves that such microorganisms can thus principally fulfill their biological energy quantum (BEQ) requirement solely by metabolizing the available mineral geochemistry of the local environment (Stevens and McKinley, 1995; Chapelle et al., 2002; Kotelnikova and Pedersen, 1997; Edwards et al., 2000; 2005; 2012; Kelley et al., 2005; Bach, 2016). This theory has thereby propitious implications for the astrobiological exploration of Mars.

All life requires energy, which should be harnessed from its host environment. Free energy ($\Delta_r G$: Free Gibs Energy) should thus be abundant at finite minimum levels so that microbial communities are able to harvest it and should be delivered at finite minimum rates to support basic biochemical integrity and function (Morita, 1997). The biological energy quantum (BEQ) and maintenance energy (ME) requirements are key parameters in assessing the bioenergetic potential of extreme environments (Hoehler, 2004) and are summarized via the following distinctive levels of biological activity:

- Growth: cells are actively creating new biological material and order. In the growth stage, they require the highest level of energy intake.

- Maintenance: cells can support basic metabolic function and activity, including biogeochemical cycling, but without new growth in biomass.

- Survival: cells retain viability by supporting the integrity of amino acids against racemization and nucleic acids against depurination but are not otherwise metabolically active.

Hoehler (2004), showed that temperature exerts the strongest control on the BEQ and the three levels of the ME requirements, and that is the most significant parameter in evaluating the habitability of subsurface environments. Furthermore, numerical modelling studies on the mineralogies and water-rock interactions within mid-ocean ridge hydrothermal systems (basaltic rocks reacting with seawater; Bach, 2016) have shown that in these low-energy environments, appreciable quantities of H_2, CH_4 and other nutrients are released after basaltic rock – water interactions; yielding a much higher than previously thought bioenergetic potential for subsurface aqueous environments. In conclusion, the possibility of similar past or even present biogeochemical activity on Mars, is a key question for current astrobiological research.

1.6.3 Life under Extreme Conditions on Mars?

So, what are the criteria for the habitability Mars? If life ever existed on Mars, then it should have been dependent on the following physicochemical conditions:

- On water-rock reactions, that provide redox energy and availability of Fe^{2+}, Fe^{3+}, Mg, H_2, SO_2 and CH_4 to lithotrophic species of microorganisms (Edwards et al., 2000; 2005; 2012; Bach, 2016), with H_2 being the most probable energy source - nutrient for methanogenic microorganisms surviving and even thriving under extreme energy limitations in extraterrestrial, subsurface environments (Taubner, 2018; Hoehler, 2022; Sauterey et al., 2022).

- On the effects of ionizing radiation on inducing catalytic reactions on the Martian surface and subsurface (Cockell and Raven, 2004) which are not necessarily lethal to radioresistant and even to radiosensitive bacteria (Kim et al., 2002; Dartnell et al., 2007).

- The abundance of solvents through which electrochemical transformations occur; such solvents concern aqueous media (water, fluids etc.) which act as shells to proteins and are requisites for the proteins' interaction with the substrates (Ball, 2008).

1.6.4 Abiotic or/& Biotic Origin for CH_4 on Mars

Recent unambiguous observations through the Mars Science Laboratory (MSL) have revealed seasonal variations and enhanced spikes of CH_4 with values reaching 7 parts per billion by volume (ppbv) and a baseline level of CH_4 at 0.4 ppbv (Webster et al., 2018). It is not yet certain whether these spatiotemporal abundances of CH_4 in the Martian atmosphere are associated with purely abiotic geochemical processes or vigorously interpreted as evidence for biosignatures (Lefèvre and Forget, 2009; Webster et al., 2013; 2015; 2018; 2020; Ten Kate, 2018; Yung et al., 2018). For example, subterranean methanogenic-hydrogenotrophic biomasses could hypothetically reside beneath the Martian surface and be responsible for the consumption of H_2 and for the subsequent release of CH_4 (Atreya et al., 2007; Mumma et al., 2009). On the other hand, CH_4 could have been released via currently active abiotic geochemical reactions beneath the Martian crust (serpentinization of olivine or pyroxene; Oze and Sharma, 2005), or potentially triggered by the high-obliquity orbit that causes thermodynamic and UV radiation fluctuations on the planet's surface and subsurface (Keppler et al., 2012; Schuerger et al., 2012).

Currently, the most plausible astrobiological scenarios for Mars are those related to the observed variations of the CH_4 atmospheric concentrations (Webster et al., 2018; Sauterey et al., 2022). Pathways for the production of CH_4 on Mars are distinguished in abiotic and biogenic and are presented as follows:

<u>Abiogenic sources</u>:

- Reduction of C by H_2 via Fischer Tropsch Type (FTT) reactions (e.g., Sabatier reaction or CO_2 hydrogenation), where H_2 is previously produced during iron oxidation, serpentinization, and/or radiolysis (Sauterey et al., 2022);

  e.g.: $CO_2 + 4\ H_2 \rightarrow CH_4 + 2\ H_2O$ or
  $CH_3COOH \rightarrow CH_4 + CO_2$

- UV alteration of organics delivered by meteorites (Keppler et al., 2012).

- Volcanically degassed CH_4 on Mars or ancient volcanic CH_4 stored in clathrates (Chastain and Chevrier, 2007). This hypothesis though is in contradiction with the observed volcanic CH_4 emissions on Earth. Hence, this scenario cannot robustly justify a putative volcanically triggered CH_4 production on Mars.

- Impact metamorphism of meteoritically delivered organics (Etiope et al., 2011; Oehler and Etiope, 2017).

Biogenic sources:

- CH_4 could be produced by hypothesized extant methanogenic microorganisms that have been using inorganic substrates (minerals) to obtain reducing equivalents for biosynthesis or energy conservation (i.e.: adenosine triphosphate production) via aerobic or anaerobic respiration (Yung et al., 2018; Webster et al., 2018; Sauterey et al., 2022). The production of CH_4 on Mars today should be dependent, however, on hydrous/hydrothermal activity and subsequent water-rock reactions in the deep subsurface. Periodical aqueous circulation events could be releasing chemical nutrients through water – rock reactions. If methanogenic communities have been in a dormant state (not extinct) in the deep Martian crust during its geological history, such aqueous processes could potentially lead to a periodical reactivation of methanogenic microbial metabolisms to grow and colonize the most hospitable hydrothermal niches.

- Similarly, putative extinct biomass of methanogens on Mars should have left appreciable quantities of organic matter preserved in the subsurface. Small impact events or/and convection through weak upwellings in systems such as recurring slope lineae, could occasionally heat the subsurface and organic deposits therein, and enable the conversion to CH_4. CH_4 will later be either trapped in sealed reservoirs, or released into the Martian atmosphere (Oehler and Etiope, 2017).

During ancient geological times, impact-induced and volcanogenic hydrothermal systems may have been the most habitable environments on planetary bodies (Mojzsis

et al., 1996; Abramov and Mojzsis, 2009; Abramov and Mojzsis, 2016; and references therein). On Earth, hydrothermal flows within the porous rocks of volcanic or impact craters can release appreciable quantities of chemical nutrients after hydrothermal fluid-rock reactions (Christou, 2018; Christou and Bach, 2019, Christou et al., 2019a). The quantities of such hydrothermally induced nutrients can even be abundant and remain available for microbes for an estimated minimum average period of 2-4 My after the impact (Christou, 2018; Christou and Bach, 2019; Christou et al., 2019a). Hence, as on Earth, impact craters could have also comprised havens for the survival, growth and evolution of primitive chemolithotrophic lifeforms on Mars. However, this hypothesis has not been thoroughly studied for Mars yet, and so, the bioenergetic potential of early Martian hydrothermal systems remains unknown. Therefore, a primary objective of this PhD research is to quantify the potential bioenergetics (habitability) of early Martian impact-induced and volcanogenic hydrothermal systems.

Preliminary thermodynamic simulations have indicated that the time needed for bioenergetics on Earth to occur under stable hydrothermal conditions ranges from 0.1 My to 10 My (Bach, 2016; Christou, 2018). Nevertheless, the requirements for the transition from abiotic to biotic conditions remain unexplored, and further research work on analogue extreme habitats on Earth is required. The aforementioned findings imply that larger Martian impact craters (diameter $\geq$ 10-15 km; Abramov and Kring, 2005; Jõeleht et al., 2005), that may have hosted hydrothermal activity for more than 0.1 My, could contain biosignatures of extinct or dormant methanogenic – hydrogenotrophic species within their subsurface. Large Martian impact structures even currently manifest a much higher CH_4 and H_2 atmospheric concentration above their ground surface than the baseline level (e.g.: Gale crater, as measured by Lefèvre and Forget, 2009; Grotzinger et al., 2015). Conclusively, these impact structures should be a top priority for the astrobiological exploration of Mars.

Understanding how CH_4 is produced on Mars today will shed new light on the habitability and bioenergetic potential of the Red Planet. On Earth, several phenomena linked to the survival and evolution of microbial life under extreme environments have only recently been observed and deciphered. For instance, recent studies have discovered microbes living on electricity and magnetism (Westheimer, 1987; Nitschke and Russell, 2009; Rowe et al., 2015), and these findings alone have significant

implications for astrobiological scenarios of microbial life thriving under extravagantly, electrically conductive oceans beneath Europa's and Enceladus' icy crusts. Therefore, uncovering the mysteries of abiogenesis, prebiotic evolution and the limitations of life here on Earth, are highly essential research objectives prior to selecting exploration targets in our Solar System, robustly assessing the astrobiological potential of other planetary bodies, and eventually detecting life beyond Earth.

1.6.5 A New Perspective for Planetary Habitability

The presence of liquid water at a planetary surface has been appraised as a crucial factor for determining the habitability of a planetary body. The discovery of microbial life that can persevere at 2.5 km depth beneath the seafloor, solely by harvesting chemical nutrients (Inagaki et al., 2015; Trembath-Reichert et al., 2017), challenges this thesis of habitability, especially for the moons of Jupiter and Saturn. So, this new revolutionary thesis of astrobiology could place Mars within the conservative habitable zone of our Solar System, considering that surficial brines (nutrients) and more significantly, subterranean ice and even liquid water reservoirs have been detected on the Red Planet (Ojha et al., 2015; Orosei et al., 2018). Some of the Jovian and Kronian moons (e.g.: Europa, Enceladus, Ganymede, Io) have never been modelled within the CHZ but are now seen as the most promising sites for astrobiology, as they host oceans beneath their icy crusts, active cryovolcanism, and even hydrothermalism (Coustenis et al., 2009; Coustenis and Blanc, 2012; Solomonidou et al., 2016; and references therein).

Planetary habitability is so far determined through the analysis of extensive telescopically obtained datasets and via remote sensing. Hence, it is mainly defined via empirical relations deriving from the modelling of astronomical and atmospheric parameters that describe a planetary body. Deterministic approaches that incorporate geochemical – cosmochemical analyses coupled with astronomical observations have not been introduced yet, as rock sampling from planetary objects has extreme limitations and concerns only a few planetary bodies within our planetary neighborhood (e.g.: Moon, Mars, asteroids, passing comets etc.). Rock samples provide a unique insight into the thermodynamic processes that have accreted and differentiated a

planetary object, and can deliver enlightening knowledge for its habitability and astrobiological potential. Conclusively, it is imperative that future astrobiological research should revise the definition of circumstellar habitability by incorporating, where attainable, high-precision geochemical samples' analyses and by enhancing this theory via further geochemical - cosmochemical modelling coupled with astrophysical simulations. In this way, planetary bodies with appreciable concentrations of ice - liquid water and organics by mass (i.e., Mars, Europa, Enceladus, Ganymede, Ceres) will reformulate more accurately the theory of the CHZ. Such exploration targets should be thus, reinvestigated via coupled astronomical, geophysical and geochemical approaches. Therefore, by following this rationale, a great focus and scientific investment should be given on rigorous geochemical analyses of planetary mission-return samples and meteorites, as these extraterrestrial rocks will enhance our insights into planetary habitability.

1.7 Meteorites from Mars: Geochemical Insights into Ancient Mars

So far, we have no samples collected and returned from the surface of Mars via rovers. Fortunately, 48.5 tons of extraterrestrial material fall on Earth per day (according to NASA). 353 / 61100 meteorites found on Earth are Martian rocks that have been ejected from the surface of Mars due to asteroid and comet impacts, and subsequently delivered to Earth after a long trip through interplanetary space. The ejection of planetary material due to impacts and traverse of meteorites through the Solar System was a quite controversial hypothesis initially, but was then widely accepted. For over than two centuries we have known that meteorites were extraterrestrial rocks (first hypotheses disseminated by Chladni (1794) and Biot (1803)), and even managed to group them into similar types of rocks later (e.g., Shergottite-Nakhlite-Chassignite (SNC) group of Martian meteorites, Howardite-Eucrite-Diogenite (HED) group of achondritic meteorites). However, their exact origin was remaining unknown up until the Apollo sample return missions. The lunar sample return missions allowed us to directly compare a known Moon rock with a meteorite and conclude that these rocks originated from the same body (i.e., the Moon). The earliest confirmed discoveries of lunar meteorites here on Earth were made by Mason (1982) and by Treiman and Drake (1983). Robust analyses of the impact–mechanics and dynamics that generate the spallation phenomenon and ejection of meteorites from parent bodies (fig. 1.14; Croft, 1980; Melosh, 1984; Melosh; 1989; Melosh; 2003; Kurosawa, 2015; Kurosawa et al., 2018) followed afterwards. Furthermore, measurements on the cosmic ray exposure of meteorites additionally concurred to this theory and provided satisfactory estimates for the duration of the meteorites' trajectory (Gladman et al., 1996; Gladman, 1997; Eugster et al., 1997; Eugster, 2003).

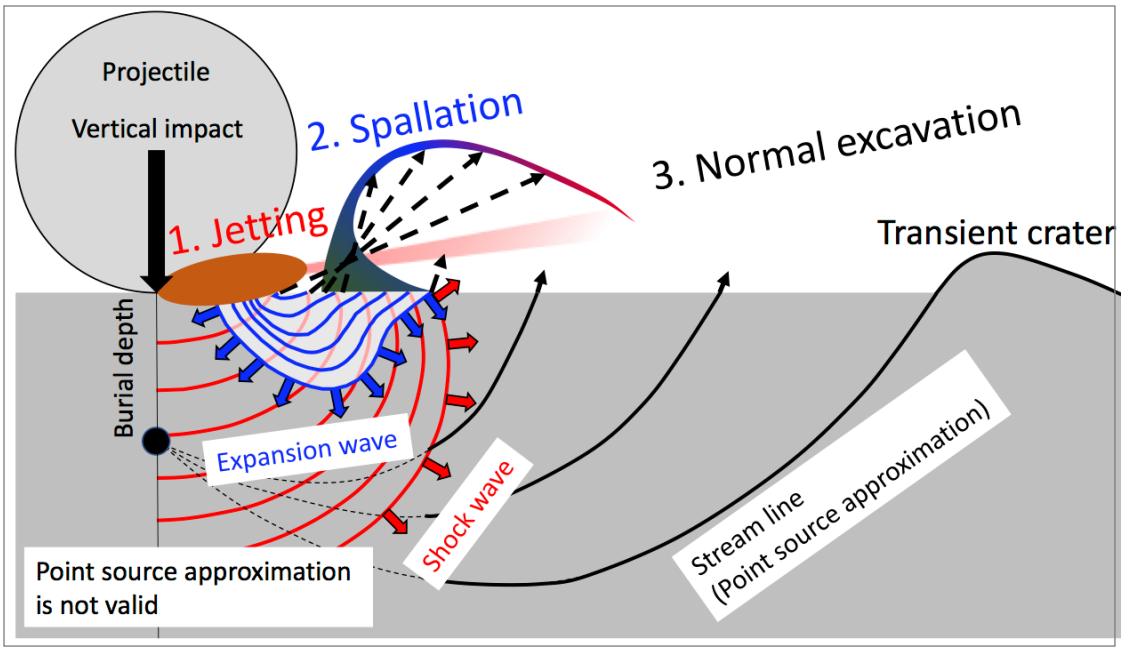

Fig. 1.14. Schematic model for the mechanics of the transition from jetting to spallation and normal excavation of rocks from a planetary surface. The isochrones and isobaric curves for the shock waves and the ejecta curtain derive from impact experiments by Kurosawa et al. (2015). The impact-cratering hydrodynamic field is computed via the Z-EDOZ model (Croft, 1980; Kurosawa, 2015).

1.7.1 Shergottite - Nakhlite - Chassignite (SNC) group of Meteorites

The formation ages of the SNC meteorites along with their evident volcanic mineralogies, atmospheric signatures and aqueous alteration products provided the solid confirmation that these rock samples originate from a planetary body that should have been hosting volcanism, an atmosphere, and a hydrological cycle, respectively. Other than Earth, the only planetary body in our Solar System that has endorsed this combination of geological processes is Mars. The only available rock samples originating from Mars are the Martian meteorites, most of which are lithologically classified into shergottites (mainly basaltic and some ultramafic rocks), nakhlites (clinopyroxenites) and chassignites (olivine cumulates), comprising the SNC (Shergottites-Nakhlites-Chassignites) group of meteorites; and there are also and a few other Martian rocks that do not fit petrologically in the SNC group, such as the rare Martian orthopyroxenite (OPX) Allan Hills (ALH) 84001 and the recently discovered Martian regolithic breccias (NWA 7034 and its paired rocks; in: Agee et al., 2013;

Wittmann et al., 2015). Fig. 1.15 summarizes the meteoritical classification based on the mineralogical and isotopic compositions, and highlights the uniqueness of the Martian rocks, in comparison with other more abundant types of meteorites. The fact that some of these meteorites originate from Mars was established after surface and atmospheric observations of the Viking landers on the Red Planet, and the confluence of the acquired Viking datasets with the observed abundances and isotopic ratios of noble gases (Ar-Kr-Xe-N) that were trapped within these rocks (Owen et al., 1977; Bogard and Johnson, 1983; Bogard et al., 1984; Smith et al., 1984; Becker and Pepin, 1984; McSween, 1984; Pepin, 1985; Wiens et al., 1986; Treiman et al., 2000).

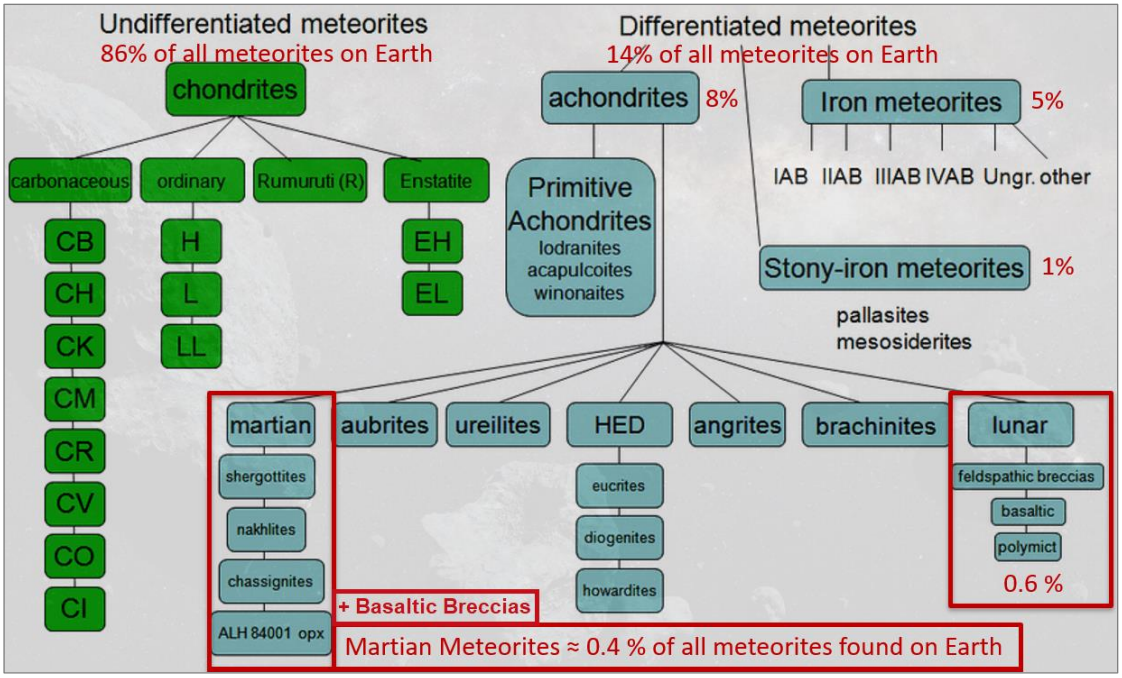

Fig. 1.15. Meteorites are divided into two broad categories: the chondrites (86% of all meteorites) which are undifferentiated (unmelted) asteroids; and the achondrites (14%) which are differentiated (melted). Martian and Lunar meteorites account for only 1% of all meteorites that have been discovered on Earth (image ©: Astromaterials Curation - NASA).

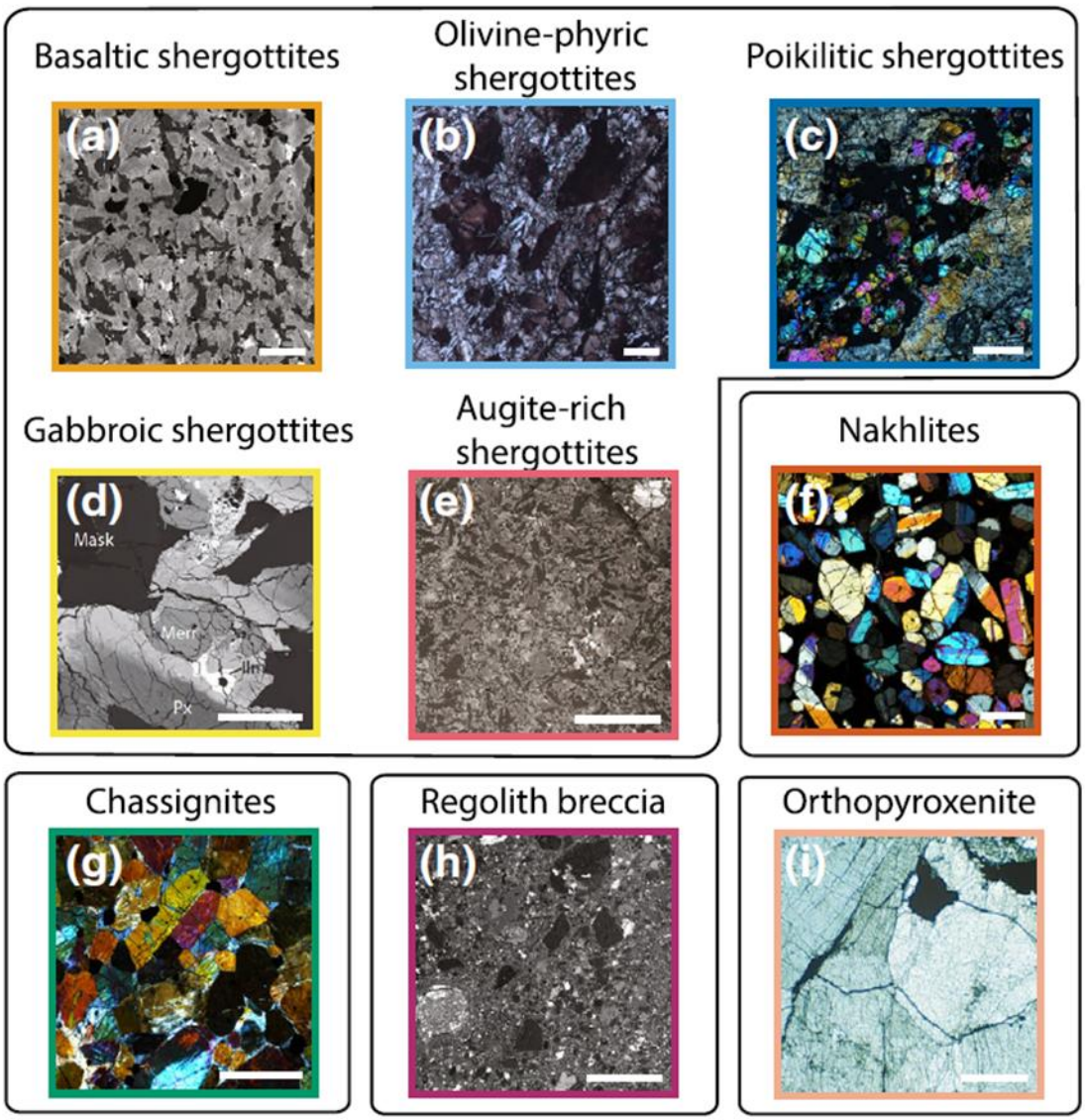

Fig. 1.16. Overview figure by Udry et al. (2020) of the different types of Martian meteorites based on their petrographic and textural characteristics (after compiling SEM-BSE images from: Udry et al., 2017; Filiberto et al., 2014; Filiberto et al., 2018; Hewins et al., 2019; and other references therein; for more information, please see: Udry et al., 2020). From (a) to (e): the five different types of shergottites, (f): nakhlites, (g): chassignites, (h): regolith breccia NWA 70134, (i): Orthopyroxenite ALH 84001.

The Martian meteorites provide powerful information on the geology, geochemistry and habitability of the Martian surface and sub-surface. Martian rocks can also answer many questions concerning the planetary evolution of Earth-like and habitable planets, since the most ancient geology on Mars is well preserved, in contrast to planet Earth. Plate tectonics on Earth have destroyed almost all evidence of the primitive crustal formation and of differentiation processes (Mojzsis et al., 1996; Wilde et al., 2001).

Conceivably, the most ancient lifeforms that emerged during Hadean Earth could be biogeochemically investigated through the prism of ancient Martian habitability, as the approximate time of emergence, and more significantly the exact environment of origin of the most ancient biomolecules in the Solar System remain unknown.

1.7.1.1 Shergottites

The shergottites' classification name derives from the Shergotty meteorite, which fell at Sherghati, India in 1865. The shergottites are quite diverse and more abundant in comparison with other Martian groups of meteorites (89% by number of the entire Martian meteorite suite, and 82% by mass), and are divided into five different types based on their composition (Udry et al., 2020). The major difference between the Martian basaltic rocks and Earth's basalts is the higher Fe/(Fe+Mg) ratio and lower Al_2O_3 content of Martian volcanic rocks (Nyquist et al., 2001). In addition, shergottites can be classified by their relative abundance (enrichment or depletion) in incompatible trace elements (ITE), and this implies that their ITE compositions should originate directly from their mantle source (Udry et al., 2020). The variety of ITE abundances in shergottites should have occurred during the planetary differentiation processes of early Mars, and through its magma-ocean crystallization around the pre-Noachian (Borg and Draper, 2003; Borg et al., 2016; Lapen et al., 2017; Udry et al., 2020). On the other hand, trace-element enriched shergottites could either be a product of subsequent partial melting, mantle metasomatism or crustal assimilation (McSween, 2015; Lapen et al., 2017; Day et al., 2018; Udry et al., 2020). Furthermore, the parental magmas of shergottites could have had an appreciable water content before the volcanic eruption / lava ascent, as the depletion of shergottites in distinctive volatiles indicates volatile loss via degassing processes (McCubbin et al., 2012; Herd et al., 2017; Udry et al., 2020).

In addition to their geochemical classification, shergottites can be classified into different groups also according to their texture (Fig. 1.16 (a-e); i.e., grain size, shapes, and modal abundances). Udry et al. (2020) suggest that the variety in shergottitic textures portray processes of mineral precipitation through emplacement in the shallow Martian subsurface, or eruptive processes at the Martian surface. Therefore, Udry et al.

(2020), distinguish shergottites into five distinct groups (fig. 1.16) in order of abundance: basaltic shergottites (highest in abundance samples; e.g.: NWA 8657, fig. 1.16a), olivine-phyric shergottites (e.g.: LAR 06319, fig. 1.16b; fig. 1.17), poikilitic shergottites (e.g.: NWA 4468, fig. 1.16c), gabbroic shergottites (e.g.: NWA 6369, fig. 1.16d), and augite-rich shergottites (lowest in abundance and rarest samples; e.g.: NWA 8159 (fig. 1.16 e), NWA 7635, NWA 13467).

The basaltic shergottites consist predominantly of clinopyroxene (augite and pigeonite) and plagioclase, and have a basaltic, or sometimes diabasic texture. These Martian basalts are relatively olivine-poor rocks, with cumulated pyroxene and strongly foliated textures (fig. 1.16a), indicating crystallization after magma fractionation (Herd et al., 2002; McSween, 2015; Day et al., 2018) via near-surface dikes or lava flows. Then, olivine-phyric shergottites are predominantly porphyritic, they host olivine phenocrysts and their olivine, pyroxene, and maskelynite crystals are indicative of later-crystallization processes (fig. 1.16b; fig. 1.17).

Poikilitic shergottites (the third group of shergottites, previously termed as lherzolitic shergottites; fig. 1.16c) are olivine rich with significant assemblages of clinopyroxene and chromite, and coarse-grained poikilitic pigeonite around olivine phenocrysts (Treiman et al., 1986; Treiman et al., 1994; Treiman et al., 2000; Goodrich, 2002; Herd, 2002). Fayalite (FeO-rich olivine), pigeonite, augite and maskelynite, are some of the most dominant mineralogical phases encountered in the interstitial phases of poikilitic shergottites. This implies a great similarity of these poikilitic rocks from Mars with the basaltic shergottites based on their identical mineralogies and presumed early crystallization from magmas. For this reason, Martian poikilitic (lherzolitic) rocks are also classified as shergottites (Treiman et al., 1994; 2000; Goodrich, 2002; Mikouchi, 2005; Mikouchi and Kurihara, 2008; Udry et al., 2020). Furthermore, many shergottites have been discovered and thoroughly examined within the last decade that are representative of distinctive magma compositions due to their higher plagioclase content (>10% plagioclase; e.g.: Los Angeles, NWA 2969, NWA 7635, QUE94201; after McSween et al., 1996; Rubin et al., 2000; McCubbin et al., 2012; Walton et al., 2012).

The fourth group of shergottites are the gabbroic shergottites (fig. 1.16d), described by their cumulate pyroxene or plagioclase content (Udry et al., 2020; and references therein). Recent discoveries and examinations of gabbroic specimens, including NWA 6963 (pyroxene cumulate) and NWA 7320 (plagioclase cumulate) (Filiberto et al., 2014; Filiberto et al., 2018; Hewins et al., 2019; Udry et al., 2020). Gabbroic shergottites share similarities with basaltic shergottites, except for the fact that they are characterized by large cumulus grains of pyroxene or plagioclase (1 - 5 mm in diameter); hence, this cumulus texture of gabbroic shergottites is indicative of crystal accumulation and may be also associated with differentiation and crystallization of parental magma sources of basaltic shergottites (Filiberto et al., 2018; Hewins et al., 2019; Udry et al., 2020).

Finally, the newly discovered augite-rich shergottites NWA 8159 and NWA 7635 comprise the fifth group of shergottites, as they are quite distinctive from the other four types, and the rarest shergottite samples (Udry et al., 2020; fig. 1.16e). They have intergranular texture consisting of augite, plagioclase, olivine, magnetite, orthopyroxene, and show an absence of pigeonite (Herd et al., 2017; Herd, 2023; Christou et al., 2019; Christou et al., 2021; Udry et al., 2020). The petrogenetic history, bulk elemental and isotopic composition, and the textural characteristics of the augitic shergottites imply that they have originated from a distinct mantle reservoir, and that they have crystallized under relatively oxidized conditions. Interestingly, the isotopic composition of the inferred parental melt of NWA 8159 and NWA 7635 appears quite unique and evolved (Ca-rich, Ti-poor and LREE-depleted), when compared to the isotopic compositions of potential magmatic sources of other SNC rocks (Herd et al., 2017; Herd, 2023; Udry et al., 2020).

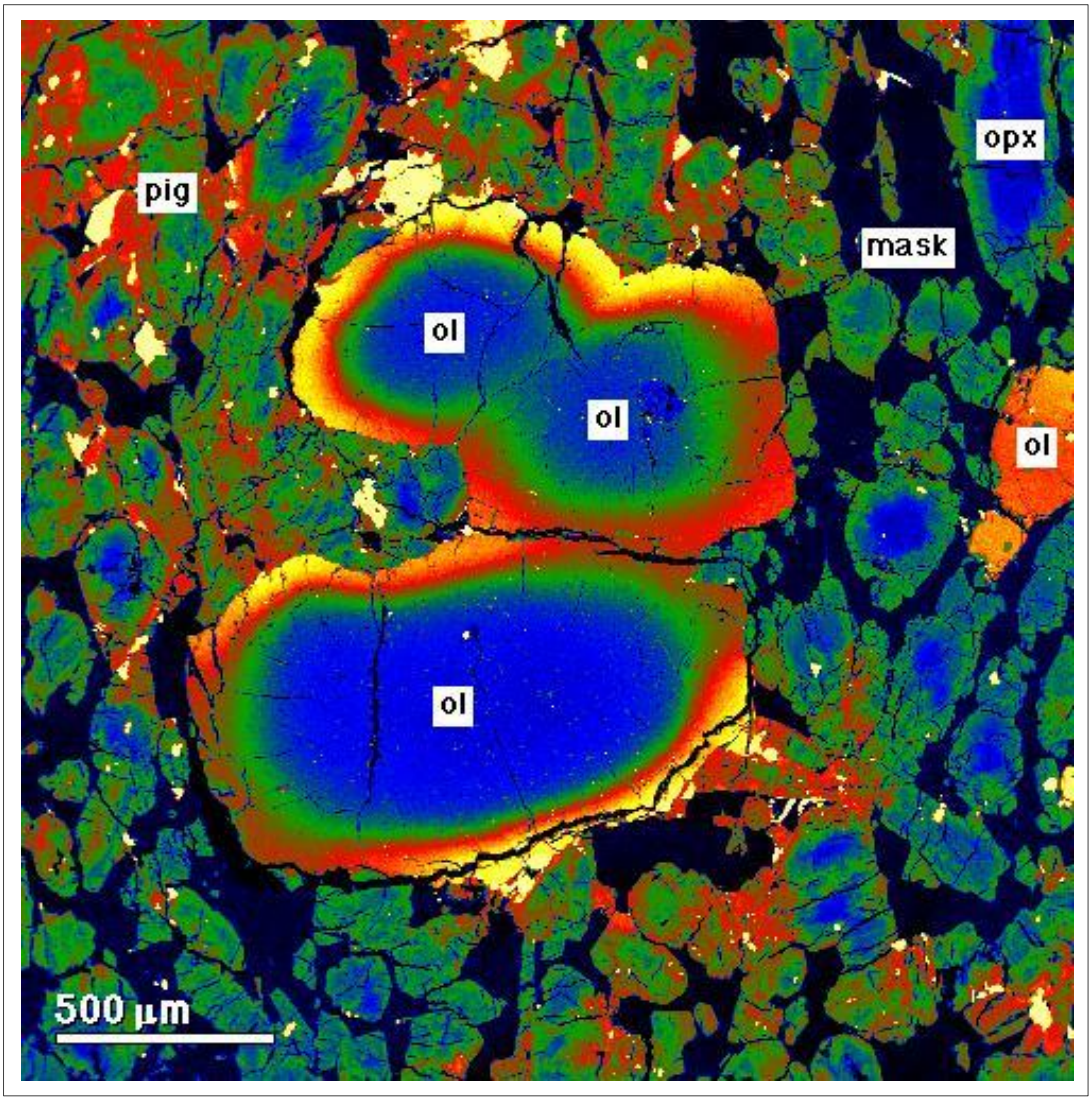

Fig. 1.17. False-colour backscattered electron image of the Olivine-phyric Shergottite NWA 2046, exhibiting strong compositional zoning in subhedral olivine phenocrysts (ol; green to red to yellow), orthopyroxene microphenocrysts (opx; blue), and groundmass pigeonite (pig; green), maskelynite (mask; black), chromite and ilmenite (both white); Irving et al., 2004.

Shergottites were considered to comprise the youngest group of all SNC meteorites, since most of these meteorites have been very accurately and precisely dated to have formed between 575 – 150 Ma (Nyquist et al., 2001). Nevertheless, the chronological constraints for the shergottites are now being controversial, as their formation ages vary between 2.40 – 0.15 Ga. This argument derives from geochemical and geochronological analyses on the newly discovered NWA 8159 and NWA 7635 shergottites, which have been recognized with calculated ages of 2.30 ± 0.25 Gyr and 2.40 ± 0.14 Gyr, respectively (Herd et al., 2017; Herd, 2023). Additionally, both early Amazonian shergottites NWA 8159 and NWA 7635 should originate from a depleted

mantle source that is distinct from the depleted shergottites based on Cr, Nd, W, and Pb isotopic geochemical signatures (Herd et al., 2017; Bellucci et al., 2020; Herd, 2023).

Cosmic radiation exposure ages for shergottites are diverse (0.5 – 19 Ma), implying that several impact events should have occurred in the recent history of Mars, in order to eject all these basaltic rocks from the planet's crust (Eugster et al., 1997; Nyquist et al., 2001; Fritz et al., 2005; Herd et al., 2017; Váci and Agee, 2020). Based on hydrodynamic simulations and topographical measurements, McEwen et al. (2005) suggested the Zunil crater as the source crater for some of the basaltic shergottites. This is consistent with the crystallization and ejection ages of the youngest shergottites, their composition, and the fact that Zunil is the sole crater with a less than 10 Ma age and a greater than 10 km diameter, able to produce abundant high-velocity ejecta fragments. However, other hypotheses suggest that all shergottites originate from the Mojave crater (Werner et al., 2014), but the variety of the cosmic radiation exposure ages cannot establish this hypothesis.

1.7.1.2 Nakhlites

The Nakhlites are named after the Nakhla meteorite which fell in the El-Nakhla province (Egypt) in 1911. It had an estimated weight of 10 kg and is the only nakhlite seen to fall. Nakhlites are clinopyroxenites consisting of augite (~80%) and olivine (~15%). Their crystallization ages (about 1.35 Ga, Middle Amazonian) imply that they formed in a large volcanic province and so, they may potentially originate from the Tharsis, Elysium or Syrtis Planum, according to crater count chronological models (Treiman, 2005). Recent $^{40}Ar/^{39}Ar$ geochronological analyses suggest that the nakhlites crystallized during four temporally discrete volcanic eruptions that occurred between 1416 ± 7 Ma to 1322 ± 10 Ma on Mars (Cohen et al., 2017; fig. 1.18). Most nakhlites were ejected from Mars from 3.9 ± 0.4 Ma to 12.1 ± 0.7 Ma due to an asteroid impact and fell to Earth within the last 10 Ky (Nyquist et al., 2001; Eugster et al., 2002; Okazaki et al. 2003). Ten nakhlite samples have been distinguished so far, and these are also illustrated in fig. 1.17. Briefly, the 10 nakhlites are: Nakhla, Lafayette, Yamato (Y), Antarctic Miller Range (MIL), Governador Valadares, NWA 817 / 998 / 5790 / 6148,

and Caleta el Cobre 022. All nakhlites exhibit aqueous alteration attributed to infiltration by Martian liquid water; iddingsite, smectite, Fe-oxide-hydroxide, gypsum and halite crystals are observable in sub-μm scale, implying that low-temperature aqueous alteration has affected the nakhlites' host rock (Bridges et al., 2001; Hallis and Taylor, 2011; Hallis et al., 2011; 2012a; 2012b; Lee et al., 2015a; 2015b).

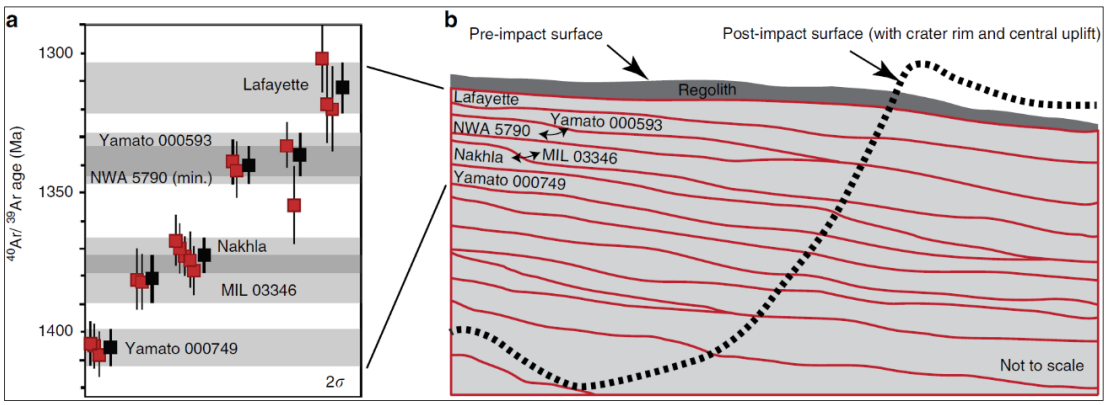

Fig. 1.18. Stratigraphic model for the nakhlite meteorites by Cohen et al. (2017); (a): Results for the $^{40}Ar/^{39}Ar$ age dating of the nakhlite meteorites. Red squares represent aliquots and highly reproducible plateau ages for each nakhlite. Black squares and horizontal grey bars account for weighted mean ages. The $^{40}Ar/^{39}Ar$ results show that the nakhlites were erupted in at least four temporally discrete volcanic eruptions within 93 ± 12 My. All uncertainties are 2σ; (b): Outline of the impact-crater morphology and schematic model for the layered lava flow sequence and the nakhlites' stratigraphy.

The mean observed modal mineralogy of the nakhlites consists of high-Ca clinopyroxene (~80%), Fe-rich olivine (~11%) and mesostasis (~9%); i.e., plagioclase, feldspar, pyrrhotite (± chalcopyrite), Fe-Ti oxides, gypsum, halite, salts, and aqueous alteration products collectively referred to as iddingsite (Treiman and Gooding, 1991; Bridges et al., 2001; Treiman, 2005; Day et al., 2006; Hallis and Taylor, 2011; Hallis et al., 2012a; 2012b; Lee et al., 2013; Lee et al., 2015a; 2015b; Corrigan et al. 2015; Daly et al., 2019a; 2019b). The source magma for nakhlites was depleted in Al_2O_3 and enriched in incompatible elements (REE) compared to terrestrial clinopyroxenites (Treiman, 2005; Terentiev and Santosh, 2017; 2020; Day et al., 2018; Udry et al., 2020). Thus, the aforementioned scientific contributions have concluded that the nakhlites originate from a long-lived magmatic source and may be genetically linked to either a periodic recharging of fractionated magmatic chambers, or to mantle metasomatism (Treiman, 2005; Lee et al., 2015a; 2015b; Cohen et al., 2017; Day et al., 2018; Daly et al., 2019a; 2019b; Udry et al., 2020; Griffin et al., 2022).

Generally, all Martian clinopyroxenites seem to have formed after accumulation of pyroxene and olivine and should have experienced a plethora of igneous crystallization and cooling conditions that are distinctive for each sample, as indicated by their varying textures (Treiman, 2005; Day et al., 2006; Daly et al., 2019a; 2019b; Griffin et al., 2022). Specifically, the MIL and Yamato samples appear to have partially crystallized in the shallow subsurface (as evidenced by their quench textured mesostasis). Whereas other nakhlites do not exhibit this texture (e.g.: Lafayette and Nakhla; Treiman, 2005; Mikouchi, 2005).

After the nakhlites' crystallization, and according to the thermodynamic conditions that persisted in their environment of emplacement, these igneous rocks were then aqueously altered by fluids that were transiently flowing on the Martian surface or within the shallow subsurface (Mikouchi et al., 2005; Ehlmann et al., 2009; Changela and Bridges, 2010; Bridges and Schwenzer, 2012; Tomkinson et al., 2013; Lee et al., 2013; 2015a; 2015b). Because of these nakhlite–Martian fluid reactions, olivine and Si-rich glass species were dissolved, and replaced by assemblages of iddingsite (smectite clays and hydrous Fe-oxides), gypsum, halite and other evaporitic minerals (Changela and Bridges, 2010; Lee et al., 2013; 2015a; 2015b; fig. 1.19: aqueously formed veins in the Nakhla meteorite; Lee et al., 2015a).

Furthermore, the nakhlite samples have helped a lot to constrain the shock pressures (less than 45 GPa) that these rocks experienced during their spallation/ejection processes (Fritz et al., 2005; Griffin et al., 2022). In particular, nakhlites host shock melt inclusions and shock veins in their crystalline plagioclase that, through mineralogical analyses, provide insights into the pressure under which those shocked mineral assemblages formed (Greshake et al., 2004; Daly et al., 2019a; 2019b; Griffin et al., 2022). Thus, this helped establish the range of shock pressures that nakhlites experienced during the impact cratering event and their subsequent ejection.

After their delivery to Earth, nakhlite rocks should have resided on Earth's surface for an extended period (Hyr – Kyr; Treiman, 2005) as they appear affected by terrestrial weathering processes; except for Nakhla, which fell in 1911 in Egypt and was collected within 2 months, and Lafayette, which probably fell in 1919 and was collected a few

months or years after; O'Brien et al., 2022). Thus, Nakhla and Lafayette should be exhibiting the lowest degree of terrestrial contamination, in contrast to other nakhlites.

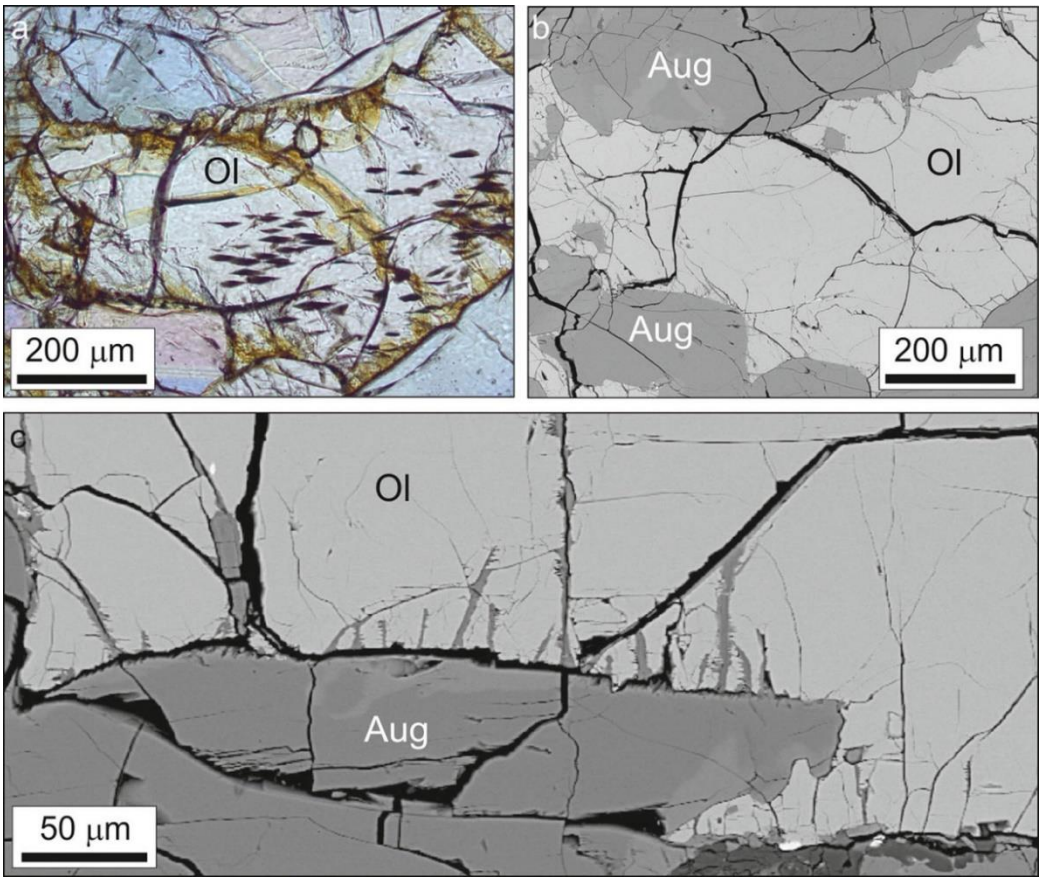

Fig. 1.19. Images of iddingsite veins in olivine (Ol) grains from a Nakhla thin section; provided by Lee et al. (2015a). (a): Plane polarized transmitted light image of an olivine (Ol) grain that is cross-cut by iddingsite veins (orange). Black oval shaped inclusions in the olivine (Ol) are symplectites. (b): Backscatter Secondary Electron (BSE) image of the same region of interest, where augite (Aug) surrounds olivine (Ol). (c): BSE image of an olivine (Ol) – augite (Aug) contact. Discontinuous iddingsite veins are abundant within olivine and close to the intergranular boundary; only a few veins penetrate further into the olivine due to etching (Lee et al., 2013; 2015a) but are absent within augite.

1.7.1.3 Chassignites

The original chassignite is the Chassigny meteorite, which fell on the 3rd of October 1815 in the Chassigny province of Haute-Marne, in France. Both chassignites and nakhlites may have been ejected from Mars simultaneously as they have the same crystallization ages (circa 1.3 Gyr; Eugster et al., 2002; Eugster, 2003; Bogard and

Garrison, 2008; Korochantseva et al., 2011; Park et al., 2014; McSween, 2015; Hewins et al., 2020) and a potential comagmatic origin (McCubbin et al., 2013). Apart from Chassigny, there are only two other known chassignites: (1) the ″Diderot″ meteorite or NWA 2737, that was retrieved from the Saharan dessert in 2000, with an identical petrography and geochemical composition to Chassigny, and (2) the NWA 8694 meteorite, which is a 55 g dunite obtained in Agadir, in July 2014. NWA 8694 has been just recently characterized as a ferroan chassignite with an intermediate composition to Chassigny and the nakhlites. Thus, NWA 8694 has expanded the chassignite suite (Hewins et al., 2020).

All three chassignites are of dunitic composition, they differ substantially from the shergottites, and are somewhat also dissimilar to nakhlites, as they have a distinctive noble gas content that is probably a geochemical signature of the Martian mantle's composition (Johnson et al., 1991). Chassignites are cumulative dunites consisting entirely of cumulus olivine (~91.5%; fig. 1.20), with intercumulous pyroxene (~5%), feldspar (~2%), chromite (~1.5%), and accessory phases of oxides and Fe-sulfides (Floran et al. 1978; Johnson et al., 1991; Magna et al., 2015; Lorand et al., 2018). They are far more depleted in REE than the nakhlites, and by additionally considering their dunitic composition and noble gas content, these facts imply that the chassignites' magmatic environment of origin has undergone partial melting (at temperatures between 900 °C - 1230 °C (Johnson et al., 1991). This has also been attested by the presence of exolved pyroxene and Ca-zoning of olivine in these samples (Mikouchi et al., 2005; Treiman et al., 2007; Hewins et al., 2020).

Finally, after their magmatic emplacement on the Martian surface, the chassignites' geological history on Mars seems rather "dry". Chassignites contain no evidence for Martian alteration (Mikouchi et al., 2005; McCubbin et al., 2013; Hewins et al., 2020), in contrast to nakhlites (Lee et al., 2013; 2015a; 2015b). Some evidence of aqueous alteration is indeed present, but this is associated to terrestrial alteration after the meteorite's fall to Earth (Misawa et al., 2005; Treiman et al., 2007). Conclusively, after their emplacement, these volcanic rocks should have not been affected by any alteration processes during their residence time on the Red Planet. Shocked alkali-feldspar in chassignite rocks reveals that two impact events (a stronger initially, and a postcedent weaker one; after Treiman et al., 2007) affected the host rock environment by

subsequent post-impact shock waves, prior to the ejection of the rocks to interplanetary space, at about 10-12 Ma (McCubbin et al., 2013).

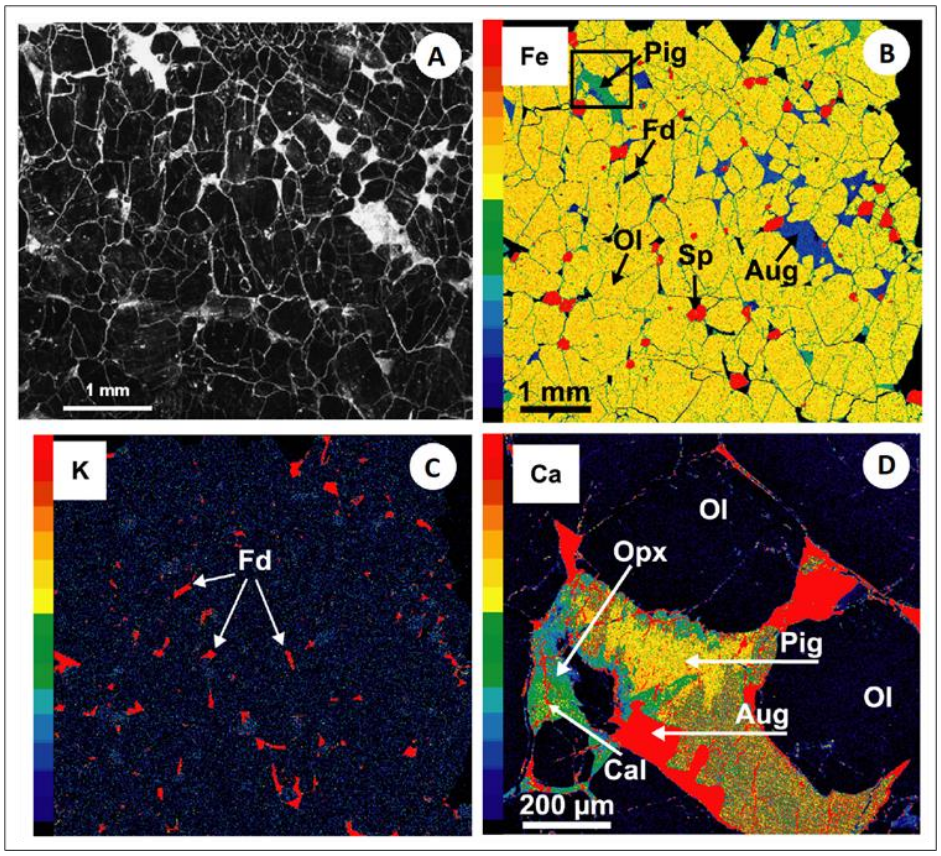

Fig. 1.20. (A): Binocular microscope image of a chassignite NWA 2737 thin section via radial illumination and white light (Treiman et al., 2007). The rock has a cumulate texture (typical for chassignites) and is dominated by dark, anhedral to subhedral olivine (mm-sized) crystals, together with euhedral chromite (dark), pyroxene, maskelynite and glass (clear and transparent). The white irregular fractures are filled with carbonates (calcite or aragonite). (B): Fe chemical map of the same NWA 2737 ROI shown in sub-caption A. The mineralogy of the NWA 2737 meteorite: Aug: augite; Ol: olivine; Pig: pigeonite; Sp: spinel; Fd: K rich feldspar. (C): K chemical map of the ROI revealing the distribution of K-rich feldpsar (Fd). (D): Ca chemical map revealing interstitial coexisting pyroxenes in the same ROI. This thin section indicates that chassignite rocks do not exhibit aqueous alteration and so, their host environment on Mars should have been unaffected by altering fluids after their emplacement (Misawa et al., 2005; Treiman et al., 2007; McCubbin et al., 2013).

1.7.2 Bizarre or/& Ungrouped & Most Ancient Martian Meteorites

In general, most SNC rocks have young crystallization ages (< 1.3 Ga; Treiman, 2005; McSween, 2015; Cohen et al., 2017;) and the only exceptions of Martian meteorites with crystallization ages older than 2 Gy are the following exotic and intriguing Martian rocks:

- The ″Black Beauty″ meteorite (or Northwest Africa (NWA) 7034) and its paired rocks were found in the Sahara Desert in 2011. NWA 7034 is classified as a basaltic - regolithic breccia and contains the oldest Martian zircons (4.42 ± 0.07 Ga; after U-Pb geochronology) ever identified (Hu et al., 2019; Udry et al., 2020). The zircons are contained in basalt, basaltic andesite, trachyandesite and igneous clasts, and also in the NWA 7034 matrix (Hu et al., 2019), implying intense volcanism on pre-Noachian Mars. In parallel, other geochemical analyses have also confirmed that Black Beauty contains approximately 10× more indigenous water than most SNC meteorites (Agee et al., 2013; Bouvier et al., 2018; Cassatta et al., 2018). Therefore, Black Beauty can be seen as the most precious Martian meteorite sample to date, as it provides evidence for the evolution of the Martian crust from the early pre-Noachian (first 100 My after planetary accretion) until the Amazonian (before its ejection; at circa 5 Ma; Cartwright et al., 2014). Furthermore, NWA 7034 and its paired rocks comprise the sole brecciated regolithic samples from Mars; with compositions that are quite distinctive from those of the SNC meteorites.

- The NWA 8159 that is an unusually old shergottite of early Amazonian age (2.37 ± 0.25 Ga; Herd et al., 2017) that was affected by aqueous alteration and weathering processes. However, it is yet unclear whether these geochemical signatures in NWA 8159 (Herd et al., 2017; Bellucci et al., 2020) are associated with alteration phases of Martian origin, or whether they are products of terrestrial alteration and weathering after the meteorite's fall to Earth, or possibly, a combination of both (Hallis et al., 2016; Christou et al., 2019b; 2020; 2021b; 2022).

- The NWA 7635 shergottite, of a similarly unusual Amazonian age (2.40 ± 0.14 Ga). The NWA 7635 isotopic composition is rather peculiar and implies that this rock derived from the same depleted mantle source from which the group of 327-574 Ma

depleted shergottites also originated (Lapen et al., 2017). Hence, NWA 7635 exhibits evidence of a Martian volcano that had been erupting continuously for almost 2 Gy.

As more than 80% of Martian meteorites belong to the shergottite group (Udry et al., 2020), NWA 8159 and NWA 7635 also seem petrologically related to the shergottites (Herd et al., 2017; Lapen et al., 2017; Christou et al., 2019; Udry et al., 2020). However, NWA 8159 and NWA 7635 show distinctive petrological characteristics from the other shergottites, the most important of which are: their enrichment in augite, the inferred Nd and Pb isotopic composition of their mantle source, and their older crystallization ages, which greatly prolong the magmatic history of shergottites (2.40 ± 0.14 Gyr for NWA 7635 and 2.30 ± 0.25 Gyr for NWA 8159; (after Herd et al., 2017; Bellucci et al., 2020; Herd, 2023). Furthermore, it has been concluded that the petrological attributes of NWA 8159 and NWA 7635 derive from redox reactions either between the melt source and the primary (early-crystallization) mineral phases, or during sub-solidus cooling (Herd et al., 2017; Shearer et al., 2019; Herd, 2023). These scientific findings propose a much more complex petrogenetic history for NWA 8159 and NWA 7635, that renders them as the most distinctive and unique shergottites. Finally, Herd (2023) supported that these two most ancient shergottites may have originated from the very same parental melt, as they share multiple petrogenetic and geochemical affinities.

- The NWA 13467 meteorite is another augite-rich basalt from Mars with significant petrogenetic and mineralogical links to NWA 8159 and NWA 7635 (Staddon et al., 2022); and that it is currently being thoroughly investigated (after personal communications with Dr. Leanne Staddon). Soon, more potential findings and subsequent detailed investigations of similarly intriguing augite-rich shergottites shall shed new light on the compositional characteristics of their parental melt, their crystallization ages, and on the magmatic and geologic evolution of Mars.

- The Allan Hills (ALH) 84001 is a rare orthopyroxenite from Mars with an igneous crystallization age of 4.09 ± 0.03 Gyr (Jagoutz et al., 1994; Wadhwa and Lugmair, 1996; Lapen et al., 2010). This implies that ALH84001 formed during the pre-Noachian period; a geological period during which Mars should have had abundant

liquid water on its surface, and the most habitable (warmest and wettest) conditions (Halevy et al., 2011; Ehlmann et al., 2011). Hence, ALH84001 is an essential sample for exploring the thermodynamic interactions between the crust-hydrosphere-atmosphere of early Mars. ALH84001 is an ungrouped orthopyroxene cumulate which has been affected by aqueous fluids on the surface of Mars, impact events, fracturing, and thermal and shock metamorphism, as revealed by examinations of its carbonates and their nitrogen (N) bearing phases (Mizuho et al., 2020 and references therein). The N-content of SNC meteorites can help reconstruct the co-evolution of the Martian crust, atmosphere and hydrosphere; moreover, on Earth, nitrogen is a crucial element for the formation and evolution of protein, DNA and RNA (Kounaves et al., 2014). So far, it is unclear whether the organics preserved in ALH84001 are of Martian origin, as the meteorite has been affected by terrestrial contamination after its fall to Antarctica (Steele et al., 2007; Lapen et al., 2010). Subsequently, from these organic compounds derives no evidence, or implication, for any biosignatures from early Mars, as previously misunderstood (McKay et al., 1996; Gibson et al., 2001).

Conclusively, the only Martian meteorites that cannot be classified into the SNC subgroups are the orthopyroxenite Allan Hills (ALH) 84001, and the ″Black Beauty″ meteorite (NWA 7034) with its paired samples. Both meteorites are the oldest samples that we have from the surface of Mars and have no petrological and textural similarities with the other SNC rocks (Black Beauty age: 4.42 ± 0.07 Ga; after Bouvier et al., 2018; Cassatta et al., 2018; Hu et al., 2019; and ALH84001 age: 4.09 ± 0.03 Ga; after Lapen et al., 2010). Thus, they comprise two other sub-categories of Martian rocks.

1.7.3 Martian Meteorite Samples Explored in this PhD Research

1.7.3.1 The Northwest Africa (NWA) 8159 Meteorite

NWA 8159 comprises a unique sample of the early Amazonian era and lithology of Mars (2.37 ± 0.25 Ga; Herd et al., 2017; fig. 1.21) and has derived from a relatively evolved, Ca-rich, Ti-poor and LREE-depleted mantle source (Herd et al., 2017;

Bellucci et al., 2020). Together with NWA 7635, this Martian meteorite is the sole sampling from the early Amazonian crust (older than 2.3 Ga; Herd et al. 2017; Lapen et al., 2017). The retrieval of NWA 8159 from the Sahara Desert, and subsequent thorough examination, eventually solved the "Shergottite Age Paradox" (Nyquist et al., 1998), which was an inconsistency caused by the very young crystallization ages of the shergottites (180 – 575 Ma) in contrast with the ages of all Martian meteorites from the nakhlite and chassignite sub-groups (Nyquist et al., 2001). The discovery, petrological classification and dating of the first early Amazonian shergottites (NWA 8159 and NWA 7635) resulted in the expansion of the shergottite suite. Today, these two shergottites comprise the most ancient samples of the entire SNC group of Martian meteorites, as all nakhlites and chassignites are younger than 1.3 Gyr (Cohen et al., 2017; Herd et al., 2017; Lapen et al., 2017).

The NWA 8159 shergottite consists of augite (~50%), plagioclase (~40%), olivine (~5%), magnetite (~3%) and orthopyroxene (~2%), with minor ilmenite, merrilite, Cl-apatite and Cr-spinel (Agee et al., 2014; Hallis et al., 2016; Vaci et al., 2016; Herd et al., 2017; Sharp et al., 2019; Shearer et al., 2019). Olivine core compositions in NWA 8159 indicate that olivine crystals are xenocrysts (in both NWA 8159 and NWA 7635) because of a discrepancy in their Mg content, after comparing the Fe/Mg ratios of olivine cores to those of augite cores (Herd, 2023). Furthermore, all olivine phenocrysts exhibit an assemblage of orthopyroxene and magnetite at their rims, proving that NWA 8159 olivine grains were affected by mineralogical replacement at their margins (Herd et al., 2017; Shearer et al., 2019). Such magnetite-orthopyroxene intergrowths (confirmed in NWA 8159; Herd et al., 2017; Christou et al., 2019b; 2020; 2021b; Herd, 2023) have been associated with magmatic and very late-stage magmatic to sub-solidus reactive processes that are highly dependent on oxygen fugacity (fO_2; Herd et al., 2017; and references therein).

NWA 8159 also exhibits veins of aqueously formed mineral assemblages (Hallis et al., 2016). It is not known whether these veins represent one long-lived episode of fluid flow, or multiple shorter events, or if these aqueous mineralogies are products of Martian alteration or of terrestrial weathering processes after the meteorite's fall on Earth (Hallis et al., 2016; Herd et al., 2017; Christou et al., 2019b; 2020; 2021b). What we know for sure is that NWA 8159 resided in the terrestrial desert for a long period,

since the rock appears heavily weathered, containing carbonate veins that crosscut all NWA 8159 samples (Hallis et al., 2016). Furthermore, NWA 8159 olivine exhibits aqueous alteration as evidenced by Fe-rich phyllosilicate (Hallis et al., 2016; Vaci et al., 2016) that is present not in the form of veins, but in the cores of olivine grains. Conceivably, the olivine core alteration in NWA 8159 could be linked to oxidation on Mars or later terrestrial oxidation.

In addition to Fe-phyllosilicate, the hydrothermal mineral laihunite has been reported in NWA 8159 (Vaci et al., 2016). Laihunite is a product of the high-temperature (400 °C – 800 °C) hydrothermal oxidation of olivine (Banfield et al., 1990) and could imply the presence of a high-temperature hydrothermal fluid in NWA 8159. Laihunite has also been reported in the Miller Range nakhlites (Hallis et al., 2011; and references therein). All these observations and analyses of the NWA 8159 rock and the consequent hypotheses provide strong incentives for future extensive research on the NWA 8159 meteorite.

Partial transformation of labradorite in NWA 8159 to jadeite has helped to constrain the meteorite's shock pressure range from 15 GPa to 23 GPa (Herd et al., 2017). NWA 8159 mineral assemblages of Ca-Na-majoritic garnet and sodic-clinopyroxene that seem to have crystallized from shock melt, indicate a crystallization pressure of approximately 16 GPa (Herd et al., 2017; Sharp et al., 2019). Results from shock recovery experiments, where plagioclase of $An_{50.4–63.5}$ composition remains completely crystalline up to a maximum shock pressure of 26 GPa (Stöffler et al., 1986), also concur to the NWA 8159 plagioclase's composition and assessed shock pressure range. In conclusion, this relatively low to mean peak shock pressure experienced by NWA 8159 during its ejection argues against the presence of a transient impact-induced hydrothermal flow; as appreciable hydrothermal flows are most likely initiated when the shock pressure (and the associated post-impact temperature) experienced by the target lithologies after an impact-cratering event is higher than 20-22 GPa (Melosh, 1989; Ivanov, 2005; Ivanov and Pierazzo, 2011). This means that if laihunite is present in NWA 8159, then it could have not been produced via an impact-induced hydrothermal mechanism.

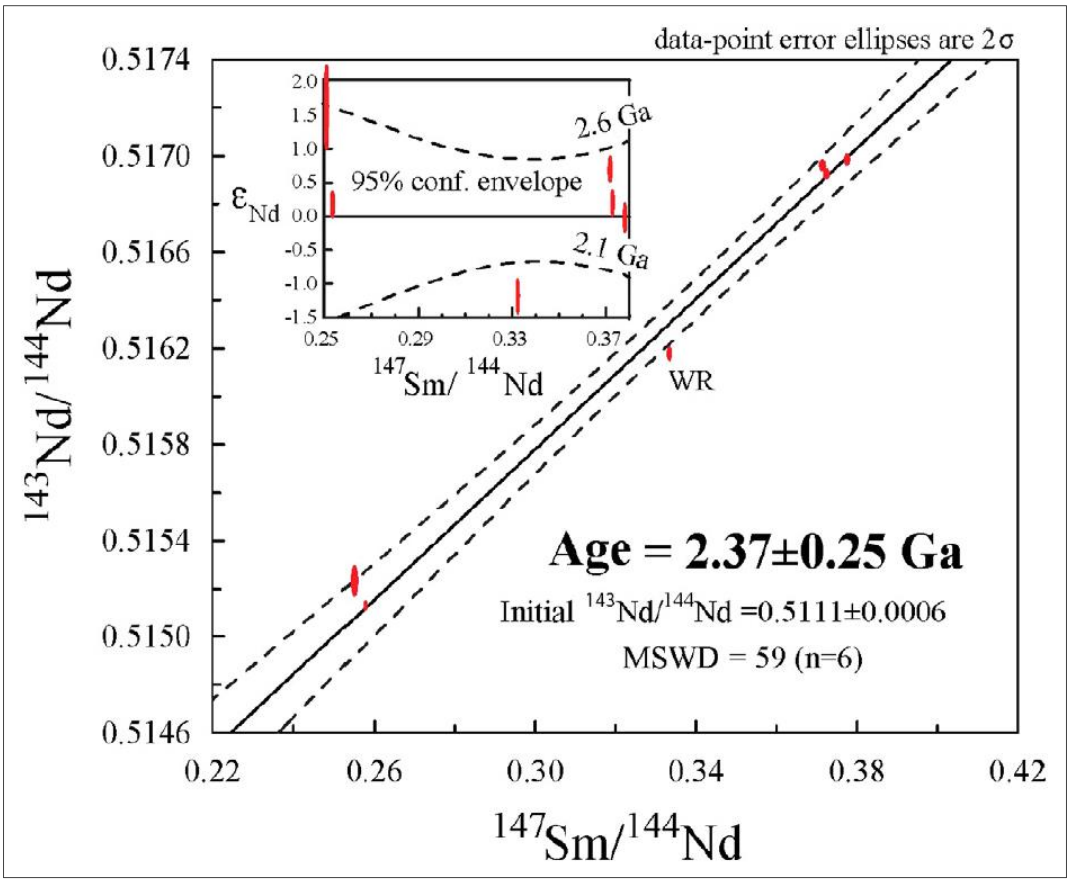

Fig. 1.21. (a) Sm/Nd isochron diagram for the entire NWA 8159 rock, calculating an average crystallization age of 2.37 ± 0.25 Gyr (2σ) for this augitic basalt (Herd et al., 2017). Sm/Nd isochronic measurements were performed on fragments with a high maskelynite/plagioclase concentration (lower Sm/Nd values) and on fragments with a high pyroxene concentration (higher Sm/Nd values). WR: whole rock sample (and WR fragments on which Sm/Nd isochronic measurements were also performed).

1.7.3.2 The Lafayette Meteorite

It has been unknown for quite a long time the location from which the Lafayette meteorite was retrieved, since it was firstly discovered and identified as a meteorite among other rocks in the Purdue university geological collection in 1931 by O. Farrington (Nininger, 1935). The meteorite's name derives from the region where it was identified; Lafayette, in Indiana. Lafayette appears to be a pristine Martian sample (Lee et al., 2015b) and non-targeted metabolomics analysis by O'Brien et al. (2022) showed that terrestrial plant-derived organic contaminants are present in this meteorite.

Furthermore, based on the plant species that were identified in this meteorite, and on the previously reported fall location (Nininger, 1935), O' Brien et al. (2022) constrained further the year (most probably in 1919) and geographical location of the Lafayette fall to the Tippecanoe County (for more details, please see: O'Brien et al., 2002).

The Lafayette meteorite exhibits a flow texted fusion crust, indicating a very fresh fall and contains no terrestrial weathering, except for plant-derived organic contaminants (O'Brien et al., 2022). Geochronological measurements of ^{39}Ar-^{40}Ar on Lafayette suggest a crystallization age of 1330 ± 15 Ma (Podosek, 1973; Cohen et al., 2017) that is in accordance with the crystallization ages of other nakhlites, and previous chronological estimates (Treiman, 2005). Lafayette's cosmic radiation exposure age is approximately 12.36 Ma (Korochantseva et al., 2011) implying that the host rock could have been ejected from Mars 1 My sooner than other nakhlites.

Lafayette is a Ca-rich nakhlite with a modal mineralogy of (~75%) augite, (~12.5%) olivine, (~6.5%) mesostasis, (~3.5%) iddingsite, (~1.5%) orthopyroxene and (~1%) Fe–Ti oxide (Tomkinson et al., 2013; Daly et al., 2019a). The texture of Lafayette is similar to that of other nakhlites (Nakhla), and its mesostasis is rich in magnetite crystals with a size range from 100 μm to 600 μm, consisting mainly of plagioclase and K-feldspar, Fe-rich clinopyroxene, Fe-Ti oxides, pyrite, K-Na-rich aluminosilicate glass and iddingsite phases (Boctor et al., 1976; Treiman et al., 2013; Korochantseva et al., 2011; Lee et al., 2015a; 2015b). In addition, Rb-Sr geochronological modelling on Lafayette's iddingsite and K-phyllosillicate has yielded formation ages of 679 ± 66 Ma (Shih et al., 1998) and 633 ± 23 Ma (Borg and Drake, 2005), respectively. These estimates should represent the hydrous flows that interacted with the meteorite's host rock, induced alteration and precipitated the iddingsite about 650 Ma. Secondary and low thermal alteration events are also present in the meteorite, but it is yet unclear whether these mineralogical indicators post-date the formation of the iddingsite (Borg and Drake, 2005; Lee et al., 2015b; fig. 1.22: iddingsite veins in Lafayette and evidence for aqueous alteration; Lee et al., 2015b).

Changela and Bridges (2010) have previously suggested that H_2O and CO_2 could have been released after impact-induced heating of reservoirs in the Martian crust, resulting to the formation of sawtooth fractures in the nakhlite host rock. However, such fractures

in nakhlite samples were later identified as crystallographically controlled (Lee et al., 2015a; 2015b; Daly et al., 2019b; Griffin et al., 2022). Lafayette alteration veins may be a product of an olivine carbonation mechanism via which CO_2 is sequestered into olivine from the Martian atmosphere in the presence of water (Tomkinson et al., 2013). In this way, impact-induced hydrothermal fluids could not have produced these iddingsite veins (primary alteration; fig. 1.22) or/and low-thermal alteration (secondary) products in Lafayette (Tomkinson et al., 2013; Lee et al., 2015b), as olivine carbonation requires the long-term presence of liquid water in the meteorite's environment of origin, and low temperature conditions that are totally irrelevant to impact-induced alteration (Lee et al., 2015a; 2015b).

Nevertheless, a variety of mechanisms that can explain the formation of iddingsite exists. According to Lee et al. (2015a; 2015b) other mechanisms include potential melting of subsurface H_2O and CO_2 due to low temperature volcanogenic flows, degassing of lava flows, or percolation of CO_2 – charged fluids in basaltic magmas. Therefore, determining the formation mechanism of nakhlite aqueously formed minerals is highly essential, as fluid longevity and flux provide a stable and potentially habitable environment, whereas occasional, transient flows do not.

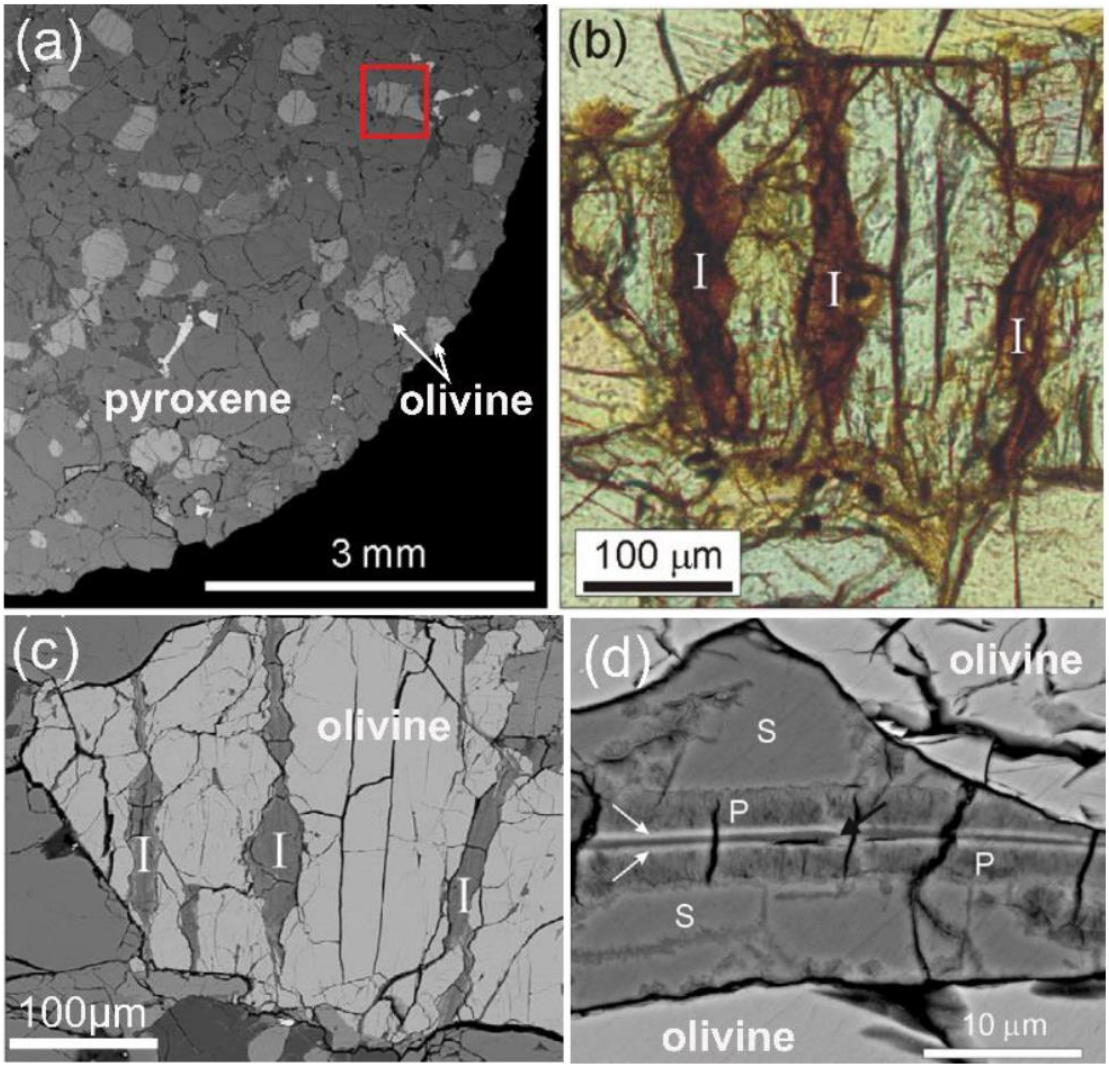

Fig. 1.22. Martian aqueously formed veins in Lafayette olivine; modified after Lee et al. (2015b). Red box in (a) indicates the location of the olivine grain shown in (b-d). Iddingsite veins appear rust coloured under optical light (b), and mid-grey in BSE images (a-c-d). Minerals within these veins (d) include siderite, Fe-rich phyllosilicate, Fe-oxide (white arrows), titanomagnetite (white), gypsum, and salts, and reveal the aqueous alteration process that affected the primary mineralogy of the Lafayette host rock.

1.7.3.3 Rationale for Investigating the NWA 8159 & Lafayette Samples

NWA 8159 and Lafayette are two Martian meteorite samples included in the meteorite collection of the University of Glasgow. NWA 8159 and Lafayette are augite-rich basaltic rocks that have distinctive chemical compositions and geological histories. These Martian meteorite samples were selected for exploration in this PhD research, as they can constrain further the bulk geochemical compositions and physical properties of the distinctive geological environments from which they originate, and the aqueous alteration processes that have affected each rock via microscopy analyses (Hallis, 2016; Christou, 2019b; 2020; 2021b; 2022). However, NWA 8159 is severely affected by terrestrial contamination, and this poses an obstacle toward distinguishing the origin and composition of the altering fluids (Martian versus terrestrial) that interacted with the rock on Mars (prior to its ejection) and on Earth (after its fall). Furthermore, NWA 8159 is a unique Martian meteorite that samples the early Amazonian crust (Herd et al., 2017) and that remains understudied. Establishing the origin, nature and evolution history of its shergottitic environment requires primarily the identification of both Martian mineralogies and aqueous alteration products.

On the other hand, Lafayette appears unaffected by terrestrial weathering. Therefore, Lafayette can be used as a benchmark tool for distinguishing the primary and secondary mineralogies that are of Martian origin in SNC meteorites from the terrestrial weathering products (e.g.: as identified in NWA 8159). A thorough investigation and comparison of NWA 8159 mineralogies with Lafayette mineralogies will shed new light on the distinctive volcanic and aqueous processes that these rocks experienced on Mars, and on their far more recent journey that resulted to their fall and weathering here on Earth.

More importantly, analytical investigations of the mineralogies and physical properties of NWA 8159 and Lafayette can contribute towards the main objective of this PhD research, which is to model the thermodynamic evolution and habitability of their host volcanic settings on Mars. By investigating the samples through detailed microscopy techniques (Scanning Electron Microscopy) and by processing the results through imaging softwares (ImageJ), the porosity of each Martian rock can be determined. Such findings can help constrain the thermodynamic conditions under which fluid –

mineral reactions could have occurred within the Martian surface and subsurface, and develop robust models for the fluid-mechanics of aqueous circulation in Martian hydrous or hydrothermal systems. Such findings and datasets will comprise powerful tools in constructing reliable numerical simulations for the thermodynamics, geochemical reaction pathways and habitability of the meteorites' host environments on Mars.

1.8 Research Aims of this PhD Research

State-of-the-art analytical examinations of Martian meteorites have been providing thorough insights into the planetary accretion and geological evolution of Mars, and have been enhancing our understanding of the physicochemical processes that have rendered Mars a potentially habitable planet. In parallel, numerical modelling research contributions have recognized the importance of hydrothermalism in astrobiology via simulations for both terrestrial and Martian hydrothermal systems. Moreover, computational research has constrained further the post-impact thermodynamics on early Mars, including impact-induced aqueous circulation.

However, previous numerical studies and experimental geochemical analyses have not quantitatively determined potential bioenergetic pathways that may have been generated under a variety of volcanogenic or impact-related hydrothermal / hydrous conditions on early Mars. In addition, published models, as explained in the previous sections, seem to have conservatively explored impact-induced hydrothermal systems on Mars, by inadvertently underestimating the basal heat flux, geothermal gradient and thermal energy availability in the early Martian lithosphere. I recognize, nevertheless, that numerical models simulate chaotic natural systems governed by numerous physical parameters, and that there will always be contradicting arguments related to a few initial conditions used in modelling approaches. Hence, computational experiments should at some point conclude on the initial parameterization and finalize the performance of

numerical simulations (which has also been a complex investigative task in this PhD research).

Therefore, the primary aim of this PhD research is to determine whether hydrothermalism or hydrous processes on ancient Mars could induce and preserve potential habitable niches for microbial life. The original scientific contributions of this PhD research and its objectives are the following:

- Numerical simulations and interpretations for the thermodynamics and hydromechanics in a variety of impact-induced and volcanogenic hydrothermal / hydrous systems on early Mars, which could be representing hydrogeological phenomena from the pre-Noachian until the late Amazonian period.

- Computations and quantitative assessments for potential bioenergetic pathways induced after Martian water – basaltic rock interactions within the Martian crust; including numerical models for the habitability of hydrothermal or hydrous environments in the Martian subsurface and simulations for the thermodynamic requirements of putative microbial life to survive and even colonize aqueous environments on Mars.

- New insights into the mineralogy, aqueous history and physical properties (porosity) of the NWA 8159 and Lafayette Martian meteorite samples via high-precision analytical techniques (mentioned in the methodology chapter (§2)). Furthermore, by extracting petrological information from these Martian meteorite samples through microscopy analyses, mineralogical datasets can efficiently interrogate and enhance the initial thermodynamic conditions (physical and chemical input parameters) and consequent results of thermodynamic and habitability simulations.

§2 MATERIALS & METHODS

2.1 The HYDROTHERM Software: An Efficient Code for Modelling the Ancient Hydrological Activity on Mars.

2.1.1 HYDROTHERM 3 Numerical Simulations

The computer code HYDROTHERM (HT; by Hayba and Ingebritsen, 1994) was used in this PhD research to simulate the thermodynamics of putative hydrothermal systems on Mars. The constructed simulations focused particularly on assessing the magnitude of water mass flux and the thermal landscape of such aqueous environments during earlier geological epochs; with numerical experiments investigating the Noachian to mid-late Amazonian Martian hydrothermalism.

A full quantitative description of flow in a hydrothermal system requires the solution of mass and energy conservation equations, coupled with equations of state appropriate for the thermodynamic conditions of a geological setting. The HT code has been reportedly used to simulate volcanic and impact-induced hydrothermal systems on Earth and Mars (e.g., Rathbun and Squyres, 2002; Abramov and Kring, 2004; 2005; 2007; Sanford, 2005; Christou, 2018). For this study, the newest HT version (#3) of the U.S. Geological Survey (USGS) was utilized, which operates via the HYDROTHERM Interactive (HTI) software (by Kipp, Hsieh and Charlton, 2008; and firstly developed by Hayba and Ingebritsen, 1994) that provides the coupled equations and solutions for the mass and energy conservation in volcanic and impact-induced hydrothermal systems, and with a much higher resolution and computing efficiency than previous HT versions.

Numerical simulations were constructed similarly to the methodology followed by Rathbun and Squyres (2002); and Abramov & Kring (2005) to model the hydrous circulation in putative early Martian volcanic and impact-induced hydrothermal systems, and establish the lifetime of the aqueous activity and geochemical interactions therein. The simulations focused primarily on determining the evolution of temperature

distribution, water mass flux, heat flux, pressure, enthalpy, porosity and permeability of the putative basaltic aqueous environments.

The governing equations used in HTI are expressions of mass and energy conservation that are posed in terms of pressure and enthalpy. The pressure - enthalpy formulation uniquely specifies the thermodynamic state of the fluid in two-phase conditions, and avoids the difficult numerical problems associated with the critical point (Ingebritsen and Hayba, 1994; and also, in the initial HT code by Hayba and Ingebritsen, 1994). The code incorporates data from various sources to develop consistent equations of state for conditions ranging from 0 °C to 1200 °C and from 0.5 to 10 kbar (50 KPa to 1 GPa). The equations of state (EOS) are formulated in HTI using a standard finite-difference approach. The equations, however, are strongly coupled and highly nonlinear, because the variables of relative permeability, density, and viscosity vary widely with pressure and enthalpy (Hayba and Ingebritsen, 1994). The nonlinear coefficients are treated using Newton-Raphson iteration that leads to a system of linear equations that are solved iteratively.

In the HT 3 simulations of this work, the initial temperature and pressure conditions at specific domains were computed after iSALE (impact-Simplified Arbitrary Lagrangian Eulerian) impact-physics simulations (Collins et al., 2016; and references therein, including previous versions of the code). Then, temperature and pressure distributions were introduced in the form of contours within the computational grid of HT 3. The governing equations of HT3 were then calculating the thermodynamic state of the fluid under both single and two-phase conditions. Computations for the evolution of thermodynamic gradients (enthalpy, pressure, thermal conductivity, viscosity, density, flux) after each pressure-enthalpy pair were then performed in every time-step and for every computational cell of the HT 3 grid (4365 cells in total). Hence, the program solved the mass and energy conservation equations for every single cell and time step as defined in the boundary conditions of the model. The final step in the computational process was to simulate the water (liquid, steam, super-critical) mass flux vectors and temperature distribution in the lithological medium.

The spatial gradients in the EOS were discretized via the following finite-difference algorithm which includes the mass and energy conservation equations:

$$\left.\begin{aligned}&\partial[\Phi S_w\rho_w + \Phi S_s\rho_s]/\partial t - \nabla\bullet[kk_{rs}\rho_s/\mu_s \bullet (\nabla P - \rho_s g\nabla D)]\\&-\nabla\bullet[kk_{rw}\rho_w/\mu_w \bullet (\nabla P - \rho_w g\nabla D)] - R_m = 0\end{aligned}\right\}\quad \text{Eq. (2.1)}$$

$$\left.\begin{aligned}&\partial[\Phi S_w\rho_w H_w + \Phi S_s\rho_s H_s + (1-\Phi)\rho_R H_R]/\partial t\\&-\nabla\bullet[kk_{rs}\rho_s H_s/\mu_s \bullet (\nabla P - \rho_s g\nabla D)]\\&-\nabla\bullet[kk_{rw}\rho_w H_w/\mu_w \bullet (\nabla P - \rho_w g\nabla D)]\\&-\nabla\bullet(K_m\nabla T) - R_H = 0\end{aligned}\right\}\quad \text{Eq. (2.2)}$$

where Φ: porosity, S_w: water saturation and S_s: solid saturation ($S_{vol} = S_w + S_s = 1$), ρ: density, t: time, k: intrinsic permeability, k_r: relative permeability ($0 \leq k_r \leq 1$), μ: dynamic viscosity, P: pressure, g: gravitational acceleration (3,721 m/s² for Mars), D: depth, H: enthalpy, K_m: medium's thermal conductivity, T: temperature, R_m: mass source/sink flow rate and R_H: energy source/sink flow rate. The subscript letters w, s, and R denote liquid water, steam, and the rock medium, respectively. Hayba and Ingebritsen (1994) refined the Newton-Raphson (N-R) iteration technique for the HT code by developing an algorithm-system of linear equations which can handle the fully coupled and nonlinear equations 2.1 and 2.2 via a 3D N-R iteration solver.

The HT 3 code computes lithostatic pressure as the dependent variable for fluid flow, since potentiometric-head function is impertinent to density fields that depend on temperature. Eq. 2.3 describes the water-component flow equation (after Faust and Mercer, 1979; Huyakorn et al., 1983; Huyakorn, 2012) that derives from the conservation of water mass in a volume element, and which is related to Darcy's law for multiphase flow through a porous medium in HT 3 (incorporated to the HT code by Kipp et al. (2008)):

$$\left.\begin{aligned}&\frac{\partial}{\partial t}[\phi(\rho_w S_w + \rho_s S_s)] - \nabla\cdot\frac{\mathbf{k}k_{rw}\rho_w}{\mu_w}[\nabla p + \rho_w g\hat{\mathbf{e}}_z]\\&-\nabla\cdot\frac{\mathbf{k}k_{rs}\rho_s}{\mu_s}[\nabla p_g + \rho_s g\hat{\mathbf{e}}_z] - q_{sf} = 0\end{aligned}\right\}\quad \text{Eq. (2.3)}$$

where e_z: the unit vector in the z-coordinate direction (dimensionless), q_{sf} : flow-rate intensity of a fluid-mass source (kg/s - m^3), p_g: fluid pressure in the gaseous phase (bar/Pa/atm), p: fluid pressure in liquid phase (bar/Pa/atm), k: porous-medium permeability tensor (m^2), g: gravity acceleration (applied for Mars in this work: 3,721 m/s^2), and subscript letters w and s denote water in its liquid and gas states, respectively. S_p: saturation of water in state p, with p = w (water) or p = s (steam), k: porous-medium permeability tensor (m^2). The interstitial or pore velocity (v_p) for water in state p is obtained through HT 3 from Darcy's law:

$$\mathbf{v}_p = -\frac{\mathbf{k}k_{rp}}{\phi S_p \mu_p}[\nabla p + \rho_p g \hat{\mathbf{e}}_z] \qquad \text{Eq. (2.4)}$$

The partial-differential equation of thermal energy transport in HT 3 derives from Faust and Mercer (1977) and Huyakorn et al. (1983) and is conditioned by the conservation of enthalpy in both the liquid and solid states of the porous medium in a volume element of the simulated domain. The following equation (Eq. 2.5) couples the rate of enthalpy change of a fluid and porous-medium to the net conductive enthalpy flux, to the net advective enthalpy flux, and to the heat source. Hence, the equation of thermal energy transport is formulated in HT 3 for a unit volume containing liquid, gas, and solid phases, and enthalpy is a derived property containing both internal energy and flow energy (Kipp et al., 2008):

$$\left.\begin{aligned}&\frac{\partial}{\partial t}[\phi(\rho_w h_w S_w + \rho_s h_s S_s) + (1-\phi)\rho_r h_r] - \nabla \cdot K_a \mathbf{I} \nabla T \\ &+ \nabla \cdot \phi(S_w \rho_w h_w \mathbf{v}_w + S_s \rho_s h_s \mathbf{v}_s) - q_{sh} = 0\end{aligned}\right\} \qquad \text{Eq. (2.5)}$$

where h: specific enthalpy of the fluid phase (J/kg), h_r: specific enthalpy of the porous matrix solid phase (rock/sediment; J/kg), ρ_r: is the density of the porous matrix solid phase (rock or sediment; kg/m^3), K_α: effective thermal conductivity of the bulk porous medium (combined liquid, gas, solid phases; W/m - °C), I: identity matrix of rank 3, T: temperature (°C), q_{sh}: flow-rate intensity of an enthalpy source (W/m^3).

Based on the method of general conjugate residuals (GMRES; Kipp, Hsieh and Charlton, 2008), the iteration technique which solves equations 2.1 – 2.5 was further refined in the development of HT 3. Thus, the GMRES solver is a new functional characteristic of the HT version 3 code which is over 10 times faster for solving this problem than the original HT code. During the simulations via the older solver, the nonlinear behavior of the equations led to non-convergent conditions and required several adjustments for the simulations to continue through the entire computing time needed for each scenario. Further details on the equations of state, that were also used in this work, are provided in the HTI - v.3 user's manual (USGS;). The HT software includes and operates through three simple components: the Fortran source code - script, the HT preprocessor, and the HTI postprocessor. The Fortran script or/and the preprocessor are used for the data input, and the definition of the boundary conditions and parameters of a model. Generally, the Fortran script should be preferred when trying to produce a higher resolution simulation. The HTI postprocessor generates the output data, displays the results, and controls the processing of the simulations. The revised HT code is enhanced via specific advancements and updates on its source script that are provided by the United States Geological Survey (USGS).

Preliminary modifications to both the pressure (e.g., 0.007 bar) and temperature range (0 °C – 2300 °C) were conducted in this research to investigate the hydrothermal response of the simulated environments under minor changes in the EOS. But the benchmarking tests indicated that no changes occur to the patterns of hydrothermal circulation in the Martian crust, when an initial $p_{surface}$ = 0.007 bar versus an initial $p_{surface}$ = 0.5 bar are used. Accordingly, when the initial temperature in an impact-induced or magmatic induced hydrothermal environment exceeds the temperature of 1200 °C (e.g.: $T_{initial}$ = 2000 °C) negligible differences are observed, and the thermodynamic evolution of the system does not exhibit differences in the lifetime of hydrothermal circulation. Similar implications were also obvious in the work of Abramov and Kring (2004; 2005; 2007) that experimented with similar extensions of the temperature limits of the code. These effects should be treated as artefacts of the simulations, and so, further software development research is needed to fix such artefacts. Unfortunately, this has not been possible within the timeframe of this PhD research. The current developers of the code in the USGS are, however, willing to solve this issue and expand the thermodynamic range of the EOS in the near future.

Fluid flows of T > 500 °C are characterized as super-critical mass fluxes and 2-phase (water-steam) mass fluxes. High precision microscopy (nanoscale) analyses of Martian meteorite samples (NWA 8159 and Lafayette) were additionally performed in this work to identify mineral assemblages that may be indicative of hydrothermal alteration in the environments of origin of these basaltic rocks from Mars (to be mentioned in the following sections). Subsequently, simulations for several thermodynamic processes that might have affected these ancient basaltic environments on Mars were performed via the HT v.3 code, and the constructed models were then compared with findings of mineralogical analyses of the two Martian samples (shergottite: NWA 8159, nakhlite: Lafayette).

Starting from the initial physical parameters of the simulations, the input conditions were defined via Fortran programming and the HT interactive programming environment. A geological setting of a 200 km horizontal distance and a maximum depth of 10 km from the surface of planet Mars were designed in 2D. For the 3D model a 200 x 200 x 10 km^3 grid was programmed. The code's gravitational acceleration value was decreased by 62% in all simulations (according to Abramov and Kring, 2005) to account for the gravity acceleration on Mars (3,721 m/s^2).

Gravity poses a significant control on the permeability and porosity of the rocks of a planetary crust. The number of fractures decreases with depth due to the increase of the geostatic gradient and so, permeability in these models decays exponentially with depth similarly to porosity (Melosh, 1989). Moreover, porosity and permeability are the factors dictating the hydrodynamics of a geological system. Due to the lower gravity on Mars, fractures should reach a 2.5 - 3.0 times greater depth than on Earth (Abramov and Kring, 2005). Thus, permeability on Mars decreases far more gradually with depth than on Earth. Porosity in the models of this work decreases exponentially with depth, accounting for the closing of pore spaces by lithostatic pressure, following the approach suggested by Binder and Lange (1980) for the lunar crust, which I also adopted for the Martian crust in this work:

$$\Phi(z) = \Phi_0 \exp(-z/K), \qquad \text{Eq. (2.6)},$$

where Φ_0 is surface porosity (20%) and K is the decay constant which scales with gravity. The decay constant is 1.07 km for Earth and 2.80 km for Mars (Clifford, 1993). The depth z is measured with respect to the assumed topography. Permeability is also a function of temperature, approximating the effect of the brittle/ductile transition at about 360 °C (Foumier, 1991) by log linearly decreasing permeability with increasing temperature between 360 °C and 500 °C, described by the following set of equations (Eq. 2.7):

$$k(z) = k_0 \exp(-z/K) \quad T < 360\ °C \qquad T < 360\ °C$$
$$\log k(z, T) = [[\log k(z) + 11 / 140] \times [(500 - T)]] - 11 \qquad 360\ °C \leq T \leq 500\ °C$$
$$k = 10^{-23}\ m^2 \qquad T > 500\ °C \qquad \text{Eq. (2.7).}$$

Thus, reverse modelling techniques applied on the sets of equations 2.6 and 2.7 for the permeability and porosity of these Martian samples via the HTI code could also suggest the depth at the Martian crust where these basalts were emplaced and affected by aqueous flows and hydrous alteration. For all simulations, the top boundary of the simulative grid was programmed to represent the icy ground – Martian atmosphere boundary (T_{min} = 0 °C). HT cannot currently reach temperatures below 0 °C, as the convergence thermodynamic criteria cannot be satisfied during a computational run with $T_{surface} < 0$ °C, and this leads to the unsuccessful termination of a simulation.

The thickness of water-ice is computed no greater than 2m, and the average thickness of the upper regolith is circa 100 meters in these simulations (after Gilmore, 1999; Schwenzer et al., 2012). The physical and chemical properties of the rocks beneath the regolith represent those of permeable basaltic and brecciated rocks. Deeper rock units comprise low permeability ($k = 10^{-18}$) basalts and gabbroic rocks ($k = 10^{-21}$), at a depth of 10 km. Precipitation and runoff rates are adjusted to 0.5 and < 0.1 mm/day for this early Martian environment, respectively (Ramirez et al., 2020). The basal heat flux was adjusted to a 10 km depth and was programmed at 17.5 mW/m^2 (T_{max} = 175 °C) for low temperature hydrothermal scenarios. The basal heat flux by a plutonic source (at a depth of 10 km) in moderate (360 °C ≤ T ≤ 500 °C) and high (T_{max} > 500 °C) temperature scenarios was programmed at 30 mW/m^2 and 50 mW/m^2, respectively. The geothermal gradient of the setting is 17 °C/km for both sets of simulations. The use of a 25 - 50 °C / km geothermal gradient for the high temperature scenarios (where T_{max} > 500 °C)

would be erroneous, as such a range of geothermal gradients has never been reported or suggested for hydrothermal systems on Mars. Additionally, the open-system thermodynamic equations of the code that physically describe in this case the cold and semi-arid surface and sub-surface of Mars (z < 1km), where $T_{surface}$ = - 20 °C and T_{1km} = 17 °C, cause computational divergence when the geothermal gradient is greater than 25 °C/km.

The boundary conditions for the physical properties of all rock units that comprise the simulative grid of the putative Martian geological setting in my HTI computations are shown in table 2.1 (below). All physical properties of the rocks, including their permeability and porosity values, were adjusted according to detailed catalogues of the petrophysical characteristics of fractured rocks in highly pressurized impact-induced, or volcanic settings, provided by Abramov and Kring (2004; 2005; 2007), Lamur et al. (2017) and Haffen et al. (2017). Finally, the thermodynamic models of Connolly et al. (2009) were adopted to investigate the hydrothermal response of the lower crustal rocks and the thermodynamic behavior of the Martian asthenospheric mantle.

Additionally, for the impact-induced thermodynamic scenarios, post-impact temperature distributions were determined analytically in the code (script), or defined and benchmarked graphically by trial-and-error in the HT 3 Interactive preprocessor (parameterization interface). Specifically, when the analytical expressions of post-impact temperature distribution within the simulative environment were leading to computations that would not satisfy the convergence thermodynamic criteria (as specified in HT 3; for more detail, please see the HT v.3 guide, § 3.6 (pp. 17 – 22: Equation Solution: https://pubs.usgs.gov/tm/06A25/pdf/TM6-A25.pdf.)), then the simulations were unsuccessfully terminated. In such cases, the algorithm computations for the initial post-impact temperature distribution were either underestimating or overestimating temperature values in at least one computational cell of the grid. Eventually, this would lead to at least one temperature - enthalpy profile being in non-convergence with other thermodynamic properties such as the geostatic gradient, post-impact shock pressure or fluid pressure. Hence, an auxiliary method in this numerical modelling work via which initial post-impact temperature distribution was defined, was graphically, via the use of both the graphical interface (HTI preprocessor) and by using the analytical equations. In all constructed simulations of this work, both analytical

expression calculations (through the HT 3 code), and trial-and-error definitions (through the HT 3 graphical interface) were made to accurately determine and benchmark the initial post-impact temperature distribution in each scenario.

The initial shock-induced heating in the simulative grid was computed by the Murnaghan equation of state (eq. 2.8) for specific waste heat (ΔE_W; Kieffer and Simonds, 1980):

$$\left.\begin{aligned}\Delta E_w = \frac{1}{2}\left[PV_0 - \frac{2K_0V_0}{n}\right]\left[1-\left(\frac{Pn}{K_0}+1\right)^{-1/n}\right] \\ + \frac{K_0V_0}{n(1-n)}\left[1-\left(\frac{Pn}{K_0}+1\right)^{1-(1/n)}\right]\end{aligned}\right\} \text{ Eq. (2.8);}$$

where P: peak shock pressure, K_0: adiabatic bulk modulus at zero pressure (193 Kbar for Martian basaltic rocks; after Schwenzer et al. (2012)), n: the pressure derivative for the bulk modulus of Martian basalt (5.5), and V_0: specific uncompressed volume ($1/\rho_0$). The above parameters have already been used and tested for impact-cratering processes on Mars by Rathbun and Squyres (2002), Abramov and Kring (2005), and Schwenzer et al. (2012). The post-impact temperature distribution in the setting is initially calculated by equation 2.8 and then divided by the heat capacity of the target rock of each scenario (e.g., basalt: 1000 J/Kg×K; please see table 2.1). The computed geothermal gradient of the Martian crust (with experimental range values: 17 °C / km to 50 °C / km) was also added to the shock-generated heat in each case (according to the methodology followed by Schwenzer et al. (2012)). In all impact cratering simulations, shock pressure (P) decreases with distance r from the impact centre, and rapidly within seconds after the impact. The relation between impact-shock pressure and impactor radius has been determined by Pierazzo and Melosh (2000) via the following equation:

$$P = A\left(\frac{r}{R_{pr}}\right)^{-k} \qquad \text{Eq. (2.9);}$$

where R_{pr}: projectile's radius, k: decay exponent, and A: pressure at r = R_{pr}. The decay exponent k is expressed as a function of impact angle (Pierazzo and Melosh, 2000) and velocity (Ahrens and O'Keefe, 1987). Hence, k can be calculated by the following relation:

$$k \approx -0.625 \times \log(U) - 1.25; \qquad \text{Eq. (2.10);}$$

where U: impact velocity (km/s) (Ahrens and O'Keefe, 1987; Schwenzer et al., 2012). Furthermore, A in equation 2.9 has been thoroughly investigated and established by Collins et al. (2002):

$$A = \frac{\rho v_i^2}{4} \qquad \text{Eq. (2.11);}$$

where ρ: impactor and target density (adjusted to 2800 – 3300 kg/m^3 in computational experiments of this work, and by following the methodology of Abramov and Kring (2005) and Schwenzer et al. (2012)), v_i: impact velocity (km/s). Eventually, a density of 3000 kg/m^3 was used for the larger impact craters (D = 100, 200 km), and a density of 2900 kg/m^3 seemed to fit better the impact cratering model for the smaller (D = 10 km) crater on Mars (Pierazzo et al., 2005; Ivanov and Pierazzo, 2011).

Furthermore, impact-generated melt is calculated by equation 2.12, which uses the geometric mean of melt volume formulas, firstly introduced by Croft (1985) and Kring (1995), and refined by Abramov and Kring (2005) for Martian impact craters:

$$Vmelt = 1.23 \times 10^{-8} \frac{\rho_P}{\rho_t} \times g^{0.18} \times D_{tc}^{0.83} \times D_{pr}^{2.35} \times v^{1.63} \times sin^{1.63}(\theta) \qquad \text{Eq. (2.12)}$$

where, ρ_p: density of the projectile (2900 – 3300 kg/m^3), ρ_t: density of the target (2700 – 3000 kg/m^3), g: acceleration due to gravity on Mars (3.72 m/s^2), D_{tc}: transient crater diameter, D_{pr}: projectile diameter, v: impact velocity (7000 m/s), and θ is the impact angle (45º). Numerical impact cratering experiments performed in this work computed an impact-generated melt volume (V_{melt}) of 3970 km^3 in the 200-km in diameter crater, and a melt volume of 952.8 km^3 in the 100-km in diameter crater on Mars. Finally,

transient crater diameter in this work is computed according to the methodology followed by Schwenzer et al. (2012), which utilizes the Pi-scaling laws of Holsapple and Schmidt (1982), and Schmidt and Housen (1987):

$$D_{tc} = 1.16 d^{0.78} v_i^{0.44} g^{-0.22} \qquad \text{Eq. (2.13);}$$

where d: impactor diameter, v_i = 7000 m/s, and g: acceleration due to gravity on Mars (3.72 m/s^2). The rim-to-rim diameter of each crater is calculated after the scaling laws of Melosh (1989), and its refined expressions by Abramov and Kring (2005):

$$D = 0.91 \frac{D_{tr}^{1.125}}{D_Q^{0.09}} \qquad \text{Eq. (2.14);}$$

where D: rim-to-rim diameter of the final crater, D_{tr}: rim-to-rim diameter of the transient crater, D_Q: simple-to-complex transition diameter (= 8.4 km for Mars, after Abramov and Kring (2005)). This methodology on calculating crater diameter (eq. 2.13 – 2.14) and the initial post-impact thermodynamics (eq. 2.1 – 2.12) has already been tested and benchmarked by Abramov and Kring (2005), and Schwenzer et al. (2012), and is thereby utilized respectably in the numerical models of this PhD research.

The HYDROTHERM code (version 3.2.0) is freely available, and its components and installation instructions can be downloaded from the USGS website: (https://volcanoes.usgs.gov/software/hydrotherm/). In the USGS website you can find the HT source code version 3.2.0 as a zip file (2.5 MB), which operates as a Fortran program. The HYDROTHERM Interactive software (PC Windows version 3.2.0) which is an executable file containing a graphical user interface can also be downloaded from this website, and it can used used on any computer platform running the Microsoft Windows operating system. Extensions and executable examples of the HT code can also be downloaded from the host website of HT 3. More importantly, a thorough analysis on the finite-differential equations for flow and heat-transport, on the property functions and transport coefficients, and on the boundary conditions of the HT version 3 code can be accessed here: https://pubs.usgs.gov/tm/06A25/pdf/TM6-A25.pdf.

Table 2.1. HTI initial conditions and input of parameters for the simulations of the aqueous and hydrothermal activity in the Martian crust.

Petrophysical Properties	**Lower Crustal Rocks**	**Basalts**	**Melt Rocks**	**Sediments**	**Regolith**
Permeability (k) {m^2}	k_z = f(d,T), k_x = f (d,T)	k_z = f(d,T), k_x = f (d,T)	k_z = f(d,T), k_x = f (d,T)	k_z = f(d,T), k_x = f (d,T)	k_z = f(d,T), k_x = f (d,T)
Porosity (φ) {%}	φ = f (d,T)	φ = f (d,T)	φ = f (d,T)	φ = f (d,T)	φ = f (d,T)
Thermal Conductivity {W/m·K}	2.7	2.5	2.4	2.3	2.3
Specific Heat Capacity {J/kg·K}	1200	1000	1000	900	900
Density {kg/m^3}	2750	2600	2500	2300	2300
Surface Permeability {m^2}	9.00E – 21	9.00E - 18	9.00E - 17	9.00E - 15	9.00E - 14
Surface Porosity ($\varphi_{surface}$)	0.5 %	2.0 %	5.0 %	20.0 %	25.0 %

2.1.2 Impact-Physics (iSALE) Simulations for the Parameterization of the HT 3 Models.

To simulate the impact-induced hydrothermal activity on ancient Mars via the HT 3 code, the initial thermodynamic distributions within the impact craters after their formation were computed via the iSALE-2D shock physics code (Amsden et al., 1980; Collins et al., 2004; Wünnemann et al., 2006). The iSALE source code and all programming components used in this work can be accessed here: https://github.com/isale-code. Although the input thermodynamic conditions could be putatively determined via HT 3, iSALE-2D was used to accurately constrain and indicate the most representative initial temperature and pressure parameters of the impact-generated hydrothermal systems on Mars. According to the methodology suggested by Manske et al. (2021), who simulated via iSALE-2D the generation of melt during basin formation for early Mars, a cylindrical geometry and a resolution of 12016 cells ($17 \times 15^2 \times \pi$) were applied for the simulative grid. A spherical impactor with a resolution of 8 cells per projectile radius (8 CPPR, in analogy to final crater's size through iSALE) was considered for each impact scenario, as such resolution can still yield reliable results for the calculations of melt volumes (after Manske et al., 2021; Wünnemann et al., 2008). The impact processes were simulated by using the ANEOS set of equations (Analytical Equations of State) which were developed for computations in hydrocodes and included in iSALE (Stewart et al., 2020). The computational methodology for melt production in impact simulations has been thoroughly described and effectively applied in the newest version of the iSALE code (Pierazzo et al., 1997; Wünnemann et al., 2008; Emsenhuber et al., 2018; Manske et al., 2021). Specifically, melt production computations utilize the peak shock pressure which determines the increase in entropy upon impact-generated compression, and that yields post-shock temperatures after the crater's formation (Manske et al., 2021). Through this way, the post-impact temperature distribution for each cratering setting could be determined.

iSALE computations in this PhD research focused specifically on the temperature distribution in the geological environment after the impact, so that the thermal constraints of iSALE could later be used as quantitative input datasets for the hydrothermal simulations. For this reason, iSALE numerical models of this work did not focus on reproducing the exact morphology, excavation or/and crater collapse processes of known impact-structures on Mars, as this would require extensive computational investigations which would not be concluded within the time-frame of this research (as such objectives would comprise another entire research project). Furthermore, simulating large impact events and reproducing the formation and morphology

of observed simple or complex impact craters is a rather difficult research task due to stress-strain uncertainties and time-dependent factors that affect the transient crater's formation along the cavity wall (Elbeshausen et al., 2009).

In this research, 20-25 impact simulations via iSALE were performed for each of the three simulated Martian impact structures (10-km, 100-km, 200-km; as follows in §3.1). From those sets of numerical experiments, the most accurate ones were determined based on the least run-time errors and imbalances in the governing equations at each iteration step of the solver, and according to the satisfaction rate of the convergence criteria of the code. On average, 15 simulations for each impact-structure were terminated unsuccessfully due to intolerance of the convergence criteria. Hence, the iSALE computations presented in this PhD thesis are those of the highest accuracy and resolution that could be achieved within the time frame of this project.

The models focused on describing post-impact melt generation and thermal distribution based on mantle convection and crustal thickness models developed by Plesa et al. (2016), and as also used by Manske et al. (2021). Based on previous findings from hydrocode simulations for early Mars (Abramov et al., 2012; Abramov and Mojzsis, 2016; Plesa et al., 2016; Manske et al., 2021), a thin Martian crust model with a thickness of 45 km and its associated thermal profile were selected for the iSALE simulations of this work, as such boundary thermodynamic conditions should represent better the basaltic crust of Mars (Abramov et al., 2012; Abramov and Mojzsis, 2016).

Impactor velocity was adjusted to 17 km/s and target materials were described by the ANEOS for basalt and dunite. The upper 15-20 km of the Martian crust in the iSALE models of this work represent basalt, (including a basaltic-regolithic surface), and the lower crustal domains (depth $\geq$ 20 km) are physically represented by dunite. Furthermore, water-ice deposits were introduced for the Martian surface and subsurface with a thickness of 100 – 200 m, and a surface water column with a maximum depth of 30 m was also utilized for the lithostratigraphic setting (after Dickeson and Davis, 2020; Sokolowska et al., 2022). A dry case for the basaltic crust was not used in this work, as previous reports indicate that the presence of such small volumes of $H_2O_{(s)}$ or/and $H_2O_{(l)}$ deposits can moderately affect transient crater's morphology and volume of ejecta blanket. Such findings do not associate with the objectives of this work, as the latter focus on determining the thermal distribution within the impact-induced geological setting. More importantly, over time and during a large crater's (diameter $\geq$ 10 km)

modification and collapse (3-10 minutes after the impact), water and ice deposits are affected by either sublimation or evaporation depending on their location. Then, after the transient crater's modification, the final depression known as a complex impact structure forms (Melosh, 1989; Ivanov, 2001). Hence, the presence of small volumes of water or/and ice in hydrocode simulations does not indicate appreciable differences in the post-impact thermodynamic status of the computational grid (Abramov and Kring, 2005; Ivanov and Pierazzo, 2011; Abramov et al., 2012; Abramov and Mojzsis, 2016). Therefore, the aforementioned geological settings were selected for the iSALE impact scenarios for Mars. The results of the constructed iSALE models were then used to define the initial thermodynamic distributions within the HT 3 computational grids, and to subsequently describe the induced hydromechanics of impact-generated Martian hydrothermal systems.

2.2 The PHREEQC code: A Program Suitable for Modelling Water – Rock Reaction Pathways.

The PHREEQC code (version 1: Appelo and Parkhurst, 1998; version 2: Parkhurst and Appelo, 1999; version 3: Parkhurst and Appelo, 2013; Appelo et al., 2014) is a computer program developed in C and C++ programming languages that simulates a wide range of water – rock reactions. The code includes two ion-association aqueous models, a Pitzer specific-ion-interaction aqueous model, and the SIT (Specific ion Interaction Theory) aqueous model (USGS report, techniques and methods, 6-A43, 2013). PHREEQC is eligible to compute the equilibrium state of solid and aqueous species in a fluid, the saturation of the fluid in relation to minerals. Additionally, the code conducts numerical models for reversible or irreversible reactions in an open or closed thermodynamic system, within a specific thermal range or polythermally (GWB; Bethke, 1996). In this work, PHEEQC v.3 (Parkhurst and Appelo, 2013) was utilized for simulating geochemical reaction pathways and thermodynamic equilibrium states in the Martian basaltic crust, under the influence of impact-induced and magmatic-induced aqueous circulation.

The initial conditions in a PHREEQC simulation involve equilibrium thermodynamics of an aqueous fluid interacting with minerals and gases (Martian basalt interacting with a fluid of seawater composition (after Millero et al. (2008) in this work). The initial thermodynamic system can be precisely defined, and the simulation is initiated by computing the system's equilibrium state. The code then calculates temperature and pressure changes (by processing the input from HT 3 simulations, in this research), and changes the water-rock system by adding or removing reactants. In this way, the simulation calculates the evolution of the varying compositions of minerals and aqueous fluids and this process is the reaction path (Parkhurst and Appello, 2013). By utilizing the aforementioned water – rock reaction pathway models, PHREEQC can perform:

- mineral and aqueous species computations related to the saturation of the environment (as produced via the HT simulations in this work);

- 1D aqueous solution transport simulations with both reversible and irreversible geochemical reactions. The PHREEQC models in this work focused on computations for the solid-liquid-gas species produced after water-rock reactions and mineral dissolution. The reactions in PHREEQC can also be kinetically controlled and influenced by thermodynamic (pressure, temperature, enthalpy) changes.

- Inverse modelling and benchmarking tests with other publicly available USGS codes and softwares (such as the HT 3, and the VSDRTI code), that have been used in this PhD research. This feature of PHREEQC contributed essentially to assessing the validity of the HT 3 simulations, and the water-rock reaction pathways (including habitability computations), and vice versa.

The PHREEQC code is publicly available and can be downloaded from: https://www.usgs.gov/software/phreeqc-version-3. For further information about how the code works please visit the USGS website and the analytical report issued by (Parkhurst and Appello, 2013).

In this work, the PHREEQC initial conditions were defined by the computed thermodynamic values of the HT 3 simulations. The putative Martian basaltic rock compositions that were affected by impact-induced or magmatic-induced fluid flows, were also included in the initial

settings of each simulation. The geochemical reaction pathways between Martian basalts, subsurface and surface fluids were computed by using a polyhedral approach, in true kinetics mode. The computations allow to examine (beyond a plethora of geochemical processes and products) the roles of substrate compositions, the rates of primary and secondary mineral dissolution and more significantly, the hydrogen (H_2 aq) and methane (CH_4) release, as a product of the basaltic glass - fluid (initial fluid: saline water) interactions within the shallow depths of the ancient Martian crust.

For modelling efficiency, the reactions of a fluid (e.g.: aqueous fluid of seawater composition, after Millero et al. (2008)) with a rock (e.g.: Martian basalt), the dissolution and precipitation of minerals, the dissociation and association of aqueous or surface complexes, and the potential reduction and oxidation (redox) reactions were simulated. The PHREEQC code is powerful in tracing such reactions, in which kinetic rate laws control the time rate at which these reactions proceed. It uses a simple rate law to compute mineral dissolution and precipitation which takes the form:

$$r_k = A_s \, k_+ \, (1 - Q/K) \qquad \text{Eq. (2.15).}$$

In Eq. (2.15), r_k is the reaction rate (mol/s, positive for dissolution), A_s is the mineral's surface area (cm^2), k_+ is the rate constant (in mol/cm^2 sec), and Q and K are the activity product and equilibrium constant for the dissolution reaction, respectively. By this equation, a mineral precipitates when supersaturated, and dissolves when it is undersaturated at a rate that depends on its rate constant and surface area. PHREEQC calculates the surface area (in cm^2/g) for each kinetic mineral. The value of the rate constant, or an activation energy E_A and pre-exponential factor A, for the Arrhenius equation were also incorporated to the code:

$$k_+ = A \, e^{-E_A / RT_K} \qquad \text{Eq. (2.16);}$$

so that the program can determine k_+ as temperature varies. Here, R is the gas constant and T_K is absolute temperature in Kelvins. Kinetic rate laws can be set, for minerals swapped into the initial system and in equilibrium with the fluid. The same can be done also for minerals set as reactants. However, a kinetic mineral must exist in some amount; otherwise, its surface area will be zero and it will never precipitate. The time span, the rate constants for minerals (in

mol/cm^2 sec) and a specific surface area (in cm^2/g) for each mineral can then be defined. After adjusting these parameters in a kinetic reaction path model, the simulations may commence.

In this way, kinetic reaction path models were constructed for putative ancient Martian geological settings. The initial thermal conditions of each reaction model were determined in PHREEQC according to the 250-bar thermodynamic database compiled from SUPCRT92 (Johnson et al. 1991) to describe the properties of Martian basaltic rocks. The output of these simulations constrained further the simulation period for each PHREEQC reaction path. Specifically, the mean curve of the spatiotemporal thermal distributions of the HYDROTHERM simulations - results was plotted and assigned to reflect the initial temperature conditions for each geochemical reaction path model. The simulations performed through the code focused on the geochemical reactions of the basaltic glass and olivine dissolution. A seawater composition (Millero et al., 2008; table 2.2) was used for the initial hydrothermal fluid in equilibrium state, and the basaltic glass was computed as the reactant (kinetic glass; table 2.2). Finding the exact and true equilibrium state of seawater though is somehow a philosophical pursuit because mineral precipitation from seawater is too slow to observe. However, the input parameters account for its generally accepted composition and state.

Bach (2016) provided a kinetic reaction path model in which basaltic glass and olivine dissolution were assigned as the rate limiting steps through REACT code computations of the GWB software (which is essentially similar to, and can operates via the PHREEQC code). In the research work by Bach (2016), the basalt glass was set as the reactant and the seawater as the initial fluid in a thermodynamic equilibrium state. Furthermore, Bach (2016) provided equilibrium thermodynamic calculations of potential hydrogen supply by the basaltic glass dissolution, and then estimated the hydrogen demand by hydrogenotrophic microorganisms (after Hoehler, 2004).

The same strategy was followed in this work and kinetic reaction pathways were constructed for modelling the dissolution of mineralogies in the Martian basalt after interacting with a hydrothermal fluid of a seawater composition (table 2.2). For this reason, I used the 250-bar thermodynamic database compiled from SUPCRT92 (Johnson et al. 1991), so that I could calculate the kinetic reaction pathways, in which the Martian volcanic glass governed the rate-limiting step. In the database the mid-ocean ridge basaltic glass has already been included as a

phase, as its thermodynamic properties have been imported via entropy, volume and free energy datasets from Chermak and Rimstidt (1989) and Holland (1989) by using a polyhedral approach (Oelkers and Gislason, 2001). I formulated the 250-bar thermodynamic database by adding an assumed Martian basaltic-glass composition (after geochemical measurements performed by the Mars Exploration Rover Spirit at Gusev crater, and particularly on Adirondack class rocks and on sites/specimen such as Irvine, Backstay, and Wishstone which are indicative of unaltered and aphanitic basaltic rocks from Mars (McSween et al., 2006a; 2006b; Peretyazhko et al., 2018; Thorpe et al., 2022)):

$[Ca_{0.220}\ Na_{0.126}\ K_{0.048}\ Fe^{++}_{0.032}\ Fe^{+++}_{0.052}\ Mg_{0.174}\ Al_{0.318}\ Si_{1.00}\ O_{3.068}]$.

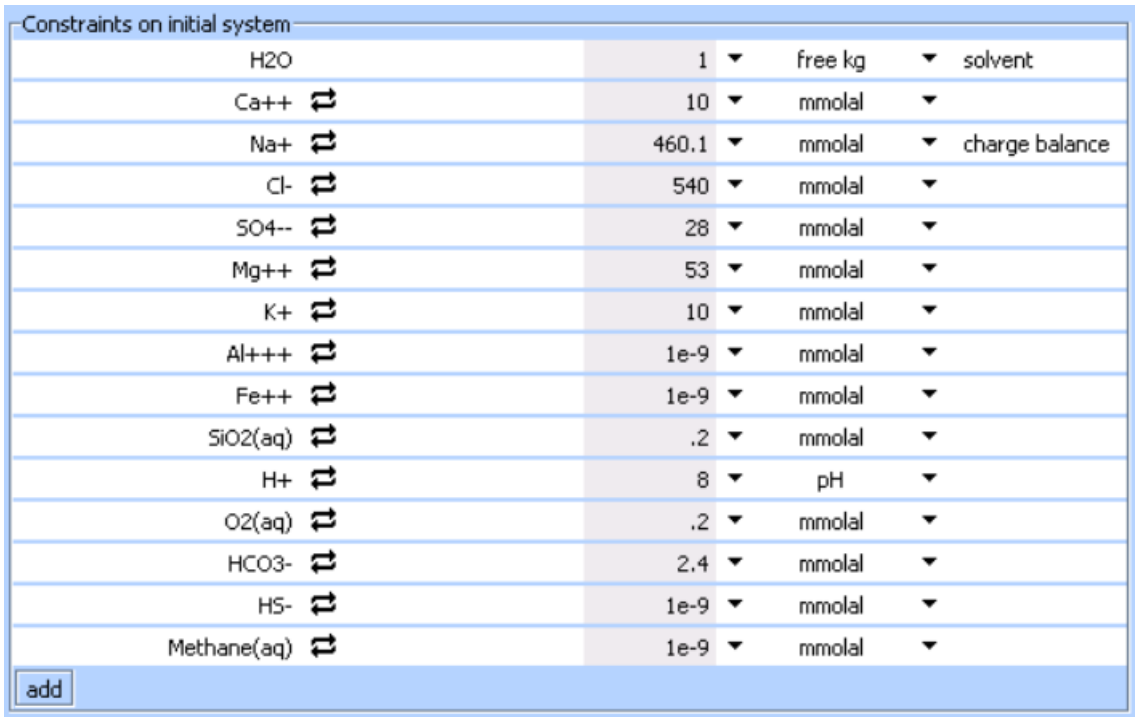

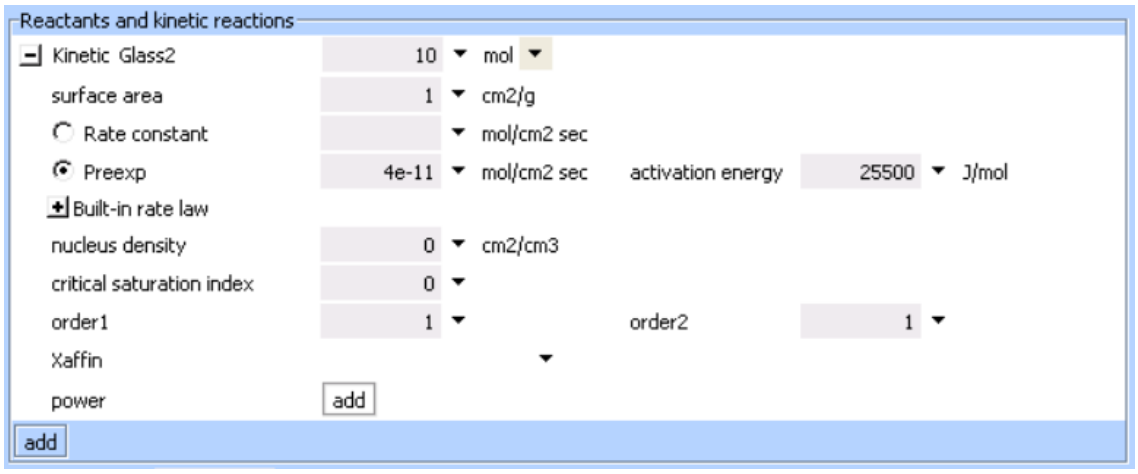

Table 2.2. The initial equilibrium state for the computed hydrothermal fluid in the PHREEQC simulations has been defined with a seawater composition (constraints on initial system: upper domain) via the geochemical reaction pathway interface (REACT). The lower domain (reactants and kinetic reactions) shows the interface via which the thermodynamic parameters for the reactants were defined, and where "Kinetic glass 2" models the Martian basaltic glass composition: [$Ca_{0.220}$ $Na_{0.126}$ $K_{0.048}$ $Fe^{++}_{0.032}$ $Fe^{+++}_{0.052}$ $Mg_{0.174}$ $Al_{0.318}$ $Si_{1.00}$ $O_{3.068}$]. Minimum activation energy (E_A) limits for the geochemical reactions to occur have been adjusted to 25.5 kJ/mol. The exact parameterization and model can be reproduced via both the GWB (Bethke, 1996) and PHREEQC software; and via any other geochemical modelling tool (e.g.: Wolery, 2010) thanks to the user-friendly interface (REACT paths) for defining the initial constraints of the simulative thermodynamic system.

The Arrhenius parameters for the Martian basaltic glass dissolution were adjusted to match the mean elemental composition of terrestrial suevitic and basaltic glass, as provided by Hect et al. (2004; Chicxulub suevitic glass) and Seyfried et al. (2007; mid-ocean ridge basaltic glass), respectively. The Martian basaltic glass dissolution is used as the rate limiting step (boundary proxy) for the dissolution of olivine, apatite and other primary mineralogies; and of any subsequently produced mineral species that the code predicts. A specific surface area (SSA) of 1 cm^2/g was assumed in all kinetics calculations (highest resolution for the geochemical simulations) and serves as an efficient approximation for the SSA of Martian basalts.

2.3 Habitability Simulations based on Hydrothermal (HT 3) & Geochemical Reaction Pathway (PHREEQC) Models.

The central goal of the geochemical reaction path modelling was to provide the equilibrium thermodynamic calculations of potential nutrient production through the Martian fluid (seawater) - rock reactions, and specifically through volcanic glass dissolution. This should then allow the construction of a bioenergetic model able to assess the habitability of these Martian environments. According to this rationale, the habitability can then be determined by

quantifying the mass of nutrients produced from these fluid-rock reactions (hydrogen, methane, ferric iron, nitrate etc.), and the nutrient demand of potential chemolithotrophic microorganisms to sustain their biomass in the subsurface realm of early Mars. This work focuses particularly on the release of H_2 in the subsurface basaltic realm of Mars, as hydrogenotrophic microbes are the most likely microbial species to thrive under extremely low energy, non-photosynthetic and anoxic conditions (Hoehler, 2004; Bach, 2016).

The range of potentially habitable space on Earth, and elsewhere in the solar system, would be greatly expanded by the existence of microbial communities that can be sustained solely by the energy supplied by water-rock chemistry. Such systems should be characterized by low-energy anaerobic conditions and the absence of the photosynthetic process. Hydrogenotrophic communities have been inferred for oceanic basaltic and ultramafic crust, where microorganisms may be supported by H_2 generated during the interaction of ferrous rocks with water (Chapelle et al., 2002; Edwards et al., 2012; Bach, 2016), also for granitic (Kotelnikova and Pedersen, 1997) and mixed mineralogy environments (Lin et al., 2002) where H_2 may be generated through water radiolysis. Hoehler (2004) demonstrated that biological energy requirements are significant in the context of such environments and that they may represent an important constraint on life in the subsurface realm.

For all organisms, free energy Δ_rG must be available at levels equal to or larger than a certain finite minimum, so that it is conserved. All known organisms utilize a common molecule, ATP (adenosine triphosphate), for storing energy and driving cellular energy-requiring processes. Therefore, free energy (Δ_rG) must be present at levels sufficient to drive the synthesis of ATP from ADP (adenosine diphosphate) and thus, to be utilized by life. The minimum energy required to be liberated and stored during metabolism is a fraction (1/n) of the total energy needed to synthesize ATP. The ATP synthesis energy ($\Delta_rG_{ADP\rightarrow ATP}$) stoichiometry of ion release during ATP synthesis (n) and (f) define the minimum free energy that must be available in a given environment, if it is to sustain life (Schink and Stams, 2002):

$$\Delta_rG_{min} = \Delta_rG_{ADP\rightarrow ATP} / n \cdot f \qquad \text{Eq. (2.17).}$$

The quantity Δ_rG_{min} is also referred to as the Biological Energy Quantum (BEQ) and was used as an initial constraint in the bioenergetic computations. The BEQ predicts the favourability of continuous biological activity, just as the Gibbs free energy change Δ_rG predicts the

favourability of chemical processes. Hence, the specific magnitude of the BEQ establishes quantitative boundary conditions on which environments are potentially capable of supporting life, and which are not. But if we are to understand the potential of BEQ to constrain the distribution of life in the subsurface, we need to accurately quantify this value. Though the specific magnitude of the BEQ still remains a question, a combination of theoretical and experimental considerations suggests that the BEQ required for actively growing populations is likely twice as large as that required for static populations in maintenance mode (Hoehler et al. 2001). For actively growing cultures, measured or assumed values for n, f, and $\Delta_r G_{ADP \rightarrow ATP}$ translate to $\Delta_r G_{min} \approx -20$ KJ/mol (Schink, 1997). Considering that n, f, and $\Delta_r G_{ADP \rightarrow ATP}$ may all vary under conditions of energy limitation (Hoehler et al., 2001a; 2001b), Equation 3 yields values of $\Delta_r G_{min} \approx -15$ KJ/mol and $\Delta_r G_{min} \approx -12$ KJ/mol for static and starving populations, respectively (Schink and Stams, 2002).

The maintenance energy (ME) concept suggests that organisms require a certain minimum rate of energy intake to maintain molecular and cellular integrity and function (Morita, 1997). Three levels of ME requirement have been defined, corresponding to differing levels of activity: growth, maintenance and survival. The ME levels are thoroughly explained by Morita (1997). Energy flux requirements have been estimated for natural systems by geochemical modelling, which can infer rates of microbial activity that are too low to measure. This approach though is directly applicable to the issue of life in the subsurface. Price and Sowers (2004) conclude that observed energy flux requirements in populations of natural environments cluster roughly into the three groups suggested by Morita (1997). Moreover, they observed that values of "growth" exceed those of "maintenance" by about three orders of magnitude, and those of "survival" by five or six orders of magnitude.

Temperature is observed to be the most significant parameter affecting maintenance energies in natural systems (Price and Sowers, 2004). The breakdown of biochemical molecules is a chemical process whose rate increases with temperature. The higher the temperature, the more rapid the breakdown of biomolecules, and the greater the required input of maintenance energy to fix the damage (Hoehler, 2004). For any chemical reaction, including the ones requiring ME, it is possible to define an activation energy, which describes the temperature dependence of the reaction rate. Hence, the following equation was then used to calculate the maintenance energy (ME) availability after water – rock interactions in the putative Martian hydrothermal systems:

$$ME = A \cdot e^{-Ea/RT} \qquad \text{Eq. (2.18);}$$

where E_a is the activation energy, R is the universal gas constant, T is Kelvin temperature, and A is an empirically derived constant. At biologically tolerated temperatures, minerals can store a significant free energy potential in the face of a thermodynamic driving force for abiotic reaction. Together, the BEQ and ME requirements define the energetic habitability of a mineral environment, the minimum levels and fluxes of energy that this environment should sustain to support life. Relying on abiotic processes to release the stored energy of mineral assemblages into a dissolved and biologically useful form, the most important mechanisms of this sort is the reaction of minerals with water to produce hydrogen H_2. Several mechanisms exist for producing H_2 in appreciable quantities from a variety of rock types (as provided by Hoehler (2004)). In addition, Bach (2016) suggests that all oceanic crust basement rocks release enough H_2 to support hydrogenotrophic life at low water-rock ratios. Considering further the frequent release of H_2 in geothermal emanations, we may conclude that H_2 is the strongest candidate for supporting subsurface life under anaerobic conditions.

Hoehler (2004) supported that the free energy yield of any chemical reaction depends directly on the activities of the substrates and products involved and calculated the Gibbs free energy yield under ambient conditions. The following formula was introduced to calculate the Gibbs free energy yield in an environment where methanogenesis ($CO_2 + 4H_2 \rightarrow CH_4 + 2H_2O$) occurs:

$$\Delta_r G_{rxn} = \Delta_r G^\circ_{(T,P)} + RT \cdot \ln [\ \{CH^4\} / \{CO_2\} \cdot \{H_2\}^4\ ] \qquad \text{Eq. (2.19);}$$

$\Delta_r G_{rxn}$ is the Gibbs free energy yield under ambient conditions, $\Delta_r G^\circ_{(T,P)}$ is the standard Gibbs free energy change modified to account for ambient temperature and pressure, R is the universal gas constant, T is Kelvin temperature, and $\{v\}$ is the activity. This proves that the energetic habitability of a given chemosynthetic system can be defined in terms of its ability to provide chemical substrates at biologically required levels (activities) and rates. In Equation (2.17), the BEQ requirement specifies the minimum $\Delta_r G_{rxn}$. Moreover, in most environments where methanogenesis for example has been studied, H_2 activities are limiting by six or more orders of magnitude. Then, BEQ requirements for methanogenesis may be defined in terms of a minimum H_2 activity:

$$\{H_2\}_{BEQ} = [\{CH_4\} / \{CO_2\} \cdot \exp [\ [\Delta_r G^\circ_{(T,P)} - \Delta_r G_{BEQ}] / RT]\ ]^{1/4} \qquad \text{Eq. (2.20);}$$

For Martian basaltic settings, the $\Delta_r G_{min}$, $\Delta_r G_{rxn}$, $[H_2]_{BEQ}$ and other species activities were acquired via the PHREEQC simulations, since the reaction path models constructed can compute these values. The final aim of the geochemical - bioenergetic model was to calculate the release of nutrients and their activity, and to evaluate the catabolic energy availability within the subsurface of Mars. This goal was achieved by using the quantitative formulas - equations [Eq. (2.17); (2.18); (2.19); (2.20)] that were described above. The results of the geochemical reaction pathways simulate efficiently the H_2 release generated from the aqueous fluid – basalt reactions on Mars. Eventually, I plotted the processed results of the PHREEQC simulations on the Hoehler (2004) model, that defines the nutrient demand by hydrogenotrophic microorganisms. Hence, the H_2 release/activity in the hydrothermal setting indicates whether the investigated subsurface domain could be habitable for potential hydrogenotrophic communities.

The initial parameterization of the simulations and their results do not consider a hypothetical presence of microbial communities in the Martian crust. Based on the H_2 activity computations, the rate of H_2 production and the thermal range of the Martian subsurface are the indicators about whether these basaltic environments affected by hydrothermalism and by subsequent water-rock reactions and chemical nutrients' production, could support potential hydrogenotrophic microbial communities. In a few words, these geochemical models explore the habitability of hypothesized subsurface and hydrothermal niches on Mars for hydrogenotrophic microbial species.

The general concept of this model is to provide the growth, maintenance, and survival ME requirements of a specific micro-biomass. Therefore, calculations of the log $[H_2]$ activity of any modelled subsurface environment, can be plotted on this diagram and quantitatively compared with the three levels of ME requirement. This method eventually provides a robust assessment on the catabolic energy availability and habitability of any terrestrial and extraterrestrial subsurface environment.

2.4 Analytical Methods

2.4.1 Sample Preparation

One thin-section (sample A: 7.5 × 1.3 mm) and one indium-mounted polished sample (B: 5.0 × 3.5 mm) were prepared from chips of NWA 8159. The first NWA 8159 sample had previously been prepared by mounting in an epoxy block. The second sample of NWA 8159 was mounted in pure indium at the University of Edinburgh to protect against terrestrial water contamination, in anticipation of future hydrogen isotope (D/H) analysis. Both thin sections were coated with 20nm carbon. Furthermore, one more thin section of the Lafayette meteorite (sample C: 4.0 × 2.5 mm) was also prepared by mounting in epoxy blocks and coated with 20nm carbon at the University of Glasgow. The Martian rock samples analyzed in this PhD research originate from the interior of each Martian meteorite and lack fusion crusts.

2.4.2 Scanning Electron Microscopy (SEM)

Energy Dispersive X-ray spectroscopy (EDS) maps and Back-Scatter Electron (BSE) images were collected using a Carl Zeiss Sigma - Variable Pressure - Field Emission Gun - Scanning Electron Microscope (VP-FEG-SEM; fig. 2.1) at the GEMS (Geoanalytical Electron Microscopy & Spectroscopy Centre; previously known as ISAAC) facility of the University of Glasgow to distinguish the aqueously formed minerals in NWA 8159, Lafayette and determine their stoichiometric composition. As well as BSE maps and EDS elemental maps of each sample (using AZTEC software), quantitative EDS data were produced for certain minerals, using the Oxford Instruments INCA software and a silicon drift X-ray detector. However, the NWA 8159 samples were severely altered by carbonate, and the quantitative datasets acquired via the SEM could not formulate reliable interpretations. The carbon-coated thin sections were analysed under high vacuum operating conditions, a probe beam current of 1 nA, an accelerating voltage of 20 kV, and a working distance of 8.5 mm. All the acquired SEM data were calibrated by using the mineral standards of the GEMS centre. SEM imaging, BSE and EDS maps of the samples focused on the bulk rock compositions of NWA 8159 and Lafayette meteorites, and on determining the porosity of the acquired BSE maps via the ImageJ software.

Fig. 2.1. The Scanning Electron Microscope (SEM) used in this PhD research and based in the school of Geographical and Earth Sciences of the University of Glasgow (GEMS Centre).

2.4.3 Porosity Measurements via the ImageJ Software

The ImageJ software was developed by the National Institutes of Health of the United States 35 years ago (previously known as NIH image; Schneider et al., 2012) and has been developing continuously as a pioneering tool for the analysis of scientific images, especially in the field of biomedical, chemical and geological sciences (Collins, 2007; Schneider et al., 2012). Within the realm of geosciences, ImageJ comprises a software with a user-friendly and interactive platform that can provide powerful analysis on determining the porosity of rock samples (Berrezueta et al., 2019; Hu et al., 2023). For the aims of this PhD research, ImageJ was used to determine the porosity of Martian meteorites that were previously analyzed via SEM. In particular, acquired whole-sample BSE (grey-scale) maps of the NWA 8159 and Lafayette thin-sections (NWA 8159 samples 1 and 2, and Lafayette USNM-1505, as described in §2.4.2) were processed through ImageJ workflows suggested by relevant published research (Schneider et al., 2012; Berrezueta et al., 2019; Hu et al., 2023); and via personal communications and tutoring sessions kindly offered by Dr. Joshua Franz Einsle. The rationale behind using ImageJ focuses on determining one of the most important factors that control aqueous circulation in hydrothermal settings; porosity. Therefore, by determining the porosity of the three meteorite samples studied in this PhD research, the accuracy of the numerical constraints that define the hydrothermal models can be significantly enhanced. The porosity

values, as derived via ImageJ processing for the two different NWA 8159 samples (1 and 2) and for the Lafayette sample USN 1505, could therefore inform the input parameters and thermodynamic constraints of the HT models.

The BSE images (tiff) were initially processed in ImageJ by having their scale set, according to the actual size of mineral grains that have been previously analyzed and mapped via the SEM instrument of the GEMS facility. Noise reduction and contrast enhancement filters were then applied on the grey-scale images, to enhance the contrast between the pores and solid matrix and to reduce the noise of the BSE maps. The next step was to adjust the threshold manually. Then, the 8-bit image type was selected for all processed BSE sample maps, before re-adjusting the threshold. The threshold was re-adjusted and computed to identify pore spaces in a red false-colour. After these configurations, statistical geometrical analyses were conducted via the set measurements options of the "analysis" menu-tool. The measurements were configured to calculate the total area of the sample, the fraction of the area defined as porous space, and the Feret diameter (i.e.: the size of a porous domain identified as the size of a particle through the ImageJ code, and computed along a specified direction; subsequently, its size and distribution within the sample could be calculated). Finally, analytical computations of the defined particles (pore spaces) were performed through the "display" tool. The "analyze particles" macro of the software and the "display" tool of the plugin menu allowed the overlay to be shown, and eventually after using the "summarize" macro, the results on the calculated porosity of the sample (φ) could be exported both as a very extensive dataset and summary.

§3 RESULTS

The code HYDROTHERM (version 3 - HYDROTHERM Interactive (HTI); Kipp, Hsieh and Charlton, 2008; firstly developed by Hayba and Ingebritsen, 1994) of the USGS was used in this research to model the hydrothermal activity in a variety of putative volcanic and impact-induced hydrothermal settings on ancient Mars. HYDROTHERM has already been proven a suitable code for modelling convective and conductive water and heat transport in terrestrial and martian impact craters (e.g.: Rathbun and Squyres, 2002; Abramov and Kring, 2004; 2005; 2007; Sanford, 2005).Therefore, in this PhD research I constructed and performed numerical simulations to explore the hydrothermal response in ancient geological environments that may have hosted some appreciable aqueous, and even hydrothermal activity on Mars.

The governing equations used in the updated version of the HYDROTHERM 3 (HT) code are expressions of mass and energy conservation that are posed in terms of pressure and enthalpy. The pressure - enthalpy formulation uniquely specifies the thermodynamic state of the fluid in two-phase conditions, and avoids the difficult numerical problems associated with the critical point (Ingebritsen and Hayba, 1994; as seen in the initial HT code). The code incorporates data from various sources to develop consistent equations of state for conditions ranging from 0 °C to 1200°C and from 0.5 to 10 kbar (50 KPa to 1 GPa). The equations of state are formulated in HT using a standard finite-difference approach. The equations, however, are strongly coupled and highly nonlinear, because the variables of relative permeability, density, and viscosity vary widely with pressure and enthalpy (Hayba and Ingebritsen, 1994). In HT 3, the nonlinear coefficients are treated by iteration (Newton-Raphson solver) that leads to a system of linear equations that are solved iteratively. A three-dimensional iterative technique based on the method of general conjugate residuals (GMRES) is a new functional characteristic of the HT version 3 code, and this new solver is over 10 times faster for solving this problem than the original HT code. Further details on the equations of state that contributed to the computations of this work are provided in the HT v.3 user's manual (USGS; Kipp, Hsieh and Charlton, 2008). The HT 3 package includes and operates through three simple components: the Fortran source code - script, the HT Interactive (HTI) preprocessor, and the HTI postprocessor. The Fortran script and the preprocessor were used in this work for the input parameterization, the definition of the boundary conditions, and the computational settings of all models. In general, the Fortran script should be preferred when trying to produce a higher resolution simulation through

HYDROTHERM. The HTI postprocessor generates the output data, displays the results, and controls the processing of the simulations.

The computational scenarios that follow were constructed similarly to the methodology followed by Abramov and Kring (2004; 2005; 2007), Jõeleht et al. (2005), Sanford (2005), Borović et al. (2019), that have previously constrained the hydrous circulation in a variety of martian and terrestrial geothermal aquifer systems and have suggested the lifetime of the fluid flows therein. The simulations focused primarily on determining the temperature distributions and the associated water-, steam-, supercritical fluid-mass flux, heat flux, pressure and enthalpy in these settings. For all the impact-induced hydrothermal scenarios (HT 3 models), the initial thermal profiles were determined firstly via iSALE and then introduced to the HT 3 computational grid. Therefore, iSALE was initially used to model the formation of impact cratering settings and their generated hydrothermal activity on Mars. In impact-induced and volcanogenic hydrothermal systems, fluid flows of T > 500 °C are characterized as super-critical mass fluxes and 2-phase (water-steam) mass fluxes, and these flows commonly produce specific mineral assemblages. Such distinctive mineral assemblages include pyrite, anhydrite, prehnite, pyrrhotite and zeolites that are often present in rocks samples retrieved from impact craters (Stöffler and Langenhorst, 1994; Grieve et al., 1996). Furthermore, shocked quartz, epidote and garnet (associated with the shock pressures of the impact-cratering process) are also signature mineralogies for the impact origin of rock samples retrieved from terrestrial craters (Bourgeois et al., 1987;; Stöffler and Grieve, 2007; Reimold et al., 2019). Finally, the presence of these mineral assemblages, as well as certain isotopic ratios in impact-related samples can approve or reject the computed distributions of temperature, pressure and fluid flows that the HT 3 code produces. Thus, the numerical modelling results of this study for the aqueous history of a variety of potential hydrothermal systems on Mars, should be compared and coupled in the near future with stratigraphic, geophysical and geochemical analyses performed by rover missions, or even by human expeditions on the Red Planet.

To examine and compare the aqueous activity in a series of hydrothermal systems on Mars, 290 simulations were constructed and ran in total for a variety of geothermal settings via the HT3 code. Out of these 290 simulations, those of the highest resolution and accuracy (based on the satisfaction rate of the code's convergence criteria per iteration) were finally selected for the scientific interpretations of the simulated environments. The numerical models selected and presented through this dissertation include:

- 4 sets of HT 3 simulations for post-impact hydrothermal systems on early Mars; the initial thermodynamic conditions and lithologies for each HT 3 simulation were determined after impact-physics (iSALE) models and according to previously published work (Abramov and Kring, 2005; Abramov et al., 2012; Abramov and Mojzsis, 2016; Manske et al., 2021). Three of the four highest resolution models represent settings with a crater radius of 10 km, 100 km, and 200 km. Finally, the fourth numerical experiment concerns a case of two small and simultaneous impact-events, occuring on the Martian crust within a diametrical distance x: 140 km $\leq$ x $\leq$ 200 km, generating two relatively distant hydrothermal systems, with each crater's radius being smaller than 5 km.

- 4 sets of numerical models exploring the hydrous activity in low to high temperature volcanic environments on Mars. These numerical experiments focused on the maximum temperature (T_{max}) and basal heat flux of each system that also governed the thermodynamics of the generated fluid fluxes therein. Thus, two distinctive computational sets of T_{max} = 120 °C, and T_{max} = 170 °C, at a depth of 9 km in the Martian crust were investigated for the lower temperature settings. These scenarios may well represent modern-day thermodynamic conditions and fluid flows within the Martian crust (Burr et al., 2002; Neukum et al., 2010; Changela and Bridges, 2010; Ramirez et al., 2020). Two other separate computational scenarios explored the hydrothermal activity in mid to high temperature conditions in the Martian crust, with T_{max} = 400 °C due to a volcanic pluming event, and T_{max} = 500 °C due to volcanic intrusive veins penetrating the geological units, respectively.

- 2 supplementary computational models exploring the hydrothermal response in a volcanic setting with a T_{max} = 600 °C due to volcanic pluming (by a deep basaltic source), and T_{max} = 750 °C due to intrusive peridotite veins (shown in appendix).

- 10 supplementary sets (4+4+2) for the (I), (II) and (III) categories of the selected highest resolution and accuracy computations (that were described above), in which the initial permeability and porosity parameters of the rock units have been adjusted more conservatively for each case (shown in appendix). Since permeability and porosity are the most significant factors dictating the hydrothermal flow in a geological setting, I

needed to additionally experiment with further numerical models based on the consideration of high-permeability versus low-permeability parameterization. This means that in the models of category (IV), the permeability and porosity of the rock units in their simulative grids, were decreased by one order of magnitude. In this way, I could investigate the thermodynamic response of those systems under a much less permeable and porous Martian crust for each case.

Based on the different petrophysical characteristics of the rock units that comprise each simulative set - geological setting, the initial thermodynamic conditions (temperature, pressure, and enthalpy distributions) were designed via the HT Interactive pre-processor in the form of contours, and the input of their spatial distributions and values was decided after experimental trials through the HT post-processor. In all simulations, the basal heat flux value has been adjusted via the equations of state of the source code, and according to the T_{max} assigned for each geological environment (i.e.: T_{max} calculated and used as input parameter at the bottom boundary of each simulative grid). Thus, the basal heat flux in this variety of Martian hydrothermal systems has varied between 14-70 mW/m^2 in this work. At the top boundary of the grid, a pressure of 0.07 bar and a temperature of 1°C have been assigned as constant values from initial conditions, to represent more ancient ground surface conditions on Mars. Currently, the average surface temperature on Mars is approximately -62.8 °C (Ramirez et al., 2020), but the HT 3 code cannot efficiently satisfy the thermodynamic criteria and equations of state for temperatures below 0° C. Preliminary simulations with temperatures lower than 0° C were not affecting the thermodynamic results, as the models were focusing on subsurface conditions and the hydrothermal response of the crust (from 0 to 10 km depth). In all scenarios, stream flux at the top of the geological domain (on the surface) and within the upper and thinner sedimentary layers of aeolian and fluvial deposits has also been inserted as a function (and thus, modelled as a possible thermodynamic effect) through the HTI pre-processor's parameterization.

The following sub-chapter (§3.1) examines the induced hydrothermal activity in Martian impact cratering settings right after a bolide's impact (with an assumed constant density for the impactor) on Mars, and for different time periods varying from tens of thousands to millions of years after the impact, according to each case study. The results presented in §3.1 originate directly from numerical simulations produced via the HYDROTHERM code. Sub-chapter §3.2 explores the hydrous activity in Martian basaltic environments that have been affected by volcanism after the emplacement and crystallization of the primary host rocks (low to high

temperature volcanic plumes ascending to a depth of 9.5 km in the Martian crust, and mid to high temperature intrusive veins penetrating the simulated geological setting). Numerical models presented in §3.2 have also been produced via HYDROTHERM simulations. Sub-chapter §3.3 presents results for the bioenergetic potential (habitability) of all those Martian hydrothermal environments that have been investigated in sub-chapters §3.1 and §3.2. The results of §3.3 have been produced via the USGS program PHREEQC (version 3; Parkhurst and Appelo, 2013; Webb, 2021). The initial conditions used in the PHREEQC simulations originate directly from the thermodynamic output data of the HYDROTHERM simulations (temperature, pressure, saturation, water/steam/super-critical fluid mass flux, enthalpy, viscosity, density, etc.). HYDROTHERM simulations produce extensive output thermodynamic data files (in tabular form), that can be later used as initial parameterization databases for other USGS codes and softwares (in this case, for the PHREEQC which is fully compatible and can be fully coupled with HYDROTHERM). Hence, PHREEQC simulations used the thermodynamic output of HYDROTHERM computations as their boundary conditions (initial settings), in order to perform calculations for the habitability of the Martian hydrothermal environments that are investigated in this doctoral research.

3.1 Numerical Simulations for Impact-Induced Hydrothermal Systems on Early Mars (via the HYDROTHERM Code)

3.1.1 iSALE Modelling for Constraining the HT 3 Simulations.

The iSALE models presented here were constructed with the purpose of constraining further the initial thermodynamic conditions of the hydrothermal simulations via the HT 3 code. Although the HT 3 simulations for post-impact hydrothermalism could be developed independently from iSALE and based on previously published work (Rathbun and Squyres, 2002; Abramov and Kring, 2004; 2005; 2007), the iSALE computations contributed towards increasing the reliability of input parameterization in hydrothermal simulations, and as a result they enhanced the accuracy of the developed HT 3 numerical models in this PhD research. The output video for all produced iSALE computations can be accessed through a shared link in the appendix (please see §7.4). Fig. 3.1 comprises an overview of the impact-physics models.

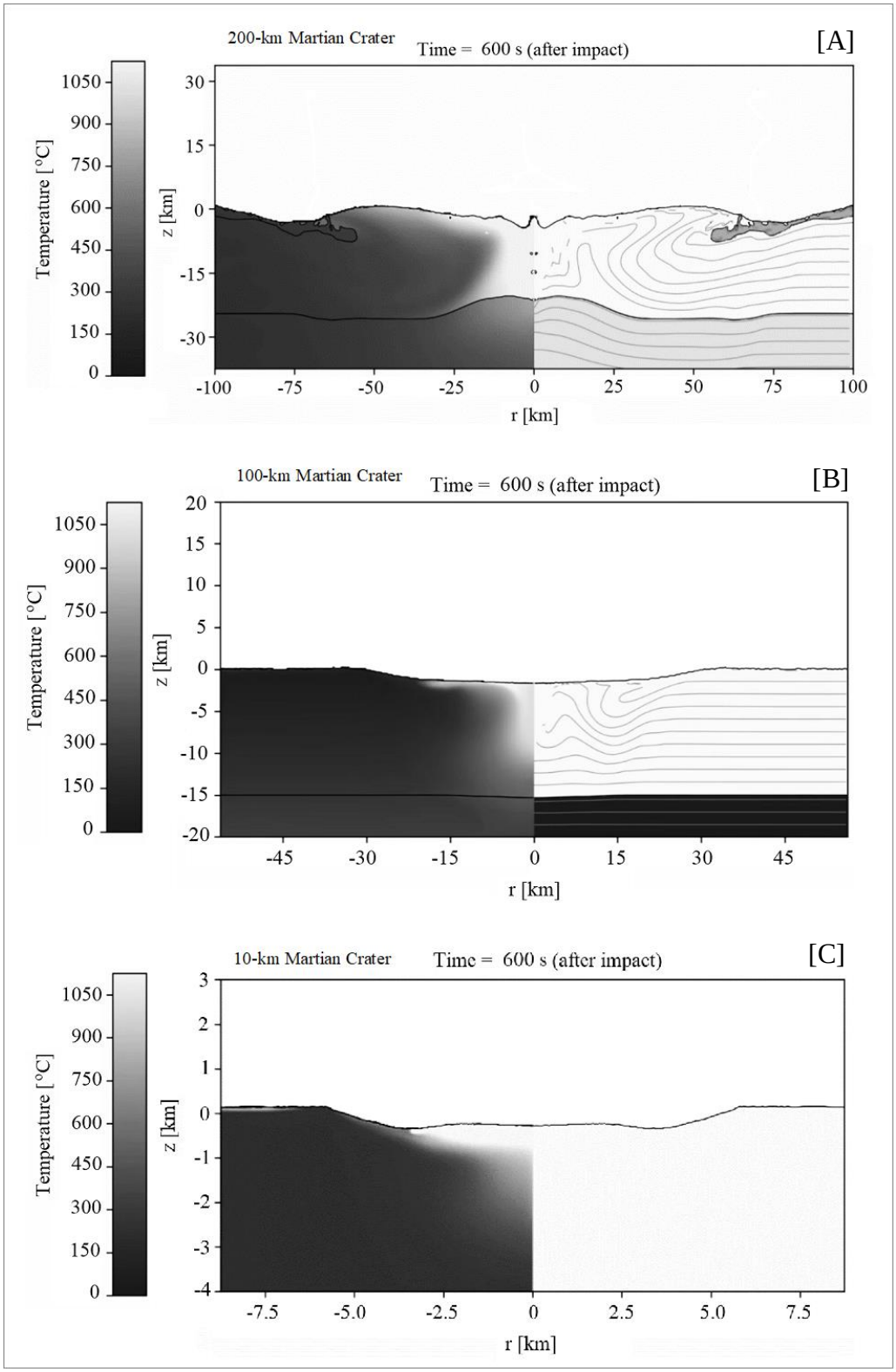

Fig. 3.1. Post-impact thermal profiles for each simulated Martian crater, after cratering modification and final crater's formation. Temperature distributions in: [A]: a 200-km in diameter Martian crater after its formation; [B]: a 100-km crater; [C]: a 12-km crater (to account for the resulting thermal distribution in a complex cratering setting (≥ 10-km), as small craters (≤ 10-km) may not induce hydrothermal activity. Simple craters form if final crater's diameter ≤ 10 km. The right-side of each simulated grid shows petrophysical differences within lithologies (e.g.: density, porosity, permeability) in the form of grey contours [A, B]. The deeper black contour illustrates a petrophysical boundary between the lower and upper crust [A, B]. For the 10-km in diameter Martian crater only a basaltic domain was assumed, as differences in petrophysical properties would not converge with the ANEOS.

The iSALE-2D models generated extensive thermodynamic output datasets that could later inform the HT 3 pre-processor (boundary and input conditions of hydrothermal simulations) and provided deeper insights into the temperature distributions for each cratering system. Impact-induced temperatures in all impact-cratering systems exceeded the temperature of 1200 °C for several minutes (0-600 s), and the distribution of the resulting thermal contours was introduced in the computational grid of HT 3 simulations. After 600 s, the peak temperatures that describe the melt sheets and ejecta blankets in all three impact cratering scenarios (fig. 3.1) are computed with a maximum value of 1200 °C through the iSALE code. However, this temperature persists for hundreds to thousands of years in each impact structure (depending on the size of the crater) and induces long-lived hydrological systems (as it will be described later in HT 3 models). Furthermore, temperature-pressure distributions from iSALE models were also used to inform the geostatic gradient and hydrostatic pressure of the computational grid of the HT 3 simulative environments, along with their associated thermodynamics (e.g.: enthalpy, density, porosity, permeability, entropy in HT 3 lithologies).

The iSALE-2D simulation for the 200-km in diameter crater reproduced a complex crater's morphology that represents the accuracy of the used resolution for the model (12016 cells), and indicated the impact-generated petrophysical differences between the different lithostratigraphic units (as shown by the grey contours; fig. 3.1). The iSALE temperature distribution was also benchmarked in terms of its accuracy through the HT 3 initial conditions. After importing the acquired temperature contours of the iSALE model into the HT 3 computational grid, the HT code can identify whether these thermodynamic conditions could satisfy the convergence criteria through iterative tests (preliminary simulations). Usually, the HT 3 iterative technique performs calculations on the satisfaction rate of the convergence criteria for the first 20000 iteration steps. During that computational phase, if the success rate on thermodynamic convergence is higher than 90% within 20000 iteration steps (circa 10% of the total number of iterations per simulation), then the computation can proceed smoothly and can be completed with high reliability. If the satisfaction of the convergence criteria is lower than 90 %, this means that errors and uncertainties in the thermodynamic input will result to the unsuccessful termination of the simulation, or to a produced simulation of very low accuracy (divergence). Therefore, the produced iSALE model for the 200-km in diameter crater was benchmarked from HT 3 preliminary tests, and its convergence thermodynamic criteria could be satisfied. A maximum temperature of 1200 °C described the induced melting process after the crater's formation and the volume of the melt (central melt sheet, melt deposits and

ejecta blanket) was computed with a value of 63400.48 km^3. The petrophysical properties of the post-impact lithologies as distinguished through the grey contouring were then used for the parameterization of the HT 3 model.

To what concerns the 100-km in diameter Martian crater, the impact-physics dictated that its subsurface morphology is indicative of a central uplift modification process for the target lithological units (please see grey contours in fig. 3.1b; and video through the appendix link). However, the iSALE simulation did not predict the formation of a central peak feature, but the morphology of a single peak ring crater. Although this may be an artefact of the simulation, no other experimental run managed to reproduce a central peak for the 100-km in diameter Martian crater. Hopefully, more thorough iSALE computational investigations in the future can solve that for this impact-cratering scenario. Nevertheless, the thermodynamic criteria that describe the subsurface of the 100-km in diameter impact crater where in convergence, and the HT code could use those as a reliable input (based on experimental iteration computations) for the subsequent development of hydrothermal models. The volume of the central melt sheet was reduced by more than 88% in this scenario when compared to the melt volume of the 200-km in diameter crater and contained within a radius of only 15-20 km (fig. 3.1a-b). The total produced melt volume was computed with a value of 7068.58 km^3 and the maximum temperature for the central melt was calculated at 1200 °C through iSALE. At this point, it should be mentioned that the total produced melt volume in these iSALE simulations represents all target lithologies that experience violent thermodynamic modifications and melting within the first few minutes after the impact event. A large proportion of the impactites, return to their solidus after the final crater's formation (600 s after impact in these scenarios; fig. 3.1), except for the central melt sheet and ejecta blankets. Therefore, the estimated iSALE melt volumes should not be confused with the melt volumes used to describe the central melt sheets of the following impact-induced hydrothermal models (§3.1.2 – §3.1.5). Additionally, the differences in the petrophysical properties of the lithologies were spatially illustrated in the form of grey contours (fig. 3.1b), and these physical parameters were later used as an input in the hydrothermal simulations for defining the computational settings of the 100-km in diameter impact crater.

Finally, the 10-km in diameter impact crater was calculated with a post-impact melt volume of 57.73 km^3 and its peak temperature after the crater's formation was observed at 1200 °C within the central region. In contrast to the large cratering scenarios, the heat source in the 10-km

crater is constrained only within a radius of 3 km. Subsequently, based on previous hydrothermal modelling reports (Rathbun and Squyres, 2002; Abramov and Kring, 2004; 2005; 2007), we can predict that the cooling process of the 10-km in diameter crater will be fast, with an estimated value of circa 10-90 Kyr. On the contrary, the lifetime of the induced hydrothermal circulation in larger craters (100 – 200 km in diameter) which have been previously predicted with hydrothermal activity that may exceed the time span of 2-6 Myr (Abramov and Mojzsis, 2016; Christou et al., 2019, Pickersgill et al., 2019; Christou et al., 2021a). The following HT 3 models (§3.1.2 – §3.1.5) will thoroughly investigate the impact-induced hydromechanics and duration of hydrological cycles.

3.1.2 Impact-Induced Hydrothermal Activity at a 200-km in diameter Martian Crater

Starting from the boundary conditions of the numerical model for the post-impact hydrothermal activity at the 200-km Martian crater, the input parameters were defined via the HT interactive programming environment and derived from the thermodynamic results of iSALE-2D simulations. A geological setting of a 200-km diametrical distance, and a maximum depth of 10 km from the surface were designed in 2D via the HT interface on a high-resolution grid of 4365 cells (97 × 45), as shown in fig. 3.2. All the input-initial petrophysical properties of the lithologies that comprise the geological setting are shown in table 3.1. The initial thermodynamic conditions (temperature, pressure, and enthalpy distributions) after the bolide's impact on the surface of Mars were programmed in the grid according to the previously presented iSALE experiments, and in accordance with previously published work on the shock physics of similar large impact-cratering processes on terrestrial planetary bodies (Abramov and Kring, 2004; 2005; 2007; and references therein). The temperature contours were designed via the HT Interactive pre-processor, and the input of their spatial distributions and values was decided after the iSALE-2D computations and initial trials via the HT post-processor.

For the simulative grid, I adjusted the basal heat flux parameter to the value of 17 mW/m^2 at the bottom boundary of the 200-km cratering setting. The basal heat flux in this simulation was defined after the average value of previously published estimates for the heat flux in the Martian crust (during both past and recent geological epochs) by Zuber et al. (2000), Jones et al. (2011), McGovern et al. (2002, 2004). The top boundary lithologically represents regolith

and surficial sediments of which a pressure of 0.007 bar and a temperature of 1°C have been assigned as a constant function for the thermodynamics of the initial conditions at the surface. Stream flux at the top of the geological domain within the thinner layers of regolith and upper aeolian and fluvial sediments has been rendered possible via boundary parameterization through the HT pre-processor. In those scenarios, the stream flows have been given a T_{min} = 1 °C at the surface. Additionally, inflow events from the ground surface to the porous rocks due to meteoric-surficial water and precipitation with T_{min} = 1 °C were also considered as possible through the HTI – preprocessor. This parameterization was conducted in order to account for surficial and colder stream flows that may have accelerated the cooling of the impact-induced hydrothermal system. These colder stream flows appear occasionally on top of, and within the upper regolith unit of the crater, and closer to the inner- and outer-slopes of the peak ring, as shown in the following simulations' results.

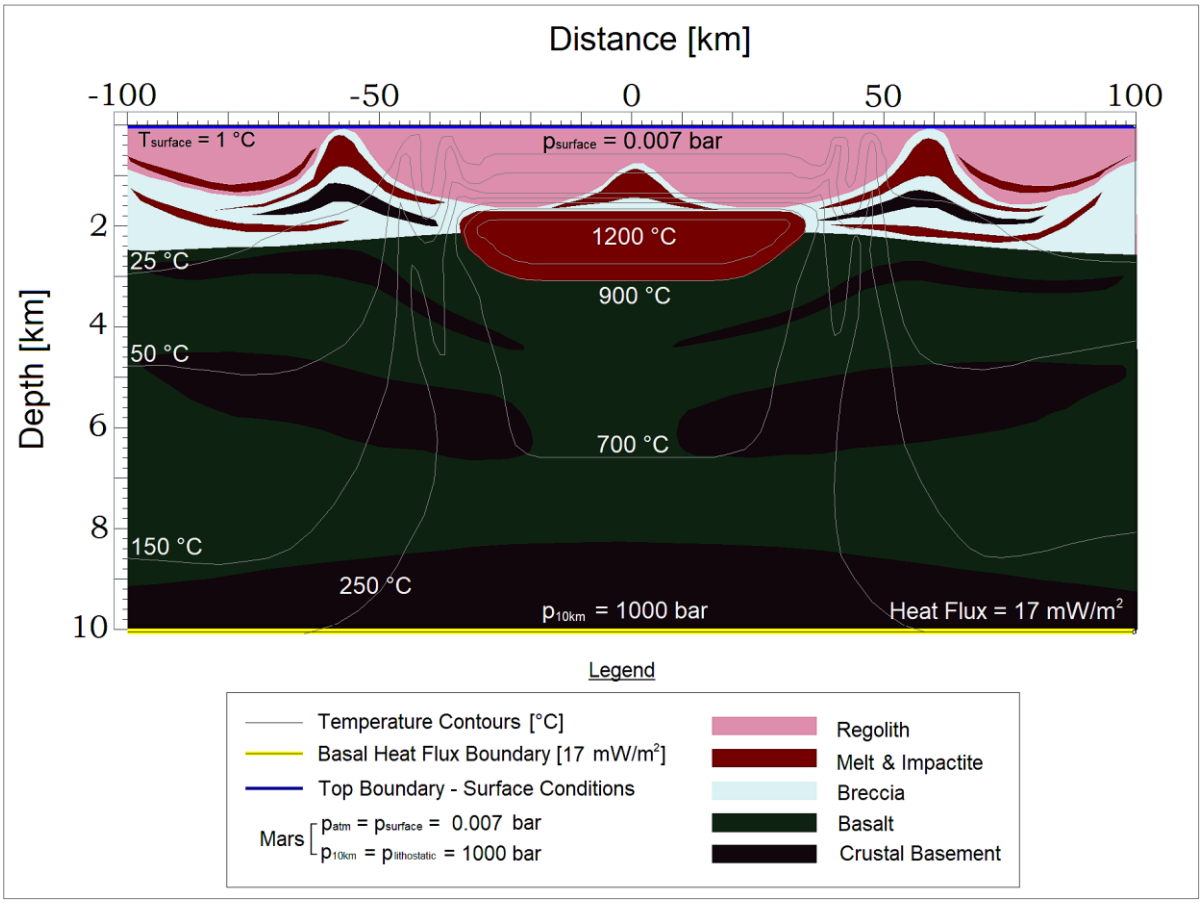

Fig. 3.2. Initial thermodynamic conditions and lithostratigraphic distribution in the simulative setting of the 200-km crater on Mars. Basal Heat Flux is assigned to a value of 17 mW/m². Atmospheric pressure at the ground surface of Mars (above the crater's valley and central region) is set at 0.007 bar and the ground temperature at 1°C. The central melt sheet formed after the impact has been given a T_{max} = 1200 °C, and the crater's morphology and lithostratigraphic distribution has been modelled according to the iSALE model (§ 3.1.1) and based on previous research findings for large impact structures by Dence (1968); Grieve et al. (1977); (1981); Grieve (1991); French (1998); Abramov and Kring (2004); (2005); (2007).

Table 3.1. HT initial thermodynamic properties of the rock units comprising the simulative grid of the 200-km Martian crater (Fig. 3.2).

Petrophysical Properties	**Lower Crustal Rocks**	**Basalts**	**Melt Rocks**	**Breccia**	**Regolith**
Permeability (k) {m^2}	k_z = f(d,T), k_x = f (d,T)	k_z = f(d,T), k_x = f (d,T)	k_z = f(d,T), k_x = f (d,T)	k_z = f(d,T), k_x = f (d,T)	k_z = f(d,T), k_x = f (d,T)
Porosity (φ) {%}	φ = f (d,T)	φ = f (d,T)	φ = f (d,T)	φ = f (d,T)	φ = f (d,T)
Thermal Conductivity {W/m·K}	2.9	2.7	2.7	2.7	1.7
Specific Heat Capacity {J/kg·K}	1200	1000	1000	900	700
Density {kg/m^3}	3000	2700	2500	2500	1700
Surface Permeability {m^2}	1.00E – 19	9.00E – 17	1.00E - 16	1.00E – 15	1.00E - 14
Surface Porosity ($\varphi_{surface}$)	2.0 %	5.0 %	7.0 %	7.0 %	15.0 %

Table 3.1 – Note: The initial thermodynamic parameters of this simulation are adapted after previous numerical models for large post-impact cratering structures on Earth and Mars (diameter ≥ 100 km) suggested by Abramov and Kring (2004); (2005); (2006); and Sanford (2005). Hence, the petrophysical properties used in the boundary conditions of this work's simulations derive from recommendations of the aforementioned research publications, and from further preliminary experiments and comparative models performed in this work, prior to determining the exact initial parameters of the simulations.

In this computational scenario of post-impact hydrothermal activity on Mars, I have examined the simulated thermodynamics in a 200-km radial distance, and 10 km depth setting of a newly formed complex impact crater. In general, beneath a depth of 10 km, the grid does not produce any flows, due to the extremely low values of permeability and porosity. Hence, for simplicity, the results of the simulation presented in this work concern a subsurface geological setting expanding from the surface of Mars and down to a depth of 10 km where minimum fluxes are observed. Hydrothermal circulation in the grid is governed primarily by the initial permeability and porosity values of the rock units that comprise the geological setting, and by the temperature and pressure distribution in the cratered geological mass right after the impact. Secondarily, all other petrophysical properties of the rocks may constrain further the duration and magnitude of flow, as explained in the methods chapter of this dissertation.

Major differences in the pattern, magnitude and duration of water mass flux, are observed only when permeability, porosity, temperature and pressure distributions change. Even minor changes in one of those governing parameters can affect the hydrodynamics of the impact-induced system drastically. Such experimentation with an order of magnitude lower values for the permeability and porosity of the impacted rocks is included in the supplementary materials (appendix) and shown in the form of exported video output from the simulation (E:/Martian Crater_200-km_Lower Permeability_.mp4). This is done for providing a comparison between the preferred simulation results that are presented within the main corpus of this thesis (herein), with the more liberal or conservative numerical experiments. The appendix's results could be evaluated as slightly less accurate, based on the experience acquired after tens (and even hundreds) of simulations that were executed for each Martian hydrothermal setting (impact-induced or volcanic). All these computations contributed towards constraining accurately the duration and thermodynamics of each aqueous system.

In the simulation scenario of the 200-km in diameter complex crater on Mars, at time zero right after the impact (Fig. 3.3: step A), we can observe a red-coloured domain of 60 km horizontal distance and 1.5 km width at the centre of the crater, with an initial temperature of 1200 °C (illustrated in red: T_{max}). This region represents the central melt sheet, expanding from the crater's centre to the inner rim. The melt can thus be considered as the focal heat source that initiates hydrothermal circulation within the impact-crater after its formation. At time zero, fluid flows (liquid water, steam and fluids under super-critical state) are present in most subsurface structures of the crater setting (Fig. 3.3: step A – strong fluxes within domains

illustrated in red colours), except for regions where melt (T = 1200 ºC) is present, or temperature reaches values greater than 500 ºC, or/and where permeability is lower than 1.0E-19 m^2. Geological structures that are of very low permeability and porosity, or/and affected by T ≥ 500 ºC, cannot allow fluid flux according to the equations of state that dictate the fluid mechanics therein, as explained in the methodology chapter. As an example, the excavated lower crustal basement rocks at depths of 8-10 km (and uplifted upper mantle material, in depths of circa 15-20 km) appear in blue colours in Fig. 3.3: A-G; the simulation shows that no flow (or minimum short-lived flow) occurs in such depths due to the effect that the geostatic gradient has on decreasing the porosity and permeability of rocks in greater depths (Hayba and Ingebritesen, 1994; Hayba and Ingebritesen, 1997).

Some very weak flows may be present in regions where the impacted-fractured rocks are of slightly higher permeability and porosity. Also, after lower permeability melt rocks or uplifted basement rocks (heated above T = 500 ºC) have crystallized and cooled, then they can allow fluids to circulate through their porous. These flows can be observed as light blue flares in the darker, blue-coloured units of the grid; Fig. 3.3: B-E. Nevertheless, flow magnitude therein is far lower than that within the other rock units of the crater. In particular, the upper impactites (Martian regolith, breccia, uplifted basalt and basaltic impactite) host the strongest observed fluid mass fluxes in every time step of the simulation, for as long as the hydrothermal system is active (Fig. 3.3: A-G; where fluid mass flux is greater than 2.0E-9 g/s×cm^2).

At t = 2 Kyr, the central melt sheet has cooled by 100-120 ºC, which does not affect the strong flows within the crater. Maximum fluid flux at t= 2 Kyr reaches a value of 3.0E-2 g/s×cm^2, and hydrothermal circulation is even observed at depths of 9.2 km, possibly due to the induced fracturing of the rocks after the impact (after Polanskey and Ahrens, 1990). Impact-physics simulations for Mars show that due to its lower gravity, the depth that impact-induced fractures can reach may be 2.5 – 3.0 times greater than it would be on Earth (Abramov and Kring, 2005). Hence, in this research work, I have adopted a similar approach and experimented with several different parameterizations in the hydrocode impact-simulations to determine the mechanics of the cratering setting. Hence, in such a large, complex impact-crater on Mars, the results reasonably indicate that impact-induced fractures may be present at a maximum depth of 9.2 km. Fractures are present in all subsurface domains of the crater that are affected by strong fluid fluxes, as shown in Fig. 3.3: A-G, and at depths greater than 8 km. This effect is represented in the different time steps by red-coloured regions at the initial phase of

hydrothermal circulation (Fig. 3.3: A-E), and by light blue-coloured regions closer to the end of hydrothermal activity (Fig. 3.3: F-G). At t = 30 Kyr, the melt sheet has cooled by 350 ºC (Fig. 3.2: C). However, water and steam mass fluxes prevail in the porous media of the setting without any decrease of the magnitude of the initial hydrothermal flux evident (water, steam, and super-critical mass fluxes present and very strong in the setting, as shown also by the very large vectors of the flow). At this time period of the simulation, the Martian crater hosts several different hydrothermal cells beneath the surface at different depths, that also appear thermodynamically inter-connected, as witnessed by the flux vectors. Hydrothermal circulation cells are present above the central melt sheet, within the inner valley of the crater. Additionally, smaller regions of intense hydrothermal activity are present around the central melt sheet of the setting, at a radial distance of 35 km beyond the centre, and at different depths (ranging from 2 to 8.25 km).

It is very interesting also to see that the major hydrothermal cells appear in the deeper regions of the cratering setting, at depths of 6-8 km, and within a basaltic domain. This deeper basaltic region that is more intensely affected by widely distributed hydrothermal fluid flux, expands from 10-30 km from the crater's centre, (depending on the cooling stage, red-coloured regions-hydrothermal cells at depths greater than 6 km in the crater, Fig. 3.3: C-E) and reaches niches at a far radial distance of even 100-km from the crater's centre. This implies that several fluid flux recharging events may have taken place, originating from the deeper hydrological cells and recharging the ones closer to the surface. Simultaneously, we should also consider that the central melt sheet which is still very hot after 30 Kyr (with T_{max} = 850 ºC; Fig. 3.3: C) significantly contributes to further recharge flows between the upper hydrothermal cells and potential sources of surficial water deposits. Surficial aqueous flows forming due to precipitation, and due to melting of ground ice at the surface of the Martian grid are modelled as present at the boundary conditions of the simulation.

Nevertheless, only a low precipitation rate of 5 mm/day was incorporated in the script, which should represent early Amazonian atmospheric conditions on Mars (after Golombek et al., 2006; Golombek et al., 2014; Ramirez et al., 2020). Induced steam and super-critical flows are present within the central melt sheet and surrounding rock units of the settings, under a pressure range of 200-650 bars and where the temperature is very close to the 500 °C limit (Fig. 3.3: B-D, purple vectors illustrate super-critical mass flux and light grey vectors represent steam mass flux). In the less permeable and heated lithological units of the central region, the two-phase

and super-critical fluxes are by 3 orders of magnitude lower than the average water mass flux of the entire grid of the hydrothermal system.

After 300 Kyr, the central melt sheet's maximum temperature has decreased by 50% (T_{max} = 600 ºC) and its margins that are in contact with the recently crystallized impactite – breccias and impactite basalts can allow fluids' circulation (Fig. 3.3: D). The inner domains of the central melt sheet that are affected by a temperature greater than 500 ºC are still impermeable though at 30 Kyr after the impact. Liquid water and steam circulation therein occurs only after 600 Kyr (see appendix: Martian Crater_200-km_Higher Permeability_.mp4); hence, more intense water-rock interactions should take place at depths of 1.5 to 5 km within the central melt sheet or within the deeper and severely fractured central basaltic units (under T_{max} = 260 ºC, and P_{max} = 570 bar) at circa 1 Myr after the impact (fig. 3.3: E). At 1 Myr, at least a dozen hydrothermal cells are still active and keep driving the circulation of fluids (fig. 3.3: E). From 2 Myr and then on, the hydrothermal system appears evidently weakened, with a calculated 85% heat loss, in comparison to its initial state right after the impact (fig. 3.3: A and F), and with fluid flows that are by 4-5 orders of magnitude lower than those observed at circa 300 Kyr of the impact-induced hydrothermal cycle (WMF_{max} = 9.19E-9 g/s×cm^2 at t = 2 Myr, in contrast to WMF_{max} = 3.6E-4 g/s×cm^2 at t = 300 Kyr).

Some hydrothermal cells appear still active even after 2 Myr, at greater depths of 7-8 km and adjacent to the lower crustal basement. Flows therein may be induced by the basal heat flux of the lower crust (which is calculated at 57 mW/m^2, at t = 2.0 Myr after the impact, according to the thermodynamic output of the simulation (exported movie file and extensive datasets of the simulation: E:/Martian Crater_200-km_Higher Permeability.mp4). These flows within the deeper subsurface regions of the crater are relatively low, with WMF_{max} = 4.7E-9 g/s×cm^2, and they do not durate for more than another 800 Kyr, before the hydrothermal activity in the Martian impact crater ceases completely.

Finally, at t = 2.8 Myr, fluid circulation is negligible at depths greater than 2 km, but some weak flows appear present at depths of 1-1.5 km beneath the peak ring, in the inner rim and inner valley regions of the crater, and at a radius of 20 to 45 km from its centre (fig. 3.3: G). During that period of impact-induced hydrological activity, the WMF_{max} is equal to 4.5E-9 g/s×cm^2 within these two main hydrothermal cells. This means that flows within these regions are still appreciable. However, at t = 2.9 - 3Myr, the thermodynamic output shows that WMF_{max}

$\leq$ 1.19E-9 g/s×cm^2, which can be considered as the time point when hydrothermal circulation ceases (based on previous HT numerical experiments and interpretations presented by Hayba and Ingebritesen (1997), Abramov and Kring (2004); (2005); (2007), and Jõeleht et al. (2005)). Additionally, at t = 2.8 Myr, the geothermal gradient of the geological setting is almost restored, as it does not exceed a value of 12 ºC / km (fig. 3.3: G; the thermal distribution in the domain is illustrated mainly by darker blue colours).

As explained in the methodology chapter of the thesis, a background geothermal gradient of 12 ºC / km has been assigned for the simulative grid of this Martian geological setting, which may be seen as a fairly conservative value, but it may represent more accurately the conditions of the Martian subsurface during the last 3 Gyr (Amazonian eon). Furthermore, if we consider a much higher background geothermal gradient (i.e.: + 7-12 ºC / km), this does not seem to significantly affect the lifetime and flow pattern of the impact-induced hydrological system, beyond an arguably prolonging effect on its duration by 100-200 Kyr (based on results of several numerical experiments that I have performed before deducing the initial thermodynamic/boundary conditions of the geological grid).

Temperature & Water Mass Flux Distribution in the Post-Impact Hydrothermal System

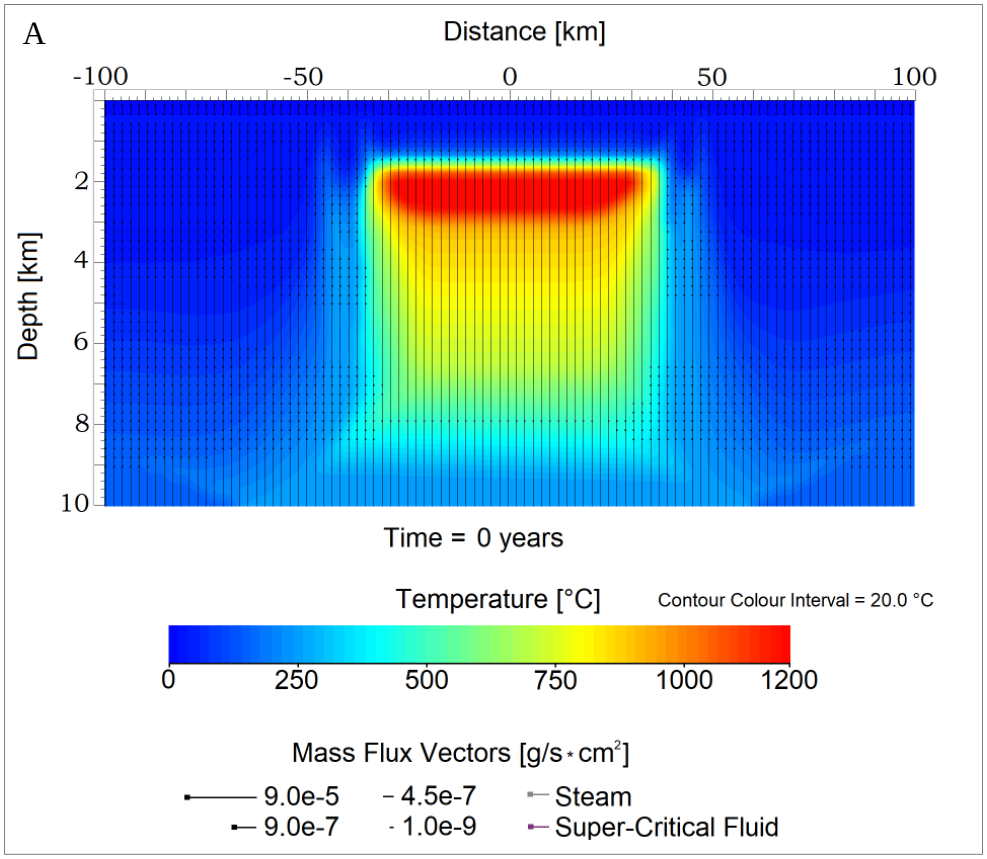

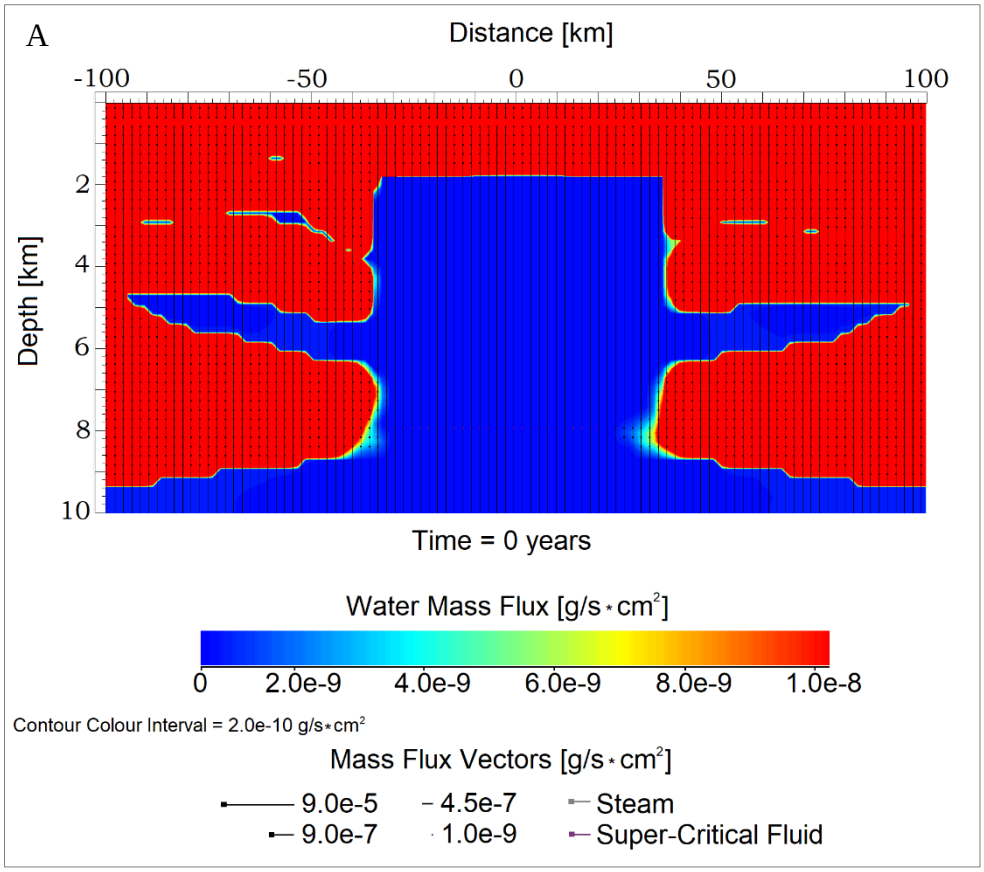

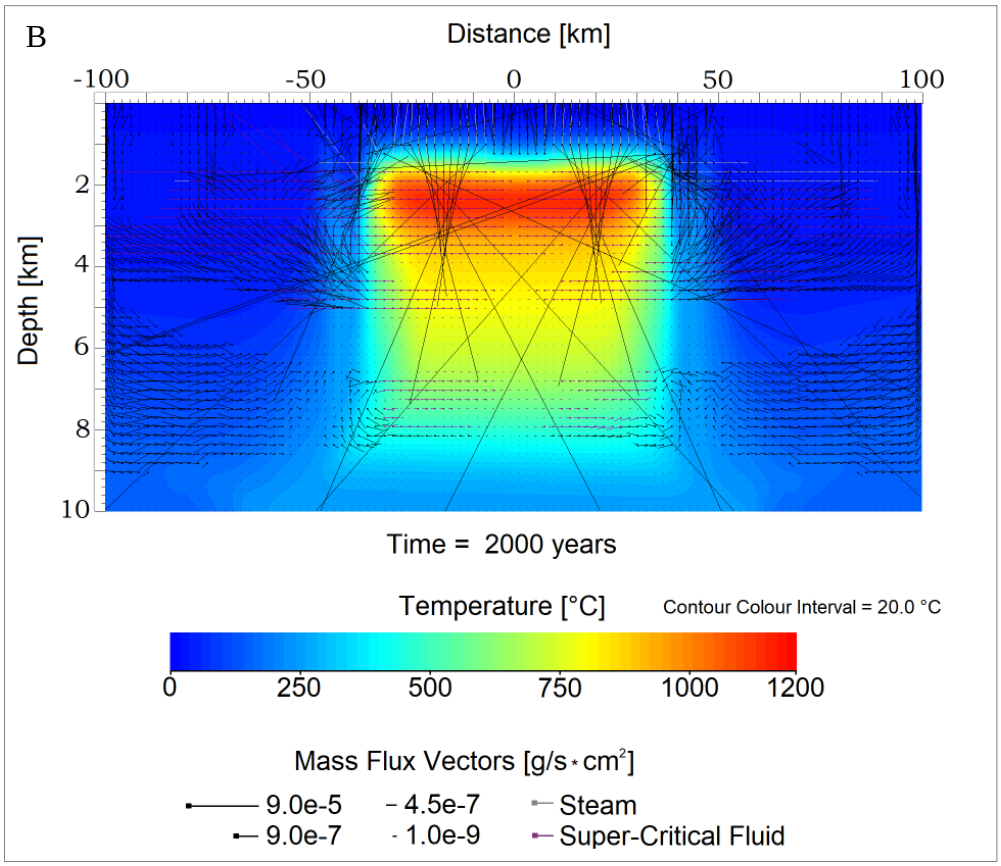
B
Distance [km]
-100
-50
0
50
100
Depth [km]
2
4
6
8
10
Time = 2000 years
Temperature [°C]
Contour Colour Interval = 20.0 °C
0
250
500
750
1000
1200
Mass Flux Vectors [g/s*cm²]
9.0e-5
4.5e-7
Steam
9.0e-7
1.0e-9
Super-Critical Fluid

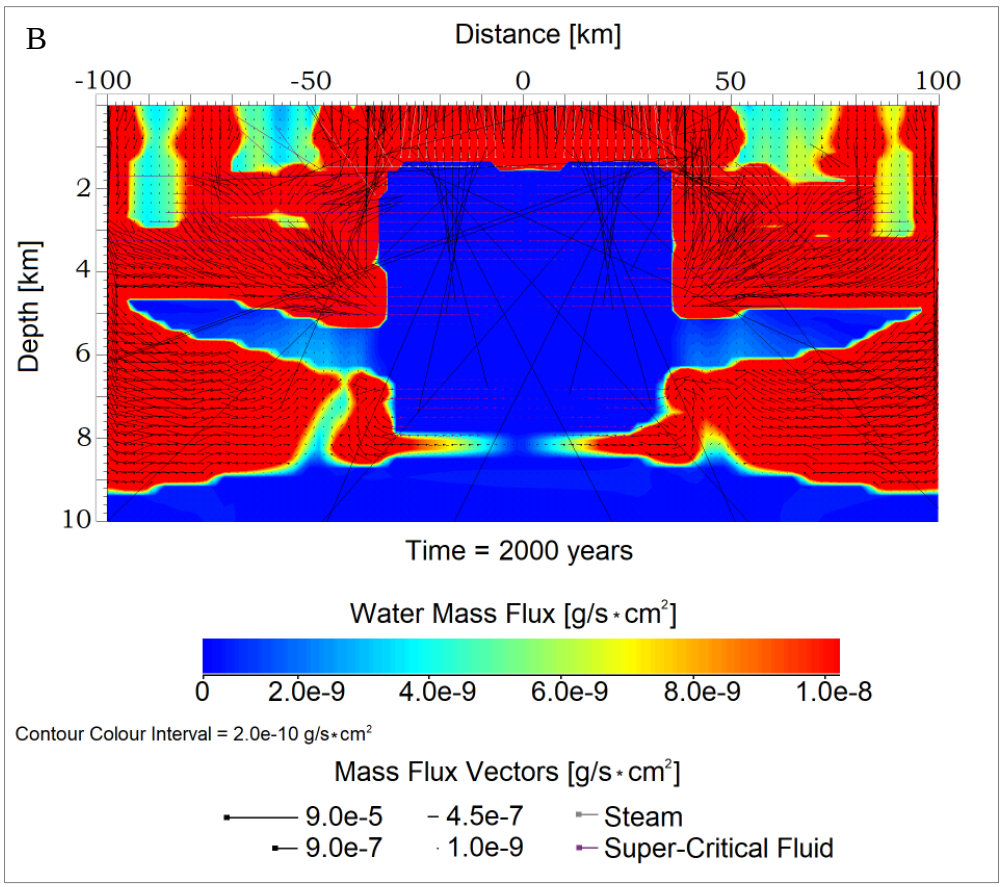
B
Distance [km]
-100
-50
0
50
100
Depth [km]
2
4
6
8
10
Time = 2000 years
Water Mass Flux [g/s*cm²]
0
2.0e-9
4.0e-9
6.0e-9
8.0e-9
1.0e-8
Contour Colour Interval = 2.0e-10 g/s*cm²
Mass Flux Vectors [g/s*cm²]
9.0e-5
4.5e-7
Steam
9.0e-7
1.0e-9
Super-Critical Fluid

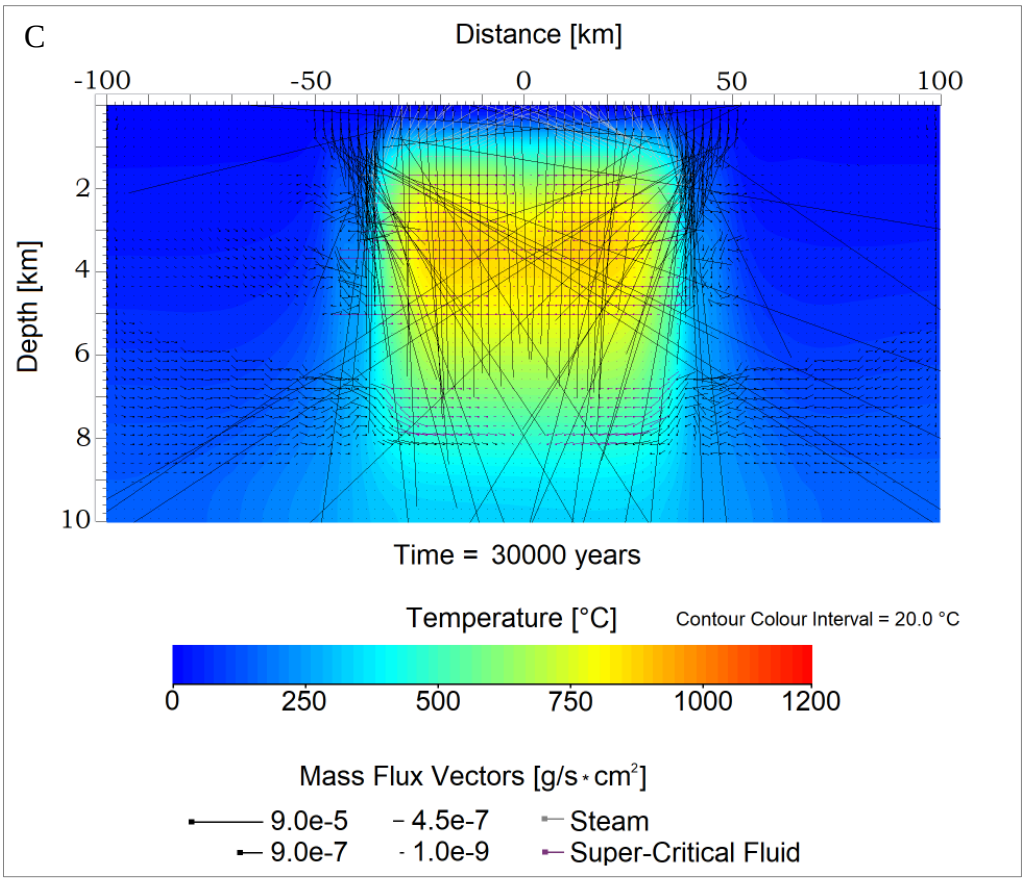
C
Distance [km]
-100
-50
0
50
100
Depth [km]
2
4
6
8
10
Time = 30000 years
Temperature [°C]
Contour Colour Interval = 20.0 °C
0
250
500
750
1000
1200
Mass Flux Vectors [g/s*cm²]
9.0e-5
4.5e-7
Steam
9.0e-7
1.0e-9
Super-Critical Fluid

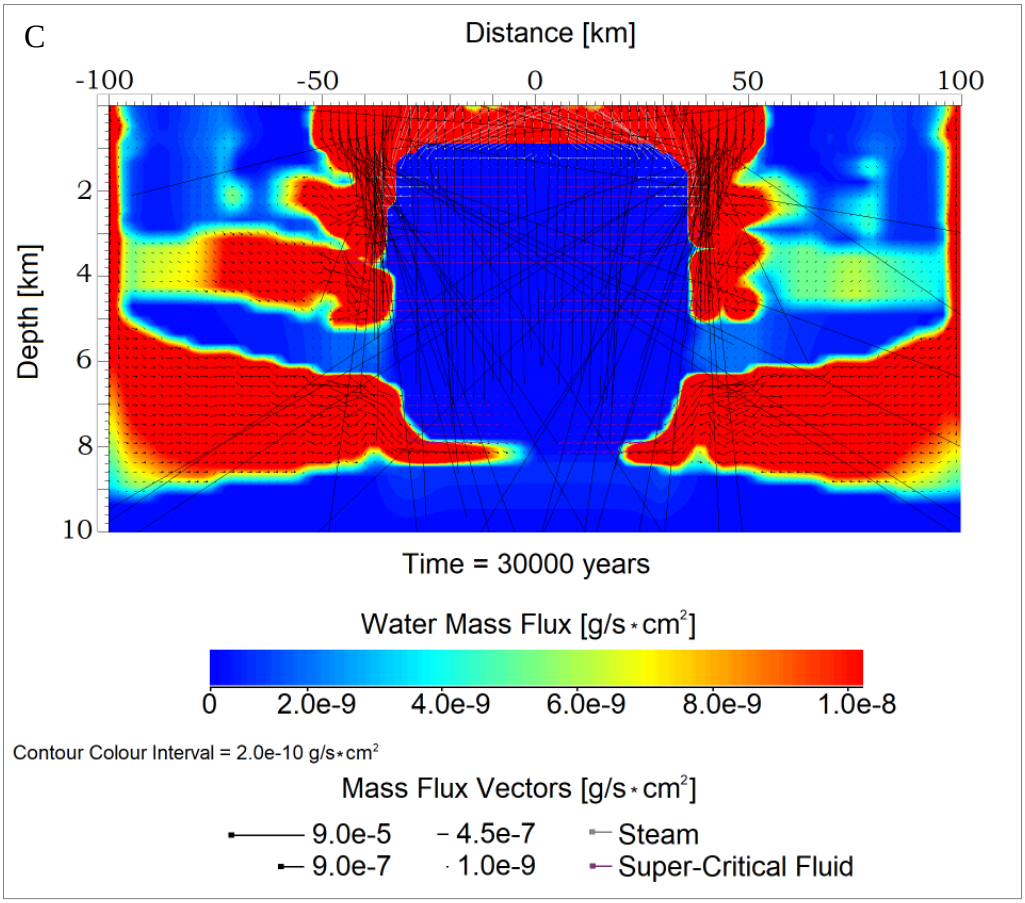
C
Distance [km]
-100
-50
0
50
100
Depth [km]
2
4
6
8
10
Time = 30000 years
Water Mass Flux [g/s*cm²]
0
2.0e-9
4.0e-9
6.0e-9
8.0e-9
1.0e-8
Contour Colour Interval = 2.0e-10 g/s*cm²
Mass Flux Vectors [g/s*cm²]
9.0e-5
4.5e-7
Steam
9.0e-7
1.0e-9
Super-Critical Fluid

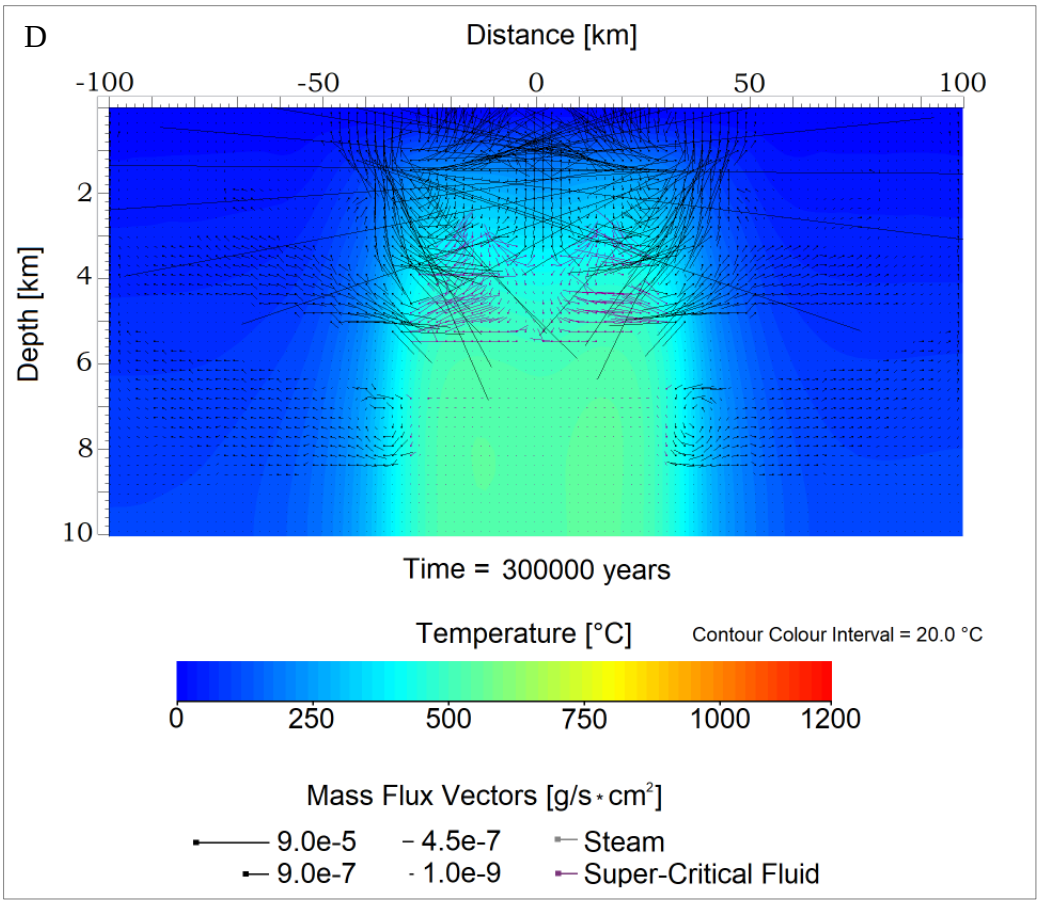
D
Distance [km]
-100
-50
0
50
100
Depth [km]
2
4
6
8
10
Time = 300000 years
Temperature [°C]
Contour Colour Interval = 20.0 °C
0
250
500
750
1000
1200
Mass Flux Vectors [g/s*cm²]
9.0e-5
4.5e-7
Steam
9.0e-7
1.0e-9
Super-Critical Fluid

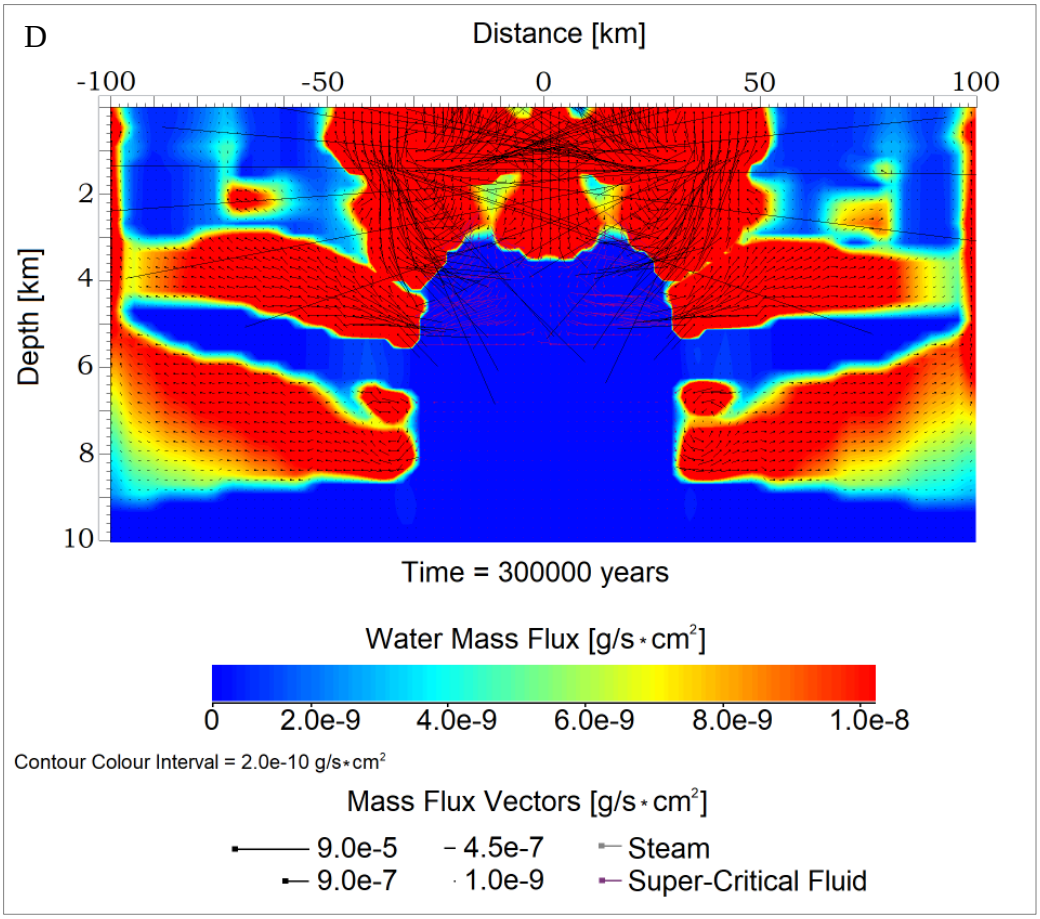
D
Distance [km]
-100
-50
0
50
100
Depth [km]
2
4
6
8
10
Time = 300000 years
Water Mass Flux [g/s*cm²]
0
2.0e-9
4.0e-9
6.0e-9
8.0e-9
1.0e-8
Contour Colour Interval = 2.0e-10 g/s*cm²
Mass Flux Vectors [g/s*cm²]
9.0e-5
4.5e-7
Steam
9.0e-7
1.0e-9
Super-Critical Fluid

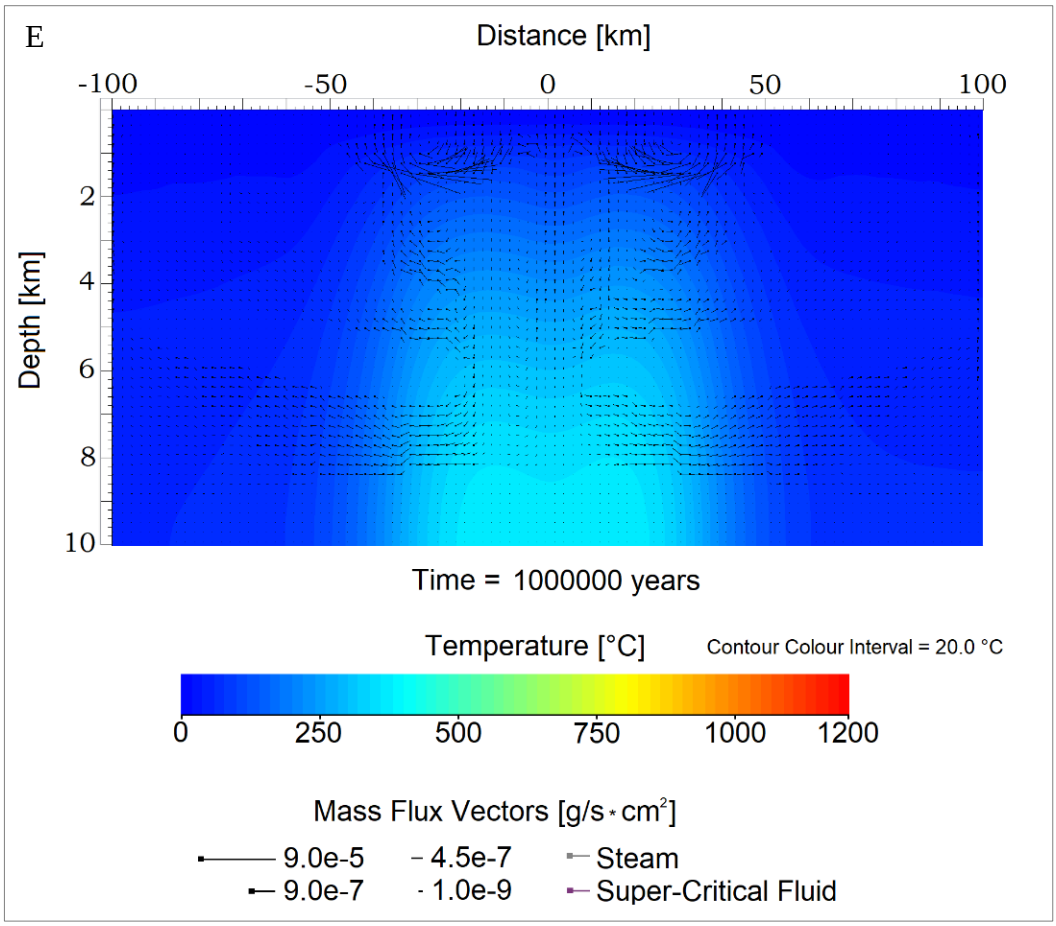
E
Distance [km]
-100
-50
0
50
100
Depth [km]
2
4
6
8
10
Time = 1000000 years
Temperature [°C]
Contour Colour Interval = 20.0 °C
0
250
500
750
1000
1200
Mass Flux Vectors [g/s*cm²]
9.0e-5
4.5e-7
Steam
9.0e-7
1.0e-9
Super-Critical Fluid

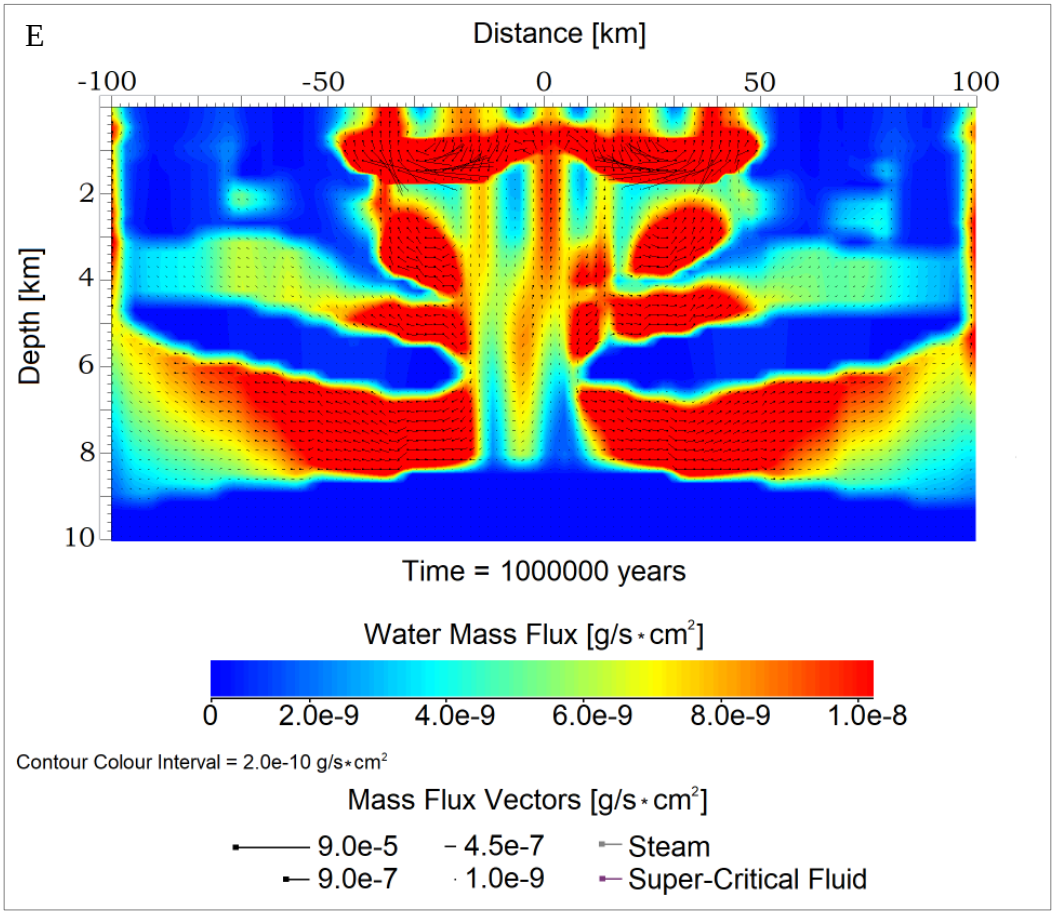
E
Distance [km]
-100
-50
0
50
100
Depth [km]
2
4
6
8
10
Time = 1000000 years
Water Mass Flux [g/s*cm²]
0
2.0e-9
4.0e-9
6.0e-9
8.0e-9
1.0e-8
Contour Colour Interval = 2.0e-10 g/s*cm²
Mass Flux Vectors [g/s*cm²]
9.0e-5
4.5e-7
Steam
9.0e-7
1.0e-9
Super-Critical Fluid

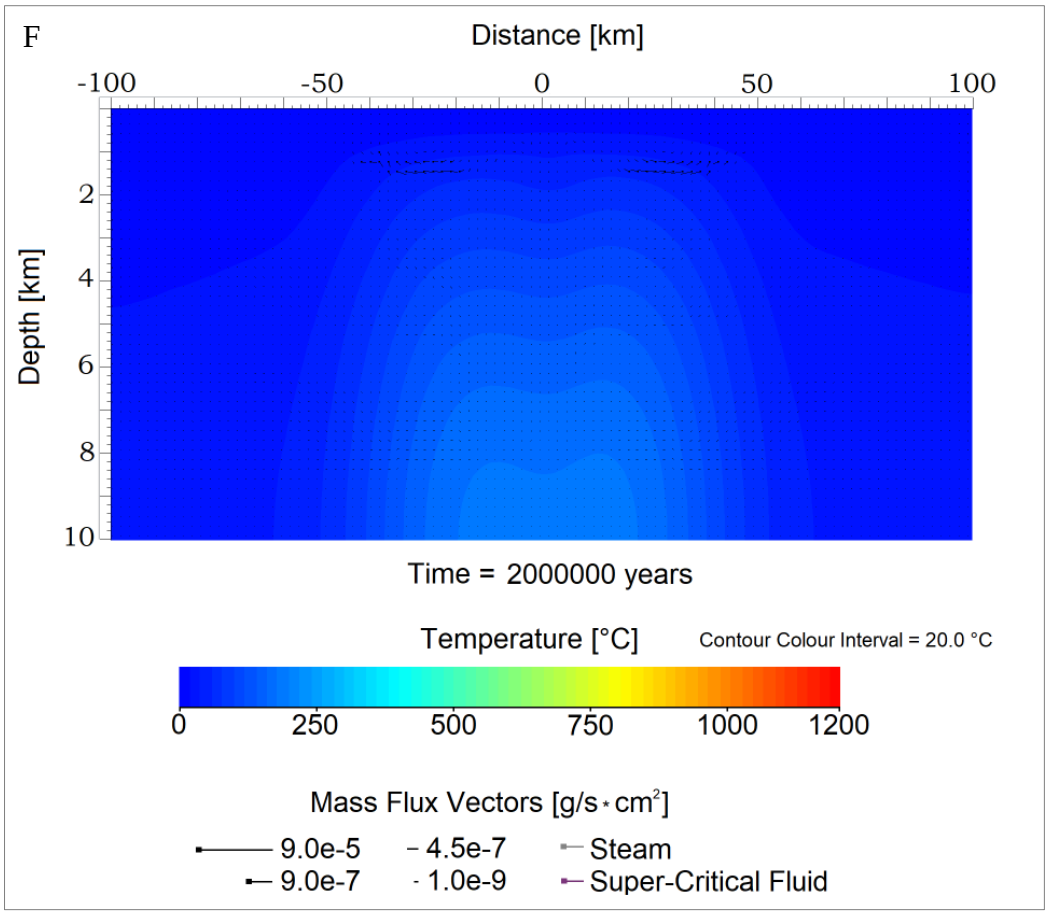
F
Distance [km]
-100
-50
0
50
100
Depth [km]
2
4
6
8
10
Time = 2000000 years
Temperature [°C]
Contour Colour Interval = 20.0 °C
0
250
500
750
1000
1200
Mass Flux Vectors [g/s*cm²]
9.0e-5
4.5e-7
Steam
9.0e-7
1.0e-9
Super-Critical Fluid

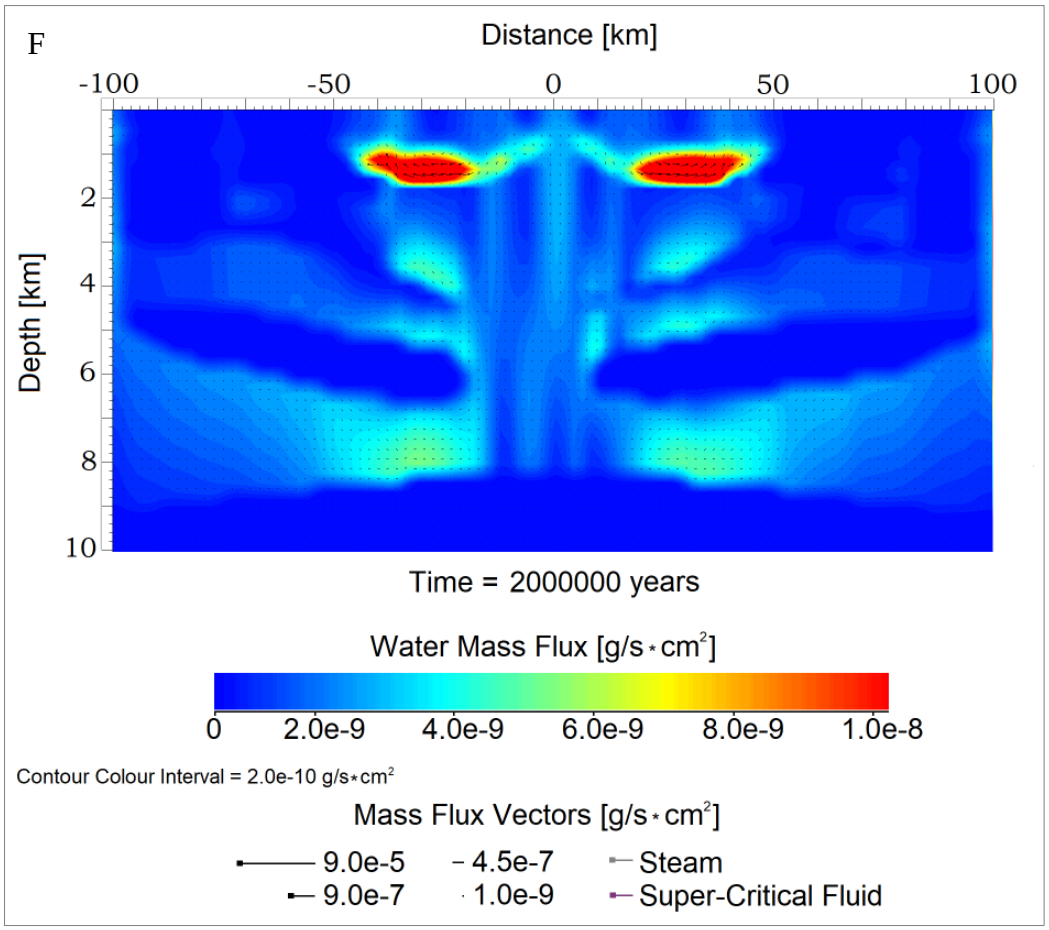
F
Distance [km]
-100
-50
0
50
100
Depth [km]
2
4
6
8
10
Time = 2000000 years
Water Mass Flux [g/s*cm²]
0
2.0e-9
4.0e-9
6.0e-9
8.0e-9
1.0e-8
Contour Colour Interval = 2.0e-10 g/s*cm²
Mass Flux Vectors [g/s*cm²]
9.0e-5
4.5e-7
Steam
9.0e-7
1.0e-9
Super-Critical Fluid

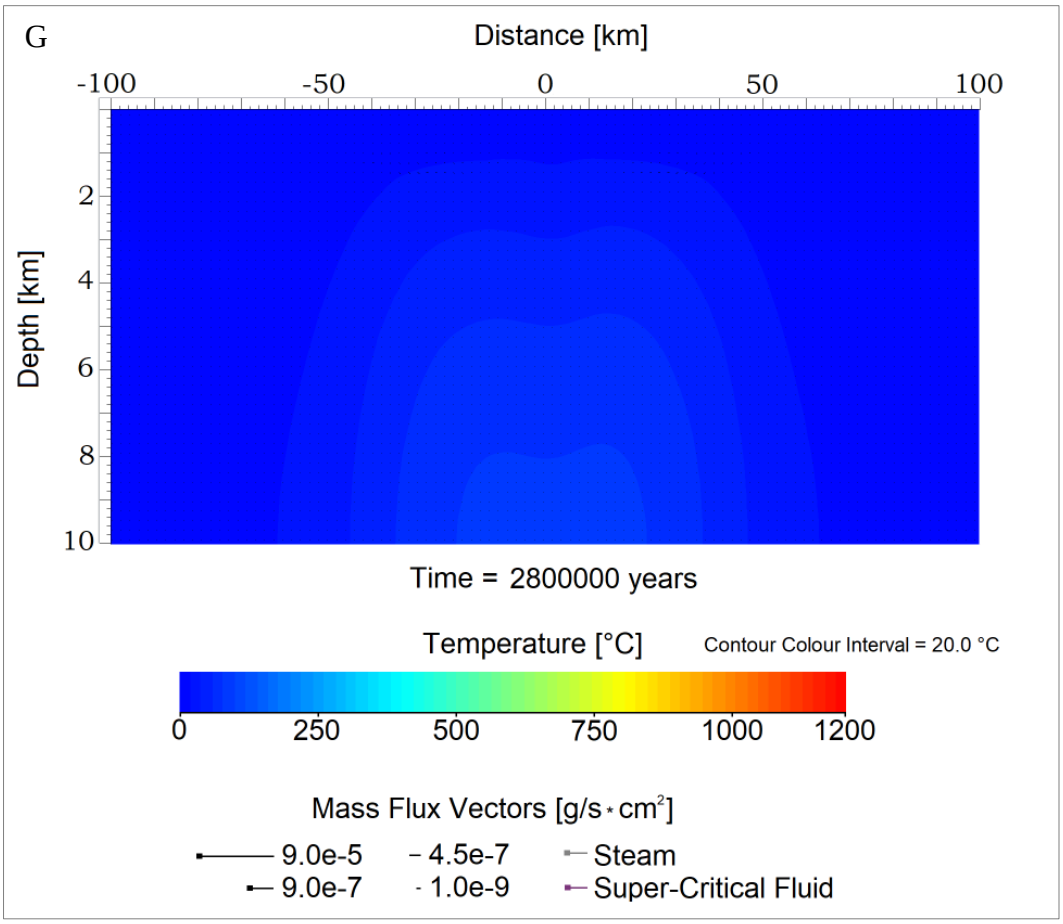
G
Distance [km]
-100
-50
0
50
100
Depth [km]
2
4
6
8
10
Time = 2800000 years
Temperature [°C]
Contour Colour Interval = 20.0 °C
0
250
500
750
1000
1200
Mass Flux Vectors [g/s*cm²]
9.0e-5
4.5e-7
Steam
9.0e-7
1.0e-9
Super-Critical Fluid

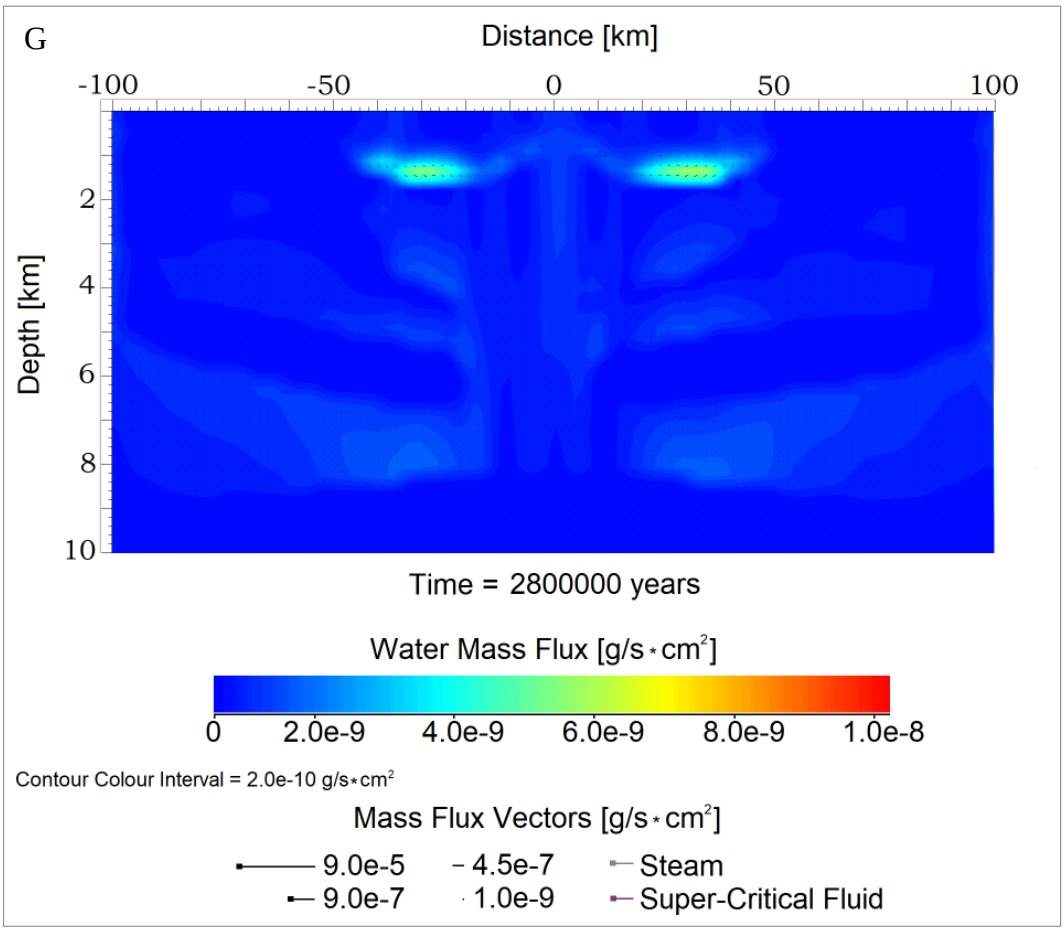
G
Distance [km]
-100
-50
0
50
100
Depth [km]
2
4
6
8
10
Time = 2800000 years
Water Mass Flux [g/s*cm²]
0
2.0e-9
4.0e-9
6.0e-9
8.0e-9
1.0e-8
Contour Colour Interval = 2.0e-10 g/s*cm²
Mass Flux Vectors [g/s*cm²]
9.0e-5
4.5e-7
Steam
9.0e-7
1.0e-9
Super-Critical Fluid

Fig. 3.3 (steps A-G). Thermal and Water Mass Flux (WMF) evolution in the impact-cratering setting from t_0 (right after the impact) and for a period of 2.8 Myr, up to the time point when the geothermal gradient of the geological setting is restored, and hydrothermal circulation has ceased: WMF_{min} = 1.0e-9 g/s×cm^2.

Temperature Distribution (steps A-G): T_{max} = 1200 °C and T_{min} = 0 °C; The central melt sheet is represented by red coloured domains at the earliest stages (A-B) of the generated hydrothermal system, where 1100 °C ≤ T ≤ 1200 °C. The cooling of the central melt sheet and of the hydrothermal system during this 2.8 Myr period is illustrated via the colour transition from warmer colours (red to yellow shades) to colder ones (green to blue shades) as time elapses. The thermal field evolution of the simulated setting shows much hotter and stronger hydrothermal fluxes at the initial stages of aqueous circulation (A-D), and colder and weaker flows during the latest stages of hydrothermal circulation (E-G). Fluid flux (liquid water flux shown in black arrows, steam in light-greyish colours, and super-critical flux in purple colours) is illustrated via vectors in each time-step of the simulation. The squared edge of each vector points to the direction of flow. At the earliest cooling stages of the hydrothermal system, fluid fluxes reach peak values (steps A-C); e.g.: Water Mass Flux $(WMF)_{max}$ at t = 2 Kyr (step B) = 3.1e-2 g/s×cm2, based on the thermodynamic output tables exported from the HT simulation. During the later period of hydrothermal cooling (t = 2.8 - 3.0 Myr), WMFmax reaches a value of 1.0e-9 g/s×cm2 and the geothermal gradient within the setting appears restored (as shown by the blue colours at steps F and G). The water mass flow limit that is set in this work to describe whether a hydrothermal system is active, has been set to 1.0e-9 g/s×cm2. (in accordance with Abramov and Kring (2004); (2005); (2007), and Jõeleht et al. (2005)). Hence, we can consider that flows below the aforementioned mass flux value are negligible, and that no hydrothermal circulation occurs.

Water Mass Flux Distribution (steps A-G): The central melt sheet ($T_{initial}$ = 1200 °C) and the surrounding lithologies appear impermeable at the earliest stages (A-D) of the impact-induced hydrothermal system (blue coloured regions in the simulative grid), and that is because permeability is also a function of temperature; when T ≥ 500 ºC, the permeability of any rock type decreases log linearly, and reaches values lower than 9.8e-23 m^2 (Hayba and Ingebritesen, 1997) due to the brittle/ductile transition at about 360 °C in silicic rocks (Fournier, 1991). Thus, mass fluxes (most probably in super-critical state) in such permeable and extremely heated rocks cannot reach values higher than 1.0e-9 g/s×cm^2. For this reason, heated regions above 500 ºC within this 200-km impact-cratering setting appear as blue at the earliest stages (steps A-D) of hydrothermal cooling. The illustrative steps (A-G) for the fluid flux evolution in this Martian crater show weaker flows with blue-ish colours (zero and minimum fluxes are represented by blue shades at the left-end of the colour-scale, with the former being darker) and stronger fluxes (≥ 6.0e-9 g/s×cm^2) are present in the yellow-, orange-, and red-coloured domains (with the latter representing maximum fluxes per time step). The magnitude of fluid flux is additionally expressed by vector's length. The squared edge of each vector indicates the direction of flow. Liquid water flux is represented by black vectors, vapour flux by light-greyish vectors, and super-critical flux by purple vectors. Each cell of the simulative grid has an appointed vector for each time step of the simulation showing the direction and magnitude of flow. At the earliest cooling stages of the hydrothermal system, fluid fluxes reach peak values (steps A-C); e.g.: Water Mass Flux $(WMF)_{max}$ = 3.1e-2 g/s×cm^2, at t = 2 Kyr (step B), based on the exported thermodynamic tables. At t = 2.8 Myr, WMF_{max} = 4.5e-9 g/s×cm^2, meaning that hydrothermal circulation is still appreciable. However, at t = 3Myr, the thermodynamic output shows that WMF_{max} = 1.02e-9 g/s×cm^2, which can be considered as the time point during which hydrothermal circulation ceases (after Abramov and Kring (2004); (2005); (2007), and Jõeleht et al. (2005).

3.1.3 Impact-Induced Hydrothermal Activity at a 100-km in diameter Martian Crater

In this numerical experiment for the impact-induced hydrothermal response in the 50 km radius cratering setting on Mars, the input parameters were defined again via the HT interactive programming environment and after iSALE computations. The lithostratigraphy was designed in a 2D mesh via the HT interface on a high-resolution grid of 4365 cells (97 × 45). The boundary conditions for the crater's geological system and impact-induced thermodynamics are summarized by fig. 3.4. The lithostratigraphic units of the impact setting and their geometrical characteristics remain similar with those in the previous case of the 200-km Martian crater, as we are still dealing with a significantly large and complex impact crater. However, the estimated volume of the fractured impactites, and of the produced melt sheet, is now reduced by 76 % in this simulation. This can be evidenced by the scale of the grid and the distribution of the rocks (i.e.: the subsurface area that they cover) therein. The melt sheet expands within a 15 km radius from the crater's center (horizontal distance), and its depth-width (vertical axis) is estimated to reach 850 m. The volume of the impact-produced melt sheet in the 200- and 100- km craters derived after computations on the geometric mean of the melt volume formulas suggested by Croft (1985), Kring (1995), Wong et al. (2005), Abramov and Kring (2005) for large impact craters. The approach that I adopted (formula shown below) yields computations that are more consistent with previously published results by Wong et al. (2005), and Abramov and Kring (2005), as their works describe more accurately impact cratering processes that occur specifically on Mars, and that are significantly affected by the Red Planet's gravitational field strength:

$$Vmelt = 1.23 \times 10^{-8} \frac{\rho_P}{\rho_t} \times g^{0.18} \times D_{tc}^{0.83} \times D_{pr}^{2.35} \times v^{1.63} \times sin^{1.63}(\theta)$$

In the above formula, ρ_p is the density of the projectile (3000 kg/m^3), ρ_t is the density of the target (2700 kg/m^3), g is the acceleration due to gravity (3.72 m/s^2), D_{tc} is the transient crater diameter, D_{pr} is the projectile diameter, v is the impact velocity (7000 m/s), and θ is the impact angle (45^o). Based on several numerical experiments performed in this work, that were also influenced by the initial parameterization used by Abramov and Kring (2005), an average volume of 952.8 km^3 was calculated for the induced melt sheet in the 100-km in diameter Martian crater (in contrast to the induced V_{melt} = 3970 km^3, in the 200-km in diameter crater).

The input thermodynamic properties of the rock units that comprise the 100-km in diameter Martian cratering system are shown in table 3.2: These are exactly the same with the ones used for the 200-km in diameter Martian cratering system. As explained in the previously presented numerical experiment for the larger crater, the initial thermodynamic conditions (temperature, pressure, and enthalpy distributions) after the bolide's impact on the surface of Mars were programmed in the grid according to shock-physics experiments for similar large impact-cratering processes on terrestrial surfaces (Abramov and Kring, 2004; 2005; 2007; and references therein). The temperature contours were designed via the HT Interactive pre-processor, and the input of their spatial distributions and values was decided after experimental trials through the HT post-processor.

The basal heat flux of the grid in this computational scenario has been assigned the same value of 17 mW/m^2 at the bottom boundary of the 100-km cratering setting, similarly to the rationale that was explained in the previous case (and according to estimates provided by Zuber et al. (2000), Jones et al. (2011), McGovern et al. (2002; 2004)). The top boundary represents the upper regolithic surface of Mars, where pressure is modelled at 0.007 bar and temperature at 1°C. The pressure and temperature constraints at the surface have been set as a constant function for the thermodynamics of the upper boundary conditions; this means that the upper surface acts like a dry and cold boundary, which despite allowing seepage of warmer upflows from the interior, any warm fluid flow is instantly cooled after reaching depths lower than 100 m. Hence, potential stream flows on the upper boundary due to spring-like hydrothermal fluxes originating from deeper regions of the crater, have been given a T_{min} = 1 °C at the surface. Additionally, inflow and fluid recharge events from the ground surface to the deeper permeable rocks of the crater, due to meteoric-surficial water and precipitation flux of T_{min} = 1 °C, were also considered as possible via the HT coding script. This thermodynamic parameterization for the 100-km crater, should allow us to explore further the hydrothermal cooling pattern (both volcanic and impact-induced) beneath the cold and arid surface of Mars, and determine the time frame under which water-rock interaction may have occurred on Mars. Furthermore, this modelling approach may also indicate niches within crater valleys on the surface of Mars, where aqueous and hydrothermal deposits may be more abundant, so that future Mars-exploration missions could utilize.

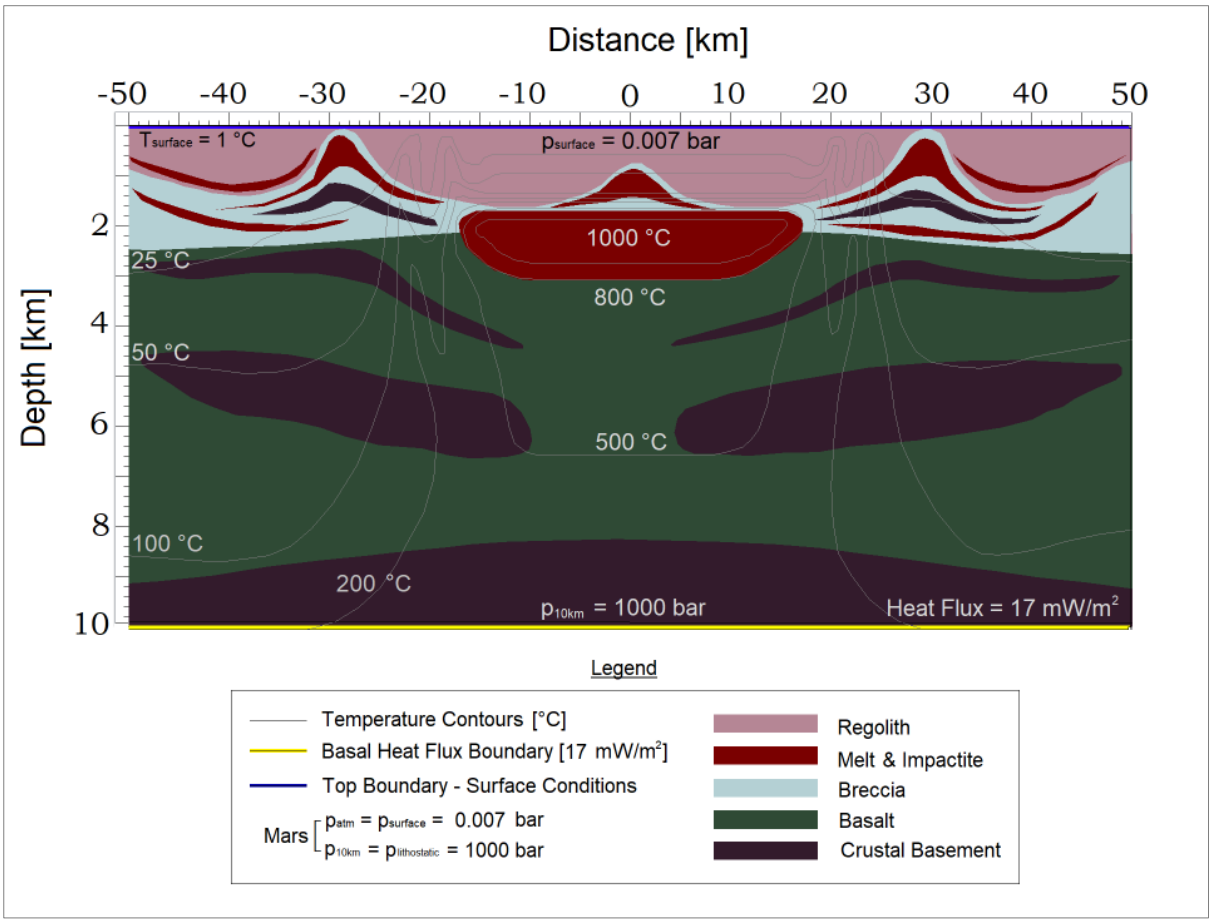

Fig. 3.4. Initial thermodynamic conditions and rock distributions in the putative 100-km cratering system on Mars. Basal Heat Flux is assigned to a value of 17 mW/m^2. Atmospheric pressure at the ground surface of Mars is set at 0.007 bar, and the ground temperature at the upper boundary of the grid is set at 1°C. The central melt sheet which comprises the main heat source of the setting has been assigned a T_{max} of 1000 °C (200 °C lower temperature than that of the central melt sheet in the case of the 200-km crater). The central melt sheet herein has been modelled with a 76% less volume than the central melt of the 200-km crater and expands at a radius of 15 km from the centre of the setting. The vertical distance - depth of the central melt sheet is set at 850 m. The crater's morphology, lithostratigraphic distribution and thermodynamic parameters have been modelled similarly to those in the 200-km case, and according to previous modelling results for large impact structures provided by Dence (1968); Grieve et al. (1977), (1981); Grieve (1991); French (1998); Abramov and Kring (2004); (2005); (2007). For this reason, the main lithologies and their geometrical characteristics remain unchanged in this simulative grid (when compared to the 200-km cratering setting), but their volume distribution within the cratering setting is reduced by 76 %, based on the impact-physics describing cratering processes on Mars (Holsapple, 1993; Abramov and Kring, 2005; Wong et al., 2005).

Table 3.2. HT boundary thermodynamic conditions for the lithologies comprising the grid of the 100-km Martian crater (fig. 3.4).

Petrophysical Properties	**Lower Crustal Rocks**	**Basalts**	**Melt Rocks**	**Breccia**	**Regolith**
Permeability (k) {m^2}	k_z = f(d,T), k_x = f (d,T)	k_z = f(d,T), k_x = f (d,T)	k_z = f(d,T), k_x = f (d,T)	k_z = f(d,T), k_x = f (d,T)	k_z = f(d,T), k_x = f (d,T)
Porosity (φ) {%}	φ = f (d,T)	φ = f (d,T)	φ = f (d,T)	φ = f (d,T)	φ = f (d,T)
Thermal Conductivity {W/m·K}	2.9	2.7	2.7	2.7	1.7
Specific Heat Capacity {J/kg·K}	1200	1000	1000	900	700
Density {kg/m^3}	3000	2700	2500	2500	1700
Surface Permeability {m^2}	1.00E – 19	9.00E – 17	1.00E - 16	1.00E – 15	1.00E - 14
Surface Porosity ($\varphi_{surface}$)	2.0 %	5.0 %	7.0 %	7.0 %	15.0 %

Table 3.2 – Note: The petrophysical properties of the rocks in this simulation are similar to those of the 200-km cratering system, except for the volume distribution of melt and impactites (heavily fractured rocks). The parameterization of the setting is also adapted after models for impact structures suggested by Abramov and Kring (2005) and Sanford (2005). The volume of the produced melt rock in this putative 100-km in diameter crater is reduced by 76%, compared to the induced volume of melt in the 200-km in diameter crater. Additionally, peak temperature in the 100-km setting was reduced by 16.66 %, when compared to the initial T_{max} of the 200-km in diameter post-impact hydrothermal system, as dictated by the impact-physics calculations for each scenario. The below parameters were used in order to reveal potential differences of the hydrothermal response in each crater.

The thermodynamics of the post-impact hydrological system in the 100-km in diameter Martian crater are summarized by the simulations time steps (A-F) of fig. 3.5 below. Significant differences can be easily observed between the two scenarios and these concern the flow patterns per each time step, the magnitude of hydrothermal flux, the number of active hydrothermal cells per time step that drive the hydrological cycle, and the resulting lifetime of the hydrothermal system (evident also through the following video in the supplementary materials: Martian Crater_100-km_Higher Permeability_.mp4). I recommend that the video and Fig. 3.5 and 3.6 should be compared to the exported results of the simulation for the 200-km sized crater. This gives a better view of the resulting fluid mechanics in the setting, and on how minor or major differences in the initial conditions of the simulative grid can produce different results. The grid is set again at 4365 cells (97 × 45), but since we are now dealing with a 50% smaller crater's diameter (compared to the 200-km sized crater), the resulting resolution for the computation is far higher. Lower resolution simulations were also performed for this model, but the results were not indicating changes on the lifetime of the hydrothermal system, or on the general flow pattern per each time step. On the contrary, some minor convective cells would not appear in the low-resolution simulations, and most numerical experiments would not converge to the equations of state and would stop abruptly, due to major thermodynamic differences on the pressure, temperature and permeability constraints between the heated domains of the crater and its surface rocks.

In this numerical experiment for the 100-km in diameter complex crater on Mars, at time zero right after the impact (fig. 3.5: A), the initial maximum temperature in the system is set at 1000 °C (as shown by the orange-coloured domains in fig. 3.5: A, and according to the temperature scale applied, representing the induced melt rock region). It is notable that lower crust material of 700 – 900 °C is uplifted from a depth of 10 km, up to a depth of 7 km beneath the central melt sheet. In the simulation for the 200-km crater, this feature was not present, and this may be due to the even higher resolution applied in this model; i.e.: 1 cell per 1.03 km on the horizontal axis, and 1 cell per 222.2 m on the vertical axis of the grid. In contrast, the simulation for the 200-km crater was using a resolution described by 1 cell per 2.06 km on the horizontal axis, and 1 cell per 222.2 m on the vertical axis. This means that the equations of state via which the HYDROTHERM code works, are not only fully capable of accurately describing the thermodynamics and hydrological activity in such systems, but they can even indicate the correct initial temperature-pressure and enthalpy distributions in a setting after a few simulation runs and experimentation with different resolution parameters. What we can observe in this

first time-step of the simulation at t_0 is that the initial thermodynamic conditions of the crater are in complete agreement with impact-physics simulations through the i-SALE code, performed in previously published work by Wünnemann et al. (2006), Collins (2014), Collins et al. (2011), and Wiggins et al. (2022).

However, the application of slightly lower or higher resolution (by 400-1000 cells) in the HYDROTHERM experiments of this work, showed that these resolution differences between computational runs did not influence the lifetime of the hydrothermal system substantially. When a lower resolution was applied in these models, some smaller hydrothermal cells that were present in higher resolution runs were absent, and on top of that, the excavated mantle and lower crust material was by 150-300 °C colder. This can also be confirmed by comparing the temperature distributions in the two different by size cratering settings (fig. 3.3: A-E and fig. 3.5: A-E). In both simulations, at t = 1 Myr, (Fig. 3.3: E and Fig. 3.5: E), the maximum temperature observed in both settings, at depths greater than 6 km and beneath the crater's centre, is between 450-500 °C, and the predictions for the hydrothermal cooling pattern by the code in each case are identical, and without the presence of any artifacts. Hence, we can safely assume that a few notable differences will be present during the initial stages of HT simulations for hydrothermal cooling, when experimenting with low resolution versus high resolution scenarios. However, the lifetime of the hydrothermal system and the thermal and water mass flux evolution of the setting will not be significantly affected, as witnessed also by Abramov and Kring (2004, 2005, 2007) in their HT numerical experiments for the impact-induced hydrological systems in terrestrial (Sudbury and Chicxulub) and putative Martian craters.

At t_0, hydrothermal flows dominate the entire upper 2-km lithological domain of the crater, and are also present in regions that are adjacent to the central melt sheet and to the excavated lower crust-upper mantle material at depths greater than 6-10 km (fig. 3.5: A; hydrothermal cells shown in red-coloured regions). At t = 2 Kyr, the central melt sheet has lost circa 10 % of its initial heat, which does not yet affect significantly the very strong hydrothermal circulation that takes place closer to the centre of the crater and above the central melt sheet (at t= 2 Kyr, T_{max} = 900 ºC, based on the thermal scale and the exported thermodynamics from fig. 3.5: B). However, at t = 2 Kyr, it can be observed that the deeper and very extensive hydrothermal cells at depths greater than 8 km that formed right after the impact and close to the uplifted lower crust region, have either ceased or appear spatially confined, with much smaller volumes (fig. 3.6: A-B). Additionally, the subsurface regions of the crater beyond its peak ring, that extend

beyond the radius of 30 km from the crater's centre (outer-rim region) seem to be affected by less strong fluxes at t = 2Kyr (WMF = 4-5E-9 g/s×cm^2). This clearly indicates that hydrothermal cooling has already started taking its toll on the hydrodynamics of the most distant subsurface regions of the outer-rim valley. Moreover, as explained in the previous simulation for the 200-km crater, the melt sheet in the central region remains impermeable for as long as its temperature is higher than 500 ºC. By the time that the rim of the central melt and its surrounding rocks crystallize, super-critical fluid flows will start being present in that domain (as shown in Fig. 3.6: B-D). At t = 300 Kyr, the system has lost around 20-25% of its initial heat (fig. 3.5: D, $T_{max} \approx 790$ ºC,), and a significant volume of the outer rim of the central melt sheet seems to have crystallized, as water mass flux appears present therein.

As convective cooling progresses, from t = 300 Kyr and then on, liquid water along with super-critical fluid can now flow through the permeable but still heated domains of the central melt sheet, and through its surrounding impactites (fig. 3.5: D-F). After 300 Kyr, hydrothermal activity takes place mainly in the upper 3-4 km of the impactites of the setting (within the regolith, breccia, melt and other excavated impactites), and within a radial distance of 30 km from the crater's centre. Hydrothermal flows do not reach regions beyond the peak ring after this time point of the hydrological system. Some very weak flows appear present at depths of 5-7 km beneath the central region, but these are negligible, as their flux magnitude is no greater than 1.0E-9 g/s×cm^2 (fig. 3.5: D, beneath the central melt sheet, slightly lighter-blue coloured fluxes are present, in contrast to the darker-blue-coloured surrounding domain where no flux takes place).

At t = 1 Myr, T_{max} = 400 ºC in the geological system and maximum fluid flux values do not exceed 1.E-8 g/s×cm^2. At that time point, we can observe only two main convective cells in the hydrothermal system that are symmetrically aligned beneath the central valley of the crater (red-coloured regions in fig. 3.5: E). It is interesting also to see some appreciable liquid water up-flows (WMF ≈ 5.0E-9 g/s×cm^2) originating from the 2-3 km deep convective cells. These up-flows seem to have persisted in the system for more than 1 Myr (fig. 3.5: A-F) and based on their direction of flow (vectors) during the entire evolution of the hydrothermal system, they should have been seeping out through the peak ring's rocks, for as long convection is active (based on the lithostratigraphy of the impact crater as presented in fig. 3.4). In both numerical simulations for the hydrothermal activity in the large impact craters on Mars (100-km and 200-km in diameter systems), these up-flows, seeping out to the surface through the peak ring's

rocks, were present in both cases and during the entire period of the hydrological cycle. By considering these results of the simulations, we can further argue on the objectives of future Mars exploration missions, and emphasize that large craters' peak rings may be the most promising and fruitful sites in terms of their astrobiological potential; since water-rock reactions and potential prebiotic nutrients' release may have persisted in peak ring lithologies of large Martian impact structures for more than 1-2 Myr during their intense impact-induced hydrological activity.

In the final time steps of the simulation, cold water recharge from the surface of Mars to the convective cells is clearly indicated through the 300 Kyr and 1 Myr time steps of the simulation (fig. 3.5: D-E). These convective events are accelerating the cooling of the hydrothermal system, since their temperature in the uppermost layer of the regolith and on the surface is adjusted to 1 °C. After 1.8 Myr, the simulation shows that recharge flows from the surface have ceased completely, implying the thermodynamic transition of the geological setting from convective to conductive cooling (fig. 3.5: F). Although some water mass flux with a maximum value of 6.0E-9 g/s×cm^2 is still present in the convective cells at depths of 2-3 km after 1.8 Myr, these do not last for more than another 100 Kyr. Since recharge flows from the surface of Mars have already cooled the system and are absent at t = 1.8 Myr, we can establish this time step as the end point of the hydrothermal system's duration. In agreement with that is also the computation for the temperature distribution in the crater at t = 1.8 Myr.

The simulation shows through fig. 3.5: step F, that the geothermal gradient is very close to its complete restoration close to the central region of the crater, and that it has already been restored in subsurface niches beyond the peak ring (in the outer-rim valley) and at a radial distance greater than 30 km from the centre. In particular, the computed value of the temperature beneath the peak ring (at 30 km radius) and at a depth of 1.5 km is 20 °C. Thus, the geothermal gradient therein can be easily deduced with a value of 13.3 °C / km, which is very close to the background geothermal gradient of 12 °C / km that I have assigned to the grid. (fig. 3.5: F; the temperature distribution in the domain is represented predominantly by darker blue colours, and proves that no fluid flux occurs in the system based on the additional absence of flow vectors).

Temperature & Water Mass Flux Distribution in the Post-Impact Hydrothermal System

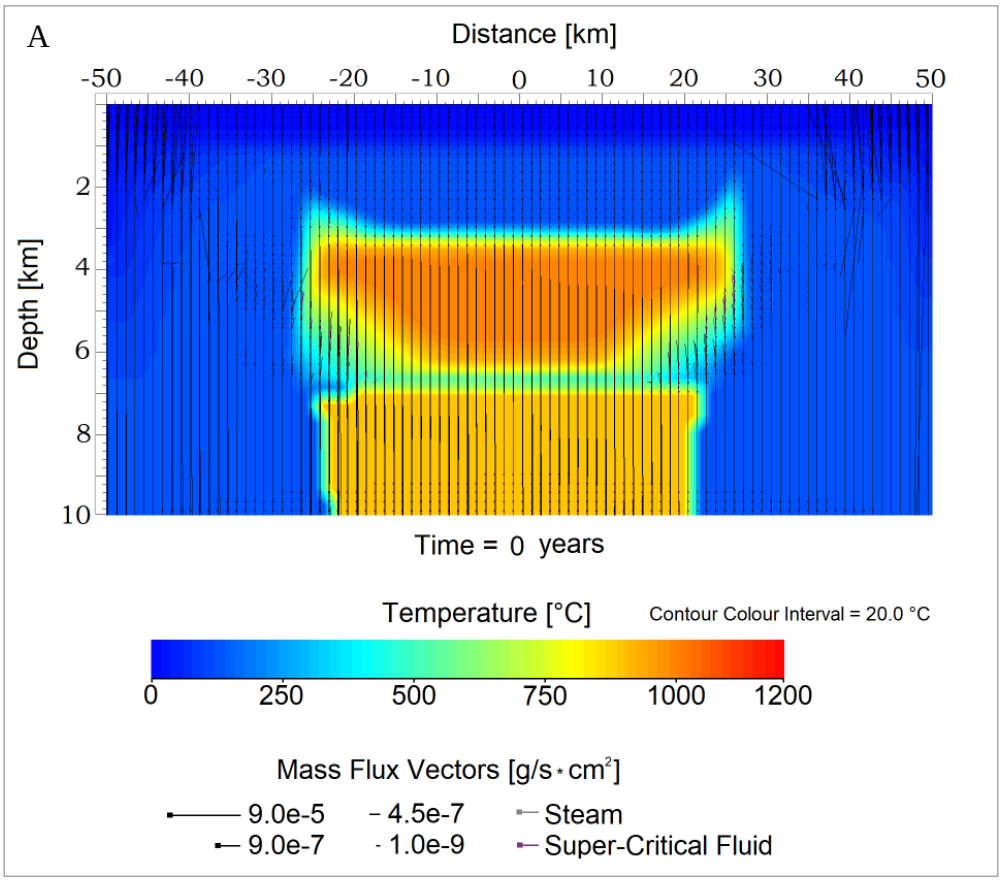

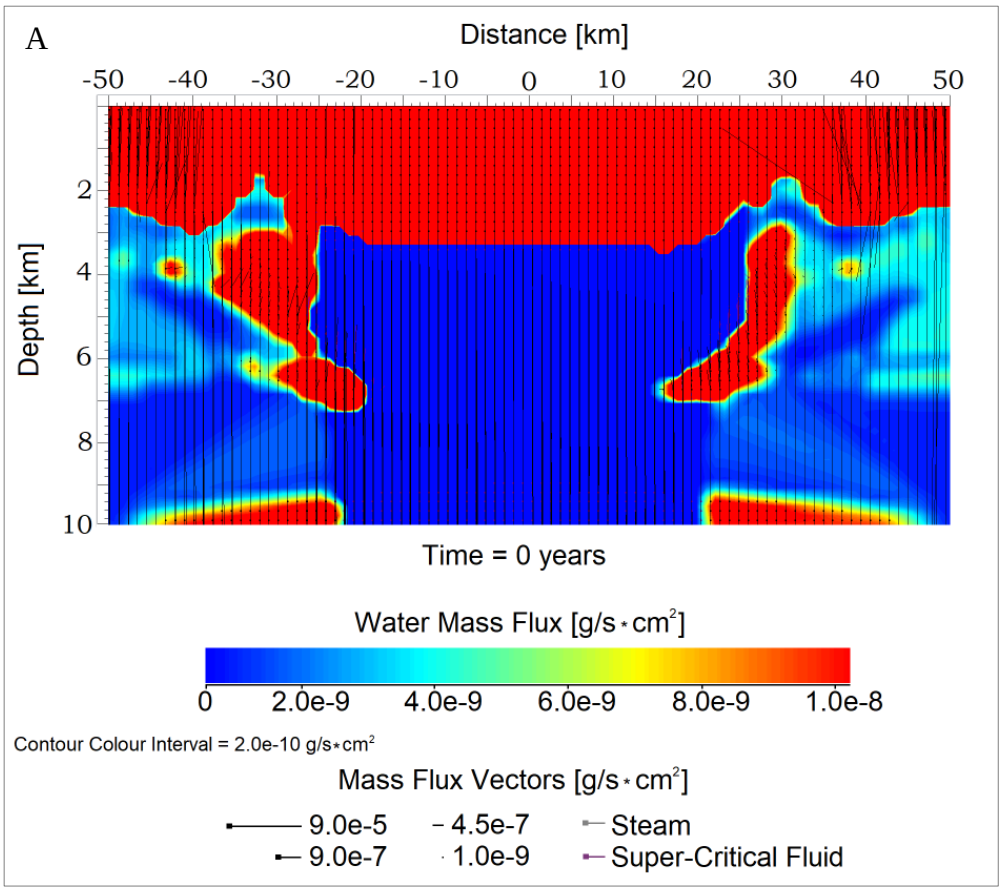

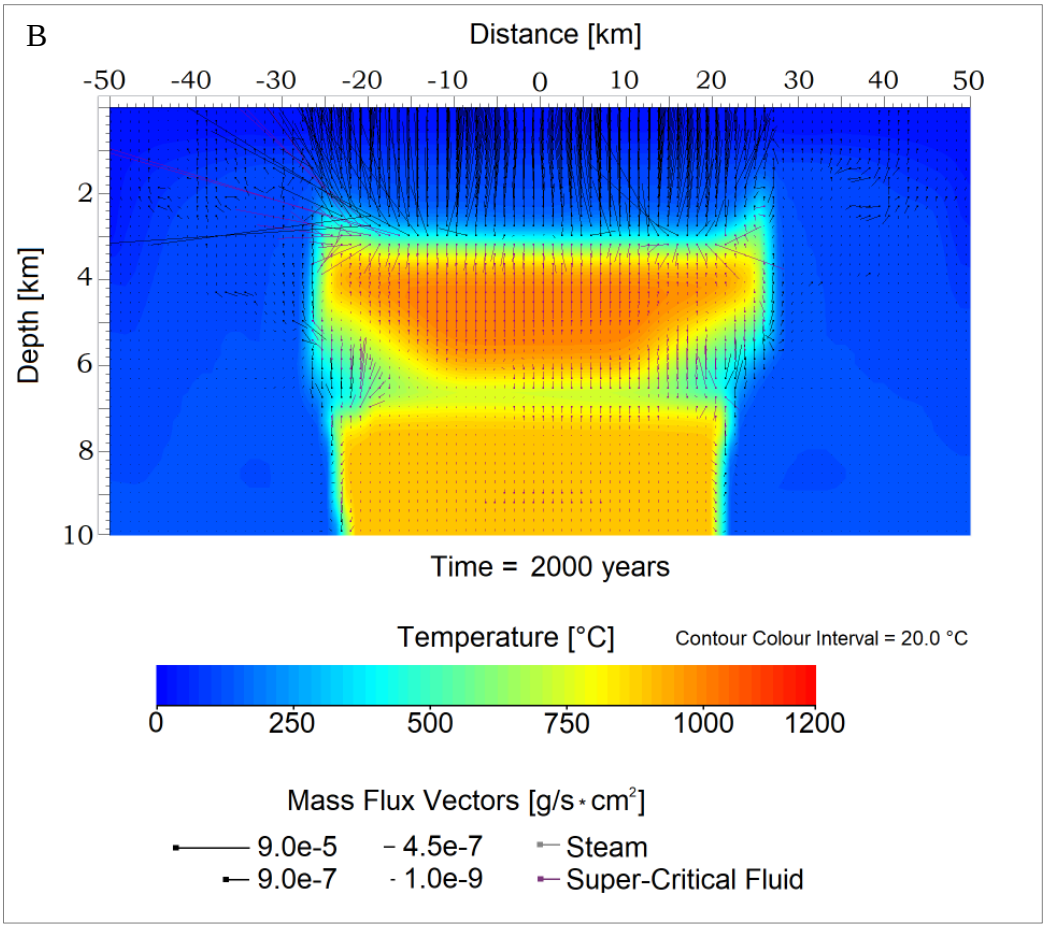
B
Distance [km]
-50 -40 -30 -20 -10 0 10 20 30 40 50
Depth [km]
2 4 6 8 10
Time = 2000 years
Temperature [°C]
Contour Colour Interval = 20.0 °C
0 250 500 750 1000 1200
Mass Flux Vectors [g/s*cm²]
9.0e-5
9.0e-7
4.5e-7
1.0e-9
Steam
Super-Critical Fluid

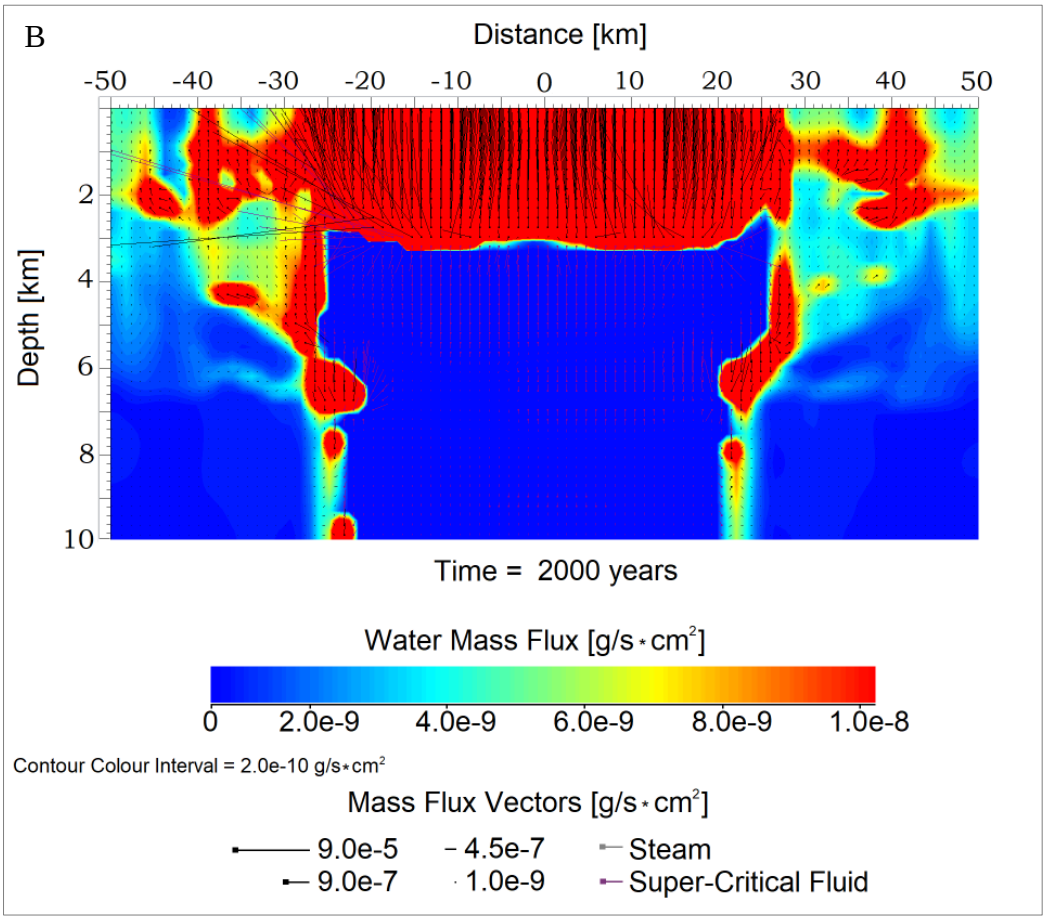
B
Distance [km]
-50 -40 -30 -20 -10 0 10 20 30 40 50
Depth [km]
2 4 6 8 10
Time = 2000 years
Water Mass Flux [g/s*cm²]
0 2.0e-9 4.0e-9 6.0e-9 8.0e-9 1.0e-8
Contour Colour Interval = 2.0e-10 g/s*cm²
Mass Flux Vectors [g/s*cm²]
9.0e-5
9.0e-7
4.5e-7
1.0e-9
Steam
Super-Critical Fluid

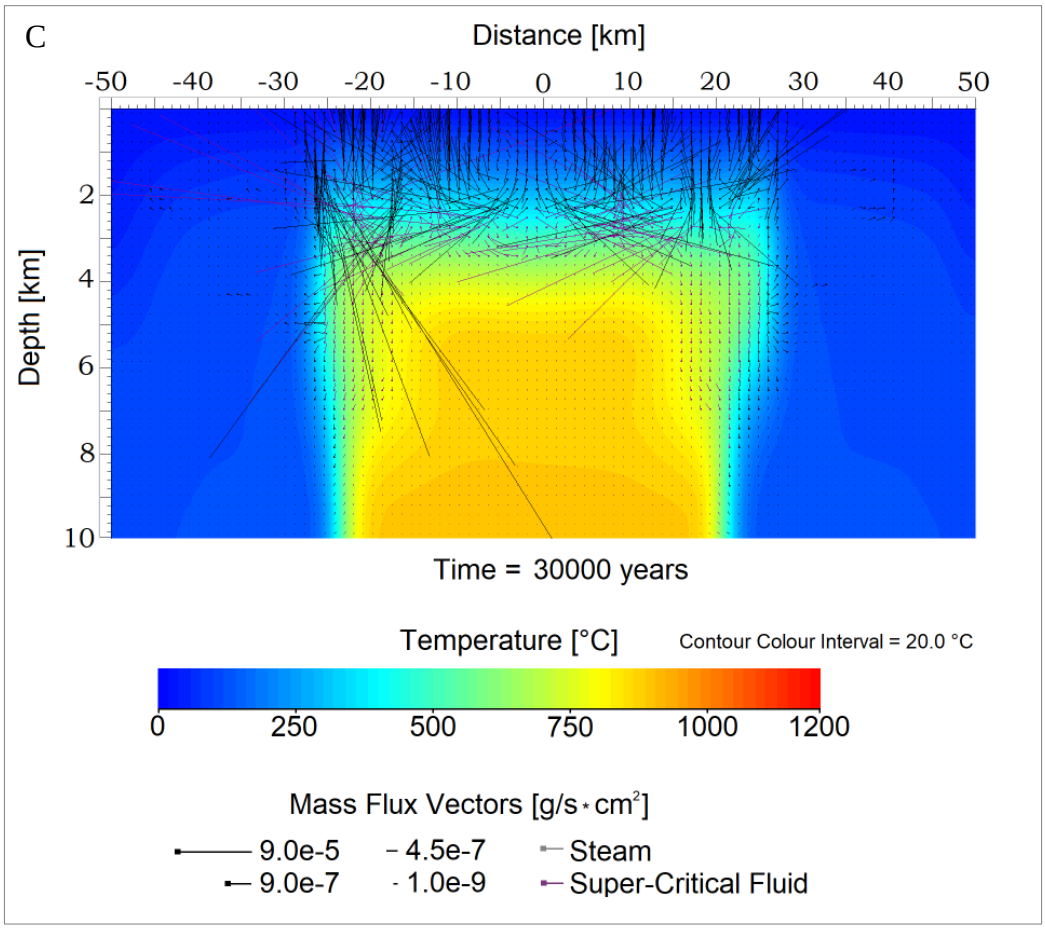
C
Distance [km]
-50 -40 -30 -20 -10 0 10 20 30 40 50
Depth [km]
2 4 6 8 10
Time = 30000 years
Temperature [°C]
Contour Colour Interval = 20.0 °C
0 250 500 750 1000 1200
Mass Flux Vectors [g/s*cm²]
9.0e-5
4.5e-7
Steam
9.0e-7
1.0e-9
Super-Critical Fluid

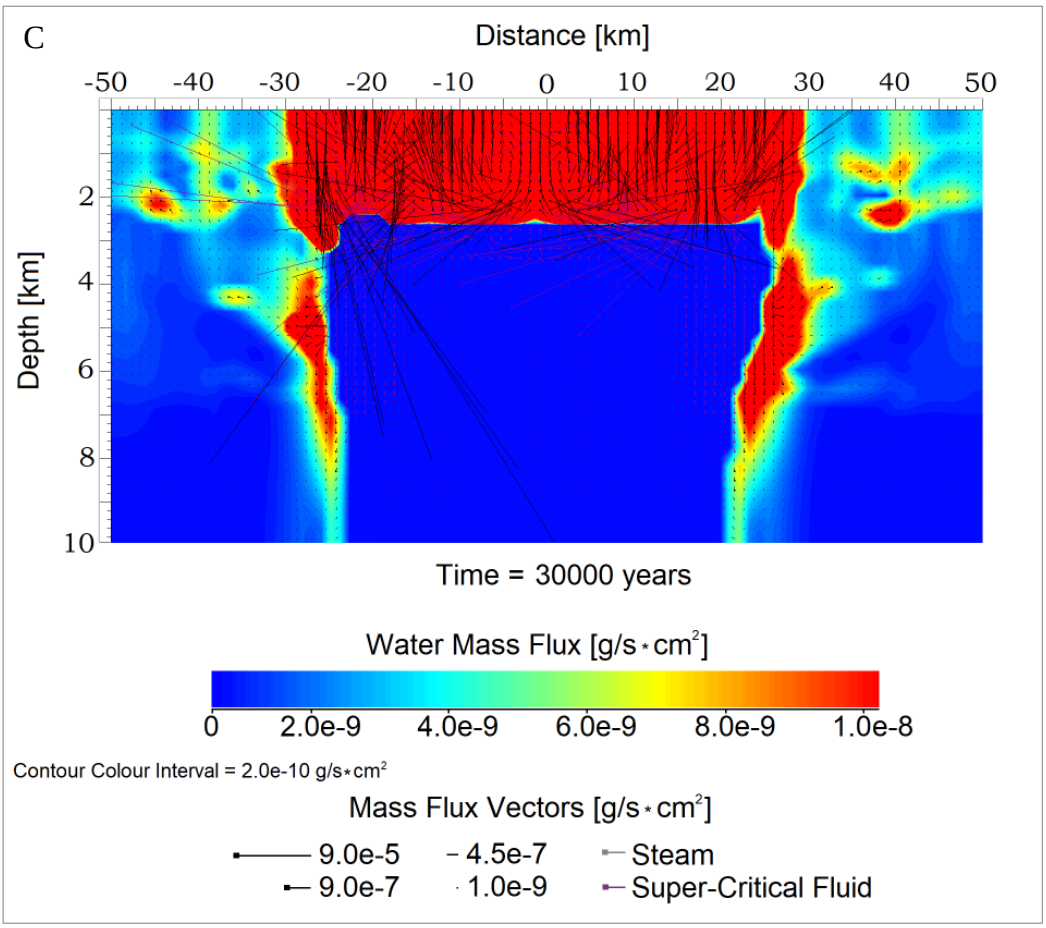
C
Distance [km]
-50 -40 -30 -20 -10 0 10 20 30 40 50
Depth [km]
2 4 6 8 10
Time = 30000 years
Water Mass Flux [g/s*cm²]
0 2.0e-9 4.0e-9 6.0e-9 8.0e-9 1.0e-8
Contour Colour Interval = 2.0e-10 g/s*cm²
Mass Flux Vectors [g/s*cm²]
9.0e-5
4.5e-7
Steam
9.0e-7
1.0e-9
Super-Critical Fluid

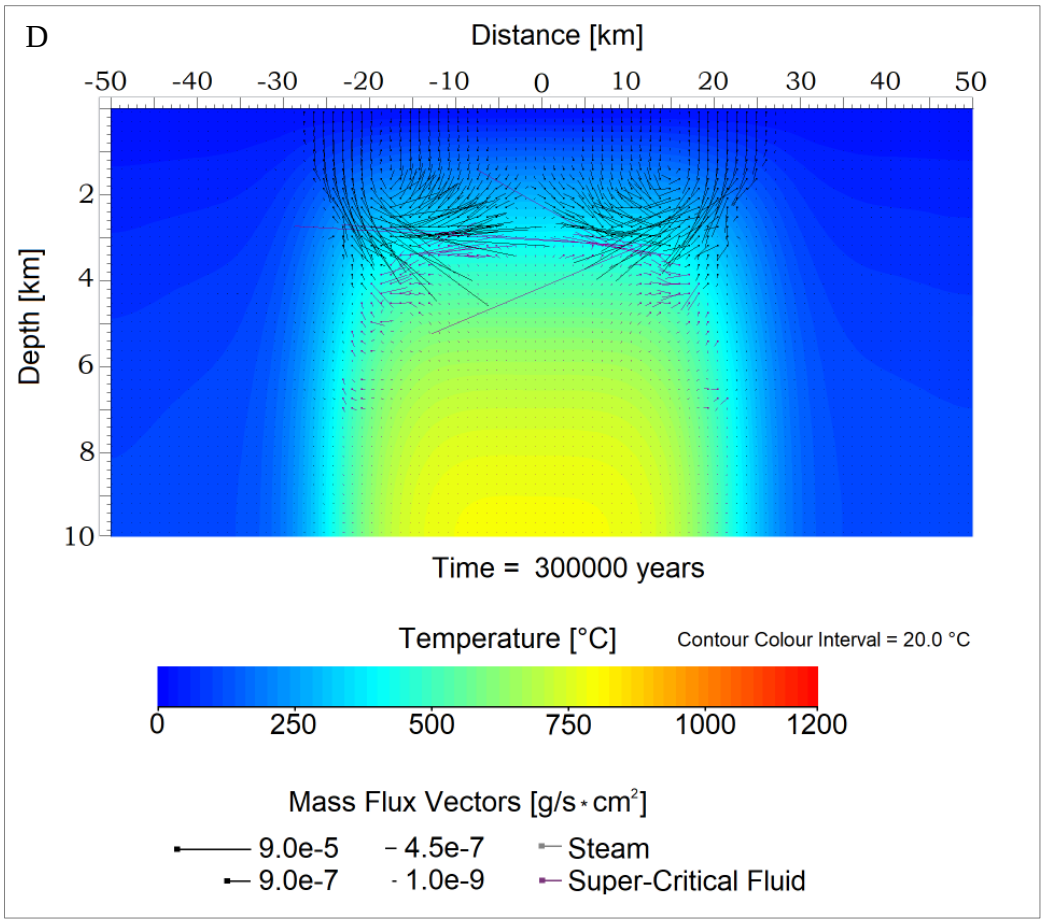
D
Distance [km]
-50 -40 -30 -20 -10 0 10 20 30 40 50
Depth [km]
2 4 6 8 10
Time = 300000 years
Temperature [°C]
Contour Colour Interval = 20.0 °C
0 250 500 750 1000 1200
Mass Flux Vectors [g/s*cm²]
9.0e-5
9.0e-7
4.5e-7
1.0e-9
Steam
Super-Critical Fluid

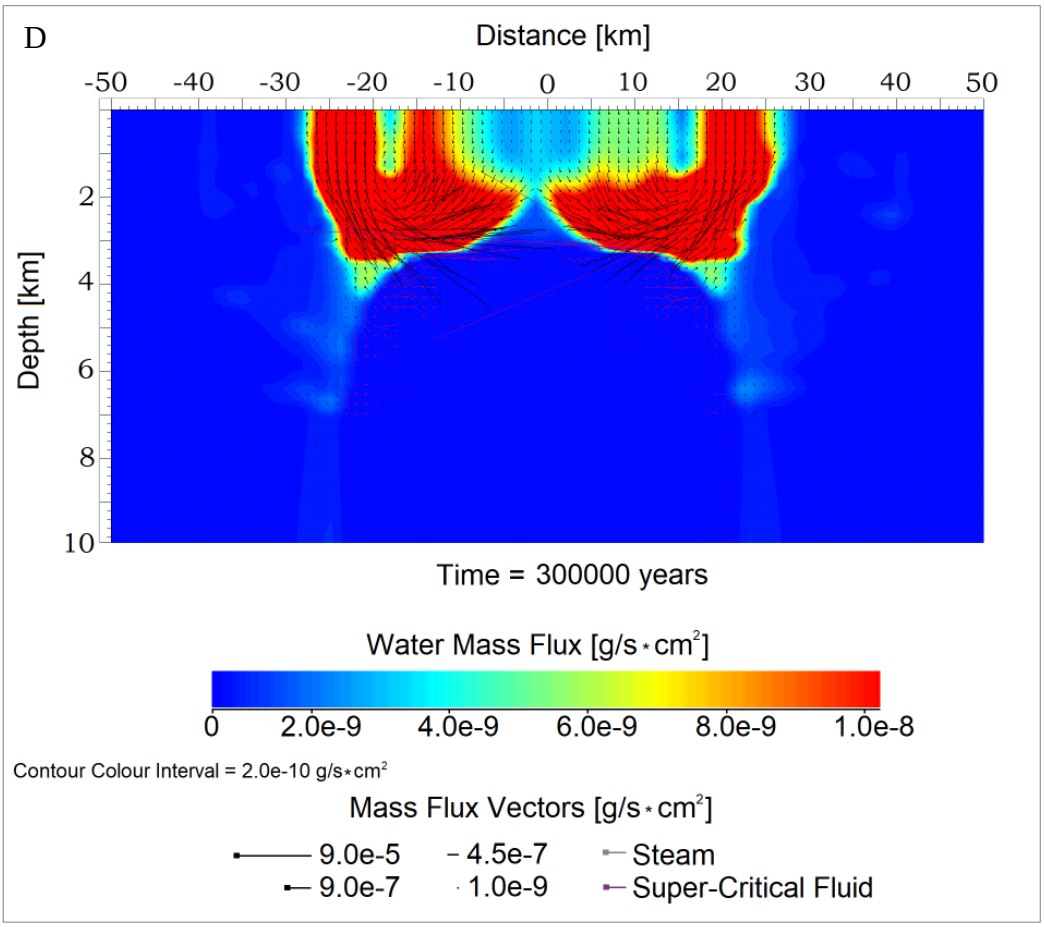
D
Distance [km]
-50 -40 -30 -20 -10 0 10 20 30 40 50
Depth [km]
2 4 6 8 10
Time = 300000 years
Water Mass Flux [g/s*cm²]
0 2.0e-9 4.0e-9 6.0e-9 8.0e-9 1.0e-8
Contour Colour Interval = 2.0e-10 g/s*cm²
Mass Flux Vectors [g/s*cm²]
9.0e-5
9.0e-7
4.5e-7
1.0e-9
Steam
Super-Critical Fluid

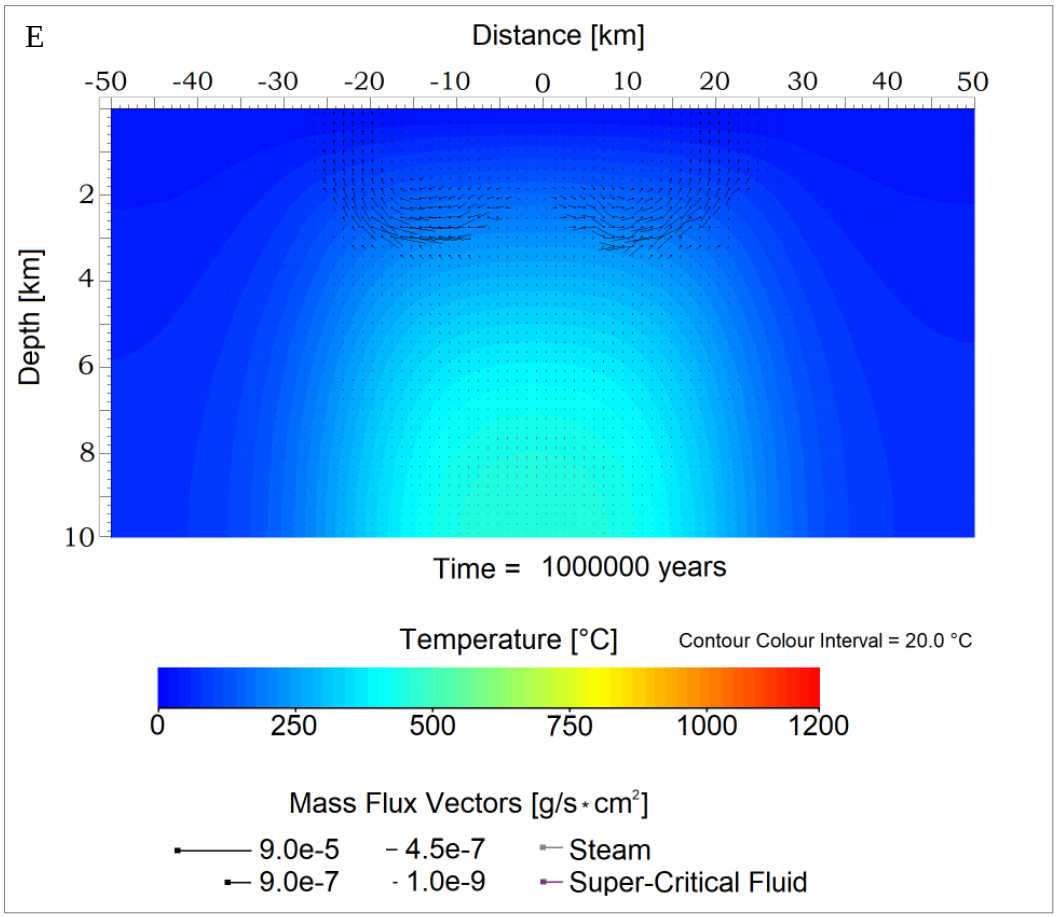
E
Distance [km]
-50 -40 -30 -20 -10 0 10 20 30 40 50
Depth [km]
2 4 6 8 10
Time = 1000000 years
Temperature [°C]
Contour Colour Interval = 20.0 °C
0 250 500 750 1000 1200
Mass Flux Vectors [g/s*cm²]
9.0e-5
4.5e-7
Steam
9.0e-7
1.0e-9
Super-Critical Fluid

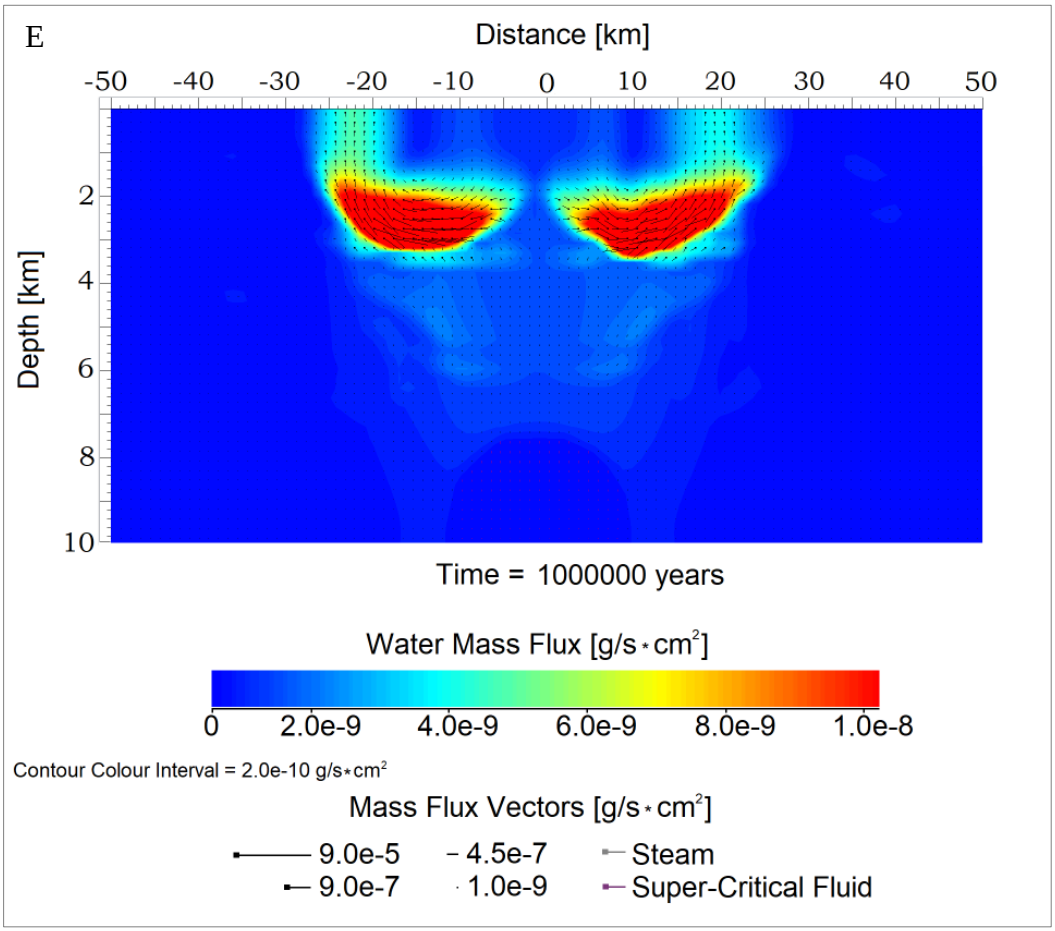
E
Distance [km]
-50 -40 -30 -20 -10 0 10 20 30 40 50
Depth [km]
2 4 6 8 10
Time = 1000000 years
Water Mass Flux [g/s*cm²]
0 2.0e-9 4.0e-9 6.0e-9 8.0e-9 1.0e-8
Contour Colour Interval = 2.0e-10 g/s*cm²
Mass Flux Vectors [g/s*cm²]
9.0e-5
4.5e-7
Steam
9.0e-7
1.0e-9
Super-Critical Fluid

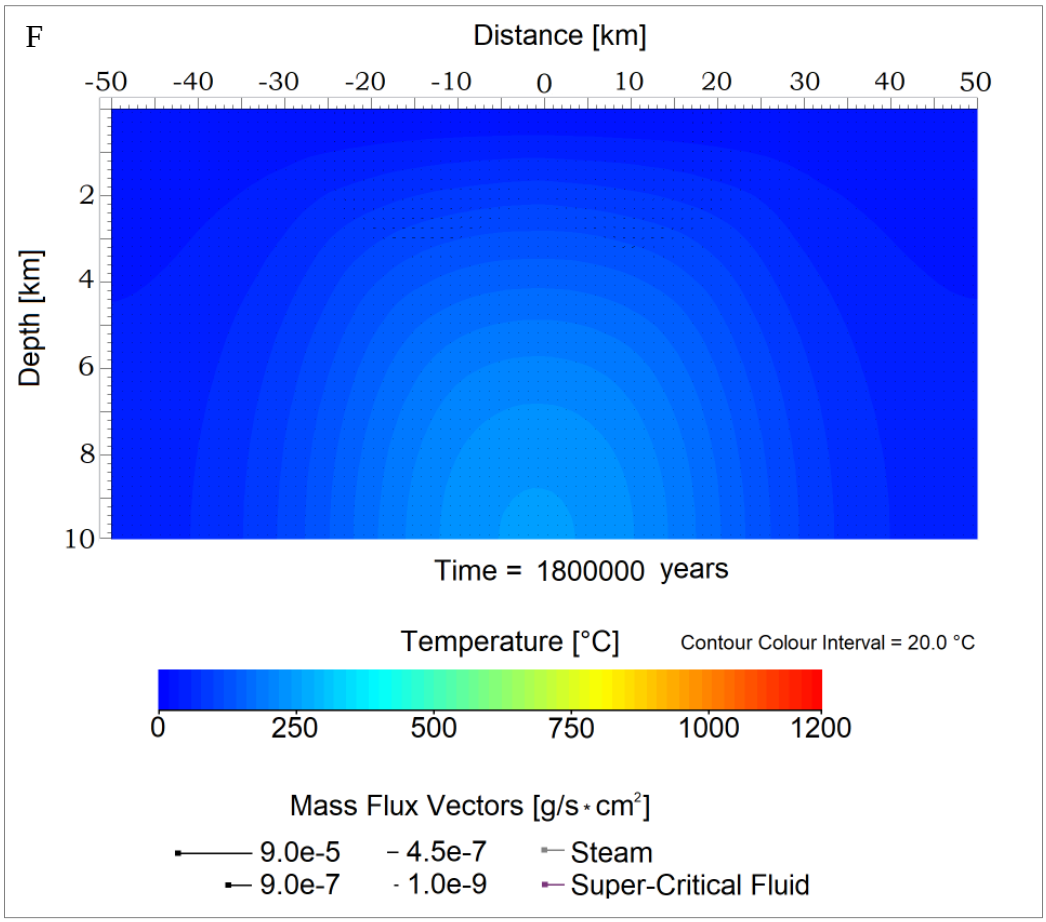
F
Distance [km]
-50 -40 -30 -20 -10 0 10 20 30 40 50
Depth [km]
2 4 6 8 10
Time = 1800000 years
Temperature [°C]
Contour Colour Interval = 20.0 °C
0 250 500 750 1000 1200
Mass Flux Vectors [g/s*cm²]
9.0e-5
4.5e-7
Steam
9.0e-7
1.0e-9
Super-Critical Fluid

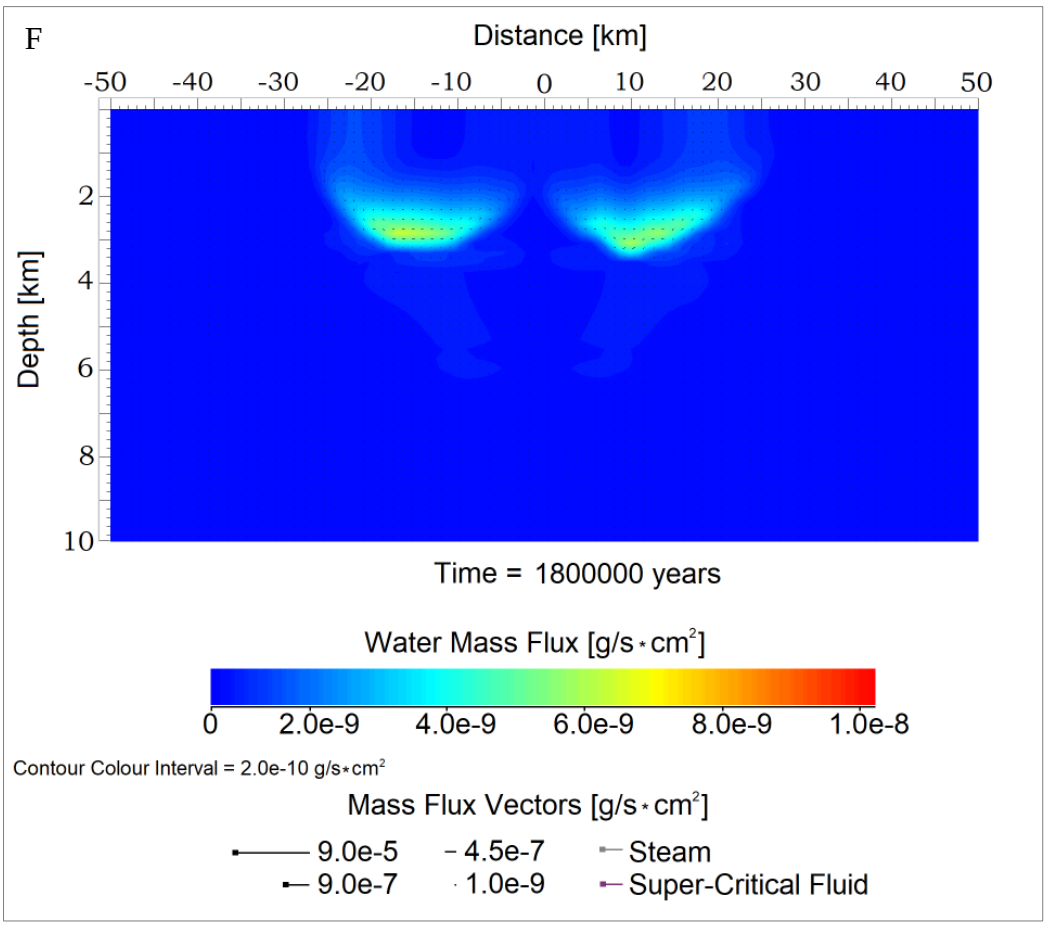
F
Distance [km]
-50 -40 -30 -20 -10 0 10 20 30 40 50
Depth [km]
2 4 6 8 10
Time = 1800000 years
Water Mass Flux [g/s*cm²]
0 2.0e-9 4.0e-9 6.0e-9 8.0e-9 1.0e-8
Contour Colour Interval = 2.0e-10 g/s*cm²
Mass Flux Vectors [g/s*cm²]
9.0e-5
4.5e-7
Steam
9.0e-7
1.0e-9
Super-Critical Fluid

Fig. 3.5 (steps A-F). Temperature and Water Mass Flux distribution in the 100-km in diameter putative Martian crater from t_0 after the impact and for a period of 1.8 Myr, up to the time point when hydrothermal circulation has ceased: WMF_{min} = 1.0e-9 g/s×cm^2.

Temperature Distribution (steps A-F): The time point in which the geothermal gradient of the setting is restored determines the halt of hydrothermal circulation. After the impact, T_{max} = 1000 °C in the entire geological domain, and the central melt sheet is represented by orange-yellowish-coloured regions (based on the temperature scale) at the earliest stages (A-B) of hydrothermal cooling. As shown previously, the cooling of the hydrothermal system during this 1.8 Myr period is represented via the transition from warmer colours (orange-yellow shades, T scale) to colder ones (green to blue shades; T scale) at the end of hydrothermal circulation. The thermal field evolution demonstrates much hotter and stronger fluid mass fluxes at the initial stages of aqueous circulation (A-D), and colder and weaker flows during the latest stages of hydrous activity (E-F). Fluid flux (liquid water flux shown in black arrows, steam in light-greyish colours, and super-critical flux in purple colours; WMF scale) is represented also by vectors in each time-step of the simulation. The squared edge of each vector shows the direction of flow. In this thermodynamic scenario, the geothermal gradient of the setting appears restored at circa t = 1.8 Myr (as blue-coloured cells prevail in the entire setting: steps E and F).

Water Mass Flux Distribution (steps A-F): The central melt sheet and its surrounding impactites appear impermeable at the earliest stages (A-D) of the hydrological cycle (blue coloured regions in the simulative grid; WMF scale), as these rocks are heated beyond the thermal limit of T ≥ 500 ºC. Steps A-F demonstrate the fluid flux evolution in this Martian crater. No flow or very weak flow is represented by blue-coloured domains in the grid, and stronger fluxes (≥ 6.0e-9 g/s×cm^2) are present by yellow-, orange-, and red-coloured domains (red-coloured regions indicate that maximum fluxes occur within the host rock unit per time step; WMF scale). The magnitude of fluid flux is additionally expressed by vector's length. The squared edge of each vector indicates the direction of flow. Liquid water flux is represented by black vectors, vapour flux by light-greyish vectors, and super-critical flux by purple vectors. Each cell of the simulative grid has an appointed vector for each time step, indicating the direction and magnitude of flow. At the initial stage of hydrothermal cooling after the impact, fluid fluxes reach peak values (steps A-C) in rock units that surround the impermeable and very hot impact-induced melt sheet at the central region of the complex crater (red cells - domains). At t = 1.8 Myr, $WMF_{max} \approx$ 5.0e-9 g/s×cm^2, meaning that hydrothermal circulation is still appreciable. Nevertheless, after less than 20 Kyr beyond that time point (i.e.: 1.82 Myr), the upper convective cells shown at time step F (WMF scale), host only minimum fluid flux of 1.02e-9 g/s×cm^2 (according to the simulations' exported video in the supplementary materials). Thus, we can assume that post-impact hydrous flows therein cease after 1.8 Myr.

3.1.4 Impact-Induced Hydrothermal Activity at a 10-km in diameter Martian Crater

Smaller impact structures are quite enigmatic in terms of their potential for generating impact-induced hydrothermal systems. In this computational scenario, I have investigated the impact-generated hydraulic effects at a Martian crater with a radius of 5 km. According to Pike (1980), the simple-to-complex transition for Martian impact structures occurs at diameters between 3 and 8 km, a theory which is also established by further investigations conducted by Grieve et al. (1981), Grieve (1987), French (1998), Dence (2004), Rae (2018). Therefore, in this case study, I have adopted a complex crater's morphological - lithostratigraphic model as a boundary condition for simulating the post-impact thermodynamics in the putative 10-km in diameter Martian crater (fig. 3.6). The lithostratigraphy of the geological setting was designed through the HT Interactive Preprocessor in a high-resolution grid of 1800 cells (60 × 30; 1 cell per 166.6 m on the horizontal axis and 1 cell per 166.6 m on the vertical – depth axis). The initial thermodynamic conditions for the impact structure after its formation on Mars were adjusted after iSALE numerical results for a 10-km in diameter crater, and based on thermodynamic constraints provided by Rathbun and Squyres (2002), Barnhardt et al. (2010). Furthermore, results from ongoing numerical experiments for smaller-scale impact cratering processes on Earth, which have been incorporated in the supplementary materials (appendix) of this thesis, have also helped determine the boundary thermodynamic conditions of this HT 3 simulation (i.e.: Christou et al. (in prep.): *Post-impact thermodynamic limits for the induced aqueous activity in small impact craters on Earth*; Vasconcelos and Christou (in prep.): *An impact-induced hydrothermal system at the Cerro do Jarau structure?*). The initial settings of the simulation conditions are summarized through fig. 3.6.

Based on the aforementioned iSALE numerical models and parameterization tests for the initial settings of this modelling scenario (fig. 3.7: impact-physics simulation through python coding), the deduced post-impact physics of the system dictate that it is highly unlikely for a central melt sheet to form under such a small-scale impact-cratering process in the Martian crust. For this reason, a volume of melt is not included in the target geological setting. However, impactites of the central region are of course overheated due to the conversion of a vast fraction of the kinetic energy of the bolide into heat. Hence, in this scenario, the heavily impacted regolith and basalt at the central region of the crater are affected by a T_{max} = 700 °C (based on previous models for the temperature distribution by Barnhart et al. (2010)) and comprise the

central heat source of the induced hydrothermal system. The basal heat flux of the grid in this computational scenario was set at 17 mW/m^2. The atmospheric conditions at the surface were adjusted to a pressure of 0.007 bar and a temperature of 1°C, so that they are consistent with the previously presented simulations for the larger Martian impact craters (100- and 200-km). Finally, we can reasonably assume that since the impact-cratering process in this scenario is of a much smaller scale (10-km crater), then the post-impact permeability and porosity values of the target lithologies should be lower than those in the 100- and 200-km craters.

So far, a scaling relationship linking the impact-induced permeability and porosity with crater's size has not been achieved for geological settings where both crystalline formations of very low permeability and units of high permeability (e.g., regolith) are present (i.e.: Martian-like crust). Hence, in this work, the post-impact parameters for the permeability and porosity of the geological units after the crater's collapse were adjusted qualitatively, based on the generic model suggested by Collins et al. (2004), and according to simplistic and preliminary experiments performed through available impact-physics coding (fig. 3.7; Barnhart et al., 2010). The boundary physical parameters of permeability and porosity in the 10-km in diameter Martian crater are shown in Table 3.3. Specifically, the permeability values of the target rocks therein have been modelled with values that are by even one order of magnitude lower than those in the previous models for the larger impact craters.

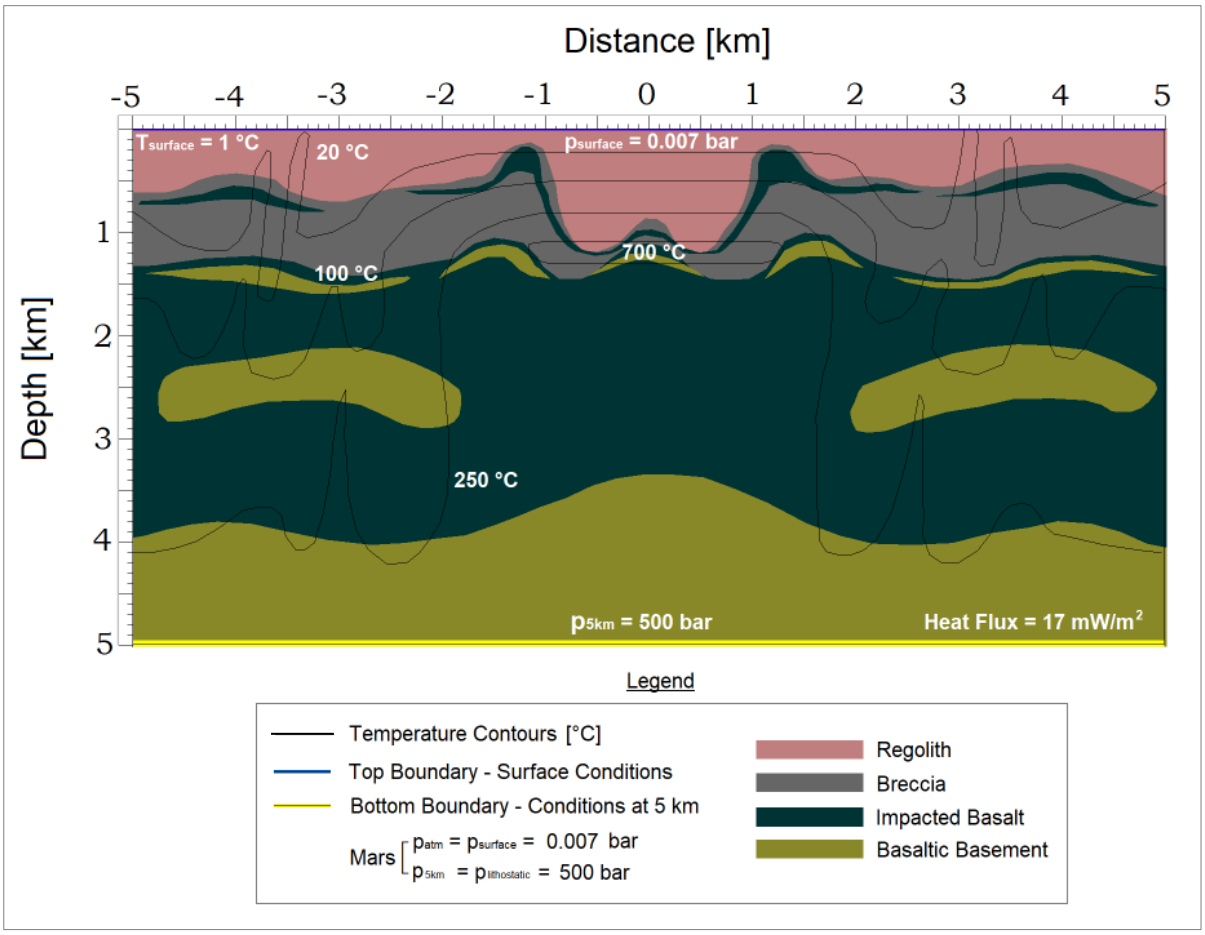

Fig. 3.6. HT boundary conditions and lithostratigraphic model for the assumed 10-km in diameter impact crater on Mars. Basal Heat Flux is modelled with a value of 17 mW/m^2, atmospheric pressure at the ground surface of Mars is set at 0.007 bar, and the ground surface temperature (upper thermodynamic boundary) is adjusted to 1°C. Numerical experiments for the impact-induced thermodynamics in craters with a smaller than 6 km radius, show that the formation of a central melt rock unit is a rare phenomenon (please see supplementary materials: Christou et al., (in prep); Vasconcelos and Christou (in prep)). Hence, in this boundary lithostratigraphic model, a central melt sheet is excluded. Nevertheless, the impacted rocks of the setting are affected by peak temperatures of 700 °C, right after the crater's formation (in accordance with numerical simulations for medium-sized impact-induced hydrothermal systems on Mars under freezing conditions, that have been provided by Barnhart et al. (2010)).

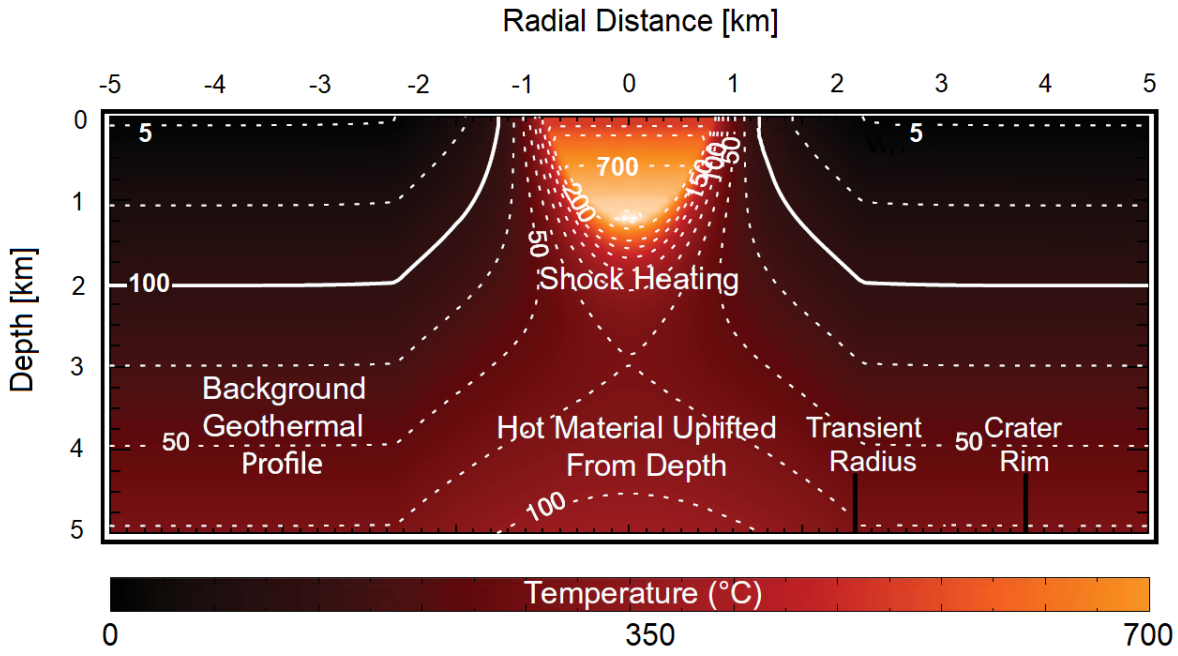

Fig. 3.7. Reproduced and modified impact-physics model after Barnhart et al. (2010), for the 10-km Martian crater. The cratering process in this scenario is triggered by an asteroid-type projectile of a 700-m diameter, and a density of 3000 kg/m^3, impacting the Martian crust with a velocity of 17 km/s. Impact angle was set at 45º. The target was adjusted to represent a Martian basalt before the impact, with an initial density of 2750 kg/m^3 (Table 3.3: basaltic impactite after the crater's formation). The result of this impact-physics simulation indicates the thermal distributions that would later be used in the boundary geological model for the HT simulation (fig. 3.6). The model shows that after the crater's collapse, peak temperature in the setting is 700 °C. Additionally, the central heat source of the generated hydrothermal system appears preserved at a depth of 1.0 -1.5 km beneath the surface. This result is also consistent with the initial benchmark calculations performed by the HT code, in order to verify the convergence of the initial thermodynamic conditions for the 10-km impact crater with the equations of state; proving that the central heat source in the impact-induced hydrothermal system expands within a radius of 1 km from the crater's centre and at a depth between 1 – 1.5 km beneath the central uplift (fig. 3.6).

Table 3.3. HT initial thermodynamic parameters for the rock units that comprise the putative lithostratigraphic setting of the 10-km in diameter Martian crater (fig. 3.6).

Petrophysical Properties	**Basaltic Basement**	**Basaltic Impactite**	**Breccia**	**Regolith**
Permeability (k) {m^2}	k_z = f(d,T), k_x = f (d,T)	k_z = f(d,T), k_x = f (d,T)	k_z = f(d,T), k_x = f (d,T)	k_z = f(d,T), k_x = f (d,T)
Porosity (φ) {%}	φ = f (d,T)	φ = f (d,T)	φ = f (d,T)	φ = f (d,T)
Thermal Conductivity {W/m·K}	2.9	2.7	2.7	1.7
Specific Heat Capacity {J/kg·K}	1200	1000	900	700
Density {kg/m^3}	3000	2700	2500	1700
Surface Permeability {m^2}	9.00E - 20	9.00E – 18	9.00E - 16	9.00E - 15
Surface Porosity ($\varphi_{surface}$)	1.0 %	4.0 %	6.0 %	15.0 %

Table 3.3 – Note: The petrophysical properties of the target rocks (permeability, porosity, heat capacity, thermal conductivity, density) and the impact-generated peak temperature in the geological setting after the crater's formation were adjusted according to previously published numerical models for smaller scale impact-cratering processes on Earth and Mars (Ivanov and Deutsch, 1999; Versh et al., 2005; Jõeleht et al., 2005; Barnhardt et al., 2010). Specifically, T_{max} of the main heat source of the hydrothermal system after the crater's formation does not exceed the value of 700 °C. The permeability and porosity values of the target rocks in this smaller in size crater are decreased by at least an order of magnitude, when compared to the values used for the more heavily fractured and shocked target rocks of the 100- and 200-km scenarios.

The numerical simulation showing the thermohydraulic evolution of the generated aqueous system in the 10-km in diameter Martian crater, implies that fluid circulation in this impact structure does not last for more than 60-80 Kyr (fig. 3.8: A-E). It is evident already from the initial phase of the hydrological system that flows are localized within a maximum radius of circa 2 km from the crater's centre. Flux vectors and the scales for the magnitude of flux in each simulative cell exhibit flows that do not reach values greater than 9.0e-6 g/s×cm^2. The main heat source that drives hydrothermal circulation is initially located at a depth of 1.0-1.5 km beneath the crater's floor (fig. 3.6), but a few months after the crater's collapse, the heat source migrates towards a greater depth (2 km; as shown in the simulations' video in the supplementary material and also by the thermal distribution in fig. 3.8: steps A-B). This may be seen as an artifact of modelling but based on previously presented patterns of hydrothermal cooling in this work, the main heat source always seems to be slightly migrating towards deeper niches of the crater as time elapses. The most logical explanation for this phenomenon is hidden in the laws of thermodynamics and equations of state via which the HT code functions. These indicate that the significant thermal difference between the heated rocks and the ground-surface of Mars results to the gradual migration of the preserved heat to a greater depth; in greater depths heat loss should be minimized, as heat flux from basement rocks should contribute to the cause of the system's conservation. Thus, this is probably why we see the central heat sheet of the system to slightly migrate towards some deeper regions of the geological setting as hydrothermal cooling progresses (fig. 3.3: A-G, fig. 3.5: A-F, fig. 3.8: A-E).

At t = 2 Kyr, the hydrothermal system has cooled by 150-200 °C, but flux is still very strong within the subsurface cylindrical domain of 2-km radius from the crater's centre. Hydrothermal cells are active down to a maximum depth of 5 km during the first 2 Kyr of hydrological activity, and upwelling flows are obvious especially at depths between 3.5 and 5 km (fig. 3.8: A-B). The upper 3-km lithological domain is mainly affected by colder flows originating from the upper-regolith layers and surficial deposits, and which seep into the lithological units of the main heat source. Subsequently, this flow pattern cools the system quite rapidly, and at 20 Kyr, the hydrothermal system does not exceed the maximum temperature value of 240 °C. At that time point, it is very interesting to see that fluid recharge from the basaltic basement and towards the surface of Mars reinvigorates the system and extends its lifetime with hotter flows (fig. 3.8: C, WMF red-coloured regions in the crater, with the annotated vectors of flow pointing towards the surface of the geological setting). This recharge cycle at t = 20 Kyr, shows flows that are greater in magnitude than those that prevailed in the system from 2 Ky to 15-20

Kyr. This hydraulic process reveals another very exciting phenomenon that has been reported in just a few magmatic-induced hydrothermal systems here on Earth. Dobson et al. (2003) reported on probable self-sealing occuring at the Yellowstone geothermal system and suggested that, although such a process may significantly decrease the permeability and porosity of the lithological units, it aggregates fluid flux along fractures, where numerous, cyclical and sporadic recharge flux episodes of higher magnitude may occur. Such an event is characterized by an explosive release of fluid overpressure, forming strong upwelling conduits that lead to phyllosilicate/clay mineral precipitation and self-sealing. Eventually, this process results to the generation of another same-pattern hydraulic cycle. Since impact craters are characterized by high fracture density, such fluid recharge fluxes are more likely to take place through such a cyclical flow pattern rather than decrease smoothly with time (as reported also in the findings of Dobson et al. (2003); Mayr et al. (2005); and Abramov and Kring (2007)).

At t = 50 Kyr (fig. 3.8: D), appreciable hydrothermal flows are still present in the system, with WMF fluxes ranging between 2.0E-9 g/s×cm^2 and 9.0E-9 g/s×cm^2 beneath the central uplift of the crater. However, the maximum temperature in the setting is no greater than 140 °C, and at a depth of 3 km where the central heat source is now located. This proves that the central heat sheet has moved by 1 km even deeper from its initial observed depth of 1.0-1.5 km at t_0 (fig. 3.6 and 3.7), and 2 km at t = 2Kyr (Fig. 3.8: B), respectively. Finally, at t = 80 Kyr (fig. 3.8: E), we can clearly see that only minimum flows are present in the system, recharge hydraulic flux is completely inactive, and that the geothermal gradient has been fully restored (T_{max} = 100 °C). Therefore, we can reasonably establish that after 50-60 Kyr (according to the exported video of the simulation too; appendix: Martian Crater_10-km_Higher Permeability_.mp4), we do not observe any substantial hydrous activity in this putative Martian subsurface system.

Conclusively, if the numerical model for this smaller-scale impact-generated hydrothermal system on Mars has accurately predicted its thermodynamic and hydraulic response through time, then the abundance of hydrothermal precipitates and alteration products may be far higher in such smaller-to-medium size craters on Mars. This means that such small-scale impact structures may have so far been under-estimated in terms of the duration of their water-rock reactive processes and their bioenergetic potential. The logic behind this is that other numerical simulations for small or even larger in size impact-generated hydrothermal systems, and in far more water-enriched environments here on Earth, have not been able to predict such explosive fluid over-pressurized upwellings and hydraulic cycles. So, it is obvious for the above reasons

that more often than rarely, numerical models can erroneously establish lower lifetimes for the post-impact hydrothermal circulation in cratering systems (Versh et al., 2005; Jõeleht et al., 2005; Pickersgill et al., 2019; Christou et al., 2019).

Temperature & Water Mass Flux Distribution in the Post-Impact Hydrothermal System

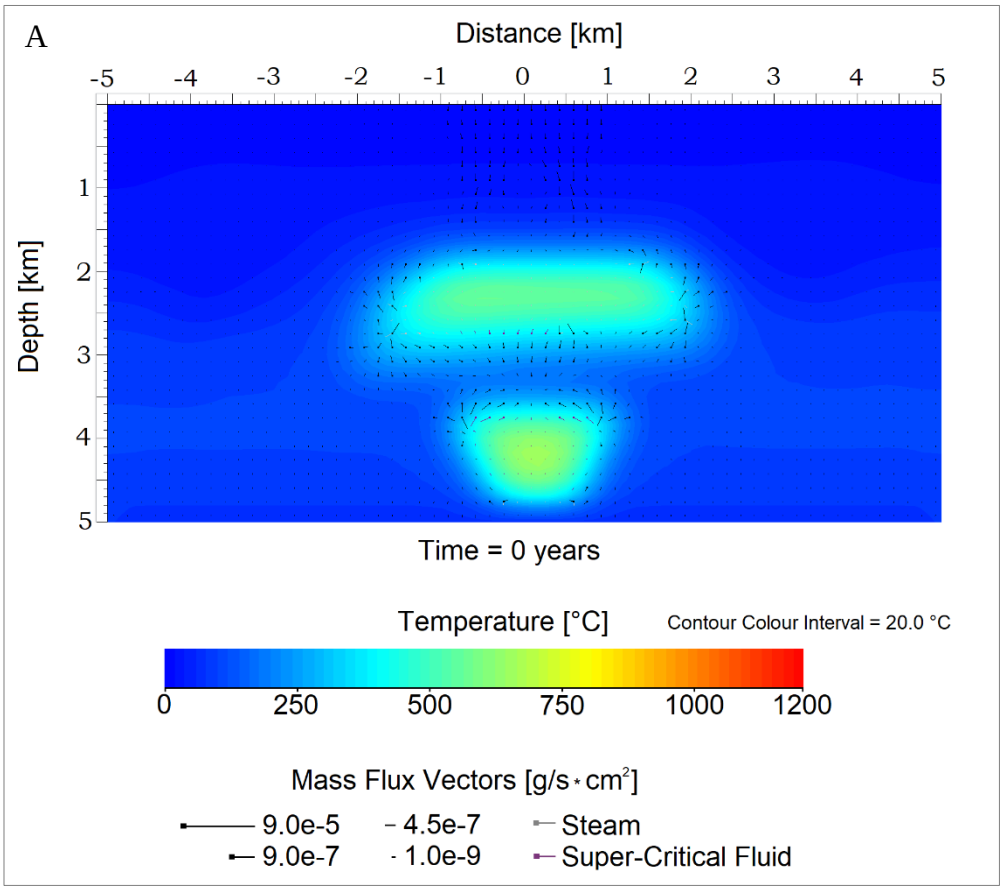

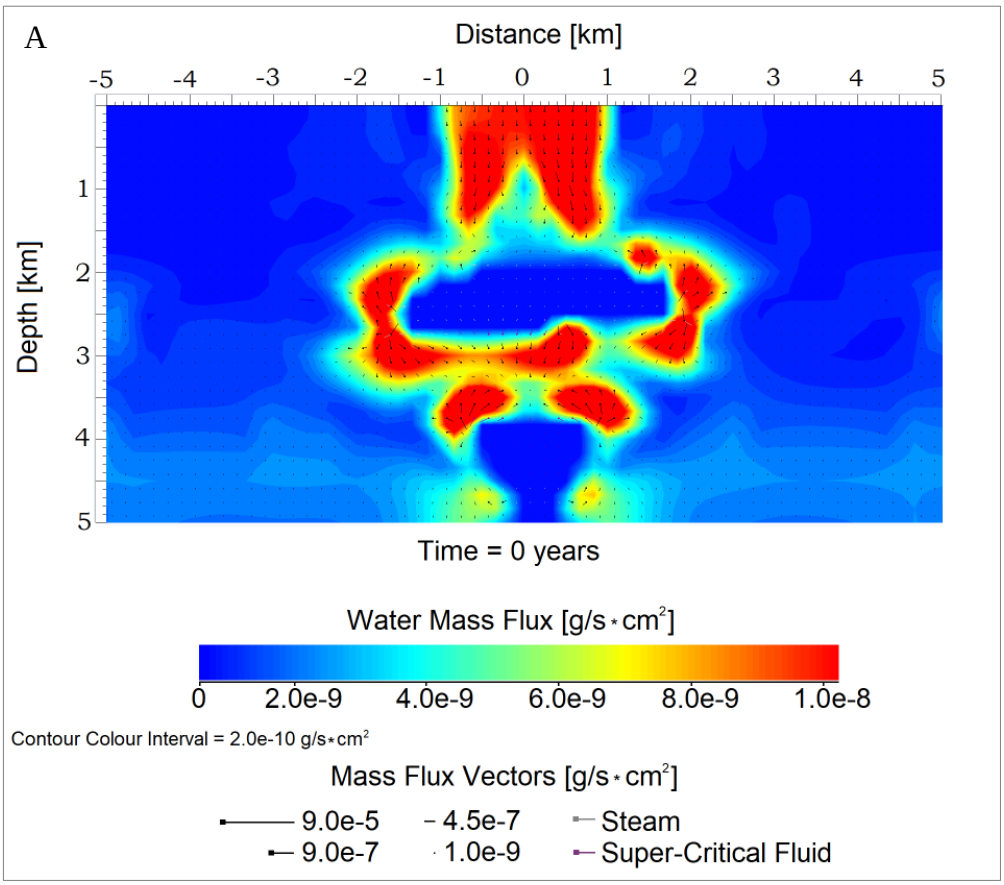

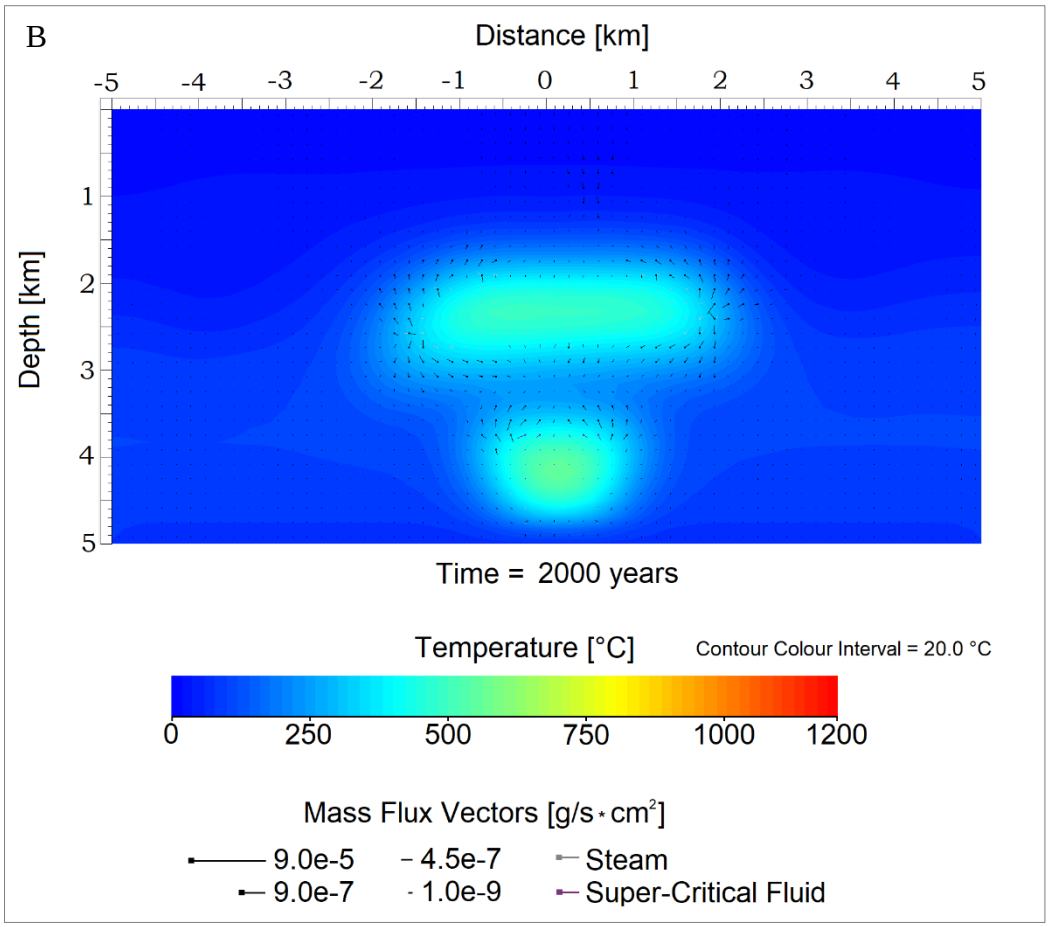
B
Distance [km]
-5 -4 -3 -2 -1 0 1 2 3 4 5
Depth [km]
1 2 3 4 5
Time = 2000 years
Temperature [°C]
Contour Colour Interval = 20.0 °C
0 250 500 750 1000 1200
Mass Flux Vectors [g/s*cm²]
9.0e-5
4.5e-7
Steam
9.0e-7
1.0e-9
Super-Critical Fluid

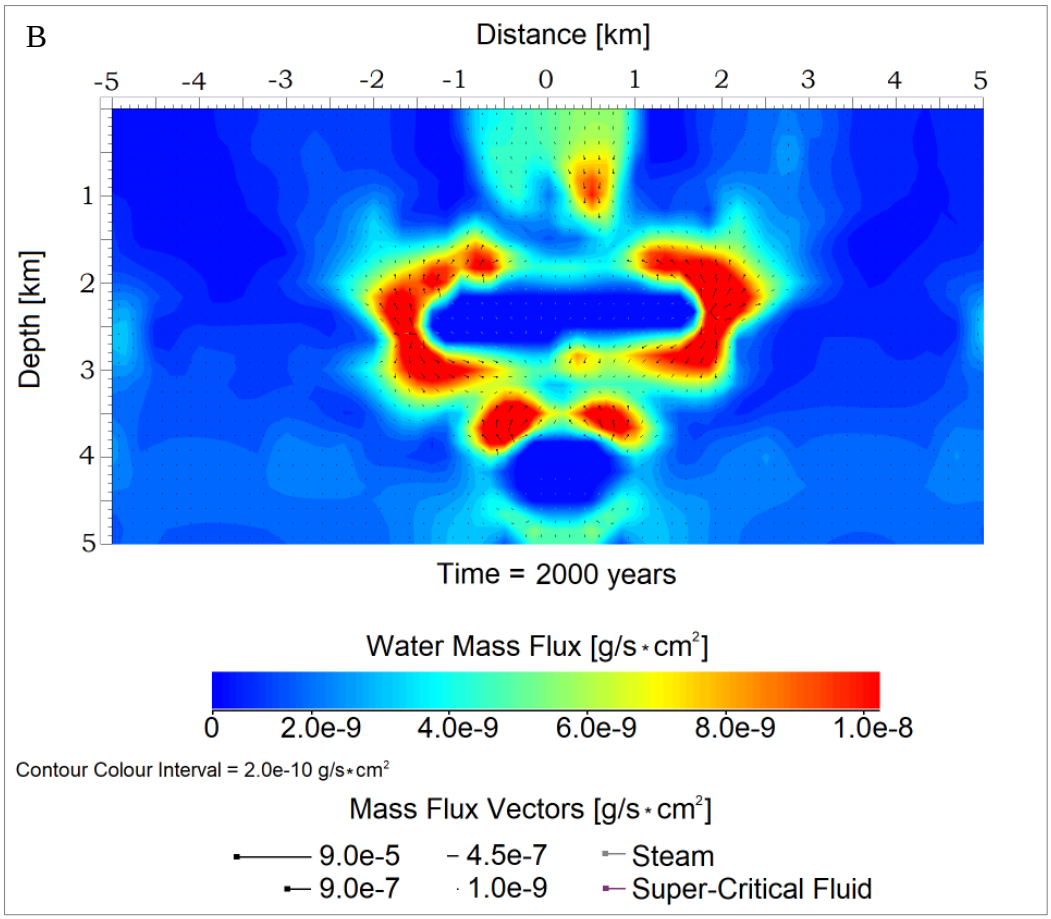
B
Distance [km]
-5 -4 -3 -2 -1 0 1 2 3 4 5
Depth [km]
1 2 3 4 5
Time = 2000 years
Water Mass Flux [g/s*cm²]
0 2.0e-9 4.0e-9 6.0e-9 8.0e-9 1.0e-8
Contour Colour Interval = 2.0e-10 g/s*cm²
Mass Flux Vectors [g/s*cm²]
9.0e-5
4.5e-7
Steam
9.0e-7
1.0e-9
Super-Critical Fluid

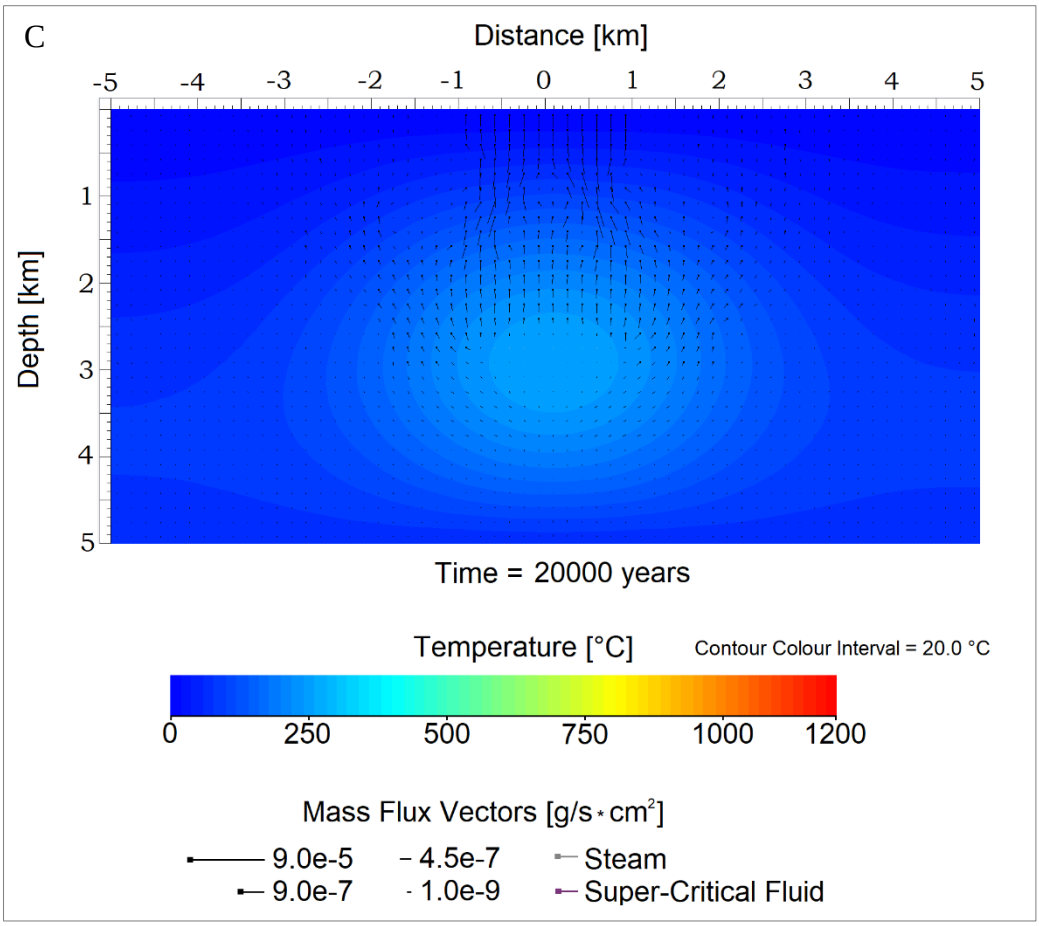
C
Distance [km]
-5 -4 -3 -2 -1 0 1 2 3 4 5
Depth [km]
1 2 3 4 5
Time = 20000 years
Temperature [°C]
Contour Colour Interval = 20.0 °C
0 250 500 750 1000 1200
Mass Flux Vectors [g/s * cm²]
9.0e-5
4.5e-7
Steam
9.0e-7
1.0e-9
Super-Critical Fluid

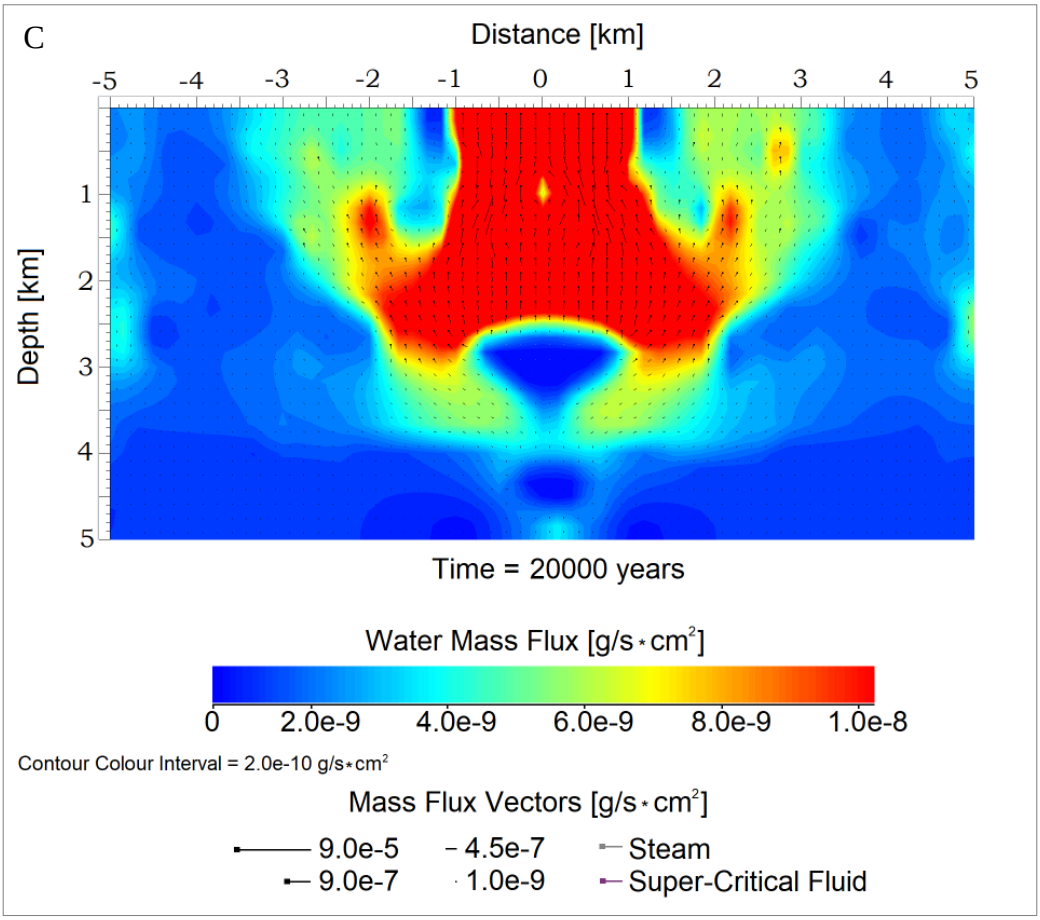
C
Distance [km]
-5 -4 -3 -2 -1 0 1 2 3 4 5
Depth [km]
1 2 3 4 5
Time = 20000 years
Water Mass Flux [g/s * cm²]
0 2.0e-9 4.0e-9 6.0e-9 8.0e-9 1.0e-8
Contour Colour Interval = 2.0e-10 g/s*cm²
Mass Flux Vectors [g/s * cm²]
9.0e-5
4.5e-7
Steam
9.0e-7
1.0e-9
Super-Critical Fluid

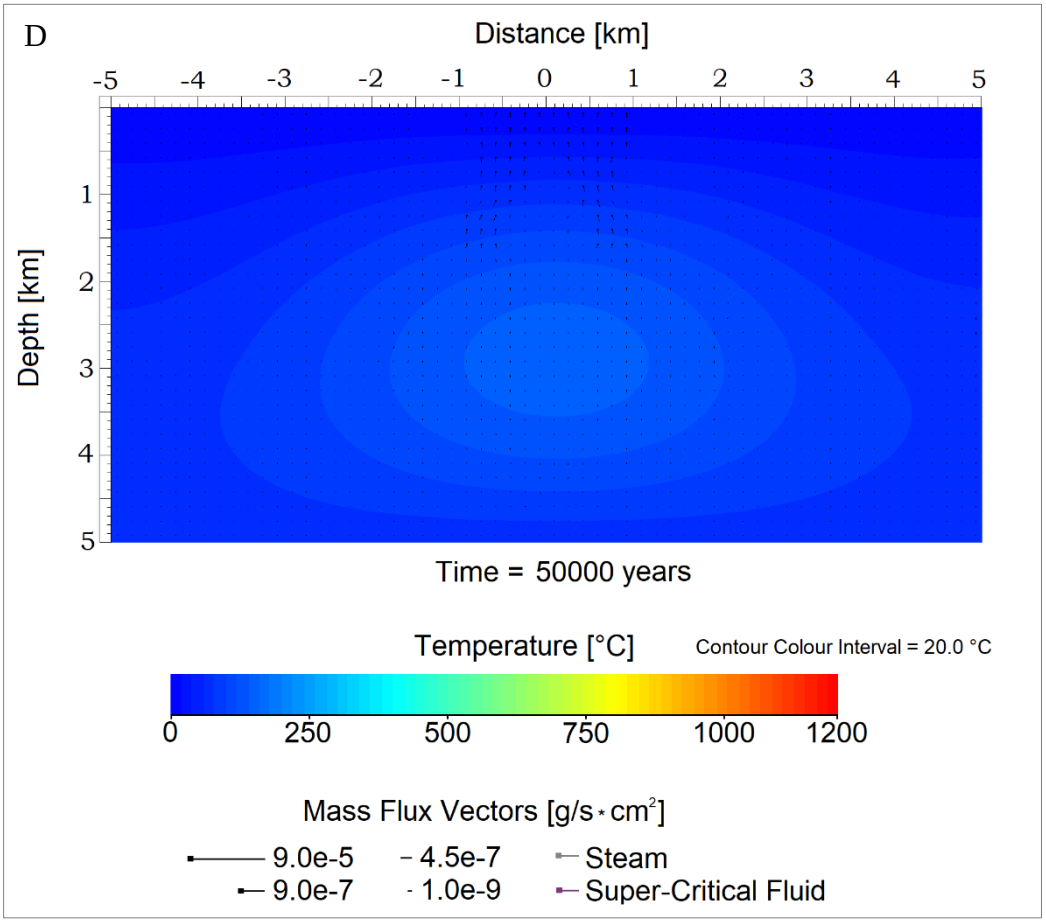
D
Distance [km]
-5 -4 -3 -2 -1 0 1 2 3 4 5
Depth [km]
1 2 3 4 5
Time = 50000 years
Temperature [°C]
Contour Colour Interval = 20.0 °C
0 250 500 750 1000 1200
Mass Flux Vectors [g/s*cm²]
9.0e-5
4.5e-7
Steam
9.0e-7
1.0e-9
Super-Critical Fluid

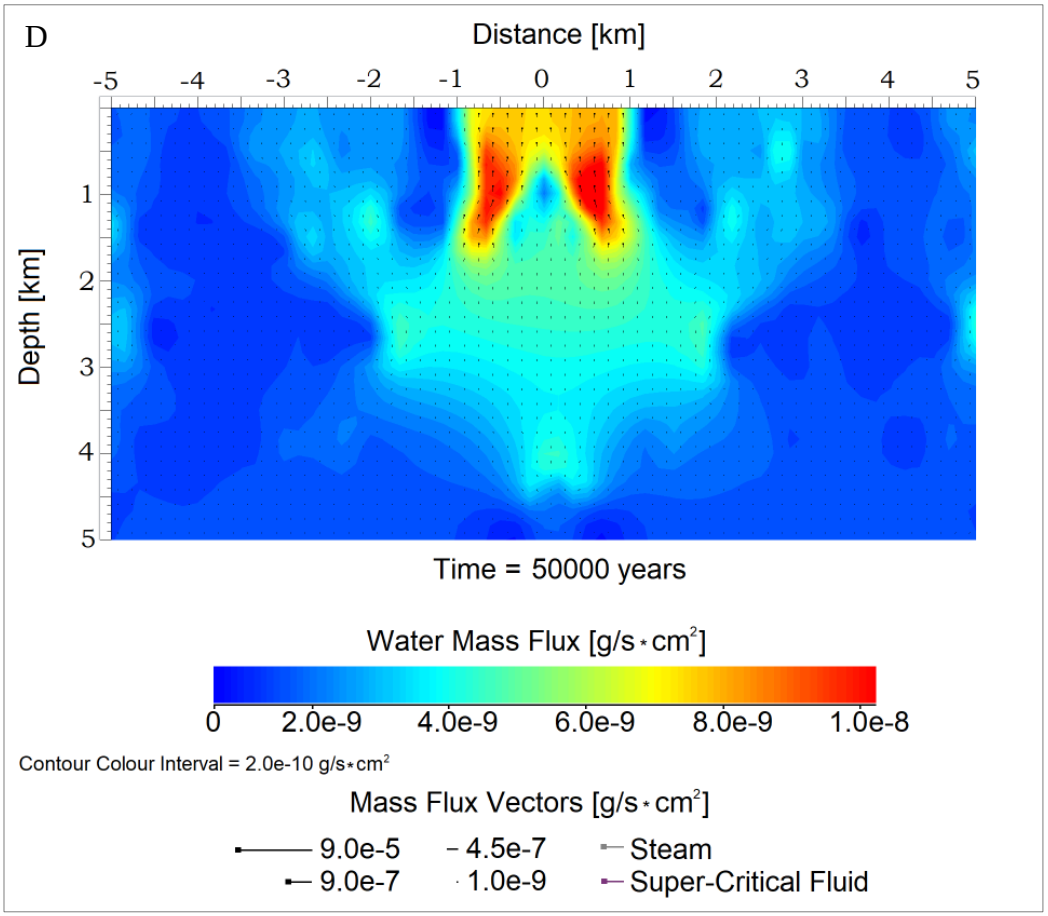
D
Distance [km]
-5 -4 -3 -2 -1 0 1 2 3 4 5
Depth [km]
1 2 3 4 5
Time = 50000 years
Water Mass Flux [g/s*cm²]
0 2.0e-9 4.0e-9 6.0e-9 8.0e-9 1.0e-8
Contour Colour Interval = 2.0e-10 g/s*cm²
Mass Flux Vectors [g/s*cm²]
9.0e-5
4.5e-7
Steam
9.0e-7
1.0e-9
Super-Critical Fluid

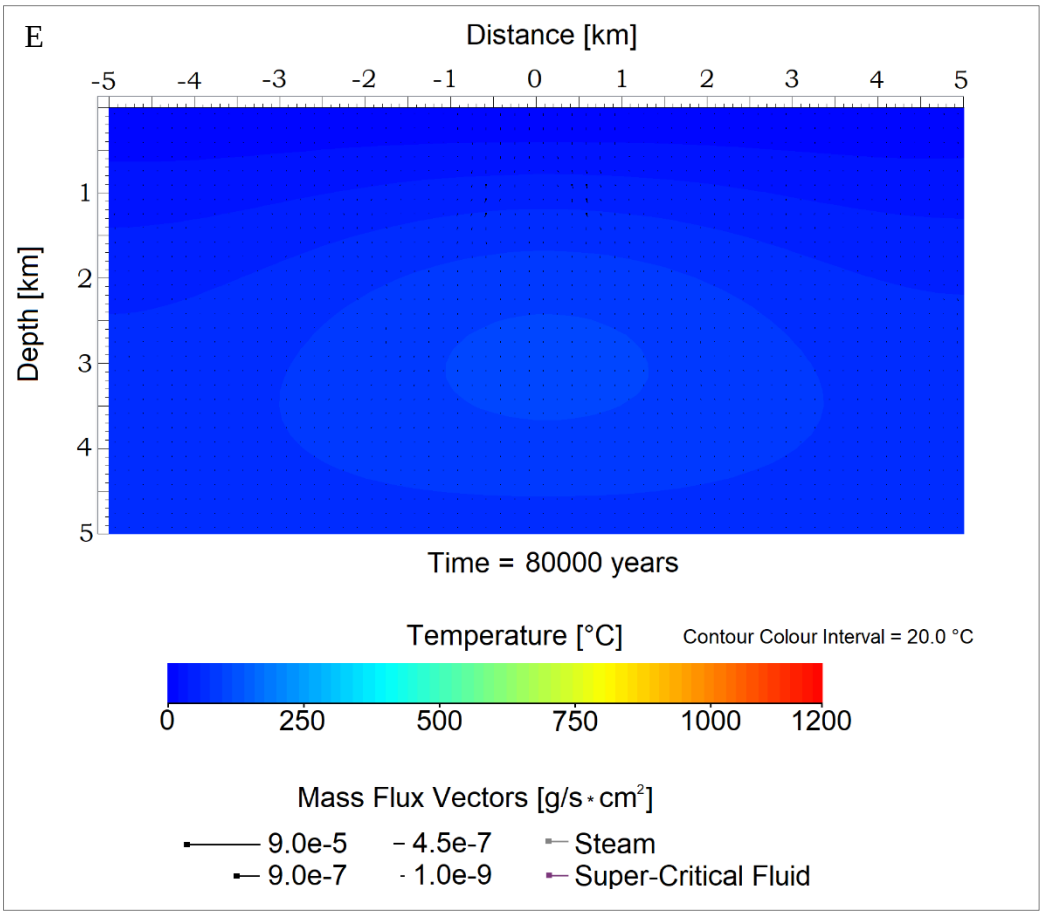
E
Distance [km]
-5 -4 -3 -2 -1 0 1 2 3 4 5
Depth [km]
1 2 3 4 5
Time = 80000 years
Temperature [°C]
Contour Colour Interval = 20.0 °C
0 250 500 750 1000 1200
Mass Flux Vectors [g/s * cm²]
9.0e-5
4.5e-7
Steam
9.0e-7
1.0e-9
Super-Critical Fluid

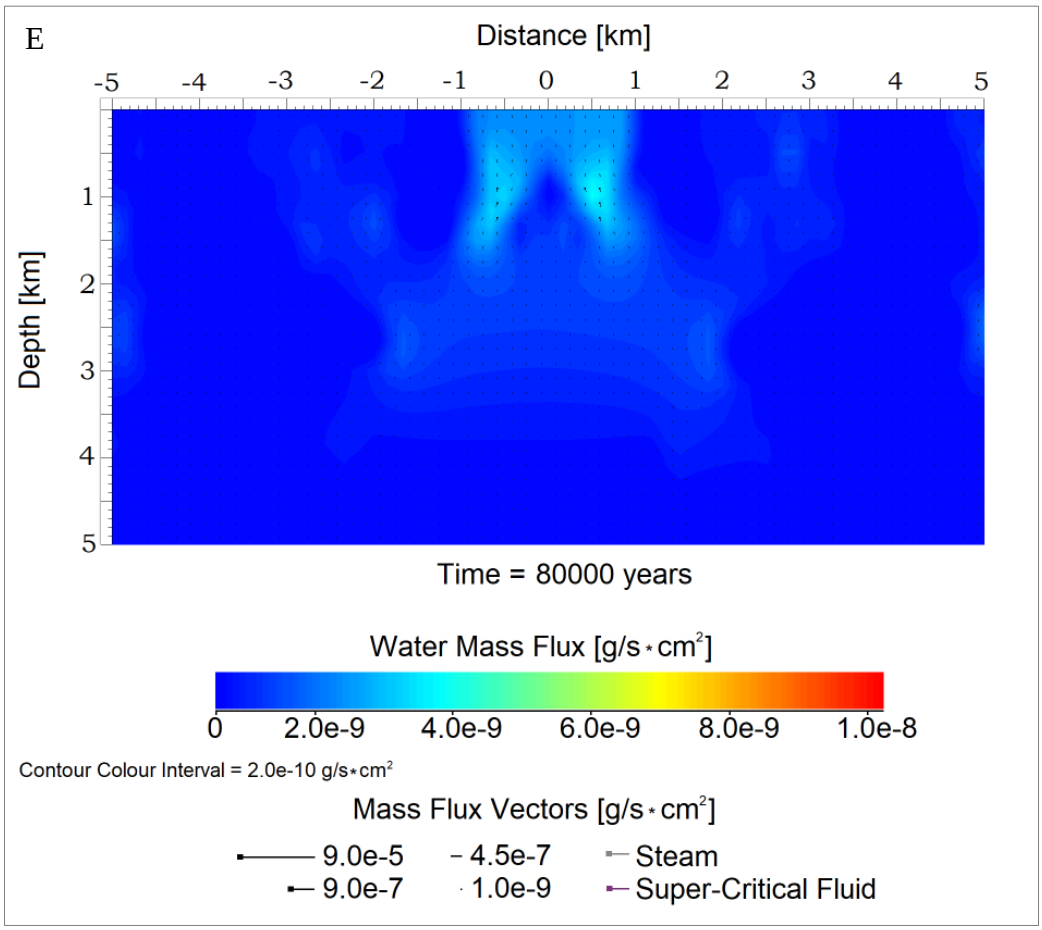
E
Distance [km]
-5 -4 -3 -2 -1 0 1 2 3 4 5
Depth [km]
1 2 3 4 5
Time = 80000 years
Water Mass Flux [g/s * cm²]
0 2.0e-9 4.0e-9 6.0e-9 8.0e-9 1.0e-8
Contour Colour Interval = 2.0e-10 g/s*cm²
Mass Flux Vectors [g/s * cm²]
9.0e-5
4.5e-7
Steam
9.0e-7
1.0e-9
Super-Critical Fluid

Fig. 3.8 (steps A-E). Temperature and Water Mass Flux (WMF) distribution in the 10-km in diameter Martian crater from just right after its formation (t_0) and for a period of 80 Kyr.

Temperature Distribution steps (A-E): The last time step of the simulation indicates the time point when the geothermal gradient of this Martian system is restored and hydrothermal circulation ceases. After the impact, T_{max} = 700 °C in the setting, and the main heat source of the hydrothermal system is illustrated in light-greenish- / azure colours within the grid during the earliest phases (steps A-B) of convective cooling. Colder and weaker hydrous flows affect the geological system from 20 Kyr to 80 Kyr. However, recharge flow events from the surface of the crater and towards the central heat source region that drives the impact-generated hydrological cycle appear active after 20 Kyr, and even after 50 Kyr (steps C-D). At t = 80 Kyr after the crater's formation, the geological system has peak temperature of T_{max} = 100 °C in the central region, and an estimated geothermal gradient of 30 °C / km in the subsurface regions beyond the crater's peak ring (and at a radial distance of 2 km from the crater's centre). At t = 100 Kyr after the impact, the geothermal gradient has reached the value of 15 °C / km. Even if the geothermal gradient is not fully restored, by the time that thermal distributions within the crater's geological system are indicating the absence of recharge convective flows (in this case, at t = 50–80 Kyr; steps D and E), we can establish that impact-generated hydrothermal circulation ceases at that time point. Therefore, in this scenario, we can conclude that after 50 Kyr, negligible water flux is present within the hydrological system.

Water Mass Flux Distribution (steps A-E): The heated target rock units of the setting and their surrounding impactites appear impermeable at the earliest phases of hydrothermal cooling (steps A-C; blue coloured regions in the simulative grid), as these rocks are heated beyond the thermal limit of T ≥ 500 ºC (as explained in Fig. 3.2, 3.3, 3.5 and 3.6). Blue-coloured domains in the grid represent lithological regions where no flows or very weak flows are present. Red-coloured regions indicate that maximum flux occurs within the host lithology per time step. Stronger fluxes (≥ 6.0e-9 g/s×cm^2) are present by yellow- and orange-coloured cells. The magnitude of fluid flux is additionally expressed by vector's length. The squared edge of each vector indicates the direction of flow. Liquid water flux is represented by black vectors, vapour flux by light-greyish vectors, and super-critical flux by purple vectors. Each cell of the simulative domain has an appointed vector per time step that shows the direction and magnitude of flow. At the initial phase of hydrothermal cooling, fluid flux reaches peak values (steps A-C) in regions of the geological setting where T ≤ 500 °C, especially in rock units that surround the impermeable and hot (500 °C ≤ T_{max} ≤ 700 °C) impactites. At t = 80 Kyr, WMF_{max} ≈ 4.0e-9 g/s×cm^2, meaning that hydrothermal circulation is still ongoing. Nevertheless, between the time steps of 50 Kyr and 80 Kyr, we observe that no recharge flows occur according to the flows' length and direction, and thus we can reasonably assume that shortly after t = 50 Kyr hydrothermal circulation ceases. Some minor hydrous fluxes still appear at t = 80 Kyr (step E), but these are spatially confined beneath the crater's central valley (within a 1-km radius), and may be due to the water-saturation increase of the rock formations that were affected by more intense hydrous activity (steps A-D).

3.1.5 Simultaneous Small-Scale Impact Cratering Events on the Martian surface (≤ 10 km in diameter hydrothermal environments) within a radial distance of 200 km.

On Mars, within the area of its highland terrains, approximately 4000 impact craters with a diameter equal to or larger than 10 km have been counted, with the majority of those to have formed between 4.2 – 3.9 Ga (Barlow, 1990; Kring and Cohen, 2002; Strom et al., 2005; Norman and Nemchin, 2012). Based on impact-cratering rate calculations for such events on the Hadean Earth (Abramov and Mojzsis, 2009) and Noachian Mars (Abramov and Mojzsis, 2016), and on observations from lunar cratering chronologies (Hartmann and Neukum, 2001; Ivanov, 2001) and lunar meteorite impact-melt ages (Cohen et al., 2000), we can deduce that the Martian crust should have been severely affected by impact-induced hydrothermal systems earlier in its geological history. In addition, Noachian Mars is believed to have been warmer, wetter and may have hosted greenhouse climatic phenomena with rainfall and surface runoff being the most frequent aqueous processes on its surface (Carr et al., 1990; Craddock and Maxwell, 1993; Carr, 1999; 2006; Craddock et al., 2013). However, the evidence for a warm and wet early Mars remains ambiguous (e.g., Squyres and Kasting, 1994; Gaidos and Marion, 2003; Fairen, 2010). Additionally, phyllosilicates in the Noachian crust (Fe, Mg clays) should have precipitated after alteration processes that were induced by subsurface hydrothermal systems, rather than weathering associated with surficial fluvial processes (Ehlmann et al., 2011).

To investigate the aforementioned and contradicting theories about the origin of the aqueous activity on Noachian Mars, in this simulative scenario, I have computed the impact-generated hydrological activity in the Martian crust after two simultaneous and nearby (within a 200 km radius) smaller-scale asteroidal impacts on Martian regolithic and basaltic units. The craters' diameters have been set at 10-km and 7-km for the west and east structure, respectively; as illustrated in fig. 3.9: A, where the central heat source is represented with brighter colours in the thermal field depiction and appears impermeable right after the impact due to $T_{max} \geq 500$ °C (illustrated with dark blue colours in fig. 3.9: WMF: step A). The craters' diameters vary by 3 km, as the probability for the simultaneous formation of two identical-in-diameter craters in the defined circular area of 31416 km^2 is reasonably far lower, than that for the formation of two less identical in size structures. For simplification, previous insightful computations by Schwenzer et al. (2012), that describe the post-impact thermodynamic effects on the Martian cryosphere, have not been investigated in this scenario, as a Martian cryosphere layer on the

top boundary of the cratered crust, would meddle with the hydrous circulation pattern of the generated hydrothermal systems.

In this modelling approach, I have incorporated a much hotter and wetter boundary setting for the Noachian crust, to investigate whether most of the hydrothermal upwellings are recharged by either surficial or subsurface aqueous sources, or both. The ground surface temperature was set at 5 °C, the atmospheric pressure at 0.5 bar, and the geothermal heat flux gradient was adjusted to a value of 60 mW/m^2 (after Schwenzer et al., 2012); which is at least three times higher than the heat flux gradient used for simulating the impact-generated hydrothermal systems in the Amazonian crust. The petrophysical characteristics and lithostratigraphy of the target rocks, and of the broader non-impacted geological setting (domain beyond the crater' rim region) remain the same with the parameterization used in the 10-km cratering simulation, and that is described by fig. 3.6 and table 3.3.

The rationale behind incorporating two smaller-scale impact events within a radial distance of 200 km, derives from estimates on the impact flux rate on Noachian Mars after calculations provided by Werner et al. (2014); these calculations describe the number of impacts that should have occurred on the Red Planet per unit area and per unit time. The impact flux on Noachian Mars has been assessed as far greater than on Earth, by a factor of ~4.5 (Horner et al., 2009; JeongAhn and Malhotra, 2015). However, the classical Late Heavy Bombardment (cLHB) scenario contradicts this hypothesis, as it assumes that the extent of the LHB is only ~100 Myr (between 3.9 – 3.8 Ga, after Morbidelli et al., 2012), with a constant bombardment flux described by a Mars/Earth impact flux ratio of 1.75, and a Mars/Moon impact flux ratio of 2.76, as reported by Le Feuvre and Wieczorek (2011), and simulated by Abramov and Mojzsis (2009); (2016). On the other hand, the duration for the Sawtooth LHB is estimated at 400 Myr, with the impact flux declining between 4.1 – 3.7 Ga (Morbidelli et al., 2012; Lagain et al., 2022). The cumulative crater-size and frequency distribution model for the different geological periods on Mars that was released by Werner and Tanaka (2011), indicates that in a 31400 km^2 area of the simulative grid in this computational scenario, two impact events with a resulting crater's diameter between 5-10 km each, could have occurred during the Noachian (after also considering the Werner et al. (2014) isochron model which dictates that the isochron-derived cumulative crater-production rate for craters with a diameter ≥ 16 m is $3.6 \times 10^{-7}/km^2/year$. More liberal parameterizations could imply that numerous cratering events with resulting diameters between 1-10 km could have affected an area of 31416 km^2 within a period of 1 - 10

Kyr during the Noachian eon. Nevertheless, for computational efficiency, this simulative scenario is designed conservatively in terms of the impact-flux rate that affected this Noachian Mars setting and includes only two simultaneous major impacts. Furthermore, HT simulations cannot satisfy the convergence criteria for the equations of state when more than one cratering events are incorporated during different time steps in a simulation, and this can be an objective for future research work. The focus of this work nonetheless, is to assess the impact-induced hydrothermal upwellings on ancient Mars. Since in this scenario I am exploring the post-impact hydrothermal effects within the Noachian crust, the logic is to primarily determine the origin of the upwellings and establish the duration of the hydrological cycle.

Fig. 3.9 depicts the evolution of the thermal field and aqueous flows in the Noachian crust, respectively. In all time steps of the simulation, but especially in step E which represents the duration's end point for aqueous flow, we can clearly observe that the geological domain remains much warmer even after the entire period of aqueous circulation, than in the previous simulative scenarios of the Amazonian crust (as shown by the slightly lighter blue colours in fig. 3.9: E; in contrast to the darker-blue coloured domains shown in the final time steps of the thermal field simulations performed for the 10-, 100-, and 200-km cratering systems). This is due to adjustments of higher basal heat flux (60 mW/m^2) and geothermal gradient for the geological system.

Furthermore, the results show that the aqueous circulation in each impact structure, does not extend below a depth of 4-5 km during the initial phase of more intense hydrothermal flow (fig. 3.9: steps A-B) which is consistent with the produced thermodynamic results for the 10-km in diameter crater. In addition, it is notable that at t_0 after the impacts, the whole geological setting is hydraulically active down to a depth of 8-9 km and within a 100 km radius (fig. 3.9: A). This means that after the impact the heat exchange occuring between the main heated sources of the target rocks and the appreciably warmer, deeper Noachian lithologies, is able to activate flows within the whole cylindrical domain. As the background geothermal gradient is adjusted to a value of 20 °C / km, we can assume that deeper lithologies beneath the cratering centres and down to depths of 5-7 km, are not only recipients of thermal conduits from the impact-induced heat sources, but additionally, stable heat flux contributors to the hydrological systems. Hence, the basal heat flux of 60 mW/m^2 may be decelerating the convective cooling and thus, preserving both systems for a much longer period.

At t = 250 yr, water mass flux in both craters reaches peak limits, with WMF_{max} = 9.0E-4 g/s×cm^2 at the west structure, and 3.0E-4 g/s×cm^2 at the east structure (fig. 3.9: B-E, as shown by the extremely long flux vectors). Furthermore, hydrothermal fluxes with values equal to or slightly lower than 9.0E-5 g/s×cm^2 durate close to the main heat source regions of the craters for more than 20 Kyr (fig. 3.9: B-D).

Comparatively, the maximum impact-induced fluxes in the Amazonian crust of the 10-km crater (previously presented simulation) appeared by at least two orders of magnitude lower value in each time step (fig. 3.9: A-E). Flows in the Amazonian 10-km crater did not last with values higher than 9.0E-7 g/s×cm^2 for a period greater than 20 Kyr. This indicates that the warmer background geothermal profile of the Noachian period contributes drastically to the prolonging of impact-induced hydrothermal systems.

Significantly, the flux pattern of each hydrothermal system seems to be governed predominantly by subsurface fluids that recharge the convective cells. Seep-in flows are also present but based on the results of the flow patterns and their associated temperature that we can observe at the later stages of hydrothermal cooling (fig. 3.9: C-E), we can argue that the temperature contours of the hydrous fluids are indicative of recharge originating from the subsurface of Mars.

In particular, the recharge flows in this Noachian setting appear enriched by subsurface water-saturated lithological units and aquifers, or/and by the dissolution of hydrous mineral phases that release aqueous solutions after hydrothermal fluid-rock reactions in the Martian subsurface. Any of the above probable scenarios, results to the release of highly pressurized and heated fluids within the Martian subsurface. Later, these fluids recharge the impact-induced thermodynamic system and contribute to the specific hydraulic pattern that we observe through the output of the numerical simulation (fig. 3.9: steps A-E). The fluxes therein indicate that water is seeping out through the porous and permeable rocks of the impact structure towards the surface. These fluid upflows cool after reaching shallower niches of the crater (e.g., rims, peak-ring, central uplift in the case of the 10-km Noachian crater), and so, if fractures of the upper-lithostratigraphic layers are not affected by self-sealing, then these colder flows return to the hydrothermal system as coolants. Otherwise, if the self-sealing of fractures in the upper-regolith and other sedimentary structures has occurred, then this should have restricted the thermodynamic interaction between surficial and subsurface aquifers. According to the

simulations' results, during the Noachian or later periods, such hydrothermal upwellings on a one-way trip to the Martian cold surface, should have significantly contributed to the water mass of crater lakes within the inner-rim regions of impact structures.

On top of that, one exciting implication of the simulation is that after 2 Kyr, the two impact-generated hydrological systems seem to start being thermodynamically inter-connected within a radius of approximately 120 km. This is evident by flow events with vectors pointing inwards to the central region of the simulative grid; the region which represents the non-impacted geological setting (within a 50 km radius from the centre of the grid), but it is unsure whether this is an artifact produced by the code or a probable natural process.

Later on, this peculiar phenomenon can be confirmed as a natural process, as at t = 20 Kyr, four more smaller in size but strong convective cells form at a farther distance from the impact structures and within the depth of 2 km beneath the Martian surface. This means that warmer flows travelling from the impact-structures to the inner regions of the grid, start to develop a thermodynamical network of minor convective cells that gradually migrate farther from the impact structure. This may have been due to probable impact-induced heat conduits originating from the basal lithologies of the setting towards the surface. The geothermal gradient uplift after impact events has been thoroughly investigated via hydrocode experiments (Melosh and Ivanov, 1999; Ivanov, 2004; Pierazzo et al., 2004). Thus, the presence of these small-scale impact-induced heat sources closer to the Noachian surface, may have disrupted the "quiescence" of the basal rocks' thermal field by expanding it further to shallower depths. This should have subsequently affected the flow pattern of the more distant convective cells.

Eventually, flows that are shown to migrate horizontally from the main impact-induced heat sources to the central non-impacted regions of the simulative grid, may have gradually increased the porosity of nearby lithological units and formed minor convective cells. These minor convective regions are not evident during the first 2-10 Kyr of hydrothermal circulation. However, after 12 Kyr (appendix: Martian Cratering_2x Impacts_Noachian.mp4), and as time elapses and hydrothermal circulation is ongoing, the porous space in rock formations that are affected by hydrothermal flows increases due to induced alteration and dissolution. Finally, these more distant and initially minor convective cells evolve to a subsurface convective network of six major interconnected hydrothermal cells at a depth of 2km. This hydrological network preserves the aqueous circulation at a depth of 2 km within the Martian crust for a

total period of 150 Kyr, and up to the point when the geothermal gradient is fully restored, and no further recharge flow events are evident (fig. 3.9: E).

At this point, I should emphasize that the same simulation was performed for a single 10-km wide hydrothermal system on Noachian Mars, and that the resulting duration of the hydrological cycle is estimated at 70 Ky in this case (shown in the supplementary materials: Martian Cratering_1x Impact_10-km_Noachian.mp4). Thus, these observations imply that simultaneous or less synchronous (by a few Kyr?) small-scale impact cratering events that may occur within a substantial kilometric distance (50-150 km?) may form a subsurface hydrodynamic cycle with a $3 - 5 \times$ greater radial expansion than that of a single impact-induced and same-scale hydrothermal system (according to the preliminary results of this experiment). More importantly, the duration of aqueous circulation in such a subsurface system seems to be prolonged by at least a factor of 2.

This opens a new area of research, in which the parameters of the time difference and distance between impact-cratering processes within a confined area of planetary crust, need to be thoroughly explored through numerous computer simulations, in order to generate a scaling relation for such phenomena. So far, the available hydrodynamic and impact-physics softwares and codes cannot produce models for simultaneous or relatively synchronous impact events.

For this reason, further investigations of this hypothesis could not be conducted during this PhD research. However, this idea comprises an incentive for future research on the physical constraints that govern the induced hydrological activity after small-scale multi-impact events on a planetary crust. Ideally, this hypothesis may have considerable applications in planetary exploration and colonization missions, as minimum-scale controlled cratering on arid or/and on icy planetary crusts, may provide appreciable amounts of water, organics and minerals needed for the establishment of inter-planetary colonies.

Temperature & Water Mass Flux Distribution in the Martian Crust after 2 Adjacent (within a 100-km radius) and Simultaneous Small-Scale Impact Cratering Events

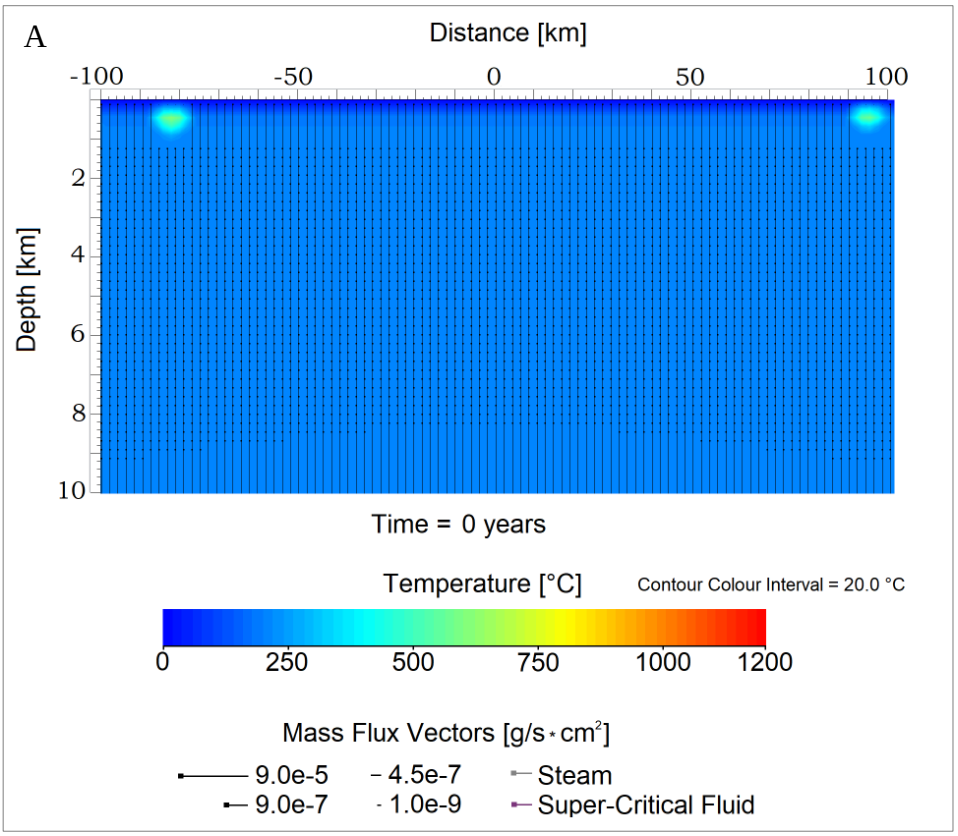

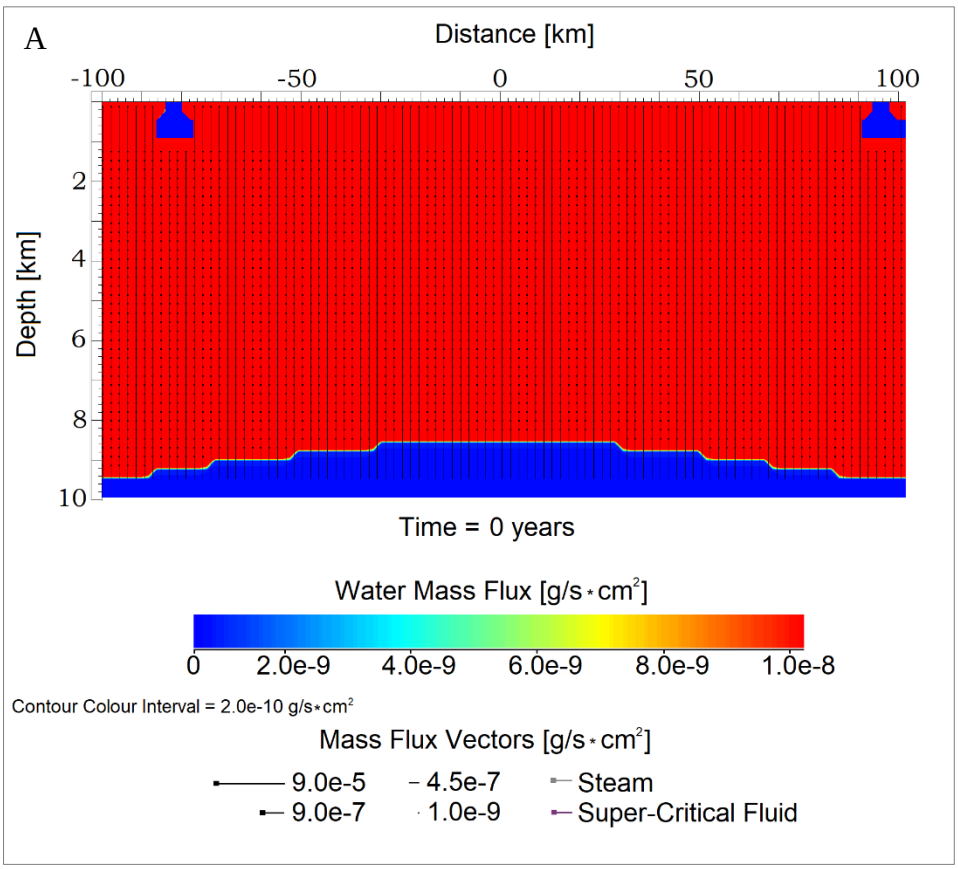

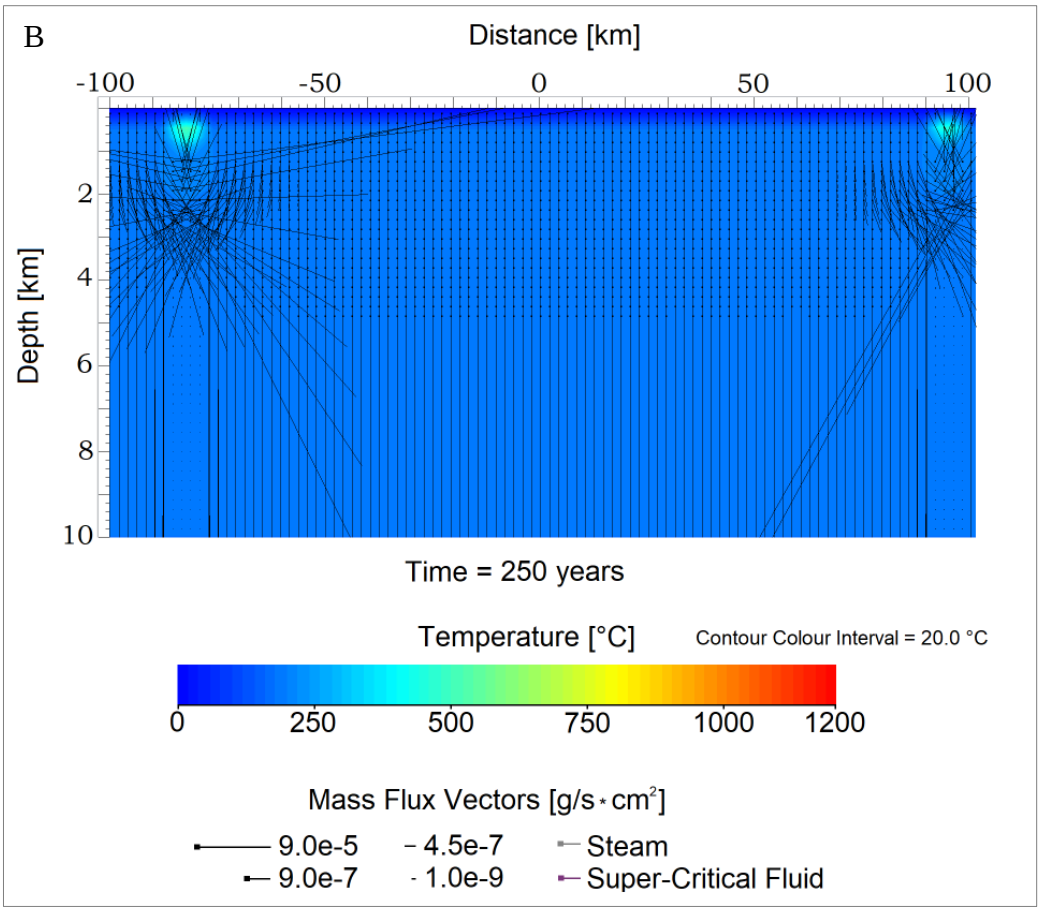
B
Distance [km]
-100
-50
0
50
100
Depth [km]
2
4
6
8
10
Time = 250 years
Temperature [°C]
Contour Colour Interval = 20.0 °C
0
250
500
750
1000
1200
Mass Flux Vectors [g/s*cm²]
9.0e-5
4.5e-7
Steam
9.0e-7
1.0e-9
Super-Critical Fluid

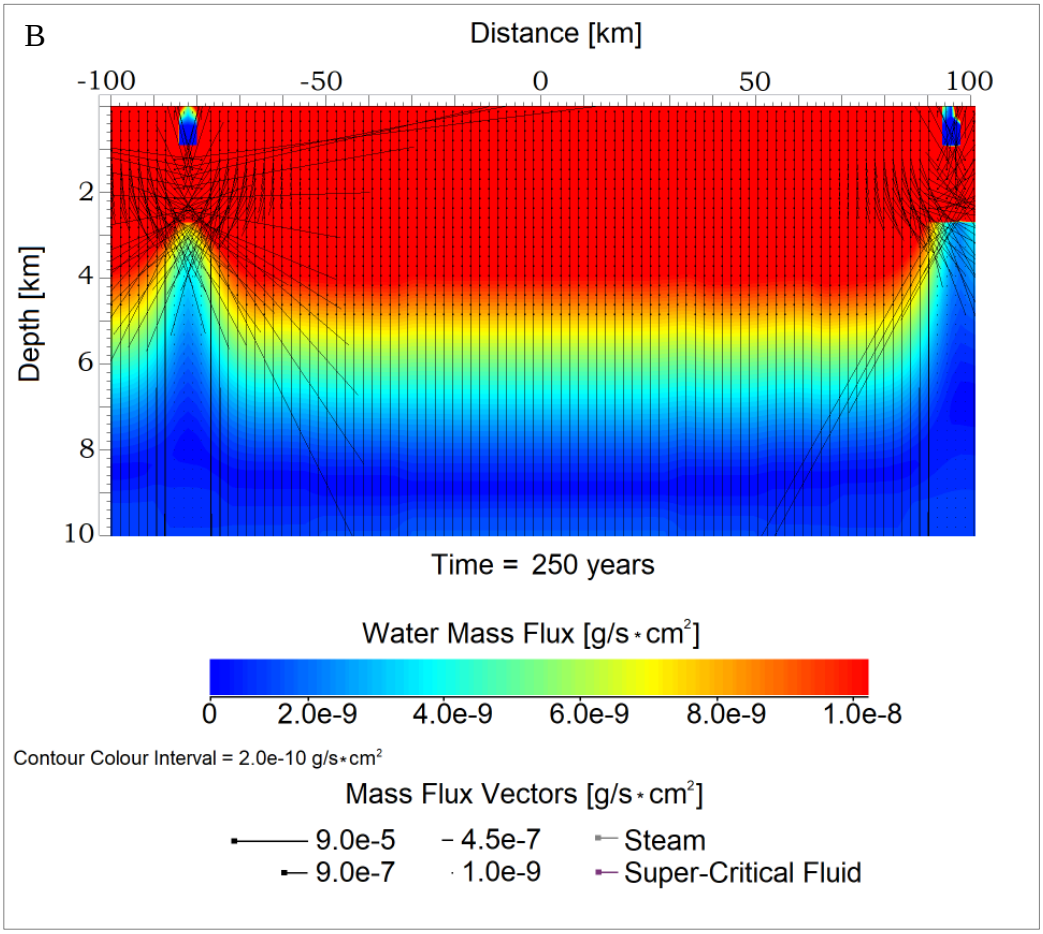
B
Distance [km]
-100
-50
0
50
100
Depth [km]
2
4
6
8
10
Time = 250 years
Water Mass Flux [g/s*cm²]
0
2.0e-9
4.0e-9
6.0e-9
8.0e-9
1.0e-8
Contour Colour Interval = 2.0e-10 g/s*cm²
Mass Flux Vectors [g/s*cm²]
9.0e-5
4.5e-7
Steam
9.0e-7
1.0e-9
Super-Critical Fluid

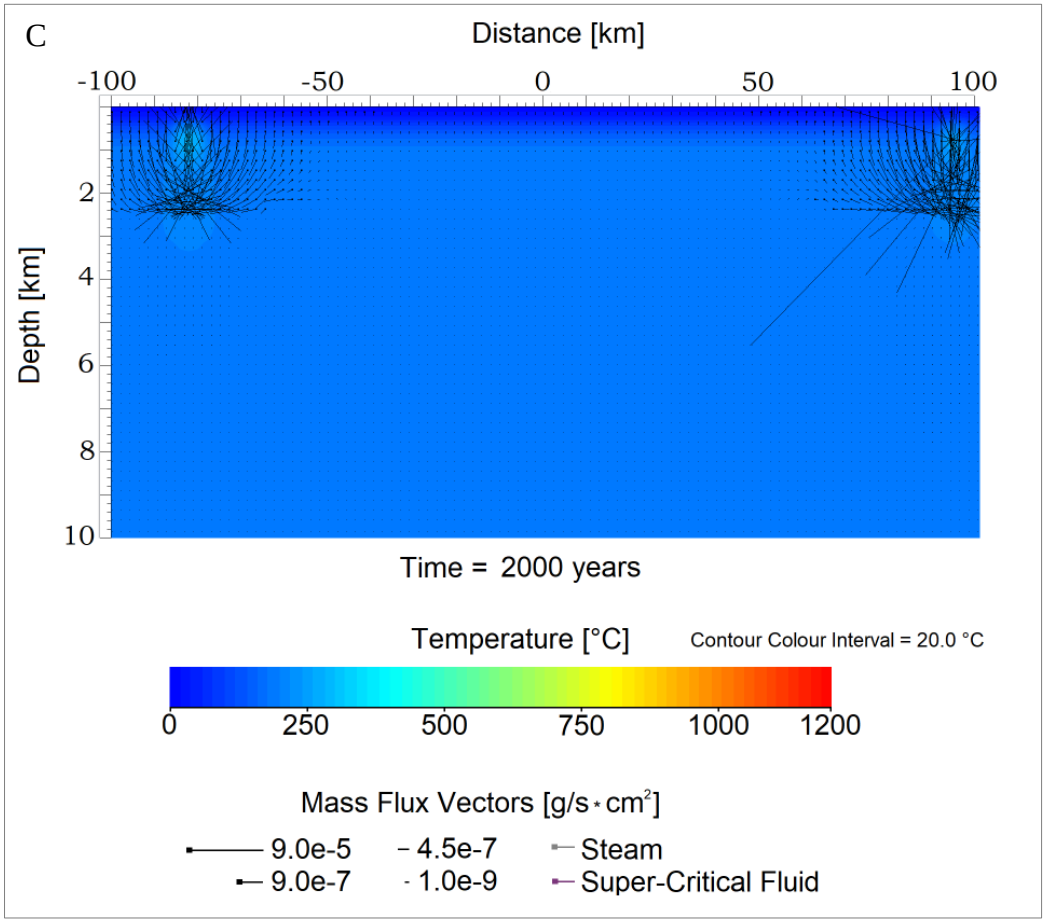
C
Distance [km]
-100
-50
0
50
100
Depth [km]
2
4
6
8
10
Time = 2000 years
Temperature [°C]
Contour Colour Interval = 20.0 °C
0
250
500
750
1000
1200
Mass Flux Vectors [g/s*cm²]
9.0e-5
4.5e-7
Steam
9.0e-7
1.0e-9
Super-Critical Fluid

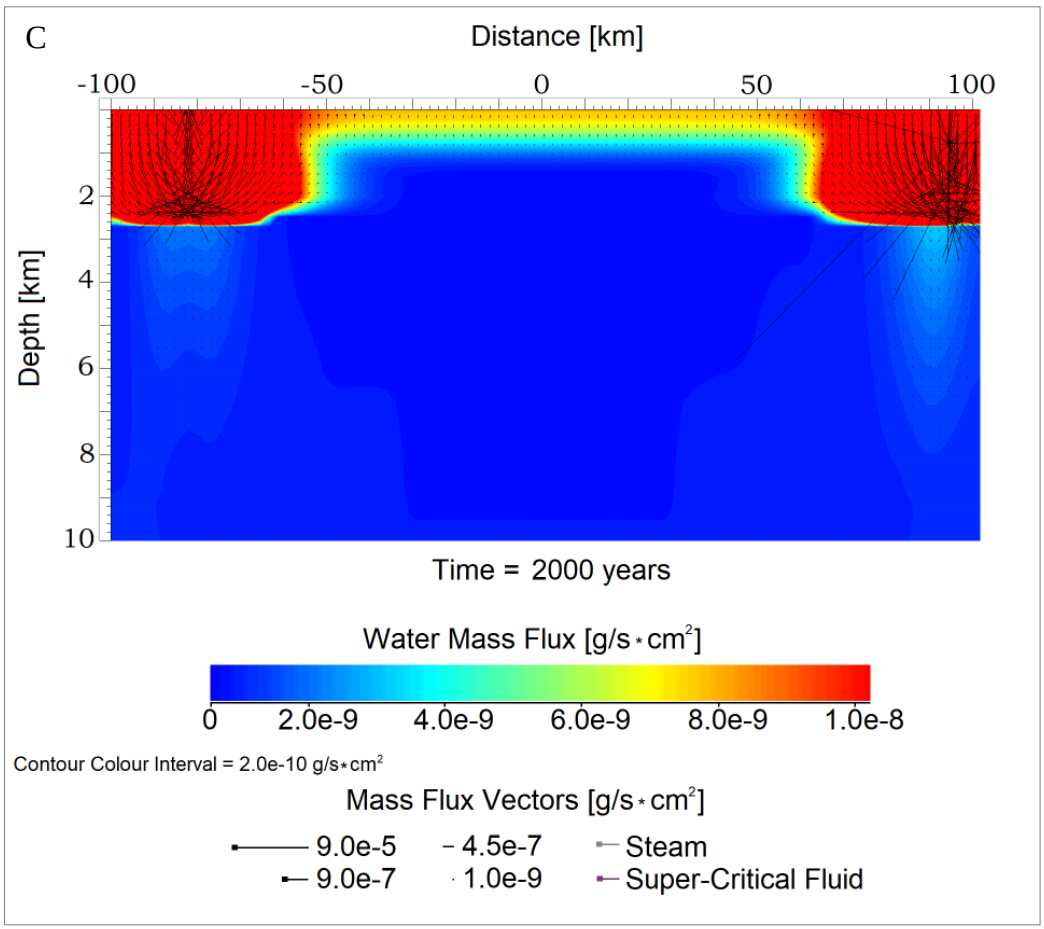
C
Distance [km]
-100
-50
0
50
100
Depth [km]
2
4
6
8
10
Time = 2000 years
Water Mass Flux [g/s*cm²]
0
2.0e-9
4.0e-9
6.0e-9
8.0e-9
1.0e-8
Contour Colour Interval = 2.0e-10 g/s*cm²
Mass Flux Vectors [g/s*cm²]
9.0e-5
4.5e-7
Steam
9.0e-7
1.0e-9
Super-Critical Fluid

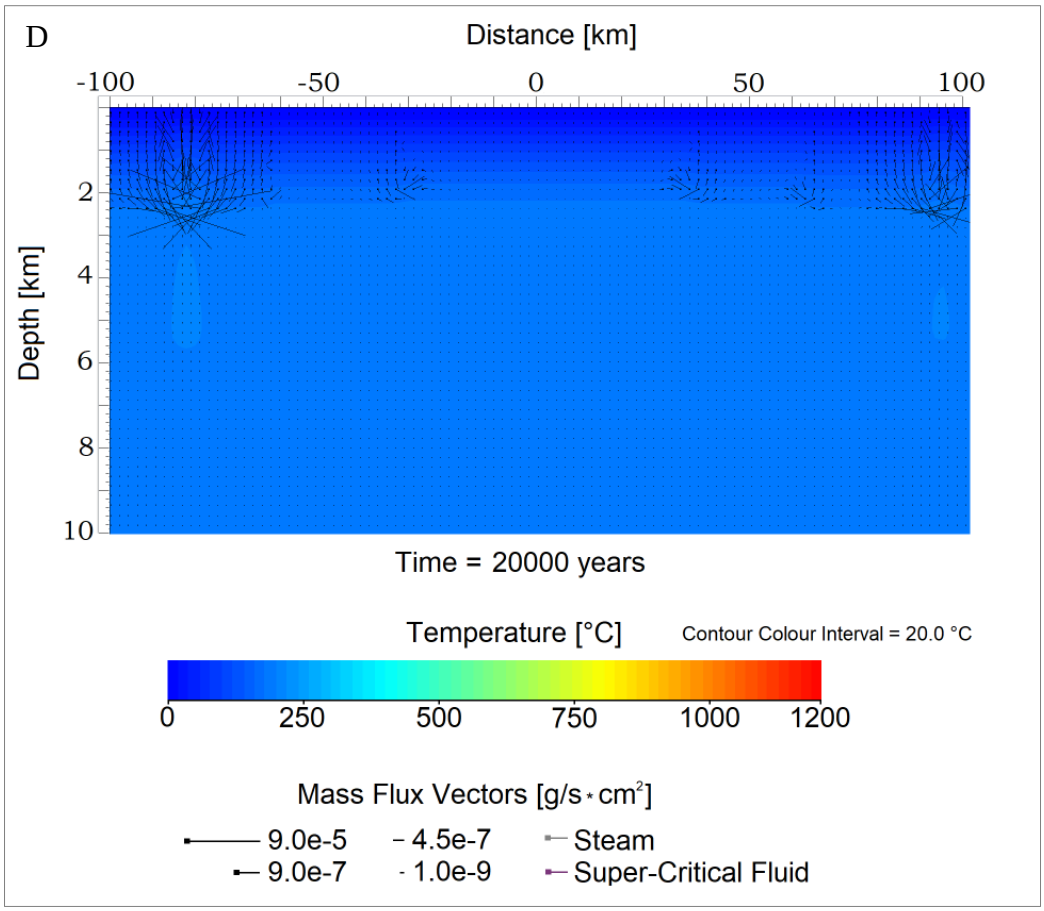
D
Distance [km]
-100
-50
0
50
100
Depth [km]
2
4
6
8
10
Time = 20000 years
Temperature [°C]
Contour Colour Interval = 20.0 °C
0
250
500
750
1000
1200
Mass Flux Vectors [g/s*cm²]
9.0e-5
4.5e-7
Steam
9.0e-7
1.0e-9
Super-Critical Fluid

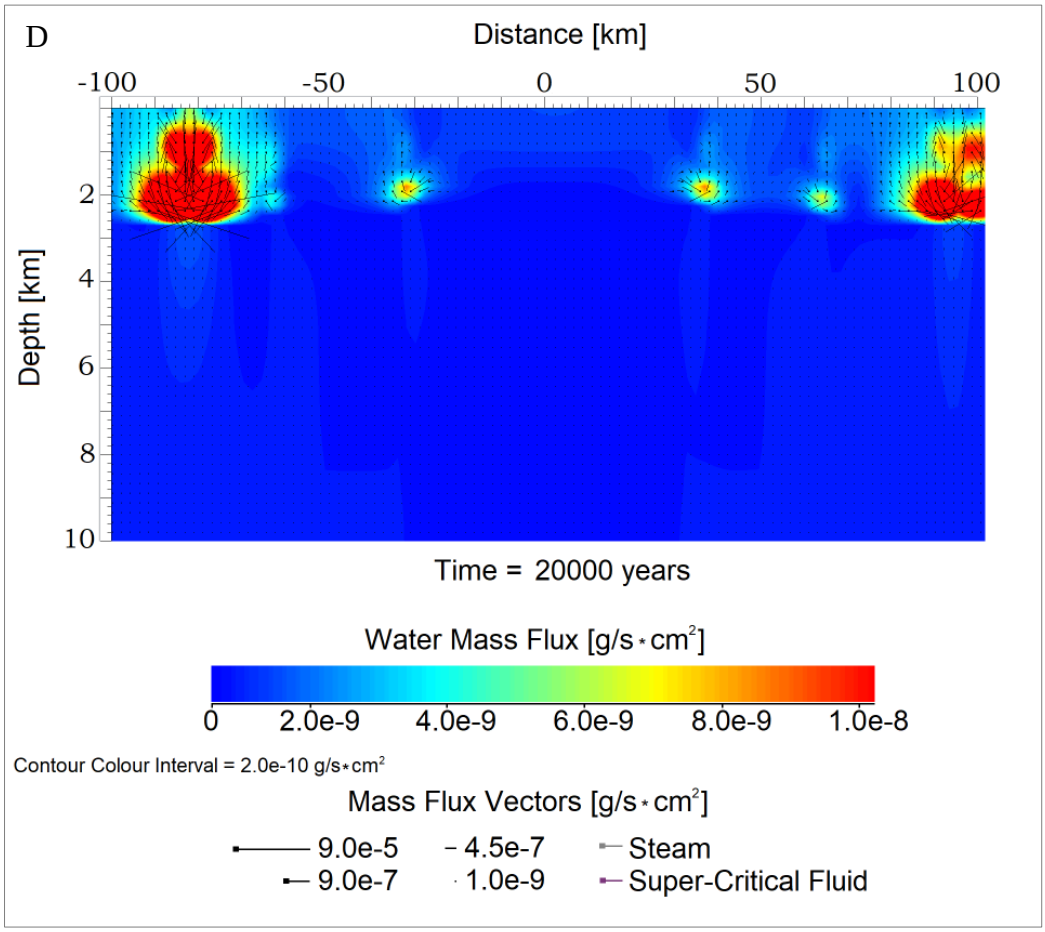
D
Distance [km]
-100
-50
0
50
100
Depth [km]
2
4
6
8
10
Time = 20000 years
Water Mass Flux [g/s*cm²]
0
2.0e-9
4.0e-9
6.0e-9
8.0e-9
1.0e-8
Contour Colour Interval = 2.0e-10 g/s*cm²
Mass Flux Vectors [g/s*cm²]
9.0e-5
4.5e-7
Steam
9.0e-7
1.0e-9
Super-Critical Fluid

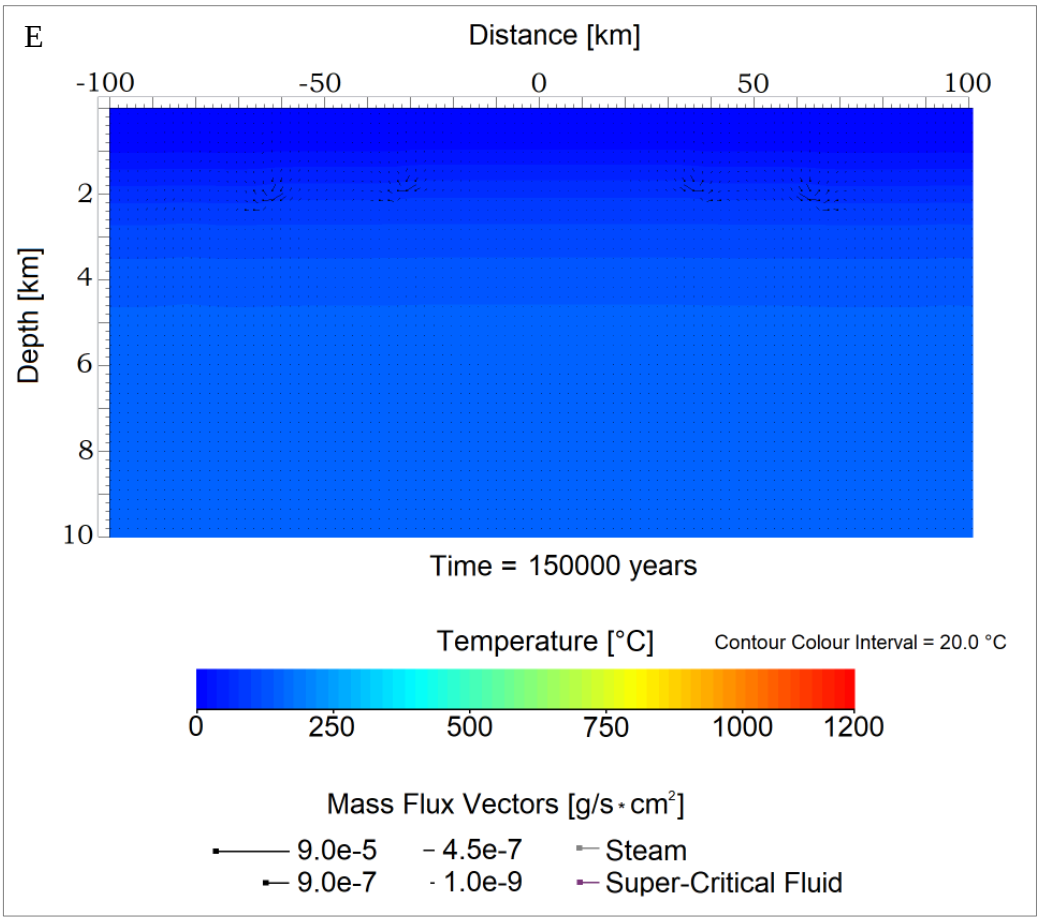
E
Distance [km]
-100
-50
0
50
100
Depth [km]
2
4
6
8
10
Time = 150000 years
Temperature [°C]
Contour Colour Interval = 20.0 °C
0
250
500
750
1000
1200
Mass Flux Vectors [g/s*cm²]
9.0e-5
4.5e-7
Steam
9.0e-7
1.0e-9
Super-Critical Fluid

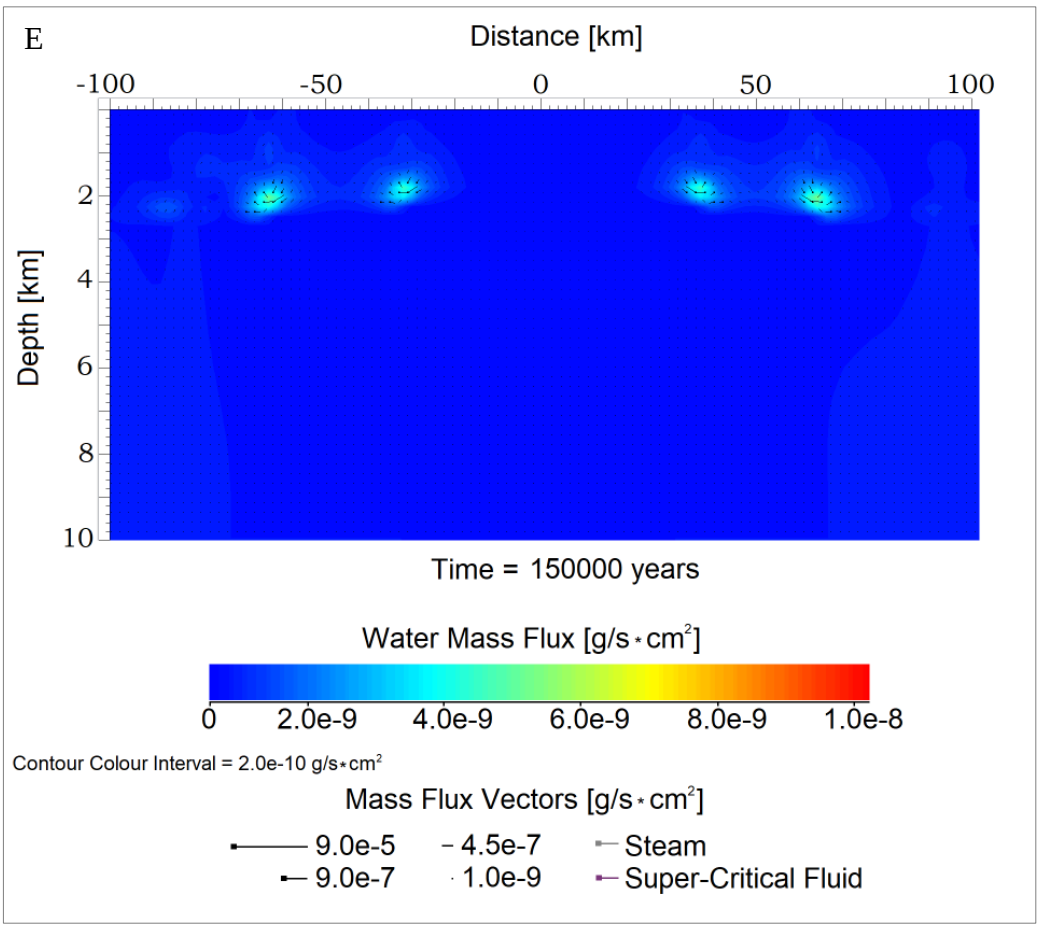
E
Distance [km]
-100
-50
0
50
100
Depth [km]
2
4
6
8
10
Time = 150000 years
Water Mass Flux [g/s*cm²]
0
2.0e-9
4.0e-9
6.0e-9
8.0e-9
1.0e-8
Contour Colour Interval = 2.0e-10 g/s*cm²
Mass Flux Vectors [g/s*cm²]
9.0e-5
4.5e-7
Steam
9.0e-7
1.0e-9
Super-Critical Fluid

Fig. 3.9 (steps A-E). Thermal and hydromechanic evolution in a putative Martian Noachian setting affected by two simultaneous impact cratering events. Both craters' diameters are ≤ 10-km.

Thermal Evolution (steps A-E): After the impact, T_{max} = 700 °C in the heavily impacted rocks at the centre of each crater. The main heat sources of each hydrothermal system are illustrated in light-greenish-/azure colours during the earliest stage of hydrothermal cooling (steps A-B), and are shown within the grid at the following [x,y] positions-coordinates: West Impact-Induced Cratering System: -78 km to -88 km on the x axis, 200 m to 800 m on the y axis; East Impact-Induced Cratering System: 91 km to 98 km on the x axis, 200 m to 800 m on the y axis. Relatively cold and weaker hydrous flows start being evident in the Martian system between 2-20 Kyr (steps C-D), with the weakest ones exhibiting the last evidence for aqueous circulation at circa 150 Kyr. At t = 150 Kyr, the geothermal gradient of the impact-induced hydrothermal system has been restored, with T_{max} = 140 °C, at a depth of 4.5 km, which is consistent with the initially programmed geothermal gradient of 30 °C / km. The basal heat flux of the Noachian crust was adjusted to 60 mW/m^2 at 10-km depth (lower boundary). We can establish that hydrothermal flows in the Noachian system cease at t = 150 Kyr.

Water Mass Flux Evolution (steps A-E): After the impacts, the whole geological domain seems to be thermodynamically affected (red-coloured regions) except for the regions where: [1]: $T_{max} \geq 500$ °C (based on the equations of state, flows cannot occur beyond this upper thermal limit) and, [2]: permeability ≥ 1.0E-20 m^2. The heated target rock units of the setting and their surrounding impactites appear impermeable at the earliest phases of hydrothermal cooling (steps A-B; blue coloured regions in the simulative grid: the central heat sources are shown in the following [x,y] positions-coordinates: West Impact-Induced Cratering System: -78 km to -88 km on the x axis, 200 m to 800 m on the y axis; East Impact-Induced Cratering System: 91 km to 98 km on the x axis, 200 m to 800 m on the y axis). Blue-coloured domains in the grid represent lithologies where no flows or very weak flows are present. Red-coloured regions represent maximum fluxes (≥ 9.0e-9 g/s×cm^2) within the host rock per time step. The magnitude of fluid flux is expressed by vector's length and the squared edge of each vector indicates the direction of flow. Each cell of the simulative grid has an assigned vector per time step, showing the direction and magnitude of flow. Liquid water flux is represented by black vectors, vapour flux by light-greyish vectors, and super-critical flux by purple vectors. At the initial stage of hydrothermal cooling, fluid flux appears with peak values (especially in step B: $WMF_{max} \approx$ 9.0E-4 g/s×cm^2. Maximum fluxes are hosted in niches of the geological system that surround the main heat sources. At t = 150 Kyr (step E), four main hydrothermal cells appear still active, with $WMF_{max} \approx$ 4.0e-9 g/s×cm^2, in each centre of convection. At t = 150 Kyr, minimum recharge flows occur but these are moderately weak. Therefore, through the WMF results we can conclude that shortly after t = 150 Kyr hydrothermal flow halts.

3.2 Numerical Simulations for the Hydrous Activity in Volcanic Systems on Early Mars (via the HYDROTHERM Code)

The most common type of hydrothermal systems on Earth are those induced by magmatism, and this may have been the case for Mars during its ancient geological periods, when the Red Panet was warmer and had abundant surface and subsurface water deposits (Levy et al., 2010; Ehlmann et al., 2011; Wray, 2013a; Ojha, 2015). Nevertheless, current evidence even suggests that the most ubiquitous hydrothermal systems on Mars may have been induced by radiogenic heat deep within the crust (Ojha et al., 2021). Such systems remain undetected and subsequently unexplored though, as they would form in depths greater than 10 km beneath the Martian surface. In contrast to volcanic or impact-induced hydrothermalism, radiogenic-induced hydrothermal systems could have survived for more than 100 Myr, because of the billion-year duration of half-lives of radioactive elements (e.g., U, Th, and K). As the thermodynamics and controversial hydraulics of such potential environments deep within Mars' lower crust or/and upper mantle remain unknown, in this PhD research, I have focused on the two mostly known and explored types of hydrothermalism based on Earth and Mars; i.e.: impact-induced and magmatic-induced hydrothermal systems.

In this section, numerical models for the induced hydrothermal systems under a variety of heat flux and geothermal gradient parameters for the Martian crustal setting (in a modelled geological domain with a maximum depth of 10 km and a horizontal/distance of 200 km in 2D). The same high-resolution discretization for the simulative grid was used for all the following scenarios, which is represented by 4365 computational cells (97 cells for the horizontal axis × 45 cells for the vertical axis) for the 2D volcanic environment of each case. According to the associated type of geothermal system the following scenarios have been investigated in this work:

Sections 3.2.1 and 3.2.2 explore hydrothermal flux due to seasonal variations on the heat flux and the associated geothermal gradient within the Martian crust, with T_{max} = 120 °C and 170 °C, respectively (similar to the implications of modelling provided by Gaidos (2001)). These models should represent domains of the Martian crust during the early- to late-Amazonian

period (or even present-day subsurface thermodynamic conditions). Sub-chapter 3.2.3 demonstrates 2D computational results from induced-hydrothermal flows due to volcanic pluming, with T_{max} = 400 °C in the Martian geological setting. This numerical simulation should account for regions that have been appreciably affected by volcanism during the early-mid Amazonian period, or should represent the thermodynamic processes of the much warmer and more geothermally active Martian crust during the Hesperian and Noachian periods.

Sub-chapter 3.2.4 explores flows in the same simulative grid of the Martian crust under the influence of intrusive veins (serpentine) with T_{max} = 500 °C. Such volcanic events and their induced hydrothermal processes should have been limited to only a few occasions during the Amazonian period, but should have been more ubiquitous during more ancient geological epochs.

All aforementioned computational scenarios have been explored under lower permeability and porosity parameterization too, and their results are included in the form of videos/movies in the appendix (e.g.: Hydrothermal Flows _ T_{max} = 120 °C _ Lower Permeability.mp4, E:/Hydrothermal Flows _ T_{max} = 170 °C _ Lower Permeability.mp4, etc.). Furthermore, in the supplementary materials of this thesis, additional HT simulations have been performed for different geothermal constraints. Such simulations derive from variations in the T_{max} present in the geological setting, which are a result of the initial boundary conditions on the type of volcanism that has been modelled. More precisely, investigations of pluming effects with T_{max} = 300 °C and T_{max} = 600 °C (in addition to the computations presented in 3.2.3) are presented in the forms of videos in the appendix, with both lower and higher permeability parameterization for each scenario. Finally, simulations for hydrothermal flows with T_{max} = 750 °C due to intrusive veins have also been conducted, to compare the duration of hydrothermal circulation and the patterns of water mass flux therein, with the thermodynamic results of scenario 3.2.4, where T_{max} = 500 °C (T decreased by 250 °C).

All the following sub-chapters explore the hydrothermal response of the Martian crust under low temperature versus high temperature effects of volcanism, and aim to determine the lifetime of hydrous circulation and the hydraulic pattern in each case study. The thermodynamic results of the simulations below will be later used in sub-chapter 3.3. to assess the bioenergetic potential of the subsurface realm of Mars for each case scenario. The following

models will help constrain further the subsurface regions in which water-rock reactions and a potential release of nutrients may have occurred under specific thermodynamic conditions. Furthermore, the numerical models that follow may also indicate the abundance and distribution of aqueous and hydrothermal deposits within the present-day Martian crust; aqueous reservoirs that should have probably formed due to the intensity and duration of hydrothermal circulation (impact-induced, magmatic or cryovolcanic) in ancient or more recent geological epochs.

3.2.1 Hydrothermal Flows of T_{max} = 120 °C in a Martian Geological Setting due to Basal Heat Flux

The initial thermodynamic conditions for the geological grid in which the simulated hydrothermal flows do not exceed a T_{max} = 120 °C, are presented in fig. 3.10, and the petrophysical properties of the rocks that comprise the geological setting are summarized in table 3.4. In this setting, I assumed that hydrothermal flows originate from a putative transient increase in the basal heat flux of the setting. The background geothermal gradient was adjusted to 12 °C / km in the boundary conditions of the simulation. However, the associated basal heat flux of the Martian setting was increased to 40 mW/m^2, instead of using an associated value of 17-25 mW/m^2. This putative 15 mW/m^2 increase in basal heat flux along with the presence of a correlated thermal contour of T_{max} = 120 °C at a depth of 8 km results to inducing hydrothermal flows with $T_{initial}$ = 120 °C at a depth of 8 km. Such events may occur regularly on present-day or late-Amazonian Mars due to seasonal changes of heat flows at such depths (7-20 km). Gaidos (2001) showed that ephemeral increase in surface temperature (due to climate change) or heat flow (due to transient volcanic events) on Mars can induce melting of ground ice, and the formation or recharge of aqueous deposits within the Martian subsurface. Thus, the modelling results of this study were considered as initial parameters for adjusting the geothermal profile and basal heat flux of this setting. The HT code showed that this difference in the basal heat flux satisfies the convergence criteria of the equations of state used in this simulation. Thus, we can hypothesize that such a transient basal heat flux increase could be probable in Martian geological settings.

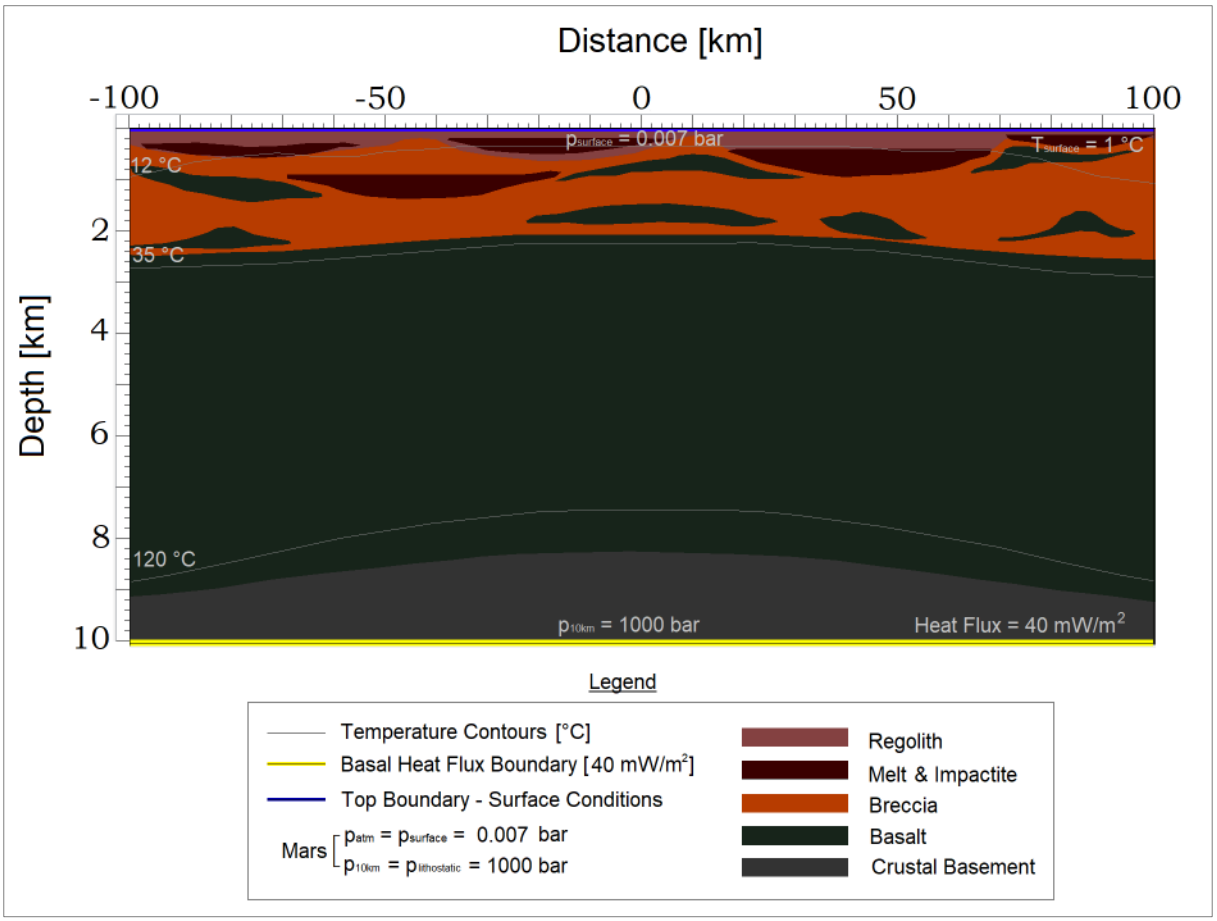

Fig. 3.10. HT thermodynamic conditions and geological model for the 200 km in horizontal distance and 10 km in depth 2D Martian subsurface environment. Basal heat flux is modelled with a value of 40 mW/m^2, atmospheric pressure at the ground surface of Mars is computed to 0.007 bar, and the ground surface temperature is set to 1°C. Maximum temperature in this setting is adjusted to 120 °C at a depth of circa 9-8 km, and represents the maximum temperature of hydrothermal flows that form due to the transient increase of the basal heat flux in the setting (from 20 mW/m^2 to 40 mW/m^2, at a depth of 10 km). In this model, impactites and volcanic rocks of higher thermal conductivity have been considered, to represent the heavily impacted Martian surface - shallow subsurface and the deeper volcanic or/and plutonic units, respectively.

Table 3.4. HT boundary parameters for the lithologies that comprise the 2D Martian subsurface environment (200 km in horizontal distance × 10 km depth: fig. 3.10). The petrophysical properties of the rocks shown below were adjusted according to the thermodynamics of models presented in sub-chapter 3.1, and correspond to the physical properties of the heavily affected by meteorite impacts Martian surface and subsurface.

Petrophysical Properties	**Crustal Basement**	**Basalt**	**Melt Rocks**	**Breccia**	**Regolith**
Permeability (k) {m^2}	$k_z = f(d,T)$, $k_x = f(d,T)$	$k_z = f(d,T)$, $k_x = f(d,T)$	$k_z = f(d,T)$, $k_x = f(d,T)$	$k_z = f(d,T)$, $k_x = f(d,T)$	$k_z = f(d,T)$, $k_x = f(d,T)$
Porosity (φ) {%}	$\varphi = f(d,T)$	$\varphi = f(d,T)$	$\varphi = f(d,T)$	$\varphi = f(d,T)$	$\varphi = f(d,T)$
Thermal Conductivity {W/m·K}	2.9	2.7	2.7	2.7	1.7
Specific Heat Capacity {J/kg·K}	1200	1000	1000	900	700
Density {kg/m^3}	3000	2700	2500	2500	1700
Surface Permeability {m^2}	1.00E – 19	9.00E - 17	1.00E - 16	1.00E – 15	1.00E - 14
Surface Porosity ($\varphi_{surface}$)	2.0 %	5.0 %	7.0 %	7.0 %	15.0 %

The numerical simulation indicates that, at t_0 after the ascension of the 120 °C isotherm at a depth of circa 8 km, the geological setting hosts intense hydrous flows starting from the deeper subsurface realm at circa 9.4 km depth to the shallowest subsurface – near-surface regions (illustrated by the red-coloured domain in fig. 3.11: A). T_{max} in the geological domain does not exceed the value of 120 °C, with the warmest flows being present at greater depths. Colder flows with $T_{max} \leq 25$ °C prevail within the upper-subsurface realm, at depths no greater than 1.6 km (fig. 3.11: A). This hydrous flow pattern appears consistent with results of previous models suggested by Gaidos (2001) and Ojha et al. (2022), indicating that flows within the shallow subsurface of Mars (≤ 1km) could not exceed the thermal limit of 20 °C. Maximum flows appear within the deeper domain of the setting, at depths between 8 and 9 km, according to the flux vectors therein which indicate a far greater magnitude (almost 3 orders of magnitude greater flux; with $WMF_{max} \approx$ 9.0e-5 g/s×cm^2).

At t = 100 yr, hydrothermal cooling seems to be affecting flows within the deeper domains of the setting. At that time point, maximum flows seem to have decreased by at least 2 orders of magnitude, with $WMF_{max} \approx$ 9.0e-7 g/s×cm^2 at lower depths (0.1 – 5 km; fig. 3.11: B). Furthermore, maximum hydrothermal flows seem to be associated with a $T_{max} \leq 75$ °C, and within a depth range from 3.4 to 5.5 km below the Martian surface (fig. 3.11: B). At depths between 8 and 9 km, hydrothermal flows do not exceed the value of 6.0e-9 g/s×cm^2, although their temperature plots closer to the 100°C isotherm under an estimated pressure of circa 800 bar (fig. 3.11: B).

At t = 160 yr the hydrothermal system seems to host hydrous fluxes that are decreased by at least 4 orders of magnitude in comparison to the initial maximum flux in the system (fig. 3.11: C). After 160 yr, maximum fluxes do not exceed a value of 1.0e-8 g/s×cm^2 and are present only in the upper 2-km subsurface domain of the hydrothermal setting, where the temperature is no greater than 25 °C (fig. 3.11: C). Eventually, we can assume that fluxes in this Martian subsurface environment do not durate for more than 230 yr; as at t = 230 yr, minimum flux has a computed value lower than 1.2e-9 g/s×cm^2 and the vectors' length implies that if any aqueous flows are present, then these are of negligible magnitude (fig. 3.11: D).

Significantly, more conservative parameterization (lower permeability) on this simulative model indicates that the lifetime of the hydrothermal setting will be by 20 yr greater; this is probably due to the fact that the lower permeability of the rock units contributes to a lower rate

of heat loss for the hydrothermal system as time elapses. As a result, in the scenario where the permeability of all rock units (as presented in table 3.4) is by one order of magnitude lower, the hydrothermal system expands its lifetime to 250 yr, as a more conductive cooling pattern prevails in the setting (appendix: Hydrothermal Flows _ T_{max} = 120 °C _ Lower Permeability.mp4). In the higher permeability simulation, the main pattern of hydrous circulation is governed by convective cooling and this is evident by the Nusselt number measurements of the simulation (appendix: Nusselt Number Measurements: T_{max} = 120 °C _ Lower Permeability.mp4 vs. Higher Permeability.mp4). The Nusselt number (Nu) indicates the ratio of convective to conductive heat transfer at a boundary in a fluid, as described in the methodology chapter of the thesis (§2). To rewind, in this modelling approach, Nusselt values below 1 represent heat transfer by pure conduction. Nu values between 1 and 10 are characteristic of lamirar flows, and Nu values between 10-100 are indicative of predominantly convective flows (Hayba and Ingebritsen, 1997; Parro et al., 2017), with $100 \leq Nu \leq 1000$ representing turbulent convective flows. In the higher permeability scenario, Nu is described by values between 10 and 30 in the domains where hydrothermal circulation occurs. However, in the lower permeability scenario, Nu is no higher than 2 in most of the regions of the Martian subsurface realm. Only a few exceptions are present at depths between 8-9 km, within a spatially constrained domain and for a period no greater than 30 yr (at the initial stage of the hydrothermal cooling process) where Nu is computed with values of 10-20 but for a very short period of time.

In conclusion, this set of simulations shows that a minor increase in the basal heat flux, and a subsequent ascension of the 100-120 °C isotherms at depths of 7-8 km, may induce some appreciable flows for a maximum period of 230-250 yr, depending on parameterization. Moreover, these computations may reveal the thermodynamic conditions within the Martian subsurface during the more recent late-Amazonian period, and the induced aqueous processes after slight temperature increases in the geothermal profile of such volcanic lithological domains. Subsequently, the resulting thermodynamics of this simulative setting and the calculated lifetime of aqueous circulation therein can additionally provide an insightful view into the potential bioenergetics in such low energy anaerobic environments in the present-day Martian subsurface realm. The question focusing on whether prebiotic chemical products can be released under such thermodynamic conditions in the Martian subsurface, and on their potential to support microbial life under low energy and duration limitations, will be analytically discussed in the following sub-chapter (§3.3).

Temperature & Water Mass Flux Distribution in the 2D Martian Geothermal Setting [T_{max} = 120 °C]

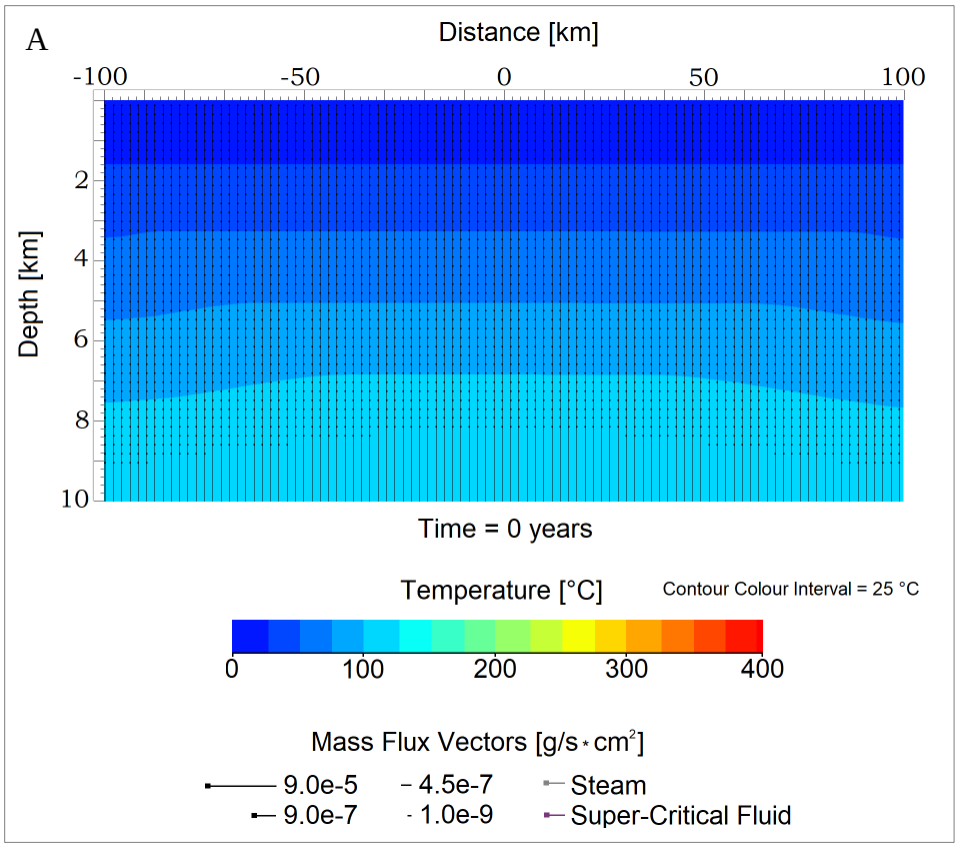

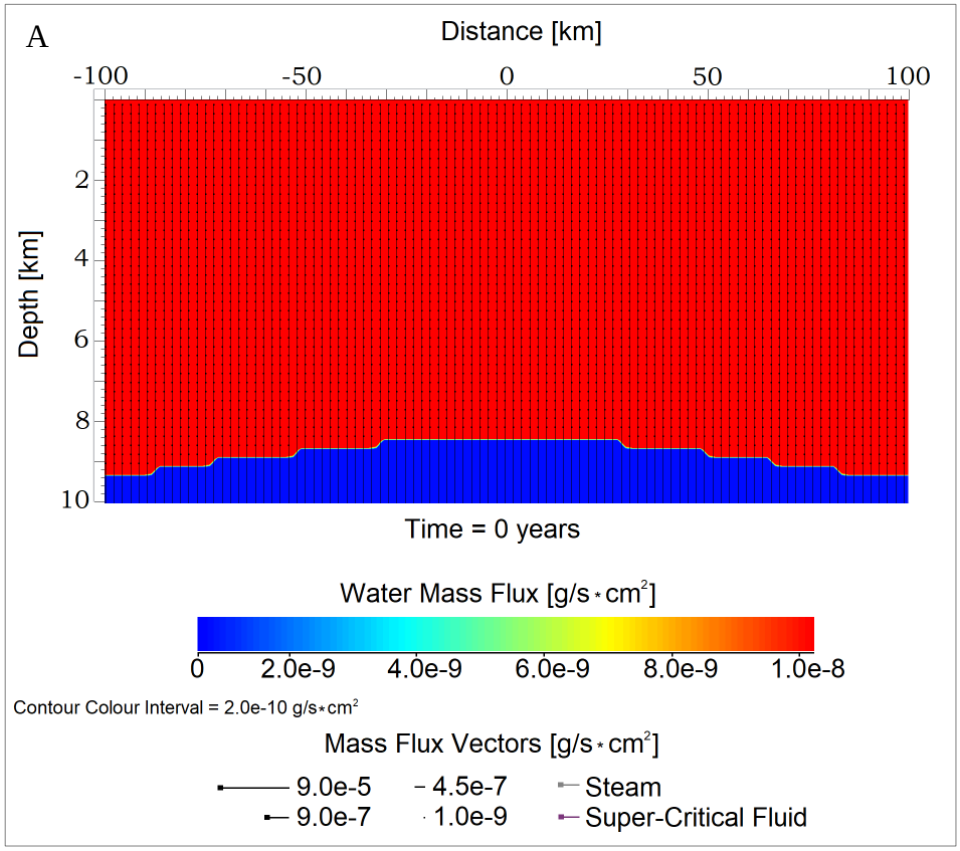

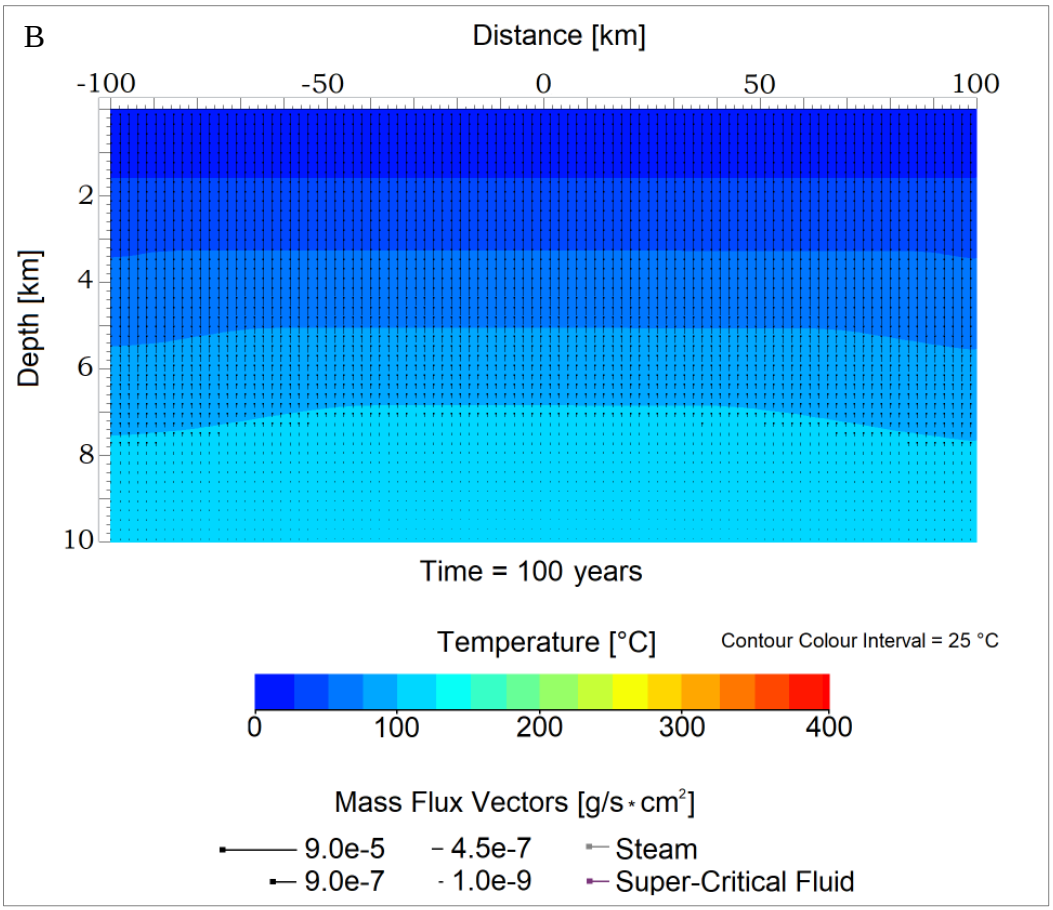
B
Distance [km]
-100
-50
0
50
100
Depth [km]
2
4
6
8
10
Time = 100 years
Temperature [°C]
Contour Colour Interval = 25 °C
0
100
200
300
400
Mass Flux Vectors [g/s*cm²]
9.0e-5
4.5e-7
Steam
9.0e-7
1.0e-9
Super-Critical Fluid

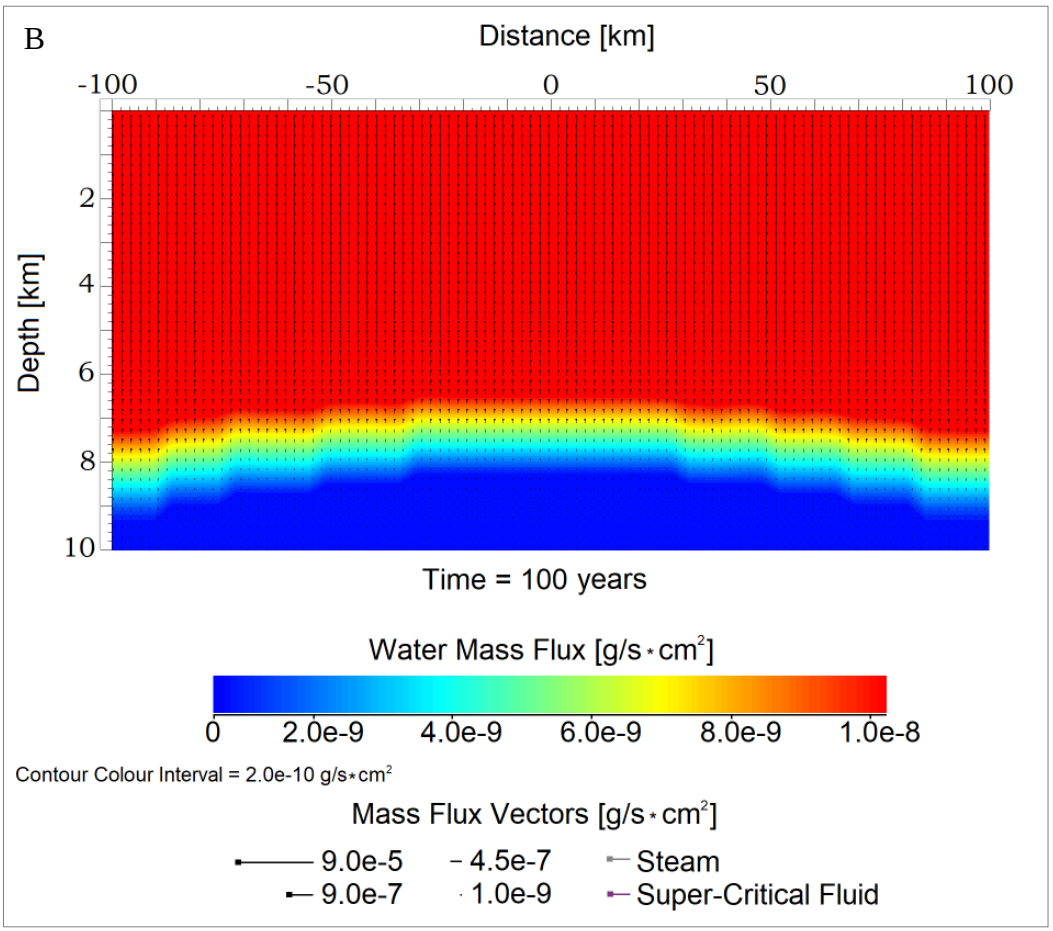
B
Distance [km]
-100
-50
0
50
100
Depth [km]
2
4
6
8
10
Time = 100 years
Water Mass Flux [g/s*cm²]
0
2.0e-9
4.0e-9
6.0e-9
8.0e-9
1.0e-8
Contour Colour Interval = 2.0e-10 g/s*cm²
Mass Flux Vectors [g/s*cm²]
9.0e-5
4.5e-7
Steam
9.0e-7
1.0e-9
Super-Critical Fluid

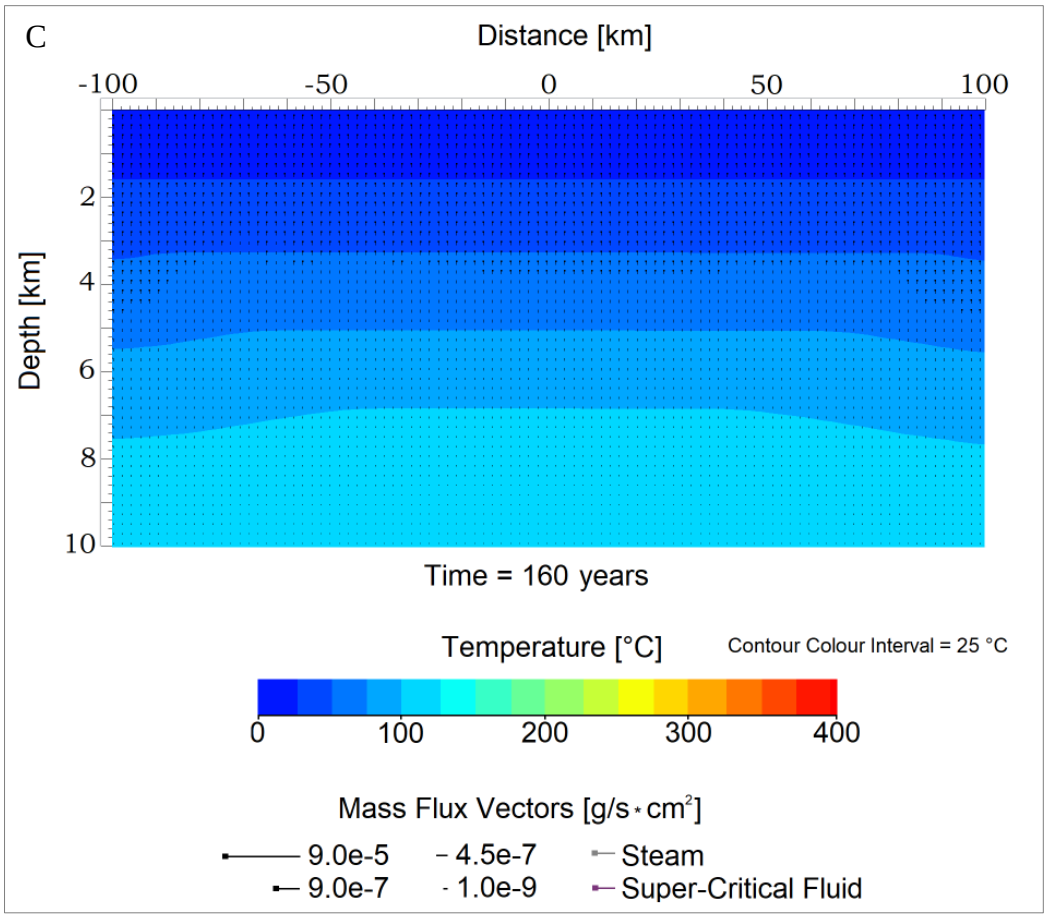
C
Distance [km]
-100
-50
0
50
100
Depth [km]
2
4
6
8
10
Time = 160 years
Temperature [°C]
Contour Colour Interval = 25 °C
0
100
200
300
400
Mass Flux Vectors [g/s*cm²]
9.0e-5
4.5e-7
Steam
9.0e-7
1.0e-9
Super-Critical Fluid

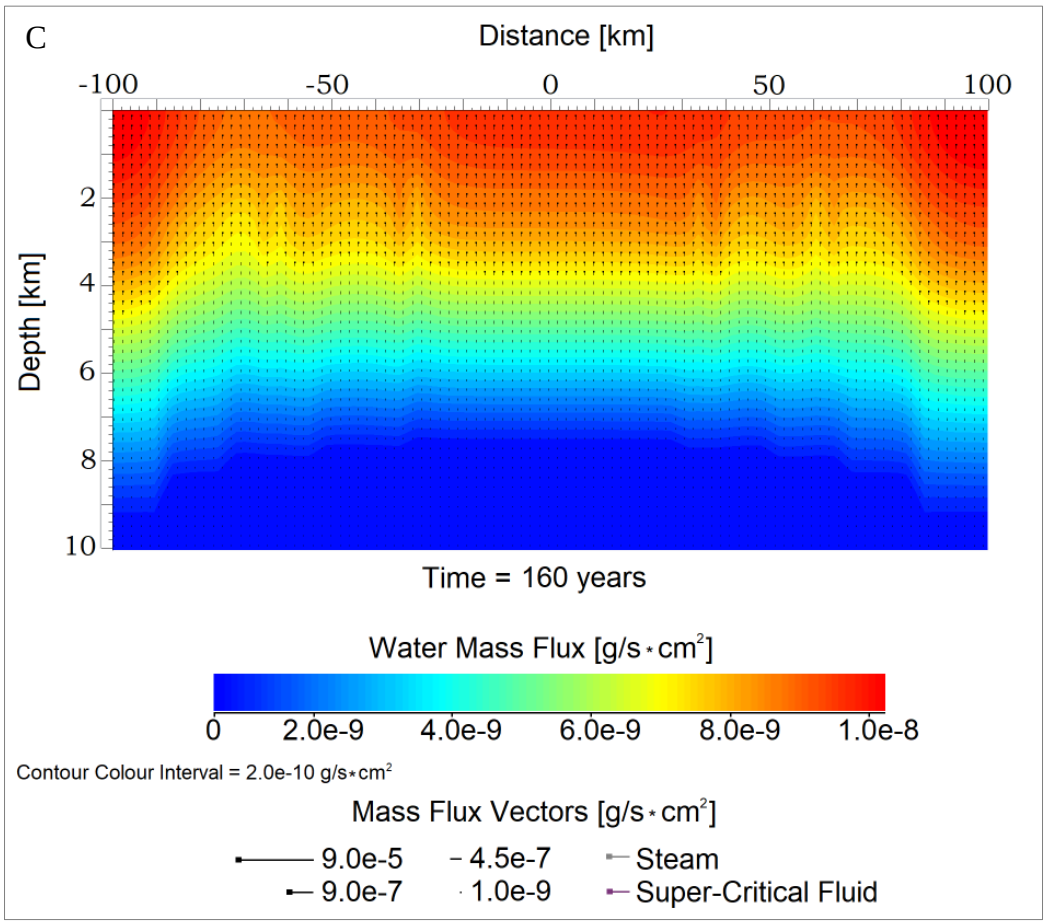
C
Distance [km]
-100
-50
0
50
100
Depth [km]
2
4
6
8
10
Time = 160 years
Water Mass Flux [g/s*cm²]
0
2.0e-9
4.0e-9
6.0e-9
8.0e-9
1.0e-8
Contour Colour Interval = 2.0e-10 g/s*cm²
Mass Flux Vectors [g/s*cm²]
9.0e-5
4.5e-7
Steam
9.0e-7
1.0e-9
Super-Critical Fluid

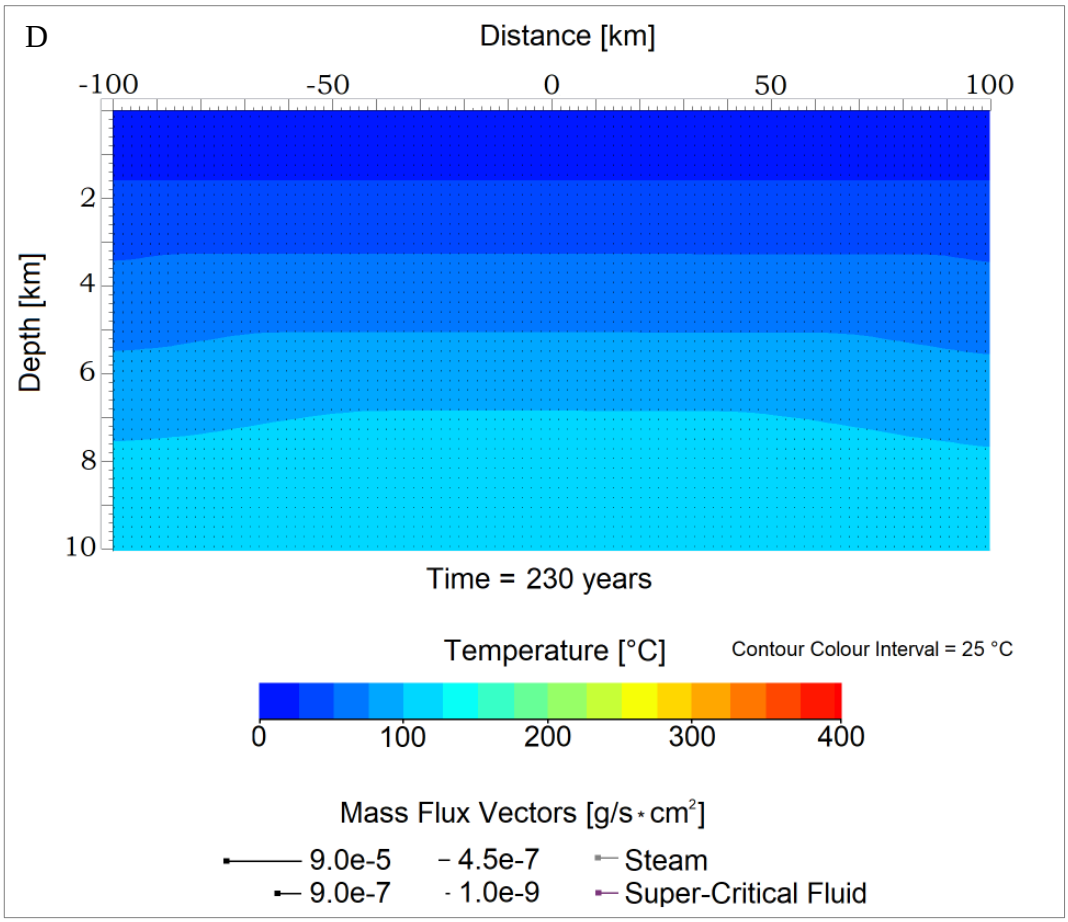
D
Distance [km]
-100
-50
0
50
100
2
4
6
8
10
Depth [km]
Time = 230 years
Temperature [°C]
Contour Colour Interval = 25 °C
0
100
200
300
400
Mass Flux Vectors [g/s * cm²]
9.0e-5
4.5e-7
Steam
9.0e-7
1.0e-9
Super-Critical Fluid

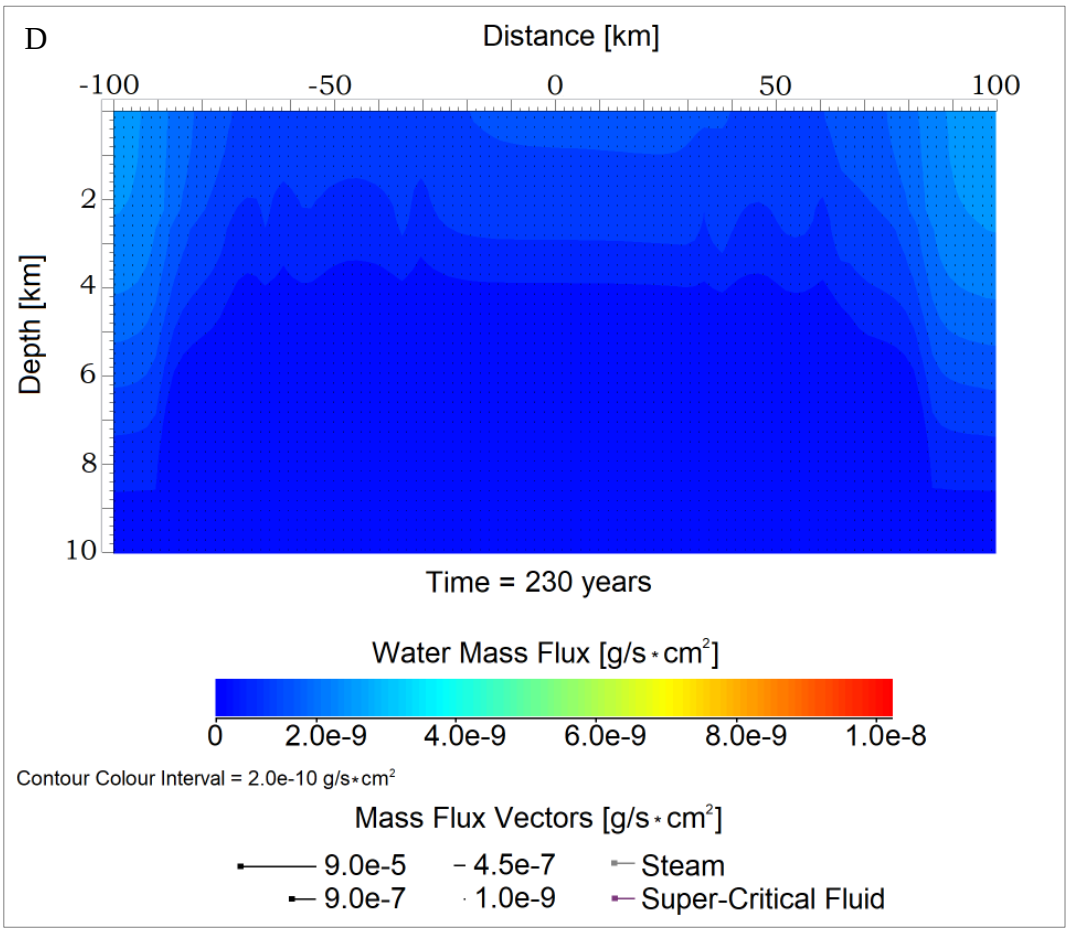
D
Distance [km]
-100
-50
0
50
100
2
4
6
8
10
Depth [km]
Time = 230 years
Water Mass Flux [g/s * cm²]
0
2.0e-9
4.0e-9
6.0e-9
8.0e-9
1.0e-8
Contour Colour Interval = 2.0e-10 g/s * cm²
Mass Flux Vectors [g/s * cm²]
9.0e-5
4.5e-7
Steam
9.0e-7
1.0e-9
Super-Critical Fluid

Fig. 3.11 (steps A-D). Thermal and hydromechanic evolution of the Martian basaltic crust, after a minor increase in the basal heat flux and the associated geothermal gradient of the setting, with T_{max} = 120 °C.

Thermal Distribution (steps A-D): Darker-blue-coloured regions in the grid show colder domains of the setting, where $T_{max} \leq 25$ °C. Azure-coloured regions of the geological grid indicate domains where T = T_{max} = 120 °C. The magnitude of fluid flux is represented by vector's length and the squared edge of each vector shows the direction of flow. Each cell of the computational grid includes a fluid flux vector per each time step that indicates the direction and magnitude of flow. Liquid water flux is represented by black vectors, vapour flux by light-greyish vectors, and super-critical flux by purple vectors. It is evident through time steps A-D that the geothermal profile of the system does not change after the ascending of the 120 °C isotherm from a depth of 10 km to a depth of 7 km at t_0; and that the geothermal gradient is stabilized as constant during the entire simulation. However, hydrous flows circulate within this subsurface realm, for as long as the thermal conductivity, porosity and permeability of the lithological units dictate the rate of heat loss and the subsequent generation of temperature- and permeability-dependent aqueous$_{(liquid)}$ flows. From t = 230 yr and then on, the computed values of water flux imply that any flows in the setting can be considered as negligible.

Water Mass Flux Distribution (steps A-D): Blue-coloured regions in the grid indicate geological domains where no flows or very weak flows are present. Red-coloured regions show maximum fluxes ($\geq$ 9.0e-9 g/s×cm^2) within the host lithology per time step. The magnitude of fluid flux is represented by vector's length and the squared edge of each vector shows the direction of flow. Each cell of the simulative grid is assigned to a vector per time step that indicates the direction and magnitude of flow. Liquid water flux is represented by black vectors, vapour flux by light-greyish vectors, and super-critical flux by purple vectors. At t_0 liquid water flux reaches peak values (step A: $WMF_{max} \approx$ 9.0e-5 g/s×cm^2) at depths of 8 and 9 km from the Martian surface, as illustrated by the vectors therein in this time step. Fluid mass flux appears only in the liquid phase, as T $\leq$ 120 °C and the P-T conditions in each cell do not allow super-critical or steam flows to be generated. After t = 230 yr, $WMF_{max} \approx$ 1.2e-9 g/s×cm^2, indicating that hydrothermal flows are negligible or of the lowest potential magnitude and thus, implying the end of the aqueous activity in this Martian environment.

3.2.2 Hydrothermal Flows of T_{max} = 170 °C in a Martian Geological Setting due to Basal Heat Flux

In this computational scenario, the geological setting remains the same with the one presented in sub-chapter 3.2.1, and the petrophysical characteristics of the rocks are adjusted to the same values shown in table 3.4. The only difference between this simulation and the previously presented case is the use of a slightly greater value for the basal heat flux at a depth of 10 km (45 mW/m^2), and the presence of a warmer isotherm at a depth of circa 7.5 – 9 km (170 °C; fig. 3.12). The different thermal parameters at such depths were used to account for a hypothesis of a much warmer crustal basement and of a subsequently hotter geothermal profile; as these parameters should describe volcanic lithologies in the Red Planet's crust which may have been affected by warmer heat currents and a higher geothermal gradient during more ancient times of the Amazonian period. This hypothesis contrasts with most of the present-day Martian subsurface domains where basal heat flux should be closer to the average calculated value of 19 mW/m^2 (with heat flow values ranging from to 14 to 25 mW/m^2; after Parro et al. (2017)). Thus, this simulation is more optimistic in terms of the heat abundance in the investigated Martian geothermal setting, and may be representative of ancient subsurface environments of the early- to mid-Amazonian period. The focus of this simulation is to assess how the duration and flow pattern of the geothermally induced aqueous activity may be influenced under warmer conditions, when compared to the previous thermodynamic model of the late-to-present-day Amazonian crust.

The results of this model show that there are some minor changes in the flow pattern and thermodynamic evolution of the hydrothermal system, based on the comparison with the results of scenario 3.2.1. Fistly, the duration of the hydrothermal system seems to be extended by a further period of 70 years (fig. 3.13: D) in this case, and on top of that, deeper regions within the crustal setting appear affected by appreciable flows (WMF ≈ 4.0e-9 g/s×cm^2) at depths of 9-10 km after t = 160 yr (fig. 3.13: C). Whereas, in scenario 3.2.1, flows of such magnitude were not evident at depths greater than 7 km from t = 160 yr and then on (fig. 3.11: C-D). This is obviously due to the presence of a higher in temperature isotherm at a depth of approximately 8 km (170 °C) and due to the slight increase of the basal heat flux of the geothermal system by 5 mW/m^2 at a depth of 10 km. These changes decelerate to a notable degree the cooling process and result to those deeper regions of the geological setting being affected by induced aqueous flows of higher temperatures (fluids of 125 to 150 °C, at depths from 6 to 10 km, and under a

pressure range of 600 – 1000 bar, respectively; fig. 3.13: B-D). Such hydrothermal flows were not evident in the previous case of the 120 °C isotherm present at a depth of approximately 8 km in the setting, and by considering a 40 mW/m^2 basal heat flux at a depth of 10 km.

However, the magnitude of flow and pattern of circulation remain similar to those of scenario 3.2.1, with no water-recharge events being present. In particular, the direction of flow (water mass flux vectors in fig. 3.13: A-D) shows that water seeps out predominantly from the interior of the geological setting to the surface of Mars. There are no colder flows present in the hydrological system, with flux vectors pointing towards the basal boundary of the setting, that could originate from the surface of Mars, and that could subsequently penetrate the porous of the volcanic rocks and move towards deeper regions of the hydrothermal system (evident through both fig. 3.11: A-D and fig. 3.13: A-D). In addition, the strength of maximum flows after t = 160 yr, is decreased by at least four orders of magnitude in both simulative scenarios (3.2.1 and 3.2.2) when compared to the initial WMF_{max} present in the hydrological system.

Furthermore, this modelling approach indicates that geothermally-induced aqueous flows may have been present at even greater depths within the Martian crust during the early- to mid-Amazonian period; when the interior of Mars should have been supposedly warmer and more abundant in H_2O-bearing deposits to a depth range of 5 – 10 km in Amazonian terrains (Hoffmann, 2000; Changela and Bridges, 2011). Hydrothermal circulation is governed by the permeability, porosity and fracture density of the rocks in a geological setting. Since the average gravitational acceleration on Mars is about 38% of that of Earth, Abramov and Kring (2005) calculated that the maximum depth of permeable, porous or/and fractured rocks in Martian hydrothermal systems should be 2.5 times greater than it would be on Earth. Moreover, they showed that permeability should decrease more gradually with depth on Mars.

Therefore, the model presented in this chapter is consistent with this hypothesis and indicates that Martian low-temperature geothermal systems may have hosted transient aqueous flows at depths greater than 8 km. The assessed duration of hydrological activity therein, however, generates critical questions about whether such ephemeral aqueous flows are able to produce prebiotic nutrients through hydrothermal fluid – volcanic rock interactions and under what energy and time limitations. The habitability of the simulated scenarios 3.2.1 and 3.2.2, that indicate similar durations (ranging from 230 to 300 yr, respectively) for the aqueous circulation

in this putative low-temperature geothermal environment on Mars, will be analytically computed and assessed in sub-chapter § 3.3.

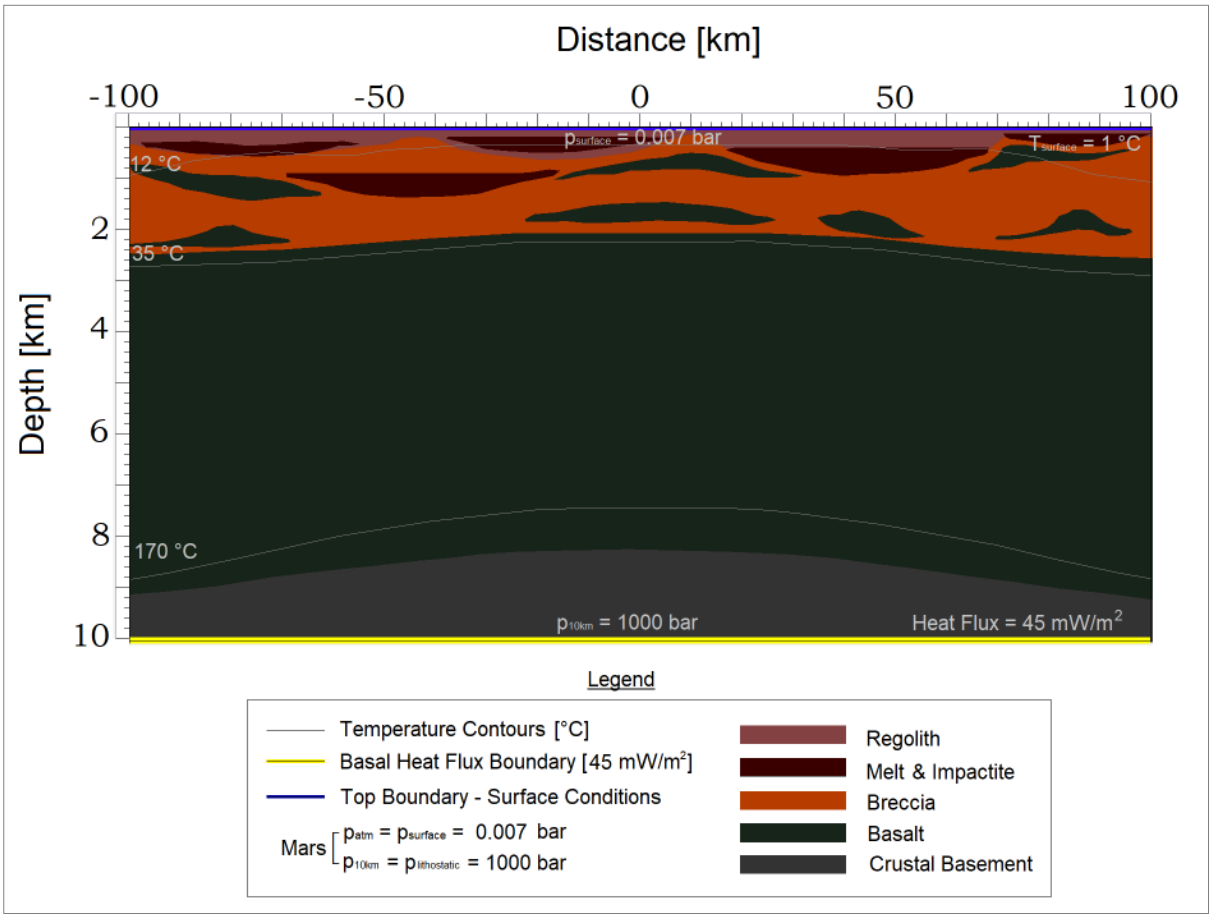

Fig. 3.12. Initial thermodynamic conditions and geological settings for the 200 km in horizontal distance and 10 km in depth 2D Martian subsurface environment. Basal heat flux is modelled with a value of 45 mW/m^2 and the associated thermal contour of 170 °C was adjusted to a depth of circa 7.5 – 9 km in the geothermal profile. The thermal contour of 170 °C also represents the domain of the setting that is affected by the maximum temperature present in the grid, and the region from which the hydrothermal flows originate, due to the increase of the basal heat flux from 20 mW/m^2 to 45 mW/m^2 (at 10-km depth). The atmospheric pressure at the Martian surface is set to 0.007 bar, and the ground surface temperature is computed to 1°C. The petrophysical properties of the rocks and the lithostratigraphy of the geological system have been kept the same with those of scenario 3.2.1 (fig. 3.10 and Table 3.4) to allow comparison on the computed circulation pattern and duration of aqueous activity between the two low-temperature (120 °C ≤ T ≤ 170 °C) hydrothermal scenarios for the Martian subsurface.

Temperature & Water Mass Flux Distribution in the 2D Martian Geothermal Setting [T_{max} = 170 °C]

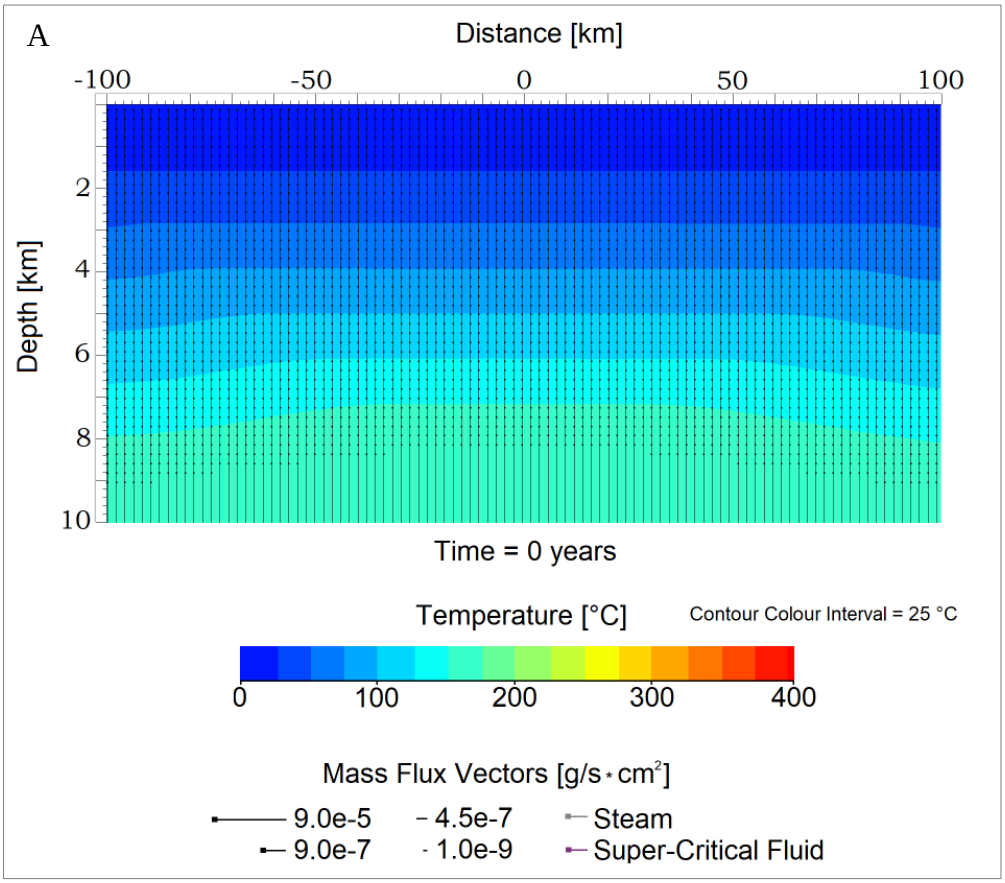

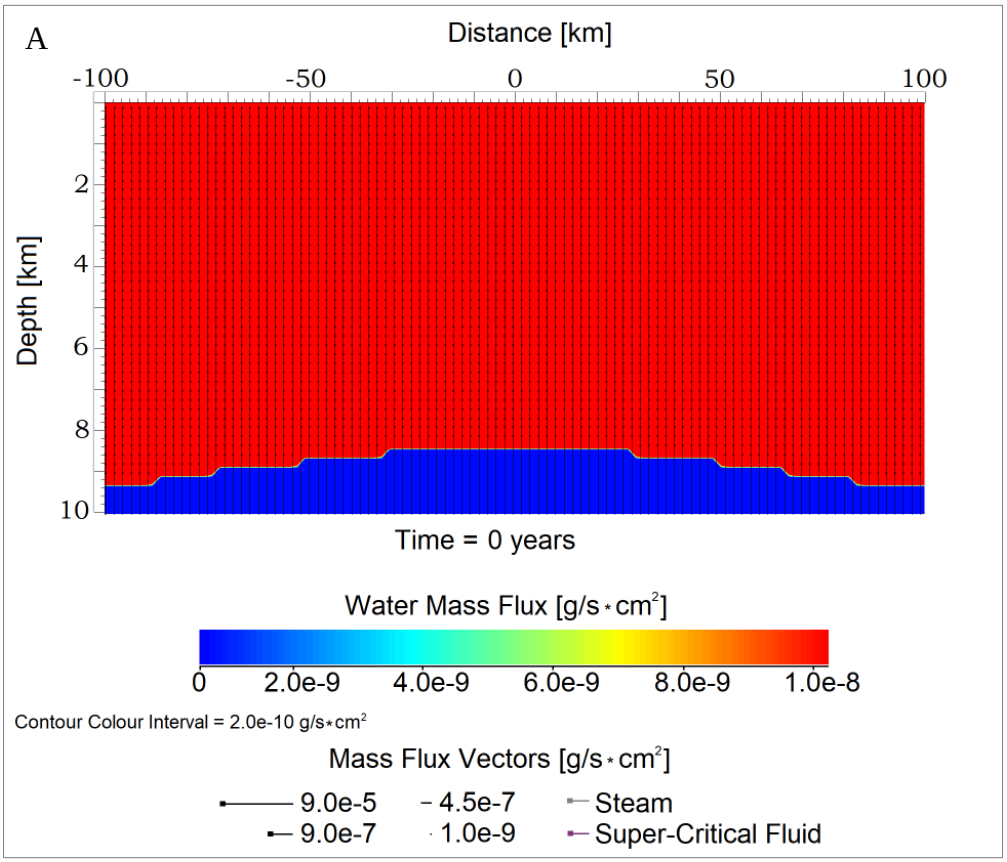

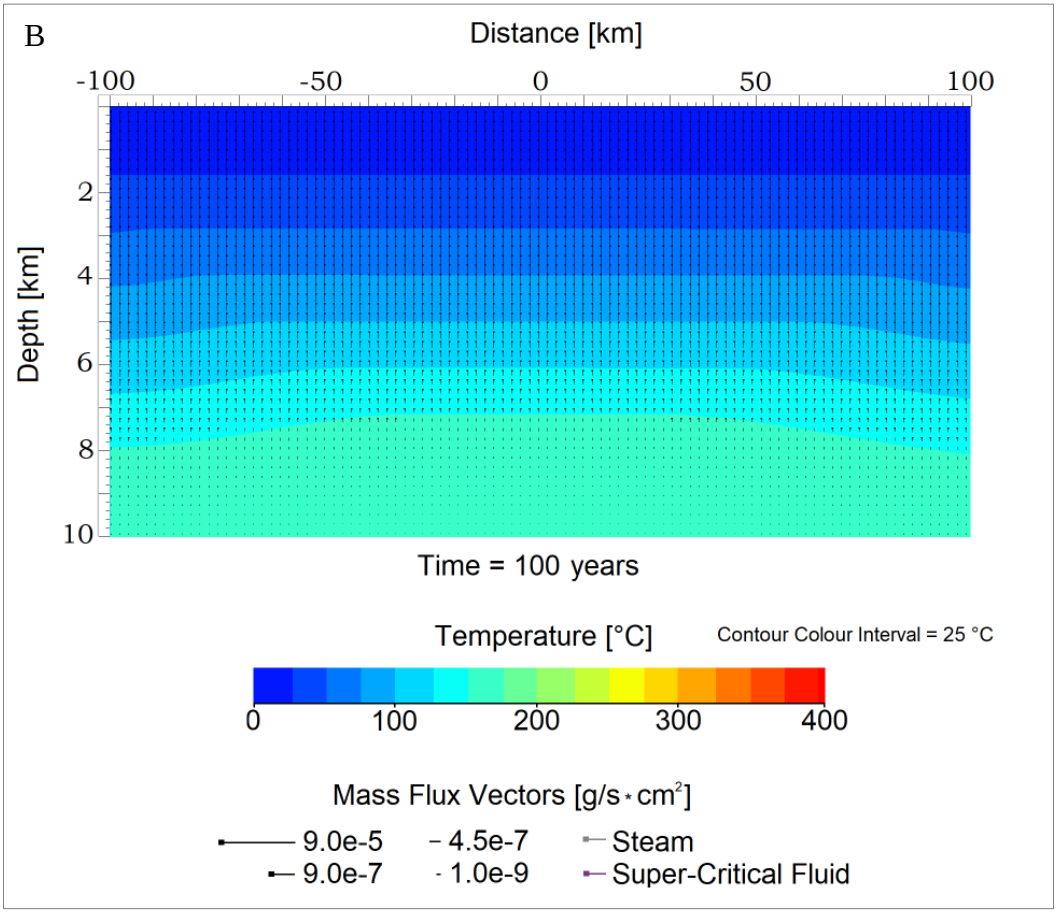
B
Distance [km]
-100
-50
0
50
100
Depth [km]
2
4
6
8
10
Time = 100 years
Temperature [°C]
Contour Colour Interval = 25 °C
0
100
200
300
400
Mass Flux Vectors [g/s*cm²]
9.0e-5
4.5e-7
Steam
9.0e-7
1.0e-9
Super-Critical Fluid

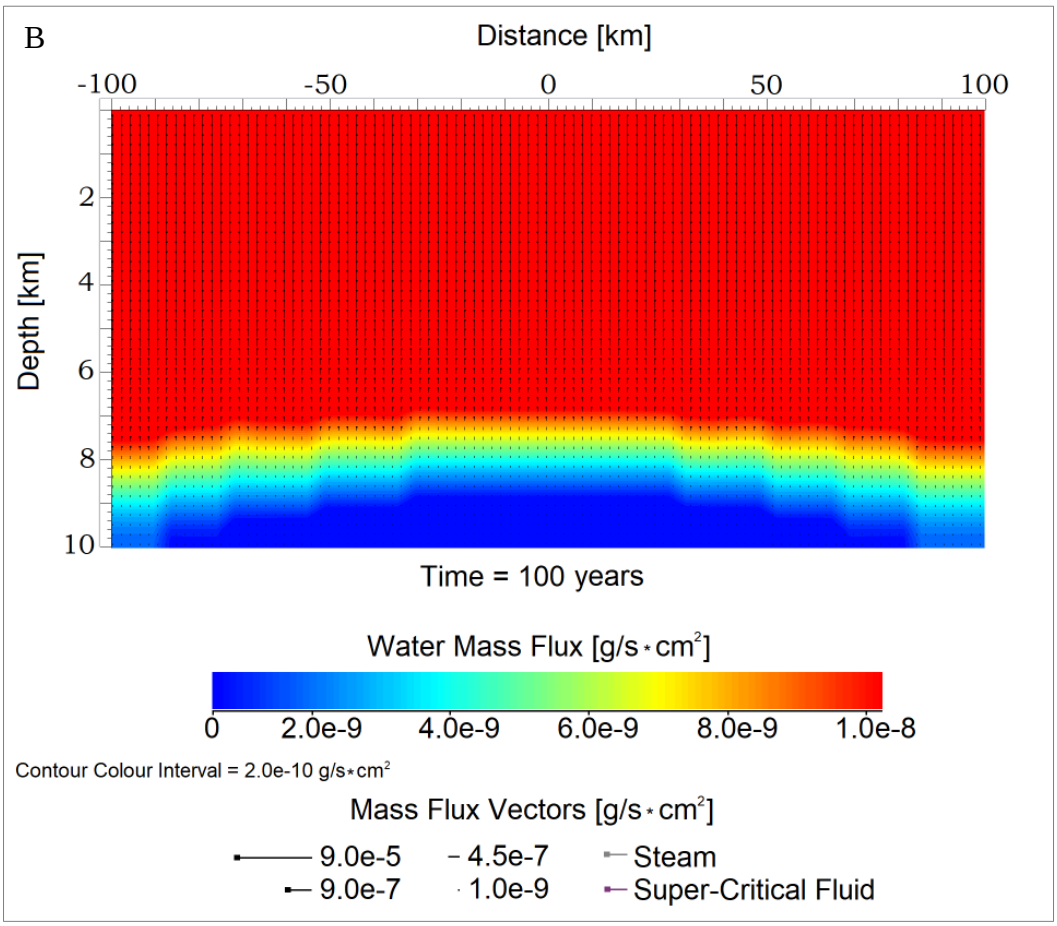
B
Distance [km]
-100
-50
0
50
100
Depth [km]
2
4
6
8
10
Time = 100 years
Water Mass Flux [g/s*cm²]
0
2.0e-9
4.0e-9
6.0e-9
8.0e-9
1.0e-8
Contour Colour Interval = 2.0e-10 g/s*cm²
Mass Flux Vectors [g/s*cm²]
9.0e-5
4.5e-7
Steam
9.0e-7
1.0e-9
Super-Critical Fluid

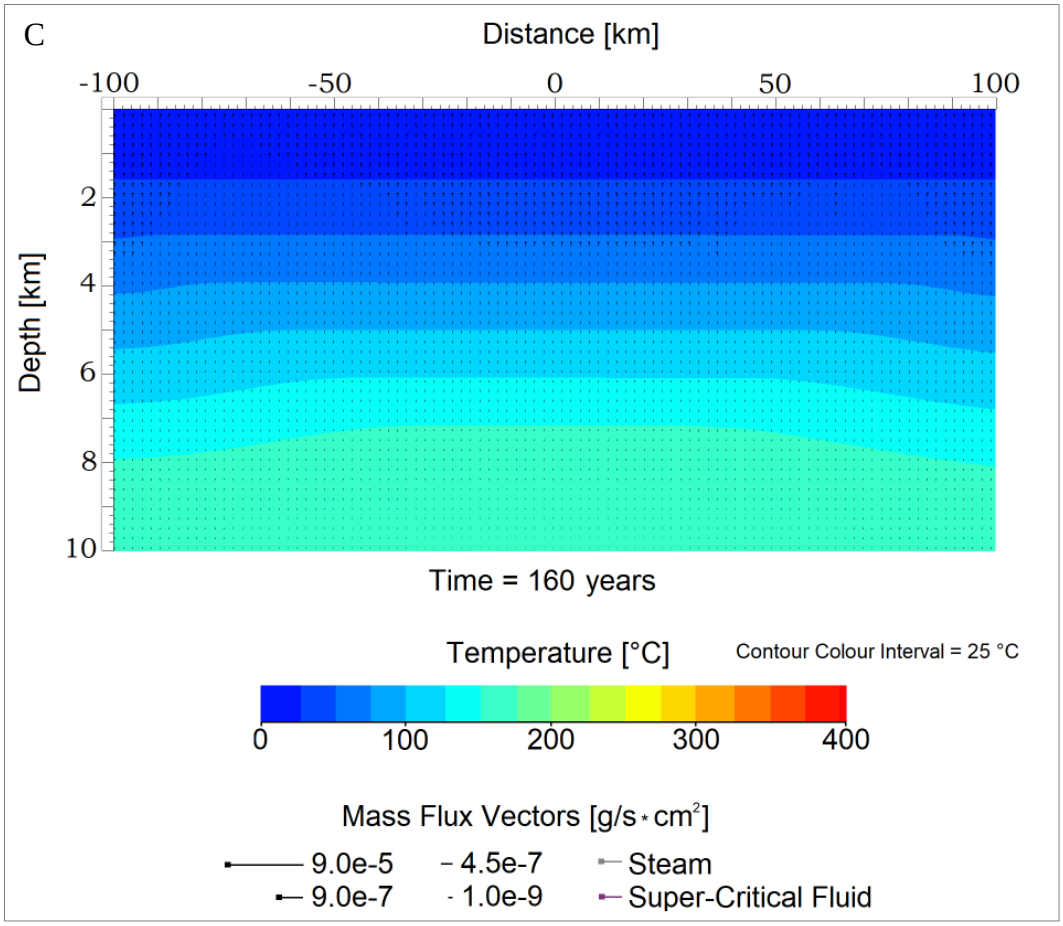
C
Distance [km]
-100
-50
0
50
100
2
4
6
8
10
Depth [km]
Time = 160 years
Temperature [°C]
Contour Colour Interval = 25 °C
0
100
200
300
400
Mass Flux Vectors [g/s*cm²]
9.0e-5
4.5e-7
Steam
9.0e-7
1.0e-9
Super-Critical Fluid

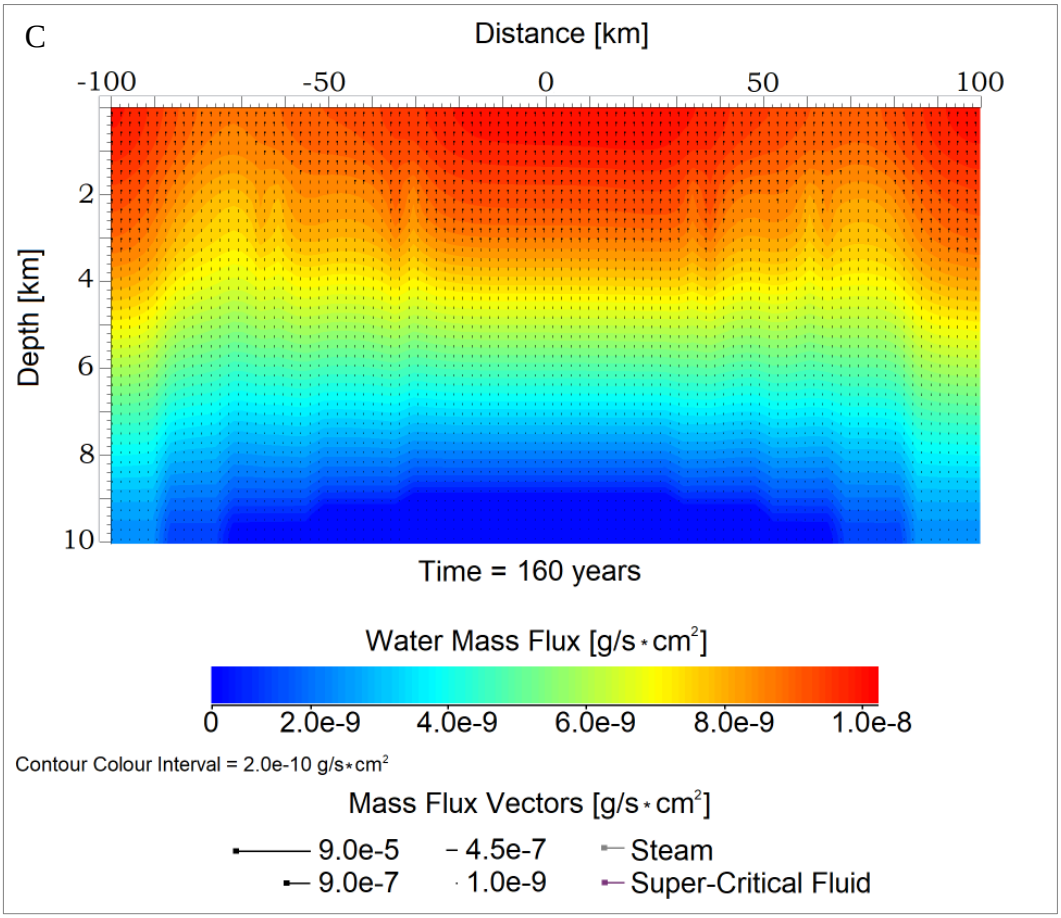
C
Distance [km]
-100
-50
0
50
100
2
4
6
8
10
Depth [km]
Time = 160 years
Water Mass Flux [g/s*cm²]
0
2.0e-9
4.0e-9
6.0e-9
8.0e-9
1.0e-8
Contour Colour Interval = 2.0e-10 g/s*cm²
Mass Flux Vectors [g/s*cm²]
9.0e-5
4.5e-7
Steam
9.0e-7
1.0e-9
Super-Critical Fluid

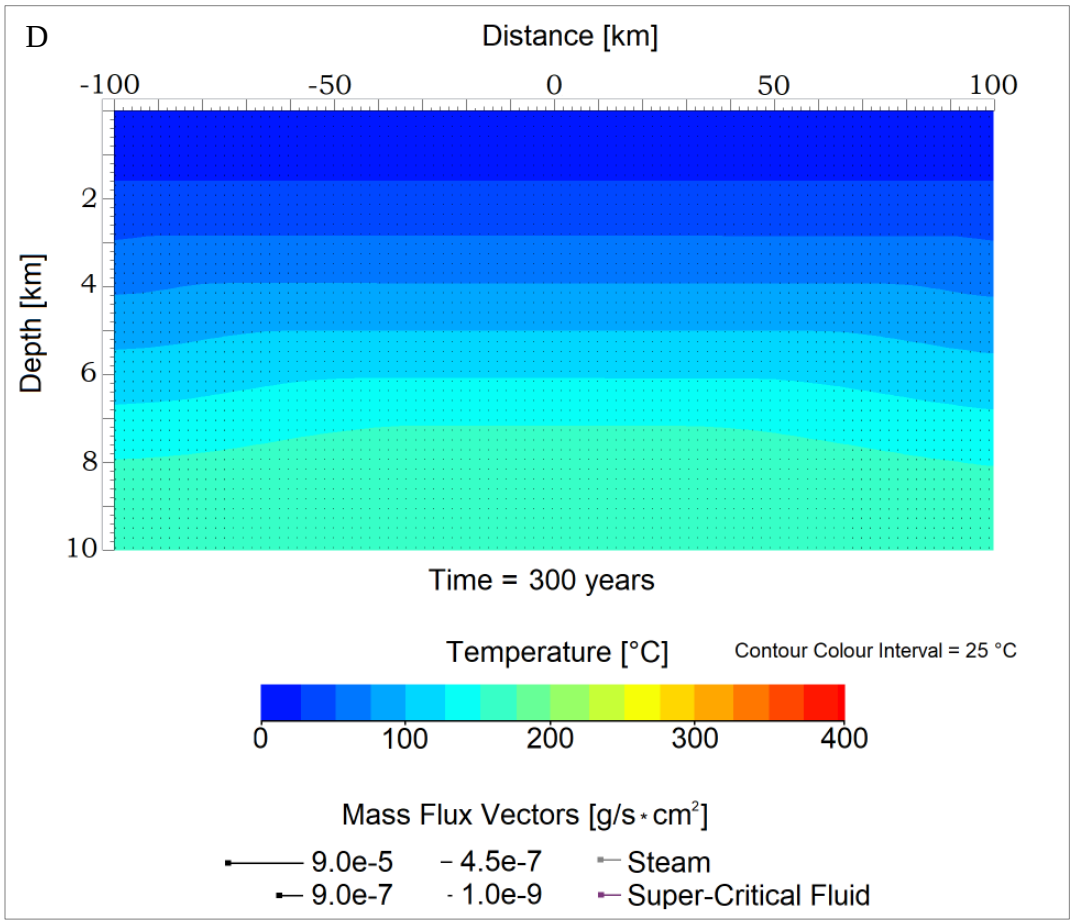
D
Distance [km]
-100
-50
0
50
100
Depth [km]
2
4
6
8
10
Time = 300 years
Temperature [°C]
Contour Colour Interval = 25 °C
0
100
200
300
400
Mass Flux Vectors [g/s*cm²]
9.0e-5
4.5e-7
Steam
9.0e-7
1.0e-9
Super-Critical Fluid

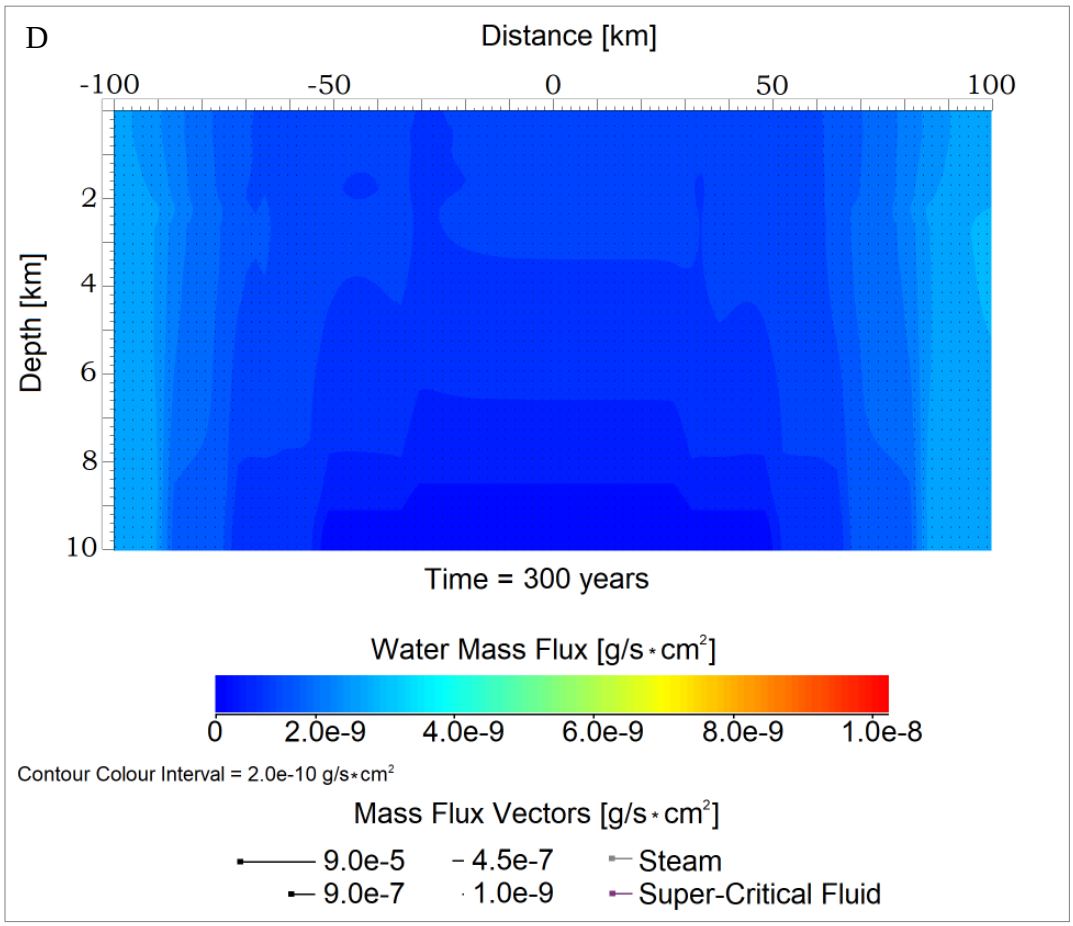
D
Distance [km]
-100
-50
0
50
100
Depth [km]
2
4
6
8
10
Time = 300 years
Water Mass Flux [g/s*cm²]
0
2.0e-9
4.0e-9
6.0e-9
8.0e-9
1.0e-8
Contour Colour Interval = 2.0e-10 g/s*cm²
Mass Flux Vectors [g/s*cm²]
9.0e-5
4.5e-7
Steam
9.0e-7
1.0e-9
Super-Critical Fluid

Fig. 3.13 (steps A-D). Temperature and Water Mass Flux (WMF) distribution in the Martian geothermal setting during selected time steps (t_0, 100 yr, 160 yr and 300 yr).

Temperature Distribution (steps A-D): T_{max} = 170 °C at a depth of circa 8 km in this geothermal environment which is represented by an isotherm. The elevation of the 170 °C – isotherm is induced after an increase in the basal heat flux (from 20 to 45 mW/m^2), and a subsequent increase in the associated geothermal gradient of the setting (from 12 °C / km to 21.25 °C / km). Darker-blue-coloured domains represent colder regions of the geological environment, where $T_{max} \leq$ 25 °C. Azure-light-greenish- coloured domains of the simulative grid represent niches where T_{max} = 170 °C. Water flux is shown with black vectors, vapour flux by light-greyish vectors, and super-critical flux by purple vectors. As indicated also in the previous scenario (3.2.1), the geothermal profile of the setting does not change throughout the entire simulation, and it seems that the heat transfer induced by the 170 °C – isotherm yields fluid flows only for a short period of time (300 yr in this case, 230 yr in scenario 3.2.1). This implies that it takes about 300 yr for all fluids trapped within the heated (by T_{max} = 170 °C) rocks of this 200 km × 10 km geothermal system to be mobilized and escape towards the surface of Mars. After 300 yr, fluid flows may have either seeped out to the surface through the regolith, or, they may have resulted in mineral precipitation and the formation of H_2O-bearing phases at greater depths, and possibly in the self-sealing of the fractures and pores of the system's rocks. This is well-shown by step D (better seen in fig. 3.13: D), where, at t = 300 yr, although minimum flows can be considered as negligible, the peripheral lithologies closer to the vertical boundaries of the setting still seem to be hosting some appreciable aqueous phases that appear stagnant in terms of their computed water mass flux and fluid's velocity. This may be an artifact of the computational grid, but it can also imply a significant increase in the water-saturation of these rocks due to hydrothermal flows, and a potential storage of H_2O deposits within the subsurface of Mars, down to depths of 9 – 10 km, or even greater.

Water Mass Flux (WMF) distribution (steps A-D): Blue-coloured regions in the simulative grid show regions of the Martian subsurface where no flows or very weak flows are present. Red-coloured regions show maximum fluxes ($\geq$ 9.0e-9 g/s×cm^2) within the host rock units via each time step calculation. The fluid flux magnitude is represented by vector's length and the squared edge of each vector shows the direction of flow. Every computational cell of the domain is represented by a vector in each time step which shows the direction and magnitude of flow. Liquid water flux is represented by black vectors, vapour flux by light-greyish vectors, and super-critical flux by purple vectors. Initially, water flux is maximum (step A: $WMF_{max} \approx$ 9.0e-5 g/s×cm^2) at depths of 8 and 9 km, as shown by the vectors' greater length present in the deepest regions of the grid in this time step (i.e.: the vectors close to the boundary between the red-coloured and blue-coloured domain). In the setting there are no steam or super-critical fluids present, as the equations of state in this simulation allow only aqueous$_{(liquid)}$ phases to circulate within this hydrothermal environment based on the thermodynamics of the system (basal heat flux = 45 mW/m^2, T_{max} = 170 °C, associated pressure range for the isotherm of T_{max} = 170 °C is 700 – 1000 bar). At t = 300 yr, $WMF_{max} \approx$ 1.4e-9 g/s×cm^2, indicating that hydrothermal flows are described by their lowest potential flux. Hence, after 300 yr, we can logically assume that aqueous flows are negligible and that geothermally induced hydrothermal activity has ceased. This can be verified also via the exported movie of the simulation that is included in the appendix (E:/Hydrothermal Flows _ T_{max} = 170 °C_.mp4), showing that shortly after 300 yr (from 301 yr to 310 yr), WMF $\leq$ 1.0e-9 g/s×cm^2. An interesting feature of this simulation is that after 300 yr, stagnant H_2O-bearing phases appear in peripheral volcanic rocks and at depths greater than 9-10 km (step D). This suggests that water-enriched volcanic rocks and hydrothermal deposits may be ubiquitous at greater depths within the Martian crust, and that these may have formed after transient or periodical aqueous flow events. In contradiction, these indications for the presence of liquid water in the peripheral regions (close to the vertical boundaries) of the geological system, after the geothermal profile has been restored (t = 300 yr), may be an artifact generated by the computational grid.

3.2.3 Hydrothermal Flows of T_{max} = 400 °C in a Martian Geological Setting due to Basal Heat Flux

In this HT simulation, a much greater value of basal heat flux is used as an input parameter for the lower boundary of the geological environment (70 mW/m^2) and the warmest isotherm in the setting is set to an associated maximum temperature of 400 °C at depths between 7.5 and 9 km. Such parameterization should represent the Hesperian and Noachian subsurface of Mars, when the average heat production in the Martian crust should have been by circa 4 times greater than the present-day heat transfer. This theory derives from observations performed by the GRS (Gamma-Ray Spectrometer) instrument on board the 2001 Mars Odyssey orbiter, and based on established geochemical ratio measurements of K/Th and K/U which indicate that ^{40}K was predominantly governing the heat production in the subsurface of Mars during geological periods before the mid-late Amazonian (Parro et al., 2017; and references therein). Therefore, in this numerical simulation basal heat flux is 1.75 times greater (with a value of 70 mW/m^2) than the boundary heat flux of the already warmer Amazonian subsurface that was simulated through computational scenario 3.2.1 (where background heat flux was initially set to 20 mW/m^2 and then increased to 40 mW/m^2).

The boundary lithostratigraphy in this scenario has remained similar to that used in scenarios 3.2.1 and 3.2.2, as illustrated via fig. 3.14. Through the schematic representation of this Martian subsurface domain the differences between the settings of this simulation and those of previous scenarios can be identified. These main differences concern: (a) the maximum temperature contour present in the setting which has an assigned maximum value of 400 °C at a depth of 7.5 – 9 km within the lower basaltic and crustal basement units; (b) the basal heat flux of the setting, from which the hottest isotherm and the associated heat currents originate, is shown with value of 70 mW/m^2 (1.75× higher); (c) the atmospheric pressure at the surface of the geological setting has been adjusted to 0.5 bar to represent atmospheric conditions of the Hesperian and possibly of the Noachian surface of Mars, in contrast to the atmospheric pressure on the surface of Mars during the Amazonian period (0.007 bar).

The following HT thermodynamic evolution model for the subsurface of ancient Mars indicates that the warmer initial conditions result in a circa 10× greater lifetime for the hydrological activity in this geothermal system (Fig. 3.20 and 3.21). We can assume that the essentially larger duration of hydrothermalism in this Martian geological environment is due to the

presence of a more than 2× greater T_{max} present in the system, and due to the approximately 2× greater rate of heat production. Nevertheless, in accordance with the flow patterns observed in scenarios 3.2.1 and 3.2.2 (fig. 3.11 and fig. 3.13), aqueous flows in this case do not seem affected by surficial – recharge fluids originating from the surface of Mars (fig. 3.15: steps A-D, as shown by the direction of the flow vectors that is pointing towards the surface). Such a volcanic scenario should be quite indicative of low-to-mid temperature pluming events that may have been quite ubiquitous during the Hesperian and Amazonian periods, or/and even during to the Amazonian. Moreover, the suspected presence of relatively young volcanism (<100 Ma) in the form of pluming events should have also been present during the late Amazonian; as deduced by a hypothesized existence of depleted-in REEs low-to-mid temperature plumes underneath nearly all large martian volcanoes (Belleguic et al., 2005; and Day et al., 2018, respectively). Hence, such a simulative approach may also represent the plumed-fed volcanoes of the host-geological environment of the nakhlites (according to Cohen et al., 2017) or even those of shergottites and chassignites.

The numerical simulation shows that hydrological activity in the setting does not last for more than 2 Kyr, with significant water fluxes present in the system for a period of 1 Kyr. Although the initial ambient geothermal gradient seems restored only after 100-200 Kyr (fig. 3.15: A-D, and appendix: Hydrothermal Flows _ T_{max} = 400 °C _ Higher Permeability.mp4), the hydrological cycle is extremely weakened in terms of fluids' velocity and flux after 1-2 Kyr (fig. 3.15: A-D). This implies that although the isotherm of 400 °C increases the lifetime of the aqueous activity by 10 times, when compared to the lower in temperature initial parameters of scenarios 3.2.1 and 3.2.2, this thermal range cannot induce flows for a period greater than 2 Kyr. Although appreciable heat currents are present in the system for a period of 200 Kyr, it seems that the deeper (3 – 10 km depth) thermodynamic domain between 200 – 400 °C and under a pressure of 400 – 1000 bar should have been severely affected by the colder and drier upper subsurface conditions. The upper domain of the setting (0 – 2 km) is governed by temperatures less than 30 °C, and this may supposedly result in the rapid cooling of fluids and subsequent self-sealing of fractures and pores under such a thermodynamic range.

Conclusively, the simulation results imply that warmer fluid flows that reach niches of the setting above a 2 km depth are cooling rapidly. The interaction of fluid flows with these shallower lithologies may take place by inducing hydrothermally altered mineral-phases within the host rock units during the first 2 Kyr of hydrological activity and when $T_{initial} \geq 50$ °C (as

shown in the methods sub-chapter: §2.2, regarding the thermodynamic range of potential fluid mass flux).Alternatively, if no water-rock interactions are possible, as under a temperature range of 1-50 °C (0 – 3.5 km depth) water-rock reactions would be extremely sluggish (after Bach, 2016), then this would result either to the self-sealing of pores and fractures, or to the seeping-out of flows to the Martian surface through the upper volcanic lithologies and regolith. Such seeped-out fluids would most probably freeze on the Martian surface and thus, these would not be capable of inducing further recharge flows within the upper subsurface domain, so that the hydrological cycle could be extended in duration.

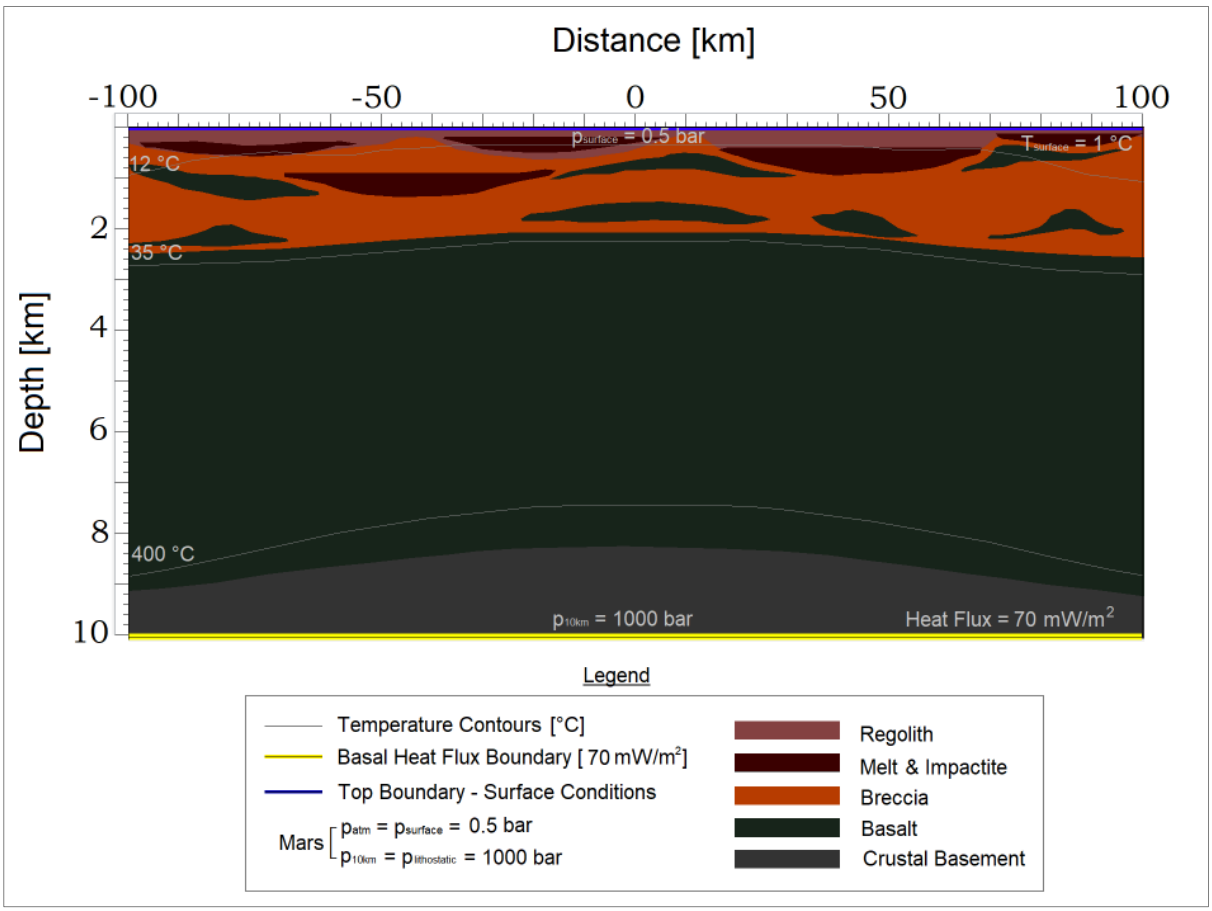

Fig. 3.14. Input thermodynamic conditions and lithostratigraphic model for the 200 km in horizontal distance and 10 km in depth 2D Martian geothermal environment. Basal heat flux is modelled with a value of 70 mW/m^2 resulting to the presence of a 400 °C – isotherm contour at a depth of circa 7.5 – 9 km in the geological setting. All other thermodynamic properties of this Martian geological setting, including the petrophysical properties of the lithologies that comprise it have been set the same with those of scenarios 3.2.1 and 3.2.2 that were presented previously. The petrophysical characteristics of the rock units are summarized in table 3.4. This boundary thermodynamic model should allow further investigations into how subsurface geological systems on Mars would respond under a much higher increase in the basal heat flux (from 20 mW/m^2 to 70 mW/m^2) originating from a depth of 10 km. This geothermal setting should be quite representative of hydrothermal conditions in the Martian crust during the early-Amazonian, or most probably, during the Hesperian and Noachian periods. The atmospheric pressure at the Martian surface is adjusted to 0.5 bar and the surface temperature is set to 1°C.

Temperature & Water Mass Flux Distribution in the 2D Volcanic Geological Setting [T_{max} = 400 °C]

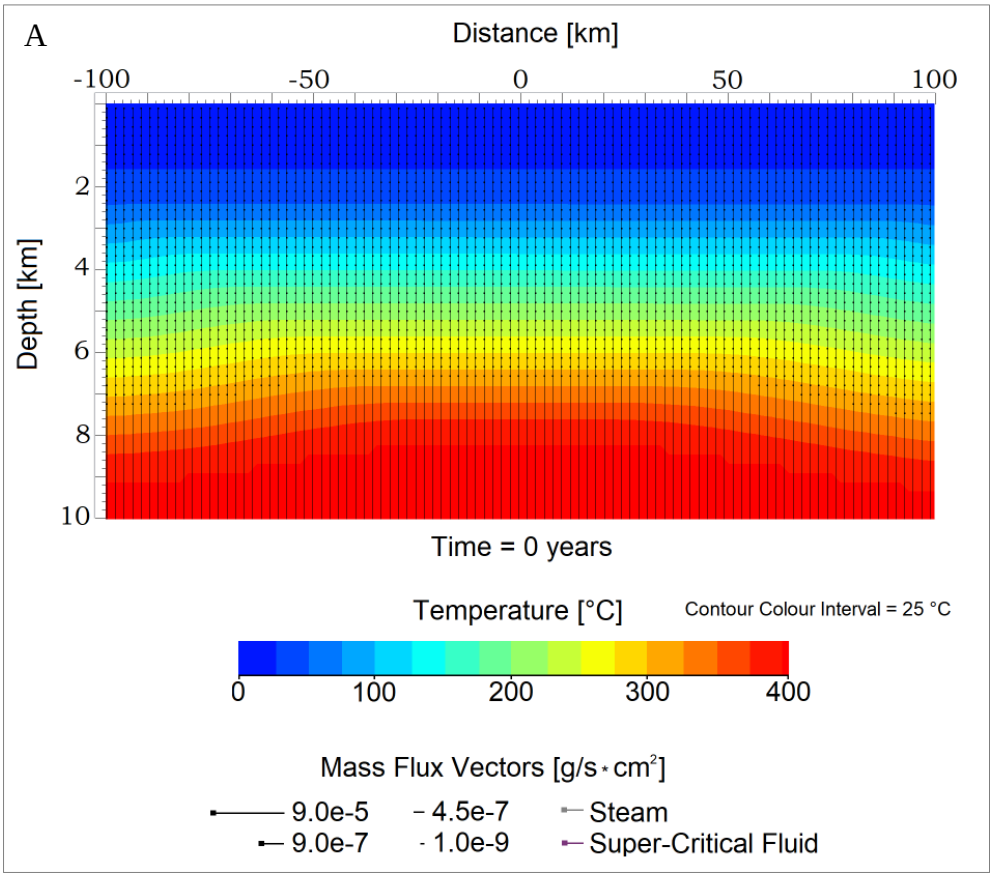

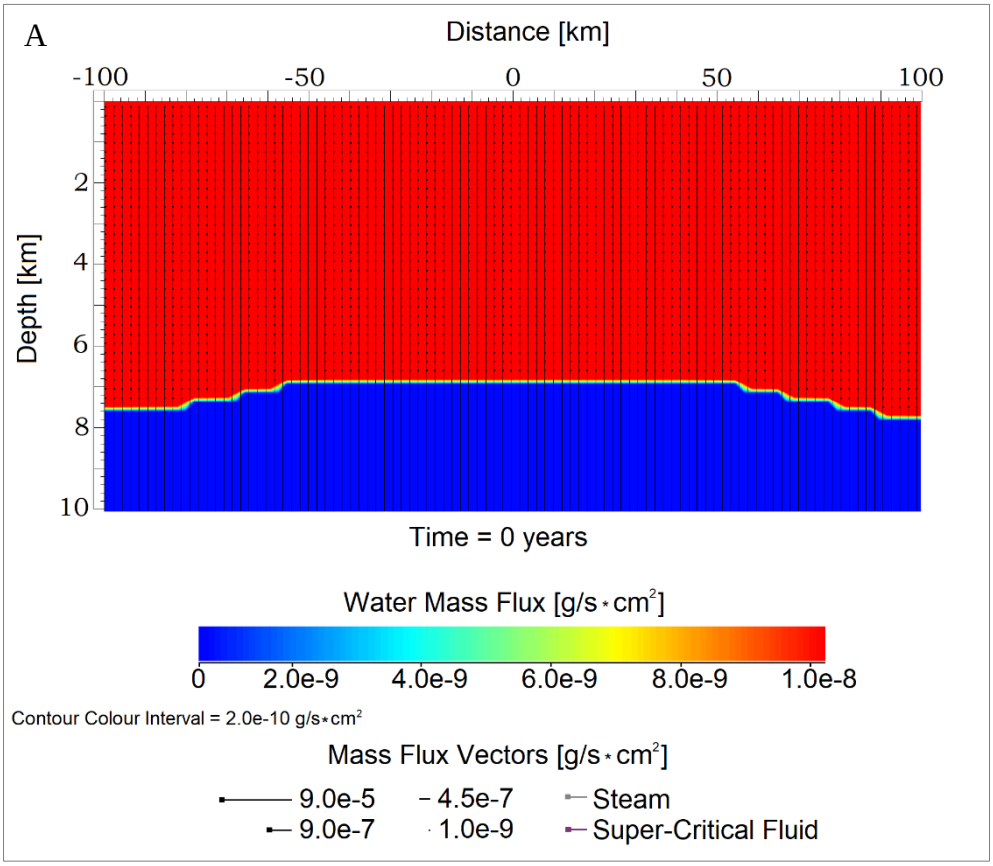

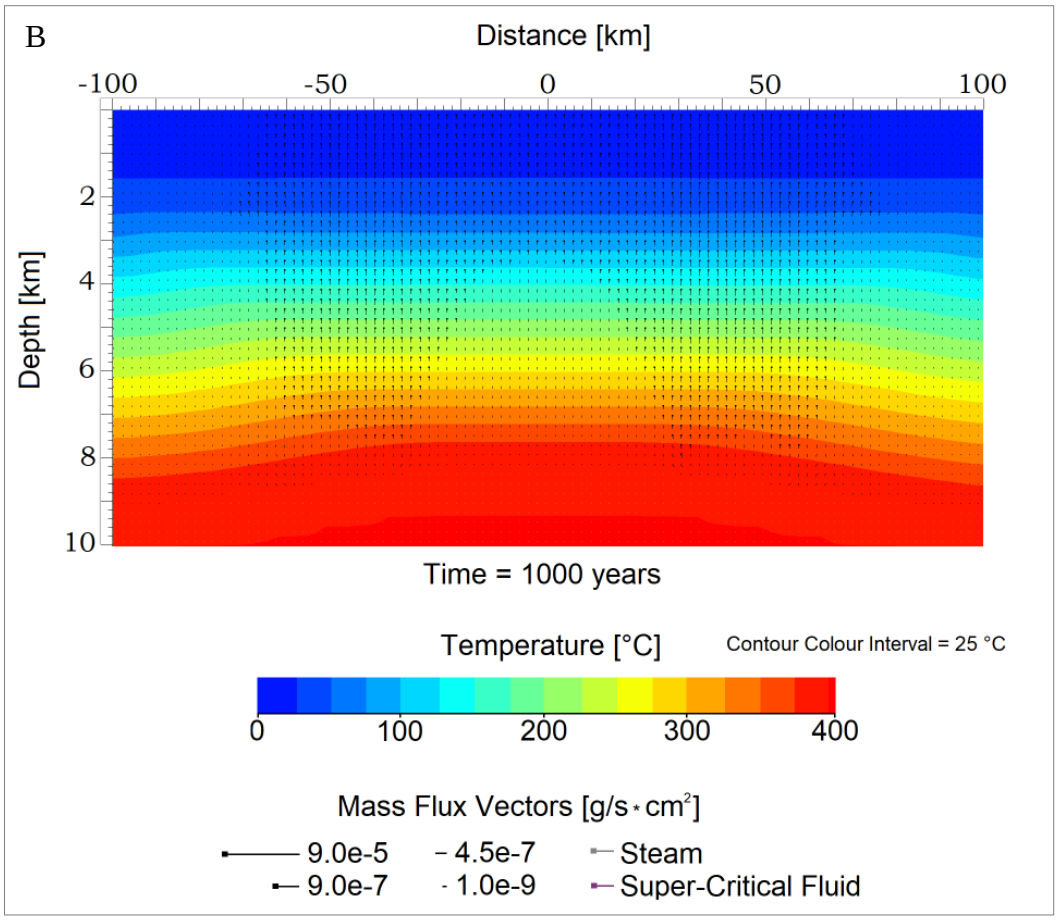
B
Distance [km]
-100
-50
0
50
100
Depth [km]
2
4
6
8
10
Time = 1000 years
Temperature [°C]
Contour Colour Interval = 25 °C
0
100
200
300
400
Mass Flux Vectors [g/s*cm²]
9.0e-5
4.5e-7
Steam
9.0e-7
1.0e-9
Super-Critical Fluid

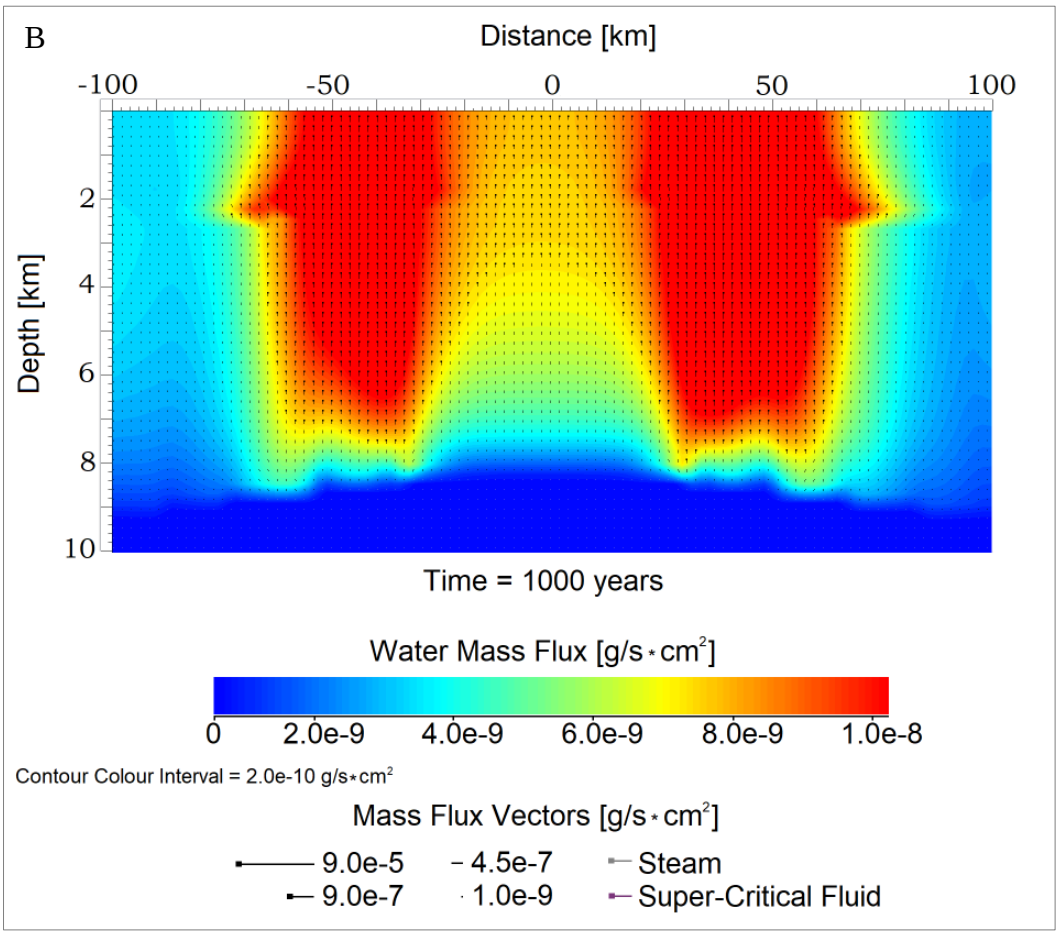
B
Distance [km]
-100
-50
0
50
100
Depth [km]
2
4
6
8
10
Time = 1000 years
Water Mass Flux [g/s*cm²]
0
2.0e-9
4.0e-9
6.0e-9
8.0e-9
1.0e-8
Contour Colour Interval = 2.0e-10 g/s*cm²
Mass Flux Vectors [g/s*cm²]
9.0e-5
4.5e-7
Steam
9.0e-7
1.0e-9
Super-Critical Fluid

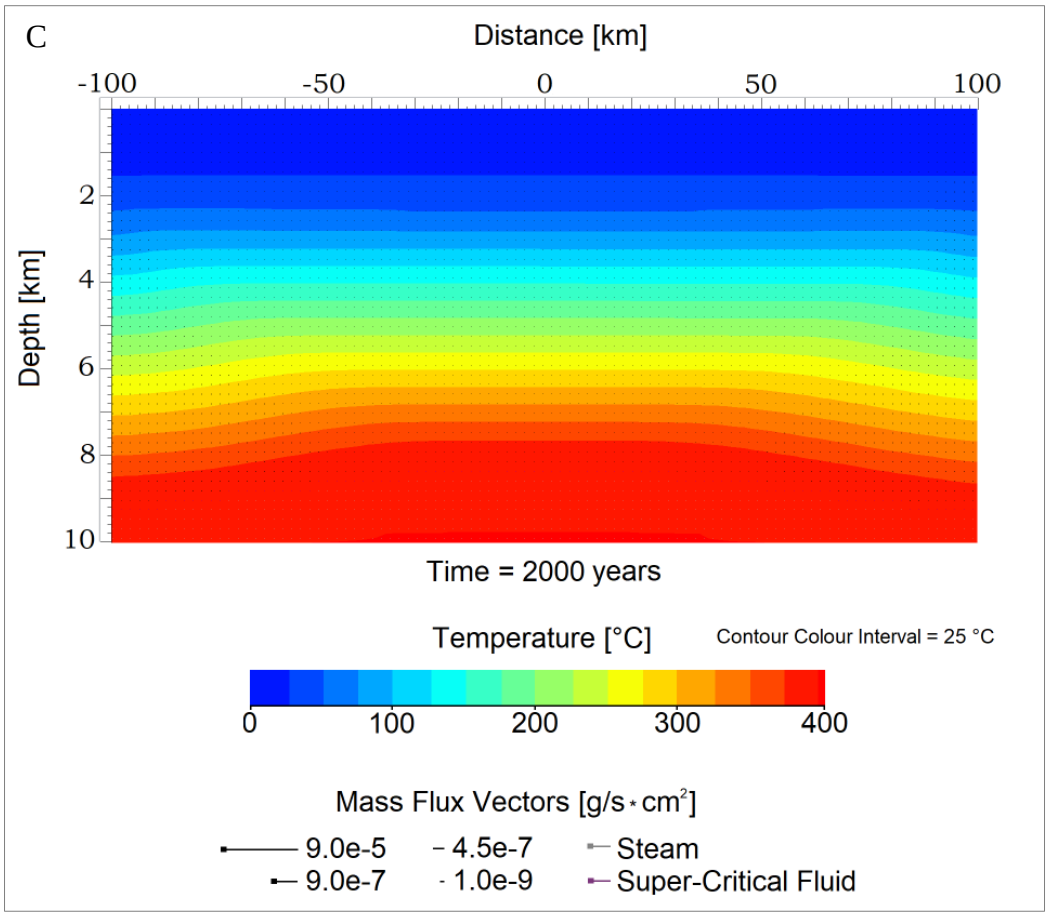
C
Distance [km]
-100
-50
0
50
100
Depth [km]
2
4
6
8
10
Time = 2000 years
Temperature [°C]
Contour Colour Interval = 25 °C
0
100
200
300
400
Mass Flux Vectors [g/s*cm²]
9.0e-5
4.5e-7
Steam
9.0e-7
1.0e-9
Super-Critical Fluid

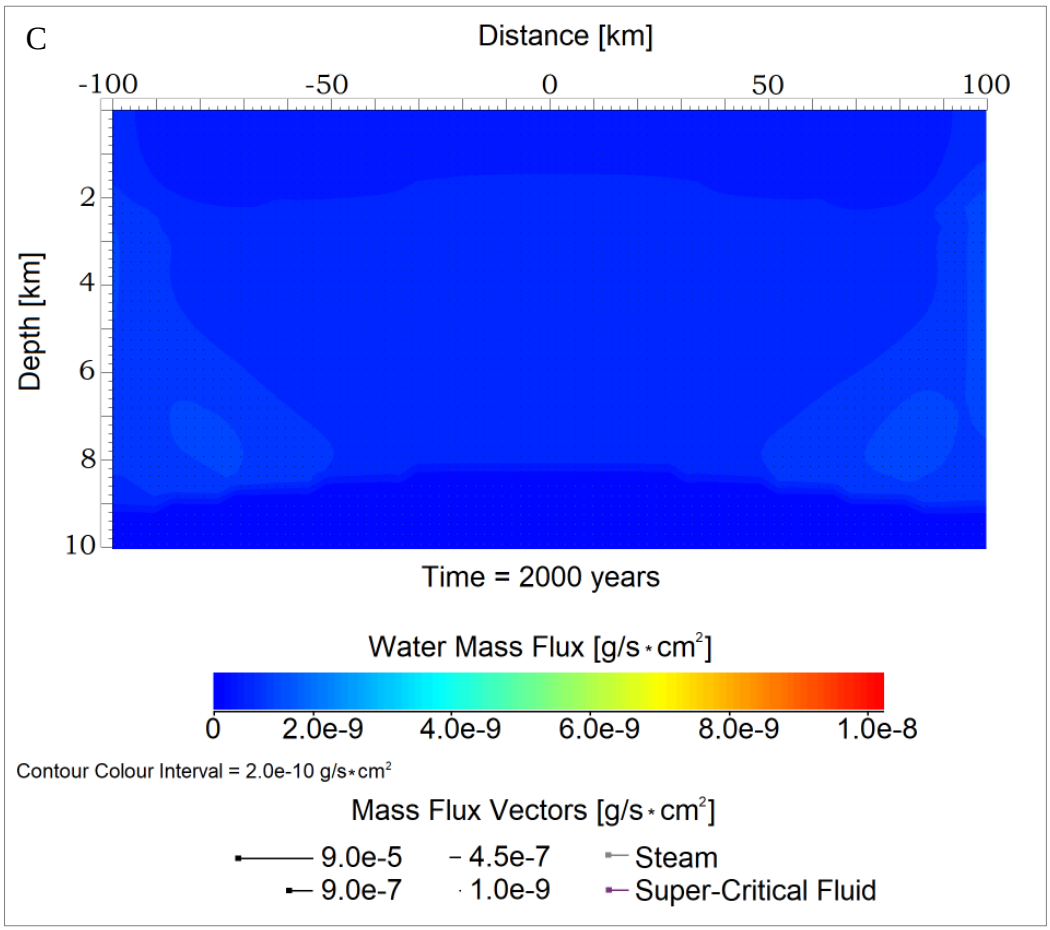
C
Distance [km]
-100
-50
0
50
100
Depth [km]
2
4
6
8
10
Time = 2000 years
Water Mass Flux [g/s*cm²]
0
2.0e-9
4.0e-9
6.0e-9
8.0e-9
1.0e-8
Contour Colour Interval = 2.0e-10 g/s*cm²
Mass Flux Vectors [g/s*cm²]
9.0e-5
4.5e-7
Steam
9.0e-7
1.0e-9
Super-Critical Fluid

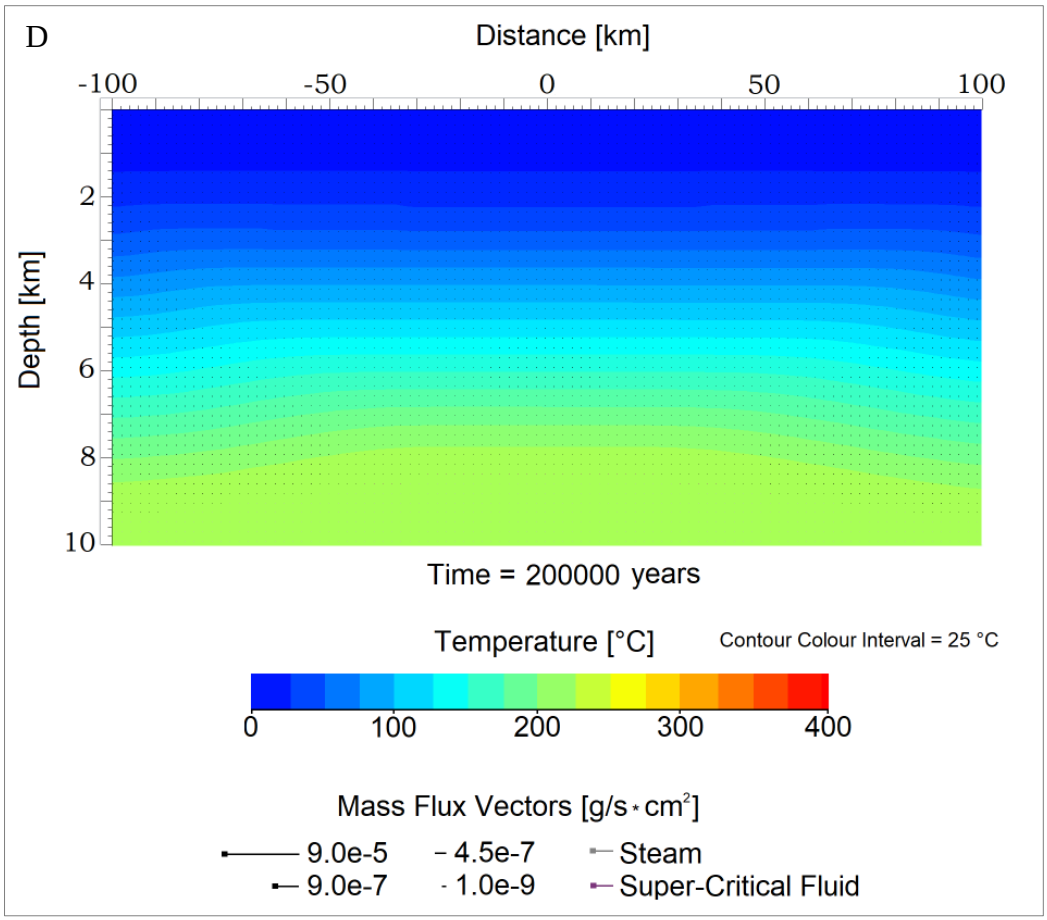
D
Distance [km]
-100
-50
0
50
100
Depth [km]
2
4
6
8
10
Time = 200000 years
Temperature [°C]
Contour Colour Interval = 25 °C
0
100
200
300
400
Mass Flux Vectors [g/s*cm²]
9.0e-5
4.5e-7
Steam
9.0e-7
1.0e-9
Super-Critical Fluid

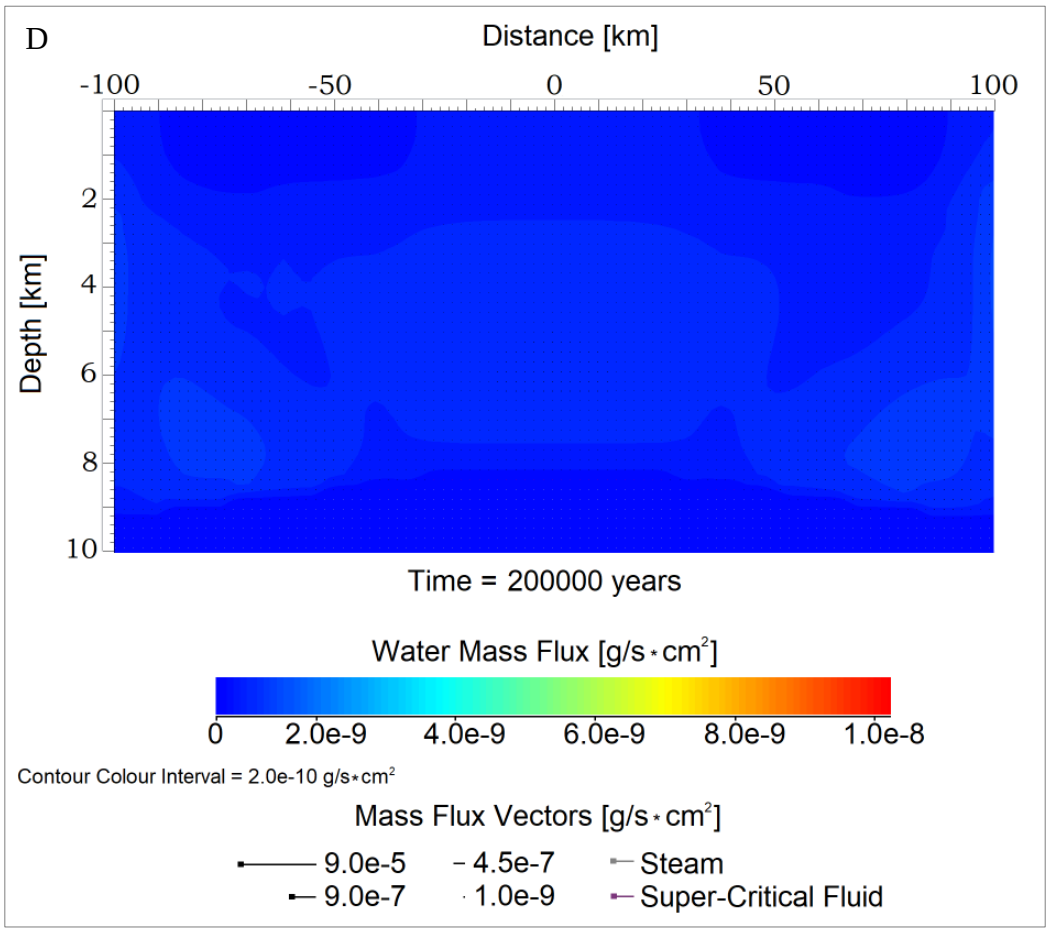
D
Distance [km]
-100
-50
0
50
100
Depth [km]
2
4
6
8
10
Time = 200000 years
Water Mass Flux [g/s*cm²]
0
2.0e-9
4.0e-9
6.0e-9
8.0e-9
1.0e-8
Contour Colour Interval = 2.0e-10 g/s*cm²
Mass Flux Vectors [g/s*cm²]
9.0e-5
4.5e-7
Steam
9.0e-7
1.0e-9
Super-Critical Fluid

Fig. 3.15 (steps A-D). Thermal and aqueous flux (WMF) evolution in the Martian geothermal environment where T_{max} = 400 °C at a depth of approximately 8 km, and basal heat flux = 70 mW/m^2 at 10 km depth (lower boundary of the grid).

Temperature Distribution (steps A-D): Dark-blue-coloured regions in the simulative domain represent colder regions of the geological environment, where $T_{max} \leq 25$ °C. Red-coloured regions of the geological grid represent regions where $T = T_{max}$ = 400 °C. Fluid flux magnitude is shown through vector's length and the squared edge of each vector indicates the direction of flow. Liquid water flux is represented by black vectors, vapour flux by light-greyish vectors, and super-critical flux by purple vectors. The basal heat flux of 70 mW/m^2 induces fluid flows that last for a period of approximately 1 – 2 Kyr (steps B and C). However, despite the system restores its geothermal gradient after circa 200 Kyr (step D), most of the available water that has been present in the host rocks of the geological setting seems to have been mobilized during the initial 2 Kyr period; after 2 Kyr, fluxes in the hydrological system seem to be negligible and any water in the system has either reached shallower regions of the setting or it may have escaped through the regolith to the Martian surface. This thermal evolution model indicates that isotherms of 400 °C present at depths of 7-9 km, may have induced hydrological activity in the Martian crust for a limited period (ranging from 1 to 2 Kyr, depending on conservative versus liberal parameterization, respectively; please also see the lower permeability (conservative) scenario in the appendix (Hydrothermal Flows _ T_{max} = 400 °C _ Lower Permeability.mp4). Steps C and D also demonstrate that although higher temperature isotherms (400 – 200 °C) are present at depths of 7-9 km, the initial input parameters that describe the abundance of water on the Martian surface, the precipitation and runoff rates, and the thermodynamics of the regolith lithologies are extremely limiting in terms of sustaining the hydrological activity in deeper domains of the setting, where basal heat flux is appreciable. Thus, we can assume that the same geothermal system on Earth could have potentially survived for a much longer period, and even up to the time point of 200 Kyr, when the background geothermal profile of the geological system has been fully re-established.

Water Mass Flux Distribution (steps A-D): Dark blue-coloured regions show niches of the environment where no flows or very weak flows are present. Red-coloured regions indicate maximum fluxes ($\geq$ 9.0e-9 g/s×cm^2) within the host lithologies. The fluid flux magnitude is represented by each vector's length in a computational cell, and the direction of flow is shown by the squared edge of each vector. Liquid water flux is shown by black vectors, vapour flux by light-greyish vectors, and super-critical flux by purple vectors. Water flux reaches maximum values during the first 1 Kyr (step A: $WMF_{max} \approx$ 4.5e-4 g/s×cm^2) at depths of 8 and 9 km, and can still be considered appreciably strong at t = 1 Kyr (step B: 9.0e-7 g/s×cm$^2 \leq WMF_{max} \leq$ 9.0e-8 g/s×cm^2). Steam fluxes are also present but with minimum values at circa 1 Kyr (step B: white dots in the blue-coloured domain which represents the crustal basement rocks). Furthermore, the isotherm of 400 °C, which also accounts for the T_{max} present in this geothermal environment, dictates impermeable conditions according to the temperature-dependent nature of permeability and porosity under such a pressure range (600-1000 bar) and associated depth. For this reason, at steps B and C, we see only negligible fluxes of water and steam within the deeper domain of the setting (between 8.5 – 10 km depth). Hence, at circa 2 Kyr, when the hydrological activity ceases, any liquid water or steam flows that may have been present in the host lithologies should have already resulted in a rapid self-sealing of fractures and pores. This explains why the fluid flow magnitude and flux pattern does not change from t_C = 2 Kyr to t_D = 200 Kyr. A significant indication of the simulation at steps C and D is also that, if any minimum fluxes and hydrothermal cells are still present beyond the time point of 2 Kyr, then these should be constrained at depths between 2 and 8 km within the subsurface realm. As explained in the thermal evolution model, this is due to the presence of a low-energy and cold barrier formed by the regolith (and upper-volcanic units) at a depth of circa 0.5 km, and due to the thermodynamics that describe the arid and cold Martian surface.

3.2.4 Hydrothermal Flows of T_{max} = 500 °C Induced by Intrusive Veins in a Martian Geological Setting

The previously presented models explored putative cases of Martian hydrothermal activity induced by either an increase to the basal heat flux (cases 3.2.1 and 3.2.2, with isotherms of T_{max} = 120 °C and T_{max} = 170 °C present in the thermodynamic system, respectively), or due to the ascending of a mid-to-low temperature plume at a depth of 10 km (with a T_{max} = 400 °C at a depth of 7.5 – 9 km). Such thermodynamic scenarios may be quite representative of geothermal processes that have affected volcanic provinces of the Martian crust predominantly during the Amazonian period (when considering the lower temperature range scenarios, where $T_{max} \leq 170$ °C) or during the early- and pre-Amazonian geological epochs ($T \leq 400$ °C).

The model presented below investigates a hypothetical volcanic scenario in the Martian crust where intrusive veins of a T_{max} = 500 °C have penetrated the upper volcanic lithologies and have reached the shallowest subsurface domains of the crust (fig. 3.16). The temperature distribution in these shallower niches of the setting ranges from 250 – 350 °C at depths between 4 and 2 km, and the upper regolith units are affected by fluid mass fluxes of 100 °C ≤ T ≤ 300 °C, due to heat loss as fluids reach the colder ambient of the shallower subsurface (fig. 3.16). As a result, the warmer fluids that reach the upper-subsurface, which is geologically comprised by the regolith or/and by other surficial volcanic units (impact-breccias, basalts, melt rocks), gradually heat up the shallower parts of the crust, and may even seep-out to the surface of Mars with a much higher temperature (25 °C ≤ T ≤ 75 °C) than that observed in previous simulated scenarios (12 °C ≤ T ≤ 25 °C, in 3.2.1, 3.2.2, 3.2.3). Therefore, this case is significantly different from scenario 3.2.3, where T_{max} = 400 °C at a depth of 7.5 – 9 km, as the volcanic plume's thermodynamic effect appears constrained within the greater depths of the Martian subsurface (7.5 – 10 km) and its heat loss does not induce flows for more than 2 Kyr (fig. 3.17).

This modelling approach induces fluid flows with a much higher initial temperature at depths between 2 and 5 km and yields a hydrothermal system that seems to be interacting with the shallowest subsurface or even surficial regions of Mars (fig. 3.17 steps A-F). The basal heat flux of the system is set to 80 mW/m^2, but since this heat flux is pertinent to a depth of 10 km, its thermodynamic effects are minimized because of the presence of the 500 °C hot peridotite veins at depths above 5 km. Fig. 3.17 (steps A-F) describes the thermodynamic evolution of

the setting with a focus on the thermal distribution and water mass flux, respectively. At t_0 after the intrusive events take place and the peridotite is emplaced, we can observe the shift towards a much hotter geothermal profile for the setting; this is evident by the vertical boundaries of the grid, where the background geothermal gradient shows an isotherm of 25 °C present at a depth of circa 1.4 km. The central region of the setting that is affected by the intrusive peridotite veins experiences temperatures higher than 200-300 °C at depths between 3 and 4 km, and at this initial time point $WMF_{max} \approx 9.9e\text{-}3$ g/s×cm^2 in the system (fig. 3.17: A-C). Thus, peridotite veins that reach niches shallower than 4 km in depth seem to cool instantly after their emplacement and to be rendered permeable. This is evident through fig. 3.17: A (WMF) where only peridotite units at depths greater than 4 km appear impermeable (blue-coloured domains) and maintain their initial thermal profile of 500 °C. Deeper regions of the geological setting where temperature slightly exceeds or is equal to the thermal limit of 500 °C appear blue in colour, which indicates that no liquid water flows are hosted therein (in accordance with the thermodynamic criteria for the aqueous flux potential incorporated in the HT code; Hayba and Ingebritsen, 1994; 1997).

At t = 1 Kyr, some regions of the peridotite have already reached temperatures lower than 400 °C, and seem to host sub-to-super-critical fluid or steam flows (purple or whitish vectors/dots) that are present at greater depths (5 – 7 km) within the central region of the setting. However, the fluid mass flux in those regions does not reach a value higher than 9.0e-7 g/s×cm^2, and super-critical fluids that may have also affected the surrounding basaltic rocks via thermal metamorphism are present in the system for only a period of 10 Kyr after the emplacement of the peridotite veins (fig. 3.17: B-C, or appendix: Hydrothermal Flows _ Intrusive Veins _ T_{max} = 500 °C _ Higher Permeability.mp4).

From 1 Kyr to 10 Kyr, we can observe through time steps B and C of the simulation in fig. 3.17 that numerous, quite extensive and strong hydrothermal cells are active in the setting, and that these grow weaker in terms of the hosted fluids' flux as time elapses. During this period, intensive hydrothermal circulation affects mainly the deeper regions of the setting (≥ 2 km) that are closer to the heat sources, i.e.: the peridotite veins with $T_{initial}$ = 500 °C. Nevertheless, after 100 Kyr, it seems that the hydrothermal cycle is predominantly maintained by the formation and evolution of hydrological cells at depths of 1 – 2 km from the surface of Mars. This ascending of the hydrological activity to a shallower depth can be explained by the evolution of the petrophysical properties of the peridotite and volcanic rocks after their

crystallization at circa 100 Kyr. After that time point, most of the intrusive veins and their surrounding host-rocks that should have melted after the penetration of the peridotite, have crystallized and are under a permeable state. This can be observed in fig. 3.17: D, where only regions of the peridotite and the volcanic basement rocks, which are located at depths greater than 8.5 – 9 km, are described by temperatures closer to the 500 °C limit, and are thus impermeable. Hence, since heat is still available in the system, with isotherms of 100 – 150 °C present at depths of 2 – 2.5 km in the central region of the volcanic setting (with the geothermal gradient = 58 °C / km therein), hydrothermal fluids of $50\ °C \leq T \leq 100\ °C$ should be escaping, due to the porous and permeable nature of the regolith and upper volcanic rocks, to the surface of Mars (Fig. 3.17: D). Interestingly, at t = 100 Kyr, we can observe that significant recharge flow events take place and keep the hydrothermal circulation ongoing. This can be seen through the vectors of the fluid flows that start from the upper domain of the grid and that point towards the deeper regions of the setting.

This simulated phenomenon strongly suggests that fluid recharge cycles are present in the hydrothermal system, and a potential mixing of the magmatic-induced hydrothermal fluids with surficial-water deposits from the surface or shallow subsurface of Mars (most probably at depths ≤ 0.2 km). Furthermore, in previous scenarios (3.2.1, 3.2.2, 3.2.3) where fluids reached surficial domains of the setting, it was indicated that these reached very low temperatures (1 – 25 °C) far more rapidly and within a period ranging from 0.2 to 2 Kyr, depending on the $T_{initial}$ of the fluids. In those cases, this effect would later result in the mineral deposition and subsequent self-sealing of the pores at shallow depths. Thus, this low temperature range and its associated inactivity in terms of the heat transfer (hydrothermal heating) towards the upper surficial domain of the grid, explains why recharge events were not possible in the previously simulated Martian volcanic environments.

In this model, the aqueous circulation pattern after 100 Kyr is still supported by the significant heat offered from the deeper peridotite niches of the setting with T_{max} = 350 °C at a depth of 6 km (fig. 3.17: D). More significantly, surficial regions (shallower than 0.2 km) of this volcanic province seem to be heated up for as long as hydrothermal activity persists with essentially higher-in-temperature fluids that reach the surface of Mars ($50\ °C \leq T \leq 100\ °C$). This effect of hydrothermal heating causes the mobilization of surficial water or/and other precipitates that were computed in the initial conditions of the setting, and induces recharge flow events that revive the hydrothermal circulation (as observed in fig. 3.17: D-E). Nevertheless, these

recharge flow events seem to gradually cool the system as time elapses and as they penetrate through the porous of rocks and interact with hotter domains of the volcanic system. At t = 500 Kyr, the system is still hydrothermally active with major hydrological cells present at depths of circa 2 km. (fig. 3.17: E). This result of the simulation is surprisingly consistent with observations and interpretations performed by Orosei et al. (2018), suggesting the presence of aqueous or water-ice deposits at depths of 2 km depth beneath the surface of Mars (via processing radar data obtained from the Mars Advanced Radar for Subsurface and Ionosphere Sounding (MARSIS) instrument deployed on the Mars Express spacecraft). Finally, this numerical simulation implies that hydrothermal circulation ceases; hence, the geothermal gradient is restored after 1.5 Myr in this Martian volcanic environment (fig. 3.17: F).

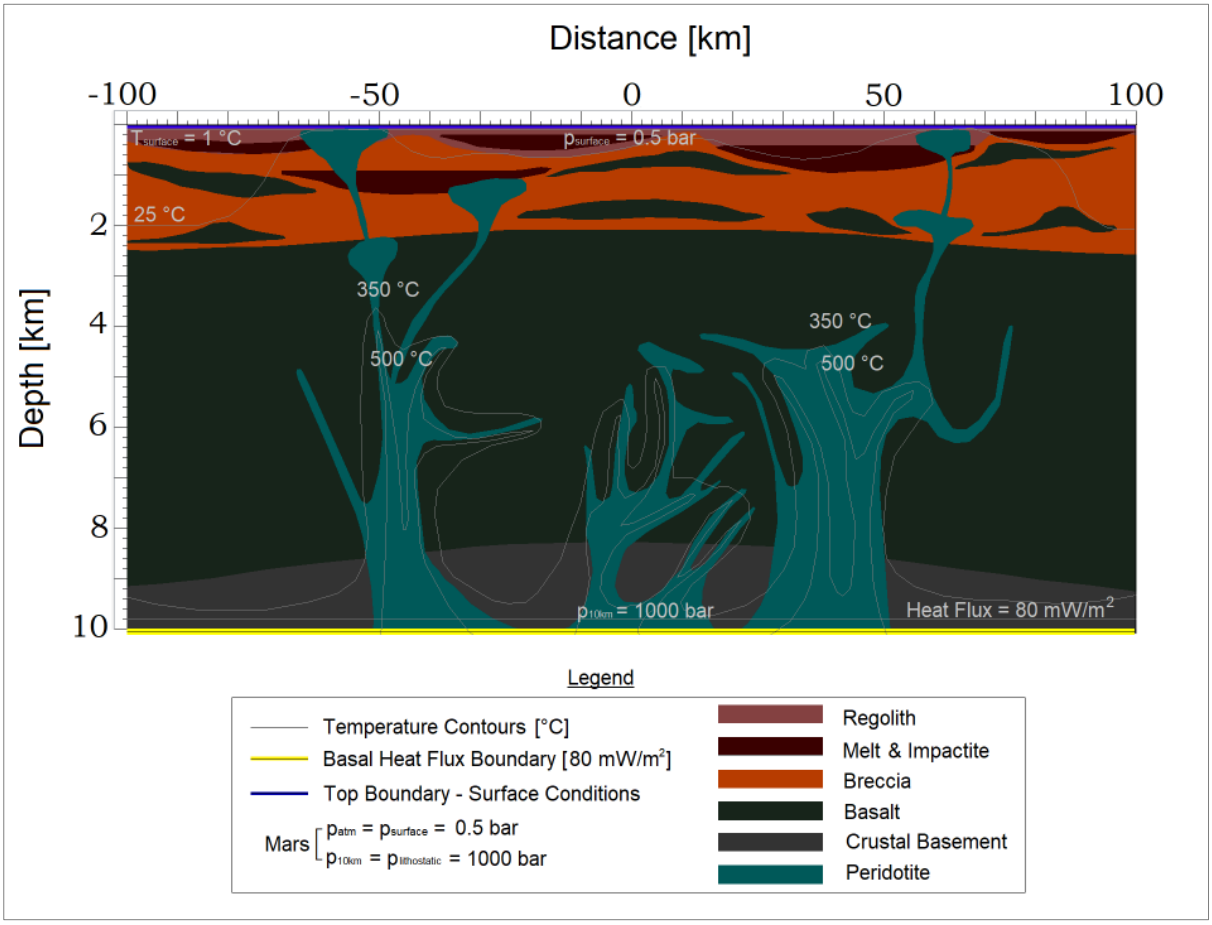

Fig. 3.16. Initial thermodynamic and lithostratigraphic model for the Martian geothermal environment that is affected by intrusive peridotite veins with a maximum temperature of 500 °C at a depth of 4 km. Isotherms of 500 – 350 °C affect the geological domain at depths between 10 and 3 km, with much higher in temperature isotherms (500 °C ≤ T ≤ 900 °C) considered at depths > 10 km (included in the basal heat flux parameterization of the coding script). Therefore, the basal heat flux of the setting has been adjusted to 80 mW/m^2 to accurately represent

purely volcanic conditions within this Martian crustal setting. The petrophysical characteristics of all geological units shown in the schematic model and its legend are summarized in Table 3.5 below. The same high-resolution grid of 4365 cells (97 × 45) was used to simulate this 2D volcanic environment. Such subsurface conditions should represent the thermodynamics of the Martian crust during more ancient geological epochs; more likely, the Hesperian and Noachian crust. Although the temperature on the surface of Mars may have been higher during more ancient geological periods, this model follows a more conservative approach by adjusting the $T_{surface}$ to 1°C and the $p_{surface}$ to 0.5 bar. Such parameters for the upper boundary of the simulation could allow a better comparison between this scenario and the previous ones (3.2.1, 3.2.2, 3.2.3) which are more representative of the Amazonian crust. A higher temperature or pressure input for the Martian surface in this simulation could have meddled with an overestimate on the recharge fluids of the hydrological system and may have not allowed a good comparison between the volcanism of the Noachian – Hesperian and the geothermics of the Amazonian crust.

Table 3.5. Petrophysical properties of the lithologies that comprise the 2D Martian crust model of fig. 3.16. The physical parameters of the rock units shown below were set similarly to the thermodynamic scenarios of cases 3.2.1, 3.2.2 and 3.2.3. The basic difference in this scenario is the use of the intrusive peridotite veins that have been added to the grid with the similar values as those describing the crust's basement rocks.

Petrophysical Properties	**Crustal Basement and Peridotite**	**Basalt**	**Melt Rocks**	**Breccia**	**Regolith**
Permeability (k) {m^2}	k_z = f(d,T), k_x = f (d,T)	k_z = f(d,T), k_x = f (d,T)	k_z = f(d,T), k_x = f (d,T)	k_z = f(d,T), k_x = f (d,T)	k_z = f(d,T), k_x = f (d,T)
Porosity (φ) {%}	φ = f (d,T)	φ = f (d,T)	φ = f (d,T)	φ = f (d,T)	φ = f (d,T)
Thermal Conductivity {W/m·K}	2.9	2.7	2.7	2.7	1.7
Specific Heat Capacity {J/kg·K}	1200	1000	1000	900	700
Density {kg/m^3}	3000	2700	2500	2500	1700
Surface Permeability {m^2}	1.00E – 19	9.00E - 17	1.00E - 16	1.00E – 15	1.00E - 14
Surface Porosity ($\varphi_{surface}$)	2.0 %	5.0 %	7.0 %	7.0 %	15.0 %

Temperature & Water Mass Flux Distribution in the 2D Volcanic Geological Setting [T_{max} = 500 °C]

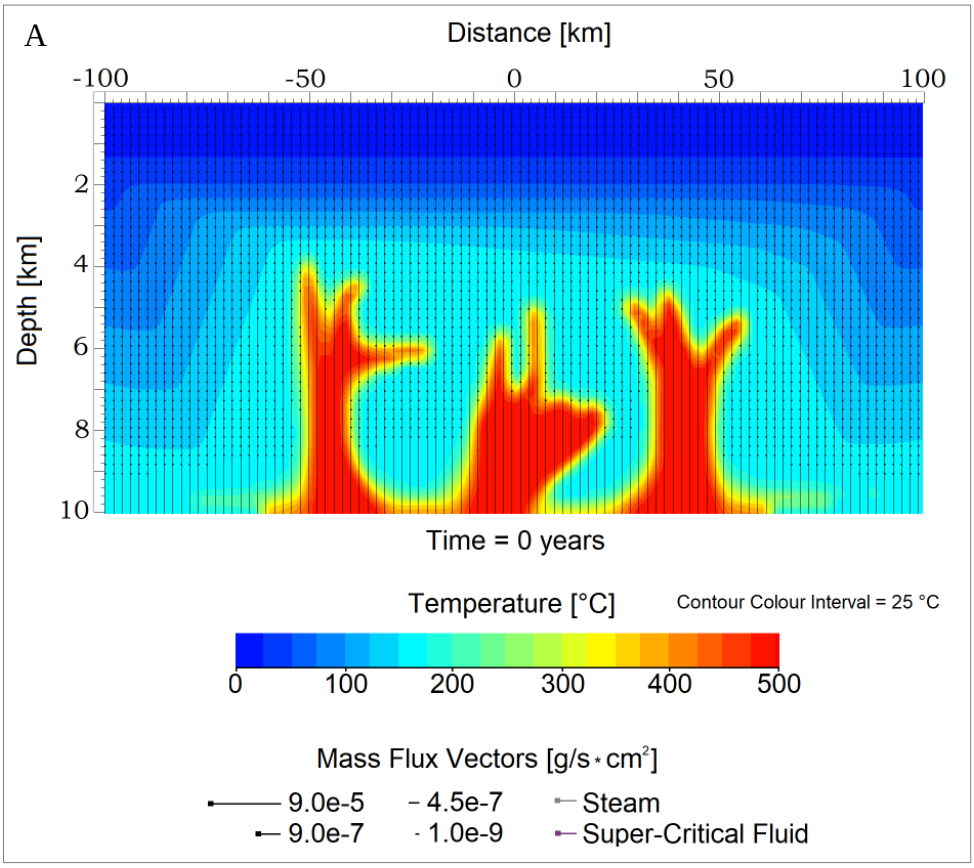

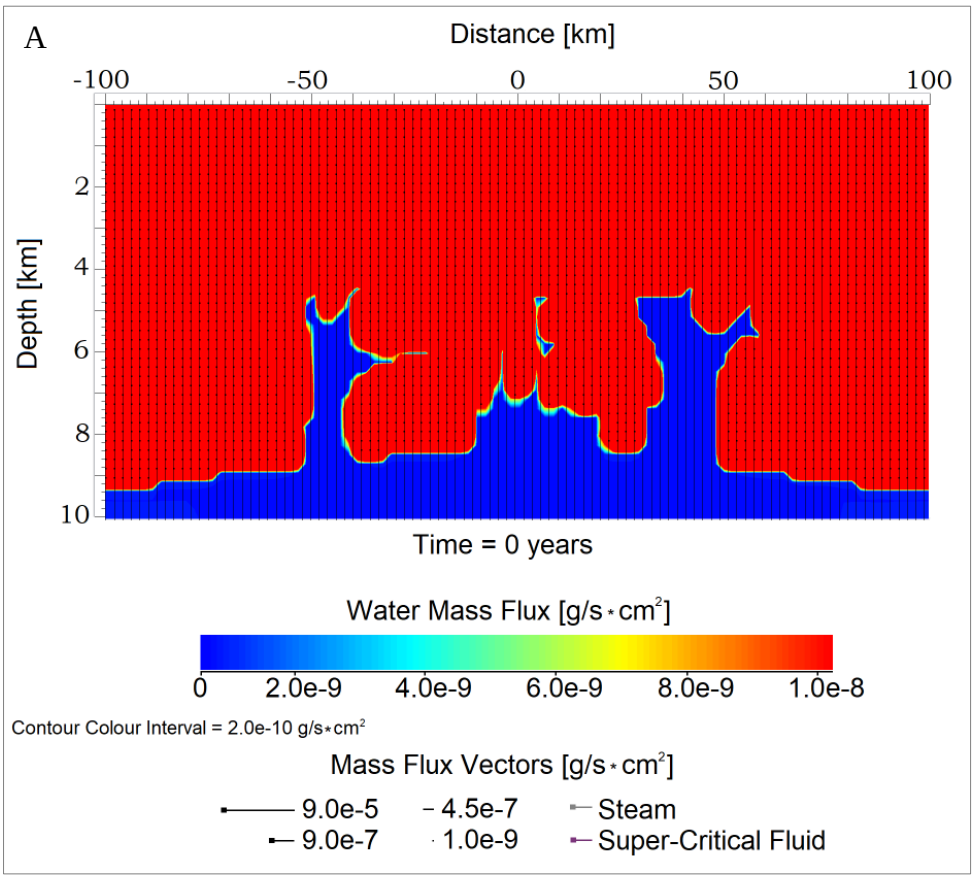

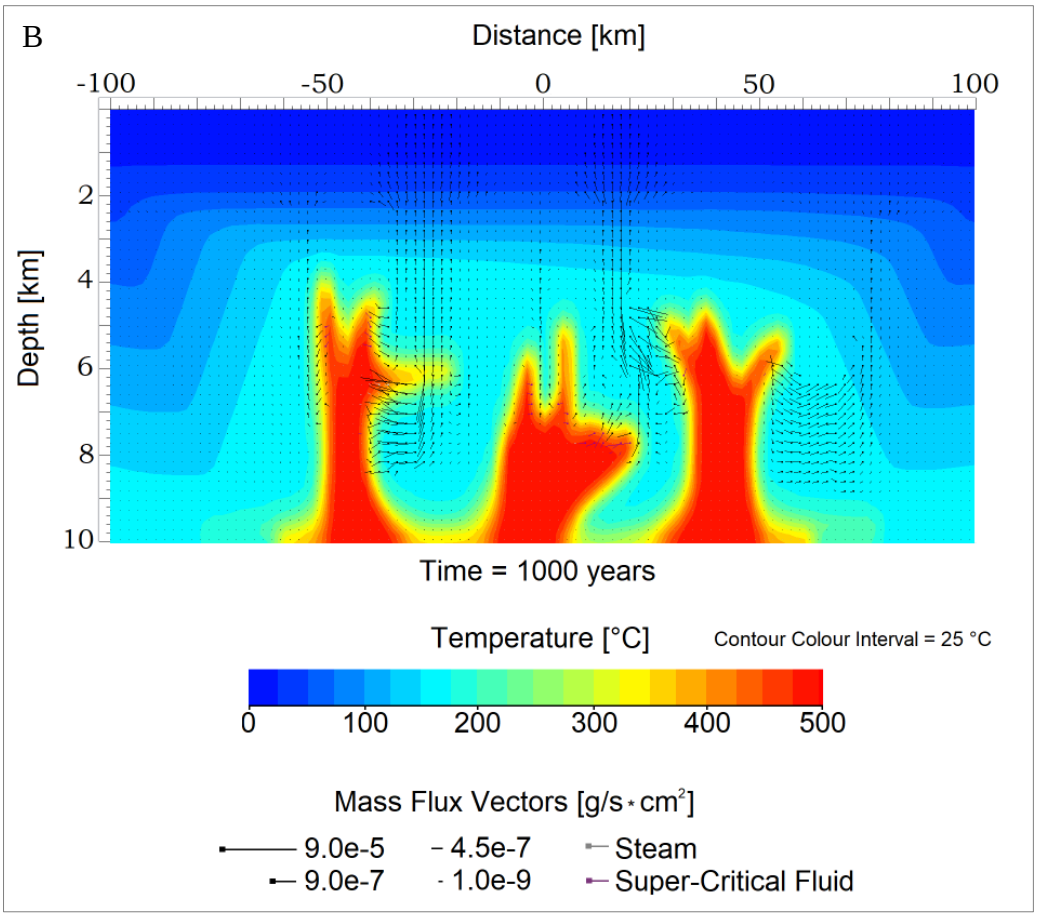
B
Distance [km]
-100
-50
0
50
100
Depth [km]
2
4
6
8
10
Time = 1000 years
Temperature [°C]
Contour Colour Interval = 25 °C
0
100
200
300
400
500
Mass Flux Vectors [g/s * cm²]
9.0e-5
4.5e-7
Steam
9.0e-7
1.0e-9
Super-Critical Fluid

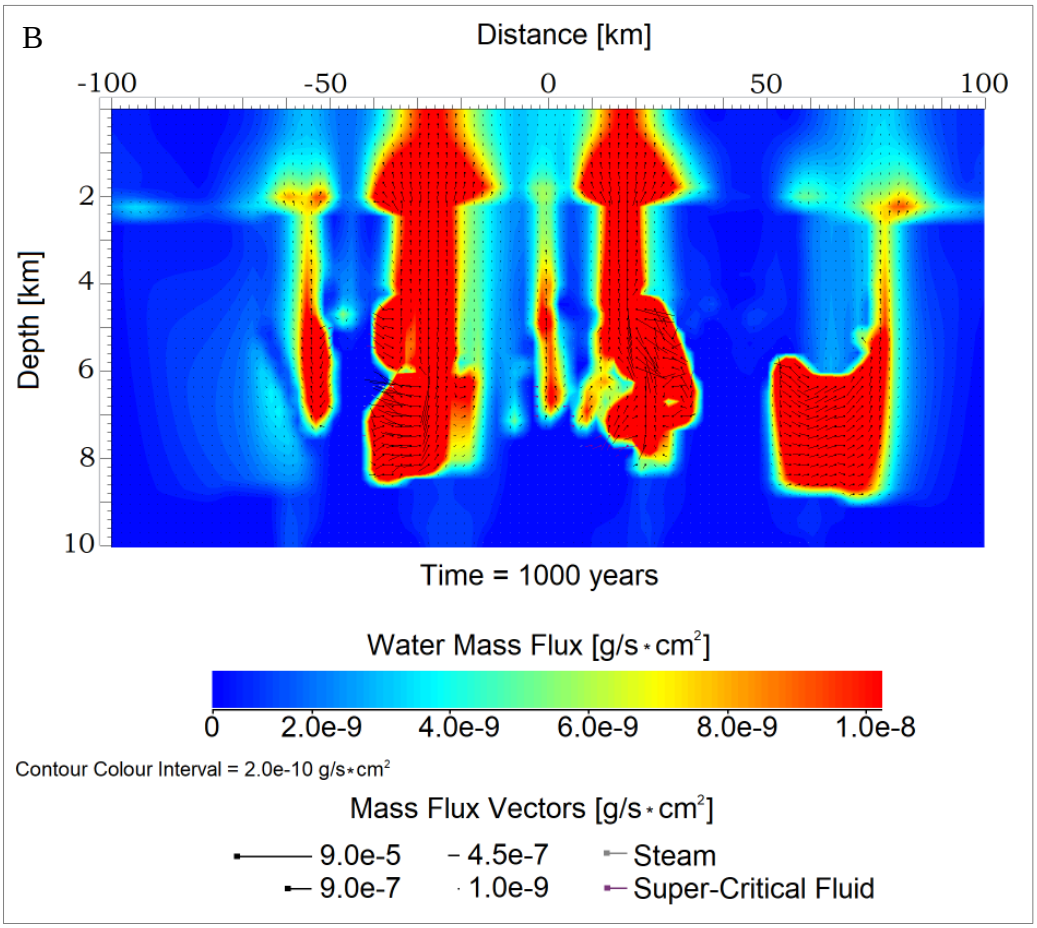
B
Distance [km]
-100
-50
0
50
100
Depth [km]
2
4
6
8
10
Time = 1000 years
Water Mass Flux [g/s * cm²]
0
2.0e-9
4.0e-9
6.0e-9
8.0e-9
1.0e-8
Contour Colour Interval = 2.0e-10 g/s*cm²
Mass Flux Vectors [g/s * cm²]
9.0e-5
4.5e-7
Steam
9.0e-7
1.0e-9
Super-Critical Fluid

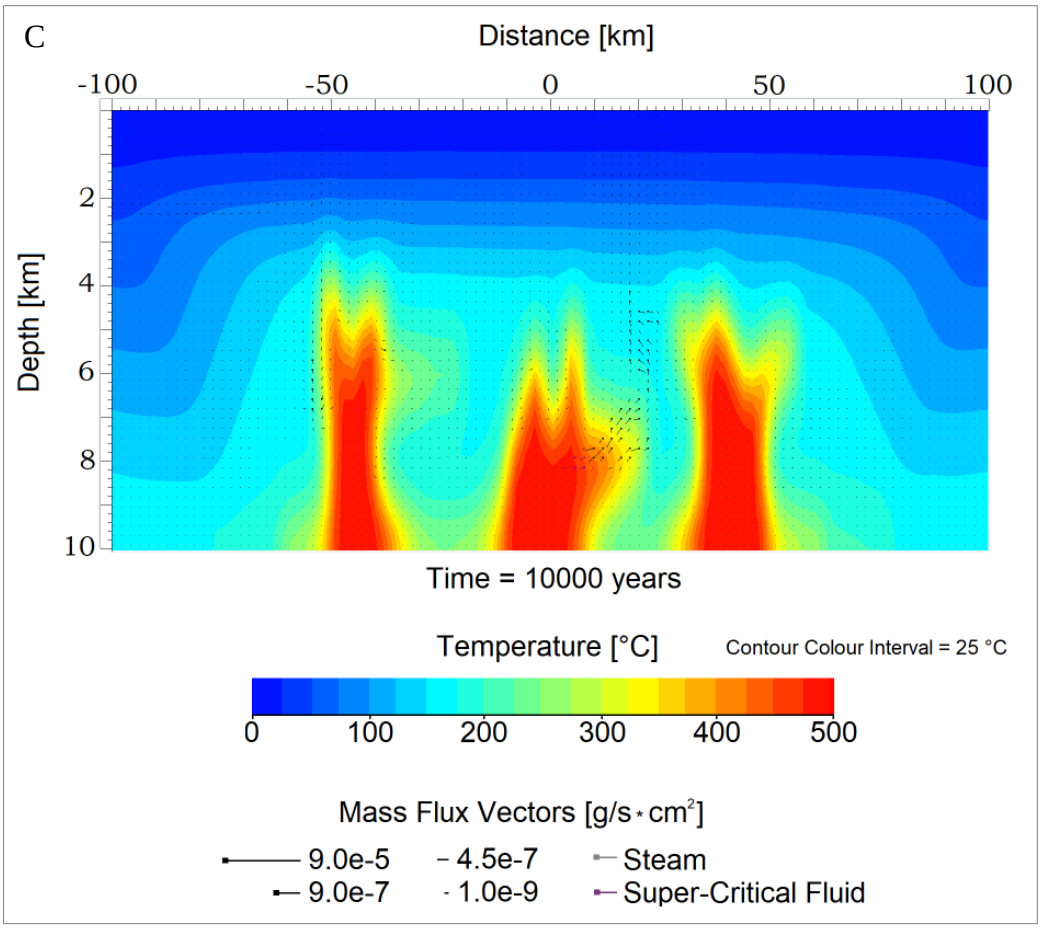
C
Distance [km]
-100
-50
0
50
100
Depth [km]
2
4
6
8
10
Time = 10000 years
Temperature [°C]
Contour Colour Interval = 25 °C
0
100
200
300
400
500
Mass Flux Vectors [g/s*cm²]
9.0e-5
4.5e-7
Steam
9.0e-7
1.0e-9
Super-Critical Fluid

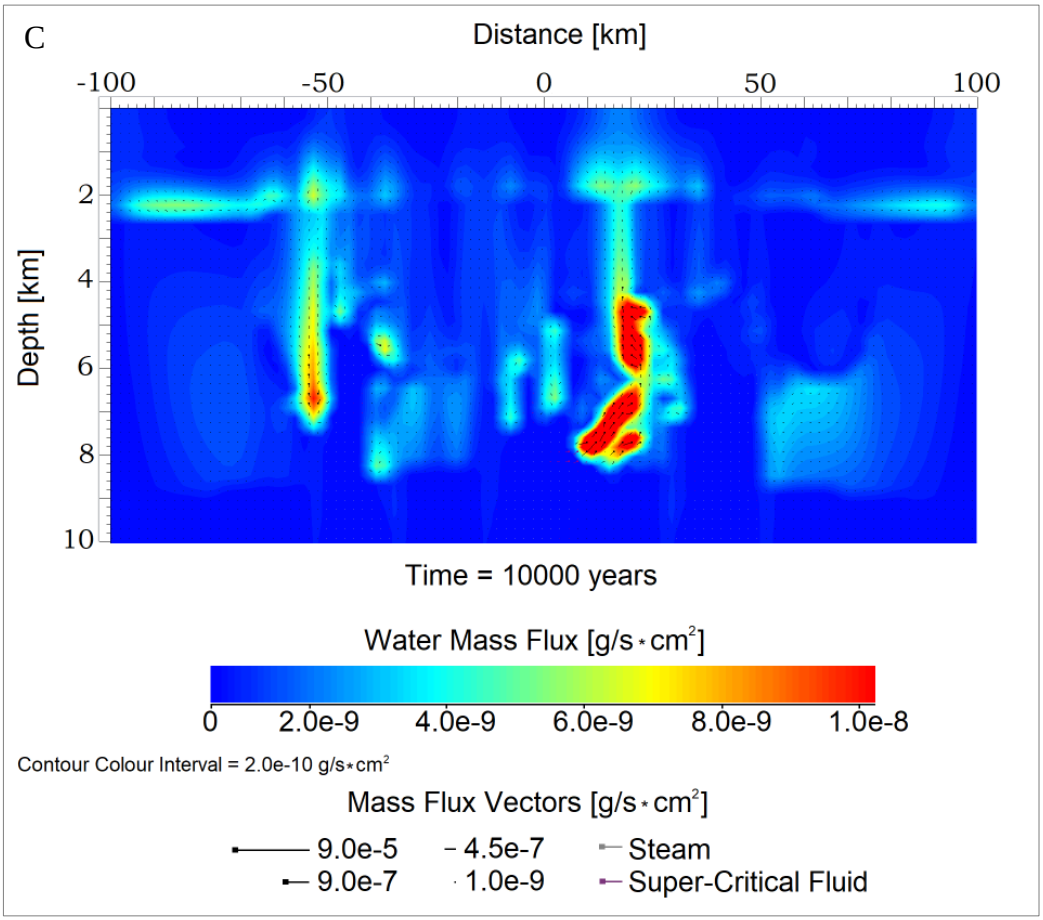
C
Distance [km]
-100
-50
0
50
100
Depth [km]
2
4
6
8
10
Time = 10000 years
Water Mass Flux [g/s*cm²]
0
2.0e-9
4.0e-9
6.0e-9
8.0e-9
1.0e-8
Contour Colour Interval = 2.0e-10 g/s*cm²
Mass Flux Vectors [g/s*cm²]
9.0e-5
4.5e-7
Steam
9.0e-7
1.0e-9
Super-Critical Fluid

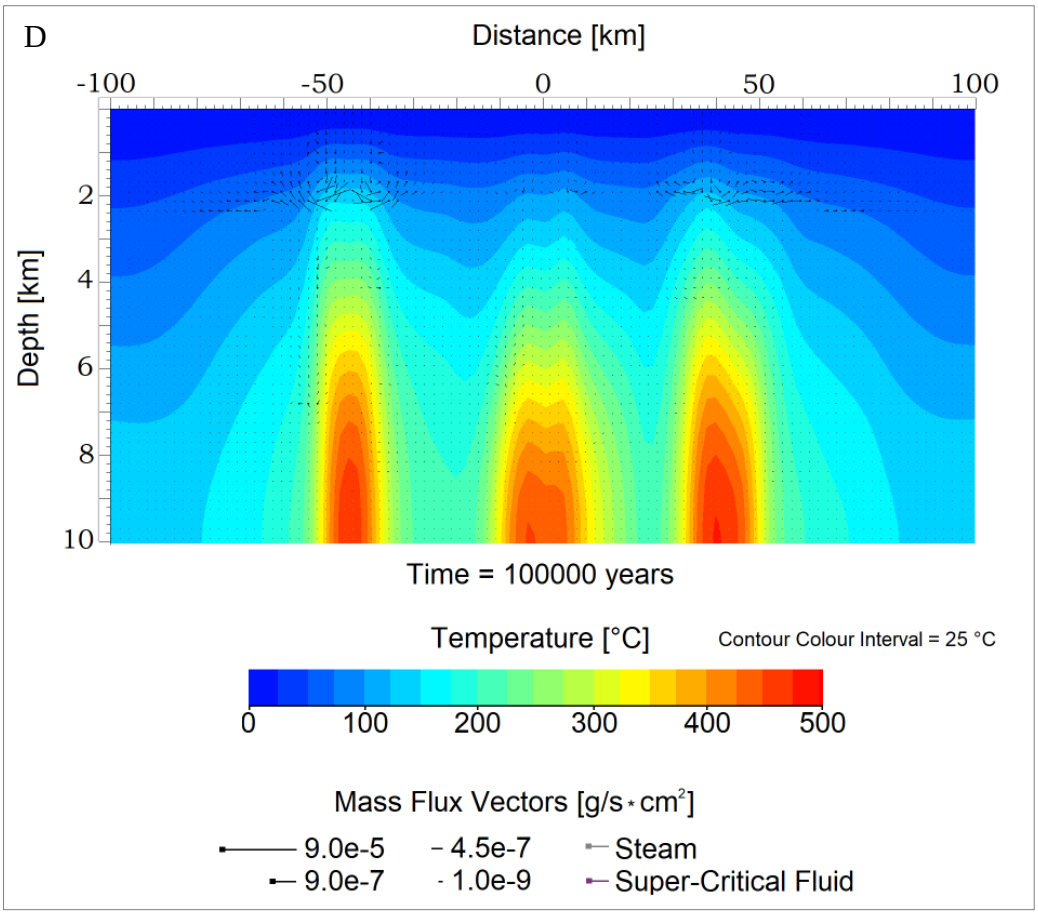
D
Distance [km]
-100
-50
0
50
100
Depth [km]
2
4
6
8
10
Time = 100000 years
Temperature [°C]
Contour Colour Interval = 25 °C
0
100
200
300
400
500
Mass Flux Vectors [g/s * cm²]
9.0e-5
4.5e-7
Steam
9.0e-7
1.0e-9
Super-Critical Fluid

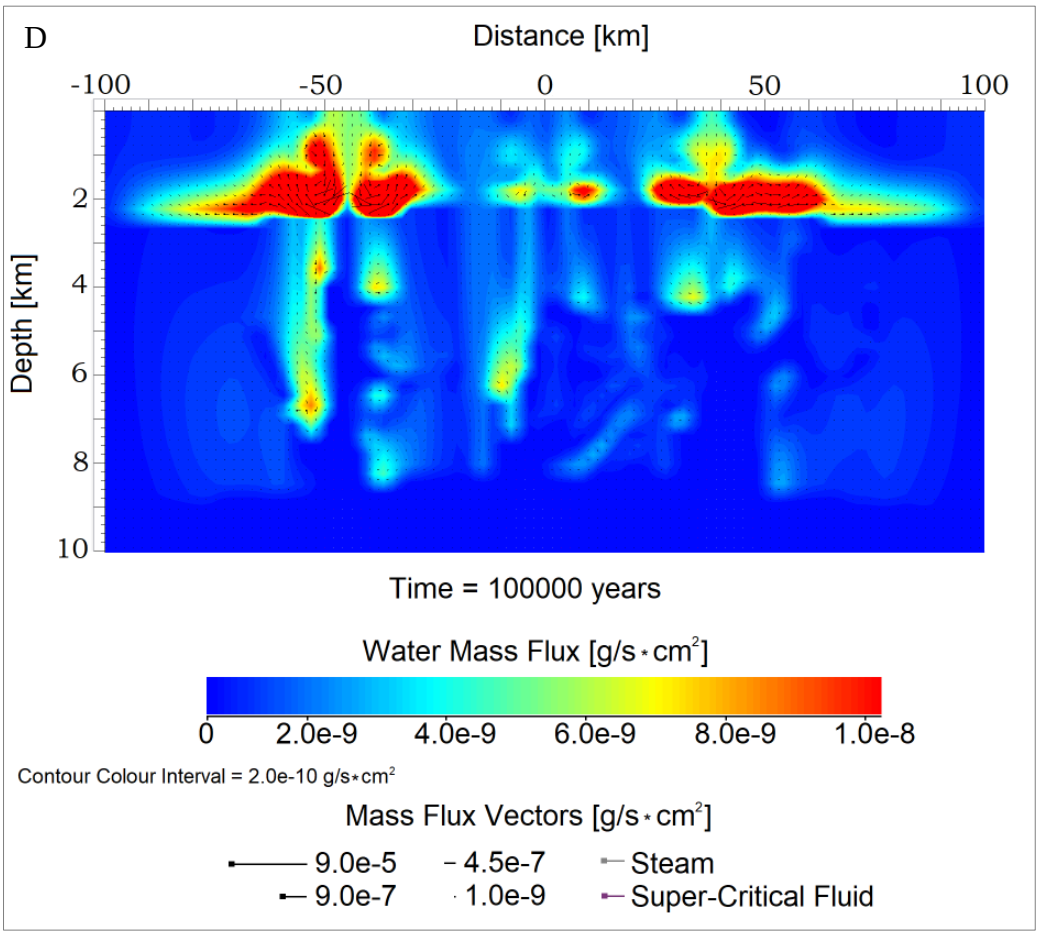
D
Distance [km]
-100
-50
0
50
100
Depth [km]
2
4
6
8
10
Time = 100000 years
Water Mass Flux [g/s * cm²]
0
2.0e-9
4.0e-9
6.0e-9
8.0e-9
1.0e-8
Contour Colour Interval = 2.0e-10 g/s*cm²
Mass Flux Vectors [g/s * cm²]
9.0e-5
4.5e-7
Steam
9.0e-7
1.0e-9
Super-Critical Fluid

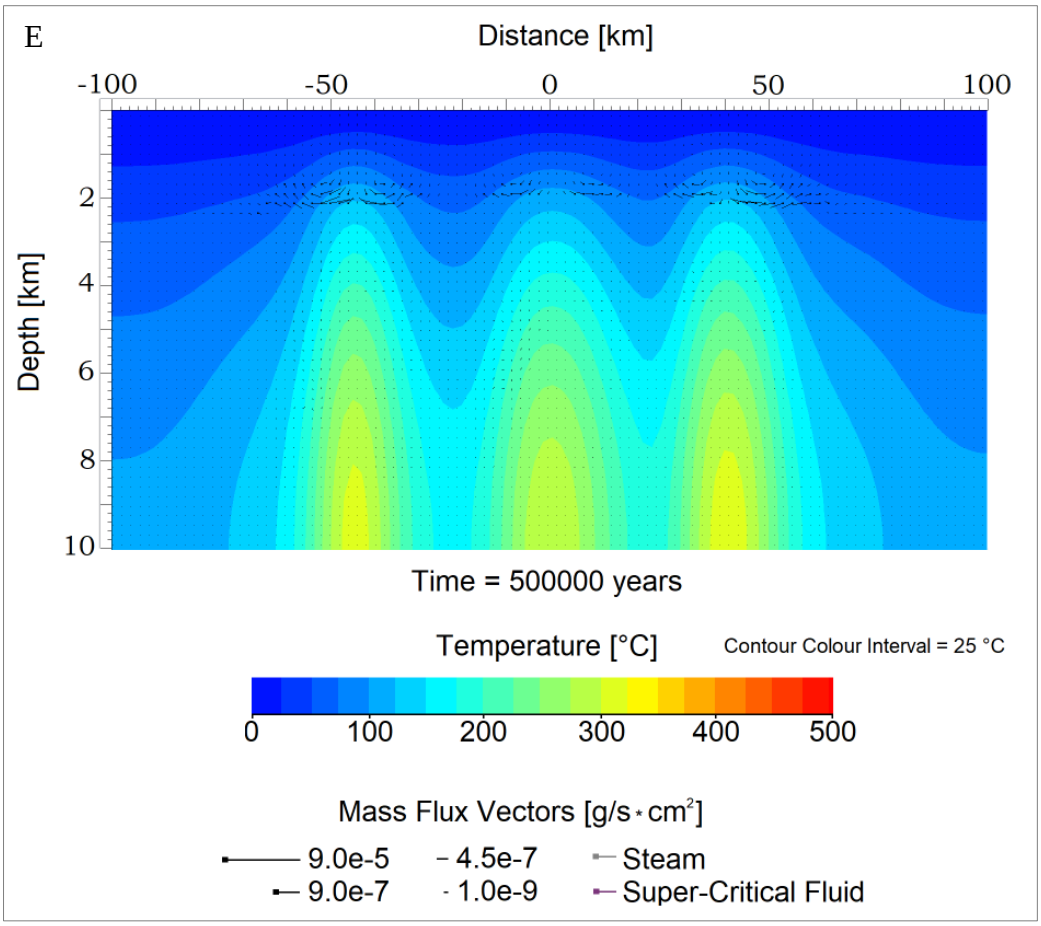
E
Distance [km]
-100
-50
0
50
100
Depth [km]
2
4
6
8
10
Time = 500000 years
Temperature [°C]
Contour Colour Interval = 25 °C
0
100
200
300
400
500
Mass Flux Vectors [g/s*cm²]
9.0e-5
4.5e-7
Steam
9.0e-7
1.0e-9
Super-Critical Fluid

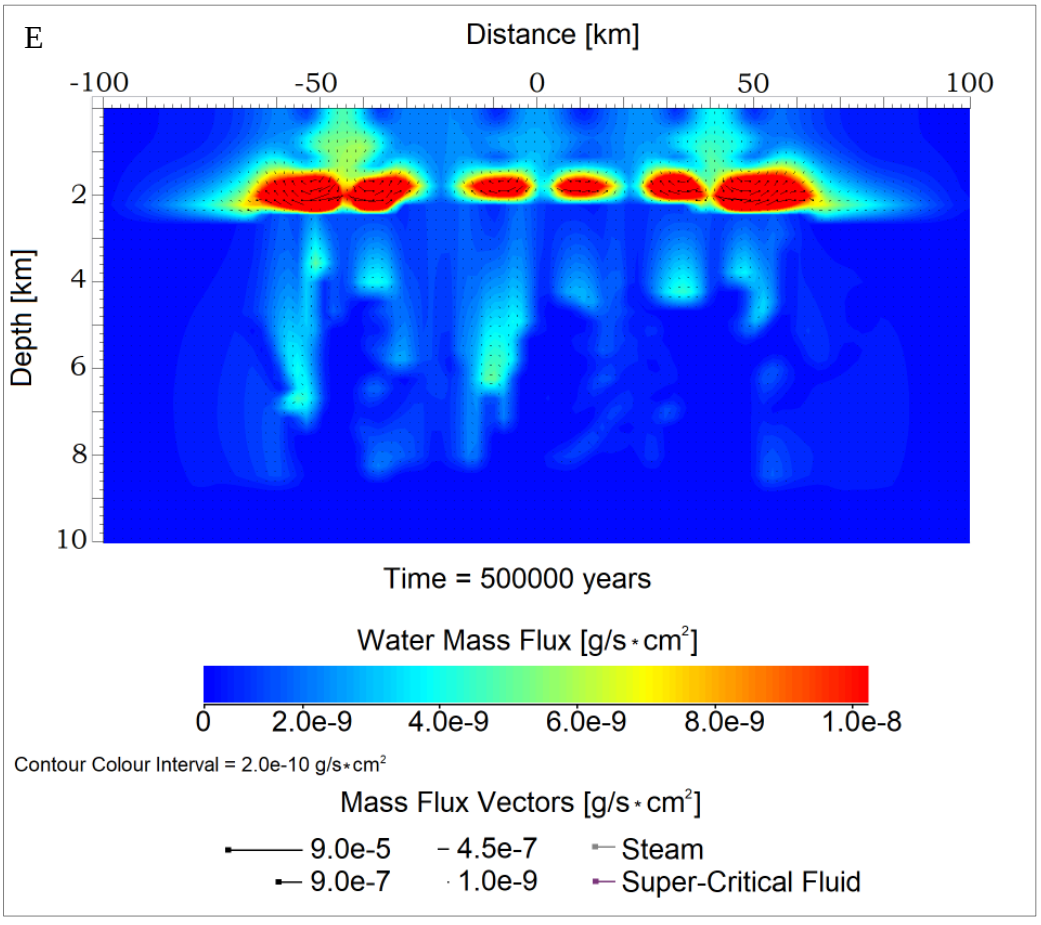
E
Distance [km]
-100
-50
0
50
100
Depth [km]
2
4
6
8
10
Time = 500000 years
Water Mass Flux [g/s*cm²]
0
2.0e-9
4.0e-9
6.0e-9
8.0e-9
1.0e-8
Contour Colour Interval = 2.0e-10 g/s*cm²
Mass Flux Vectors [g/s*cm²]
9.0e-5
4.5e-7
Steam
9.0e-7
1.0e-9
Super-Critical Fluid

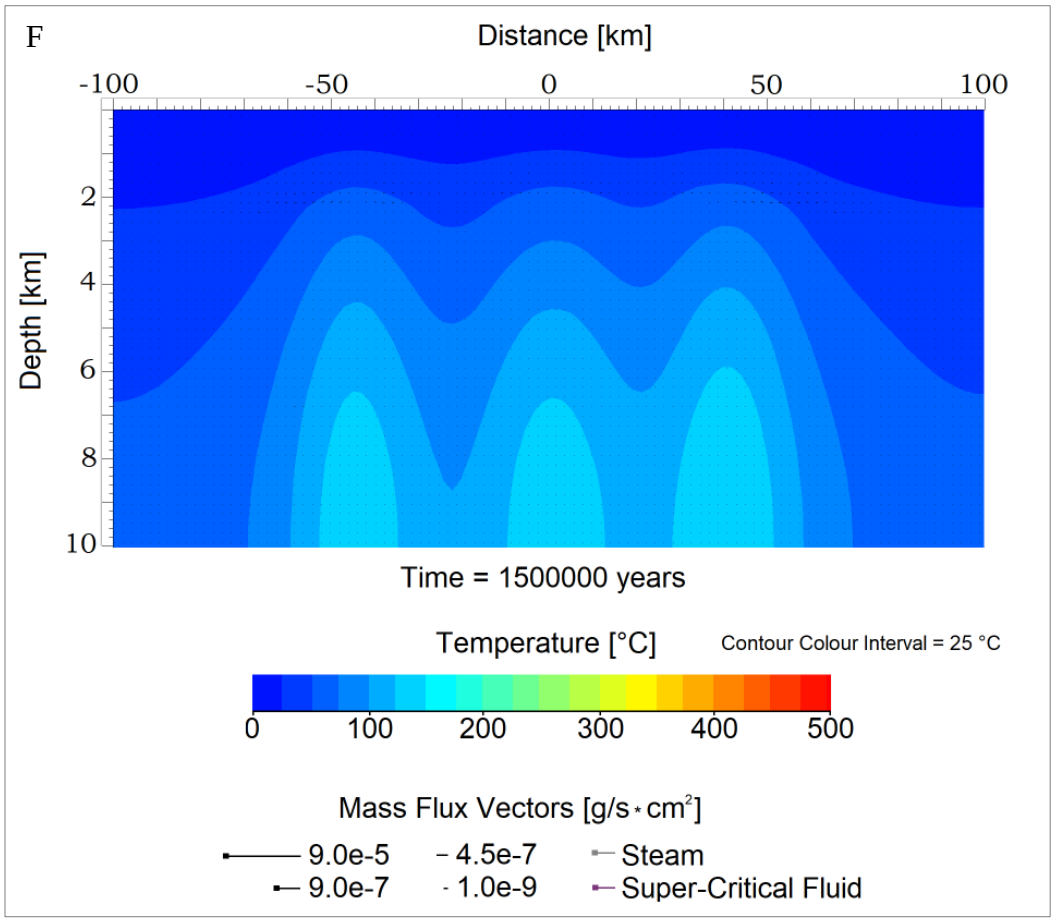
F
Distance [km]
-100
-50
0
50
100
Depth [km]
2
4
6
8
10
Time = 1500000 years
Temperature [°C]
Contour Colour Interval = 25 °C
0
100
200
300
400
500
Mass Flux Vectors [g/s*cm²]
9.0e-5
4.5e-7
Steam
9.0e-7
1.0e-9
Super-Critical Fluid

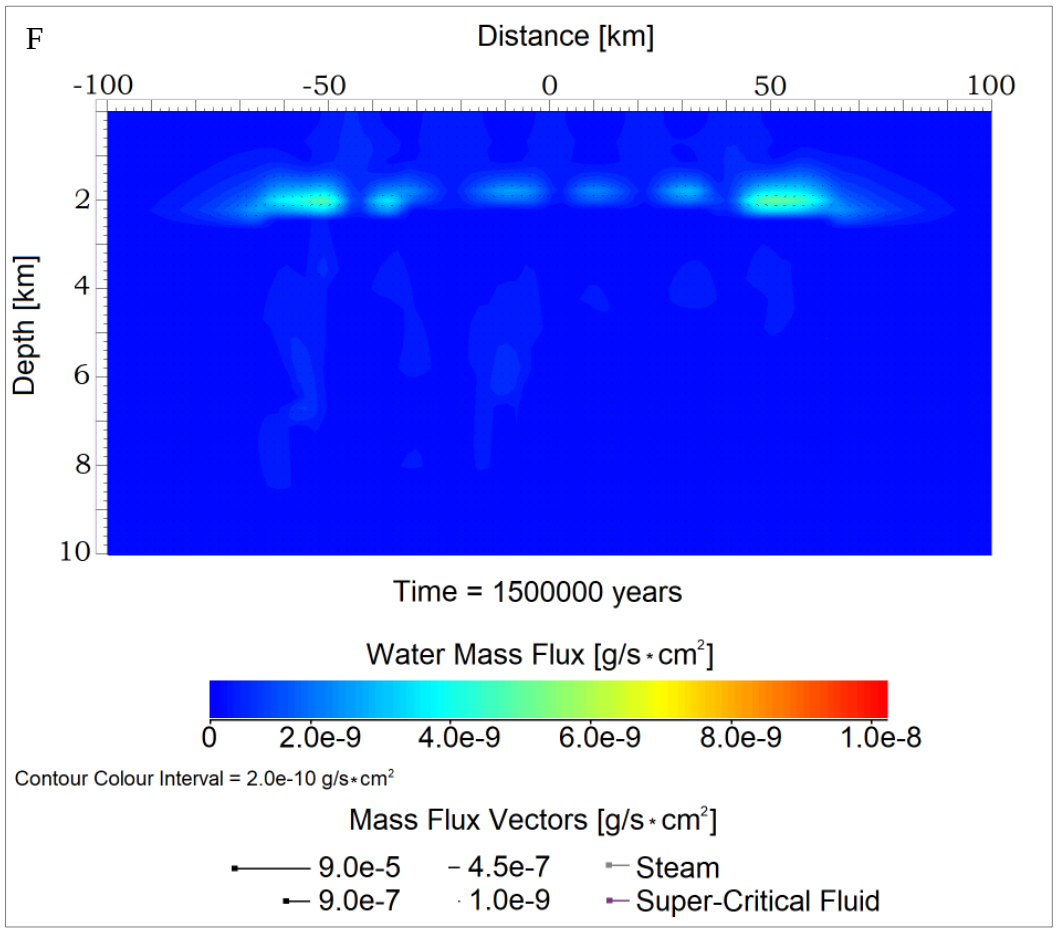
F
Distance [km]
-100
-50
0
50
100
Depth [km]
2
4
6
8
10
Time = 1500000 years
Water Mass Flux [g/s*cm²]
0
2.0e-9
4.0e-9
6.0e-9
8.0e-9
1.0e-8
Contour Colour Interval = 2.0e-10 g/s*cm²
Mass Flux Vectors [g/s*cm²]
9.0e-5
4.5e-7
Steam
9.0e-7
1.0e-9
Super-Critical Fluid

Fig. 3.17 (steps A-F). Thermal and aqueous flux distribution in the Martian volcanic setting for a period of 1.5 Myr, where T_{max} = 500 °C at a depth of approximately 4 km, and basal heat flux with a value of 80 mW/m^2 is computed present through the code at 10 km depth.

Thermal Distribution (steps A-F): Dark blue-coloured regions in the schematics show colder domains of the environment, where $T_{max} \leq 25$ °C. Red-coloured regions of the grid represent domains where $T = T_{max} = 500$ °C. As in previous models, the magnitude of fluid flux is indicated by vector's length and the squared edge of each vector shows the direction of flow. Liquid water flux is represented by black vectors, vapour flux by light-greyish vectors, and super-critical flux by purple vectors. Intrusive peridotite veins of a T_{max} = 500 °C at depths between 10 and 4 km cause significant heating in the upper crust. As a result, warmer flows with 25 °C $\leq T \leq$ 50 °C reach the upper-subsurface or even surface of Mars and seem to induce significant recharge flow events (steps B-E: from 1 Kyr to 500 Kyr). This effect is probably due to the significantly higher temperature of warmer flows reaching the surface of Mars (25-50 °C higher than in previous scenarios), heat transfer from the intrusive peridotitic veins to the regolith, and a potential mixing and subsequent recharge of hydrothermal flows with surficial runoff and precipitated colder water. The recharged fluids are observed to penetrate the regolith again and flow inwards to the deepest regions of the setting inducing an appreciable hydrothermal cycle. The basal heat flux of the volcanic setting is computed to 80 mW/m^2 at a depth of 10 km, and the system seems to be hydrothermally inactive only after 1.5 Myr, when the geothermal gradient seems restored (step F). In step F it is notable that subsurface regions of the deeper crust are affected by a shift of hotter isotherms to shallower depths, which is what we could expect in only recently inactive and geologically young magmatic or impact-induced hydrothermal settings.

Water Mass Flux Distribution (steps A-F): Blue-coloured regions show domains where no flows or very weak flows are present. Red-coloured regions represent maximum fluxes ($\geq$ 9.0e-9 g/s×cm^2) within the host rocks. The magnitude of fluid flux is depicted by vector's length. The squared edge of each vector indicates the direction of flow, and every cell of the simulative grid is represented by a vector in each time step that shows the direction and magnitude of flow. Liquid water flux is shown in black vectors, vapour flux in light-greyish vectors, and super-critical flux in purple vectors, as presented in the previous models. At t_0 liquid water mass flux is shown with peak values (step A: $WMF_{max} \approx$ 9.0e-3 g/s×cm^2) at depths between 9 and 5 km. In the shallower regions of the setting (0-5 km) flux is plotted in red colour and with a calculated $WMF_{max} \approx$ 9.0e-6 g/s×cm^2. Steps B-E indicate that numerous and quite extensive hydrothermal cells form due to the presence of intrusive veins at various subsurface locations. These hydrological cells stay active for more than 500 Kyr, with several recharge events occuring during the entire period of intense hydrous activity. Recharge flows are obvious through time steps C – E, where the direction of flow points from the Martian surface inwards to the deeper niches of the environment. Weaker steam and supercritical fluxes (white and purple vectors, respectively) appear only within the peridotitic veins from 1 to 100 Kyr, with 300 °C $\leq T \leq$ 500 °C. The super-critical and steam flux however, is by 2 orders of magnitude lower ($\leq$ 9.0e-7 g/s×cm^2); probably due to the high temperature and low permeability of the peridotite veins. Eventually, the magmatic-induced hydrothermal activity persists for a period of 1.5 Myr. The heat transfer by the intrusive network of peridotite veins at depths between 4 and 10 km, and the presence of a magmatic chamber at a depth $\geq$ 10 km (evident through the basal heat flux value of the setting) should be the mechanisms responsible for such a long duration. The most significant implication of the model is that hydrological cells appear active at depths $\geq$ 2 km, which means that deep subsurface niches of volcanic provinces on present-day Mars, should be quite enriched in aqueous deposits; a thesis which is also consistent with observations and interpretations by Orosei et al. (2018).

3.3 Numerical Models for the Bioenergetic Potential of Ancient Volcanic & Impact-Induced Hydrothermal Systems on Mars

The previously presented numerical models that were produced via the HT code yielded an extensive output of thermodynamic datasets, including computations for the water mass flux in these putative Martian hydrothermal systems. The calculations pertinent to the water flow in each setting were then used to assess the bioenergetic potential and habitability of these systems. To accomplish this objective, the PHREEQC program of the USGS (version 3; Parkhurst and Appelo, 2013) which allows coupling between the thermodynamic output of HT 3 simulations and experimental (PHREEQC) geochemical reaction models that can also be benchmarked via the GWB software (Bethke, 1996) or the EQ3/6 code (Wolery and Jarek, 2003), was used to perform further computations for the habitability of the simulated Martian subsurface hydrothermal environments. This part of my PhD thesis examines the hydrogen release in these geological systems after interactions of impact-induced or magmatic-induced aqueous fluids with Martian basalt or peridotite, within the computed duration of hydrothermal circulation in each scenario. Therefore, these computations are time-constrained and governed by the thermodynamic input and output variables of the HT simulations.

This approach also enabled the benchmarking of the geochemical reaction path models, by allowing validity checks on whether the computed herein water-rock reactions take place within the thermodynamic window of the HT simulations (as explained in §2). In this work, due to the complexity of these thermodynamic reaction path computations, only H_2 is examined as the primary nutrient for a potential hydrogenotrophic subsurface biosphere on Mars. The H_2 release in each thermodynamic scenario is then assessed against the demands of hydrogen for fulfilling the survival, maintenance or growth bioenergetic criteria of putative hydrogenotrophic microbial communities (provided by Hoehler (2004)).

The HT simulations provided thorough insights into the water availability, fluid mass flux and duration of aqueous activity in these Martian geological systems. Therefore, thermodynamic computations for the availability of H_2 were reproducible, reliable, and time-efficient; in contrast to the computations for the availability of other potential nutrients (O_4S^{-2}, Fe(II), Fe(III), CO_2, CH_4, $C_2H_3O_2^-$ etc.). Hence, in this sub-chapter several computational scenarios

for the H_2 availability are explored to determine whether the Martian impact- or magmatic-induced hydrothermal systems could support microbial life under low energy and anaerobic conditions within the subsurface of the Red Planet.

3.3.1 Habitability Computations Dependent on Thermal and H_2 Availability Constraints for the explored Martian Impact-Induced Hydrothermal Systems.

The bihydrogen activity induced by the post-impact hydrothermal circulation in the putative Martian cratering systems is explored in this section. The evolution of the thermodynamic properties (temperature, pressure, enthalpy, H_2O-mass flux, etc.) after each impact scenario comprised the initial-boundary thermodynamic conditions for computing the H_2 availability in each cratering setting. The following results conclude on the habitability of different sized Martian craters for potential methanogens – hydrogenotrophic microbes.

Initially, fig. 3.18 shows the H_2 availability in the 200-km in diameter crater for as long hydrothermal circulation and subsequent water-rock interactions are active in the geological system. At the beginning, the computations consider distant areas of the crater where the temperature does not exceed the limit of 121 °C. However, due to intense hydrothermal fluxes being present in the entire setting, and at a radius of 100 km after the impact, even niches that were quite remote from the central melt sheet and the peak temperatures of the central cratering valley (i.e.: $T \geq 1200$ °C), still appear affected by fluid fluxes of $T \geq 121$ °C in later periods of the hydrothermal cycle. The HT simulations for the 200-km crater, showed that hydrothermal flow events induced by the central melt sheet affected domains that are even beyond a radius of 100-km. Thus, even colder and more distant subsurface regions of the crater got warmer and eventually hosted significant quantities of hydrothermal flux.

As the hydrothermal cooling of the crater progresses, regions that plot within the thermal range of 25 °C $\leq T \leq$ 121 °C are gradually more ubiquitous, especially during the latest stages of hydrothermal cooling, and those can be considered as the habitable niches of the setting. Therefore, we can assume that the habitability volume of the setting should increase as time elapses after the impact. Nevertheless, water-rock interactions should simultaneously be active in order to ensure the nutrient release in the system.

Estimates regarding the habitable rock volume of the setting have not been reliable yet through the code's configurations. This is because in different time-steps, specific thermodynamic parameters may imply the thermal habitability of the setting, but at the same time, they diverge from the chemical-based habitability. Preliminary habitable rock volume calculations showed on the one hand that the habitable volume of the system constantly increases as time elapses. On the other hand, the chemical-based habitability computations indicated that when the hydrothermal system is much colder, no water-rock interactions take place and thus, H_2 activity decreases and the environment is rendered unhospitable for microbial life. Thus, the approach that I have adopted in these bioenergetic simulations is dependent not only on the thermal habitability parameterization of the geological domain, but also on the chemical species availability for lithotrophs to exploit for their survival, maintenance and growth metabolic functions.

The model presented through fig. 3.18 indicates that from 0 to circa 50 Kyr after the impact, no region in this Martian cratering system is habitable. The possible explanations for that are the following:

- The temperature in subsurface domains that are far away from the heated (and conclusively sterilized region) have not been affected yet by fluxes of $T \geq 121$ °C, in order for water-rock reactions to produce a significant amount of chemical nutrients.

- Intensive hydrothermal fluxes take place in the sterilized domain (closer to the central and peak ring regions of the crater). Although the abundance of chemical nutrients after water-rock reactions therein should have peaked during the first 100 Kyr of hydrothermal cooling, the temperatures that dominate those niches are prohibitive for the survival of microbial life.

- The chemical species released under such thermally habitable conditions may have been too toxic ($pH < 3$, or $pH > 9$) for the hypothetical lithotrophic communities. The parameter of pH is included in the habitability computations and is directly dependent on temperature (as is the auto-dissociation activity of water which increases with an increasing temperature in the code).

From approximately 52 Kyr after the impact until 60 Kyr, the simulation appears a habitable thermodynamic window for potential microbial life but this lasts for only a short period of 8 Kyr. After 60 Kyr, regions of the setting that plot within the habitable range become sterilized as they are affected by hydrothermal fluxes of $T \geq 121$ °C. These fluxes persist in these domains from 60 Kyr to 226 Kyr and affect these previously habitable niches of the geological setting with 125 °C $\leq T \leq$ 160 °C. These intense hydrothermal fluxes release significant amounts of bihydrogen in the geological system and so, when the temperature decreases below 121 °C, from 226 Kyr and up to 410 Kyr, the thermodynamic conditions and H_2 activity are optimal for the metabolic growth of potential hydrogenotrophic communities. Thus, the simulation indicates that during this 184 Kyr period (226 – 410 Kyr), the growth criteria of methanogens have been satisfied. Hence, we can assume that the potential biomass of such life forms should have colonized any habitable volume in the porous of the host Martian geological environment. Later, from 410 Kyr to 800 Kyr, the geological system's bioenergetics cannot support the growth criteria of potential microbes as the H_2 activity data points are computed with values below the growth curve's limits. Nevertheless, the potential hydrogenotrophic biomass in the crater should not have lost any volume during that phase and should have had the energy availability in the system to support its maintenance mode (as shown by the H_2 activity plot – shown in bright blue colour). After 800 Kyr and up to the final time-step of the simulation (2.8 Myr) the bihydrogen activity in the Martian subsurface of the crater has been reduced by circa 4.5 orders of magnitude below the optimum range for microbial growth, but the survival mode of hydrogenotrophs can still be ensured (as H_2 activity plots above the survival mode curve).

This bioenergetic simulation indicates that even after impact-induced hydrothermal activity has ceased, the H_2 availability in the host rock units of this Martian crater still supports the survival of microbial life for a period greater than 2.8 Myr. Conclusively, we can deduce that large impact craters ($r \geq 100$ km) on Mars that formed during ancient geological periods, could have fulfilled the bioenergetic functions of microbial life for even more than 2 – 3 Myr after the impact. Thus, geological samples that may be retrieved from large Martian impact craters by present and future rover missions may be proven fruitful for astrobiological findings.

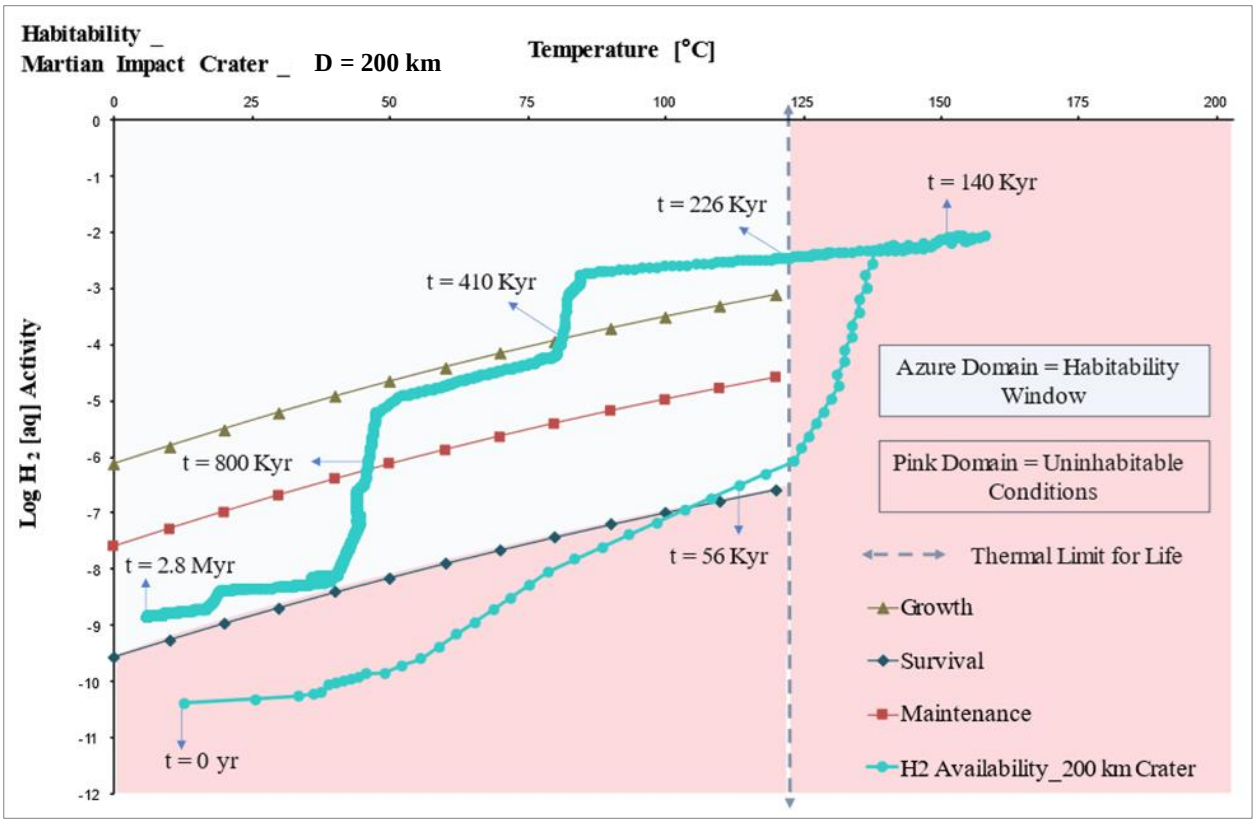

Fig. 3.18. H_2 release and habitability computations for the geological setting of the putative 200 km in diameter Martian crater. The hydrogenotrophic biomass demand limits (survival, maintenance and growth) were provided by Hoehler (2004). As the upper temperature limit for life is established at 121 °C (Kashefi and Lovley, 2003), areas of the hydrothermal setting that plot beyond this upper thermal limit during the period of hydrothermal circulation or after the hydrological cycle has ceased, can be considered as uninhabitable and hostile for microbial life (pink domain). On top of that, niches of the setting where water-rock reactions release amounts of H_2 that plot below the survival mode curve for microbial activity (blue curve in the legend) are also determined as poor in terms of their bioenergetic potential. The thermodynamic properties of the environment and duration of Martian basalt – water interactions, and the subsequent H_2 release, depend on the HT simulation results (output) of scenario 3.1.1.

In continuation to the rationale and investigation of the impact-induced bioenergetics in the 200-km Martian crater, fig. 3.19 depicts the computational results for the habitability of the smaller by 50 km in radius crater (diameter = 100 km). The hydrothermal setting and its habitability have been assessed in this case for a total period of 1.8 Myr, which means that the nutrient availability in this geological system has been evaluated for an additional period after the post-impact hydrothermal circulation has halted.

In the hydrothermal system of the 100-km in diameter crater, habitable conditions do not appear up to the time point of 23 Kyr. Similarly to the previous case (200-km cratering setting), strong and hotter than 121°C hydrothermal fluxes do not reach the more distant niches of the crater

within the first 23 Kyr. Additionally, the central valley, peak ring and closer outer-rim regions that are affected by the heat currents of the central melt sheet are sterilized and so, they are unhospitable for life. After 23 Kyr, the central melt sheet cools significantly, and the impact-induced heat conduits and fluxes reach the more distant regions of the crater. After that time point water-rock reactions occur far more rapidly under much warmer conditions. Thus, the nutrient release in the geological environment increases by approximately 3-4 orders of magnitude when compared to the H_2 activity during the first 10 Kyr of impact-induced hydrothermal circulation.

From 24 Kyr to 100 Kyr, both the survival and maintenance mode criteria of microbial metabolic function are satisfied, and the Martian subsurface system of the crater can be characterized as habitable. Nevertheless, even when H_2 activity in the geological system has peaked under the habitable conditions' window (at circa 80 – 100 Kyr), the nutrient availability cannot support microbial growth. Hence, this model suggests that Martian craters with diameters equal to or smaller than 100 km may have not supplied enough energy for microbes to grow their colonies. However, not only the survival but also the maintenance mode of microbial activity are supported under such hydrothermal conditions. This also implies that cratering systems of such a size may have also attracted microbial communities from other nearby geological domains of the subsurface of Mars that may have been struggling with their survival under cold and arid conditions and very low energy limitations (if microbial life ever existed during ancient geological epochs on Mars).

Moreover, from 100 Kyr to 208 Kyr, all of the initially habitable regions of the crater appear affected by harmful-for-life hydrothermal fluxes ($T \geq 121$ °C). This means that all microbial life may be eradicated after experiencing such temperatures around that time point. This leads to the conclusion that whatever microbial communities may have been present in the hydrothermal system or migrated towards it from other nearby regions of the subsurface realm of Mars may have gone extinct between 100 – 208 Kyr. On top of that, although the nutrient release (H_2 availability) in the system increases by at least 3 orders of magnitude when temperature exceeds 100 °C, as shown through the plotted H_2 activity data from 24 Kyr to circa 40 Kyr, and reaches peak values when the temperature in the host rock is close to 150 °C, the post-sterilization habitability should possibly be considered as ambiguous.

After 208 Kyr, the bioenergetics of the system dictate that the maintenance mode of microbial activity is fulfilled, and that any potential microbial biomass should persist in the system by supporting its metabolic maintenance for a period of circa 772 Kyr (from 208 Kyr to 980 Kyr). From 980 Kyr and then on, the energy availability in the geological system seems to be unable to support the maintenance mode of microbial life. Thus, after that time point microbes will shift their metabolic function from their maintenance to their survival mode.

Even after hydrothermal circulation has ceased, the geothermal gradient has been restored, and water-rock interactions are not possible anymore, it seems that the H_2 availability in the system is marginally above the survival limits of thermophilic hydrogenotrophs (at the final time-step of the simulation: t = 1.8 Myr). Nevertheless, as bihydrogen is extremely volatile, we expect that its availability in this Martian geological system will decrease significantly after a few tens of Kyr, and since the final time-step calculation shows it closer to the survival limits. Therefore, we can conclude that this 100 km Martian crater which hosted impact-induced hydrothermal flows, and appreciable water-rock interactions and even potential bioenergetics for a period greater than 1.5 Myr, is rendered uninhabitable shortly after 1.8 – 1.9 Myr.

The implications of this simulation are, nevertheless, supportive of the hypothesis that potential microbial habitats may have persisted on Mars under impact-induced hydrothermal conditions. In comparison with the habitability simulation for the 200 km in diameter crater and its induced hydrothermalism, these two models indicate that the larger the crater, the more prolonged the hydrothermal activity, and so, the higher the abundance of chemical nutrients released through water-rocks reactions during the post-impact geological period.

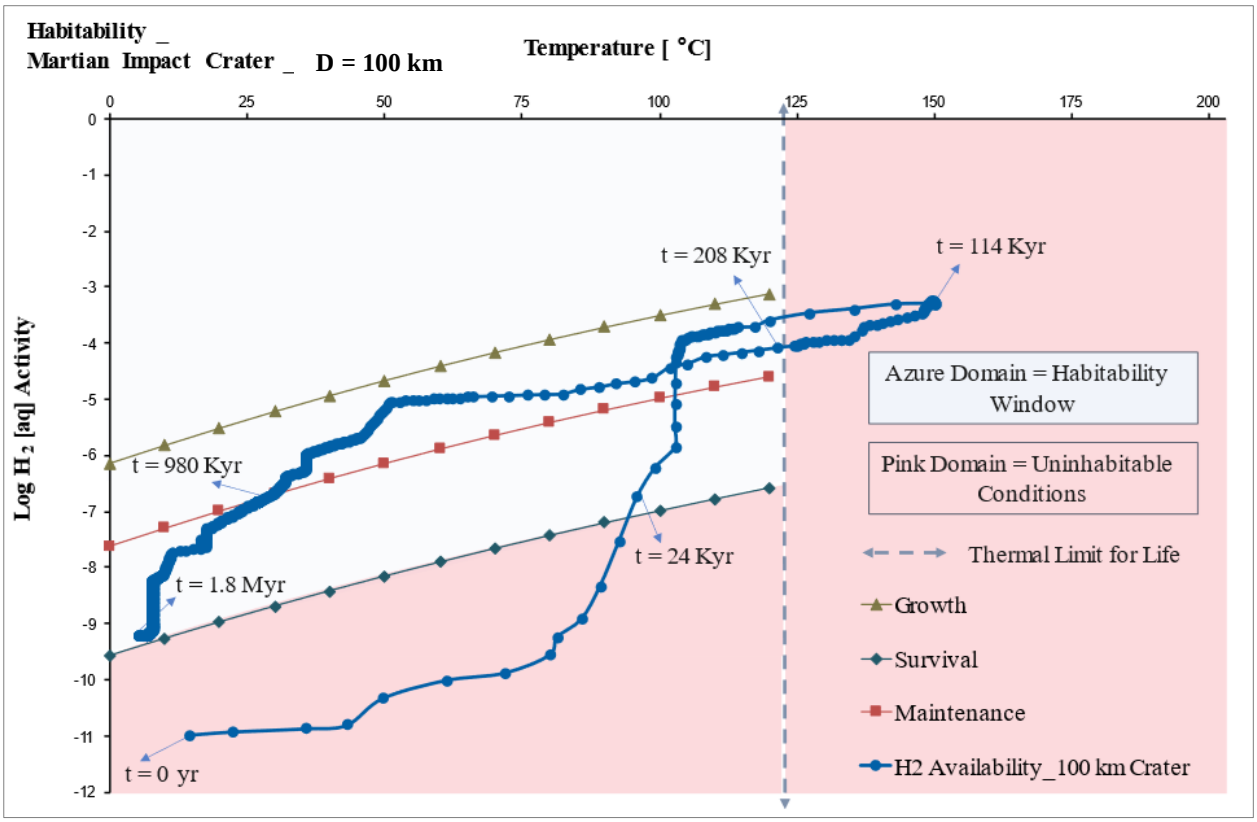

Fig. 3.19. H_2 availability for the impact-induced hydrothermal system of the 100 km in diameter Martian crater. The hydrogenotrophic biomass demand limits (survival, maintenance and growth) were provided by Hoehler (2004). The upper temperature limit for life has been computed at 121 °C (after Kashefi and Lovley, 2003). Hence, domains of the geological environment that are computed with isotherms that exceed this upper thermal limit during or after the period of hydrothermal circulation, are characterized as hostile for microbial life (pink domain). Regions of the geological system where water-rock reactions yield H_2 activity that plots below the survival mode curve for microbial activity (blue curve in the legend) are also distinguished as uninhabitable based on their bioenergetic potential. The thermodynamic window of the setting, the duration of Martian basalt – water reactions, and the simulated H_2 production, depend on the HT simulation results (output) of scenario 3.1.2.

Finally, the last bioenergetic simulation related to Martian impact-induced hydrothermal activity and habitability is represented by fig. 3.20. As previously presented, the HT simulation for the 10-km in diameter Martian crater established that such a post-impact hydrological system could have lasted for an approximate period of 80 – 100 Kyr. Taking advantage of the 20x shorter duration of the system, the water-rock interactions in this system and its habitability are investigated for a total period of 300 Kyr. The two previous models for the larger craters (D = 100 km, D = 200 km) produced extensive thermodynamic datasets and hence, it was quite difficult in terms of the available computational capacity to explore the H_2 activity in those settings for an additional period of 200-500 Kyr; i.e.: long after water-rock interactions in the geological system have ceased. The 10-km in diameter crater, however, allows to investigate

the habitability of the setting for a far longer (2 × greater) period after the geothermal gradient has been restored and hydrous flows are absent.

In this scenario, habitable space in the crater forms at 21-22 Kyr after the impact, as revealed by the H_2 activity curve (coloured in green in fig. 3.20). Again, at this time point, most of the habitable niches should be located remotely from the crater's center; as at the central valley the temperature is close to 700 °C right after the impact, far beyond the thermal limit for life (121 °C; after Kashefi and Lovley, 2003). This means that regions closer to the crater's peak ring and center stay sterilized for a period that is greater than 22 Kyr. Nevertheless, any potential microbial communities that may have existed should follow the same pattern of migration that was previously described; firstly, the more remote areas of the hydrothermal system will be colonized as temperature therein should not exceed 121 °C. Then, as hydrothermal cooling progresses and the central melt sheet loses about 75% of its initial heat within the first 20 Kyr (scenario 3.1.3; fig. 3.8), regions closer to the inner-rim, peak ring and surficial rocks of the central valley could start being colonized by microbes. Thus, microbial communities should gradually migrate from the outer-rim regions of the crater to the inner-rim domains, where heat (within the habitable window), water and nutrients are considerably more abundant in these geological niches.

An exciting feature of this habitability simulation is that sterilization (due to fluid flows with temperature beyond the thermal limit of 121 °C) does not occur to the newly formed habitable domain within the crater. In the computational scenarios for the larger craters', the hydrothermal currents from the central melt sheet were affecting periodically the newly formed habitable niches of the crater with temperatures higher than 121 °C, leading to their sterilization. In this 10-km in diameter crater, hydrothermal cooling occurs more rapidly, and after 50 Ky, T_{max} in the entire setting is no higher than 160 °C at a depth of 3 km (fig. 3.8: step D). Therefore, the habitable space should be negligibly affected by hydrothermal flows with T ≈ 121 °C. This explains why no thermal sterilization is evident in this simulation after 22 Kyr.

From 22 Kyr to 72 Kyr, H_2 activity reaches a peak value and the temperature is within the range between 95 – 110 °C. These are optimal conditions for potential hydrogenotrophs to support not only their survival metabolic function but also the maintenance of their biomass. At 32 Kyr after the impact, hydrogenotrophs have fulfilled their maintenance criteria and up to the time point of 72 Kyr their bioenergetic activity is well above their maintenance mode. However, the

water-rock interactions in the hydrothermal system seem to not yield abundant bihydrogen in order to boost the growth rate of potential microbial life. Eventually, from 72 Kyr to approximately 150 Kyr, the availability of H_2 decreases slowly (≈ 50 % decrease). From 150 Kyr to 190 Kyr H_2 activity drops below the maintenance criteria. Hence, after that time point, any potential hydrogenotrophs in the crater should shift to their survival metabolic state. At 290 – 300 Kyr after the impact, this Martian subterranean domain can be considered unhospitable for life, with cold and arid conditions persisting in the entire geological setting. Conclusively, if microbial life was ever present in smaller (D ≤ 10 km) Martian impact-induced hydrothermal systems, then it would have been very difficult for it to potentially grow its biomass; but it should have significantly supported its metabolic functions of survival and maintenance.

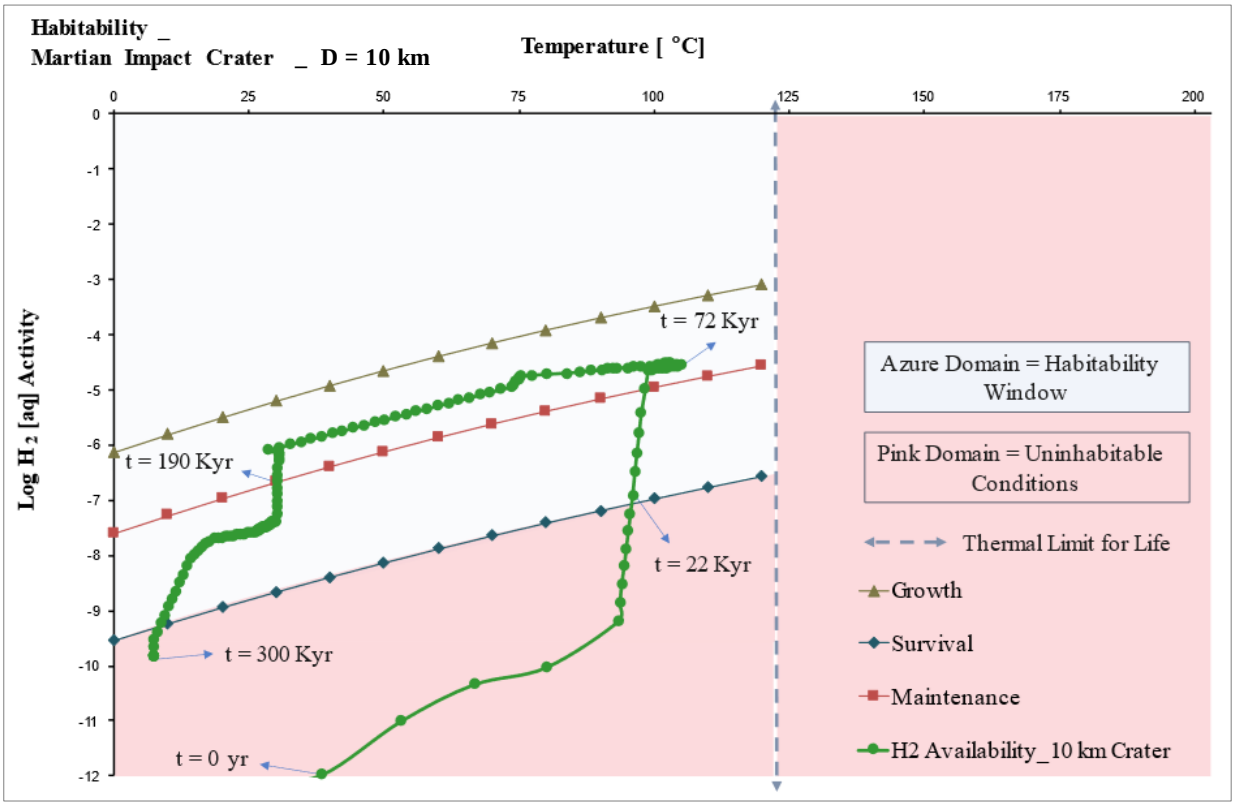

Fig. 3.20. Thermodynamic simulation for the H_2 production and bioenergetics in the subsurface environment of the 10 km in diameter Martian crater. The hydrogenotrophic biomass demand limits (survival, maintenance and growth) were incorporated from Hoehler (2004). Since the upper temperature limit for life is at 121 °C (Kashefi and Lovley, 2003), niches of the geological system, that plot beyond this upper thermal limit during or after the period of hydrothermal circulation, can be considered as uninhabitable and hostile for microbial life (pink domain). On top of that, domains of the impact-induced hydrothermal system where water-rock reactions release amounts of H_2 that plot below the survival mode curve for microbial activity (blue curve in the legend) can also be characterized as uninhabitable in terms of their bioenergetic potential. The thermodynamic properties of this Martian subsurface environment, the duration of Martian basalt – water interactions, and the subsequent H_2 release, depend on the HT simulation results (output) of scenario 3.1.4).

3.3.2 Habitability Computations Dependent on Thermal and H_2 Availability Constraints for the explored Martian Volcanic Settings

Following the strategy presented for the habitability simulations of the impact-induced hydrothermal systems, in this section, the habitability of magmatic-induced hydrothermal systems is also investigated. Starting with hydrothermal scenarios 3.2.1 and 3.2.2 that were presented in the HT simulations sub-chapter, fig. 3.21 and fig. 3.22, summarize the computations for the habitability in the two low-temperature Martian geothermal systems where the maximum temperature value reaches 120 °C, and 170 °C, respectively.

The first bioenergetic simulation (fig. 3.21) shows that no sterilization occurs in the hydrothermal setting, as T_{max} = 120 °C (safely below the upper thermal limit for life, according to Kashefi and Lovley (2003)). As hydrous circulation in this Martian geological system does not last for more than 230 yr, the hydrogen yield in the system cannot reach values that can help overcome the survival mode of microbial metabolic function. Although all domains of the setting that is affected by a low-T (120 °C) geothermal flux are thermally habitable, the chemical nutrients' availability therein can barely and ambiguously support microbial maintenance for a maximum period of 30 yr (as shown by the fuchsia-coloured curve's data plotted between 80 and 110 yr). From 110 yr to 200 yr, H_2 activity in the lithostratigraphic environment still supports the survival state of methanogens, but shortly before 210 yr, the nutrient availability in the system drops below the chemical/lithotrophic limit for life. Thus, we can conclude that such seasonal variations in the geothermal heat flux within the Martian crust, at depths between 0 and 10 km, cannot support potential microbial growth through induced, short-lived water-rock interactions, and neither can they reinforce the maintenance state of any potential microbial species that we are so far aware of.

The habitability simulation which examines the same Martian basaltic rock setting (200 km in horizontal distance × 10 km in depth, 2D grid) under the influence of a higher in temperature flux (with T_{max} = 170 °C; fig. 3.22) is only slightly more promising for potential microbial activity and in a somewhat extended period, when compared to the results of the previous model (fig. 3.21). The bioenergetic model of fig. 3.22 shows that sterilization occurs in the setting between t = 60 yr and t = 135 yr after the induction of warmer geothermal fluxes in the Martian setting. Although T_{max} = 170 °C at a depth of circa 8 km, induced warmer water flows

with T ≥ 121 °C affect all potentially habitable niches of the geological system, even those that are very close to the surface. This simulation's results are contradicting the biogeochemical model of the 10-km in diameter Martian cratering setting, where no sterilization occurs in the newly formed habitable niches of that system.

The explanation for this controversy relies on the parameterization of the computations that were conducted herein. Firstly, the habitable domains in the case of the 10-km Martian crater are located far away from the crater's center. The heat source of the cratering setting, the melt sheet, is spatially constrained within a radius no greater than 1.7 km from the central uplift. Although T_{max} = 700 °C in that region, the cooling pattern significantly differs, and the distant habitable domains of the crater do not get affected by flows with T ≥ 121 °C. In particular, as the central melt sheet cools, hydrothermal flows within the habitable domain do not exceed the temperature of 110 °C. Thus, the spatially constrained heat source in this simulation dictated a significantly localized circulation pattern (within a radius of 2 km: fig. 3.8) of harmful-for-life hydrothermal flows (T ≥ 121 °C), and this resulted to the habitable lithostratigraphic volume remaining unaffected by thermal sterilization. On the contrary, in the scenario of the Martian geothermal setting experiencing geothermally induced flows with T_{max} = 170 °C, the heat source and the generated hydrothermal fluxes dominate the entire deep subsurface realm of the grid (at a depth ≥ 8 km), since the heat source is extended at a 200 km horizontal distance in 2D / diameter in 3D. Thus, these ubiquitous hydrothermal flows that originate from a depth of approximately 8 km transfer heat to all shallower regions of the setting. As a result, the sterilization of any recently formed habitable niches in the shallower lithologies occurs during the period of substantial hydrothermal activity.

Nevertheless, fig. 3.22 shows that after 135 years from the initiation of hydrothermal activity, temperatures in the habitable domains do not exceed the limit of 121 °C. Furthermore, the yield of molecular hydrogen in the geological system due to the ongoing water-rock reactions is considerable for fulfilling the maintenance mode of microbial metabolic activity. From 135 yr to 190 yr, hydrogenotrophs can support the maintenance of their biomass, but after circa 195 yr, they should be shifting towards their survival metabolic state. After 260 yr, although this Martian geological system is thermally habitable, the availability of chemical nutrients is rendering the setting unhospitable for life.

It is noteworthy that, since in this scenario, the T_{max} of the geothermal system is by 50 °C higher than that in the previous case (T_{max} = 170 °C versus T_{max} = 120 °C scenarios), we observe the prolonging effect that this thermal condition has, not only on the duration of the hydrothermal cycle (by 70 years), but also on the perseverance (by 50 years) of hydrogenotrophic life under such bioenergetic limitations. The simulations for the two low-temperature geothermal settings (where T_{max} = 120 °C, and 170 °C) that are described through fig. 3.21 and 3.22, indicate that potential periodical or arbitrary increases in the heat flux within the Martian crust (at depths ≤ 10 km) may induce water-rock reactions and subsequent bioenergetics that cannot persist for a period longer than 210 and 260 yr, respectively. Finally, these two habitability models imply that such geothermally induced water-rock reactions and subsequent biogeochemical processes on Mars may have been occuring during the early-to-late Amazonian period, when the crust is much colder and more arid, and characterized by an average heat flux of circa 21 mW/m^2 (Plesa et al., 2016; Parro et al., 2017).

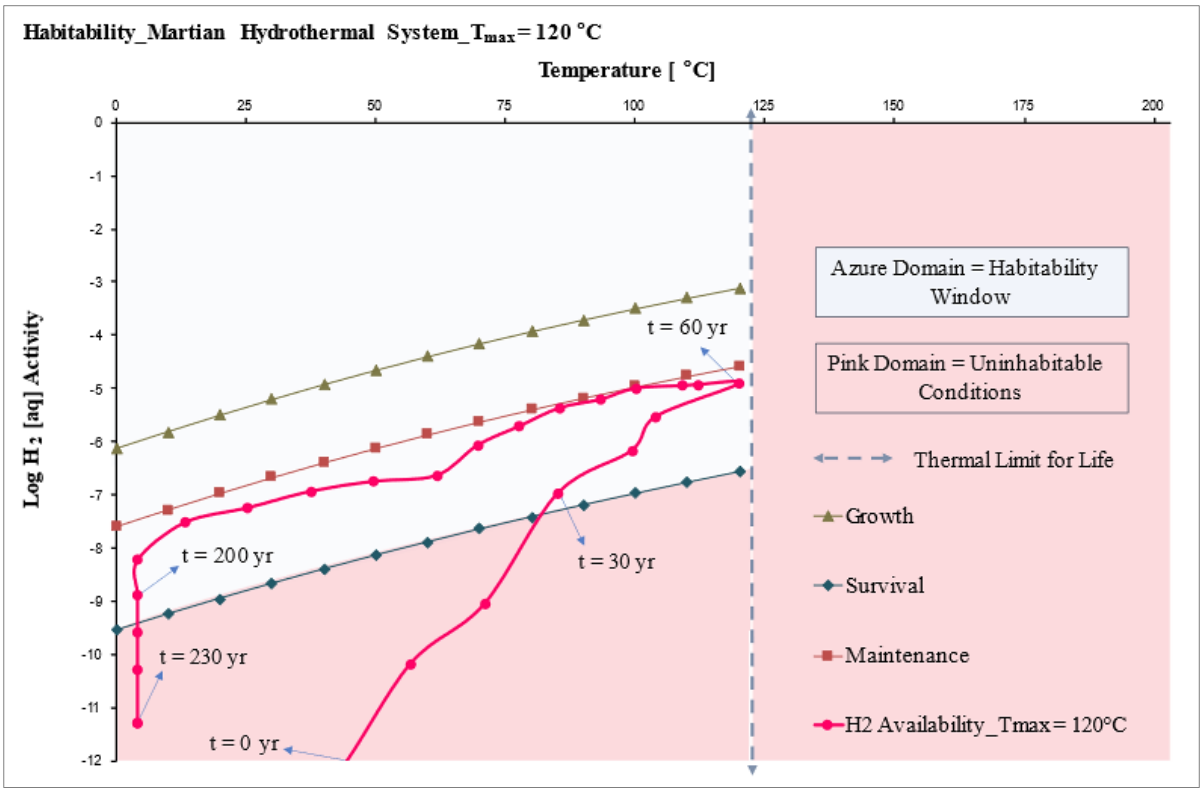

Fig. 3.21. Computed values for the H_2 release and habitability of a Martian basaltic environment under a maximum temperature of 120 °C. The bioenergetic limits for a potential hydrogenotrophic biomass (survival, maintenance and growth, as suggested by Hoehler (2004)) were used to assess the habitability of this Martian basaltic environment. Similar to the computational scenarios for the habitability of the impact-induced hydrothermal systems on Mars, the upper thermal limit for life is set again at 121 °C (according to Kashefi and Lovley, 2003). However, as T_{max} = 120 °C in this simulated geological setting, the main parameter dictating the habitability of this system is the H_2 availability after water-rock reactions. The period during which these aqueous fluid – basaltic rock interactions are ongoing ends at t = 230 yr, and the results show that the system is uninhabitable after t = 200 yr. The bullet points of the curve represent different time periods of the simulation where major changes in H_2 release and temperature have been observed. The time step for each calculation in this simulation was adjusted to 1 day and the bullet points of the curve represent the evolution of the H_2 availability in the system during distinctive periods (hence, the distribution of time frames on the curve (uniformly adjusted to 10 yr) should not be confused with the time step for each calculation (1 d)). During the period of hydrothermal activity from approximately 30 yr to 200 yr, the simulation implies that the system was habitable for a total period of 170 yr, and more specifically, that the thermodynamic system could support the survival, and marginally, the maintenance mode of potential microbial life.

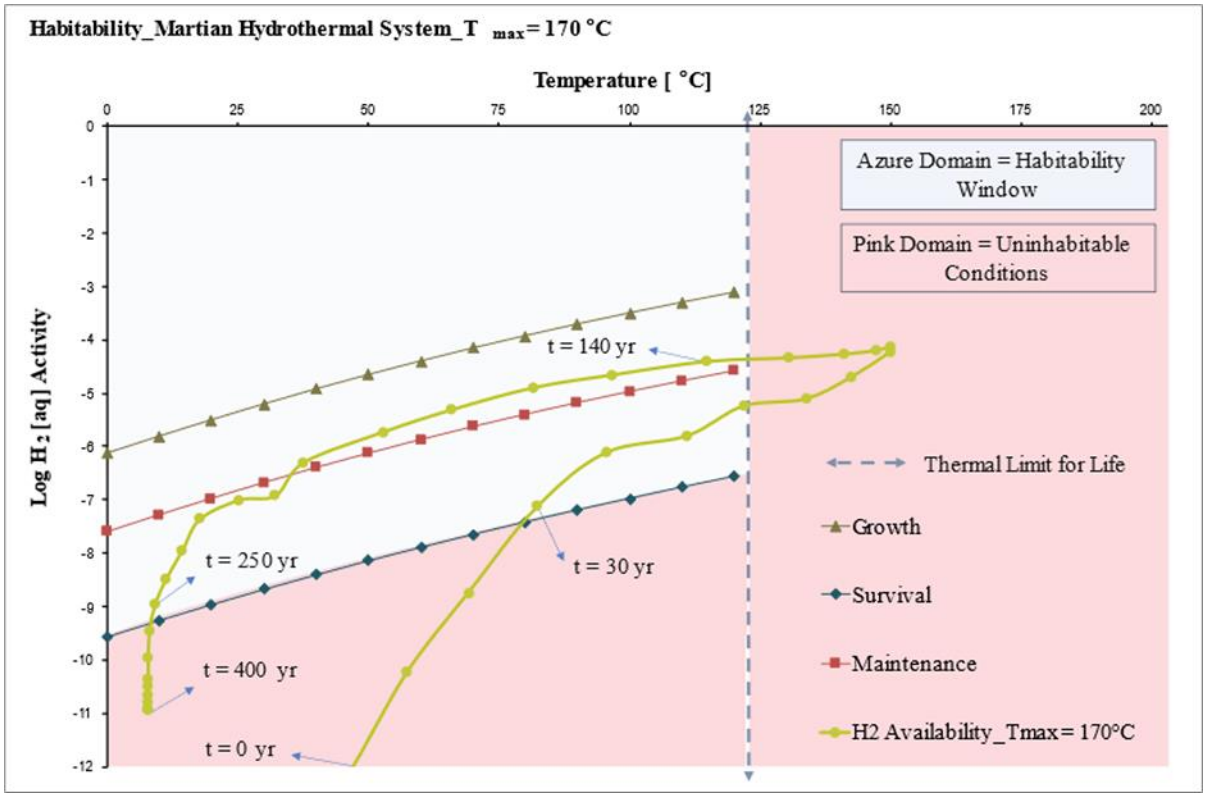

Fig. 3.22. Thermodynamic and habitability model computing the H_2 release of the same Martian basaltic environment under a maximum temperature of 170 °C. The hydrogenotrophic biomass demand limits (survival, maintenance and growth) of Hoehler (2004) were used as a boundary condition for the bioenergetic habitability, and the upper temperature limit for life (121 °C, after Kashefi and Lovley (2003)) governs the thermal habitability of the system. Water-rock interactions occur in the system for a limited period of 400 yr, and the system seems to be rendered hostile for any potential hydrogenotrophic microbial communities after t = 250 – 260 yr. As H_2 release is highly dependent on temperature, the isotherm of 170 °C offers a significant amount of heat in the geological system, and thus, the subsequent production rate of H_2 after water-rock reactions is higher in this case (when compared against the previous scenario: where T_{max} = 120 °C). Moreover, this simulated environment stays habitable for a total period of 220 yr and can even support the maintenance mode of a potential microbial biomass for a period of circa 60 yr (from t = 135 yr to t = 195 yr). The bullet points of the curve represent distinctive time frames of the simulated period where major changes in H_2 release and temperature have been observed. The time step for each calculation in this simulation is set to 1 day and the bullet points of the curve represent time frames (not time steps) that indicate the evolution of H_2 availability in distinctive periods. The distribution of data points on the curve is set to 10 yr. After t = 250 – 260 yr, the computations show that no microbial life could thrive under such energy and thermal limitations; hence, we can assess this Martian geological setting as unhospitable for microbial life after that time point.

The following habitability simulation examines the same putative volcanic province of Mars, with the exception now that the T_{max} in the setting is 400 °C and the basal heat flux is adjusted to 70 mW/m^2. According to the HT simulation in scenario 3.2.3, hydrothermal flows in the system are present for a period of circa 2 Kyr, and some transient and very weak flows ($WMF_{max} \leq$ 2.0E-8 g/s×cm^2) may persist for an additional 2-4 Kyr. Thus, we observe in this simulation that by having extended the T_{max} of the setting to 400 °C (more than 2× greater, when compared to the T_{max} = 170 °C of the previous case) the simulation yields a 10× greater duration of hydrothermal circulation. Hence, water-rock reactions in this Martian geological setting should be occuring continuously during this 2-4 Kyr period of hydrothermal activity. Based on the previously presented HT computations for the thermodynamic evolution of this magmatic environment, it seems that the heat source – plume of this basaltic environment (with T_{max} = 400 °C, at a depth of approximately 8 km; fig. 3.15) cools completely after 4 Kyr.

To fully explore how the bioenergetics of this hydrothermal system are affected, even long after the geothermal gradient has been restored and water flows are negligible, the habitability simulation explores a period of 6 Kyr (fig. 3.23). As in the previous lower temperature geothermal case of T_{max} = 170 °C, sterilization is also evident in this scenario since the plume dominates the entire subsurface realm, from the west to the east vertical boundary of the simulative grid, at a depth of 8 km. The first habitable niches in the setting start forming at circa 200 yr after the emplacement of the plume at a depth of 8 km beneath the Martian surface. The induced water-rock reactions due to the hydrothermal currents that penetrate the upper lithologies of the setting yield appreciable quantities of H_2 during the first 200 yr. Hence, as Fig. 3.23 illustrates, after t = 200 yr, potential microbial life can support its basic survival metabolic function.

However, after 600 yr, much warmer flows with 121 °C ≤ T ≤ 400 °C affect all the newly formed habitable niches of the system and thus, sterilize the subsurface realm of this volcanic province. The basaltic environment stays sterile for about 1.2 Ky (from 600 yr to 1.2 Kyr) but in the meantime, these hydrothermal fluxes boost water-rock reactions and the production of H_2 in the system. After 1.8 Kyr, this Martian subsurface realm can be considered both thermally and chemically habitable. The bihydrogen availability in the system is enough to support the maintenance mode of microbial metabolism, but it cannot reach any concentration that is close to fulfilling the growth metabolic criteria of hydrogenotrophs. For a period of 0.9 – 1 Kyr (from 1.8 Kyr to 2.7 Kyr) the maintenance criteria of microbial life are fulfilled, and this time window

is even shortly after considerable hydrothermal flows have halted. Nevertheless, after this period, any potential microorganism in this geological environment should go into its survival - hibernation state, as the nutrients' availability in the environment plots below the maintenance curve's bioenergetic criteria. Finally, after 4.2 Kyr, the H_2 activity in the system cannot support any basic metabolic function of microbial life and thus, the system is chemically unhospitable, despite being thermally habitable.

We can assume that low to moderate temperature volcanic provinces similar to the simulated one herein, may have been more ubiquitous on Mars during the geological periods of the early Amazonian and Hesperian. Therefore, the results of this Martian habitability model (fig. 3.23) indicate that such magmatic environments on Mars may have not been able to support the growth of any potential (hyper-)thermophilic biomass and the subsequent colonization of the Martian subsurface by microbes. Some spatially constrained microbial communities may have benefited from the conditions of the hydrothermal environment and may have persisted in the system through maintaining their biomass for a few (2-6) Kyr.

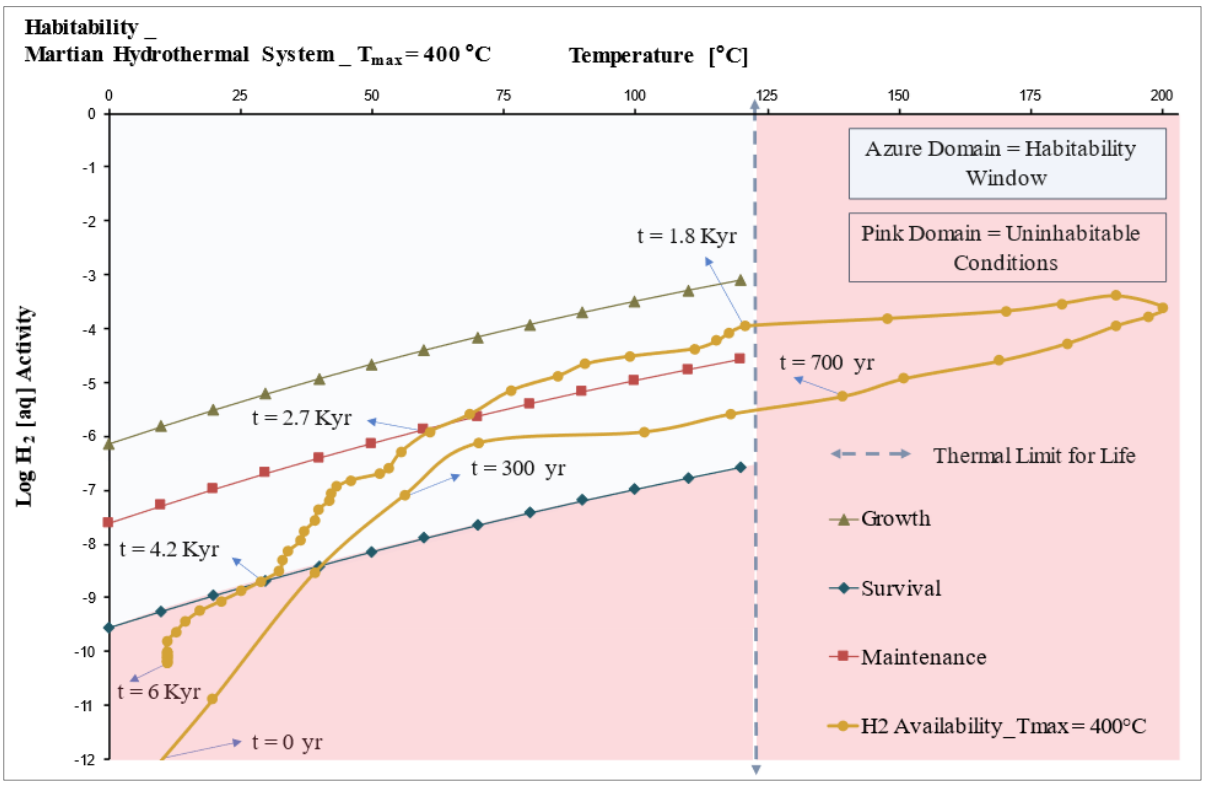

Fig. 3.23. Thermodynamic simulation for the H_2 release and habitability in a Martian subsurface volcanic realm, and under the influence of a T_{max} = 400 °C isotherm. The hydrogenotrophic biomass demand limits (survival, maintenance and growth) provided by Hoehler (2004) were used as the boundary conditions for the bioenergetic

habitability of the simulative environment. As in previous computational scenarios, the upper temperature limit for life is set with the value of 121 °C (Kashefi and Lovley, 2003) and dictates the thermal habitability of the system. In this thermodynamic scenario, the results indicate that water-rock reactions persist in the system for a total period of 6 Kyr; for as long as hydrothermal circulation is active. Although the growth mode of a hypothetical hydrogenotrophic biomass cannot be supported according to the availability of catabolic energy in the system, the environment stays habitable (maintenance and survival mode criteria are satisfied) for a period of circa 2.4 Kyr. Interestingly, the model shows that even though habitable conditions prevailed during an earlier period of hydrothermal activity and within domains where $T_{max} \leq 120$ °C, (approximately from t = 300 yr to t = 600 yr), sterilization occurred soon after t = 600 yr due to the excessive temperature ($T \geq 120$ °C) that was affecting the geological system from circa t = 600 yr to t = 1.8 Kyr. The bullet points of the curve represent time frames of the computed H_2 availability in the geological system, with a constant resolution of 100 yr. The time step for each computation of H_2 release in this simulation was set to 31 days.

Fig. 3.24 and fig. 3.25 represent the computations for the habitability of the same magmatic system on Mars under the influence of intrusive veins with T_{max} = 500 °C and T_{max} = 750 °C, respectively. Both models show that intrusive veins that penetrate this putative domain of the Martian crust produce hydrothermal systems that last for an extensive period of about 2-3 Myr. In the T_{max} = 500 °C scenario (as explained in the previous HT simulations chapter), the combination of the intrusive veins that reach depths of circa 3.5 – 4 km from the surface with 350 °C ≤ T ≤ 500 °C, and the presence of a lower crust – upper mantle plume at a depth of circa 9 km with T_{max} = 500 °C, produces a long-lasting hydrothermal system; a system which yields intense aqueous flows that then interact with the mineralogies of the lithostratigraphic units of the setting during an entire 1.75 Myr period. The HT simulation for the same intrusive volcanism scenario under the influence of a T_{max} = 750 °C (shown in the appendix: Hydrothermal Flows _ Intrusive Veins _ T_{max} = 750 °C _ Higher Permeability.mp4) generates a hydrological system that durates for approximately 3 Myr. Hence, fig. 3.24 and fig. 3.25 (as shown below) summarize the biogeochemical status for this Martian volcanic environment during a period of 1.75 Myr and 3 Myr, respectively.

As presented in the previous cases with the lower thermal boundary conditions (fig. 3.22 - 3.23), sterilization takes place in both of the following simulative scenarios (fig. 3.24 - 3.25), but the duration of the sterilizing effect differs. In the model of fig. 3.24, sterilization persists for a period of 23 Kyr, although in the model of fig. 3.25 sterilization affects all habitable niches of the hydrothermal environment for an extended period of 84 Kyr (from 22 Kyr to 106 Kyr). It is again unclear whether such a sterilization effect may have extinguished all life forms that may have previously colonized habitable areas where abundant heat and water were

present. Aqueous circulation patterns in intrusive volcanic and impact-induced hydrothermal environments, however, imply that warm enough, but non-sterilizing hydrous flows may be affecting the peripheral niches of each setting (as shown in HT scenarios / §3.1 – 3.2). Thus, if microbial species have been in a dormant state at a safe distance from the harmfully hot ($T \geq 121$ °C) hydrothermal cells, then at the later stages of hydrothermal cooling, their initial habitat may get affected by hydrothermal currents transferred via permeable and porous rocks. Such an event could hypothetically trigger the migration of microbial species towards the warmer areas of the hydrothermal setting, after the thermodynamic conditions are favorable for life. Moreover, the thermodynamic and bioenergetic pattern shown in these two simulations is also consistent with the habitability evolution of the impact-induced hydrothermal settings that were described earlier.

The models of fig. 3.24 and 3.25 show that H_2 activity in the volcanic province reaches values that are well above the minimum bioenergetic limit for microbial growth in both thermodynamic cases. Fig. 3.24 indicates that microbial growth in the hydrothermal system should have been possible for a period of almost 0.9 Myr (from 45 Kyr to 900 Kyr). This should be an extensive time and thermodynamic window of opportunity for potential lithotrophic organisms to harvest the chemical nutrients that are being released in the system and build their biological colonies. Additionally, fig. 3.25 implies that the duration of habitable conditions that can reinforce microbial growth in the same volcanic province under the influence of a $T_{max} = T_{initial} = 750$ °C, is doubled and approximately close to 1.7 Myr. Therefore, this scenario along with the bioenergetic models of the 200- and 100-km in diameter craters, represent optimistic hypotheses for the habitability of Martian hydrothermal systems.

As indicated in the bioenergetic simulation of fig. 3.25, the $T_{max} = 500$ °C scenario demonstrates that after 1.75 Myr, the system can be considered marginally habitable, since the H_2 availability in the system is slightly above the minimum bioenergetic limit of microbial survival. Nevertheless, H_2 activity at the latest stage of hydrothermal cooling seems to be significantly stabilized. Thus, based on the evolution of the H_2 curve (grey-coloured in fig. 3.24), we can assume that microbial survival could be sustained for another 200 – 300 Kyr (after 1.75 Myr), before H_2 activity decreases below the lower bioenergetic limit for survival. Comparatively, the last habitability simulation (fig. 3.25: $T_{max} = 750$ °C) proves that microbial survival is fulfilled even long after water-rock interactions have ceased, and the volcanic system has been rendered inactive. At the latest stages of hydrothermal cooling, we can deduct

from fig. 3.25 that, not only microbial survival is bioenergetically supported by the geochemical substrates, but also the maintenance requirements of the putative biomass (from 1.86 Myr to 2.7 Myr, when water mass fluxes are somehow negligible: $WMF_{max} \leq$ 2.0E-8 g/s×cm^2). Consequently, at t = 3 Myr, H_2 activity in the system plots between the survival and maintenance limits of microbial metabolism. If we were to sample this hypothetical biogeochemical province of Mars, based on how microbes' metabolisms function and evolve here on Earth, we can speculate that some of our sampled Martian microbes should have been observed in a semi-dormant state; whereas a considerable population of hydrogenotrophs could be possibly releasing lower-than-average quantities of methane, as a byproduct of its sluggish metabolic function under such thermodynamic conditions.

The habitability simulations represented by fig. 3.24 and 3.25 indicate that such a volcanic environment on Mars, with a maximum temperature present in the geological system between 500 °C and 750 °C, can host optimal conditions for the metabolic growth of microbial life for hundreds of Kyr, and result to the subsequent microbial colonization of this hydrothermal province. Since such geothermal systems can host a hydrological cycle for more than a couple of Myr, provinces of the Red Planet that provide evidence of active volcanism during earlier geological epochs (e.g., the Tharsis and Elysium volcanic provinces) should be primary candidate sites for the search of biosignatures in the Martian subsurface.

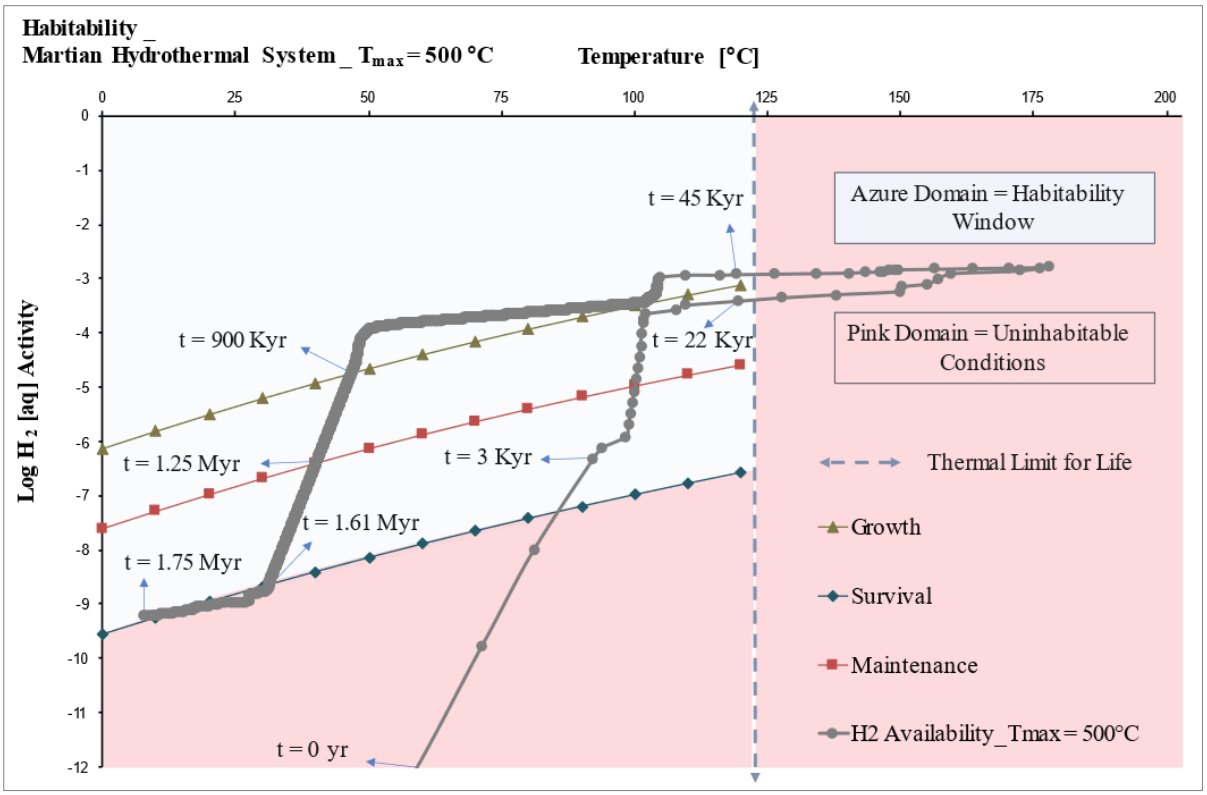

Fig. 3.24. Thermodynamic simulation for the H_2 release and habitability in the Martian basaltic crust, under the influence of a T_{max} = 500 °C. The hydrogenotrophic biomass demand limits (survival, maintenance and growth) provided by Hoehler (2004) define the boundary conditions for the habitability of the hydrothermal environment. The simulation shows that hydrothermal fluid – basaltic rock reactions in the geological setting are ongoing for a total period of 1.5 Myr, and that the growth mode bioenergetic criteria of a potential hydrogenotrophic community have been satisfied for a total period of 855 Kyr (from t = 45 Kyr to t = 900 Kyr). Additionally, at the latest stages of hydrothermal cooling, from 900 Kyr to 1.25 Myr, the H_2 availability in the volcanic setting fulfils the maintenance mode of a potential microbial community. On top of that, the habitability computations show that even after hydrothermal circulation has ceased (after approximately 1.5 Myr), the geological system has appreciable H_2 quantities to support the survivability of microbes. As in previously presented habitability models for the Martian basaltic crust, it is also evident in this scenario that, when isotherms of T ≥ 120 °C affect the potentially habitable niches of this Martian subterranean environment, sterilization occurs from circa 22 Kyr to 45 Kyr (due to the thermal limit for life being set at 121 °C in the simulation, after Kashefi and Lovley (2003)). The bullet points of the curve represent time frames of the computed H_2 availability in the hydrothermal environment with a step resolution of 1 Kyr. The time step for each computation of H_2 release in the system after water-rock reactions was set to 100 yr.

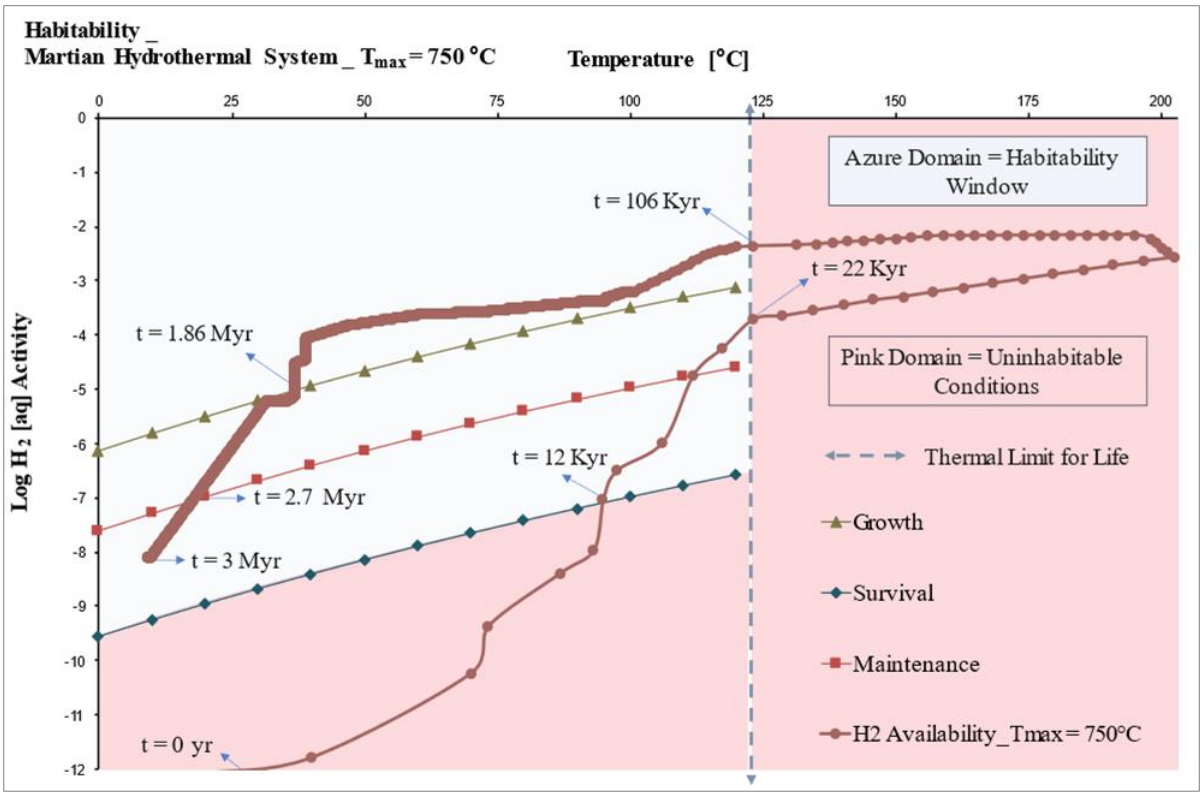

Fig. 3.25. Numerical simulation for the H_2 release and habitability in the Martian basaltic crust, under a T_{max} = 750 °C. The hydrogenotrophic biomass demand limits (survival, maintenance and growth) provided by Hoehler (2004) define the boundary conditions for the bioenergetic habitability of this Martian volcanic setting. The thermal limit for life was set again at 121 °C (after Kashefi and Lovley (2003)). This simulation calculates the H_2 release in the geological environment after the interaction of Martian peridotite and basalt with hydrothermal fluids (initial seawater composition was assumed for the hydrothermal fluid). These geochemical reactions occur and produce H_2 for as long as hydrothermal circulation is active, i.e.: for a total period of circa 2 Myr. The growth mode criteria of a potential hydrogenotrophic biomass appear fulfilled for a total period of circa 1.9 Myr (from t = 106 Kyr to t = 2 Myr). This implies that any potential hydrogenotrophs could have thrived under such magmatic conditions within the Martian crust. The simulation indicates that from 2 Myr to 2.7 Myr, the maintenance mode criteria of microbial life have been satisfied. Moreover, even long after hydrothermal circulation is inactive (after approximately 2 Myr), the H_2 reserve that accumulated during this period in the setting can support the survival of hydrogenotrophic microbial life not only from 2.7 Myr to 3 Myr, but logically for a much longer period after that time point (based on the computed H_2 value at t = 3 Myr, which significantly exceeds the bioenergetic criteria of the survival mode). The bullet points of the curve represent time frames of the computed H_2 availability in the hydrothermal environment with a step resolution of 2 Kyr. The time step for each computation of H_2 release in the simulated Martian geological environment after aqueous fluid – volcanic rock reactions was adjusted to 1 Kyr.

3.4 Microanalyses of Martian Meteorite Samples Supporting the Numerical Models for Hydrothermalism on Mars

The microscopy investigation aims of this PhD research were primarily focusing on thorough high precision microscopy (micro-, and nano-scale elemental composition) analysis of Martian meteorite samples to:

- Establish the porosity of the NWA 8159 and Lafayette rock samples by processing their exported SEM-BSE maps (tiff) via the ImageJ software. Porosity comprises a significant factor that governs hydrothermal circulation in volcanic or impact-induced settings. Therefore, determining the porosity of NWA 8159 and Lafayette would constrain efficiently and benchmark the hydrothermal simulations of this PhD research.

- Examine the NWA 8159 and Lafayette Martian meteorite samples through SEM (by acquiring SEM-BSE and SEM-EDS elemental composition maps) to assess the geochemistry of their volcanic environments of origin on Mars.

- Simulate the geochemistry reaction pathways of the Martian water-rock systems via the PHREEQC code and validate the developed PHREEQC simulations based on SEM observations.

- Establish an origin for the fluids that have affected the meteorites' host rocks on Mars and compare their aqueous alteration products with the assumed aqueous activity of distinctive geological periods.

- Distinguish the Martian alteration from the terrestrial weathering products via SEM-EDS elemental composition maps.

- Reliably determine via the HYDROTHERM code the duration of the aqueous activity that has affected these meteorite samples and compute fluid mass flux, pH, enthalpy, Gibbs free energy and other thermodynamic parameters of their host environments on Mars.

- Assess the habitability of the Martian palaeoenvironments that these basaltic rocks sample via PHREEQC simulations.

The COVID-19 pandemic prohibited lab-based microscopy analyses during the lockdown periods. Furthermore, it severely impacted microscopy analysis after the reopening of research facilities at the University of Glasgow and at other collaborating research institutes (University of Edinburgh - UK, University of Sydney - Australia, Smithsonian Institute -USA, Arizona State University - USA), as the state and performance of high precision analytical instruments could not allow the acquisition of reliable datasets, due to maintenance issues of the instruments after extensive periods of lockdowns. Therefore, this PhD research eventually focused on simulating the thermodynamics of hydrothermal systems on Mars and on computing the habitability of Martian hydrothermal environments mainly via numerical modelling techniques.

Nevertheless, detailed microscopy investigations were performed during the academic year 2018-2019, and some insightful elemental composition datasets from two Martian meteorite samples (NWA 8159 and Lafayette) were also obtained during the period March 2020 – August 2022. These mineralogical and elemental composition datasets significantly assisted the parameterization of the numerical simulations of this work and their subsequent interpretations. Particularly, several indications of the constructed numerical models regarding hydrothermal circulation in the Martian crust were proven consistent with the elemental composition results of microscopy analyses and with the input porosity values of numerical models. ImageJ software processing established the porosity for each of the three Martian rock thin-sections (NWA 8159 samples 1 and 2, and Lafayette sample USNM 1505-5) and yielded porosity results that agree with the input porosity parameters used to construct the hydrothermal simulations. Additionally, the micro-, and nano-scale analysis of the NWA 8159 and Lafayette meteorite samples revealed the presence of phyllosilicate in their primary mineralogies (in apatite and olivine), which is in accordance with the HT 3 simulations; as HT3 hydrothermal models predicted the self-sealing of pores and fractures due to precipitation of clay/phyllosilicate minerals in Martian permeable and porous lithologies during hydrothermal cooling.

The nature of the phyllosilicate in NWA 8159 has yet to be established as Martian or terrestrial in origin, since the sample suffers by extensive terrestrial contamination (Christou et al., 2019).

Thus, more thorough nano-scale analyses in the near future via correlative Electron Probe Micro-Analysis (EPMA), Transmission Electron Microscopy (TEM), Nano – Secondary Ion Mass Spectrometry (Nano – SIMS) and Atom Probe Tomography (APT) are required to determine the origin of phyllosilicate in NWA 8159, and to correlate and validate such mineralogical findings with the numerical modelling results of this work. SEM-EDS investigations focused further on detecting minerals that are of hydrothermal origin (e.g.: laihunite; Vaci et al., 2016) in the NWA 8159 and Lafayette samples, but the results were negative; i.e., no minerals of hydrothermal origin were detected. Nevertheless, due to preliminary findings that support the presence of hydrothermal minerals in NWA 8159 (Vaci et al., 2016) more thorough APT and nano-SIMS examinations are needed in order to confirm the presence or absence of hydrothermal mineralogies in these Martian rock samples. Finally, the bulk rock compositions of NWA 8159 and Lafayette reported previously (Lee et al., 2015b; Herd et al. 2017; and references therein), and as observed through SEM research in the GEMS facility of the University of Glasgow, accord with the thermodynamic database input parameters that describe the Martian basaltic rocks of the PHREEQC simulations (McSween et al., 2006a; 2006b; Peretyazhko et al., 2018; Thorpe et al., 2022; and as discussed in § 2.2).

3.4.1 Scanning Electron Microanalyses of the Martian Rocks NWA 8159 & Lafayette

3.4.1.1 SEM-EDS Analysis of the NWA 8159 Meteorite

Two samples of the Martian meteorite NWA 8159 were analysed during this PhD research project, revealing the basaltic composition of this volcanic rock from Mars. SEM-EDS observations on NWA 8159 sample 1 (7.5 × 1.3 mm) revealed 48 apatite grains greater than 10 μm in size (fig. 3.26 – 3.29). These apatites are mainly associated with magnetite phenocrysts. NWA 8159 sample 2 (5.0 × 3.5 mm) has similar apatite abundance and texture (fig. 3.30). Through SEM analyses of NWA 8159, several anhedral apatite grains less than 10 μm in size, with a sub-grain granular texture (fig. 3.31) and with identical intergrown magnetite and a Si-rich phase were identified (fig. 3.26 – 3.31). NWA 8159 apatite undoubtedly exhibits extensive aqueous alteration, but through SEM observations it remains unclear whether this alteration is related to ancient aqueous activity on Mars or terrestrial contamination after the meteorite fell to Earth. However, SEM-EDS analyses were quite efficient in identifying the

effects of terrestrial weathering on this meteorite, as calcite veins cross-cut the meteorite in numerous places (as shown through the SEM-EDS elemental composition maps: fig. 3.26 – 3.30). In general, the BSE and EDS analyses on the two NWA 8159 samples revealed a basaltic shergottite that exhibits both Martian alteration and terrestrial weathering.

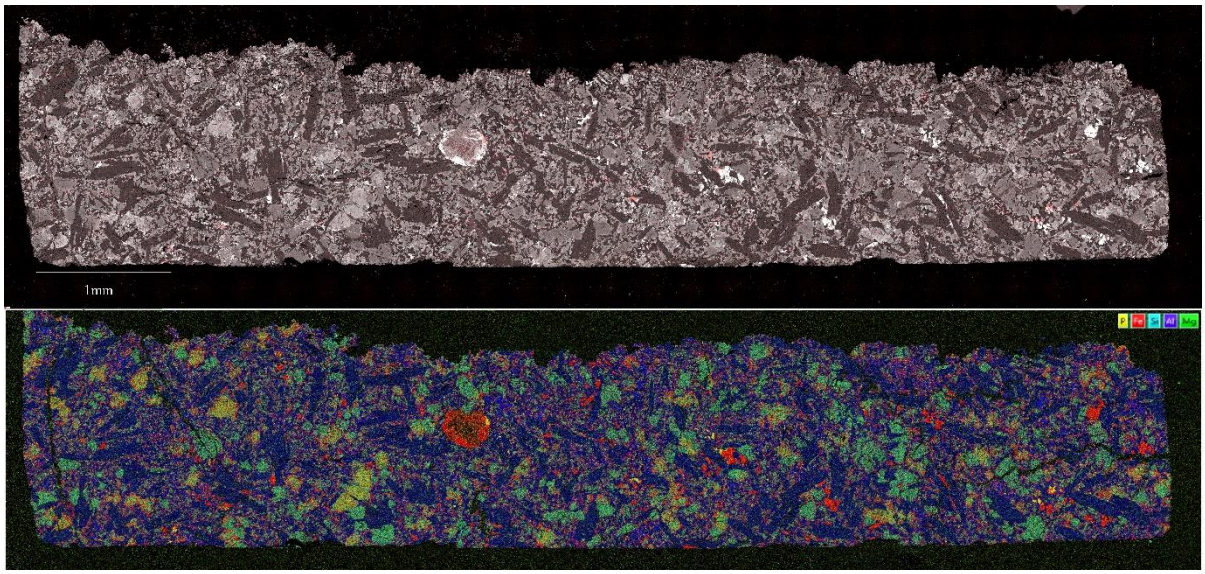

Fig. 3.26. BSE map (up) and SEM-EDS (false-coloured) map of the NWA 8159 sample 1 (thin section) with apatite revealed in false-coloured pink (BSE map) or shiny yellow (false-coloured map) regions (zoom-in needed). The mineralogy and alteration phases in NWA 8159 were identified through SEM-EDS analysis at the GEMS facility of the University of Glasgow. NWA 8159 sample 1 _ SEM overview (linked to Fig. 3.27 – 3.29). Resolution (Width): 13926 pixels; Resolution (Height): 3532 pixels; Pixel Size: 3.54713 µm; Dwell Time: 35µs. SEM was operated at an accelerating voltage of 20.00 kV, and a moderate-low beam current of 1nA was applied.

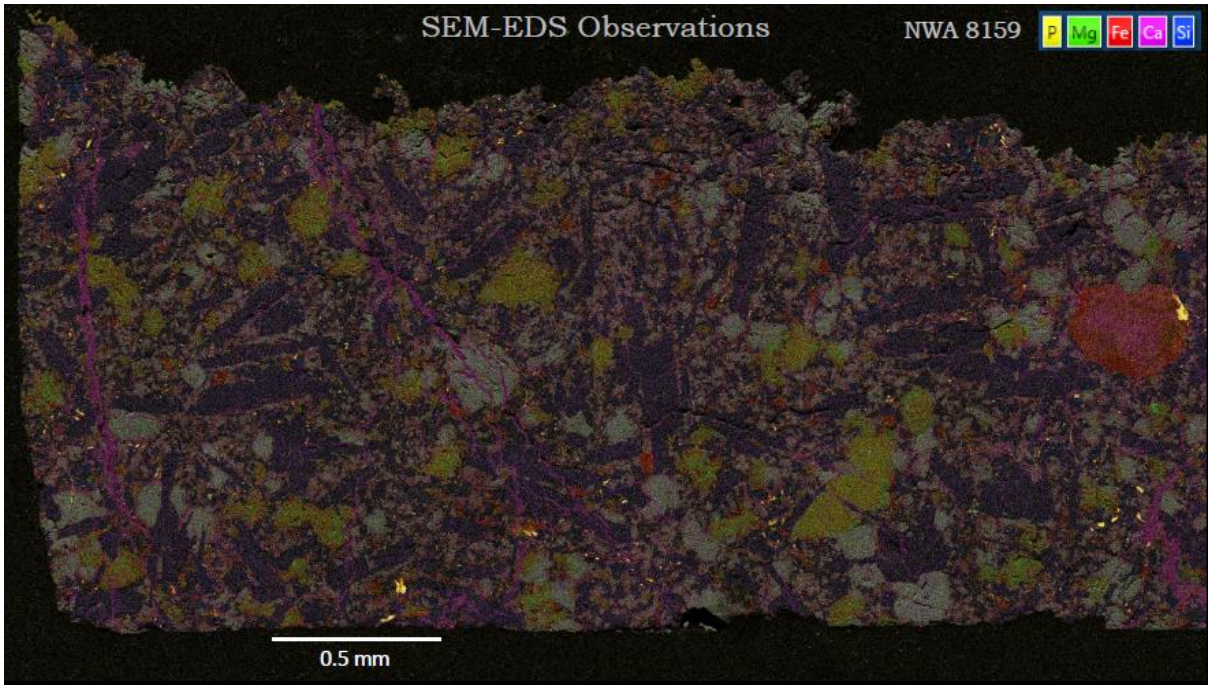

Fig. 3.27. SEM-EDS false coloured map for the western segment of the NWA 8159 thin-section 1. Calcite veins are shown in pink colour, olivine grains in olive-green colour, Fe-oxides/hydroxides in red, pyroxenes in grey-light blue colour; apatite grains are tiny (≤ 15µm in size), but can be indentified as false-coloured shiny yellow minerals, representing a high P content. Image Resolution (Width): 3674 pixels; Resolution (Height): 1697 pixels Pixel Size: 0.70368 µm; Dwell Time: 35µs. SEM was operated at an accelerating voltage of 20.00 kV, and a moderate-low beam current of 1nA was used for the SEM analysis of NWA 8159.

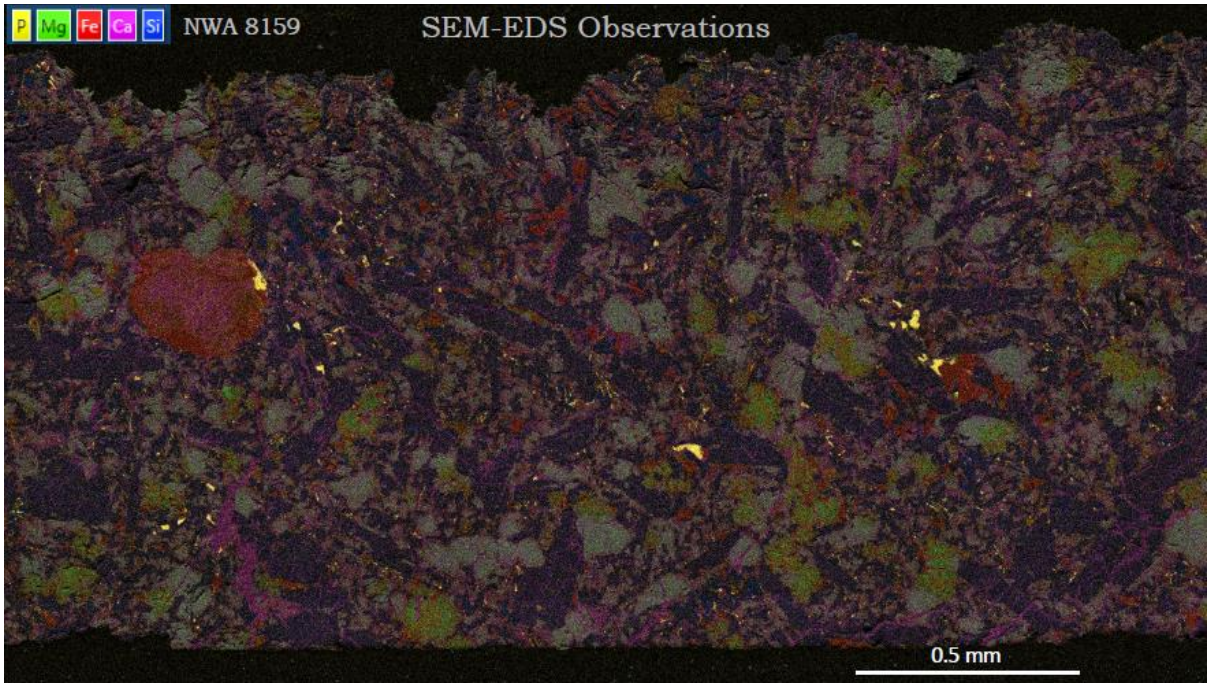

Fig. 3.28. SEM-EDS false coloured map for the central segment of the NWA 8159 thin-section 1. Calcite veins are shown in pink colour, olivine grains in olive-green colour, Fe-oxides/hydroxides in red, pyroxenes in grey-light blue colour; and apatite grains can be identified as false-coloured shiny yellow minerals, representing a high P content. Image Resolution (Width): 3458 pixels; Resolution (Height): 1641 pixels; Pixel Size: 0.78680 µm; Dwell Time: 35µs. SEM was operated at an accelerating voltage of 20.00 kV and under a moderate-low beam current of 1nA.

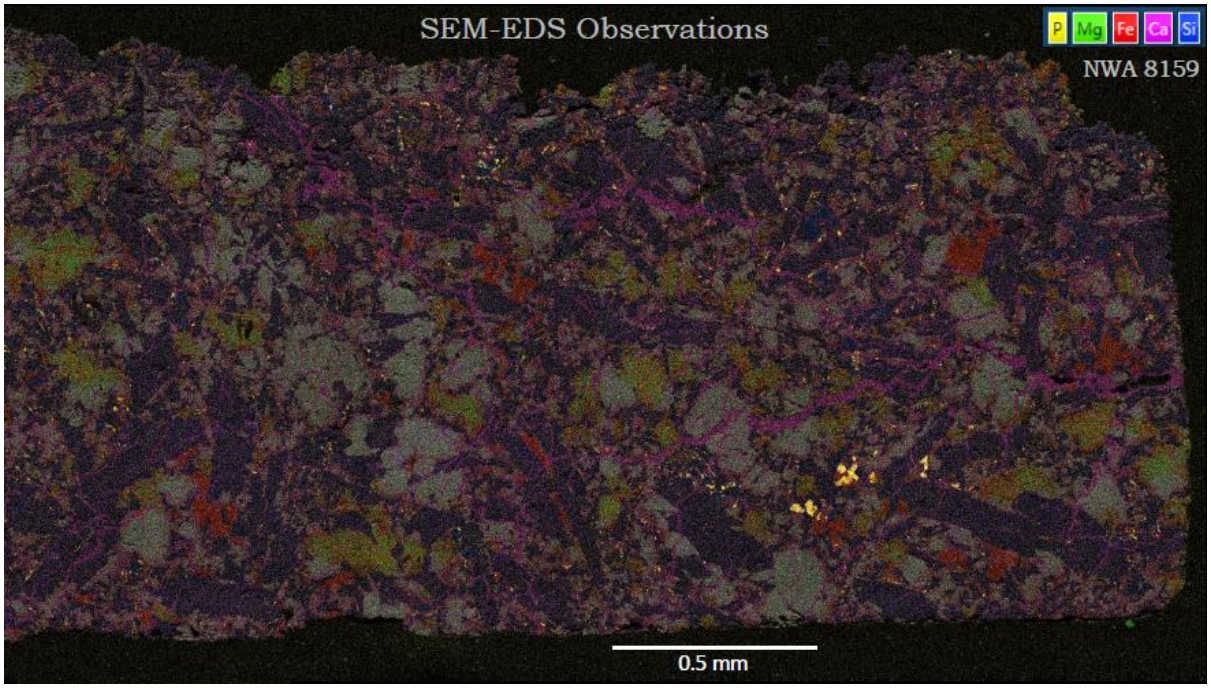

Fig. 3.29. SEM-EDS false coloured map for the eastern segment of the NWA 8159 thin-section 1. Calcite veins are shown in pink colour, olivine grains in olive-green colour, Fe-oxides/hydroxides in red, pyroxenes in grey-light blue colour; and apatite grains can be identified as false-coloured shiny yellow minerals, representing a high P content. Image Resolution (Width): 3321 pixels; Resolution (Height): 1579 pixels; Pixel Size: 0.79077 µm; Dwell Time: 35µs. SEM was operated at an accelerating voltage of 20.00 kV, and SEM analysis was performed under a moderate-low beam current of 1nA.

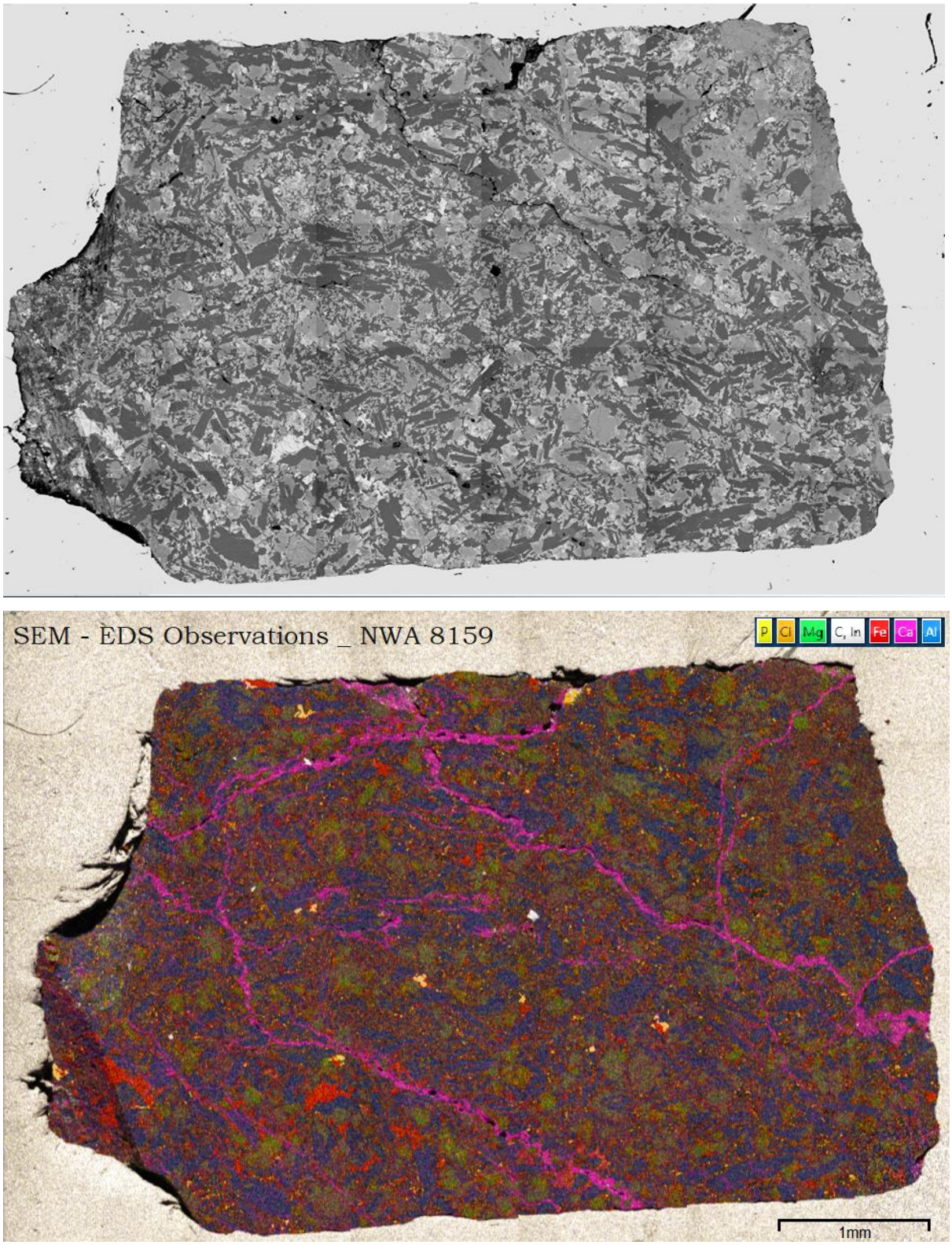

Fig. 3.30. SEM-EDS false coloured map for the central segment of the NWA 8159 thin-section 2. Calcite veins are shown in pink colour, olivine grains in olive-green colour, Fe-oxides/hydroxides in red, pyroxenes in grey-light blue colour; and apatite grains can be identified as false-coloured shiny yellow minerals, representing a high P content. Resolution (Width): 5734 pixels; Resolution (Height): 3594 pixels; Pixel Size: 2.40368 µm. SEM instrument was operated at an accelerating voltage of 20.00 kV, and analyses were conducted under a moderate-low beam current of 1nA.

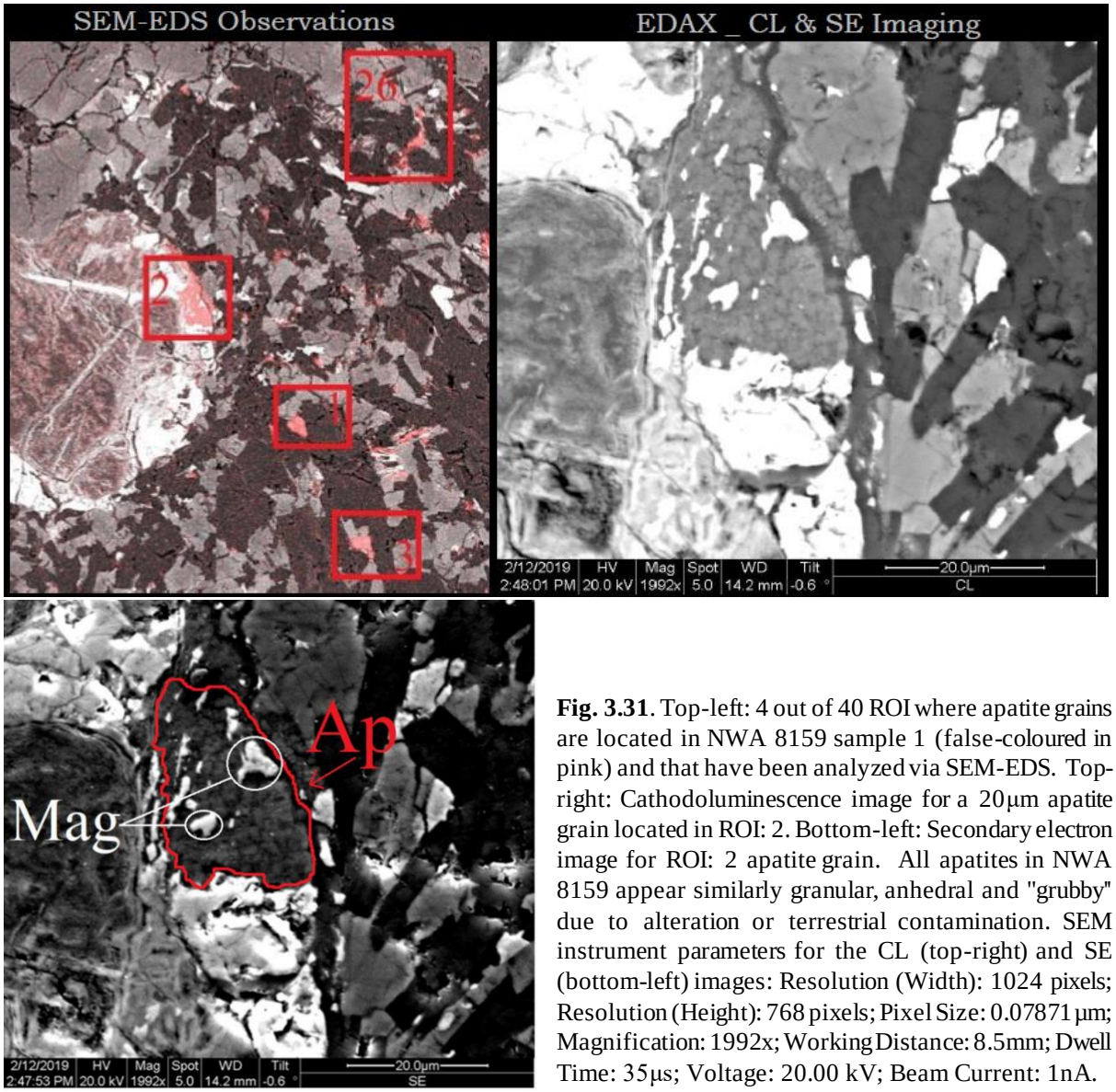

Fig. 3.31. Top-left: 4 out of 40 ROI where apatite grains are located in NWA 8159 sample 1 (false-coloured in pink) and that have been analyzed via SEM-EDS. Top-right: Cathodoluminescence image for a 20µm apatite grain located in ROI: 2. Bottom-left: Secondary electron image for ROI: 2 apatite grain. All apatites in NWA 8159 appear similarly granular, anhedral and "grubby" due to alteration or terrestrial contamination. SEM instrument parameters for the CL (top-right) and SE (bottom-left) images: Resolution (Width): 1024 pixels; Resolution (Height): 768 pixels; Pixel Size: 0.07871 µm; Magnification: 1992x; Working Distance: 8.5mm; Dwell Time: 35µs; Voltage: 20.00 kV; Beam Current: 1nA.

3.4.1.2 SEM-EDS Analysis of the Lafayette meteorite

SEM-EDS microanalyses were also performed at the GEMS facility of the University of Glasgow to identify the aqueous primary minerals and alteration phases in one Lafayette thin section sample (Fig. 3.32 and 3.33). Nakhlites exhibit Martian aqueous alteration more ubiquitously than any other group of Martian meteorites (Treiman, 2005). Specifically, Lafayette contains veins of alteration within olivine grains that are indicative of nakhlitic rock – fluid interactions on Mars. The observed alteration veins in the nakhlite group are of phyllosilicate, Fe-oxide, hydroxide and carbonate composition (Changela and Bridges, 2011). Furthermore, the alteration minerals in nakhlite rocks should have precipitated during the Amazonian period, which is the latest and driest period in Mars' history (Okazaki et al., 2003). The acquired SEM-EDS montage maps (fig. 3.32 and fig. 3.33) revealed more than 20 large enough apatite grains (> 25 μm in diameter; ROI) in thin section USNM 1505-5 from which the elemental content of apatite, olivine and augite crystals could be further constrained. However, due to the lockdown or due to maintenance issues of the lab facilities, no further analysis could be performed prior to the completion of this PhD thesis.

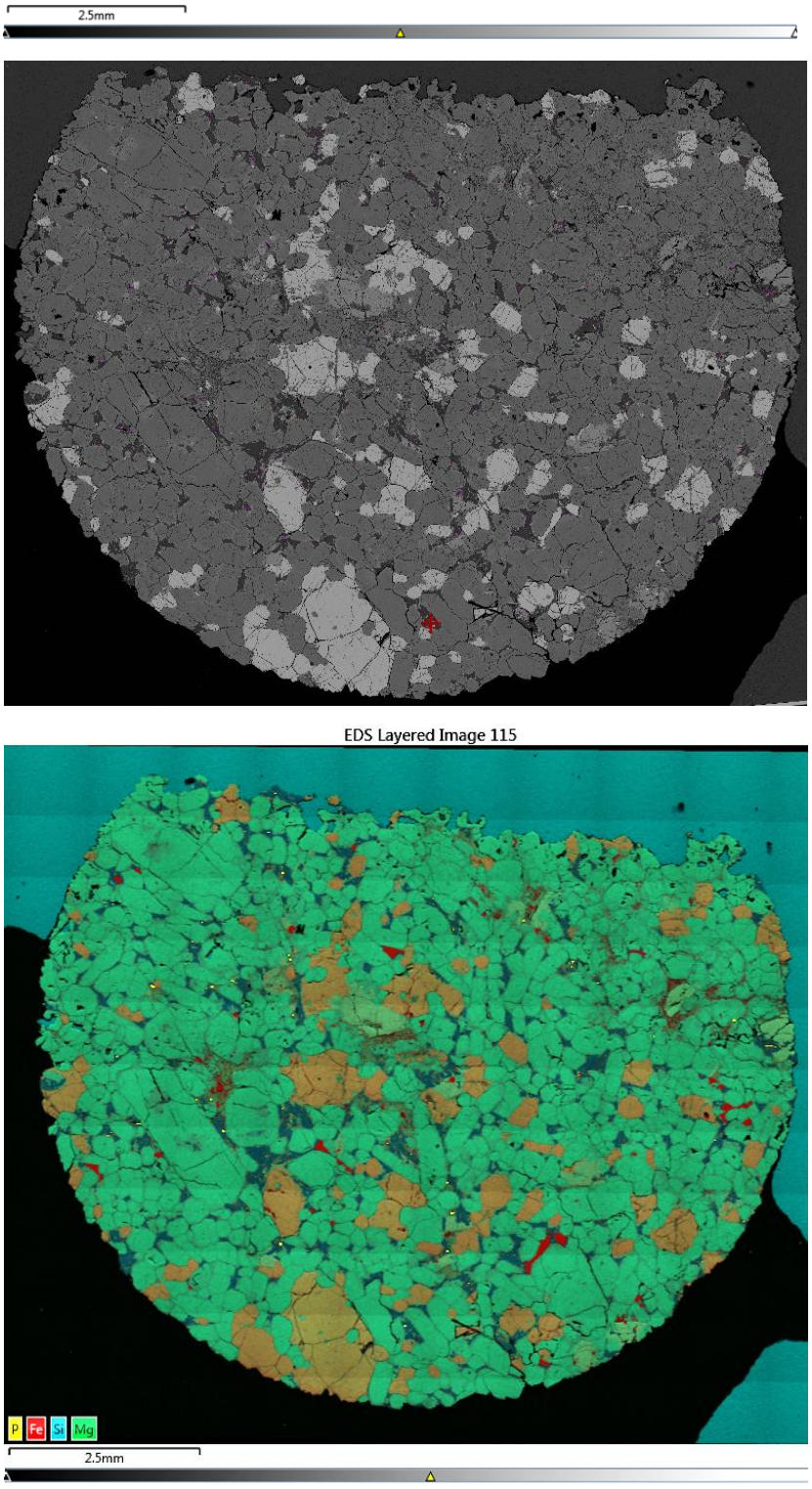

Fig. 3.32. BSE map (upper) and SEM-EDS (false-coloured; lower) map of the Lafayette thin section in which apatite grains are illustrated in yellow (false-)colour by zooming in. False-coloured pale beige grains illustrate olivine grains, the ubiquitous azure-greenish grains represent augite, and red-coloured crystals indicate the Fe-oxides in the sample. The mineralogies and alteration phases in Lafayette were identified through SEM-EDS analysis at the GEMS facility of the University of Glasgow. Image Resolution (Width): 4724 pixels; Resolution (Height): 3818 pixels; Pixel Size: 2.40736 µm; Dwell Time: 35µs; SEM instrument was operated at an accelerating voltage of 20.00 kV, and a moderate-low current of 1nA was adjusted for the beam.

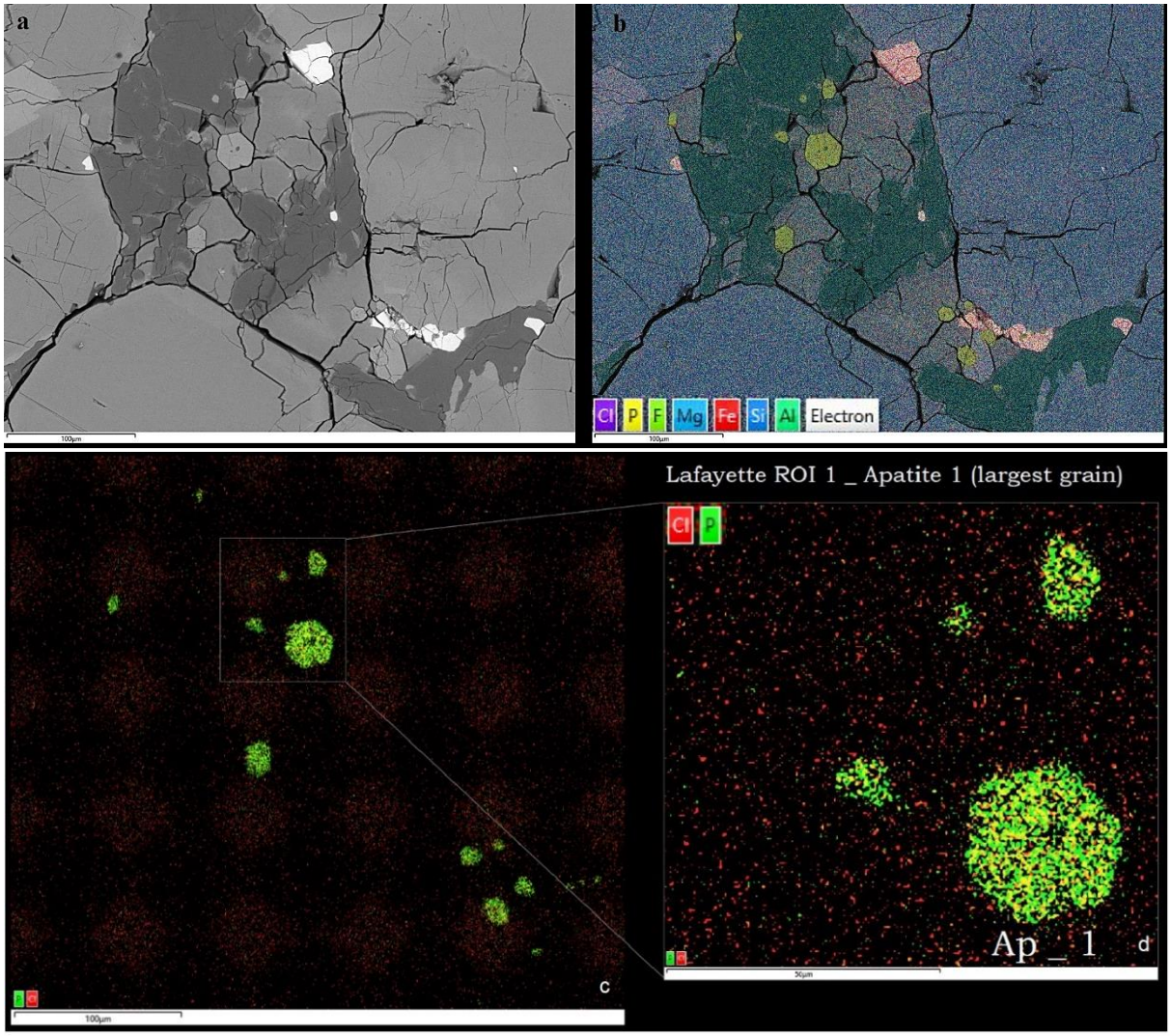

Fig. 3.33. BSE Image from ROI 1 (a). SEM-EDS (false coloured) map of the ROI 1 (b) in which one sufficiently large apatite grain (Ap 1 size > 25 µm) ideal for nano-scale analyses has been identified. Zoomed-in SEM-EDS phosphorus (P) and chlorine (Cl) map of ROI 1, revealing the elemental content (c-d) of the larger apatite grain and of the smaller crystals in its vicinity. Apatite in Lafayette appears much more enriched in chlorine (Cl), which is also the case for most nakhlitic apatite (McCubbin et al., 2013), when compared with apatite in NWA 8159. SEM instrument parameters for the BSE and EDS maps (a-c): Resolution (Width): 1024 pixels; Resolution (Height): 768 pixels; Pixel Size: 0.27307 µm; Magnification: 1102x; Working Distance: 8.5 mm; Accelerating Voltage: 20.00 kV; Beam Current: 1 nA. SEM instrument parameters for the zoomed-in SEM-EDS map (d): Resolution (Width): 1024 pixels; Resolution (Height): 876 pixels; Pixel Size: 0.07245 µm; Magnification: 3823x; Working Distance: 8.5mm; Accelerating Voltage: 20.00kV; Beam Current: 1 nA.

3.4.2 Determining the Porosity of the NWA 8159 & Lafayette Meteorites via ImageJ.

Three BSE (tiff) images which comprise whole-sample BSE maps of the three Martian meteorite samples studied through SEM in this PhD research, (two thin-sections of NWA 8159 (samples 1 and 2) and the Lafayette thin section USNM 1505-5), were thoroughly processed via the ImageJ software to determine the porosity of these Martian rock samples (fig. 3.34). Porosity is a significant physical parameter that governs hydrothermal circulation alongside permeability. For this reason, establishing the porosity of these Martian rock samples could constrain further and enhance the robustness of the HT simulations for the hydrous and hydrothermal activity on Mars.

The processed tiff (BSE map) of NWA 8159 sample 1 through ImageJ shows that the porosity of NWA 8159 sample 1 is calculated with a value of 5.27% (fig. 3.34(a) and table 3.7). This result agrees with the porosity values used for the basaltic rocks of the simulated impact-cratering settings via HT. Specifically, porosity was adjusted to 5% for the basalts of the simulated larger impact structures (100-, and 200-km in diameter), and 4% for the 10-km in diameter crater (please see tables 3.1 – 3.4). Similarly, the porosity of the Lafayette USNM 1505-5 sample was calculated with a value of 4.93 % via ImageJ processing, which is also in accordance with the 4 – 5 % porosity input values used in the fluid-mechanics models to account for the basaltic rocks of Martian hydrothermal systems (fig. 3.34(c) and table 3.7). Conclusively, as larger impact structures are expected to exhibit higher (impact-generated) porosity in their target rocks than smaller impact structures (Abramov and Kring, 2004; 2005; 2007), the ImageJ analyses on the Martian meteorites' BSE maps indicate that the input parameterization of the HT models is accurate and that the resulting hydrothermal simulations are reliable (please compare the porosity values of table 3.7 with the HT input porosity values of tables 3.1 – 3.4).

However, ImageJ analysis on the BSE map of NWA 8159 sample 2 yielded a porosity value of just 2.2 %. Although both NWA 8159 thin sections originate from the same chunk of this Martian meteorite, they do not exhibit the same distribution of pores and cracks, as evidenced through SEM analysis and from the ImageJ results shown in table 3.7 and fig. 3.34. This heterogeneity of porosity in the two NWA 8159 samples may be a result of sample preparation, or most likely, it may be linked to the heterogenous distribution of terrestrial alteration and weathering that evidently affected this Martian meteorite during its entry into Earth's

atmosphere, or/and after its fall in the Moroccan desert (Hallis et al., 2016; Christou et al., 2019; 2020; 2021). On another note, if we implausibly assume that the ImageJ calculation for the porosity of NWA 8159 sample 2 is the most accurate one (and ignore the values of 4.93 % and 5.27 % for Lafayette and NWA 8159 sample 1, respectively), this would contradict previous modelling results from Abramov and Kring (2005); who calculated that impact-induced porosity in the Martian crust could be distributed in far greater depths than on Earth due to the significantly lower gravity (3.71 m/s^2) of the Red Planet, and that lower-crustal basement rocks of Martian craters should exhibit impact-generated porosity and permeability to a greater degree than impactites of cratering settings on Earth.

The result form the ImageJ processing on the BSE map of NWA 8159 sample 2 proves that determining the physical properties of the Martian crust and mantle based on a few grams of Martian rock is a scientific approach defined by proximetry, and that extensive and thorough petrological analyses should be performed prior to formulating a hypothesis about the geological evolution of Mars. Nevertheless, Martian meteorites are the only rock samples that we currently have on Earth from the Red Planet, and that we can thoroughly study via advanced microscopy and chemical techniques.

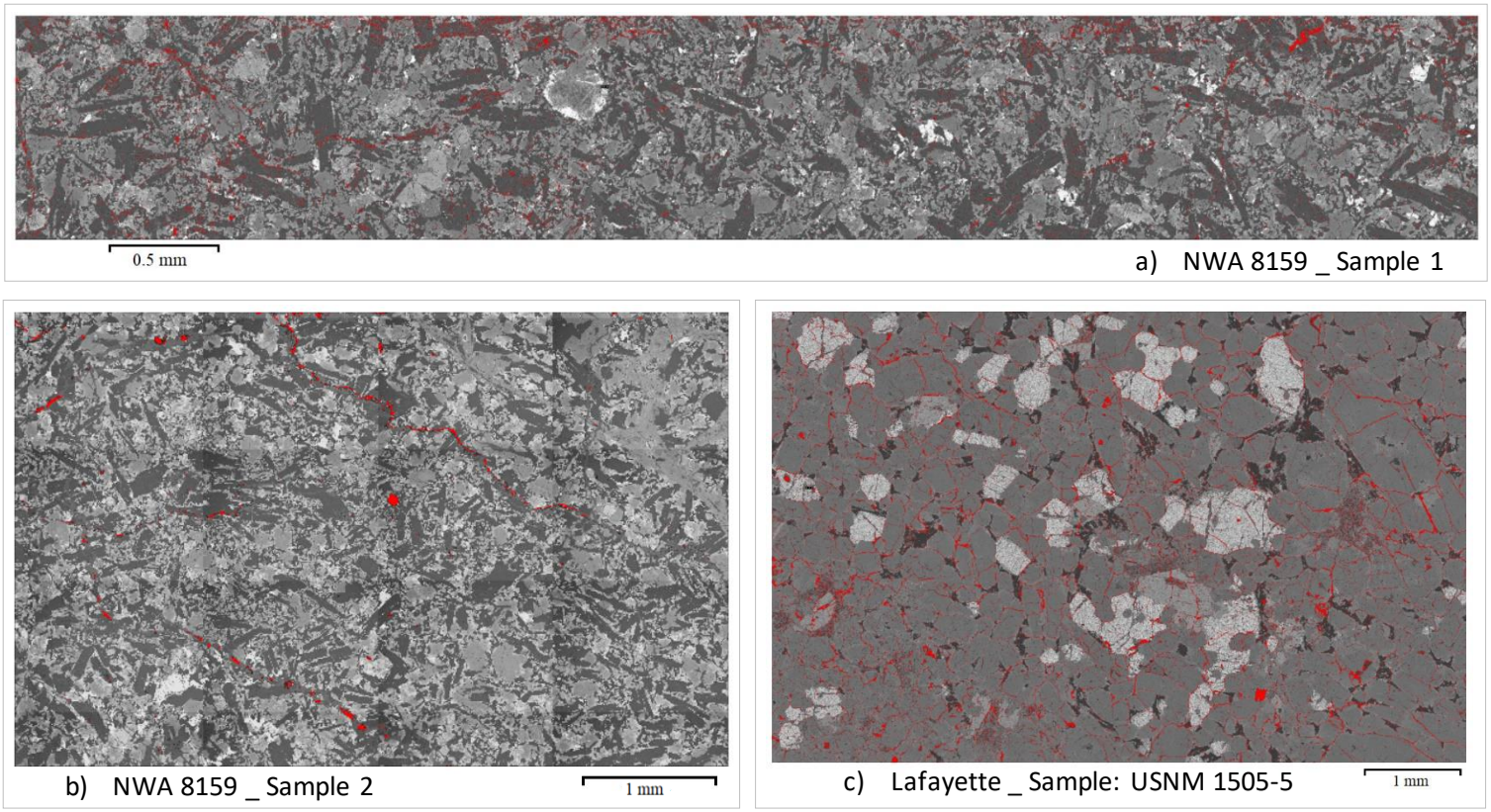

Fig. 3.34. Processed BSE maps of the three different Martian meteorite samples via the ImageJ software: (a) NWA 8159 sample 1, (b) NWA 8159 sample 2, (c) Lafayette sample USNM 1505-5. Regions annotated in red (false-)colour indicate porous spaces within each rock sample, and account for the calculated porosity. Porosity calculations were performed by the ImageJ code after considering the total area, pixel count, and average size of particles in each BSE map (tiff. image); and by adjusting the image type (8-bit), scale and threshold for each image. The porosity of each sample was finally determined via ImageJ analysis of its BSE map; i.e.: by calculating the percentage of the total area that displays in red false-colour (hence, as porous space area) through the software.

Table 3.7. Porosity measurements for the NWA 8159 and Lafayette meteorite samples after processed BSE maps (tiff.) images through the ImageJ software. NWA 8159_Sample 1 porosity is calculated with a value of 5.27 % and NWA 8159_Sample 2 porosity has been measured at 2.20 %. Lafayette sample porosity has been calculated with a value of 4.93 %. The datasets from which these calculations derived can be accessed through the appendix (please see § 7.5).

Thin Section	Count	Total Area	Average Size	%Area = Porosity (%)	Feret	FeretX	FeretY	FeretAngle	MinFeret
NWA 8159_sample 1_.tiff	94140.00	394129.79	4.19	**5.27**	3.07	6164.25	904.50	109.18	1.53
NWA 8159_sample 2_.tiff	1219.00	38913.58	31.92	**2.20**	5.75	1479.70	645.77	114.80	2.56
Lafayette_sample: USNM 1505-5	63840.00	6716977.74	105.22	**4.93**	16.14	1570.26	1107.77	125.20	7.02

§4 DISCUSSION

4.1 Duration of Hydrothermal Systems on Mars

4.1.1 Mechanics of Martian Impact-Induced Hydrothermal Systems

The numerical simulations performed in this work yielded insights into the thermodynamics and hydraulics of hypothetical impact-induced and magmatic-induced hydrothermal systems on Mars. The post-impact hydrothermal systems in all computational scenarios were governed by a major, central heat source (hotspot) at the center of the crater. Additionally, in the hydrothermal scenarios of the larger craters (100-, and 200-km in diameter), apart from the central melt-hotspot, smaller melt sheets in more distant areas of the crater were also considered (obvious through Fig. 3.1 and 3.4). Such melt sheets in these Martian impact craters were evident in the peak ring lithologies, and in those of the annular trough and even of the outer margin and were generating more complex hydrothermal systems. Thus, all melt sheets computed in the simulative impact-induced hydrothermal environments were contributing to the hydrothermal cycle pattern by extending it both spatially and in duration for each scenario.

The scenario of the 10-km in diameter crater on Mars, however, exhibits only a central heat source (shock-emplaced heat from the overheated rocks after the impact, with T_{max} = 700 °C; Fig. 3.7) that generates large hydrothermal upwellings beneath the surface of the central basin. This induced hydrological system is simpler in terms of identifying the main hydrothermal cells and circulation patterns in the lithological setting. Generally, we can conclude that the presence of melt-rock sheets or/and shock-emplaced heated lithologies is a major triggering mechanism for hydrothermal upwellings in the host domains of the simulative grid in HT3.

Furthermore, the initial peak-temperatures for each hydrothermal scenario depend on the target lithologies and significantly affect the fluid mechanics of the impact-induced hydrothermal systems. In this work, the simulations did not experiment with different lithological compositions and assumed target rocks of igneous origin. As several different petrophysical and geothermal parameters were explored to determine how the generated hydrothermal system is affected in each scenario, the assumption of different lithologies would have opened new areas of investigations that would expand beyond the objectives of this thesis.

As explained in the methodology chapter of this thesis, temperatures that are higher than 500 °C render the host lithology impermeable and do not allow fluid flows to penetrate those overheated domains. Heat is transferred via both conduction and convection to the surrounding rocks (e.g., breccia, regolith, brecciated basalt, crystallized melt-rocks) and induces hydrological circulation in the areas adjacent to the heat sources. After impactites and melt rocks that are initially characterized by temperatures higher than 500 °C solidify, fluids can enter and circulate through the heated porous and permeable domains of those still heated lithologies. Eventually, fluid flows within the newly crystallized rock units enrich the hydrothermal system with high-temperature liquid water, steam, or even super-critical mass fluxes.

Moreover, the background geothermal gradient in the subsurface of Mars should also be interacting with the post-impact thermal distribution of the cratering setting. However, the available fluid flow codes have been unable so far to suggest whether basal heat flux from the lower crust and upper mantle of Mars affects considerably the impact-induced hydrological cycle, and subsequently, the duration of hydrothermal activity. Such numerical experiments were performed in this work by changing only the geothermal heat flux in the impact-induced hydrothermal scenarios, but the observed differences can be established as insignificant; as changes in the geothermal heat flux of the simulative grid did not seem to significantly affect the duration of hydrothermal activity (Fig. 4.1 and 4.2). In nature, this might not be the case though, as such hydrothermal systems should be exchanging heat at a great extent with the warmer deeper regions of the lower crust, or the shallower colder regions of the near surface. Hence, such thermodynamic interaction processes, that are characteristic for open-thermodynamic systems in nature, could not be observed in the HT3 simulative environments of this work. Thus, this may lead to the conclusion that some of the hydrothermal systems may have been over- or under-estimated in terms of their hydrological activity.

Finally, water-ice presence and precipitation in a geothermal environment play a significant role in the enrichment of a hydrothermal system with colder fluids. Surficial fluids and precipitation were considered in the HT3 simulations of this work, but the differences in the hydrological cycles and cooling pattern were in all cases negligible. We can suspect further that the presence of an appreciable mass of water-ice deposits deep within the Martian crust should also be considered in this dissertation's numerical models (according to findings by Orosei et al. (2018)). Unfortunately, when water-ice deposits were used as input units in the

lithological setting (in the form of horizontally elongated sheets between rock formations) the convergence of the thermodynamic criteria for heat and flow transport between rock units and water-ice reserves could not be satisfied. Such simulative scenarios were getting automatically aborted after a few time steps (between 0-100 years) in each simulation run. For this reason, the presence of large in mass deposits of water-ice in the Martian crust could not be modelled.

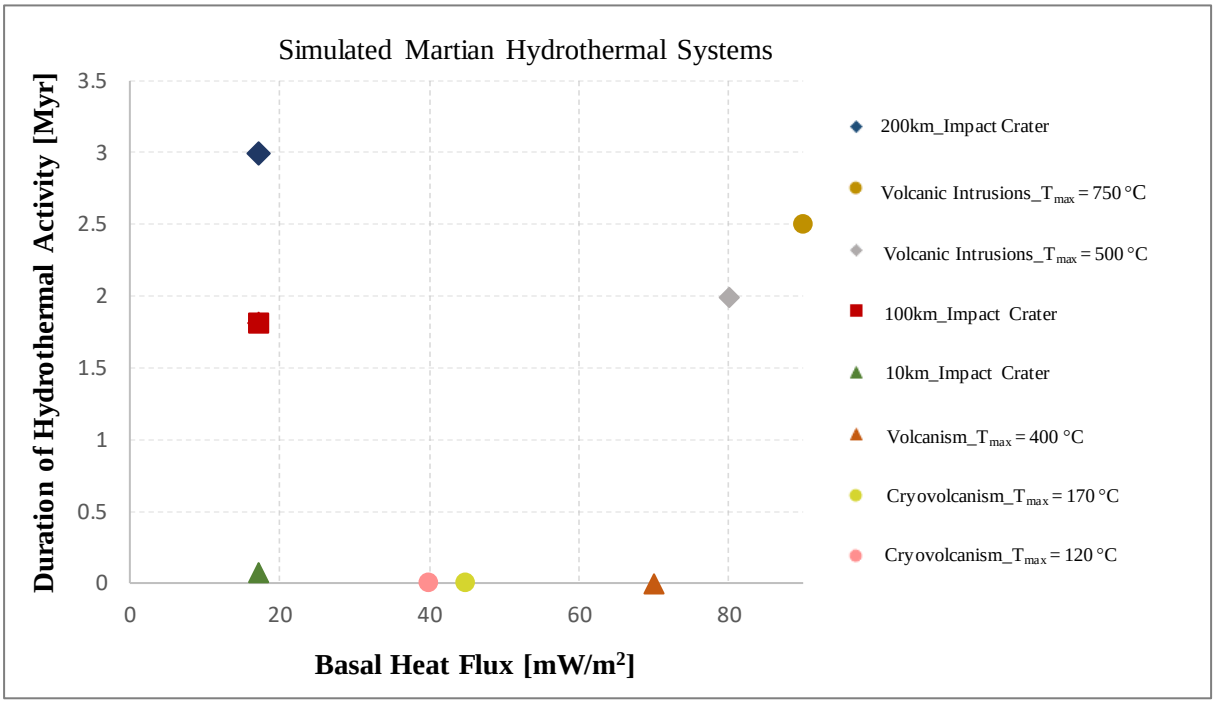

Fig. 4.1. Plotted values of the duration of hydrothermal activity versus geothermal heat flux in the simulated hydrothermal environments of this work. This graph indicates that the duration of hydrothermal activity is independent of the basal heat flux in the HT3 simulations. Nevertheless, in natural (open-thermodynamic) systems, geothermally induced heat flux should be interacting with the heat sources of the impact-generated melt sheets. The modelling results strongly indicate that the hydrothermal settings with the very low heat flux (17 mW/m^2) have significantly higher lifetimes of hydrothermal circulation. This is contrasted by the computed lower lifetimes of magmatic-induced hydrothermalism, as these geothermal systems have been initially assigned to much greater basal heat flux in the simulations (ranging from 40 to 90 mW/m^2). Thus, other governing factors should be affecting the pattern and duration of hydrological circulation in both impact-induced and magmatic-induced hydrothermal systems on Mars.

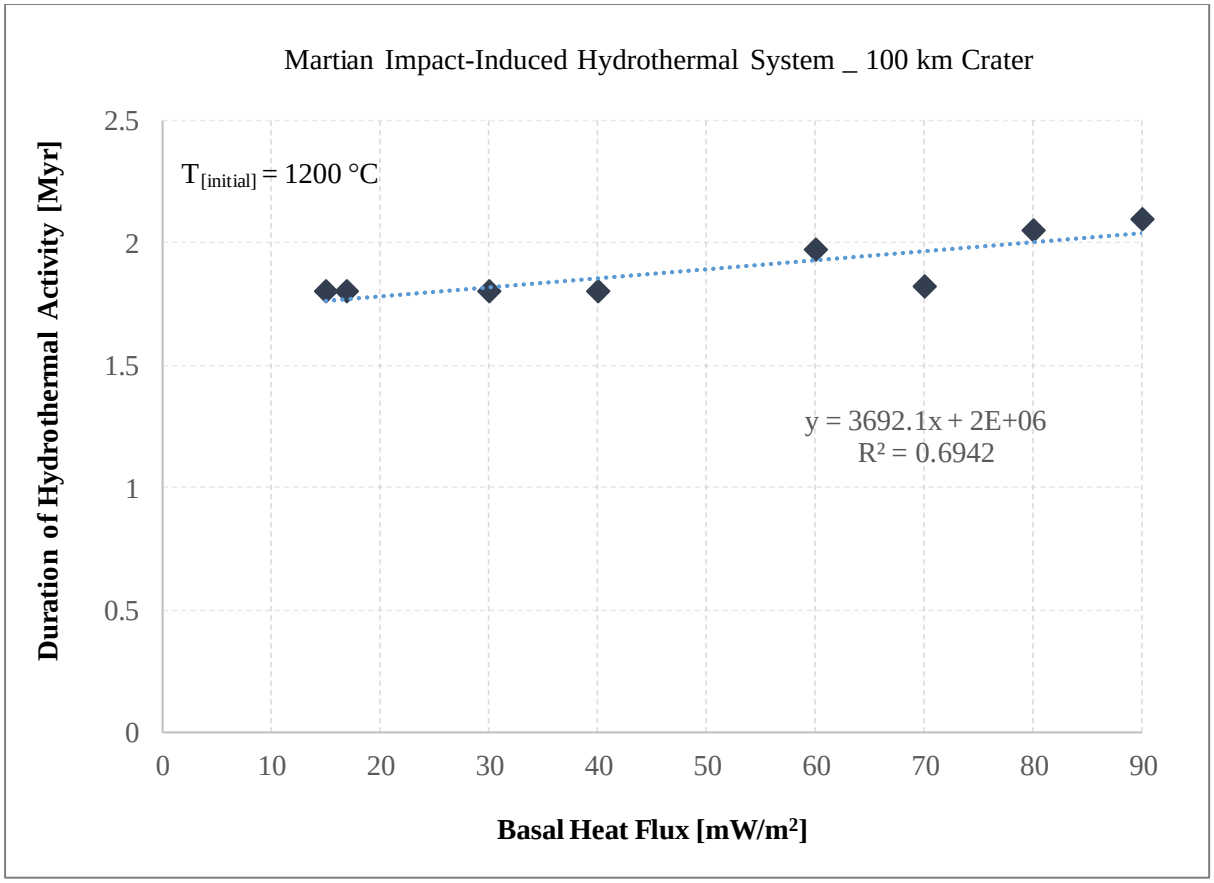

Fig. 4.2. This plot shows the weak correlation between the duration of hydrothermal activity and geothermal heat flux in the simulations performed for the 100-km crater. In this investigation, the $T_{initial}$ [°C] and all other petrophysical properties of the crater's geological environment were kept constant, in order to monitor the change in the duration of hydrothermal circulation after changes in the geothermal (basal) heat flux of the setting. The regression analysis indicates that since $R^2 = 0.6942$, subsequently, $p = 0.010216$ which is > 0.01 (the result is considered significant at $p < 0.01$, in these HT3 models). Nevertheless, if the significance criteria are adjusted more liberally and a p-value is considered significant at values < 0.05, we can conclude that there is indeed a significant correlation between the basal heat flux and the duration of hydrothermal circulation in impact-generated geothermal setting; which is what we should expect in field observations of similar open-thermodynamic natural systems. By additionally considering the results of Fig. 4.1., we can suggest that impact-generated hydrothermalism is more significantly dependent on other physical parameters of the cratering environment, and secondarily on the background geothermal heat flux of the geological setting.

4.1.2 Mechanics of Martian Magmatic-Induced Hydrothermal Systems

In comparison with the impact-induced hydrothermal simulations, the scenarios for the magmatic-induced hydrological systems on Mars, are governed primarily by an increase in the basal heat flux at the bottom boundary of the simulative grid, and a resulting increase of the temperature of the isotherms at depths greater than 5 km. Additionally, intrusive volcanism scenarios exhibit higher temperature isotherms (300 °C ≤ T ≤ 750 °C) at depths between 3.5 – 6 km from the surface. Such geothermal parameterization in HT3 simulations resulted to the generation of multiple hydrothermal cells at depths between 2 – 7 km in the Martian subsurface. In the scenarios of intrusive volcanism (T_{max} = [500 °C, 750 °C]), upwelling events were also evident at depths between 0 – 2 km from the surface, and flows were seeping out through the regolith to the Martian surface. Hence, the computational hypotheses for the magmatic-induced hydrothermalism on Mars experiment with variations in the basal heat flux and associated temperature of volcanic-induced isotherms. Therefore, we can assume that these models (the lower temperature scenarios: 3.2.1, 3.2.2; versus the higher-temperature scenarios: 3.2.3, 3.2.4) should represent the geothermics of putative Martian volcanic provinces dating from the Noachian period, when the interior and atmosphere of Mars were much warmer, until present, when much colder conditions characterize the Red Planet, respectively.

Hydraulics in the Martian volcanic systems explored in this work are initiated by the increase in geothermal heat flux and the temperature difference (ΔT) between the deeper domains of the subsurface (depth ≥ 3.5 km) and the upper-subsurface lithologies. In the lower temperature scenarios (120 °C ≤ T ≤ 170 °C), aqueous fluxes persisted in those systems for no more than 260 years and are observed only in the form of upwellings; with a direction of flux pointing only towards the surface. After hydrothermal fluids in those scenarios escape through the porous and permeable lithologies to the Martian surface, they seem unable to re-penetrate the surficial regolith with a far lower temperature (probably due to freezing). For this reason, hydrothermal cycling is not evident in those numerical experiments, and these Martian geothermal systems host upwelling flows only for a limited period. Thus, these low-temperature simulations should be representing the fluid mechanics processes of short-lived, transient flows during the Amazonian period, as described by Changela and Bridges (2011) and Ojha et al. (2015).

On the contrary, the formation of hydrothermal cells is ubiquitously evident in the numerical experiments of the higher temperature scenarios that were previously presented and analysed (3.2.3, 3.2.4, and in the appendix: E:/Hydrothermal Flows _ Intrusive Veins _ T_{max} = 750 °C _ Higher/Lower Permeability.mp4). The pattern of hydrothermal circulation therein is governed by numerous hydrological cells that develop in even shallower depths (≤ 2 km), and transfer heat and fluids to the upper surficial lithologies. As a result, the regolith and breccia formations of the near surface get heated, and so, hydrothermal cycling is initiated and can persist between the colder surficial lithologies of the geothermal setting and the heat sources for hundreds of Kyr.

4.1.3 Limitations of Numerical (HT 3) Simulations

4.1.3.1 Initial Thermodynamic Conditions of Hydrothermal Scenarios

The numerical experiments that were conducted through this work implied that the lifetimes of the investigated Martian hydrothermal systems are highly dependent on the initial heat source of the setting. This was particularly evident in the impact-induced hydrothermal scenarios (3.1.1, 3.1.2, 3.1.3), where the initial temperature distribution of the central melt sheet dictated to an appreciable degree the lifetime of hydrothermal circulation. However, as the duration of hydrothermal circulation depends on multiple thermodynamic and petrophysical variables, in such heat and flow transport computational methodologies, it is essential to investigate how the hydrothermal activity is affected under the influence of the initial thermal distribution as the sole independent variable.

Therefore, more simplistic simulations regarding impact-induced hydrothermal scenarios were performed, in order to explore how strongly the initial temperature of the heat source affects the hydrothermal activity in such Martian impact cratering settings. Parameters such as the porosity, permeability, thermal conductivity, heat capacity and lithostratigrahy (Martian basaltic target rock) of the setting were kept the same in all of these investigative cases. Hence, eight different simulations were constructed and performed for a putative Martian impact-induced hydrothermal environment under a $T_{initial}$ ranging from 500 °C to 2000 °C. Fig. 4.3 illustrates the results of this meta-analysis, and indicates that there is a significantly strong

correlation between the initial temperature of the heat source and the duration of hydrothermal circulation. Conclusively, it is not surprising that giant impact cratering events which generate excessive volumes of melt sheets with $T_{initial} \geq 1000$ °C, induce hydrothermal cycles that can last for more than 1.0 Myr in these simulative approaches. On the other hand, when the impact crater's diameter is essentially smaller ($D \leq 50$ km), then $T_{initial} \leq 800$ °C in these impact-induced hydrothermal scenarios for the basaltic crust of Mars. Thus, for smaller impact-cratering settings, the volume of the central heat source is much smaller, and so is the peak initial temperature. For this reason, the duration of hydrological activity ranges from 50 Kyr to 300 Ky for the lower $T_{initial}$ (500 °C – 800 °C) hydrothermal cases.

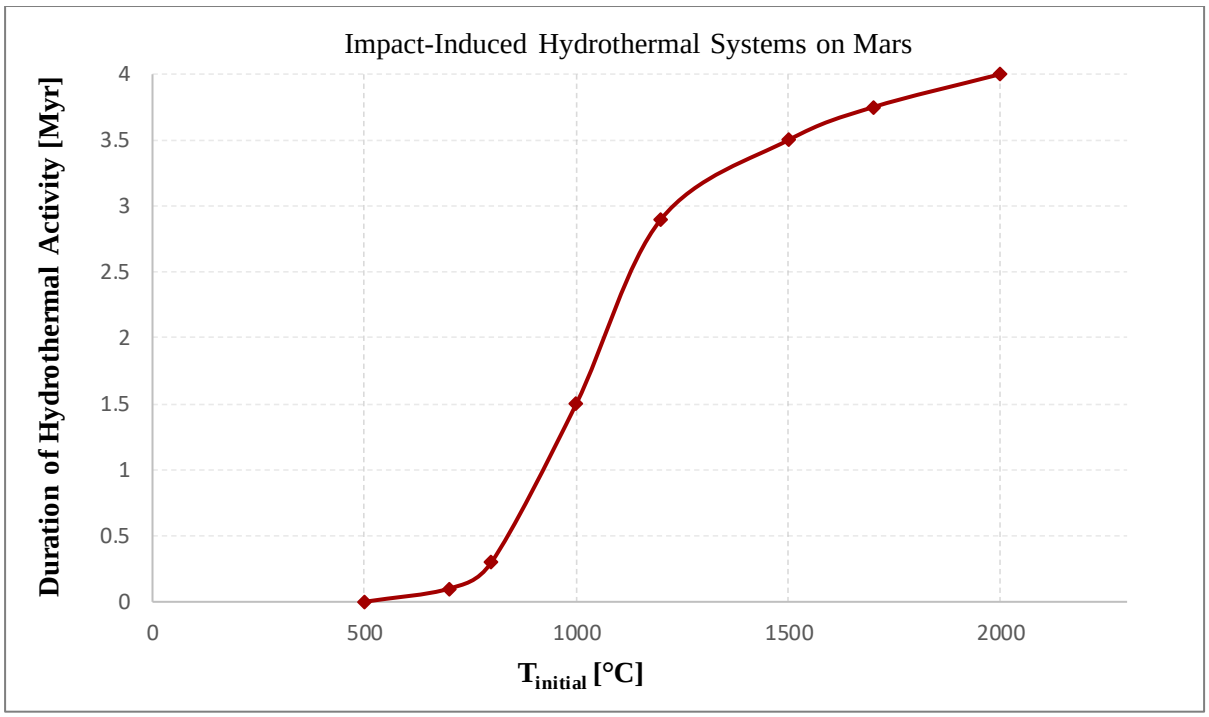

Fig. 4.3. Analysis on the correlation between duration of hydrothermal activity and initial temperature ($T_{initial}$) of the heat source (melt sheet(s)) via 8 different impact-induced hydrothermal modelling experiments in this work (for the 10-, 100- and 200-km craters under constant values for permeability, porosity, thermal conductivity and heat capacity of rocks). In this quantitative analysis, simulations with each of the following $T_{initial}$ (°C) parameters: [500, 700, 800, 1000, 1200, 1500, 1800] were performed for associated sizes (non-correlated variable in the regression analysis) of impact cratering systems (i.e.: $T_{initial}$ [°C] = [500, 700, 800] for the 10-km crater; $T_{initial}$ [°C] = [1000, 1200] for the 100-km crater; and $T_{initial}$ [°C] = [1500, 1800] for the 200-km crater.

4.1.3.2 Major Controls on the Duration of Hydrothermal Activity

Permeability and porosity are the most significant petrophysical parameters that govern the duration and mechanics of hydrothermal circulation (as presented also in HT simulations by Abramov and Kring (2004); (2005); (2006)). Further numerical experiments were conducted to investigate how permeability and porosity would affect the previously explored geological niches of the Martian crust. To monitor the effects of these factors on hydrothermal duration and fluid mechanics, a more simplified simulative setting was used; this was solely comprised by brecciated rock, and the initial temperature of the heat source (impact-generated melt) was adjusted to a value of 1200 °C in all explored models. Fig. 4.4 and 4.5, illustrate the results of computational experiments, where permeability and porosity are the independent variables, respectively. The dependent variable in both investigative hypotheses is the duration of hydrothermal activity. Accordingly, in the plotted models of Fig. 4.4, the porosity of the brecciated rock is held constant at 20% and the effects of varying permeability have been explored. Similarly, Fig. 4.5 represents numerical experiments for the hydrothermal duration in the same geological setting, but by assigning a constant value to the permeability of the brecciated rock (9.0E-17 m^2) and by using a varying porosity with values between 0% and 60% to investigate how the duration of hydrothermal activity will be affected.

Fig. 4.4 shows that permeabilities between 1.0E-15 m^2 and 9.0E-15 m^2 maximize the duration of hydrological activity in the brecciated rock. The simulations with permeability values $\geq$ 9.0E-12 m^2 suggest that the pattern of hydrothermal circulation is dictated by convective patterns of rapid cooling, since the distribution of highly permeable spaces in the rock results to a far more rapid and greater heat loss. The HT simulations also indicate that in all numerical experiments, conduction and convection seem to be antagonizing for dominance. In extremely low permeability scenarios (where $k \leq$ 1.0E-19 m^2) heat conduction is far greater than convection. This results to a simulated phenomenon in which fluids, that move through the low permeability rock and towards the impact-generated melt by convection, are heated by conduction so fast that their movement is halted due to buoyancy. In parallel, when warmer fluids have managed to reach niches of the crater that are far away from the heat source (despite moving through a low permeability rock), then these fluids are cooled by conduction so fast, that their buoyancy is rendered negligible. As a result, such fluids cannot maintain their mechanical activity under such low permeability limitations. This observation offers a complementary thermodynamic explanation on why low permeability geological units cannot

allow hydrothermal flows to persist for long periods, apart from the obvious reason which is the unavailability of permeable space.

To explore how varying porosity affects the duration of hydrothermal circulation in impact-generated breccia, an equilibrium on conductive versus convective cooling was used, which is represented by a constant value for the permeability of the simulative grid ($k = 9.0E\text{-}17\ m^2$). The experimental results for the evolution of hydrothermal duration under varying porosity conditions indicate accordingly that a very high ($\geq 50\%$) or very low ($\leq 3\%$) porosity of the rock unit results to a very low duration of aqueous activity. Furthermore, porosities between 17% and 35% are yielding lifetimes of hydrothermal circulation that are by even 20 times greater than those observed in extremely porous ($\geq 50\%$) or non-porous ($\leq 5\%$) rock settings (Fig. 4.5).

The findings of this meta-analytical investigation are also consistent with indications of previously published research (Abramov and Kring, 2004; 2005; 2007; Sanford, 2005), where the controlling effects of permeability and porosity on the lifetime of hydrothermal circulation were also observed. Particularly, these contributions experimented with varying values of porosity and permeability in their simulated post-impact hydrothermal settings. Consequently, they identified the range of porosity and permeability values that either maximize or minimize the duration of hydrothermal flow. Nevertheless, hydrothermal systems are controlled by numerous physicochemical factors that dictate their formation and evolution. Such computational investigations can efficiently monitor how the constructed simulated environments respond to changes of one or maximum two independent variables per simulation, but where all other factors should be controlled (held constant) for the purpose of comparison. Hydrothermal systems on Earth and on other planetary bodies are, however, much more chaotic; petrophysical factors like thermal conductivity, specific heat capacity and density of the broader lithostratigraphic environment, and simultaneously, other factors related to the petrology of the asteroidal/cometary bolide, its velocity and angle of impact, are of great significance to the post-impact response of planetary crusts. Thus, our understanding on how impact-induced hydrothermal systems are generated and evolve remains limited via such perspectives, apart from approaches where fundamental 2D correlative models and interpretations can be conducted.

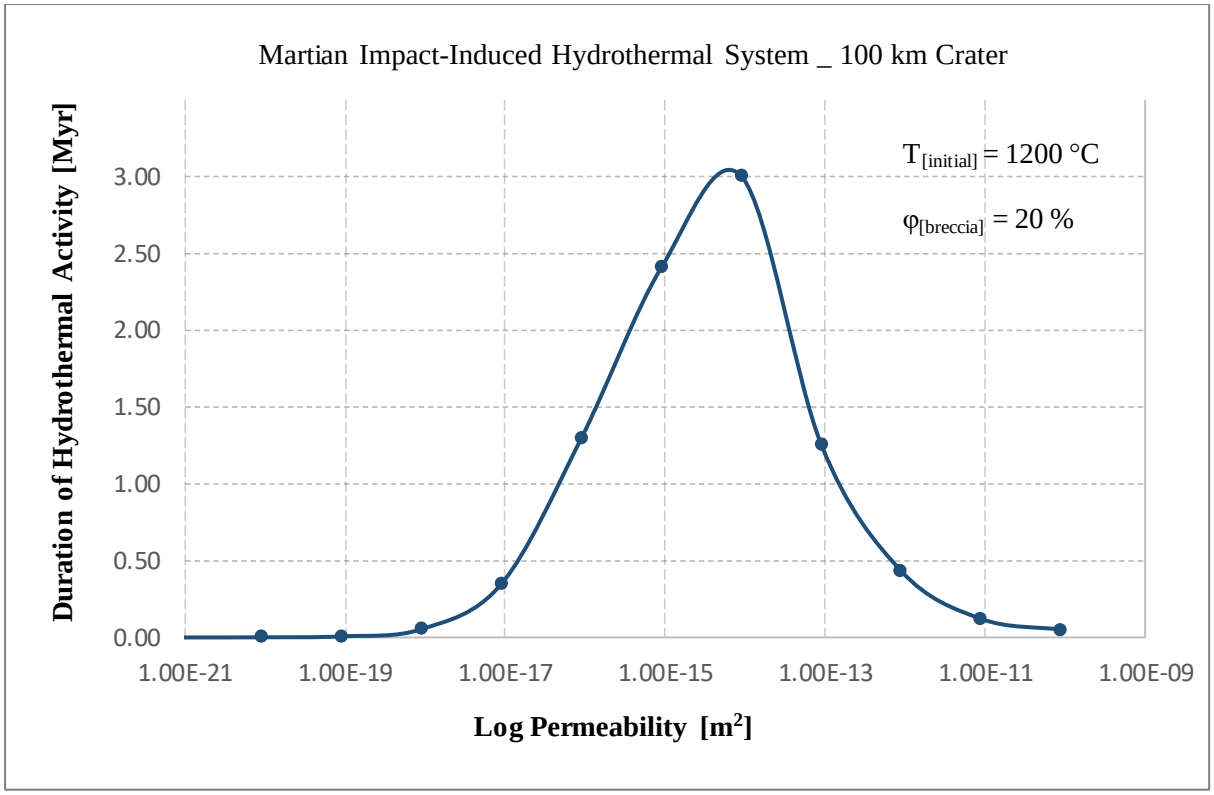

Fig. 4.4. The effects of permeability on the lifetime of hydrothermal activity at the 100-km in diameter crater, by assuming that the post-impact lithostratigraphy of the system is solely comprised by breccia. This computational grid was applied to perform more simplistic simulations of this impact-cratering setting that could record and suggest the effects that permeability poses, as the only independent variable in this modelling approach, on the hydrothermal system's duration. $T_{initial}$ was adjusted to 1200 °C, and porosity was held constant at a value of 20% during these experiments. The results from different simulations indicate that a permeability factor between 1.0E-15 – 9.0E-15 m^2 yields the maximum duration for hydrological activity in the brecciated rock. In addition, it is evident that a permeability value ≥ 9.0E-12 m^2, or ≤ 9.0E-19 m^2, significantly decreases the duration of the generated hydrological system. This implies that target rocks with permeabilities ≥ 9.0E-12 m^2 transfer rapidly significant amounts of impact-generated heat to surrounding rock units, and this results to their rapid cooling via convection. On the other hand, rocks with permeabilities ≤ 1.0E-19 m^2 are almost impermeable, and flows that may develop within such rock units are too weak to be considerable; in such very low permeability systems, conduction is the prevalent pattern of heat transport. Although the latter impact-induced heat conditions may persist in the setting for a much longer period (5-10 × longer; depending on parameterization), the duration of aqueous flows therein is much lower. This is because the porous and permeable space of the host rock in such a scenario is extremely limiting towards the formation of hydrothermal cells that are adequate in flow strength.

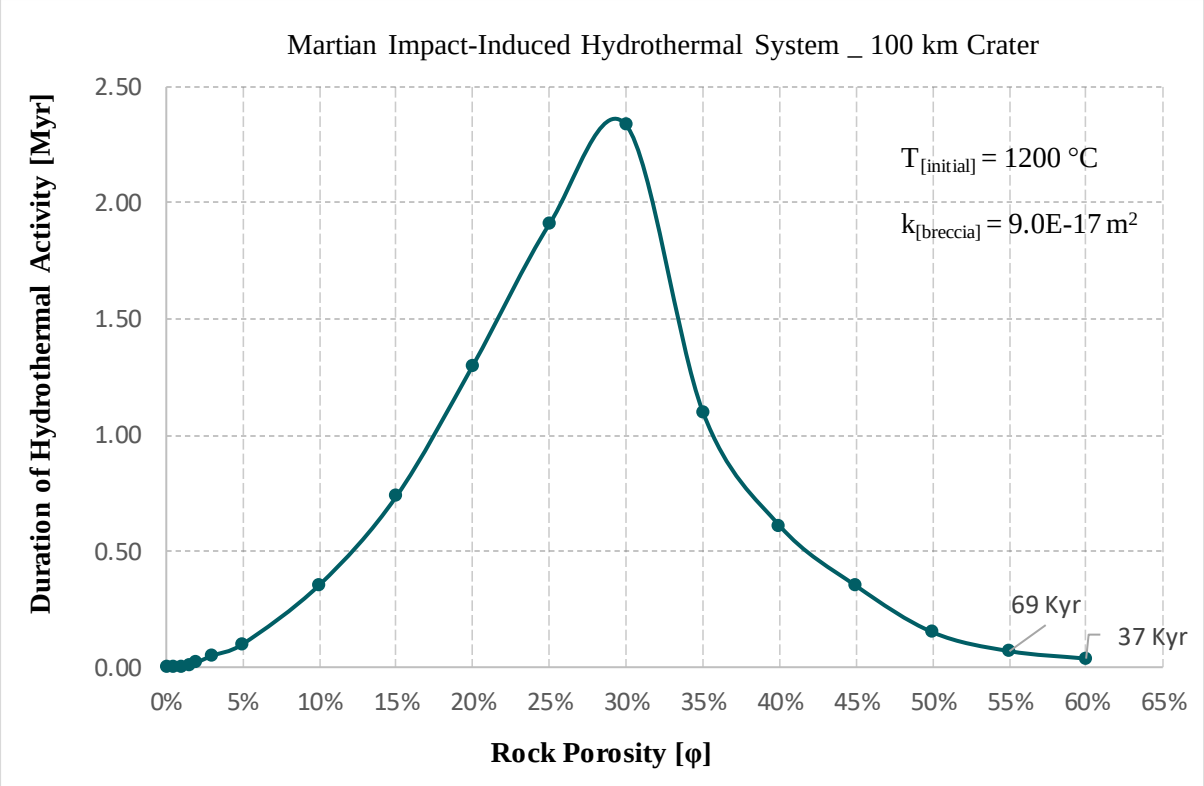

Fig. 4.5. The effects of porosity on the duration of hydrothermal activity at the 100-km in diameter Martian crater. In this model, the post-impact geological setting is comprised only by brecciated rock with a constant computed value for permeability of 9.0E-17 m^2. The simplicity in this simulated impact-induced hydrothermal environment was assigned so that the factor of porosity could be investigated as the sole independent and changeable factor influencing the hydrothermal system's duration. Porosity values of the rock below 1.5 %, generate a hydrothermal cycle that cannot persist for more than 10 Kyr given a permeability of 9.0E-17 m^2. Additionally, as shown in the graph, porosity values between 30 – 40 % decrease the duration of hydrothermal circulation by a factor of 2 – 3, respectively, and porosity values above 60 %, yield durations that are below 30 Kyr. Thus, the plotted results of these simulation experiments on the effects of porosity indicate that the duration of hydrothermal circulation is maximized when the porosity of the computed rock unit is between 25 – 33 %, under a permeability value of 9.0E-17 m^2, and an impact-generated $T_{[initial]}$ = 1200 °C. At this point, it should be noted that further simulative experiments under different boundary factors (i.e.: $T_{[initial],}$, permeability) may yield different results on the duration of the hydrothermal system, but the curve pattern that describes the effect of porosity should not change (as shown by similar investigations on the effects of permeability and porosity in Abramov and Kring (2004); (2005); (2007)).

4.1.3.3 Artefacts and Limitations of HT 3 Simulations

HT simulations comprise a very effective and reliable tool for modelling geothermal systems (Rathbun and Squyres, 2002; Abramov and Kring, 2004). However, the development of HT models requires prudence in the initial parameterization and resolution used for each simulative scenario (Abramov and Kring, 2004; 2005; 2007). This was firstly evident in the work of Rathbun and Squyres (2002), where the utilization of a radial symmetry in the older HT version (Hayba and Ingebritsen, 1994; 1997) produced erroneous calculations for the water mass flux in 3D, with the flow in the z axis being by two ordes of magnitude greater than the flow in the x and y axis of the grid. Therefore, several trial simulations should be performed prior to finalizing the geometry of the simulative grid, the spatial distribution of lithostratigraphic units, and the initial 2D or 3D resolutions of the simulative environment.

The resolution of the grid in HT simulations is also another important parameter which creates differences in the flow pattern, given that resolution varies between simulations for the same geological setting. For example, the mechanics of the hydrothermal circulation pattern in a high-resolution grid of 4365 cells will be essentially different in terms of spatial distribution from that in a model with a low-resolution grid (400-900 cells). Nevertheless, if the initial and boundary conditions of the setting (physicochemical, geometrical, and computational) have been defined correctly, a comparative investigation should not produce deviations in the thermodynamic values that describe the evolution of a simulated hydrothermal system. For example, the duration of hydrothermal circulation, or the peak temperature and water mass flux at a specific time step after Kyr, should not be different between varying resolution - forensic simulations. What would differ though in such cases would be the spatial distribution and circulation pattern of aqueous flows in regions of the setting. The cell distribution in a computational grid is discretized far more efficiently in high resolution models and thus, high-resolution simulations predict flows more accurately in each time step per cell.

On the contrary, coarse resolution in HT models involves low accuracy interpolation and discretizes a far larger area per simulative cell, which results to less detail. Thus, low-resolution models often result to flow patterns being present in areas where the thermodynamic regime would not normally allow those to a specific extent (e.g.: flows of appreciable flux magnitude relatively close to the impact-generated and overheated melt (by $T \geq 500$ °C)). As mentioned though, even in such a scenario, the order of flux magnitude and the peak temperatures should

not be deviating beyond standard levels. For all the above reasons, this PhD research experimented with both low- and high-resolution modelling. However, the HT simulations selected for further experimentation, meta-analysis and interpretations in this thesis achieved the highest possible resolution, based on the capabilities of computational facilities at the College of Science and Engineering of the University of Glasgow.

Freezing affects significantly the latent heat release, permeability, porosity and hence, the evolution of aqueous flows. HT cannot accurately model fluids and solids below the freezing point (Barnhart et al., 2010), and so, the effects of low temperature niches (≤ 0 °C) on the duration of hydrothermal activity in these putative Martian geological systems could not be investigated through these numerical models. This implies that Martian hydrothermal activity may have been overestimated by this aspect in this work, and in previously published contributions (Rathbun and Squyres, 2002; Abramov and Kring, 2005). On the other hand, modelling approaches by Barnhart et al. (2010) which incorporated freezing for simulating the evolution of post-impact hydrothermal systems within 45-km and 90-km diameter craters on Mars, yielded durations and patterns of impact-induced hydrological activity that were quite consistent with the findings of this research and other previously published works that did not include temperatures below the freezing point of water. In particular, Barnhart et al. (2010) concluded with durations of 10^3–10^5 years for the 45-km in diameter Martian crater, and with durations of 10^3–10^6 years for the hydrothermal activity of the 90-km in diameter crater. Therefore, even though the hydrothermal models presented herein have not incorporated temperatures below 0 °C, the results are quite consonant with several previous modelling approaches and their implications.

An additional process affecting hydrothermal circulation is the self-sealing of pores and permeable domains due to mineral alteration and deposition (Dobson et al., 2003; Abramov and Kring, 2007). This was argued also in the published work of Abramov and Kring (2005) which presented simulations of putative impact-induced hydrothermal systems on Mars. However, the HT code's version that these authors used in their work was not incorporating self-sealing. The newer version of HT, the HT 3 code, allows the modelling of self-sealing by using a 2D or 3D finite-difference technique for the spatial and temporal discretization of the equations of state in a wide variety of hydrothermal transport scenarios. Hence, in the simulations of this PhD work fluid flow decreases with time, but it occurs mainly in cyclical episodes of high magnitude due to self-sealing (as suggested by Dobson et al. (2003)), rather

than following a smooth decrease pattern with time (as presented by Rathbun and Squyres (2002), and Abramov and Kring (2005)). Each fluid flow cycle in the simulated Martian environments is initiated by a release of over-pressurized fluid, which forms both transient flow conduits of higher magnitude flux, or lower magnitude fluxes which are more persistent. These two different in duration and magnitude patterns of hydrothermal circulation result in mineral precipitation and in a subsequent partial self-sealing of the permeable and porous space in each Martian lithostratigraphic setting. Eventually, this process leads to another cycle of over-pressurized fluids' release, until the porous and permeable domains have been self-sealed completely, and the heat sources have cooled completely.

Finally, it is noteworthy to mention that self-sealing occurs only as a physical and not as a chemical process in HT 3 simulations. This is explained by the fact that the HT 3 code (including older versions) assumes that hydrothermal fluid is pure water, while hydrothermal fluids not only contain dissolved solids, but their compositions may be far more acidic or alkaline when compared to pure water. Self-sealing as a chemical process should thus be included in future developments of the HT 3 code. Moreover, as the fluid used in HT 3 experiments is simply water, Martian brines could not be incorporated. Thus, aqueous solutions at the early Martian surface and subsurface should have been characterized by saline water compositions and associated with the later formation of saline brine deposits on Mars (Brass, 1980; Sawyer et al., 2000; Bullock et al., 2004). Subsequently, Martian brines should have had significant effects on the self-sealing of pores and fractures during hydrothermal circulation, and an equally important role in chemical interactions with Martian basalts under volcanic- or impact-induced hydrothermal conditions.

4.1.4 The Availability of Water in the Martian Crust

The presented models of this work assume water presence in the geological domain of the upper 10 km of the Martian crust. However, no fluvial, permafrost, lacustrine, marine, or any other shallow-water or water-ice deposits were considered for the simulated Martian geological settings. Water presence in these numerical simulations was confined by adjusting thermodynamic conditions for potential formation of liquid water on the surface, and by determining the rate of atmospheric in origin precipitation. Hence, the presence of water was

limited only in the form of post-impact or magmatic-induced aquifers in the subsurface of Mars, and in the form of precipitated and runoff water on the Martian surface. Precipitation and runoff rates were assigned to values of 0.1 mm/day and 0.5 mm/day for the early Martian surface, respectively (after Ramirez et al. (2020)).

We know that early Mars should have hosted abundant surface fluids and a thicker atmosphere, and there is even indirect evidence of current, transient fluid activity at the planet's surface (McEwen et al., 2014; Ojha et al., 2015; Martín-Torres et al., 2015; Wade et al., 2017). By considering previous findings, further experimental simulations were performed for the impact-generated and magmatic-induced hydrothermal activity with and without the presence of aqueous deposits. Numerical simulations that were considering either a completely arid, or a much more aqueously enriched Martian (sub)surface were demonstrating negligible differences in the induced magnitude and duration of hydrothermal flux; and these differences were only pertinent to the hydrological pattern observed in a few domains of the geothermal system. These experiments additionally suggested that the limiting factors dictating the hydrological activity on the surface or shallow-subsurface in each modelling scenario were the thermodynamic parameters of pressure, temperature and enthalpy that characterized the cold surface ($T \approx 1$ °C) and upper subsurface of Mars (where at depths ≤ 0.5 km, $T \leq 10$ °C). Thus, heat loss in the domains that were closer to the Martian surface was maximized and as a result, the cooling pattern and water circulation of the hydrothermal system remained almost unaffected by variations in the initially assumed water volume.

However, this may be an artefact of modelling, as larger volumes of water-ice on the surface, or water-ice deposits in the subsurface should have enriched induced hydrothermal systems with aqueous fluxes (Schwenzer et al., 2012). On the other hand, if colder water-ice deposits were present, convective cooling of the main heating sources may have taken place much faster. Nevertheless, this hypothesis should be treated as controversial, since computational tools that can simultaneously and effectively model environments characterized by both cryospheric and geothermal conditions have not been yet developed (Rathbun and Squyres, 2002; Abramov and Kring, 2005; Barnhart et al., 2010). Particularly, future developments on hydrodynamic simulations should focus on defining the equations of state for strength models that include rock and ice mixtures, and on optimizing the petrophysical parameters that describe acoustic fluidization of rock and ice deposits (after Pierazzo et al. (2005)) in Martian regolithic and basaltic environments.

Additionally, the boiling or freezing point of aqueous solutions depends on the concentrations of solutes, and subsequently on the availability of water in a specific natural system. Such parameters have not been efficiently constrained yet for early Mars. Apart from that, the HT code determines that hydrothermal fluid (water) and lithostratigraphic units are in a local thermal equilibrium (Abramov and Kring, 2005), which cannot be the case for natural terrestrial or extraterrestrial systems. Howbeit, the problem of simplified thermal equilibrium is negated when fluid flows are slow and persistent, but it causes inaccuracies in predicting the thermodynamic evolution in each simulative cell per time step, when rapid transient fluid flows exceed a water mass flux value of 10E-2 g/s×cm^2. In the numerical simulations of this work, this threshold has not been overcome, since the largest recorded water mass flux value did not exceed 3E-2 g/s×cm^2.

As previously mentioned, the composition of water on early Mars should have been much closer to that of seawater on Earth. Thus, by considering that the HT code erroneously treats hydrothermal fluid as pure water, HT models may be providing some inaccurate predictions on the evolution of Martian hydrothermal activity. It has been proven though that at supercritical temperatures the effect of solutes in H_2O is negligible (Hayba and Ingebritsen, 1997). Therefore, the simulations presented in this work should have not been affected by such inaccurate computations, as domains where hydrothermal activity was ubiquitous were thermodynamically dictated by supercritical temperatures ($T \geq 373$ °C).

Lastly, the HT code hypothesizes that the subsurface remains fully saturated in liquid water, steam, or/and supercritical aqueous fluid throughout the simulation, which implies that all pore and permeable spaces of the geological setting remain filled with aqueous phases for as long hydrothermal circulation is active. This should also be seen as an artefact of the computations. Simultaneously, the artefacts linked to saturation in the hydrothermal simulations can be easily distinguished and disregarded in interpretations. When appreciable hydrothermal flux (WMF $\geq$ 1E-8 g/s×cm^2) is present in cells of the geological grid, we expect the space to be fully saturated in water, and that is accurately reproduced by the HT simulations. On the contrary, in lithostratigraphic domains where no flux or negligible flux is present (WMF $\leq$ 1E-8 g/s×cm^2), the code erroneously predicts, in this case, that those niches are fully saturated in water. Therefore, when maximum saturation levels coincide with negligible fluxes in areas of the hydrothermal setting, these computational artefacts can be easily identified and disregarded from the reliable predictions of the code.

4.2 The Habitability of Martian Hydrothermal Systems

4.2.1 Limitations and Parameterization of Bioenergetic Modelling

Habitability, as we hypothesize it, requires liquid water, nutrients, and energy (Cockell, 2014). These requirements along with significantly limiting parameters that affect the habitability of geological environments, such as temperature, enthalpy, pressure, pH, porosity and permeability, comprise an enigma for assessing and predicting the probability for microbial life under extreme thermodynamic conditions or/and under low energy limitations (Hoehler, 2004). The identification of bioenergetic trends that may have supported the emergence and evolution of life in the Hadean Earth is interwoven with the occurrence of hydrothermal activity (Cockell, 2014; Westall et al., 2018). Nevertheless, the geological regime and combination of physicochemical parameters that should have contributed to the formation of the first biomolecules and lifeforms remain unknown. Conclusively, predictions on the water-rock interactions, energy availability, and combination of thermodynamic parameters that can support microbial life under extreme conditions and low energy limitations are only hypothetical and thus, difficult to establish. A minor change of temperature for example in the bioenergetic simulations of this work (§ 3.3.1 and 3.3.2), can determine the rate of water-rock interactions and nutrients' release in the geological system, and have devastating effects on the environment's habitability. Furthermore, major and abrupt decreases in the availability of water through geological time cannot allow stable conditions for a biogeochemical habitat to emerge and evolve. Hence, if water-rock interactions cannot persist for an appreciable geological period (e.g.: fig. 3.28, 3.29 and 3.30), the host environments are rendered chemically and thermally uninhabitable after a few hundreds of years.

Therefore, the previously presented bioenergetic results and the meta-analytical approaches developed in this section are highly reliable on the limitations of computational predictions. However, the simulations of this work managed to quantify the habitability of a variety of Martian hydrothermal systems, since they determined and constrained further some of the most significant thermodynamic factors and localities for the emergence and evolution of microbial life in the Martian crust. To summarize, the most important factors that were emphasized in the bioenergetic simulations chapter of this work (§ 3.3.1 and 3.3.2) were: temperature, water availability, water-rock interactions, and duration of aqueous fluxes in a geothermal setting.

These parameters derived from the HT computations and later governed the bioenergetic activity in the simulated hydrothermal environments.

Nevertheless, two other parameters that were not directly influenced by, and fully coupled with, the simulated and assessed thermodynamics of hydrothermalism on Mars, but by the species and metabolisms of putative microbial communities, are: the rates of microbial metabolic activity for growth, maintenance and survival (according to Hoehler, 2004) which are highly dependent on the species of microorganisms, and the availability of activation energy (Ea) in the bioenergetic environment needed for particular species to perform their basic metabolic functions.

In the selected bioenergetic simulations presented in § 3.3.1 and 3.3.2, the availability of Ea was adjusted to 69.4 kJ/mol. The metabolic rates of potential hydrogenotrophs for microbial growth, maintenance and survival were adjusted to 3.00E+12 kJ/g of dry weight per cell, 5.00E+10 kJ/g of dry weight C per cell, 5.00E+02 kJ/g of dry weight C per cell, respectively. These biological limitations have been calibrated in the computations of this work according to research findings on microbial habitats under extremely low energy limitations here on Earth; in hydrothermal vents of mid-ocean ridges or/and in sediments and basaltic rocks of the deep oceanic crust (Hinrichs et al., 1999; Bach and Edwards, 2003; Hinrichs et al., 2006; Bach, 2016). These constraints may be considered too optimistic though for the habitability of the Martian subsurface, as they derive from already confirmed microbial habitats deep within the Earth's oceanic crust. For this reason, the aforementioned biochemical parameters should be evaluated further. The following two sub-chapters represent a meta-analysis on how the habitability of the simulated Martian hydrothermal systems would be affected, if the metabolic rates of potential hydrogenotrophs and the availability of Ea for microbial bioenergetic functions are more conservatively defined. Importantly, it should be noted that that the boundary conditions for the newly assessed bioenergetic requirements for growth, maintenance and survival mode of microbial metabolisms, and the availability of Ea do not change or affect the H_2 thermodynamic computations (simulated H_2 release in the different hydrothermal scenarios), but the growth, maintenance and survival criteria – curves. Ideally, a fully coupled code should allow a deterministic correlation between the thermodynamically -, and bioenergetically - controlled habitability. As such computational tools have not been developed yet, in this work, a comparative and partially coupled quantitative assessment is applied for the thermodynamics and microbiological potential of these Martian geological systems.

4.2.1.1 The Bioenergetic Parameter of Microbial Metabolic Activity

The energy requirements for microbial growth, maintenance and survival (as suggested by Hoehler (2004)) are highly dependent on the microbial species. Life in the deep subsurface is adapted to survive and maintain its biomass under extreme energy limitations and under extreme thermodynamic conditions. Archaea species like hydrogenotrophic methanogens, which comprise the hypothesized microbial species in the bioenergetic simulations of this work, can thrive within a temperature range between 100 °C and 121 °C, and within a reported activation energy range between 69.4 kJ/mol and 110 kJ/mol (Tijhuis et al., 1993; Price and Sowers, 2004). Under such thermodynamic conditions, the growth mode of archaean metabolic rate can be satisfied. Nonetheless, species that may thrive under lower Gibbs free energy (ΔrG) limits, and subsequently, also under lower activation energy availability for microbial metabolic functions, have not been reported yet on Earth (Hoehler, 2004; Bach, 2016). For the colder and geologically less active subsurface of Mars, we can assume that the ΔrG and Ea availability should be essentially lower. In this work, the bioenergetic requirements for microbial growth, maintenance and survival were computed according to requirements of archaea in terrestrial systems, and on top of that, based on an averagely optimistic (thermodynamic and bioenergetic) approach for the habitability of these systems on Earth. For this reason, the assumption of potential Martian microbial communities in the bioenergetic models that resemble those of the Earth's deep biosphere, should be seen as a very optimistic scenario for the habitability of the Martian crust.

Therefore, readjustments on the microbial rate of the putative hydrogenotrophic species were completed, to provide a meta-analysis on the bioenergetic simulations. Fig. 4.6, 4.7, and 4.8 evaluate how the bioenergetics of the simulated hydrothermal systems would be affected, if the microbial species is more demanding in terms of energy from the lithological substrate. In particular, the following models (fig. 4.6, 4.7 and 4.8) assess Martian habitability under the condition that the variables of growth, maintenance and survival bioenergetic requirements are by one order of magnitude greater; i.e.: 3.00E+13 kJ/g of dry weight C per cell for satisfying the growth criteria of metabolic activity, 2.00E+11 kJ/g of dry weight C per cell for the maintenance requirements, and 5.00E+02 kJ/g of dry weight C per cell for survival.

The results in fig. 4.6 – 4.8 indicate that from all the previously reported and analysed hydrothermal systems, though this perspective, no environment can evidently support the

metabolic growth mode of microbial communities over geological time on Mars. Moreover, the H_2 activity in most hydrothermal systems plots well below the survival bioenergetic limits after aqueous circulation ceases. Slight exceptions to this case-pattern are the H_2 activity evolutions in the impact-induced hydrothermal settings of the 200-km and 100-km craters (fig. 4.6), which are marginally above the survival curve, and the H_2 activity in the magmatic-induced hydrothermal setting with T_{max} = 750 °C (fig. 4.8), which plots arguably above the survival curve even long after aqueous activity has ceased. Conclusively, the species of microorganisms and their associated metabolic rates should comprise another independent variable in habitability assessments. The correlation of this biological factor with the assessed thermodynamics of a geological environment is, however, not sufficiently constrained yet.

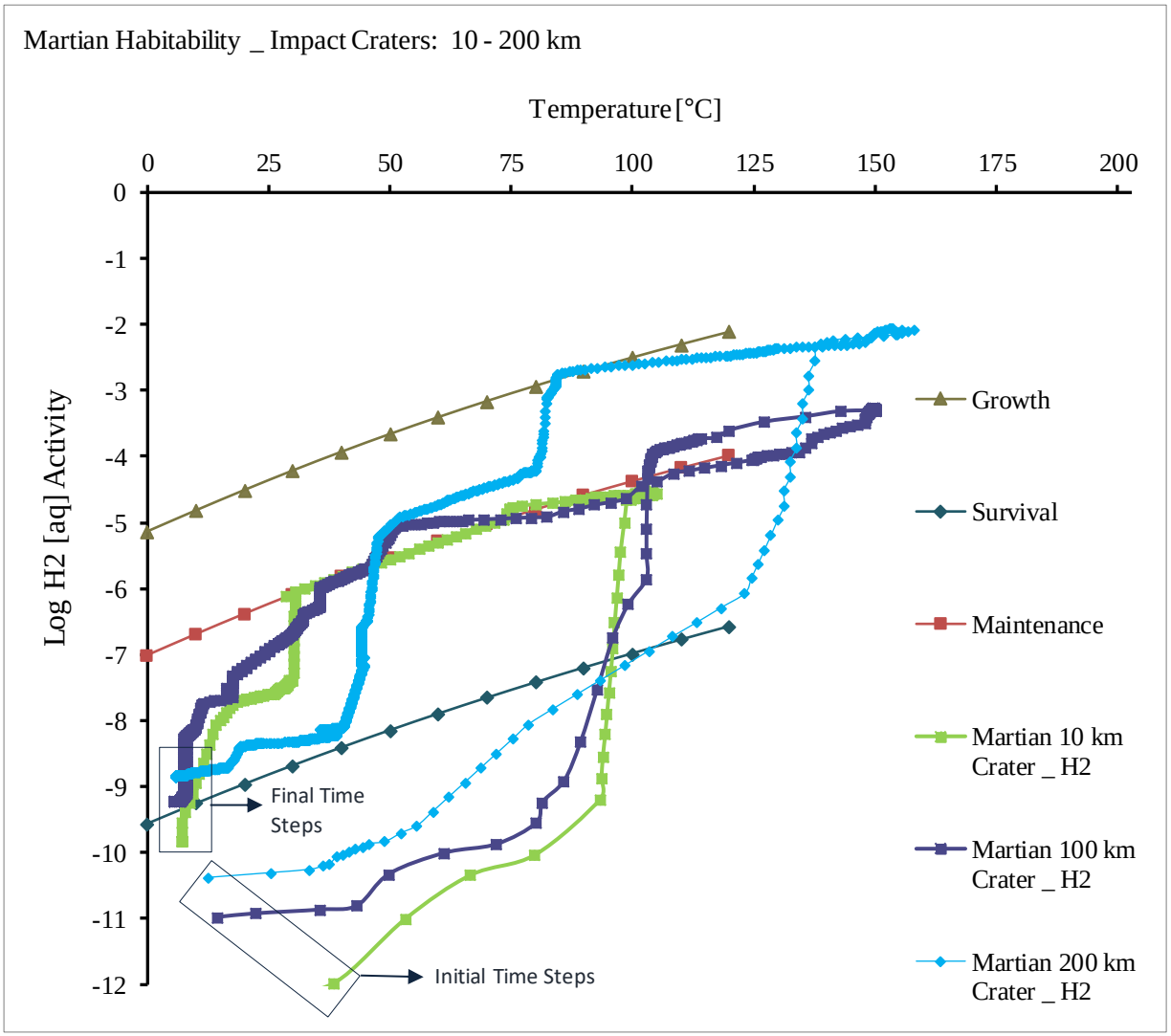

Fig. 4.6. Computations for the H_2 release and habitability in the Martian basaltic crust under impact-induced hydrothermal conditions in the putative impact cratering systems (10-, 100-, and 200-km in diameter craters). This model has reproduced the computations of fig. 3.25, 3.26, and 3.27 (presented in §3.3.1), but under the limitation that the bioenergetic requirements for growth, maintenance and survival have been more conservatively

readjusted, i.e.: 3.00E+13 kJ/g of dry weight C per cell for the growth criteria of metabolic activity, 2.00E+11 kJ/g of dry weight C per cell for the maintenance requirements of metabolic activity, and 5.00E+02 kJ/g of dry weight C per cell as a threshold for the survival requirements of metabolic activity. The activation energy of the Martian subsurface realm in this comparative simulative approach has been held constant at 69.4 kJ/mol, as in the simulations of fig. 3.25, 3.26, 3.27. The illustrated results show that the bioenergetic requirements for each microbial metabolic function (growth, maintenance, survival) are by at least an order of magnitude greater in this approach. This subsequently implies that the quantified habitability of each impact-induced hydrothermal system has been significantly reduced. Particularly, all three Martian cratering systems plot very close to or below the microbial survival limits by the end of their hosted hydrothermal activity.

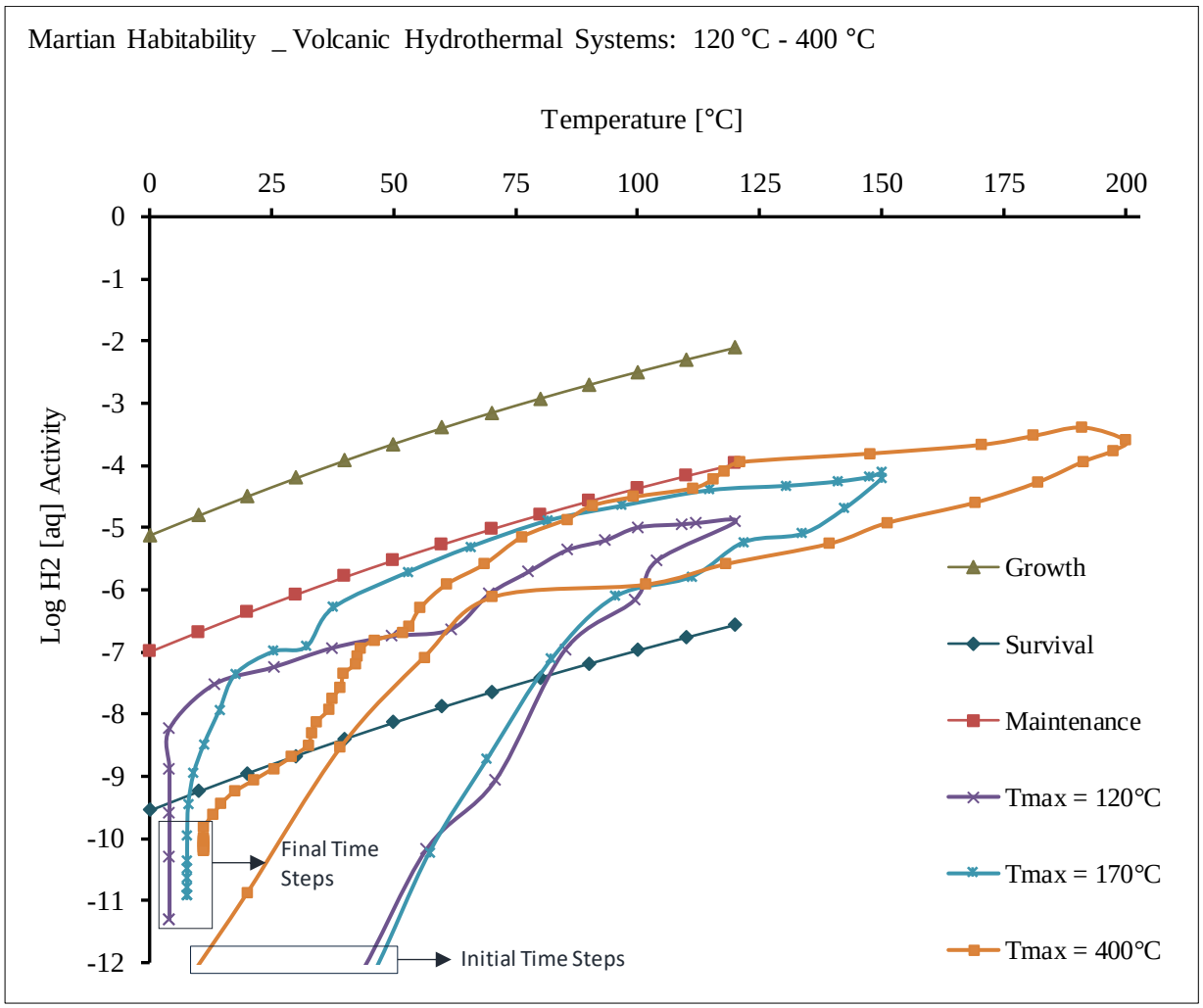

Fig. 4.7. Computations for the habitability of the Martian basaltic crust under magmatic-induced hydrothermalism and via using the same thermodynamic settings that were presented and analysed in §3.3.2 (fig. 3.28, 3.29, 3.30; for a variety of peak temperatures in these Martian geothermal systems). Similar to the modelling approach represented by fig. 4.6, in this numerical experiment, the microbial activity levels for growth, maintenance and survival have also been readjusted to: 3.00E+13 kJ/g of dry weight C per cell as a threshold for microbial growth, 2.00E+11 kJ/g of dry weight C per cell for microbial maintenance, and 5.00E+02 kJ/g of dry weight C per cell for microbial survival. The activation energy of this early Martian magmatic realm has been also held constant at 69.4 kJ/mol, as in the simulations presented in §3.3.2. The illustrated results show that the bioenergetic requirements for each microbial metabolic function (growth, maintenance, survival) are by at least an order of magnitude greater in this approach. Thus, the habitability of each magmatic in origin hydrothermal system has

been substantially reduced. The results indicate that these Martian magmatic environments are more hostile to microbial life than those of the computational scenarios (fig. 3.28, 3.29, 3.30) where more liberal parameterization on the bioenergetic requirements for microbial metabolic functions was used. This conservative limitation on the bioenergetic criteria of microbial biomass shows that water-rock interactions in magmatic-induced hydrothermal systems in the subsurface of Mars cannot support the maintenance or even survival of potential microbial communities.

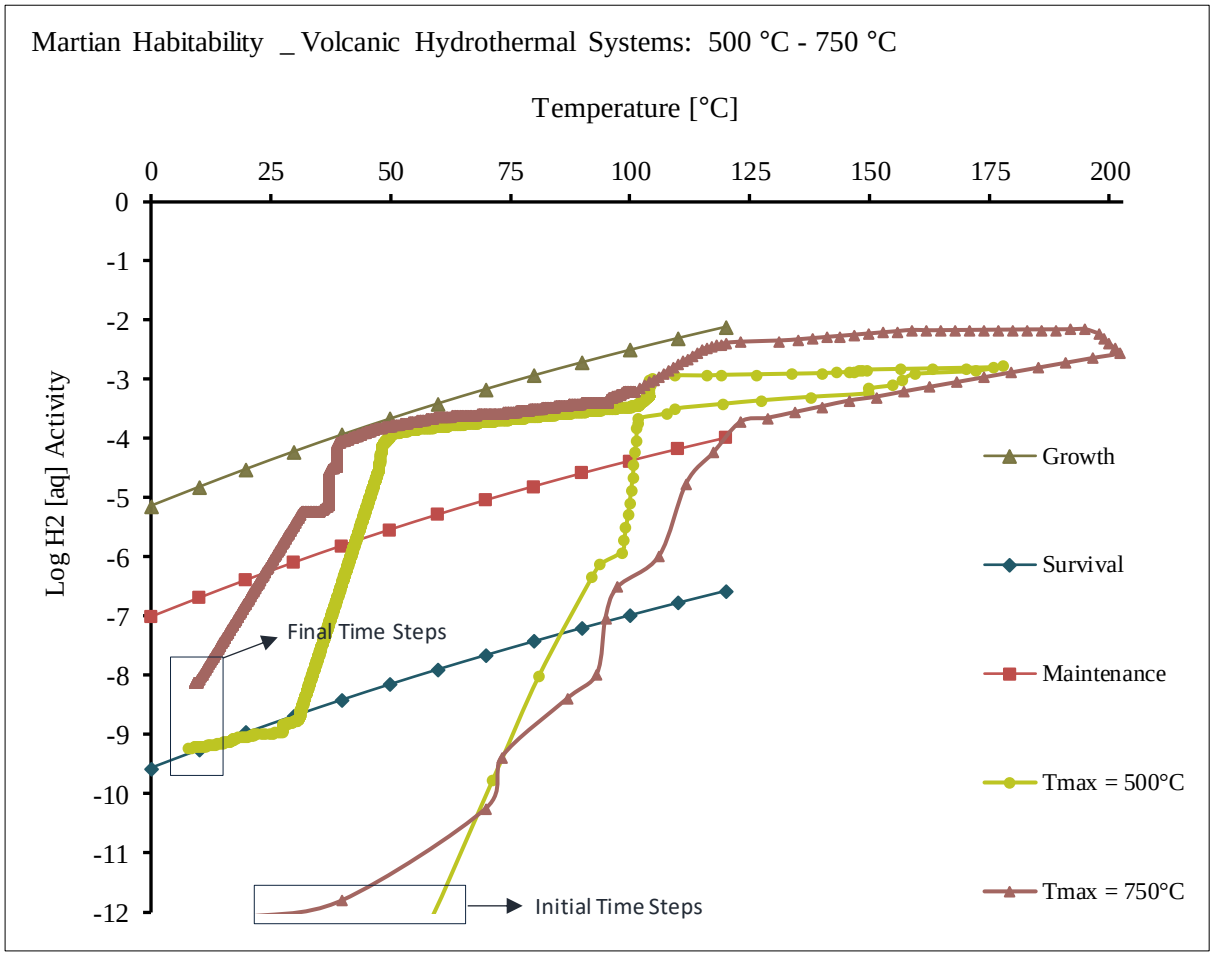

Fig. 4.8. Numerical modelling for the habitability of the Martian basaltic crust under peak temperatures of 500 °C and 750 °C and magmatic-induced hydrothermal conditions. This experimental approach has reproduced the simulations represented by fig. 3.31 and 3.32 in §3.3.2. However, the bioenergetic requirements for microbial growth, maintenance and survival have been conservatively readjusted to: 3.00E+13 kJ/g of dry weight C per cell as a threshold for microbial growth, 2.00E+11 kJ/g of dry weight C per cell for microbial maintenance, and 5.00E+02 kJ/g of dry weight C per cell for microbial survival. The activation energy in the Martian subsurface has also been held constant at 69.4 kJ/mol in this model, as in the simulations presented in §3.3.2. This model shows that that the bioenergetic requirements for microbial growth, maintenance, and survival are increased by at least an order of magnitude. Hence, the habitability of these magmatic-induced hydrothermal systems has been subsequently decreased in this approach. This is arguably evident by the evolution of the H_2 availability in the two hydrothermal settings, with plots that are well below the growth and maintenance bioenergetic thresholds, and close to the survival limits by the end point of hydrothermal activity (especially the T_{max} = 500 °C model).

4.2.1.2 The Bioenergetic Parameter of the Activation Energy (Ea) Availability

The activation energy availability in a lithic substrate poses a further control on the habitability of geological environments (Hoehler et al., 2001a; 2001b; Hoehler, 2004). Similar to the energy requirements for the metabolic rates of microorganisms that differ among microbial species, the activation energy (Ea) in a geological system, that derives from the Gibbs free energy and reaction rate, as defined via Arrhenius kinetics (Davidson and Janssens, 2006; Leifeld and von Lützow, 2014), is an extremely limiting factor for the habitability of a geological system. The rate of energy release after exothermic water-rock interactions in a geological setting determines the availability of E_a for microbes to harvest. In microbial habitats under extreme conditions on Earth, the E_a availability required for biological metabolic functions ranges from 69.4 kJ/mol and 110 kJ/mol, with the lower values characterizing some of the most challenging environments in which known life can survive (Tijhuis et al., 1993; Price and Sowers, 2004).

Herein, a critical analysis is provided on how E_a availability in the simulated Martian hydrothermal settings affects their bioenergetic potential. Fig. 4.9, 4.10 and 4.11 summarize the bioenergetic results after computing the value for E_a at 62.5 kJ/mol (10% decrease) in the basaltic rock substrates. This change of E_a in the computations implies that the habitability of the simulated Martian geological systems is affected in a significant rate and pattern, as presented also and in the previous calculations of § 4.2.1.1; i.e.: by an approximately one order of magnitude higher nutrient (log H_2) release required for the growth, maintenance and survival microbial metabolic functions. The plotted results of fig. 4.9 – 4.11 suggest that the H_2 release and activity in the assessed hydrothermal systems does not satisfy the energy requirements of potential hydrogenotrophic communities in the subsurface of Mars. Nevertheless, through a more optimistic prism for Martian habitability, the H_2 release and bioenergetics in the 200-km and 100-km in diameter craters (fig. 4.9), and those in the T_{max} = 750 °C magmatic-induced hydrothermal scenario (fig. 4.11), show that potential hydrogenotrophs could have survived, maintained their biomass, and perhaps even marginally reached the growth limits of metabolic function within a limited period of 1-2 Myr. Therefore, if microbial life ever existed on Mars, basaltic units in large impact craters ($d \geq 100$ km) or magmatic systems (where $T_{max} \geq 750$ °C) may be proven fruitful sites for astrobiological findings.

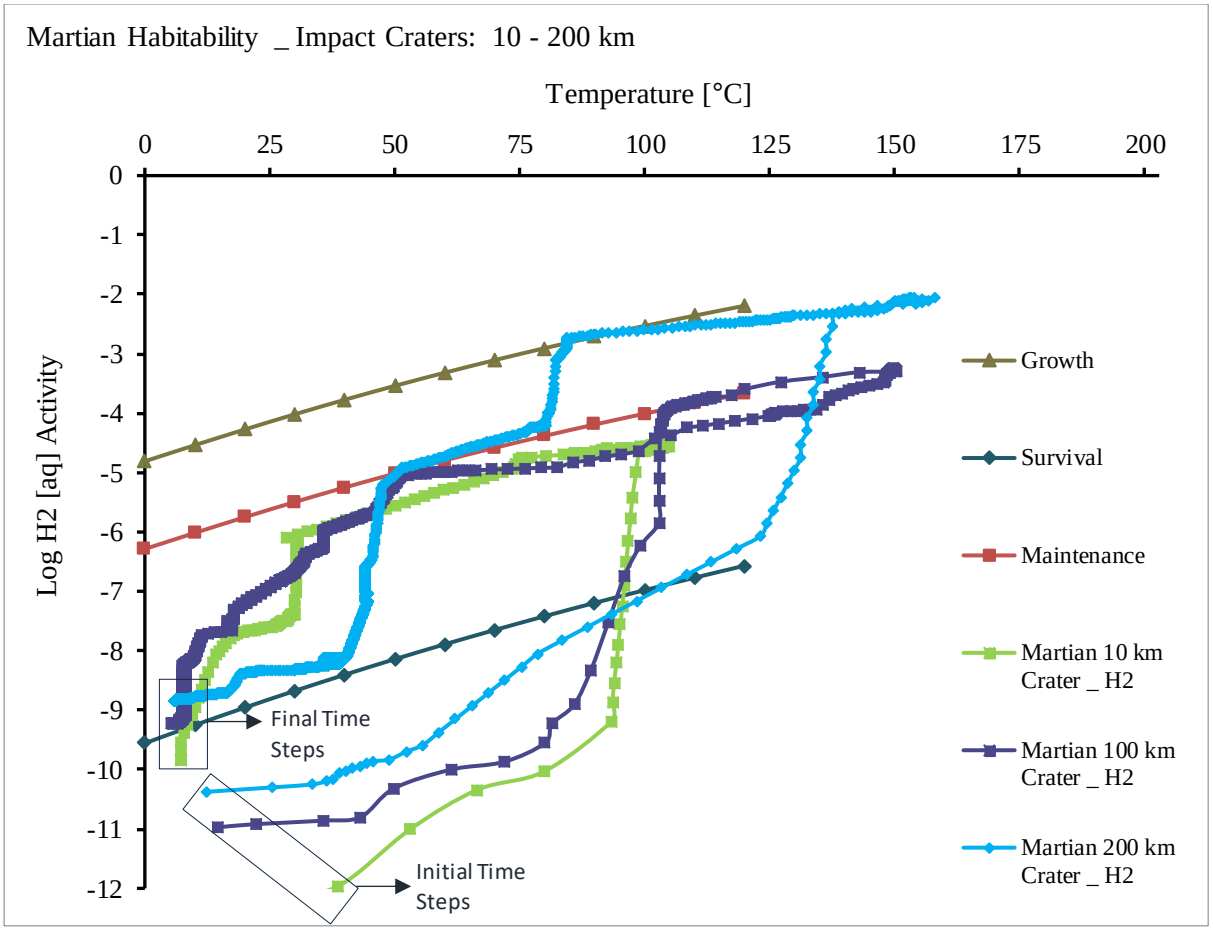

Fig. 4.9. Computations for the H_2-controlled and thermal habitability in the Martian basaltic crust under impact-induced hydrothermal conditions. This graph includes habitability models that are similar with the previously presented simulations of fig. 3.25, 3.26, and 3.27. Although in this approach the bioenergetic limits for microbial growth, maintenance and survival are adjusted with the same values as in the models represented by fig. 3.25, 3.26 and 3.27 (3.00E+12 kJ/g of dry weight C per cell for microbial growth, 5.00E+10 kJ/g of dry weight C per cell for microbial maintenance, 5.00E+02 kJ/g of dry weight C per cell for microbial survival), the availability of activation energy (Ea) due to ongoing water-rock reactions in the hydrothermal environments is decreased by 10% in this investigation (i.e.: Ea = 62.5 kJ/mol, instead of using a value of 69.4 kJ/mol as in the models of §3.3.1). The computations show that Ea comprises another limiting factor for the habitability of these thermodynamic systems. It is evident that even in the most promising scenario for habitability, which simulates an impact-generated hydrological cycle with a 2.8 Myr duration (200-km in diameter crater – H_2 curve: total duration = 2.8 Myr, after fig. 3.25), microbial growth of potential hydrogenotrophic communities can be hardly satisfied in this case. The simulated Martian impact-induced hydrothermal systems are rendered almost hostile for potential microbial life shortly after hydrothermal circulation has ceased (as revealed by the end data points of the three coloured curves above, which are slightly above or below the bioenergetic requirements for microbial survival). This is because the activation energy availability (Ea = 62.5 kJ/mol) for bioenergetic interactions therein is insufficient.

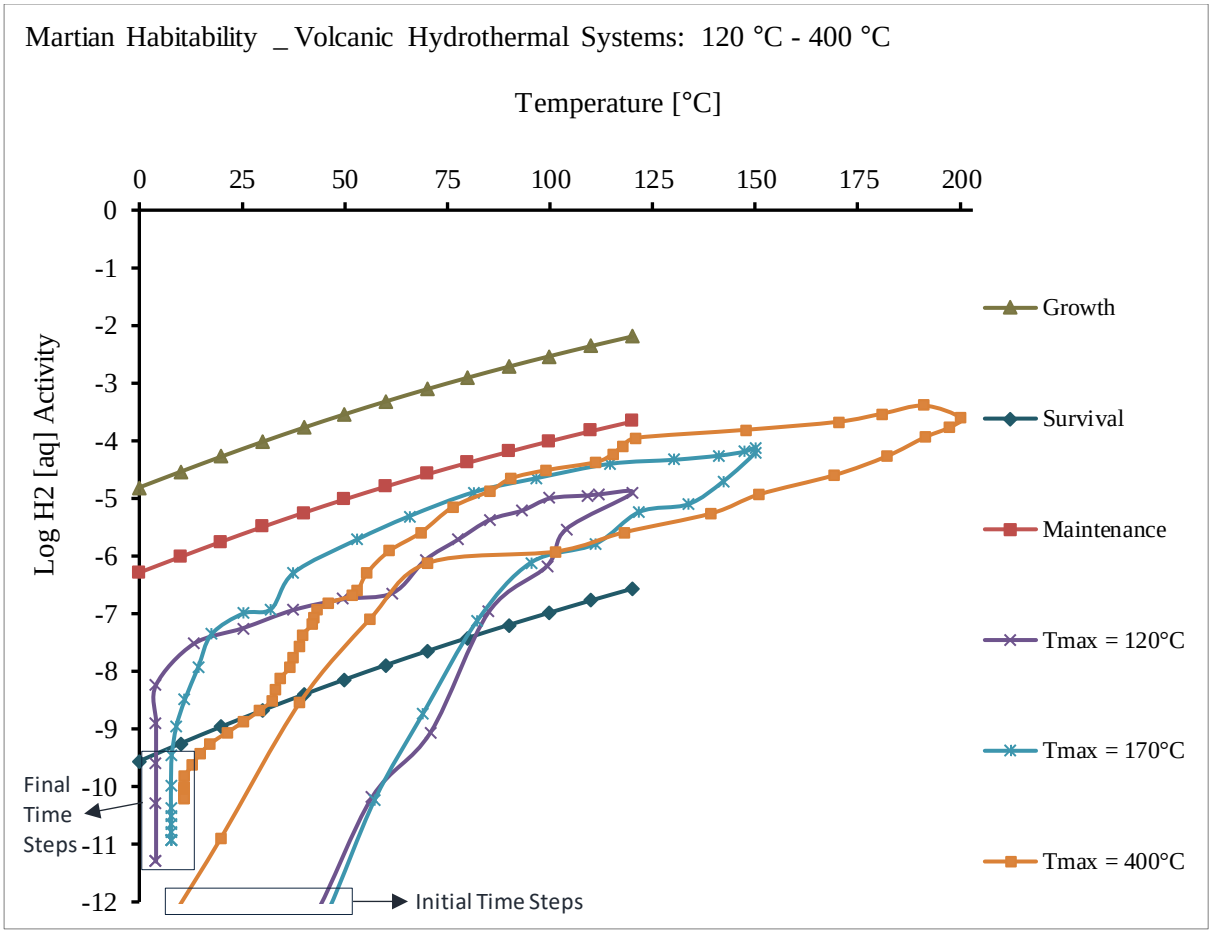

Fig. 4.10. Comparative model for the habitability of the Martian basaltic crust under magmatic-generated hydrothermal conditions. The above habitability plots are different from the models of fig. 3.28, 3.29 and 3.30 by one aspect: due to a 10% decrease in the Ea value (= 62.5 kJ/mol) in the boundary parameterization. All other thermodynamic and bioenergetic parameters of the models have been kept the same with those presented in §3.3.2. The computations indicate that the habitability of these putative geothermal environments is severely affected by this 10% decrease in Ea. More precisely, the hydrothermally generated bioenergetics cannot even fulfil the maintenance mode of microbial metabolic activity during the periods of more intense hydrothermal flux in each geothermal setting. For the end period of hydrothermal activity in each computational scenario, all plots conclude that uninhabitable conditions for microbial life should have prevailed in the Martian subsurface.

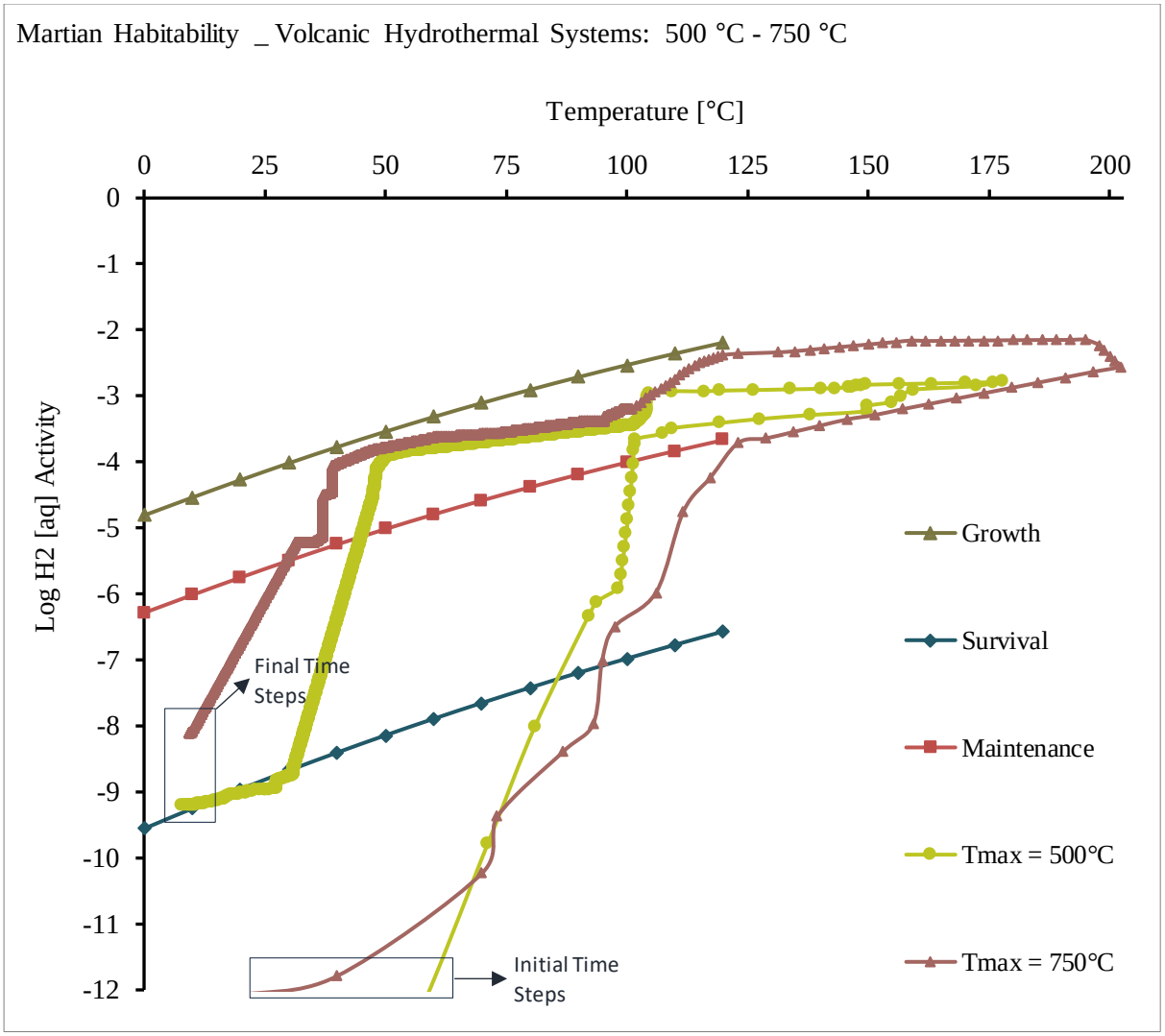

Fig. 4.11. Modelling for the habitability of the Martian basaltic subsurface under high temperature magmatic-induced hydrothermalism. The above plots are using an Ea value of 62.5 kJ/mol, as explained by the rationale of fig. 4.9 and 4.10. However, any other thermodynamic and bioenergetic parameters are adjusted according to the boundary conditions of the simulations presented in fig. 3.30 and 3.31 (§3.3.2). The plots for water-rock interactions and subsequent bioenergetics under a T_{max} = 500 °C (light green curve) show that at the end of the hydrothermal cycle, the environment does not offer sufficient energy to support the survival mode of microbial communities (Log $H_{2\,[aq]}$ = -9.21). Similarly, the model for hydrothermally generated bioenergetics under a T_{max} = 750 °C, also indicates that this Martian thermodynamic system cannot allow the maintenance mode of microbial activity after hydrothermal circulation has ceased. However, the final stage of this model reveals that the system can still allow the metabolic rate of microbial survival under such conditions. Moreover, both geothermal systems seem to support the mode of microbial maintenance under very low energy limitations (and their computed bioenergetics plot close to fulfilling the limits of microbial growth) for as long water-rock interactions are active.

4.2.2 Habitability Does Not Prove Past or/& Present Life

Suitable environmental conditions for the emergence and evolution of life require a complicated combination and equilibrium of physicochemical factors within a particular time frame and spatial domain. This amalgama of variables that dictate planetary habitability has not been efficiently explored yet. Factors such as the minimum bioenergetic requirements for microbial metabolic activity, the $\Delta_r G$ and Ea constraints of extreme terrestrial or other (exo-) planetary environments, or the rates of water-rock reactions and nutrients' release in geological realms, still do not comprise limiting factors in numerical modelling and quantification methodologies for assessing planetary habitability (Hoehler, 2004; Hoehler et al., 2007). Furthermore, such properties can be rarely sampled in surface or subsurface extraterrestrial environments. Hence, the bioenergetic parameters of habitability, although they might comprise some of the most significant variables in the preservation of microbial habitats under extremely low energy limitations (in photosynthesis-independent and anoxic environments), they remain an enigma in astrobiological research (Hoehler et al., 2007). The computational results of this work are an initial step towards coupling thermodynamic simulations for habitable environments with quantitative bioenergetic methods.

By theoretically determining a high probability for life existing under specific physicochemical conditions within a planetary crust, this rationale cannot suggest that biochemical evidence is decisively present in such an explored environment. Cockell (2014) explored hypotheses for the habitability of Mars and concluded that, if ancient Martian environments were uninhabitable or definitely uninhabited since the planet's formation, then the planet should be considered as uninhabited or uninhabitable from the Noachian until today (fig. 4.12). Additionally, in his work, Cockell argues that if Mars was definitely inhabited during its geological past, then the Red Planet may have either preserved its inhabited habitats until today, or that such habitats may have been rendered uninhabited or at least uninhabitable due to an extinction event. The results of this work, although consistent with previously published theses (Hoehler et al., 2007; Cockell, 2014), suggest that definitions on habitability are still incomplete. Thus, four complementary scenarios for the habitability of Mars, which may enrich the work of Cockell (2014), have been developed based on the thermodynamic and astrobiological simulations' results of this research:

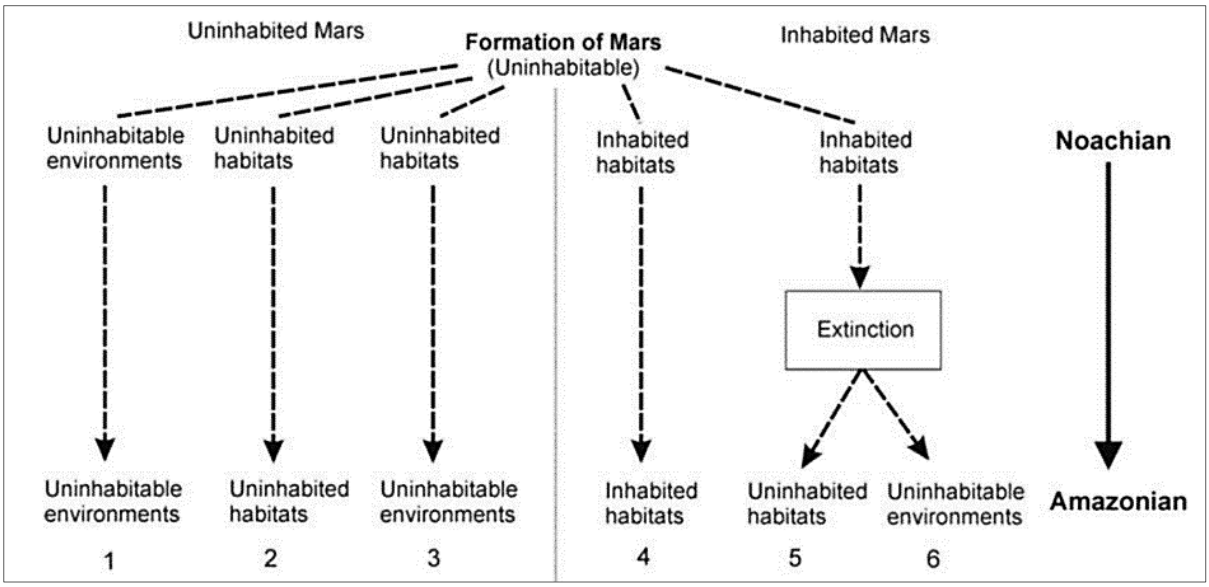

Fig. 4.12. Scenarios for the habitability of Mars through geological time by considering that Mars was either inhabited or uninhabited during the Noachian period (Cockell, 2014). The habitability models of this work investigated all the above hypotheses and experimented further with the emergence and evolution of potential microbial life under impact-induced and magmatic-induced hydrothermal conditions. Hypothesis n.4 could also represent the habitability evolution of planet Earth from the Hadean geological period until present.

[I]: If Mars was uninhabited during its ancient geological past, some of its deep subsurface environments may have been rendered habitable (but still uninhabited) later, due to ongoing water-rock interactions that could have persisted in the deep Martian crust for millions of years (e.g., bioenergetic models for the 100-, and 200-km in diameter impact-induced hydrothermal settings, and for the T_{max} = 750 °C magmatic-induced hydrothermal system).

[II]: If Mars was uninhabited during the Noachian, there might have been the possibility for the Red Planet to develop microbial (inhabited) habitats much later in its geological history, since the exact thermodynamic and bioenergetic processes and conditions, and time frame in which the first biomolecules can form and then evolve into microorganisms (mRNA, viruses prokaryotes) remains unknown.

[III]: Mars could have been inhabited during the Noachian period, but because of extinction events (large scale impact-cratering processes) sterilization may have eradicated all life forms since then. This does not mean though, that habitable conditions could not have persisted within the Martian crust from the early Hesperian until present. This scenario suggests that the planet may be uninhabited but still habitable in a few domains of the Martian subsurface.

[IV]: Martian environments could have been uninhabitable during the entire geological history of the planet, but some localities where hydrothermal conditions could have persisted deep within the crust, may have rendered those niches as habitable, and simultaneously uninhabited.

The findings of my PhD research strongly imply that habitable niches on Mars, and possibly beneath the icy crusts of Jovian and Kronian moons (according to research findings by Taubner et al. (2018); Hoehler et al. (2022)), or/and on other Earth-like (exo-)planetary bodies, may be far more ubiquitous. However, habitability assessments on such terrestrial environments should not even imply the existence of life forms where habitable conditions prevail. In other words, a planetary environment may be habitable, but it may be and may have stayed uninhabited during its entire geological history. The numerical models of this work (thermodynamic and bioenergetic) concur to the hypothesis that hydrothermalism on Mars may have formed habitable niches in the Martian subsurface for an appreciable period ranging from tens of Kyr to 2-3 Myr. Nevertheless, after hydrothermal circulation and water-rock interactions cease, the simulated (previously) habitable impact-induced and magmatic-induced hydrothermal environments of Mars are rendered uninhabitable, as the thermodynamic conditions and the availability of nutrients and energy are prohibitive for life.

4.3 Microscopy Analyses Informing the Numerical Models

4.3.1 SEM Analysis and Observations for the NWA 8159 & Lafayette Samples.

In the context of aqueous alteration processes during Mars' geological past, qualitative mineralogical observations from the NWA 8159 and Lafayette samples imply that Fe- and Mg-oxides and phyllosilicates hosted in the primary mineralogies may be associated with either primary or secondary aqueous alteration on Mars (e.g.: this should be the case for the Lafayette meteorite, as it is a quite pristine and less-affected by terrestrial contamination meteorite; Lee et al., 2015b), or may be the products of terrestrial weathering and contamination after their delivery to Earth (e.g.: several alteration phases in NWA 8159; Christou et al., 2019; 2020; 2021). The SEM-BSE and SEM-EDS observations in this work allowed to construct elemental composition maps and to identify mineral phases that have been affected by primary or secondary alteration (e.g.: apatite in NWA 8159 (fig. 3.38; Christou et al., 2019; 2020), olivine in Lafayette (Lee et al., 2015b)). Hence, alteration veins hosted within the mineralogies of NWA 8159 and Lafayette are a clear indication of aqueous processes that have affected these meteorite samples.

However, it is yet unclear whether those fluid-rock interactions occurred on the Red Planet or Earth, or both. To understand the precise origin and geochemical reaction pathways from which these alteration mineral phases originate has been proven a very complicated and multifaceted research task in this PhD research, requiring innovative and correlative nano-scale analyses through a variety of microscopy techniques. Future EPMA, TEM, nano-SIMS, and APT analyses have been scheduled, so that the characterization of Martian and terrestrial mineral species can be conducted. Furthermore, future analyses are anticipated to determine the stoichiometric and volatile composition of the fluids that have interacted with these Martian volcanic rocks on both Mars and Earth.

As the bulk rock compositions of Martian basalts have been introduced into the PHREEQC thermodynamic database according to findings by McSween et al. (2006a; 2006b), Herd et al. (2017), Peretyazhko et al. (2018) and Thorpe et al. (2022) (please see § 2.2), the PHREEQC simulations of this research utilized and compiled previous bulk rock compositional findings into the PHREEQC input parameterization; instead of relying on the SEM-EDS qualitative /

semi-quantitative elemental composition datasets acquired at the GEMS facility of the University of Glasgow, after many disruptions to lab-based research during the covid-19 pandemic. Nevertheless, the BSE and EDS maps helped determine the physical and petrological characteristics of these Martian rocks in the developed numerical models of this work. Specifically, the porosity of the NWA 8159 and Lafayette rocks was determined in this PhD research after acquiring whole-sample BSE maps via SEM analysis of their thin sections. Furthermore, as the NWA 8159 and Lafayette meteorites sample basaltic environments of ancient Mars, their volcanic petrologies and indications for aqueous alteration helped determine potential geochemical reaction pathways through PHREEQC simulations.

4.3.2 ImageJ Analysis on the BSE maps of the NWA 8159 and Lafayette Samples.

Image processing of the BSE (tiff) maps from NWA 8159 and Lafayette through the ImageJ software allowed calculations on the porosity of these Martian rocks. As the NWA 8159 and Lafayette meteorites sample the basaltic crust of Mars, the calculated porosity values through ImageJ were of major significance for constraining efficiently and for increasing the reliability of the hydromechanical models developed in this PhD research. Porosity is a major controlling factor of hydrothermal circulation together with permeability (Abramov and Kring, 2004; 2005; 2007), and so, defining analytically at least one of the two petrophysical parameters via microscopy imaging has led to enhancing the accuracy of the input thermodynamic conditions in HT 3 models, and their subsequent results.

To determine the permeability of any rock, an appreciable mass of an intact hard or soft lithology should be tested through flow pump tests (e.g.: transient pulse tests; Hsieh et al., 1981; Neuzil et al., 1981; Song et al., 2019); such methodologies require the rock to be affected by aqueous flows under lab-controlled conditions. Due to the uniqueness and short supply of Martian rock samples, permeability tests cannot be conducted; firstly, the required rock masses to be tested are unavailable, and moreover, such permeability examinations would alter or even destroy several of the chemical characteristics of these rocks (e.g.: flow pump tests would probably lead to the dissolution of Martian phyllosilicate and carbonate minerals, if the whole meteorite sample was to be tested). Furthermore, porosity measurements on terrestrial rocks also require extensive rock sampling and subsequent examinations to be able to establish the

porosity of an entire geological unit or area. Therefore, using just a couple or a few thin-sections that come from a single Martian rock sample (meteorite) is quite a restrictive approach towards characterizing the physical and chemical properties of the Martian crust. In this PhD research, this problem was also evident through a discrepancy in the calculated (through ImageJ) porosity values just between the two NWA 8159 thin-sections. As mentioned in §3.4.2., ImageJ processing on the BSE map of NWA 8159 sample 2 calculated the sample's porosity with a value of 2.2 %, even though the same methodological steps yielded porosity values of 4.93 % and 5.27 % for Lafayette USNM 1505-5 and NWA 8159 sample 1, respectively. Nonetheless, we need to appreciate that Martian meteorites still comprise the only accessible petrological samples from the Red Planet that we can extensively investigate through a variety of non-destructive microscopy and nano-scale analytical techniques here on Earth.

Eventually, the porosity of the NWA 8159 and Lafayette samples were efficiently determined via ImageJ processing in this PhD work. For the above reasons, temperature dependent (based on HT 3 thermodynamic specifications) porosity values of circa 5% were chosen to describe the Martian basaltic crust in HT 3 simulations. Thus, by establishing the porosity of the aforementioned Martian meteorite samples via microscopy imaging analysis, the input HT 3 parameters of permeability and porosity could be subsequently benchmarked and redefined through the equations of state included in the code (as discussed in §2.1; please also see equations 2.1 – 2.7). Finally, this approach enabled refining the initial parameterization in HT 3 models and informed the generated numerical simulations with both qualitative (SEM-EDS maps) and quantitative microscopy observations (e.g.: porosity calculations by processing BSE maps via ImageJ). Conclusively, utilizing the findings of microscopy investigations to inform and enhance the numerical models of this work has been proven a beneficial research strategy towards increasing the reliability and insightfulness of the developed models.

4.4 Numerical Models Consistent with Mars Spacecraft and Rover Observations

4.4.1 The Presence of Water-/Ice Deposits on & in the Martian Crust

The modelling results of this work imply that the abundance of water in the Martian crust is highly significant for supporting long-lived hydrothermal circulation and the bioenergetic potential of its host geological systems. The surface and subsurface of Mars have been observed with appreciable quantities of ice deposits via remote sensing observations (Levy et al., 2014) but it is yet unclear whether the directly observed or inferred icy deposits are associated with aqueous compositions. Fig. 4.13 summarizes the distribution of buried ice deposits on Mars and could serve as a preliminary habitability indicator (Levy et al., 2014; Grau Galofre, 2020). Where water-ice and rock reactions are possible, then the higher the probability should be for potential nutrients' release in a lithological substrate. The north and south polar ice caps of Mars are regions of great scientific interest, as Martian ice samples could establish the hydrous or anhydrous nature of these icy deposits' compositions and constrain essentially the habitability of the Red Planet. Moreover, ice core samples could be relatively easy to obtain from Mars' polar regions via future rover missions.

Geophysical surveys via the MARSIS system on the Mars Express Orbiter have revealed a high abundance of water-ice deposits in the shallow subsurface (depth $\leq$ 1 km) of Mars close to the polar regions and have even implied the presence of liquid water deposits at depths between 1.5 – 2km (Orosei et al., 2018). However, geophysical data obtained via orbiter spacecrafts have their limitations, as radar echoes cannot accurately specify the type of reflector in a surveyed lithostratigraphic setting. Although preliminary findings may be indicative of abundant aquifers in the Martian crust, without sampling the icy deposits of the Martian surface and examining their nature, interpretations may be proven too optimistic for the abundance of water and subsequent occurrence of habitable niches on Mars.

So far, several hypotheses have been put forward regarding the compositions of the inferred water-ice deposits on Mars. The most prevalent hypothesis formulates that Martian

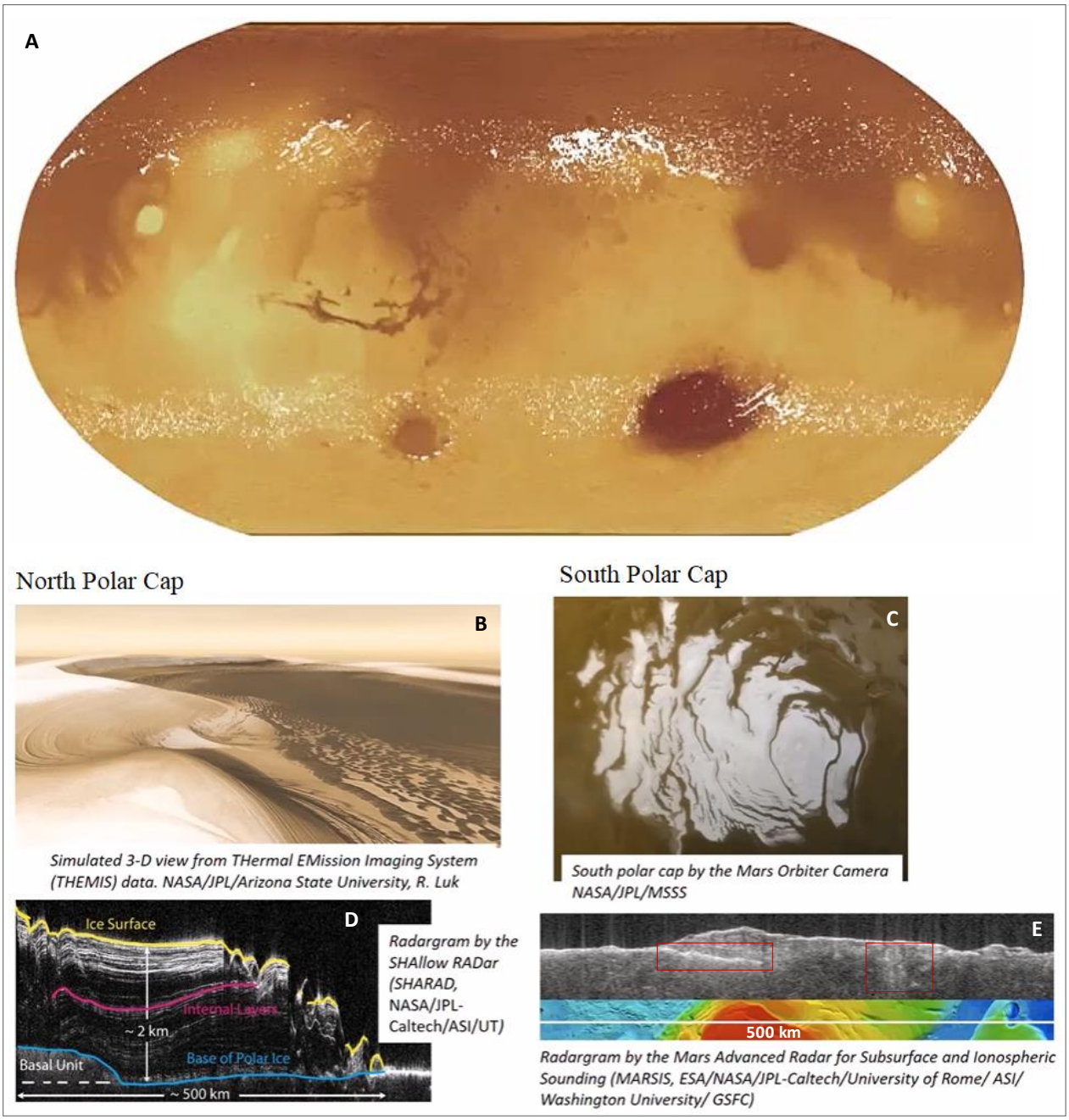

Fig. 4.13. Evidence for ice deposits on the Martian surface and subsurface via remote sensing observations. (A): Geographical distribution of buried icy formations on Mars over topography, via datasets obtained from the Mars Orbiter Laser Altimeter (MOLA) instrument (Levy et al., 2014). (B): Reconstructed 3D view of the North Polar Ice Cap on Mars via analysis of THEMIS data. (C): Image of the South Polar Ice Cap on Mars obtained through the Mars Orbiter Camera. (D) Reconstruction of radar data acquired by the SHARAD system, which reveals the lithostratigraphy of the Martian cryosphere and the contact between a basal lithology and the 2-km thick ice deposits. (E): Stratigraphic profile reconstruction (radargram) after analysis of a MARSIS's transit acquired radar datasets. The regions annotated with the red rectangles (bright regions) indicate a higher concentration of ice deposits within the subsurface. Some of these icy formations seem to have been deposited within faults, fractures and generally, within higher permeability subsurface niches. Captions B-E have been edited after Grau Galofre (2020).

water-ice deposits appear mainly in the form of frozen brines on the surface under freezing temperatures or, when found in warmer regions of the equator and in the deeper subsurface, frozen aqueous deposits should be forming liquid water flows of high salinity, as observed in the Recurring Slope Lineae (RSL) regions on Mars (Ojha et al., 2015). Microbes that are halophilic (thriving under high salinity conditions) and psychrophilic (thriving under cold – freezing temperatures) have been observed in Earth's polar regions (Chua et al., 2018; Luo et al., 2020). Therefore, if the ubiquitous icy deposits on Mars are of indeed aqueous compositions, then similar microbial species could have probably populated cold and high alkalinity habitats of the Martian polar regions or/and of the icy subsurface (depth ≥ 1.5 km).

4.4.1.1 Implications for the Presence of Water in Martian Impact Craters

Detection of liquid H_2O in Martian impact cratering structures and broadly on the Martian surface has not been possible yet. Liquid water cannot form on the planet's surface, since the Martian atmospheric pressure is about 0.006 bar, which is slightly below the vapor pressure of water. Hence, any water on the Martian surface would sublime (transit directly from solid to vapor) under warmer conditions, and vice versa, any water-vapor cooling on Mars would deposit immediately in the form of ice (Haberle et al., 2001). Evidence for ice deposits' formation due to seasonal temperature variations, and for ice deposits excavated from the subsurface after impact-cratering processes has already been reported (Levy et al., 2014). The formation process and nature of the RSL geological features on Mars remains controversial as there is no scientific consensus about their association with either hydrous flows or dry granular flows (fig. 4.14, Ojha et al., 2015; Bishop et al., 2021). As the exact composition of these icy deposits remains unknown, assigning a H_2O composition to Martian icy deposits in quantitative or qualitative analytical investigations should be treated as a mere speculation.

Impact-cratering processes on Mars may excavate ice deposits from deeper subsurface regions, and assuming a large-scale cratering formation process, impact-generated heat may induce liquid and vapor flows in such cases (Abramov and Kring, 2005). Even though we are unsure about the stoichiometry of ice deposits within the Martian subsurface, impact cratering events would inevitably melt and mobilize any volatile components within the target lithology. Therefore, in the event of an asteroid/comet impact, if any aquifer would have been present in

the affected Martian crust, then it would thermodynamically respond by inducing hydrothermal flows. However, if icy deposits are anhydrous (e.g.: CO_2, CH_4), under impact-generated conditions, no other fluid flows should be expected, other than steam fluxes.

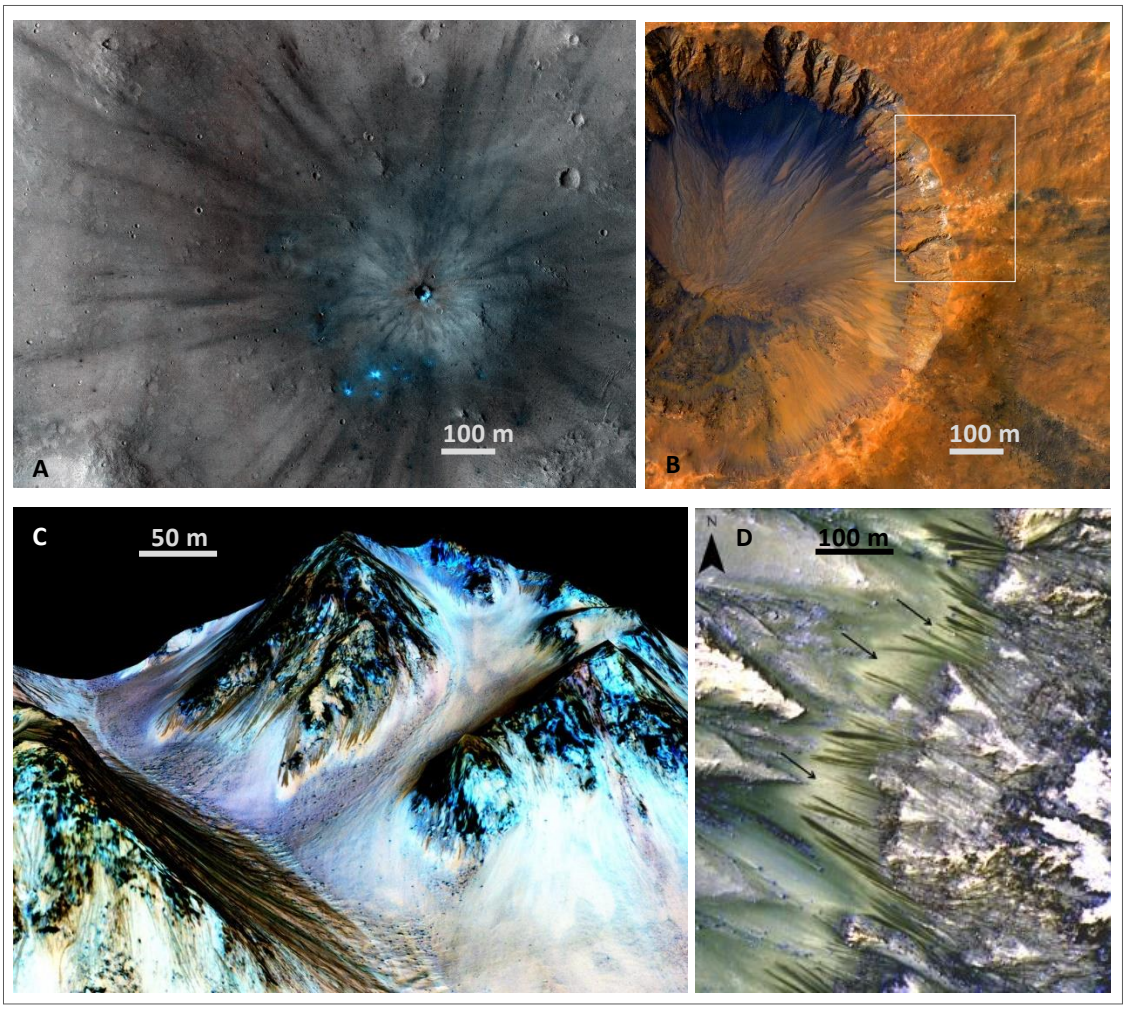

Fig. 4.14. Fresh impact structures on Mars and implications for the presence of water-ice deposits therein. (A): A new crater on Mars formed between 2012 - 2013 and firstly observed by the High-Resolution Imaging Science Experiment (HiRISE) camera on NASA's Mars Reconnaissance Orbiter on 19/11/2013. ©NASA/JPL-Caltech. The terrain where the crater formed was dusty and regolithic. Hence, the fresh crater appears blue in the enhanced colour image due to removal of the reddish dust in that area. The bright azure colours may also host represent ice deposits beneath the regolithic surface, but no quantitative geochemical data via remote sensing have been obtained yet from that region. (B): Another new impact crater on Mars, discovered in the Sirenum Fossae region on 30/3/2015 by the HiRISE camera aboard NASA's Mars Reconnaissance Orbiter. This impact crater appears recent too, as it exhibits a sharp rim and well-preserved ejecta. The inner slopes of the crater are very steep and carved by gullies, and there is a strong implication for recurring slope lineae (bright deposits implying the presence of fluids annotated by the white rectangle, ©NASA/JPL-Caltech). (C and D): Recurring Slope Lineae (RSL) at Hale Crater, Mars ©NASA/JPL-Caltech. RSL indicate that seasonal flows occur on equatorial Martian slopes. However, it is yet unclear whether these flows comprise saline water flows which occur during the warmest months on Mars, or dry granular materials that simply flow downslope. As RSL incrementally grow on steep

(25° to 40°) slopes during warm seasons and fade during cold seasons, it most likely for the RSL to represent heat-generated flows of salty water on the Martian surface (Ojha et al., 2015). An alternative hypothesis considers RSL to be Martian landslide features which are induced after geochemical reactions between sulfates and chlorine salts under either wet (presence of H_2O) or dry (absence of H_2O) conditions, or both (Bishop et al., 2021).

4.4.1.2 Implications for the Presence of Water in Martian Volcanic Provinces

Volcanic plateaus on Mars exhibit evidence for extensive lava flooding events throughout the planet's geological history (Robbins et al., 2011; Wray et al., 2013b). Most of these volcanic provinces are associated with a ubiquitous presence of flood basalts, some of which are also in the vicinity of a sequential formation of outflow channels and valley networks (Jaeger et al., 2007). Hence, if these volcanic environments were at some point, during the Martian geological history, affected by the later formation of outflow channels (significant water flows), such processes could have then initiated hydrothermal circulation and water-rock interactions in the broader volcanic province for a considerable period, as indicated by the computational results of this PhD research. Furthermore, high-precision analytical examinations of nakhlites have already identified carbonate and phyllosilicate chemistries of Martian origin in these basaltic rocks from Mars; such phyllosilicate and carbonate phases are Fe-rich, and alteration veins in nakhlites were also found to contain appreciable amounts of prebiotically important elements such as H, C, S, P, Cl, K and B (Hallis and Taylor, 2011; Hallis et al., 2012a; 2012b; Lee et al., 2013; Lee et al., 2015a; 2015b). These contributions strongly indicated that the nakhlites' host basaltic rocks should have been interacting with aqueous flows on Mars. Thereby, the subsequent release of chemical nutrients after water – rock interactions on Mars could have rendered such basaltic or other environments (e.g.: brines; Stevens and Cockell, 2023), as also suggested by the bioenergetic modelling of this PhD research.

Fig. 4.15 shows high-resolution images of lava flows on Mars obtained by the Thermal Emission Imaging System (THEMIS) - Daytime InfraRed (IR). The lava terrains of Arsia Mons and Athabasca Valles may be associated with the subsequent development of outflow channels on Mars, as they are all in a relative proximity (please see also fig. 4.18). The triggering mechanisms via which Athabasca Valles and its proximal outflow channels formed are still controversial, but the most plausible explanation is offered by Cassanelli and Head (2018), who

state in their work that late-Amazonian lava plains should have been emplaced in Athabasca Valles in the form of flood basalts. These lava flow events triggered large-scale lava-ice interactions, resulting eventually in the formation of the youngest outflow channel system on Mars. We can therefore deduce that these volcanic environments should have interacted with heterochronous aqueous flows that originated from the outflow channels, and so, the habitability potential of this volcanic province should be considerable and consistent with the quantitative analysis of the bioenergetic models of this work.

Another similar volcanic environment to Athabasca Valles is Arsia Mons, one of the three largest volcanoes in the Solar System. Arsia Mons is also associated with identical but less extensive outflow channels that postdate its formation, and which developed in the broader Tharsis volcanic plateau. The magmatic-induced flows in this volcanic province, together with the aqueous flows generated by the outflow channels, should have produced an extended and long in duration (for 2 – 3 Myr) hydrothermal environment in both the southern and easternmost provinces of the Tharsis plateau, since similar thermodynamic settings were reproduced via numerical modelling (magmatic-induced hydrothermalism simulation with T_{max} = 750 °C). Such conditions should have led to the development of habitable niches in the broader Tharsis volcanic province, which can then be seen as a very promising site in terms of its biogeochemical potential. On the other hand, the basaltic province of Hesperia Planum which exhibits wrinkle ridges does not seem to host clear evidence for basaltic rock – water interactions, as no outflow channels or any similar geomorphological features can be easily distinguished therein or in the vicinity of this flood basalt terrain.

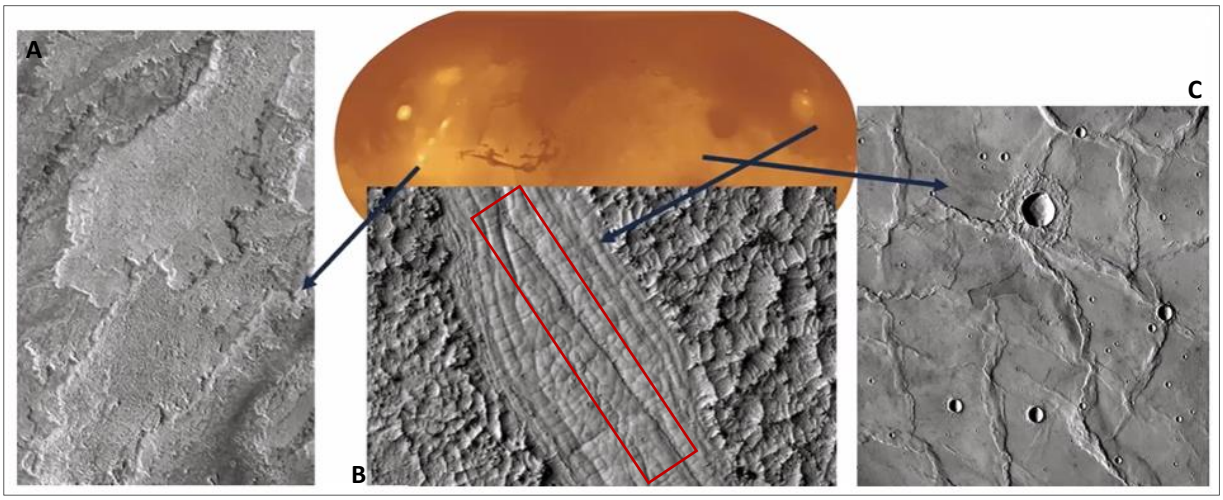

Fig. 4.15. (A): Lava flow in Arsia Mons reported by the THEMIS – Daytime IR. This lava flow is located in the Tharsis volcanic plateau which is near the equator in the western hemisphere of Mars. The Tharsis volcanic province is home to the largest volcanoes of the Solar System: known as the Tharsis Montes / shield volcanoes (Arsia Mons, Pavonis Mons and Ascraeus Mons) © NASA/ASU/JPL-Caltech. (B): Relatively recent lava flow (age: 45-50 Ma) in Athabasca Valles revealed by the HiRISE instrument. The Athabasca Valles exhibits a late-Amazonian period outflow channel system in the central Elysium Planitia region of Mars, south of the Elysium Rise (Jaeger et al., 2007); © NASA/JPL-Caltech/MSSS/UoA. Although the formation process of the Athabasca Valles system is still debated, most research outcomes concur to the hypothesis that late-Amazonian lava plains have been emplaced via a flood basalt mode. The flood basalts induced large-scale lava-ice interactions, and this should have resulted to the formation of the youngest outflow channel system on Mars. Hence, Athabasca Valles on Mars may have formed by the catastrophic outpouring from the 1235-km across semi-parallel faults/fissures (Cerberus Fossae: annotated by the red rectangle), which pulled the crust apart in the Cerberus region (Cassanelli and Head, 2018). (C): Wrinle ridges in Hesperia Planum revealed by the THEMIS – Daytime IR © NASA/ASU/JPL-Caltech. Hesperia Planum is a much older volcanic plain on Mars, which exhibits wrinkle ridges. The wrinkle ridges' occurrence on Mars is solely associated with basaltic lava flows (flood basalts). The ridges themselves are believed to be the surface expression of thrust faults developed after the lava flows were emplaced. Hence, the ridges are not of volcanic, but of tectonic origin, as they form in dense and lower permeability rocks that have undergone compressional stress (Montési and Zuber, 2003). Hesperia Planum is mainly composed by flood basalts and exhibits very weak evidence for basaltic lava-ice interactions (Gregg and de Silva, 2009), in contrast to the geological environments of Elysium Planitia and Tharsis Montes.

4.4.2 Observed Features from Mars Missions Predicted via Numerical Modelling

The numerical models of this work reproduced features of the deep Martian subsurface that are evident in data acquired by exploration orbiters (fig. 4.16). The most significant and robust simulations showed that if liquid water has been present on the Martian subsurface, then it

should be found at depths greater than 1.5 km beneath the surface. At shallower depths, the low geothermal gradient, combined with the freezing temperatures for H_2O and the very low atmospheric pressure on the surface, results to most liquid water forming ice deposits. In the simulations, it was evident that the upper regolithic units were not hosting appreciable water fluxes beyond the initial stages (1 – 20 Kyr) of hydrothermal activity, and that most active hydrothermal cells would persist at depths greater than 1.5 – 2 km. The HT3 code and PHREEQC software could not reproduce the chemical and physical formation of water-ices on the surface of Mars, but the equations of state that HT 3 uses could indeed predict a much lower water mass flux magnitude and distribution of flows in the upper regolith of the simulated geothermal settings due to low atmospheric and lithostatic pressure.

Fig. 4.16 (C) demonstrates that if any liquid water deposits are present on Mars today, or have been present during the entire Amazonian period, then these aqueous sources should be found beneath the lower regolithic units, and within the porous spaces of deeper and lower permeability sedimentary, brecciated, or basaltic lithologies. These computational results are highly consistent with geophysical interpretations provided by Orosei et al (2018) suggesting the detection of liquid water beneath subglacial regions at the South Pole of Mars after radar data acquired by the MARSIS instrument on board the Mars Express Orbiter (fig. 4.16). This suggests that the equations of state and thermodynamic specifications of the HT 3 code, and the conducted modifications for simulating the geothermics of planet Mars through this PhD work, can be considered accurate. Therefore, we can additionally conclude that aqueous environments at depths greater than 1.5 – 2 km within the subsurface of Mars could have provided favorable conditions for the development and perseverance of habitable niches for subterranean microbial life.

As mentioned, due to the very low atmospheric pressure on Mars, water cannot exist in its liquid form on the surface. Salt dissolution, however, reduces the freezing point and increases the boiling point of aqueous phases (Marion et al., 2010). Perchlorate salts in mixture with carbonates, sulfates and chlorides have been detected in regolithic soils on Mars by the Phoenix Wet Chemistry Laboratory (WCL) experiment (Hecht et al., 2009) and have been previously modelled for predicting the thermodynamic response of such saline aqueous solutions under putative Martian surface conditions (Marion et al., 2010; Toner et al., 2015a; 2015b). These previous findings highlight the effect of different perchlorate salts such as $NaClO_4$ and $Mg(ClO_4)_2$ on the freezing and boiling points of aqueous solutions, and consider saturation

solubility under varying ionic conditions with indications for the triple point of water shifting to – 4.15 °C. The thermodynamic and bioenergetic models of this work could not include temperatures below 0°C, as the convergence criteria of the HT3 code and PHREEQC program could not be satisfied.

Previously published numerical experiments via the FREZCHEM and PHREEQC codes (Marion et al., 2010; Toner et al., 2015a; 2015b) indicated that under extreme saturation conditions by mixtures of salts, liquid water may be present on Mars between – 93.15 °C and 25 °C. These researchers concluded that above this temperature range liquid water exists in the form of steam in the shallow subsurface or surface of Mars, and that below this temperature range, water exists as ice. On top of that, under these numerical simulative conditions, water held in hydrated salts was predicted only with a 0.29 wt.% concentration. Therefore, such computational tools should be further reviewed and developed for simulating cryospheric and cold Martian analogues, as their predicted values for H_2O concentrations in Martian soils and salts appear considerably lower (0.29 wt.% H_2O) than minimum estimates (1.5 wt.% and 2 wt.% H_2O) from orbital and in situ measurement of Martian soil water content findings (Toner et al., 2015a; 2015b). Lastly, if the predictions of these codes were robust, liquid water on Mars should have been ubiquitous and easily observed in RSL brines. Therefore, the assumptions of the aforementioned codes (FREZCHEM and PHREEQC) on the temperature range in which aqueous saline solutions may form on Mars should be considered as relatively liberal.

For the above reasons and due to the limitations of geochemical softwares to accurately predict water-rock interactions under putative freezing ($\leq$ 0°C) and extremely low-pressure surface conditions, this PhD research focused on simulating the thermodynamics and potential bioenergetics of the Martian crust under subsurface hydrothermal conditions. This thesis recognized that if any habitable domains formed and persisted in the Martian crust throughout the Red Planet's geological history, then these should have been in the deep subsurface, under higher temperature and lithostatic pressure constraints. Therefore, the results of this PhD research support the hypothesis that drilled core samples from far greater depths beneath the surface of Mars ($\geq$ 1 km), or samples originating from the slopes of volcanic and impact crater rims may be proven far more fruitful for the potential detection of fossilized or even currently active microbial life.

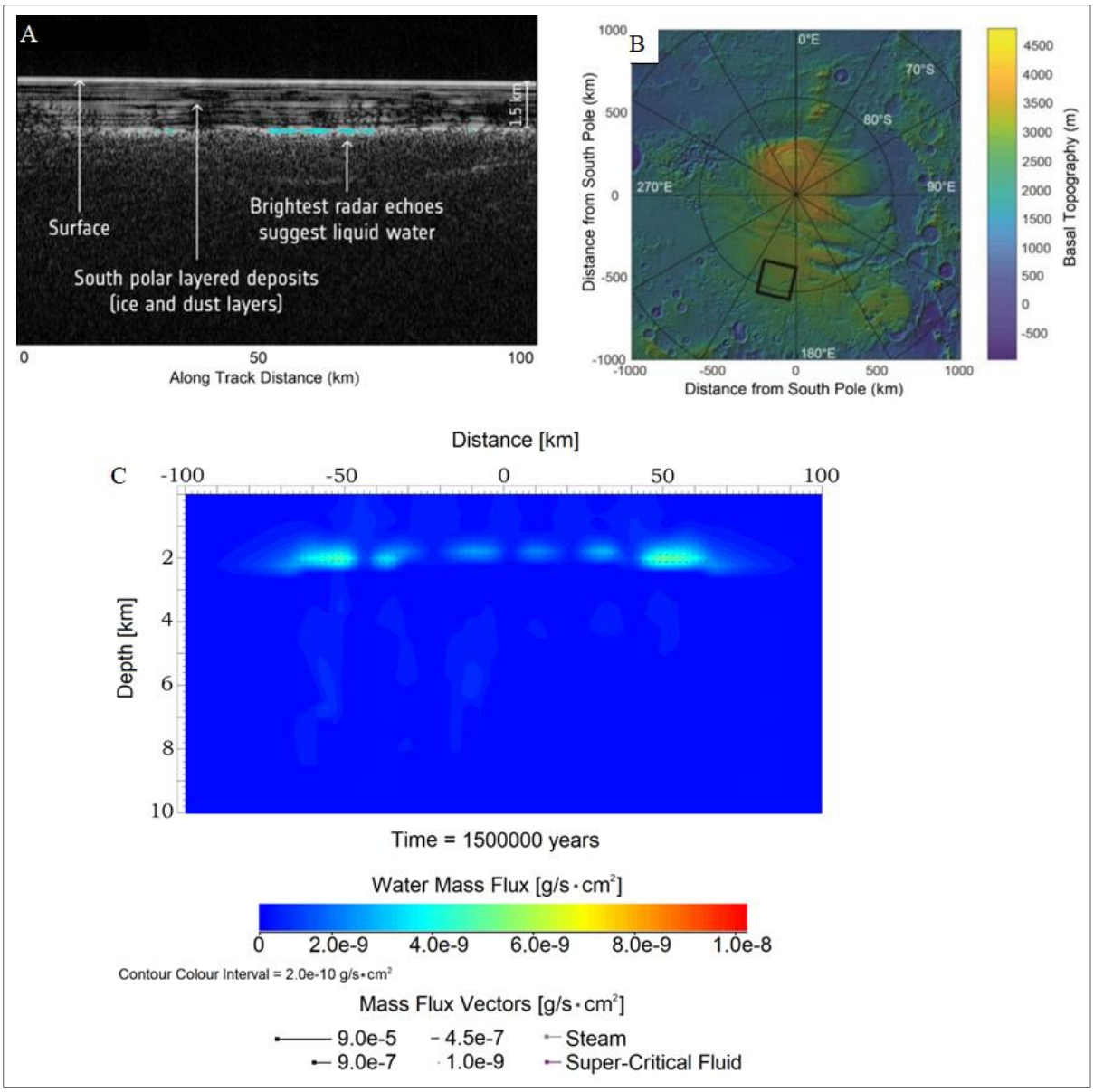

Fig. 4.16. (A): Geophysical detection of liquid water beneath subglacial regions at the South Pole of Mars via the use of the MARSIS instrument (Orosei et al., 2018). Caption A is a 2D reconstructed model which allowed the detection of reflectors in the Martian subsurface, after ground-penetrating radar echo experiments performed by the MARSIS instrument deployed on the Mars Express Orbiter. The MARSIS observations revealed potentially liquid water deposits 1.5 – 2 km beneath the Martian surface as brightest radar echoes. (B): Topography of the South Polar region that the MARSIS system of the Mars Express Orbiter surveyed and from which the radar echo reflection data originate (illustrated with a black box). (C): Numerical simulation results which indicate that after hydrothermal circulation has ceased in a magmatic-induced hydrothermal system within the Martian crust, water deposits form and are preserved at depths of circa 1.5 – 2.5 km. This simulation reproduces the indications of geophysical data obtained by the Mars Express Orbiter. Additionally, it implies that if any liquid water deposits have been present in the Martian subsurface throughout Mars' geological history, the thermal characteristics of the crust would allow those to form and persist at depths greater than 1.5 km. In shallower depths H_2O and CO_2 deposits are expected in their solid state due to the low geothermal gradient and the freezing surface temperature.

4.5 Promising Sites for the Detection of Biosignatures on Mars

4.5.1 Martian Impact Craters

Martian impact cratering systems with larger crater diameters ($D \geq 10$ km) should have hosted long-lived hydrothermal systems with durations ranging from 75 Kyr ($D \approx 10$ km) to even up to 2 – 3 Myr (when $D \geq 100$ km). As reported via the numerical simulations of this work, hydrothermal circulation in such systems, and the subsequent water-rock interactions in these settings should have provided sufficient quantities of chemical nutrients for potential microbial life to harvest and fulfill its basic metabolic energy requirements, even under extreme energy limitations (non-photosynthetic and anoxic conditions).

Therefore, it is not surprising that the Jezero crater ($D \approx 45$ km) was selected as a very promising site for the Perseverance rover to land and explore its surface and shallow subsurface for potential biosignatures on Mars, and to assess the habitability of the crater's geological environment by sampling and caching rocks and regolith soils for future return missions. Conclusively, the findings of this PhD research indicate that impact cratering structures on Mars with a large crater diameter, should be far more promising for the detection of biosignatures in their inner-rim, central valley, and peak ring slopes, as these regions should have been more heavily affected by impact-induced hydrothermal activity. To accurately predict the distribution of post-impact hydrothermal flows in ancient impact craters, the duration of hydrothermal circulation, and to determine the domains that were more severely affected by hydrothermal fluid – impactite interactions, modelling tools should be further developed to increase the resolution and robustness of thermodynamic and bioenergetic computations. Several initial conditions such as the H_2O saturation and evolution of the impact-affected environment, the crust – atmosphere thermodynamic interactions after the impact, or the presence of H_2O and CO_2 ices and brines (fig. 4.17) in the impact cratering setting have not been efficiently incorporated in hydrocodes yet. Such state-of-the-art simulation techniques will eventually guide and synchronously provide feedback to future rover missions during their astrobiological research expeditions on planet Mars. In conclusion, the development of even more sophisticated geophysical and geochemical codes that can also be coupled is imperative.

Fig. 4.17. The icy impact-cratering landscape was captured on 19/05/2022 by the High-Resolution Stereo imaging Camera (HRSC) on board ESA's Mars Express, while it was surveying the Ultimi Scopuli region near the South Pole of Mars. This crater is at the southern hemisphere and when the image was captured, it was during the spring season; hence, ice had already started retreating in elevated terrains. Dark dunes and dark dust were revealed in several regions and in the form of ridges. Dark dunes and dust deposits should be originating from erupted material that is of basaltic origin, and they are ubiquitous on Mars due to aeolian deposition © ESA/DLR/FU Berlin.

4.5.2 Martian Volcanic Provinces

Similar to impact-induced hydrothermalism, hydrothermal systems generated in volcanic settings share identical patterns of hydrothermal circulation and durations of hydrological activity. Where water-rock interactions are active for hundreds of Kyr and even up to Myr, which should be the case for major volcanic provinces of the Martian crust, the habitability of such volcanic subterranean realms increases exponentially, as shown in the bioenergetic computations of this work (particularly, in the simulated geothermal systems with T_{max} = 500 °C, and T_{max} = 750 °C).

Several volcanic provinces on Mars seem to have been affected by hydrological activity, and such hydrological events should chronologically coincide or slightly postdate the geological periods of active volcanism on Mars (Robbins et al., 2011). Basaltic lava flooding events and

intense volcanism during ancient epochs of the Amazonian period are evident in the western highlands of Mars (Tharsis volcanic plateau) and in the central Elysium Planitia region of Mars which is located south of the Elysium Rise (as analysed through fig. 4.15). After their formation, these volcanic provinces were affected by a subsequent proximal evolution of outflow channels. These hydrological features may have been interacting with recent magmatic-induced hydrothermal systems therein, or at least aqueously with the basaltic lithologies emplaced in these provinces (Jaeger et al., 2007). Therefore, volcanic rock – water/ice interactions should have been persisting in these volcanic terrains for an appreciable period during more ancient geological eons. For example, the terrain of the Tharsis volcanic plateau hosts three of the largest volcanoes of the Solar System (Wilhelms and Squyres, 1984; Neukum et al., 2007). Hydrothermal activity in such large-scale volcanic systems, as inferred from the simulations of this work and under conservative constraints (T_{max} = 750 °C), may have lasted for a minimum period of 2-3 Myr.

Fig. 4.18 (A-B) shows that the easternmost part of the Tharsis plateau is affected by the canyon system of Valles Marineris and by several outflow channels. Conclusively, outflow channels of the Valles Marineris canyon system (annotated by the red rectangle) should have been transporting significant quantities of aqueous fluids to the eastern volcanic provinces of the Tharsis plateau. Thus, slopes of these volcanic craters (on Arsia Mons, Pavonis Mons and Ascraeus Mons) should be hosting valuable evidence for basaltic rock - water interactions under either hydrothermal or hydrous conditions. The simulations of this work should therefore be indicative for the duration of hydrothermal circulation and for the bioenergetic potential of the broader Tharsis volcanic province. Such water-rock interaction cycles could have been occuring periodically, since hydrothermal activity in major Tharsis volcanoes, or the aqueous activity implied by the extent of outflow channels of Valles Marineris, could have persisted for several Myr.

However, the timescale in which hypothesized water-rock interactions may have been occuring in Valles Marineris remains a mystery, and there is still no consensus about the origin and alteration history (aeolian vs. lacustrine vs. volcanic; Chojnacki and Hynek, 2008) of the layered deposits at the greater than 15000 km^2 Valles Marineris area. Hence, future areological research should focus on solving this conundrum, as it would constrain substantially the aqueous history and habitability of the Red Planet.

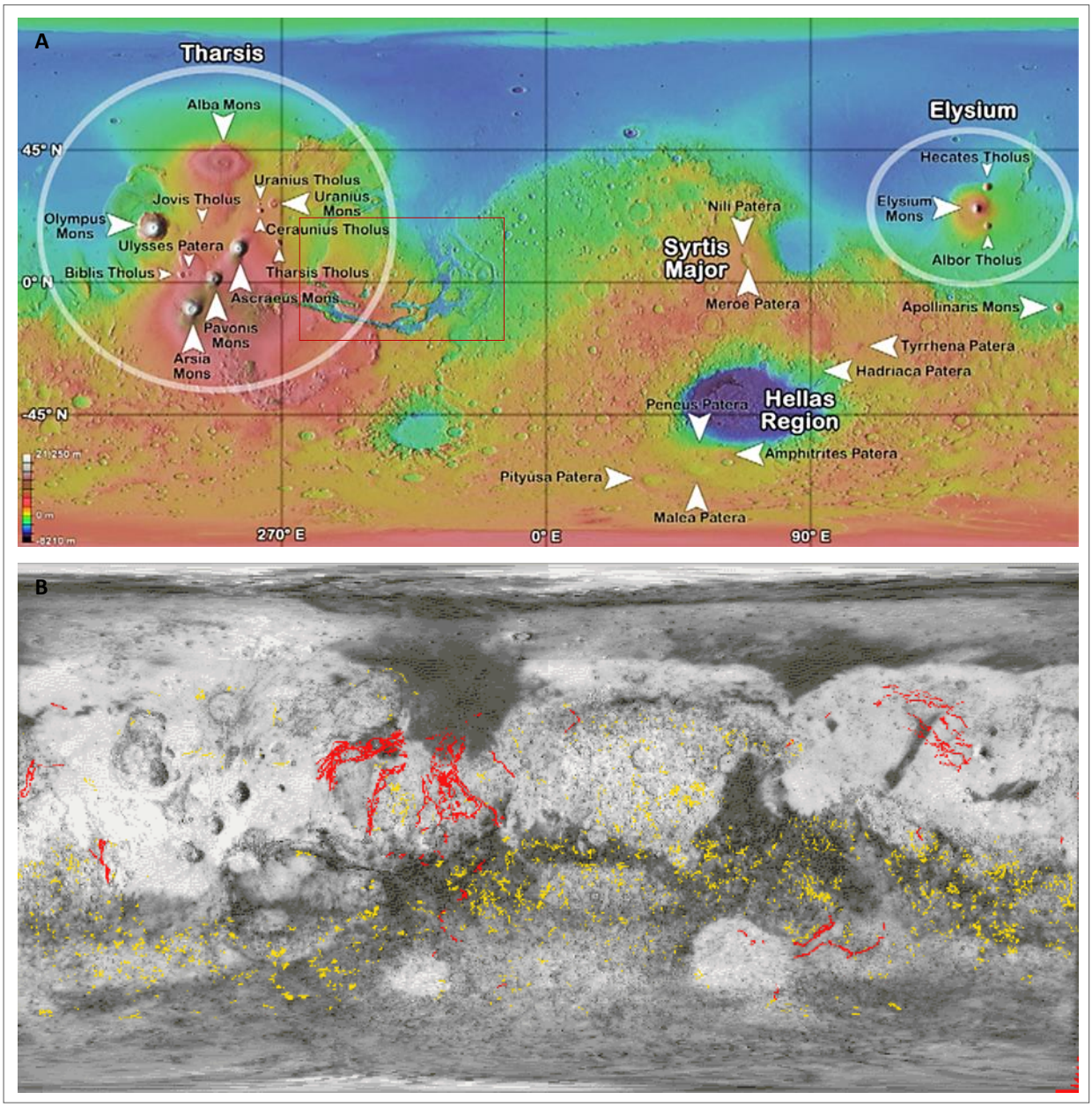

Fig. 4.18. (A): MOLA (Mars Orbiter Laser Altimeter) shaded relief topographic map (Smith et al., 2001) with plotted locations of the 24 major volcanoes of planet Mars (modified after Robbins et al., 2011). (B): Major outflow channels' (coloured red) and valley networks' locations (coloured yellow) on Mars (© Mike Caplinger, Malin Space Science Systems, 1995). Outflow channels are evident mainly in the young terrains (of Amazonian age) of the northern lowlands. Valley networks occur in the much older, and severely affected by impact-cratering processes, terrains of the Noachian and Hesperian periods. Therefore, we can deduce that the formation of outflow channels postdates the formation of valley networks on Mars. Moreover, most outflow channels are also in the vicinity of some of the largest volcanic plateaus. Thus, volcanic rock – water/ice interactions should have been more frequent in those regions during ancient geological epochs (e.g.: in the easternmost region of the Tharsis volcanic plateau, where the canyon system of Valles Marineris (annotated by the red rectangle in sub-caption A) stretches eastward from the Tharsis plateau. Outflow channels once flooded with water incrementally developed the Valles Marineris hydrological system in the eastern regions of the Tharsis volcanic province, and then extended toward the northern lowlands of Mars.

4.6 Astrobiological Implications for Cryovolcanic Systems in the Outer Solar System.

The modelling rationale of this thesis focuses on exploring the habitability of Martian environments that may have hosted water-rock interactions under hydrothermal conditions and for a significant geological period (from 100 Kyr to more than 3 Myr). The origin of life under hydrothermal conditions has already been suggested for geological systems on Earth (Holm, 1992; McCollom and Shock, 1997). This theory has strong implications for potential microbial activity under hydrothermal conditions on Mars, on other planetary bodies of the Solar System, or on other exoplanetary bodies that may be exhibiting active hydrothermalism.

This work focused on the habitability of Mars and, in particular, on computational investigations for the duration and thermodynamics of hypothesized Martian hydrothermal systems. One of the main factors that limit the habitability of Mars and that of other planetary bodies is the timescale in which hydrothermal circulation is active and able to release chemical nutrients in the lithological environment for host microbial communities to exploit. By that aspect, Mars has been quite an arid, inactive and cold geological environment during the last 3 Gyr (Catling, 2014). Therefore, the habitability computations for the simulated Martian hydrothermal systems in this research reflected on this principle, and did not imply very optimistic scenarios for the astrobiological potential of the Red Planet. Even the longest-lived hydrothermal environments (higher temperature (T = 750 °C) and large volcanic systems, or in the large impact craters ($D \geq 100$ km)) seem to be unable to support the maintenance, and sometimes even the survival mode, of microbial metabolisms after hydrothermal activity has ceased. Conclusively, one of the fundamental requirements for an increased bioenergetic potential in a geological environment, is the stability of hydrothermal conditions and long duration of water-rock interactions.

In the Solar system, primary candidates that host stable thermodynamic conditions and evidence for long-in-duration hydrothermal activity are the icy moons of Jupiter and Saturn (please see: fig. 4.19). In the Jovian and Kronian icy moons (mainly in Europa and Enceladus) the imbalance between heat production and heat loss of 1 mW/m^2 (Matson et al., 2009) induces a shell melting/freezing rate of about 100 km/Gyr. In conclusion, the diffusion timescale for an

ice shell that is 100 km thick is approximately 0.3 Gyr. Hence, these extremely long timescales indicate that ocean worlds and their host hydrothermalism beneath thick conductive ice shells could have lifetimes comparable to the Solar System's age (Nimmo and Pappalardo, 2006; 2016).

The Kronian icy moon Enceladus emits jets of H_2O from its south-polar region and apart from H_2O, the Ion and Neutral Mass Spectrometer (INMS) onboard NASA's Cassini probe detected methane (CH_4), ammonia (NH_3), carbon dioxide (CO_2), molecular hydrogen (H_2) and nitrogen (N_2) by sampling its water-vapor plume during its flyby through it (Waite et al., 2017). Water-rock interactions and active hydrothermalism have been previously hypothesized for the deep interior of Enceladus, as its core is believed to have a chondrite-like composition (Sekine et al., 2015) reacting with the deepest liquid water layer of its ocean at low to moderate ($T \leq 100$ °C) temperatures (Waite et al., 2017; Taubner et al., 2018). The most probable source for the detected H_2 in Enceladus' interior should be the oxidation of ferrous iron during the serpentinization of olivine in its chondritic core. The hydrolysis of olivine at moderate to low temperatures, as shown in the thermodynamic models of this work for putative Martian hydrothermal systems is a fundamental process for supporting hydrogenotrophic life on Earth (Mayhew et al., 2013). Since H_2 has been detected in significant quantities as a released product on Enceladus, it may comprise a potential substrate for biological CH_4 production (Taubner et al., 2018). Furthermore, the detection of CH_4 in Enceladus' plume additionally implies that the origin of CH_4 may be linked to the biological activity of hydrogenotrophic – methanogenic microbial species thriving in Enceladus' ocean (Hoehler et al., 2022).

A similar hydrothermal activity regime has been hypothesized for Jupiter's Moon Europa, as geochemical reactions at the rocky mantle – ocean interface (Dombard and Sessa, 2019) may be bioenergetically supporting habitable niches of Europa's subsurface ocean. These findings suggest that planetary habitability has not been efficiently constrained, as the subglacial ocean worlds of the Outer Solar System may be proven far more habitable through future exploration than Mars; a planet that plots within the HZ of the Solar System (Kasting et al., 1993; Kopparapu et al., 2013). Consequently, the theoretical approach for determining the habitability of a planetary body should be therefore revisited, and the CHZ definition should be reconstructed by incorporating icy moons of the Outer Solar System that evidently host cryovolcanism and hydrothermalism.

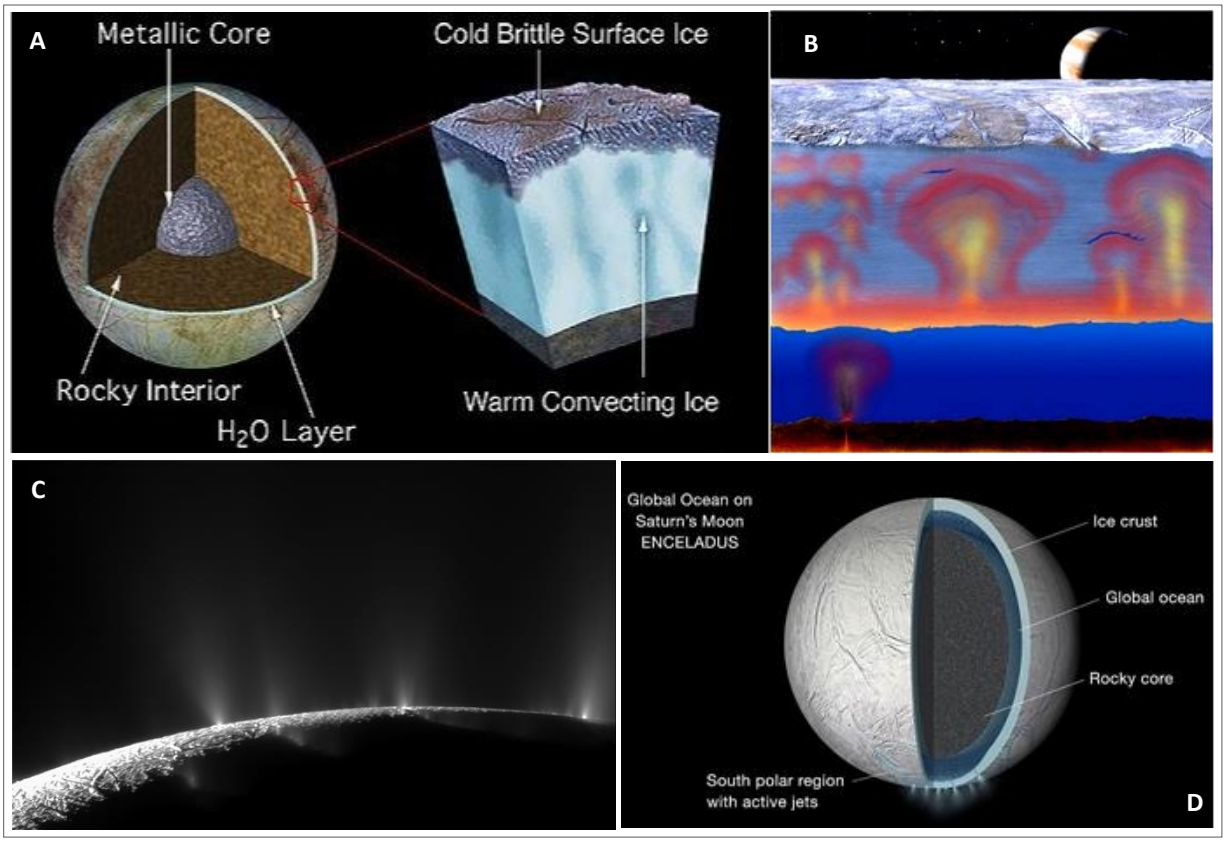

Fig. 4.19. (A) Model for the internal structure of Europa which indicates that Europa's ice shell is 15 – 25 km thick, floating on an ocean that is 60 – 150 km deep © NASA/JPL. Europa's mantle may be rocky and hot enough (due to tidal heating) to drive hydrothermal circulation. Therefore, the habitability of Europa's subsurface ocean increases significantly if active hydrothermalism induces geochemical reactions at the rocky mantle – ocean interface (Dombard and Sessa, 2019). (B) Artistic representation for hydrothermal circulation occuring within Europa's upper mantle and subsurface ocean, due to tidal heating of the Jovian moon's interior © NASA/JPL. (C): Detection of water vapour plumes on Saturn's moon Enceladus by the Cassini's Ultraviolet Imaging Spectrograph (UVIS) © NASA/JPL. These observations indicated a primary H_2O composition for the supersonic jets, constrained the plume dimensions, and implied the geochemical and geophysical processes (tidal heating) that induce water-vapour pluming phenomena on Enceladus (Taubner et al., 2018). (D): Enceladus' structure according to new data from NASA's Cassini mission (the thickness of the layers in the Fig. is not to scale) © NASA/JPL. The ice shell has an average thickness of 20-25 km, the ocean beneath the ice shell is 300 – 330 km thick, and the rocky core has a radius of circa 150-170 km. The hypothesized structure, and more importantly, the observed and sampled (by the Cassini spacecraft) vapour pluming events on Enceladus imply that active cryovolcanism due to tidal heating is inducing basaltic rock – water interactions at the rocky core – ocean interface. Hence, these processes may be rendering Enceladus' deep ocean realm habitable for potential microbial life.

4.7 A Re-Definition for (Exo-)Planetary Habitability?

As thermodynamic simulations for Martian hydrothermal systems in this work have not been generally concurring to the hypothesis that Mars has hosted favourable conditions for microbial life to thrive, it should be considered whether the definition of the circumstellar habitable zone in the Solar System has been accurately formulated. Moreover, if putative Venusian magmatic-induced hydrothermal systems would have been modelled via the HT 3 and the PHREEQC software, the findings would arguably be indicative of a sterile crust for Venus due to the extremely high temperatures and pressures. Mars (and possibly early Venus; Way and Del Genio, 2020) plot in the marginal regions of the Solar System's habitable zone (fig. 1.6; Kasting and Harman, 2013). On the contrary, moons such as Enceladus, Europa, Ganymede and Callisto, which could have been hosting cryovolcanic or/and hydrothermal activity in their interior for hundreds of Myr and characterized by favourable thermal limits for life in their subglacial oceans ($0\ °C \leq T \leq 100\ °C$; Nimmo and Pappalardo, 2006; Sekine et al., 2015; Waite et al., 2017; Hoehler et al., 2022), are inequitably considered uninhabitable, based on the principles of the CHZ hypothesis.

Consequently, a re-definition for the habitability of planetary bodies in stellar systems should be reconstructed, since tidal heating processes that induce cryovolcanism beneath icy crusts may be far more efficient in terms of energy and heat provision toward generating habitable environments, than is the effective stellar flux of the host star toward the surface habitability of an inner terrestrial planet or moon. Therefore, future research investigations on the habitability of extraterrestrial environments should aim to incorporate novel principles that can expand the perspective of habitability in our Solar System and other exoplanetary systems.

§5 CONCLUSIONS

5.1 Impact-Induced Hydrothermal Activity on Mars

The numerical experiments performed in this PhD research indicate that large impact cratering structures (D = 100, 200 km) on Mars could have hosted hydrothermal and hydrous activity for periods greater than 2.5 – 3 Myr after their formation. Specifically:

- The most conservative parameterization (shown in the Appendix) applied in the initial conditions of the models yields lifetimes for hydrothermal circulation that range between 1.5 – 2 Myr for the 100-km crater, and 1.8 – 2.5 Myr for the 200-km crater.

- The semi-conservative parameterization (used in all numerical models presented in §3.1) generated simulated post-impact hydrothermal systems that durate for 1.8 – 2 Myr in the 100-km crater, and 2.8 – 3.2 Myr in the 200-km crater.

- The use of even more liberal parameters in these HT3 models would result in non-convergence of the thermodynamic criteria of the code during computational runs, and subsequently, in the unsuccessful termination of the simulation. This implies that the use of extremely high porosities and permeabilities for the target lithologies renders these rock domains of the simulative setting thermodynamically incompatible (non-convergent) with the shock-induced pressure and heat. For example, a basaltic impactite with an initial permeability of 9.0E-14 m^2 or/and a porosity of 30% – 40% cannot describe the EOS impact-induced melt of 1200 °C for more than a few time steps (0.01 – 10y). Hence, domains with T > 500 °C experience an abrupt exponential decrease of their permeability and porosity (Hayba and Ingebritsen, 1997), and based on the thermodynamic criteria that were analysed in §2 (please see Eq. 2.1 – 2.4, and 2.7). Therefore, the initial porosity and permeability values of the lithological units in HT 3 models should be prudently defined and derive from numerical impact-cratering experiments that reliably calculate the post-impact temperature and shock-pressure distributions in the simulated environment (Eq. 2.8 – 2.12).

- The post-impact thermodynamic conditions in the 10-km crater on Mars dictate that initial peak temperatures do not exceed a value of 700 °C (§3.1.4). However, this smaller scale impact-generated heating of the Martian crust produces a hydrothermal system that can durate for approximately 80 Kyr, based on semi-liberal initial parameters (which is also the preferred and thoroughly explained modelling approach; please see §3.1.4). The use of more conservative initial thermodynamic parameters implies that such post-impact hydrological systems on Mars can persevere for about 35 – 60 Kyr.

- Simulations for two small scale post-impact hydrological systems ($D \leq 10$ km, for each) that form after simultaneous impact events and with an in-between distance of 200 km (e.g.: a possible scenario for the Martian crust during the early Noachian) generate two separate hydrological systems that soon (within the first 0.1-1 Kyr) merge and form a subsurface hydrodynamic system with a 3 – 5 × greater radial expansion. Additionally, this simulation indicated that the duration of the hydrological cycle in such a Martian subsurface is prolonged by at least a factor of 2 (please see: §3.1.5).

- In a nutshell, previous models through older versions of the HT or similar codes seem to have slightly (Abramov and Kring, 2005) or significantly (Rathbun and Squyres, 2002) underestimated the durations for post-impact hydrothermal circulation in the Martian crust, when compared to the results of this work. Conclusively, the simulations of this PhD research indicate that the lifetimes of impact-induced hydrological systems on Mars should have been appreciably longer. These findings raise significant implications for prolonged water-rock interactions within impact structures on early Mars and for potential bioenergetics under hydrothermal conditions.

5.2 Volcanogenic Hydrothermal & Hydrous Activity on Mars

The models for the volcanogenic hydrological systems on ancient Mars indicate that:

- Low temperature hydrothermal flows of 120 °C or 170 °C (§3.2.1 and 3.2.2) within the upper 8 km of the Martian crust, induced by a low temperature pluming effect at 10 km depth, and a subsequent increase of basal heat flux, cannot durate for a period greater than 230 and 300 yr, respectively. This implies that aqueous flows within the temperature range of 120 – 170 °C may have been present in the Martian crust even during the late-Amazonian period. However, the short duration (230 – 300 yr) and small magnitude of such aqueous flows interacting with host basalts could not result in a considerable release and availability of chemical nutrients for potential microbial life.

- Hydrothermal and super-critical flows induced within a magmatic environment, where T_{max} = 400 °C at a depth of 8 – 9 km in the Martian crust (pluming effect; §3.2.3), persevere for a period of circa 2 – 3 Kyr. Additionally, the simulation showed that some hydrous flows of lower temperature may persist at depths of 6 – 8 km for a slightly greater period (additional 1 – 2 Kyr). Based on the computed flux magnitude and the duration of water – rock reactions, such flows could possibly result in the self-sealing of pores and fractures in the setting within 2 – 4 Kyr.

- Intrusive volcanism in the Martian crust in the form of peridotite veins that reach the shallowest domains of the subsurface (0.1 – 2 km depth, with T_{max} = 500 °C; §3.2.4), produces an astonishingly long-lived hydrothermal cycle (duration range: 0.5 – 1.5 Myr), in contrast to pluming events of similar T_{max}. This implies that Martian geological environments, which exhibit evidence for ancient intrusive volcanism, or with outcrops of peridotite / olivine cumulate petrologies (Liu et al., 2022) could be fruitful sites for the detection of hydrothermally precipitated minerals, and possibly, even of biosignatures. If T_{max} = 750 °C, then the duration of aqueous circulation in the volcanic setting is predicted with an approximate value of 2 – 3 Myr.

- Hydrothermal circulation that may have persisted for a longer period (0.1 – 3 Myr) in impact-induced and volcanogenic environments on ancient Mars, should be constrained within deeper domains of the subsurface; i.e.: at depths ≥ 1.5 km, based on the observed

hydrodynamic patterns that the simulations produced. These computational scenarios are not only consistent with previous findings, but they have reproduced natural phenomena and features that have been detected on Mars (Orosei et al., 2018; please see Fig. 4.16) and Earth (e.g.: Caudill et al. (2021): evidence for post-impact activity of degassing pipes at the Ries impact structure; and findings of this PhD research). Therefore, this suggests the reliability and accuracy of the high-resolution numerical simulations that have been constructed through this PhD research.

5.3 The Habitability of Hydrological Systems on Mars

The Martian habitability models produced in this PhD research by coupling the thermodynamic HT 3 simulations with the bioenergetic computations of the PHREEQC code suggest that:

- Large impact craters (D = 100, 200 km) or basaltic provinces that exhibit ancient intrusive volcanism on Mars could have hosted hydrothermal activity for more than 2 – 3 Myr (based on HT 3 models). Therefore, long-lived volcanogenic or impact-generated hydrothermal environments on Mars, that have sustained water – rock reactions in the subsurface for Myr, should have comprised the most habitable niches, according to the bioenergetic models of this PhD research. Specifically, bioenergetic computations for the most habitable hydrothermal systems (based on H_2 availability; Hoehler, 2004; Hoehler et al., 2022; Sauterey et al., 2022) show that microbial metabolisms can fulfill their growth energy requirements after 124 Kyr on average of ongoing fluid – basalt reactions and consequent H_2 release.

- Habitability is governed by temperature, and by nutrient release - availability (H_2) in bioenergetic models. Hence, domains of the Martian crust affected by hydrothermal fluxes with 50 °C ≤ T ≤ 121 °C (Kashefi and Lovley, 2003; ideal conditions for mesophilic-thermophilic or even hyper-thermophilic microbial species) for a prolonged period (preferably ≥ 100 Kyr) should comprise the most promising sites for astrobiological findings.

- On the contrary, lower temperature (0 °C ≤ T ≤ 50 °C) aqueous settings do not seem to induce appreciable amounts of nutrients, as such low temperature flows need more time to produce nutrients through interactions with rocks. Thus, lower temperature flows are characterized by a lower bioenergetic potential, despite aqueous solutions being present.

- After hydrothermal circulation has ceased, a significant decrease in nutrient availability by 3 – 4 orders of magnitude occurs in all computational scenarios. For the most habitable hydrothermal environments (200-km crater, volcanogenic system with T_{max} = 750 °C) this indicates that 1 Myr after hydrothermal circulation has halted, these geological systems cannot even support the maintenance mode of potential microbial biomass. Conceivably, 2 Myr after hydrothermal circulation has ceased, these subsurface niches can no longer support the growth mode of potential microbial life. These habitability computations and their interpretations imply that if life thrived under hydrothermal conditions on Mars, then such microbiological activity should have taken place during a limited geological period (0.1 – 3 Myr).

- Aqueous flows with temperatures close to their freezing point should form ices rapidly in the shallower and colder niches of the Martian subsurface or surface. Also, if any warm water would seep through the regolith to the surface, then it would most probably sublime due to the extremely low atmospheric pressure. The simulations of this PhD research indicated that any prolonged aqueous or hydrothermal circulation should have been preserved at greater depths in the Martian crust (≥ 1.5 km from the surface). Therefore, the simulated and inferred bioenergetic potential of the deeper and warmer Martian subsurface should have been significantly higher than that of the surface or shallow subsurface during the geological periods of active hydrothermalism on Mars. Although drilled sample retrieval from great depths on Mars is currently unfeasible (limited to ≤ 2 m beneath the Martian surface; Rosalind Franklin rover: scheduled ExoMars mission), future astrobiological exploration may require drilled samples from significantly deeper subsurface lithologies (ideally from basalts or peridotites) in large impact craters or volcanic provinces to detect potential biosignatures.

5.4 Future Work

The research completed through this PhD thesis provides incentives for further explorative ventures in the scientific realm of numerical modelling and quantitative predictions of the aqueous activity and habitability of (extra-)terrestrial and even exoplanetary systems. Several improvements of the modelling tools used in this work are currently in progress via international collaboration. Firstly, the HT 3 code could be more efficiently modified and further benchmarked, so that modelling of hydrothermal and other volcanic systems on Mars can be conducted in 3D. So far, there are some bugs in the HT 3 code which prevent the export of reliable 3D models, as there are inconsistencies between in the predicted values of properties on the x,y axis and those on the z axis. For this reason, the HT 3 code is mainly used for 2D numerical modelling. Through continuous communications with the developers of HT 3 and via benchmarking feedback these minor bugs should be removed from the source code within a few academic years.

Furthermore, the thermodynamic simulations of this work indicated that the boundary conditions of the initial thermodynamic system are highly dependent on the impact-cratering formation process and on the astrophysical and geochemical characteristics of the bolide. The code iSALE (Collins et al., 2016, including previous versions of the code and references therein) is an extremely powerful tool for simulating impact cratering processes on Earth and beyond. However, iSALE does not simulate aqueous fluid mass flux and HT 3 does not simulate impact-physics. Therefore, the merging of these two very useful and sophisticated codes would be highly beneficial for reinvestigating, benchmarking and subsequently, improving the models of this work. My future aspiration is to fully-couple these two computational tools via code development techniques, and research further on (re-)modelling impact-cratering processes on Mars; and if possible, on other icy planetary bodies, such as the Jovian and Kronian moons, or those of other exoplanetary systems.

Eventually, modelling on impact-cratering processes for the cryosphere of Mars or for the enriched in icy deposits Martian crust, has been inconclusive via current simulation tools. Therefore, empirical relations for the physicochemical response of ice deposits under impact-generated thermodynamic conditions should also be incorporated in the HT 3 and PHREEQC source codes (or in any other similar thermodynamic codes and softwares), to enhance further

the simulations of this research and provide even more decisive insights into the hydrological activity of Mars, and into the quantification methods for assessing planetary habitability.

In relation to the nanoscale investigations that were conducted in this work on the Martian meteorite samples NWA 8159 and Lafayette, future analyses via APT and nano-SIMS are anticipated to establish a geochemical perspective on the stoichiometry and volatile composition of the apatite and olivine in these two distinctive basalts from Mars. NWA 8159 apatite APT needles and one NWA 8159 olivine APT needle have already been prepared at the University of Sydney (in June 2019) and are expected to be analyzed soon within this academic year, after APT experiments can be resumed by the local research group. Furthermore, the NWA 8159 sample 2 which contains 10 – 15 apatite and 20 olivine grains (ROI) ≥ 20 μm, and the Lafayette thin section USNM 1505-5 containing 20 apatite and circa 20 olivine grains (ROI) ≥ 20 μm in size, have already been sent to the University of Arizona for nano-SIMS analyses, as soon as research operations in the local facility can also be resumed. Future nanoscale analyses on the aqueous minerals (apatite and olivine) of the NWA 8159 and Lafayette meteorites via correlative TEM, APT and nano-SIMS shall:

- Establish the mineralogy, texture, and volatile chemistry of these Martian meteorite samples and unveil the thermodynamic conditions of their volcanic environment of origin on Mars.

- Determine the origin of the fluids that have interacted with these volcanic rocks on Mars (during their residence on the Red Planet), and on Earth (after their fall, due to the terrestrial weathering and contamination), and match the observed aqueous alteration products with the assumed aqueous geochemical processes of distinctive geological periods on Mars.

- Distinguish the Martian alteration mineralogies from the terrestrial weathering phases.

- Constrain further and increase the reliability and robustness of the thermodynamic simulations (via the HT 3 code), geochemical reaction pathways and habitability computations (PHREEQC models) for the explored Martian hydrothermal environments.

§6 LIST OF REFERENCES

Abe, Y., Abe-Ouchi, A., Sleep, N.H. and Zahnle, K.J., 2011. Habitable zone limits for dry planets. *Astrobiology*, *11*(5), pp.443-460.

Abramov, O. and Kring, D.A., 2004. Numerical modeling of an impact-induced hydrothermal system at the Sudbury crater. *Journal of Geophysical Research: Planets*, *109*(E10).

Abramov, O. and Kring, D.A., 2005. Impact-induced hydrothermal activity on early Mars. *Journal of Geophysical Research: Planets*, *110*(E12).

Abramov, O. and Kring, D.A., 2007. Numerical modeling of impact-induced hydrothermal activity at the Chicxulub crater. *Meteoritics & Planetary Science*, *42*(1), pp.93-112.

Abramov, O. and Mojzsis, S.J., 2009. Microbial habitability of the Hadean Earth during the late heavy bombardment. *Nature*, *459*(7245), pp.419-422.

Abramov, O., Wong, S.M. and Kring, D.A., 2012. Differential melt scaling for oblique impacts on terrestrial planets. *Icarus*, *218(2)*, pp.906-916.

Abramov, O. and Mojzsis, S.J., 2016. Thermal effects of impact bombardments on Noachian Mars. *Earth and Planetary Science Letters*, *442*, pp.108-120.

Achilles, C.N., Downs, R.T., Ming, D.W., Rampe, E.B., Morris, R.V., Treiman, A.H., Morrison, S.M., Blake, D.F., Vaniman, D.T., Ewing, R.C. and Chipera, S.J., 2017. Mineralogy of an active eolian sediment from the Namib dune, Gale crater, Mars. *Journal of Geophysical Research: Planets*, *122*(11), pp.2344-2361.

Adams, F.C., 2010. The birth environment of the solar system. *Annual Review of Astronomy and Astrophysics*, *48*, pp.47-85.

Agee, C.B., Wilson, N.V., McCubbin, F.M., Ziegler, K., Polyak, V.J., Sharp, Z.D., Asmerom, Y., Nunn, M.H., Shaheen, R., Thiemens, M.H. and Steele, A., 2013. Unique meteorite from

early Amazonian Mars: Water-rich basaltic breccia Northwest Africa 7034. *Science*, *339*(6121), pp.780-785.

Agee, C.B., Muttik, N., Ziegler, K., Walton, E.L., Herd, C.D.K., McCubbin, F.M., Santos, A.R., Burger, P.V., Simon, J.I., Peters, T.J. and Tappa, M.J., 2014, September. New Meteorite Type NWA 8159 Augite Basalt: Specimen from a Previously Unsampled Location on Mars?. In *77th Annual Meeting of the Meteoritical Society* (Vol. 77, No. 1800, p. 5397).

Ahrens, T.J. and O'Keefe, J.D., 1987. Impact on the Earth, ocean and atmosphere. *International journal of impact engineering*, *5*(1-4), pp.13-32.

Ahrer, E., Wheatley, P.J., Kirk, J., et al., 2022. VizieR Online Data Catalog: WASP-94A light curves. *VizieR Online Data Catalog*, pp.J-MNRAS.

Ahrer, E.M., Stevenson, K.B., Mansfield, M., Moran, S.E., Brande, J., Morello, G., Murray, C.A., Nikolov, N.K., Petit Dit de la Roche, D.J., Schlawin, E. and Wheatley, P.J., 2023. Early Release Science of the exoplanet WASP-39b with JWST NIRCam. *Nature*, pp.1-4.

Alexander, C.O.D., Cody, G.D., De Gregorio, B.T., Nittler, L.R. and Stroud, R.M., 2017. The nature, origin and modification of insoluble organic matter in chondrites, the major source of Earth's C and N. *Geochemistry*, *77*(2), pp.227-256.

Amsden, A.A., Ruppel, H.M. and Hirt, C.W., 1980. SALE: A simplified ALE computer program for fluid flow at all speeds (No. LA-8095). *Los Alamos National Lab*. (LANL), Los Alamos, NM (United States).

Andrews-Hanna, J.C., Zuber, M.T. and Banerdt, W.B., 2008. The Borealis basin and the origin of the martian crustal dichotomy. *Nature*, *453*(7199), pp.1212-1215.

Andrews-Hanna, J.C., 2012a. The formation of Valles Marineris: 1. Tectonic architecture and the relative roles of extension and subsidence. *Journal of Geophysical Research: Planets*, *117*(E3).

Andrews-Hanna, J.C., 2012b. The formation of Valles Marineris: 3. Trough formation through super-isostasy, stress, sedimentation, and subsidence. *Journal of Geophysical Research: Planets*, *117*(E6).

Appelo, C.A.J. and Parkhurst, D.L., 1998. Enhancements to the geochemical model PHREEQC-1D transport and reaction kinetics. *Water Rock Interaction*, *9*, pp.873-876.

Appelo, C.A.J., Parkhurst, D.L. and Post, V.E.A., 2014. Equations for calculating hydrogeochemical reactions of minerals and gases such as CO_2 at high pressures and temperatures. *Geochimica et Cosmochimica Acta*, *125*, pp.49-67.

Arny, T. and Schneider, S. (2019) Explorations: An introduction to astronomy 6 (2019). *9th edition, McGraw-Hill Education*, New York, NY.

Arvidson, R.S., Mackenzie, F.T. and Guidry, M., 2006. MAGic: A Phanerozoic model for the geochemical cycling of major rock-forming components. *American Journal of Science*, *306*(3), pp.135-190.

Atreya, S.K., 2007. The mystery of methane on Mars & Titan. *Scientific American*, *296*(5), pp.42-51.

Bach, W. and Edwards, K.J., 2003. Iron and sulphide oxidation within the basaltic ocean crust: implications for chemolithoautotrophic microbial biomass production. *Geochimica et Cosmochimica Acta, 67,* pp.3871–3887.

Bach, W., 2016. Some Compositional and Kinetic Controls on the Bioenergetic Landscapes in Oceanic Basement. *Frontiers in Microbiology, 7*:107.

Ball, B.A., Hunter, M.D., Kominoski, J.S., Swan, C.M. and Bradford, M.A., 2008. Consequences of non-random species loss for decomposition dynamics: experimental evidence for additive and non-additive effects. *Journal of ecology*, *96*(2), pp.303-313.

Barboni, M., Boehnke, P., Keller, B., Kohl, I.E., Schoene, B., Young, E.D. and McKeegan, K.D., 2017. Early formation of the Moon 4.51 billion years ago. *Science advances*, *3*(1), p.e1602365.

Barnes, J.J., McCubbin, F.M., Santos, A.R., Day, J.M., Boyce, J.W., Schwenzer, S.P., Ott, U., Franchi, I.A., Messenger, S., Anand, M. and Agee, C.B., 2020. Multiple early-formed water reservoirs in the interior of Mars. *Nature Geoscience, 13(4)*, pp.260-264.

Barnhart, C.J., Nimmo, F. and Travis, B.J., 2019. Geochemical and Geomorphological Effects of Post-Impact Hydrothermal Systems Incorporating Freezing. *Icarus,* 208, 101–117.

Basilevsky, A.T., Werner, S.C., Neukum, G., Head, J.W., Van Gasselt, S., Gwinner, K. and Ivanov, B.A., 2006. Geologically recent tectonic, volcanic and fluvial activity on the eastern flank of the Olympus Mons volcano, Mars. *Geophysical Research Letters*, *33*(13).

Beaty, D.W., Grady, M.M., McSween, H.Y., Sefton-Nash, E., Carrier, B.L., Altieri, F., Amelin, Y., Ammannito, E., Anand, M., Benning, L.G. and Bishop, J.L., 2019. The potential science and engineering value of samples delivered to Earth by Mars sample return: International MSR Objectives and Samples Team (iMOST). *Meteoritics & Planetary Science*, *54*, pp.S3-S152.

Becker, R.H. and Pepin, R.O., 1984. The case for a Martian origin of the shergottites: Nitrogen and noble gases in EETA 79001. *Earth and Planetary Science Letters*, *69*(2), pp.225-242.

Bedford, C.C., Banham, S.G., Bridges, J.C., Forni, O., Cousin, A., Bowden, D., Turner, S.M., Wiens, R.C., Gasda, P.J., Frydenvang, J. and Gasnault, O., 2022. An insight into ancient aeolian processes and post-Noachian aqueous alteration in Gale crater, Mars, using ChemCam geochemical data from the Greenheugh capping unit. *Journal of Geophysical Research: Planets*, pp.Early-access.

Belleguic, V., Lognonné, P. and Wieczorek, M., 2005. Constraints on the Martian lithosphere from gravity and topography data. *Journal of Geophysical Research: Planets*, *110*(E11).

Bellucci, J.J., Herd, C.D.K., Whitehouse, M.J., Nemchin, A.A., Kenny, G.G. and Merle, R.E., 2020. Insights into the chemical diversity of the martian mantle from the Pb isotope systematics of shergottite Northwest Africa 8159. *Chemical Geology*, *545*, p.119638.

Berger, J.A., Gellert, R., Boyd, N.I., King, P.L., McCraig, M.A., O'Connell-Cooper, C.D., Schmidt, M.E., Spray, J.G., Thompson, L.M., VanBommel, S.J. and Yen, A.S., 2020. Elemental composition and chemical evolution of geologic materials in Gale Crater, Mars: APXS results from Bradbury landing to the Vera Rubin ridge. *Journal of Geophysical Research: Planets*, *125*(12), p.e2020JE006536.

Berrezueta, E., Domínguez-Cuesta, M.J. and Rodríguez-Rey, Á., 2019. Semi-automated procedure of digitalization and study of rock thin section porosity applying optical image analysis tools. Computers & Geosciences, 124, pp.14-26.

Bethke C., 1996. *Geochemical Reaction Modeling. NewYork, NY*: Oxford University Press.

Betts, H.C., Puttick, M.N., Clark, J.W., Williams, T.A., Donoghue, P.C. and Pisani, D., 2018. Integrated genomic and fossil evidence illuminates life's early evolution and eukaryote origin. *Nature ecology & evolution*, *2*(10), pp.1556-1562.

Bibring, J.P., Langevin, Y., Mustard, J.F., Poulet, F., Arvidson, R., Gendrin, A., Gondet, B., Mangold, N., Pinet, P., Forget, F. and Berthé, M., 2006. Global mineralogical and aqueous Mars history derived from OMEGA/Mars Express data. *Science*, *312*(5772), pp.400-404.

Binder, A.B. and Lange, M.A., 1980. On the thermal history, thermal state, and related tectonism of a moon of fission origin. *Journal of Geophysical Research: Solid Earth*, *85*(B6), pp.3194-3208.

Biot, J.B., 1803. *Essai sur l'histoire générale des sciences pendant la Révolution française*. Duprat.

Bishop, J.L., Yeşilbaş, M., Hinman, N.W., Burton, Z.F.M., Englert, P.A.J., Toner, J.D., McEwen, A.S., Gulick, V.C., Gibson, E.K. and Koeberl, C., 2021. Martian subsurface cryosalt expansion and collapse as trigger for landslides. *Science Advances*, *7*(6), p.eabe4459.

Bitsch, B., Lambrechts, M. and Johansen, A., 2015a. The growth of planets by pebble accretion in evolving protoplanetary discs. *Astronomy & Astrophysics*, *582*, p.A112.

Bitsch, B., Johansen, A., Lambrechts, M. and Morbidelli, A., 2015b. The structure of protoplanetary discs around evolving young stars. *Astronomy & Astrophysics*, *575*, p.A28.

Blamey, N.J., Parnell, J., McMahon, S., Mark, D.F., Tomkinson, T., Lee, M.R, Shivak, J., Izawa, M.R., Banerjee, N.R. and Flemming, R.L., 2015. Evidence for methane in Martian meteorites. *Nature Communications*, *6*(1), p.7399.

Boctor, N.Z., Meyer, H.O. and Kullerud, G., 1976. Lafayette meteorite: Petrology and opaque mineralogy. *Earth and Planetary Science Letters*, *32*(1), pp.69-76.

Bogard, D.D. and Johnson, P., 1983. Martian gases in an Antarctic meteorite?. *Science*, *221*(4611), pp.651-654.

Bogard, D.D., Nyquist, L.E. and Johnson, P., 1984. Noble gas contents of shergottites and implications for the Martian origin of SNC meteorites. *Geochimica et Cosmochimica Acta*, *48*(9), pp.1723-1739.

Bogard, D.D. and Garrison, D.H., 2008. 39Ar–40Ar age and thermal history of Martian dunite NWA 2737. *Earth and Planetary Science Letters*, *273*(3-4), pp.386-392.

Bollard, J., Connelly, J.N., Whitehouse, M.J., Pringle, E.A., Bonal, L., Jørgensen, J.K., Nordlund, Å., Moynier, F. and Bizzarro, M., 2017. Early formation of planetary building blocks inferred from Pb isotopic ages of chondrules. *Science Advances*, *3*(8), p.e1700407.

Borg, L.E., Connelly, J.N., Nyquist, L.E., Shih, C.Y., Wiesmann, H. and Reese, Y., 1999. The age of the carbonates in Martian meteorite ALH84001. *Science*, *286*(5437), pp.90-94.

Borg, L.E. and Draper, D.S., 2003. A petrogenetic model for the origin and compositional variation of the Martian basaltic meteorites. *Meteoritics & Planetary Science, 38(12)*, pp.1713-1731.

Borg, L. and Drake, M.J., 2005. A review of meteorite evidence for the timing of magmatism and of surface or near-surface liquid water on Mars. *Journal of Geophysical Research: Planets*, *110*(E12).

Borg, L.E., Brennecka, G.A. and Symes, S.J., 2016. Accretion timescale and impact history of Mars deduced from the isotopic systematics of martian meteorites. *Geochimica et Cosmochimica Acta*, *175*, pp.150-167.

Bottke, W.F., Walker, R.J., Day, J.M., Nesvorny, D. and Elkins-Tanton, L., 2010. Stochastic late accretion to Earth, the Moon, and Mars. *Science*, *330*(6010), pp.1527-1530.

Bottke, W.F. and Andrews-Hanna, J.C., 2017. A post-accretionary lull in large impacts on early Mars. *Nature Geoscience*, *10*(5), pp.344-348.

Bottke, W.F. and Norman, M.D., 2017. The late heavy bombardment. *Annual Review of Earth and Planetary Sciences*, *45*, pp.619-647.

Bouvier, A. and Wadhwa, M., 2010. The age of the Solar System redefined by the oldest Pb–Pb age of a meteoritic inclusion. *Nature geoscience*, *3*(9), pp.637-641.

Bouvier, L.C., Costa, M.M., Connelly, J.N., Jensen, N.K., Wielandt, D., Storey, M., Nemchin, A.A., Whitehouse, M.J., Snape, J.F., Bellucci, J.J. and Moynier, F., 2018. Evidence for extremely rapid magma ocean crystallization and crust formation on Mars. *Nature*, *558*(7711), pp.586-589.

Brasser, R., 2013. The formation of Mars: building blocks and accretion time scale. *Space Science Reviews*, *174*, pp.11-25.

Brasser, R., Mojzsis, S.J., Werner, S.C., Matsumura, S. and Ida, S., 2016. Late veneer and late accretion to the terrestrial planets. *Earth and Planetary Science Letters*, *455*, pp.85-93.

Brasser, R. and Mojzsis, S.J., 2017. A colossal impact enriched Mars' mantle with noble metals. *Geophysical Research Letters*, *44*(12), pp.5978-5985.

Brasser, R., Werner, S.C. and Mojzsis, S.J., 2020. Impact bombardment chronology of the terrestrial planets from 4.5 Ga to 3.5 Ga. *Icarus*, *338*, p.113514.

Bridges, J.C. and Grady, M.M., 2000. Evaporite mineral assemblages in the nakhlite (martian) meteorites. *Earth and Planetary Science Letters*, *176*(3-4), pp.267-279.

Bridges, J.C., Catling, D.C., Saxton, J.M., Swindle, T.D., Lyon, I.C. and Grady, M.M., 2001. Alteration assemblages in Martian meteorites: Implications for near-surface processes. *Space Science Reviews*, *96*, pp.365-392.

Bridges, J.C. and Schwenzer, S.P., 2012. The nakhlite hydrothermal brine on Mars. *Earth and Planetary Science Letters*, *359*, pp.117-123.

Bristow, T.F., Rampe, E.B., Achilles, C.N., Blake, D.F., Chipera, S.J., Craig, P., Crisp, J.A., Des Marais, D.J., Downs, R.T., Gellert, R. and Grotzinger, J.P., 2018. Clay mineral diversity and abundance in sedimentary rocks of Gale crater, Mars. *Science advances*, *4*(6), p.eaar3330.

Brown, A.J., Viviano, C.E. and Goudge, T.A., 2020. Olivine-carbonate mineralogy of the Jezero crater region. *Journal of Geophysical Research: Planets*, *125*(3), p.e2019JE006011.

Brož, P., Hauber, E., Platz, T. and Balme, M., 2015. Evidence for Amazonian highly viscous lavas in the southern highlands on Mars. *Earth and Planetary Science Letters*, *415*, pp.200-212.

Brož, P., Hauber, E., Wray, J.J. and Michael, G., 2017. Amazonian volcanism inside Valles Marineris on Mars. *Earth and Planetary Science Letters*, *473*, pp.122-130.

Brož, P., Bernhardt, H., Conway, S.J. and Parekh, R., 2021. An overview of explosive volcanism on Mars. *Journal of Volcanology and Geothermal Research*, *409*, p.107125.

Brustel, C., Flahaut, J., Hauber, E., Fueten, F., Quantin, C., Stesky, R. and Davies, G.R., 2017. Valles Marineris tectonic and volcanic history inferred from dikes in eastern Coprates Chasma. *Journal of Geophysical Research: Planets*, *122*(6), pp.1353-1371.

Cardace, D. and Hoehler, T.M., 2009. Serpentinizing fluids craft microbial habitat. *Northeastern Naturalist*, *16*(sp5), pp.272-284.

Cardenas, B.T., Lamb, M.P. and Grotzinger, J.P., 2022. Martian landscapes of fluvial ridges carved from ancient sedimentary basin fill. *Nature Geoscience*, pp.1-7.

Carr, M.H. and Head, J.W., 2010. Geologic history of Mars. *Earth and Planetary Science Letters*, *294*(3-4), pp.185-203.

Carr, M.H., 2012. The fluvial history of Mars. *Philosophical Transactions of the Royal Society A: Mathematical, Physical and Engineering Sciences*, *370*(1966), pp.2193-2215.

Cartwright, J.A., Ott, U., Herrmann, S. and Agee, C.B., 2014. Modern atmospheric signatures in 4.4 Ga Martian meteorite NWA 7034. *Earth and Planetary Science Letters*, *400*, pp.77-87.

Cassanelli, J.P. and Head, J.W., 2018. Large-scale lava-ice interactions on Mars: Investigating its role during Late Amazonian Central Elysium Planitia volcanism and the formation of Athabasca Valles. *Planetary and Space Science*, *158*, pp.96-109.

Cassata, W.S., Cohen, B.E., Mark, D.F., Trappitsch, R., Crow, C.A., Wimpenny, J., Lee, M.R. and Smith, C.L., 2018. Chronology of martian breccia NWA 7034 and the formation of the martian crustal dichotomy. *Science Advances*, *4*(5), p.eaap8306.

Catling, D.C., 2014. Mars atmosphere: History and surface interactions. In *Encyclopedia of the solar system* (pp. 343-357). Elsevier.

Caudill, C., Osinski, G.R., Greenberger, R.N., Tornabene, L.L., Longstaffe, F.J., Flemming, R.L. and Ehlmann, B.L., 2021. Origin of the degassing pipes at the Ries impact structure and implications for impact-induced alteration on Mars and other planetary bodies. *Meteoritics & Planetary Science*, *56*(2), pp.404-422.

Changela, H.G. and Bridges, J.C., 2010. Alteration assemblages in the nakhlites: Variation with depth on Mars. *Meteoritics & Planetary Science*, *45*(12), pp.1847-1867.

Chapelle, F., O'Neill, K., Bradley, P., Methe, B., Ciufo, S., Knobel, L. and Lovley, D., 2002. A hydrogen-based subsurface microbial community dominated by methanogens. *Nature, 415*, pp.312–315.

Chastain, B.K. and Chevrier, V., 2007. Methane clathrate hydrates as a potential source for martian atmospheric methane. *Planetary and Space Science*, *55*(10), pp.1246-1256.

Chermak, J. and Rimstidt, J., 1989. Estimating the thermodynamic properties (ΔGf and ΔHf) of silicate minerals at 298K from the sum of polyhedral contributions. *American Mineralogist, 74*, 1023–1031.

Chladni, E.F.F., 1794. *Ueber den Ursprung der von Pallas gefundenen und anderer ihr ähnlicher Eisenmassen und über einige damit in Verbindung stehende Naturerscheinungen.* bey Johann Friedrich Hartknoch.

Chojnacki, M. and Hynek, B.M., 2008. Geological context of water-altered minerals in Valles Marineris, Mars. *Journal of Geophysical Research: Planets*, *113*(E12).

Christensen, P.R., Bandfield, J.L., Hamilton, V.E., Ruff, S.W., Kieffer, H.H., Titus, T.N., Malin, M.C., Morris, R.V., Lane, M.D., Clark, R.L. and Jakosky, B.M., 2001. Mars Global Surveyor Thermal Emission Spectrometer experiment: investigation description and surface science results. *Journal of Geophysical Research: Planets*, *106*(E10), pp.23823-23871.

Christensen, P.R., Jakosky, B.M., Kieffer, H.H., Malin, M.C., McSween, H.Y., Nealson, K., Mehall, G.L., Silverman, S.H., Ferry, S., Caplinger, M. and Ravine, M., 2004. The thermal emission imaging system (THEMIS) for the Mars 2001 Odyssey Mission. *Space Science Reviews*, *110*, pp.85-130.

Christensen, P.R., Ruff, S.W., Fergason, R., Gorelick, N., Jakosky, B.M., Lane, M.D., McEwen, A.S., McSween, H.Y., Mehall, G.L., Milam, K. and Moersch, J.E., 2005. Mars Exploration Rover candidate landing sites as viewed by THEMIS. *Icarus*, *176*(1), pp.12-43.

Christou, E., 2018, October. MSc. Thesis, *Universität Bremen*.

Christou, E. and Bach, W., 2019, July. Post-Impact Habitability at the Chicxulub Crater. In *82nd Annual Meeting of the Meteoritical Society* (Vol. 82, No. 2157, p. 6100).

Christou, E., Pickersgill, A.E. and Bach, W., 2019a. Controls on the Duration of Impact-Induced Hydrothermal Activity via Numerical Simulations. *Large Meteorite Impacts and Planetary Evolution VI*, *2136*, p.5037.

Christou, E., Hallis, L.J., Hayward, C.L. and Lee, M.R., 2019b, July. Unusual Apatite in the Unusual Martian Meteorite Northwest Africa (NWA) 8159. In *82nd Annual Meeting of The Meteoritical Society* (Vol. 82, No. 2157, p. 6283).

Christou, E., Hallis, L.J., Daly, L., McCarroll, I., Garbrecht, M., Yang, L., Hayward, C.L., Liu, Y., Cairney, J. and Lee, M.R., 2020. Martian vs. Terrestrial Alteration of Apatite in the Unique Northwest Africa 8159 Meteorite.

Christou, E., Hallis, L.J., Daly, L., Pickersgill, A.E., Keller, T., Hayward, C.L. and Lee, M.R., 2021a, March. Fluid Flow in the Martian Subsurface During the Early Amazonian Period Constrained via Numerical Simulations: Implications for Habitability. In *52nd Lunar and Planetary Science Conference* (No. 2548, p. 2556).

Christou, E., Hallis, L.J., Daly, L., Hayward, C.L. and Lee, M.R., 2021b, August. Northwest Africa 8159 Apatite Versus Lafayette Apatite: Effects of Terrestrial Weathering Versus Martian Alteration. In *84th Annual Meeting of the Meteoritical Society* (Vol. 84, No. 2609, p. 6297).

Christou, E., Hallis, L.J., Daly, L., Pickersgill, A.E. and Lee, M.R., 2022, August. A Pessimistic Perspective on the Habitability of Early Mars: Simulations for the Northwest Africa 8159

Environment. In *Meteoritics & Planetary Science* (Vol. 57). 111 River St, Hoboken 07030-5774, NJ USA: Wiley.

Chua, M.J., Campen, R.L., Wahl, L., Grzymski, J.J. and Mikucki, J.A., 2018. Genomic and physiological characterization and description of Marinobacter gelidimuriae sp. nov., a psychrophilic, moderate halophile from Blood Falls, an Antarctic subglacial brine. *FEMS microbiology ecology*, *94*(3), p.fiy021.

Claire, M.W., Sheets, J., Cohen, M., Ribas, I., Meadows, V.S. and Catling, D.C., 2012. The evolution of solar flux from 0.1 nm to 160 μm: quantitative estimates for planetary studies. *The Astrophysical Journal*, *757*(1), p.95.

Clifford, S.M., 1993. A model for the hydrologic and climatic behavior of water on Mars. *Journal of Geophysical Research: Planets*, *98*(E6), pp.10973-11016.

Clog, M., Aubaud, C., Cartigny, P. and Dosso, L., 2013. The hydrogen isotopic composition and water content of southern Pacific MORB: A reassessment of the D/H ratio of the depleted mantle reservoir. *Earth and Planetary Science Letters*, *381*, pp.156-165.

Cockell, C.S. and Lee, P., 2002. The biology of impact craters–a review. *Biological Reviews*, *77*(3), pp.279-310.

Cockell, C.S. and Raven, J.A., 2004. Zones of photosynthetic potential on Mars and the early Earth. *Icarus*, *169*(2), pp.300-310.

Cockell, C.S., 2006. The origin and emergence of life under impact bombardment. *Philosophical Transactions of the Royal Society B: Biological Sciences*, *361*(1474), pp.1845-1856.

Cockell, C.S., 2014. Habitable worlds with no signs of life. *Philosophical Transactions of the Royal Society A: Mathematical, Physical and Engineering Sciences*, *372*(2014), p.20130082.

Cockell, C.S., Schaefer, B., Wuchter, C., Coolen, M.J., Grice, K., Schnieders, L., Morgan, J.V., Gulick, S.P., Wittmann, A., Lofi, J. and Christeson, G.L., 2021. Shaping of the present-day

deep biosphere at Chicxulub by the impact catastrophe that ended the Cretaceous. *Frontiers in Microbiology*, p.1413.

Cohen, B.E., Mark, D.F., Cassata, W.S., Lee, M.R., Tomkinson, T. and Smith, C.L., 2017. Taking the pulse of Mars via dating of a plume-fed volcano. *Nature Communications*, *8*(1), p.640.

Collins, G., Melosh, H., Morgan, J. and Warner, M., 2002. Hydrocode simulations of Chicxulub crater collapse and peak ring formation. *Icarus, 157*:24–33.

Collins, G.S., Melosh, H.J. and Ivanov, B.A., 2004. Modeling damage and deformation in impact simulations. *Meteoritics & Planetary Science, 39(2)*, pp.217-231.

Collins, G.S., Elbeshausen, D., Wünnemann, K., Davison, T.M., Ivanov, B. and Melosh, H.J., 2016. iSALE: A multi-material, multi-rheology shock physics code for simulating impact phenomena in two and three dimensions. *Manual for the Dellen release of the iSALE shock physics code*.

Collins, T.J., 2007. Image J for Microscopy. *BioTechniques, 43*. S25-S30. http://dx. doi. org/10.2144/000112517.

Connelly, J.N., Bollard, J. and Bizzarro, M., 2017. Pb–Pb chronometry and the early solar system. *Geochimica et Cosmochimica Acta*, *201*, pp.345-363.

Connolly, J.A.D., 2009. The geodynamic equation of state: what and how. *Geochemistry, geophysics, geosystems*, *10*(10).

Corrigan, C.M., Velbel, M.A. and Vicenzi, E.P., 2015. Modal abundances of pyroxene, olivine, and mesostasis in nakhlites: Heterogeneity, variation, and implications for nakhlite emplacement. *Meteoritics & Planetary Science*, *50*(9), pp.1497-1511.

Coustenis, A., Atreya, S.K., Balint, T., Brown, R.H., Dougherty, M.K., Ferri, F., Fulchignoni, M., Gautier, D., Gowen, R.A., Griffith, C.A. and Gurvits, L.I., 2009. TandEM: Titan and Enceladus mission. *Experimental Astronomy*, *23*, pp.893-946.

Coustenis, A. and Blanc, M., 2012. Large habitable moons. *Frontiers in Astrobiology. Cambridge University Press, Cambridge, United Kingdom and New York, NY, USA*, pp.175-201.

Coustenis, A. and Encrenaz, T., 2013. Life beyond Earth: the search for habitable worlds in the Universe. *Cambridge University Press*.

Coustenis, A., 2021, December. Search for habitable conditions in the outer solar system. In *AGU Fall Meeting Abstracts* (Vol. 2021, pp. P14A-01).

Gregg, T. and de Silva, S., 2009. Tyrrhena Patera and Hesperia Planum. *Mars: New Insights (and Old Interpretations) from High-Resolution Imagery*, *40*, p.1700.

Croft, S.K., 1980. *Cratering flow fields: Implications for the excavation and transient expansion stages of crater formation*. Pergamon Press.

Croft, S.K., 1985. The scaling of complex craters. *Journal of Geophysical Research: Solid Earth*, *90*(S02), pp.C828-C842.

Curd, P., 2007. "Anaxagoras", *The Stanford Encyclopedia of Philosophy (Winter 2019 Edition)*.

Da Rocha Grasselli, M., do Matao, R. and Travessa, R., 1995. The Heroic Age: the intelectual enterprise of Greek mathematicians in the V century BC.

Dalrymple, G.B., 2004. *Ancient Earth, ancient skies: the age of Earth and its cosmic surroundings*. Stanford University Press.

Daly, L., Lee, M.R., Piazolo, S., Griffin, S., Bazargan, M., Campanale, F., Chung, P., Cohen, B.E., Pickersgill, A.E., Hallis, L.J. and Trimby, P.W., 2019a. Boom boom pow: Shock-facilitated aqueous alteration and evidence for two shock events in the Martian nakhlite meteorites. *Science Advances*, *5*(9), p.eaaw5549.

Daly, L., Piazolo, S., Lee, M.R., Griffin, S., Chung, P., Campanale, F., Cohen, B.E., Hallis, L.J., Trimby, P.W., Baumgartner, R. and Forman, L.V., 2019b. Understanding the emplacement of Martian volcanic rocks using petrofabrics of the nakhlite meteorites. *Earth and Planetary Science Letters*, *520*, pp.220-230.

Daly, L., Lee, M.R., Hallis, L.J., Ishii, H.A., et al., 2021. Solar wind contributions to Earth's oceans. *Nature Astronomy*, *5*(12), pp.1275-1285.

Dartnell, L.R., Desorgher, L., Ward, J.M. and Coates, A.J., 2007. Martian sub-surface ionising radiation: biosignatures and geology. *Biogeosciences*, *4*(4), pp.545-558.

Dauphas, N. and Pourmand, A., 2011. Hf–W–Th evidence for rapid growth of Mars and its status as a planetary embryo. *Nature*, *473*(7348), pp.489-492.

Dauphas, N., 2017. The isotopic nature of the Earth's accreting material through time. *Nature*, *541*(7638), pp.521-524.

Davidson, E.A. and Janssens, I.A., 2006. Temperature sensitivity of soil carbon decomposition and feedbacks to climate change. *Nature*, *440*(7081), pp.165-173.

Day, J.M., Taylor, L.A., Floss, C. and Mcsween Jr, H.Y., 2006. Petrology and chemistry of MIL 03346 and its significance in understanding the petrogenesis of nakhlites on Mars. *Meteoritics & Planetary Science*, *41*(4), pp.581-606.

Day, J.M., Tait, K.T., Udry, A., Moynier, F., Liu, Y. and Neal, C.R., 2018. Martian magmatism from plume metasomatized mantle. *Nature communications*, *9*(1), p.4799.

De Blasio, F.V., 2011. Landslides in Valles Marineris (Mars): A possible role of basal lubrication by sub-surface ice. *Planetary and Space Science*, *59*(13), pp.1384-1392.

De Wit, J., Wakeford, H.R., Lewis, N.K., et al., 2018. Atmospheric reconnaissance of the habitable-zone Earth-sized planets orbiting TRAPPIST-1. *Nature Astronomy*, *2*(3), pp.214-219.

Dick, S.J., 1984. Plurality of Words: The Extraterrestrial Life Debate from Democritus to Kant. *CUP Archive*.

Dickeson, Z.I. and Davis, J.M., 2020. Martian oceans. *Astronomy & Geophysics, 61(3)*.

Dobson, P.F., Kneafsey, T.J., Hulen, J. and Simmons, A., 2003. Porosity, permeability, and fluid flow in the Yellowstone geothermal system, Wyoming. *Journal of Volcanology and Geothermal Research*, *123*(3-4), pp.313-324.

Dodd, M.S., Papineau, D., Grenne, T., Slack, J.F., Rittner, M., Pirajno, F., O'Neil, J. and Little, C.T., 2017. Evidence for early life in Earth's oldest hydrothermal vent precipitates. *Nature*, *543*(7643), pp.60-64.

Dole, S.H., 1964. Habitable planets for man, *New York, Blaisdell Pub. Co*.

Dong, J., Fischer, R.A., Stixrude, L.P., Lithgow-Bertelloni, C.R., Eriksen, Z.T. and Brennan, M.C., 2022. Water storage capacity of the martian mantle through time. *Icarus*, *385*, p.115113.

Edson, A., Lee, S., Bannon, P., Kasting, J.F. and Pollard, D., 2011. Atmospheric circulations of terrestrial planets orbiting low-mass stars. *Icarus*, *212*(1), pp.1-13.

Edwards, K.J., Bond, P.L., Gihring, T.M. and Banfield, J.F., 2000. An archaeal iron-oxidizing extreme acidophile important in acid mine drainage. *Science*, *287*(5459), pp.1796-1799.

Edwards, K.J., Bach, W. and McCollom, T.M., 2005. Geomicrobiology in oceanography: microbe–mineral interactions at and below the seafloor. *TRENDS in Microbiology*, *13*(9), pp.449-456.

Edwards, K.J., Fisher, A.T. and Wheat, C.G., 2012. The deep subsurface biosphere in igneous ocean crust: frontier habitats for microbiological exploration. *Frontiers in microbiology*, *3*, p.8.

Edwards, C.S. and Ehlmann, B.L., 2015. Carbon sequestration on Mars. *Geology*, *43*(10), pp.863-866.

Ehlmann, B.L., Mustard, J.F., Swayze, G.A., Clark, R.N., Bishop, J.L., Poulet, F., Des Marais, D.J., Roach, L.H., Milliken, R.E., Wray, J.J. and Barnouin-Jha, O., 2009. Identification of hydrated silicate minerals on Mars using MRO-CRISM: Geologic context near Nili Fossae and implications for aqueous alteration. *Journal of Geophysical Research: Planets*, *114*(E2).

Ehlmann, B.L., Mustard, J.F., Murchie, S.L., Bibring, J.P., Meunier, A., Fraeman, A.A. and Langevin, Y., 2011. Subsurface water and clay mineral formation during the early history of Mars. *Nature*, *479*(7371), pp.53-60.

Ehlmann, B.L., Anderson, F.S., Andrews-Hanna, J., Catling, D.C., Christensen, P.R., Cohen, B.A., Dressing, C.D., Edwards, C.S., Elkins-Tanton, L.T., Farley, K.A. and Fassett, C.I., 2016. The sustainability of habitability on terrestrial planets: Insights, questions, and needed measurements from Mars for understanding the evolution of Earth-like worlds. *Journal of Geophysical Research: Planets*, *121*(10), pp.1927-1961.

Elbeshausen, D., Wünnemann, K. and Collins, G.S., 2009. Scaling of oblique impacts in frictional targets: Implications for crater size and formation mechanisms. *Icarus, 204(2),* pp.716-731.

Elkins-Tanton, L.T., Hess, P.C. and Parmentier, E.M., 2005. Possible formation of ancient crust on Mars through magma ocean processes. *Journal of Geophysical Research: Planets*, *110*(E12).

Emsenhuber, A., Jutzi, M. and Benz, W., 2018. SPH calculations of Mars-scale collisions: The role of the equation of state, material rheologies, and numerical effects. *Icarus*, *301*, pp.247-257.

Etiope, G., Oehler, D.Z. and Allen, C.C., 2011. Methane emissions from Earth's degassing: Implications for Mars. *Planetary and Space Science*, *59*(2-3), pp.182-195.

Eugster, O., Weigel, A. and Polnau, E., 1997. Ejection times of Martian meteorites. *Geochimica et Cosmochimica Acta*, *61*(13), pp.2749-2757.

Eugster, O., Busemann, H., Lorenzetti, S. and Terribilini, D., 2002. Ejection ages from krypton-81-krypton-83 dating and pre-atmospheric sizes of Martian meteorites. *Meteoritics & Planetary Science*, *37*(10), pp.1345-1360.

Eugster, O., 2003. Cosmic-ray exposure ages of meteorites and lunar rocks and their significance. *Geochemistry*, *63*(1), pp.3-30.

Farley, K.A., Stack, K.M., Shuster, D.L., Horgan, B.H.N., Hurowitz, J.A., Tarnas, J.D., Simon, J.I., Sun, V.Z., Scheller, E.L., Moore, K.R. and McLennan, S.M., 2022. Aqueously altered igneous rocks sampled on the floor of Jezero crater, Mars. *Science*, *377*(6614), p.eabo2196.

Fassett, C.I. and Head, J.W., 2008. Valley network-fed, open-basin lakes on Mars: Distribution and implications for Noachian surface and subsurface hydrology. *Icarus*, *198*(1), pp.37-56.

Faust, C.R. and Mercer, J.W., 1979. Geothermal reservoir simulation: 1. Mathematical models for liquid-and vapor-dominated hydrothermal systems. *Water resources research*, *15*(1), pp.23-30.

Filiberto, J., Gross, J., Trela, J. and Ferré, E.C., 2014. Gabbroic shergottite Northwest Africa 6963: an intrusive sample of Mars. *American Mineralogist, 99(4)*, pp.601-606.

Filiberto, J., Gross, J., Udry, A., Trela, J., Wittmann, A., Cannon, K. M., et al. (2018). Shergottite Northwest Africa 6963: A pyroxene-cumulate martian gabbro. *Journal of Geophysical Research: Planets, 123(7)*, 1823–1841. https://doi.org/10.1029/2018JE005635.

Floran, R.J., Prinz, M., Hlava, P.F., Keil, K., Nehru, C.E. and Hinthorne, J.R., 1978. The Chassigny meteorite: A cumulate dunite with hydrous amphibole-bearing melt inclusions. *Geochimica et Cosmochimica Acta*, *42*(8), pp.1213-1229.

Foumier, R.O., 1991. The transition from hydrostatic to greater than hydrostatic fluid pressure in presently active continental hydrothermal systems in crystalline rock. *Geophysical Research Letters*, *18*(5), pp.955-958.

Franz, H.B., Trainer, M.G., Malespin, C.A., Mahaffy, P.R., Atreya, S.K., Becker, R.H., Benna, M., Conrad, P.G., Eigenbrode, J.L., Freissinet, C. and Manning, H.L., 2017. Initial SAM calibration gas experiments on Mars: Quadrupole mass spectrometer results and implications. *Planetary and Space Science*, *138*, pp.44-54.

French, B.M., 1998. *Traces of catastrophe: A handbook of shock-metamorphic effects in terrestrial meteorite impact structures* (No. LPI-Contrib-954).

Frey, H. and Schultz, R.A., 1988. Large impact basins and the mega-impact origin for the crustal dichotomy on Mars. *Geophysical Research Letters*, *15*(3), pp.229-232.

Fritz, J., Artemieva, N. and Greshake, A., 2005. Ejection of Martian meteorites. *Meteoritics & Planetary Science*, *40*(9-10), pp.1393-1411.

Gaidos, E.J., 2001. Cryovolcanism and the recent flow of liquid water on Mars. *Icarus*, *153*(1), pp.218-223.

Gibson Jr, E.K., McKay, D.S., Thomas-Keprta, K.L., Wentworth, S.J., Westall, F., Steele, A., Romanek, C.S., Bell, M.S. and Toporski, J., 2001. Life on Mars: evaluation of the evidence within Martian meteorites ALH84001, Nakhla, and Shergotty. *Precambrian research*, *106*(1-2), pp.15-34.

Gilbert, E.A., Barclay, T., Schlieder, J.E., et al., 2020. The first habitable-zone Earth-sized planet from TESS. I. Validation of the TOI-700 system. *The Astronomical Journal*, *160*(3), p.116.

Gilmore, M.S., 1999, July. Craters as an indicator of martian regolith thickness. In *The Fifth International Conference on Mars*.

Gladman, B.J., Burns, J.A., Duncan, M., Lee, P. and Levison, H.F., 1996. The exchange of impact ejecta between terrestrial planets. *Science*, *271*(5254), pp.1387-1392.

Gladman, B., 1997. Destination: Earth. Martian meteorite delivery. *Icarus*, *130*(2), pp.228-246.

Glamoclija, M., Schieber, J. and Reimold, W.U., 2007, March. Microbial signatures from impact-induced hydrothermal settings of the Ries crater, Germany; a preliminary SEM study. In *38th Annual Lunar and Planetary Science Conference* (No. 1338, p. 1989).

Goldblatt, C., 2015. Habitability of water worlds: runaway greenhouses, atmospheric expansion, and multiple climate states of pure water atmospheres. *Astrobiology*, *15*(5), pp.362-370.

Golombek, M.P., Grant, J.A., Crumpler, L.S., Greeley, R., Arvidson, R.E., Bell, J.F., Weitz, C.M., Sullivan, R., Christensen, P.R., Soderblom, L.A. and Squyres, S.W., 2006. Erosion rates at the Mars Exploration Rover landing sites and long-term climate change on Mars. *Journal of Geophysical Research: Planets*, *111*(E12).

Gomes, R., Levison, H.F., Tsiganis, K. and Morbidelli, A., 2005. Origin of the cataclysmic Late Heavy Bombardment period of the terrestrial planets. *Nature*, *435*(7041), pp.466-469.

Goodrich, C.A., 2002. Olivine-phyric Martian basalts: A new type of shergottite. *Meteoritics & Planetary Science, vol. 37, Supplement, p. 31-34*, *37*, pp.31-34.

Goudge, T.A., Mustard, J.F., Head, J.W., Fassett, C.I. and Wiseman, S.M., 2015. Assessing the mineralogy of the watershed and fan deposits of the Jezero crater paleolake system, Mars. *Journal of Geophysical Research: Planets*, *120*(4), pp.775-808.

Goudge, T.A., Mohrig, D., Cardenas, B.T., Hughes, C.M. and Fassett, C.I., 2017, March. Stratigraphy and evolution of delta channel deposits, Jezero Crater, Mars. In *Lunar and Planetary Science Conference* (No. MSFC-E-DAA-TN38543).

Gourronc, M., Bourgeois, O., Mège, D., Pochat, S., Bultel, B., Massé, M., Le Deit, L., Le Mouélic, S. and Mercier, D., 2014. One million cubic kilometers of fossil ice in Valles Marineris: Relicts of a 3.5 Gy old glacial landsystem along the Martian equator. *Geomorphology*, *204*, pp.235-255.

Grasset, O., Dougherty, M.K., Coustenis, A., et al., 2013. JUpiter ICy moons Explorer (JUICE): An ESA mission to orbit Ganymede and to characterise the Jupiter system. *Planetary and Space Science*, *78*, pp.1-21.

Grau Galofre, A., Jellinek, A.M. and Osinski, G.R., 2020. Valley formation on early Mars by subglacial and fluvial erosion. *Nature Geoscience*, *13*(10), pp.663-668.

Greenberger, R.N., Mustard, J.F., Cloutis, E.A., Pratt, L.M., Sauer, P.E., Mann, P., Turner, K., Dyar, M.D. and Bish, D.L., 2015. Serpentinization, iron oxidation, and aqueous conditions in an ophiolite: implications for hydrogen production and habitability on Mars. *Earth and planetary science letters*, *416*, pp.21-34.

Greshake, A., Fritz, J. and Stöffler, D., 2004. Petrology and shock metamorphism of the olivine-phyric shergottite Yamato 980459: Evidence for a two-stage cooling and a single-stage ejection history. *Geochimica et Cosmochimica Acta*, *68*(10), pp.2359-2377.

Griffin, S., Daly, L., Keller, T., Piazolo, S., Forman, L.V., Lee, M.R., Baumgartner, R.J., Trimby, P.W., Benedix, G.K., Irving, A.J. and Hoefnagels, B., 2022. Constraints on the emplacement of Martian nakhlite igneous rocks and their source volcano from advanced micro-petrofabric analysis. *Journal of Geophysical Research: Planets*, *127*(6), p.e2021JE007080.

Grotzinger, J.P., Gupta, S., Malin, M.C., Rubin, D.M., Schieber, J., Siebach, K., Sumner, D.Y., Stack, K.M., Vasavada, A.R., Arvidson, R.E. and Calef III, F., 2015. Deposition, exhumation, and paleoclimate of an ancient lake deposit, Gale crater, Mars. *Science*, *350*(6257), p.aac7575.

Gulick, S., Morgan, J. and Mellett, C.L., 2017. Expedition 364 preliminary report: Chicxulub: drilling the K-Pg impact crater. *Preliminary report*, *364*.

Haberle, R.M., McKay, C.P., Schaeffer, J., Cabrol, N.A., Grin, E.A., Zent, A.P. and Quinn, R., 2001. On the possibility of liquid water on present-day Mars. *Journal of Geophysical Research: Planets*, *106*(E10), pp.23317-23326.

Haffen, S., Géraud, Y., Rosener, M. and Diraison, M., 2017. Thermal conductivity and porosity maps for different materials: A combined case study of granite and sandstone. *Geothermics*, *66*, pp.143-150.

Halevy, I., Fischer, W.W. and Eiler, J.M., 2011. Carbonates in the Martian meteorite Allan Hills 84001 formed at 18±4 C in a near-surface aqueous environment. *Proceedings of the National Academy of Sciences*, *108*(41), pp.16895-16899.

Hallis, L.J. and Taylor, G.J., 2011. Comparisons of the four Miller Range nakhlites, MIL 03346, 090030, 090032 and 090136: Textural and compositional observations of primary and secondary mineral assemblages. *Meteoritics & Planetary Science*, *46*(12), pp.1787-1803.

Hallis, L.J., Taylor, G.J., Nagashima, K. and Huss, G.R., 2012a. Magmatic water in the martian meteorite Nakhla. *Earth and Planetary Science Letters*, *359*, pp.84-92.

Hallis, L.J., Taylor, G.J., Nagashima, K., Huss, G.R., Needham, A.W., Grady, M.M. and Franchi, I.A., 2012b. Hydrogen isotope analyses of alteration phases in the nakhlite martian meteorites. *Geochimica et Cosmochimica Acta*, *97*, pp.105-119.

Hallis, L.J., Huss, G.R., Nagashima, K., Taylor, G.J., Halldórsson, S.A., Hilton, D.R., Mottl, M.J. and Meech, K.J., 2015. Evidence for primordial water in Earth's deep mantle. *Science*, *350*(6262), pp.795-797.

Hallis, L.J., Simpson, S., Mark, D. and Lee, M.R., 2016, August. Martian Alteration in Unique Meteorite NWA 8159?. In *79th Annual Meeting of the Meteoritical Society* (Vol. 79, No. 1921, p. 6442).

Hallis, L.J., 2017. D/H ratios of the inner Solar System. *Philosophical Transactions of the Royal Society A: Mathematical, Physical and Engineering Sciences*, *375*(2094), p.20150390.

Hansen, B.M., 2009. Formation of the terrestrial planets from a narrow annulus. *The Astrophysical Journal*, *703*(1), p.1131.

Hartmann, W.K. and Neukum, G., 2001. Cratering chronology and the evolution of Mars. In *Chronology and Evolution of Mars: Proceedings of an ISSI Workshop, 10–14 April 2000, Bern, Switzerland* (pp. 165-194). Springer Netherlands.

Hayba, D.O. and Ingebritsen, S.E., 1994. The computer model HYDROTHERM, a three-dimensional finite-difference model to simulate ground-water flow and heat transport in the temperature range of 0 to 1,200 degrees Celsius. *U.S. Geological Survey: Water-Resources Investigations Report 94-4045*. Reston, Virginia: U.S. Geological Survey, 85 p.

Hayba, D.O. and Ingebritsen, S.E., 1997. Multiphase groundwater flow near cooling plutons. *Journal of Geophysical Research, 102*: pp.12,235–12,252.

Hecht, L., Wittmann, A., Schmitt, R.T. and Stöffler, D., 2004. Composition of impact melt particles and the effects of post-impact alteration in suevitic rocks at the Yaxcopoil-1 drill core, Chicxulub crater, Mexico. *Meteoritics & Planetary Science*, *39*(7), pp.1169-1186.

Hecht, M.H., Kounaves, S.P., Quinn, R.C., West, S.J., Young, S.M., Ming, D.W., Catling, D.C., Clark, B.C., Boynton, W.V., Hoffman, J. and Deflores, L.P., 2009. Detection of perchlorate and the soluble chemistry of martian soil at the Phoenix lander site. *Science*, *325*, pp.64-67.

Herd, C.D., Borg, L.E., Jones, J.H. and Papike, J.J., 2002. Oxygen fugacity and geochemical variations in the Martian basalts: Implications for Martian basalt petrogenesis and the oxidation state of the upper mantle of Mars. *Geochimica et Cosmochimica Acta*, *66*(11), pp.2025-2036.

Herd, C.D., Walton, E.L., Agee, C.B., Muttik, N., Ziegler, K., Shearer, C.K., Bell, A.S., Santos, A.R., Burger, P.V., Simon, J.I. and Tappa, M.J., 2017. The Northwest Africa 8159 martian meteorite: Expanding the martian sample suite to the early Amazonian. *Geochimica et Cosmochimica Acta*, *218*, pp.1-26.

Herd, C.D., 2023. Insights into the petrogenetic history of the Northwest Africa 7635 augite-rich shergottite. *Meteoritics and Planetary Science*, *58*, pp.158-164.

Hewins, R. H., Zanda, B., Pont, S., & Zanetta, P. -M. (2019). Northwest Africa 10414, a pigeonite cumulate shergottite. *Meteoritics & Planetary Sciences, 54(9)*, 2132–2148.

Hewins, R.H., Humayun, M., Barrat, J.A., Zanda, B., Lorand, J.P., Pont, S., Assayag, N., Cartigny, P., Yang, S. and Sautter, V., 2020. Northwest Africa 8694, a ferroan chassignite: Bridging the gap between nakhlites and chassignites. *Geochimica et Cosmochimica Acta*, *282*, pp.201-226.

Hinrichs, K.U., Hayes, J.M., Sylva, S.P., Brewer, P.G. and DeLong, E.F., 1999. Methane-consuming archaebacteria in marine sediments. *Nature*, *398*(6730), pp.802-805.

Hinrichs, K.U., Hayes, J.M., Bach, W., Spivack, A.J., Hmelo, L.R., Holm, N.G., Johnson, C.G. and Sylva, S.P., 2006. Biological formation of ethane and propane in the deep marine subsurface. *Proceedings of the National Academy of Sciences*, *103*(40), pp.14684-14689.

Hoehler, T.M., Bebout, B.M. and Des Marais, D.J., 2001a. The role of microbial mats in the production of reduced gases on the early Earth. *Nature*, *412*(6844), pp.324-327.

Hoehler, T.M., Alperin, M., Albert, D. and Martens C., 2001b. Apparent minimum free energy requirements for methanogenic archaea and sulfate-reducing bacteria in an anoxic marine sediment. *FEMS Microbiology Ecology, 38*, pp.33–41.

Hoehler, T.M., 2004. Biological energy requirements as quantitative boundary conditions for life in the subsurface. *Geobiology, 2*, pp.205–215.

Hoehler, T.M., Amend, J.P. and Shock, E.L., 2007. A "follow the energy" approach for astrobiology. *Astrobiology*, *7*(6), pp.819-823.

Hoehler, T.M. and Jørgensen, B.B., 2013. Microbial life under extreme energy limitation. *Nature Reviews Microbiology*, *11*(2), pp.83-94.

Hoehler, T.M., Som, S.M. and Kiang N., 2018. Life's requirements. In *Handbook of Exoplanets*. H.J. Deeg and J.A. Belmonte, Eds., Springer International, doi:10.1007/978-3-319-30648-3_74-1.

Hoehler, T.M., 2022. Implications of H_2/CO_2 disequilibrium for life on Enceladus. *Nature Astronomy*, *6*(1), pp.3-4.

Hoffman, N., 2000. White Mars: A new model for Mars' surface and atmosphere based on CO_2. *Icarus*, *146*(2), pp.326-342.

Holland, T.J., 1989. Dependence of entropy on volume for silicate and oxide minerals; a review and predictive model. *American Mineralogist*, *74*(1-2), pp.5-13.

Holm, N.G., 1992. Marine hydrothermal systems and the origin of life.

Holm, N.G. and Neubeck, A., 2009. Reduction of nitrogen compounds in oceanic basement and its implications for HCN formation and abiotic organic synthesis. *Geochemical Transactions*, *10*, pp.1-11.

Holsapple, K.A. and Schmidt, R.M., 1982. On the scaling of crater dimensions: 2. Impact processes. *Journal of Geophysical Research: Solid Earth*, *87*(B3), pp.1849-1870.

Horgan, B.H., Anderson, R.B., Dromart, G., Amador, E.S. and Rice, M.S., 2020. The mineral diversity of Jezero crater: Evidence for possible lacustrine carbonates on Mars. *Icarus*, *339*, p.113526.

Hsieh, P.A., Tracy, J.V., Neuzil, C.E., Bredehoeft, J.D. and Silliman, S.E., 1981, June. A transient laboratory method for determining the hydraulic properties of 'tight'rocks—I. Theory. In *International Journal of Rock Mechanics and Mining Sciences & Geomechanics Abstracts* (*Vol. 18, No. 3*, pp. 245-252). Pergamon.

Hu, S., Lin, Y., Zhang, J., Hao, J., Xing, W., Zhang, T., Yang, W. and Changela, H., 2019. Ancient geologic events on Mars revealed by zircons and apatites from the Martian regolith breccia NWA 7034. *Meteoritics & Planetary Science*, *54*(4), pp.850-879.

Hu, Z., Zhang, R., Zhu, K., Li, D., Jin, Y., Guo, W., Liu, X., Zhang, X. and Zhang, Q., 2023. Probing the Pore Structure of the Berea Sandstone by Using X-ray Micro-CT in Combination with ImageJ Software. *Minerals, 13(3)*, p.360.

Huyakorn, P.S., Lester, B.H. and Faust, C.R., 1983. Finite element techniques for modeling groundwater flow in fractured aquifers. *Water Resources Research*, *19*(4), pp.1019-1035.

Huyakorn, P.S., 2012. *Computational methods in subsurface flow*. Academic Press.

Iess, L., Stevenson, D.J., Parisi, M., et al., 2014. The gravity field and interior structure of Enceladus. *Science*, *344*(6179), pp.78-80.

Inagaki, F., Hinrichs, K.U., Kubo, Y., Bowles, M.W., Heuer, V.B., Hong, W.L., Hoshino, T., Ijiri, A., Imachi, H., Ito, M. and Kaneko, M., 2015. Exploring deep microbial life in coal-bearing sediment down to ~2.5 km below the ocean floor. *Science*, *349*(6246), pp.420-424.

Ingebritsen, S. and Hayba, D., 1994. Fluid flow and heat transport near the critical point of H_2O. *Geophysical Research Letters*, *21*, pp.199–203.

Irving, A.J., Herd, C.D.K., Kuehner, S.M., Gregory, D.A. and Aaronson, A.A., 2004, August. Petrology and redox state of basaltic shergottite. In *Meteoritics & Planetary Science* (Vol. 39, No. 8, pp. A49-A49). Dept. Chemistry/Biochemistry, Univ. Arkansas, Fayetteville, Ar. 72701 USA: Meteoritical Soc.

Ivanov, B.A., 2001. Mars/Moon cratering rate ratio estimates. *Space Science Reviews*, *96*(1-4), pp.87-104.

Ivanov, B.A., Langenhorst, F., Deutsch, A. and Hornemann, U., 2002. How strong was impact-induced CO_2 degassing in the Cretaceous-Tertiary event? Numerical modeling of shock recovery experiments. *Special Paper of the Geological Society of America*, *356*, pp.587-594.

Ivanov, B.A., 2005. Numerical modeling of the largest terrestrial meteorite craters. *Solar System Research*, *39*, pp.381-409.

Ivanov, B.A. and Pierazzo, E., 2011. Impact cratering in H_2O-bearing targets on Mars: Thermal field under craters as starting conditions for hydrothermal activity. *Meteoritics & Planetary Science*, *46*(4), pp.601-619.

Irwin III, R.P. and Watters, T.R., 2010. Geology of the Martian crustal dichotomy boundary: Age, modifications, and implications for modeling efforts. *Journal of Geophysical Research: Planets*, *115* (E11).

Jaeger, W.L., Keszthelyi, L.P., McEwen, A.S., Dundas, C.M. and Russell, P.S., 2007. Athabasca Valles, Mars: A lava-draped channel system. *Science*, *317*(5845), pp.1709-1711.

Jagoutz, E., Sorowka, A., Vogel, J.D. and Wanke, H., 1994. ALH 84001: Alien or progenitor of the SNC family?. *Meteoritics*, *29*, pp.478-479.

Jin, Z. and Bose, M., 2019. New clues to ancient water on Itokawa. *Science advances*, *5*(5), p.eaav8106.

Jõeleht, A., Kirsimäe, K., Plado, J., Versh, E. and Ivanov, B., 2005. Cooling of the Kärdla impact crater: II. Impact and geothermal modeling. *Meteoritics & Planetary Science*, *40*(1), pp.21-33.

Johansen, A., Low, M.M.M., Lacerda, P. and Bizzarro, M., 2015. Growth of asteroids, planetary embryos, and Kuiper belt objects by chondrule accretion. *Science Advances*, *1*(3), p.e1500109.

Johansen, A. and Lambrechts, M., 2017. Forming planets via pebble accretion. *Annual Review of Earth and Planetary Sciences*, *45*, pp.359-387.

Johnson, M.C., Rutherford, M.J. and Hess, P.C., 1991. Chassigny petrogenesis: melt compositions, intensive parameters and water contents of Martian (?) magmas. *Geochimica et Cosmochimica Acta*, *55*(1), pp.349-366.

Johnson, J., Oelkers, E. and Helgeson, H., 1992. SUPCRT92: a software package for calculating the standard molar thermodynamic properties of minerals, gases, aqueous species, and reactions from 1 to 5000 bar and 0–1000 °C. *Computers in Geoscience, 18*, pp.899–947.

Johnson, B.C., Walsh, K.J., Minton, D.A., Krot, A.N. and Levison, H.F., 2016. Timing of the formation and migration of giant planets as constrained by CB chondrites. *Science Advances*, *2*(12), p.e1601658.

Kaltenegger, L. and Sasselov, D., 2011. Exploring the habitable zone for Kepler planetary candidates. *The Astrophysical Journal Letters*, *736*(2), p.L25.

Kashefi, K. and Lovley, D.R., 2003. Extending the upper temperature limit for life. *Science*, *301*(5635), pp.934-934.

Kasting, J.F., Whitmire, D.P. and Reynolds, R.T., 1993. Habitable zones around main sequence stars. *Icarus*, *101*(1), pp.108-128.

Kasting, J.F. and Harman, C.E., 2013. Inner edge of the habitable zone. *Nature*, *504*(7479), pp.221-223.

Keller, T. and Tackley, P.J., 2009. Towards self-consistent modeling of the martian dichotomy: The influence of one-ridge convection on crustal thickness distribution. *Icarus*, *202*(2), pp.429-443.

Kelley, D.S., Karson, J.A., Blackman, D.K., FruÈh-Green, G.L., Butterfield, D.A., Lilley, M.D., Olson, E.J., Schrenk, M.O., Roe, K.K., Lebon, G.T. and Rivizzigno, P., 2001. An off-axis hydrothermal vent field near the Mid-Atlantic Ridge at 30 N. *Nature*, *412*(6843), pp.145-149.

Kelley, D.S., Karson, J.A., Fruh-Green, G.L., Yoerger, D.R., Shank, T.M., Butterfield, D.A., Hayes, J.M., Schrenk, M.O., Olson, E.J., Proskurowski, G. and Jakuba, M., 2005. A serpentinite-hosted ecosystem: the Lost City hydrothermal field. *Science*, *307*(5714), pp.1428-1434.

Kenkmann, T., 2021. The terrestrial impact crater record: A statistical analysis of morphologies, structures, ages, lithologies, and more. *Meteoritics & Planetary Science*, *56*(5), pp.1024-1070.

Keppler, F., Vigano, I., McLeod, A., Ott, U., Früchtl, M. and Röckmann, T., 2012. Ultraviolet-radiation-induced methane emissions from meteorites and the Martian atmosphere. *Nature*, *486*(7401), pp.93-96.

Kerridge, J.F., 1985. Carbon, hydrogen and nitrogen in carbonaceous chondrites: Abundances and isotopic compositions in bulk samples. *Geochimica et Cosmochimica Acta*, *49*(8), pp.1707-1714.

Kieffer, S.W. and Simonds, C.H., 1980. The role of volatiles and lithology in the impact cratering process. *Reviews of Geophysics*, *18*(1), pp.143-181.

Kiefer, W.S., 2003. Melting in the Martian mantle: Shergottite formation and implications for present-day mantle convection on Mars. *Meteoritics & Planetary Science*, *38*(12), pp.1815-1832.

Kim, J.I., Sharma, A.K., Abbott, S.N., Wood, E.A., Dwyer, D.W., Jambura, A., Minton, K.W., Inman, R.B., Daly, M.J. and Cox, M.M., 2002. RecA Protein from the extremely radioresistant bacterium Deinococcus radiodurans: expression, purification, and characterization. *Journal of Bacteriology*, *184*(6), pp.1649-1660.

Kipp, K., Hsieh, P. and Charlton, S., 2008. Guide to the revised ground water flow and heat transport simulator: HYDROTHERM - Version 3: *U.S. Geological Survey: Techniques and Methods*, 6–A25, 160 p.

Kivelson, M.G., Khurana, K.K., Russell, C.T., et al., 2000. Galileo magnetometer measurements: A stronger case for a subsurface ocean at Europa. *Science, 289(5483)*, pp.1340-1343.

Kleine, T., Touboul, M., Bourdon, B., Nimmo, F., Mezger, K., Palme, H., Jacobsen, S.B., Yin, Q.Z. and Halliday, A.N., 2009. Hf–W chronology of the accretion and early evolution of asteroids and terrestrial planets. *Geochimica et Cosmochimica Acta*, *73*(17), pp.5150-5188.

Kling, A.M., Haberle, R.M., McKay, C.P., Bristow, T.F. and Rivera-Hernandez, F., 2020. Subsistence of ice-covered lakes during the Hesperian at Gale crater, Mars. *Icarus*, *338*, p.113495.

Kopparapu, R.K., Ramirez, R., Kasting, J.F., Eymet, V., Robinson, T.D., Mahadevan, S., Terrien, R.C., Domagal-Goldman, S., Meadows, V. and Deshpande, R., 2013. Habitable zones around main-sequence stars: new estimates. *The Astrophysical Journal*, *765*(2), p.131.

Kopparapu, R.K, Wolf, E.T., Arney, G., Batalha, N.E., Haqq-Misra, J., Grimm, S.L. and Heng, K., 2017. Habitable moist atmospheres on terrestrial planets near the inner edge of the habitable zone around M dwarfs. *The Astrophysical Journal*, *845*(1), p.5.

Korochantseva, E.V., Schwenzer, S.P., Buikin, A.I., Hopp, J., Ott, U. and Trieloff, M., 2011. ^{40}Ar-^{39}Ar and cosmic-ray exposure ages of nakhlites—Nakhla, Lafayette, Governador Valadares—and Chassigny. *Meteoritics & Planetary Science*, *46*(9), pp.1397-1417.

Kotelnikova, S. and Pedersen, K., 1997. Evidence for methanogenic archaea and homoacetogenic bacteria in deep granitic rock aquifers. *FEMS Microbiology Reviews, 20*, pp.339–349.

Kounaves, S.P., Carrier, B.L., O'Neil, G.D., Stroble, S.T. and Claire, M.W., 2014. Evidence of martian perchlorate, chlorate, and nitrate in Mars meteorite EETA79001: Implications for oxidants and organics. *Icarus*, *229*, pp.206-213.

Kring, D.A., 1995. The dimensions of the Chicxulub impact crater and impact melt sheet, *Journal of Geophysical Research, 100 (E8)*, 16979– 16986.

Kring, D.A, 2000. Impact events and their effect on the origin, evolution, and distribution of life. *GSA Today, 10*, pp.1–7.

Kring, D.A, 2005. Hypervelocity collisions into continental crust composed of sediments and an underlying crystalline basement: Comparing the Ries (~24 km) and Chicxulub (~180 km) impact craters. *Chemie der Erde*, *65*, pp.1–46.

Kring, D.A., Tikoo, S.M., Schmieder, M., Riller, U., Rebolledo-Vieyra, M., Simpson, S.L., Osinski, G.R., Gattacceca, J., Wittmann, A., Verhagen, C.M., Cockell, C.S., et al., 2020. Probing the hydrothermal system of the Chicxulub impact crater. *Science Advances*, *6*(22), p.eaaz3053.

Kring, D.A., Whitehouse, M.J. and Schmieder, M., 2021. Microbial sulfur isotope fractionation in the Chicxulub hydrothermal system. *Astrobiology*, *21*(1), pp.103-114.

Kurosawa, K., Nagaoka, Y., Senshu, H., Wada, K., Hasegawa, S., Sugita, S. and Matsui, T., 2015. Dynamics of hypervelocity jetting during oblique impacts of spherical projectiles investigated via ultrafast imaging. *Journal of Geophysical Research: Planets*, *120*(7), pp.1237-1251.

Kurosawa, K., Okamoto, T. and Genda, H., 2018. Hydrocode modeling of the spallation process during hypervelocity impacts: Implications for the ejection of Martian meteorites. *Icarus*, *301*, pp.219-234.

Lammer, H., Zerkle, A.L., Gebauer, S., Tosi, N., Noack, L., Scherf, M., Pilat-Lohinger, E., Güdel, M., Grenfell, J.L., Godolt, M. and Nikolaou, A., 2018. Origin and evolution of the atmospheres of early Venus, Earth and Mars. *The Astronomy and Astrophysics Review*, *26*, pp.1-72.

Lammer, H., Leitzinger, M., Scherf, M., Odert, P., Burger, C., Kubyshkina, D., Johnstone, C., Maindl, T., Schäfer, C.M., Güdel, M. and Tosi, N., 2020. Constraining the early evolution of Venus and Earth through atmospheric Ar, Ne isotope and bulk K/U ratios. *Icarus*, *339*, p.113551.

Lammer, H., Brasser, R., Johansen, A., Scherf, M. and Leitzinger, M., 2021. Formation of Venus, Earth and Mars: constrained by isotopes. *Space Science Reviews*, *217*(1), p.7.

Lamur, A., Kendrick, J.E., Eggertsson, G.H., Wall, R.J., Ashworth, J.D. and Lavallée, Y., 2017. The permeability of fractured rocks in pressurised volcanic and geothermal systems. *Scientific reports*, *7*(1), p.6173.

Langlais, B. and Thébault, E., 2011. Predicted and observed magnetic signatures of Martian (de) magnetized impact craters. *Icarus*, *212*(2), pp.568-578.

Lapen, T.J., Righter, M., Brandon, A.D., Debaille, V., Beard, B.L., Shafer, J.T. and Peslier, A.H., 2010. A younger age for ALH84001 and its geochemical link to shergottite sources in Mars. *Science*, *328*(5976), pp.347-351.

Lapen, T.J., Righter, M., Andreasen, R., Irving, A.J., Satkoski, A.M., Beard, B.L., Nishiizumi, K., Jull, A.T. and Caffee, M.W., 2017. Two billion years of magmatism recorded from a single Mars meteorite ejection site. *Science advances*, *3*(2), p.e1600922.

Lapôtre, M.G. and Ielpi, A., 2020. The pace of fluvial meanders on Mars and implications for the western delta deposits of Jezero crater. *AGU Advances*, *1*(2), p.e2019AV000141.

Leask, E.K. and Ehlmann, B.L., 2021. Evidence for deposition of chloride on Mars from small-volume surface water events into the Late Hesperian-Early Amazonian. (1.0) [Data set]. *Caltech DATA*.

Leask, E.K. and Ehlmann, B.L., 2022. Evidence for deposition of chloride on Mars from small-volume surface water events into the Late Hesperian-Early Amazonian. *AGU Advances*, *3*(1), p.e2021AV000534.

Leconte, J., Forget, F., Charnay, B., Wordsworth, R. and Pottier, A., 2013. Increased insolation threshold for runaway greenhouse processes on Earth-like planets. *Nature*, *504*(7479), pp.268-271.

Lee, M.R., Tomkinson, T., Mark, D.F., Stuart, F.M. and Smith, C.L., 2013. Evidence for silicate dissolution on Mars from the Nakhla meteorite. *Meteoritics & Planetary Science*, *48*(2), pp.224-240.

Lee, M.R., MacLaren, I., Andersson, S.M.L., Kovacs, A., Tomkinson, T., Mark, D.F. and Smith, C.L., 2015a. Opal-A in the Nakhla meteorite: A tracer of ephemeral liquid water in the Amazonian crust of Mars. *Meteoritics & Planetary Science*, *50*(8), pp.1362-1377.

Lee, M.R., Tomkinson, T., Hallis, L.J. and Mark, D.F., 2015b. Formation of iddingsite veins in the martian crust by centripetal replacement of olivine: Evidence from the nakhlite meteorite Lafayette. *Geochimica et Cosmochimica Acta*, *154*, pp.49-65.

Lee, M.R., Daly, L., Cohen, B.E., Hallis, L.J., Griffin, S., Trimby, P., Boyce, A. and Mark, D.F., 2018. Aqueous alteration of the Martian meteorite Northwest Africa 817: Probing fluid–rock interaction at the nakhlite launch site. *Meteoritics & Planetary Science*, *53*(11), pp.2395-2412.

Lefèvre, F. and Forget, F., 2009. Observed variations of methane on Mars unexplained by known atmospheric chemistry and physics. *Nature*, *460*(7256), pp.720-723.

Leifeld, J. and von Lützow, M., 2014. Chemical and microbial activation energies of soil organic matter decomposition. *Biology and Fertility of Soils*, *50*, pp.147-153.

Levison, H.F., Kretke, K.A. and Duncan, M.J., 2015. Growing the gas-giant planets by the gradual accumulation of pebbles. *Nature*, *524*(7565), pp.322-324.

Levy, J., Head, J.W. and Marchant, D.R., 2010. Concentric crater fill in the northern mid-latitudes of Mars: Formation processes and relationships to similar landforms of glacial origin. *Icarus*, *209*(2), pp.390-404.

Levy, J.S., Fassett, C.I., Head, J.W., Schwartz, C. and Watters, J.L., 2014. Sequestered glacial ice contribution to the global Martian water budget: Geometric constraints on the volume of remnant, midlatitude debris-covered glaciers. *Journal of Geophysical Research: Planets*, *119*(10), pp.2188-2196.

Lin, L.H., Onstott, T.C., Lippmann, J., Ward, J., Hall, J. And Lollar, B.S., 2002, August. Radiolytic H_2 In Continental Crust: A Potential Energy Source For Microbial Metabolism In Deep Biosphere. In *Geochimica et Cosmochimica Acta* (Vol. 66, No. 15 A, Pp. A457-A457).

Lindgren, P., Ivarsson, M., Neubeck, A., Broman, C., Henkel, H. and Holm, N.G., 2010. Putative fossil life in a hydrothermal system of the Dellen impact structure, Sweden. *International Journal of Astrobiology*, *9*(3), pp.137-146.

Liu, Y., Tice, M.M., Schmidt, M.E., Treiman, A.H., Kizovski, T.V., Hurowitz, J.A., Allwood, A.C., Henneke, J., Pedersen, D.A.K., VanBommel, S.J. and Jones, M.W.M., 2022. An olivine cumulate outcrop on the floor of Jezero crater, Mars. *Science*, *377*(6614), pp.1513-1519.

Lorand, J.P., Pont, S., Chevrier, V., Luguet, A., Zanda, B. and Hewins, R., 2018. Petrogenesis of martian sulfides in the Chassigny meteorite. *American Mineralogist: Journal of Earth and Planetary Materials*, *103*(6), pp.872-885.

Luo, W., Ding, H., Li, H., Ji, Z., Huang, K., Zhao, W., Yu, Y. and Zeng, Y., 2020. Molecular diversity of the microbial community in coloured snow from the Fildes Peninsula (King George Island, Maritime Antarctica). *Polar Biology*, *43*, pp.1391-1405.

Magna, T., Day, J.M., Mezger, K., Fehr, M.A., Dohmen, R., Aoudjehane, H.C. and Agee, C.B., 2015. Lithium isotope constraints on crust–mantle interactions and surface processes on Mars. *Geochimica et Cosmochimica Acta*, *162*, pp.46-65.

Mandon, L., Quantin-Nataf, C., Thollot, P., Mangold, N., Lozac'h, L., Dromart, G., Beck, P., Dehouck, E., Breton, S., Millot, C. and Volat, M., 2020. Refining the age, emplacement and alteration scenarios of the olivine-rich unit in the Nili Fossae region, Mars. *Icarus*, *336*, p.113436.

Manske, L., Marchi, S., Plesa, A.C. and Wünnemann, K., 2021. Impact melting upon basin formation on early Mars. *Icarus*, *357*, p.114128.

Marinova, M.M., Aharonson, O. and Asphaug, E., 2008. Mega-impact formation of the Mars hemispheric dichotomy. *Nature*, *453*(7199), pp.1216-1219.

Marion, G.M., Catling, D.C., Zahnle, K.J. and Claire, M.W., 2010. Modeling aqueous perchlorate chemistries with applications to Mars. *Icarus*, *207*(2), pp.675-685.

Martin, R.G. and Livio, M., 2012. On the evolution of the snow line in protoplanetary discs. *Monthly Notices of the Royal Astronomical Society: Letters*, *425*(1), pp.L6-L9.

Martin, R.G. and Livio, M., 2012. On the formation and evolution of asteroid belts and their potential significance for life. *Monthly Notices of the Royal Astronomical Society: Letters*, *428*(1), pp.L11-L15.

Martín-Torres, F.J., Zorzano, M.P., Valentín-Serrano, P., Harri, A.M., Genzer, M., Kemppinen, O., Rivera-Valentin, E.G., Jun, I., Wray, J., Bo Madsen, M. and Goetz, W., 2015. Transient liquid water and water activity at Gale crater on Mars. *Nature Geoscience*, *8*(5), pp.357-361.

Mason, B., 1982. *Antarctica Meteorite Newsletter 5(4)*.

Matson, D.L., Castillo-Rogez, J.C., Schubert, G., Sotin, C. and McKinnon, W.B., 2009. The thermal evolution and internal structure of Saturn's mid-sized icy satellites. *Saturn from Cassini-Huygens*, pp.577-612.

Mayhew, L.E., Ellison, E.T., McCollom, T.M., Trainor, T.P. and Templeton, A.S., 2013. Hydrogen generation from low-temperature water–rock reactions. *Nature Geoscience*, *6*(6), pp.478-484.

McCollom, T.M. and Shock, E.L., 1997. Geochemical constraints on chemolithoautotrophic metabolism by microorganisms in seafloor hydrothermal systems. *Geochimica et Cosmochimica acta*, *61*(20), pp.4375-4391.

McCollom, T.M. and Seewald, J.S., 2013. Serpentinites, hydrogen, and life. *Elements*, *9*(2), pp.129-134.

McCubbin, F.M., Smirnov, A., Nekvasil, H., Wang, J., Hauri, E. and Lindsley, D.H., 2010. Hydrous magmatism on Mars: A source of water for the surface and subsurface during the Amazonian. *Earth and Planetary Science Letters*, *292*(1-2), pp.132-138.

McCubbin, F.M., Hauri, E.H., Elardo, S.M., Vander Kaaden, K.E., Wang, J. and Shearer Jr, C.K., 2012. Hydrous melting of the martian mantle produced both depleted and enriched shergottites. *Geology*, *40*(8), pp.683-686.

McCubbin, F.M., Elardo, S.M., Shearer Jr, C.K., Smirnov, A., Hauri, E.H. and Draper, D.S., 2013. A petrogenetic model for the comagmatic origin of chassignites and nakhlites: Inferences from chlorine-rich minerals, petrology, and geochemistry. *Meteoritics & Planetary Science*, *48*(5), pp.819-853.

McEwen, A.S., Preblich, B.S., Turtle, E.P., Artemieva, N.A., Golombek, M.P., Hurst, M., Kirk, R.L., Burr, D.M. and Christensen, P.R., 2005. The rayed crater Zunil and interpretations of small impact craters on Mars. *Icarus*, *176*(2), pp.351-381.

McEwen, A.S., Dundas, C.M., Mattson, S.S., Toigo, A.D., Ojha, L., Wray, J.J., Chojnacki, M., Byrne, S., Murchie, S.L. and Thomas, N., 2014. Recurring slope lineae in equatorial regions of Mars. *Nature geoscience*, *7*(1), pp.53-58.

McKay, D.S., Gibson Jr, E.K., Thomas-Keprta, K.L., Vali, H., Romanek, C.S., Clemett, S.J., Chillier, X.D., Maechling, C.R. and Zare, R.N., 1996. Search for past life on Mars: possible relic biogenic activity in Martian meteorite ALH84001. *Science*, *273*(5277), pp.924-930.

McKeegan, K.D. and Leshin, L.A., 2001. Stable isotope variations in extraterrestrial materials. *Reviews in Mineralogy and Geochemistry*, *43*(1), pp.279-318.

McMahon, S., Bosak, T., Grotzinger, J.P., Milliken, R.E., Summons, R.E., Daye, M., Newman, S.A., Fraeman, A., Williford, K.H. and Briggs, D.E.G., 2018. A field guide to finding fossils on Mars. *Journal of Geophysical Research: Planets*, *123*(5), pp.1012-1040.

McSween Jr, H.Y., 1984. SNC meteorites: Are they Martian rocks?. *Geology*, *12*(1), pp.3-6.
Mcsween Jr, H.Y., Eisenhour, D.D., Taylor, L.A., Wadhwa, M. and Crozaz, G., 1996. QUE94201 shergottite: Crystallization of a Martian basaltic magma. *Geochimica et Cosmochimica Acta*, *60*(22), pp.4563-4569.

McSween, H.Y., Wyatt, M.B., Gellert, R., Bell III, J.F., Morris, R.V., Herkenhoff, K.E., Crumpler, L.S., Milam, K.A., Stockstill, K.R., Tornabene, L.L. and Arvidson, R.E., 2006a. Characterization and petrologic interpretation of olivine-rich basalts at Gusev Crater, Mars. *Journal of Geophysical Research: Planets*, *111*(E2).

McSween, H.Y., Ruff, S.W., Morris, R.V., Bell Iii, J.F., Herkenhoff, K., Gellert, R., Stockstill, K.R., Tornabene, L.L., Squyres, S.W., Crisp, J.A. and Christensen, P.R., 2006b. Alkaline volcanic rocks from the Columbia Hills, Gusev crater, Mars. *Journal of Geophysical Research: Planets*, *111*(E9).

McSween Jr., H.Y., 2015. Petrology on Mars. *American Mineralogist*, *100*(11-12), pp.2380-2395.

Meadows, V., Arney, G., Schmidt, B. and Des Marais, D.J., 2020. *Planetary Astrobiology*. University of Arizona Press.

Mège, D. and Bourgeois, O., 2011. Equatorial glaciations on Mars revealed by gravitational collapse of Valles Marineris wallslopes. *Earth and Planetary Science Letters*, *310*(3-4), pp.182-191.

Melosh, H.J., 1984. Impact ejection, spallation, and the origin of meteorites. *Icarus*, *59*(2), pp.234-260.

Melosh, H.J., 1989. *Impact cratering: A geologic process*. New York: Oxford University Press; Oxford: Clarendon Press.

Melosh, H.J., 2003. Exchange of meteorites (and life?) between stellar systems. *Astrobiology*, *3*(1), pp.207-215.

Mikouchi, T., 2005. Northwest Africa 1950: Mineralogy and comparison with Antarctic lherzolitic shergottites. *Meteoritics & Planetary Science*, *40*(11), pp.1621-1634.

Mikouchi, T. and Kurihara, T., 2008. Mineralogy and petrology of paired lherzolitic shergottites Yamato 000027, Yamato 000047, and Yamato 000097: Another fragment from a Martian “lherzolite” block. *Polar Science*, *2*(3), pp.175-194.

Millero, F.J., Feistel, R., Wright, D.G. and McDougall, T.J., 2008. The composition of Standard Seawater and the definition of the Reference-Composition Salinity Scale. *Deep Sea Research Part I: Oceanographic Research Papers*, *55*(1), pp.50-72.

Misawa, K., Shih, C.Y., Reese, Y., Nyquist, L.E. and Barrat, J.A., 2005. Rb-Sr and Sm-Nd isotopic systematics of NWA 2737 chassignite. *Meteoritics and Planetary Science Supplement*, *40*, p.5200.

Mitrofanov, I., Malakhov, A., Djachkova, M., Golovin, D., Litvak, M., Mokrousov, M., Sanin, A., Svedhem, H. and Zelenyi, L., 2022. The evidence for unusually high hydrogen abundances in the central part of Valles Marineris on Mars. *Icarus*, *374*, p.114805.

Mittelholz, A., Johnson, C.L. and Morschhauser, A., 2018. A new magnetic field activity proxy for Mars from MAVEN data. *Geophysical Research Letters*, *45*(12), pp.5899-5907.

Mittelholz, A., Johnson, C.L., Feinberg, J.M., Langlais, B. and Phillips, R.J., 2020. Timing of the martian dynamo: New constraints for a core field 4.5 and 3.7 Ga. *Science Advances*, *6*(18), p.eaba0513.

Mittlefehldt, D.W., 1994. ALH84001, a cumulate orthopyroxenite member of the Martian meteorite clan. *Meteoritics*, *29*(2), pp.214-221.

Mojzsis, S.J., Arrhenius, G., McKeegan, K.D., Harrison, T.M., Nutman, A.P. and Friend, C.R.L., 1996. Evidence for life on Earth before 3,800 million years ago. *Nature*, *384*(6604), pp.55-59.

Mojzsis, S.J., Harrison, T.M. and Pidgeon, R.T., 2001. Oxygen-isotope evidence from ancient zircons for liquid water at the Earth's surface 4,300 Myr ago. *Nature*, *409*(6817), pp.178-181.

Mojzsis, S.J., Brasser, R., Kelly, N.M., Abramov, O. and Werner, S.C., 2019. Onset of giant planet migration before 4480 million years ago. *The Astrophysical Journal*, *881*(1), p.44.

Montési, L.G. and Zuber, M.T., 2003. Clues to the lithospheric structure of Mars from wrinkle ridge sets and localization instability. *Journal of Geophysical Research: Planets*, *108*(E6).

Montmerle, T., Augereau, J.C., Chaussidon, M., Gounelle, M., Marty, B. and Morbidelli, A., 2006. Solar System formation and early evolution: the first 100 million years. *Earth, Moon, and Planets*, *98*, pp.39-95.

Morgan, J., Gulick, S., Mellett, C.L. and Green, S.L., 2017. Chicxulub: Drilling the K-Pg impact crater. *Proceedings of the International Ocean Discovery Program*, *364*.

Morbidelli, A., Chambers, J., Lunine, J.I., Petit, J.M., Robert, F., Valsecchi, G.B. and Cyr, K.E., 2000. Source regions and timescales for the delivery of water to the Earth. *Meteoritics & Planetary Science*, *35*(6), pp.1309-1320.

Morbidelli, A., Levison, H.F., Tsiganis, K. and Gomes, R., 2005. Chaotic capture of Jupiter's Trojan asteroids in the early Solar System. *Nature*, *435*(7041), pp.462-465.

Morbidelli, A., Brasser, R., Gomes, R., Levison, H.F. and Tsiganis, K., 2010. Evidence from the asteroid belt for a violent past evolution of Jupiter's orbit. *The Astronomical Journal*, *140*(5), p.1391.

Morbidelli, A., Lunine, J.I., O'Brien, D.P., Raymond, S.N. and Walsh, K.J., 2012. Building terrestrial planets. *Annual Review of Earth and Planetary Sciences*, *40*, pp.251-275.

Morbidelli, A., 2018. Calcium signals in planetary embryos. *Nature*, *555*(7697), pp.451-452.

Morita, R.Y., 1997. *Bacteria in oligotrophic environments* (p. 529). Chapman & Hall, New York.

Moser, D.E., Arcuri, G.A., Reinhard, D.A., White, L.F., Darling, J.R., Barker, I.R., Larson, D.J., Irving, A.J., McCubbin, F.M., Tait, K.T. and Roszjar, J., 2019. Decline of giant impacts

on Mars by 4.48 billion years ago and an early opportunity for habitability. *Nature Geoscience*, *12*(7), pp.522-527.

Mothé-Diniz, T., árcio Carvano, J. M., & Lazzaro, D. (2003). Distribution of taxonomic classes in the main belt of asteroids. *Icarus*, *162*(1), 10-21.

Mumma, M.J., Villanueva, G.L., Novak, R.E., Hewagama, T., Bonev, B.P., DiSanti, M.A., Mandell, A.M. and Smith, M.D., 2009. Strong release of methane on Mars in northern summer 2003. *Science*, *323*(5917), pp.1041-1045.

Murchie, S., Arvidson, R., Bedini, P., Beisser, K., Bibring, J.P., Bishop, J., Boldt, J., Cavender, P., Choo, T., Clancy, R.T. and Darlington, E.H., 2007. Compact reconnaissance imaging spectrometer for Mars (CRISM) on Mars reconnaissance orbiter (MRO). *Journal of Geophysical Research: Planets*, *112*(E5).

Needham, A.W., Abel, R.L., Tomkinson, T. and Grady, M.M., 2013. Martian subsurface fluid pathways and 3D mineralogy of the Nakhla meteorite. *Geochimica et Cosmochimica Acta*, *116*, pp.96-110.

Nemchin, A., Timms, N., Pidgeon, R., Geisler, T., Reddy, S. and Meyer, C., 2009. Timing of crystallization of the lunar magma ocean constrained by the oldest zircon. *Nature Geoscience*, *2(2)*, pp.133-136.

Neukum, G., Basilevsky, A., Chapman, M., Werner, S., van Gasselt, S., Jaumann, R., Hauber, E., Hoffmann, H., Wolf, U., Head, J. and Greeley, R., 2007. Episodicity in the geological evolution of Mars: resurfacing events and ages from creating analysis of image data and correlation with radiometric ages of martian meteorites. In *Seventh International Conference on Mars* (Vol. 1353, p. abstract3015). Lunar and Planetary Institute.

Neuzil, C.E., Cooley, C., Silliman, S.E., Bredehoeft, J.D. and Hsieh, P.A., 1981, June. A transient laboratory method for determining the hydraulic properties of 'tight'rocks—II. Application. In *International journal of rock mechanics and mining sciences & geomechanics abstracts* (*Vol. 18, No. 3*, pp. 253-258). Pergamon.

Nimmo, F. and Pappalardo, R.T., 2006. Diapir-induced reorientation of Saturn's moon Enceladus. *Nature*, *441*(7093), pp.614-616.

Nimmo, F. and Pappalardo, R.T., 2016. Ocean worlds in the outer solar system. *Journal of Geophysical Research: Planets*, *121*(8), pp.1378-1399.

Nininger, H.H., 1935. The Lafayette meteorite. *Popular Astronomy*, *43*, p.404.

Nitschke, W. and Russell, M.J., 2009. Hydrothermal focusing of chemical and chemiosmotic energy, supported by delivery of catalytic Fe, Ni, Mo/W, Co, S and Se, forced life to emerge. *Journal of Molecular Evolution*, *69*, pp.481-496.

Nyquist, L.E., Borg, L.E. and Shih, C.Y., 1998. The Shergottite age paradox and the relative probabilities for Martian meteorites of differing ages. *Journal of Geophysical Research: Planets*, *103*(E13), pp.31445-31455.

Nyquist, L.E., Bogard, D.D., Shih, C.Y., Greshake, A., Stöffler, D. and Eugster, O., 2001. Ages and Geologic Histories of Martian Meteorites. *Space Science Reviews*, *96*, pp.105-164.

O'Brien, Á.C., Hallis, L.J., Regnault, C., Morrison, D., Blackburn, G., Steele, A., Daly, L., Tait, A., Tremblay, M.M., Telenko, D.E. and Gunn, J., 2022. Using Organic Contaminants to Constrain the Terrestrial Journey of the Martian Meteorite Lafayette. *Astrobiology*, *22*(11), pp.1351-1362.

Odert, P., Lammer, H., Erkaev, N.V., Nikolaou, A., Lichtenegger, H.I., Johnstone, C.P., Kislyakova, K.G., Leitzinger, M. and Tosi, N., 2018. Escape and fractionation of volatiles and noble gases from Mars-sized planetary embryos and growing protoplanets. *Icarus*, *307*, pp.327-346.

Oehler, D.Z. and Etiope, G., 2017. Methane seepage on Mars: where to look and why. *Astrobiology*, *17*(12), pp.1233-1264.

Oelkers, E.H. and Gislason, S.R., 2001. The mechanism, rates and consequences of basaltic glass dissolution: I. An experimental study of the dissolution rates of basaltic glass as a function

of aqueous Al, Si and oxalic acid concentration at 25 °C and pH= 3 and 11. *Geochimica et Cosmochimica Acta*, *65*(21), pp.3671-3681.

Ojha, L., Wilhelm, M.B., Murchie, S.L., McEwen, A.S., Wray, J.J., Hanley, J., Massé, M. and Chojnacki, M., 2015. Spectral evidence for hydrated salts in recurring slope lineae on Mars. *Nature Geoscience*, *8*(11), pp.829-832.

Ojha, L., Karunatillake, S., Karimi, S. and Buffo, J., 2021. Amagmatic hydrothermal systems on Mars from radiogenic heat. *Nature communications*, *12*(1), p.1754.

Okazaki, R., Nagao, K., Imae, N. and Kojima, H., 2003. Noble gas signatures of Antartic nakhlites, Yamato (Y) 000593, Y000749 and Y000802. *Antarctic meteorite research*, *16*, pp.58-79.

Orosei, R., Lauro, S.E., Pettinelli, E., Cicchetti, A.N.D.R.E.A., Coradini, M., Cosciotti, B., Di Paolo, F., Flamini, E., Mattei, E., Pajola, M. and Soldovieri, F., 2018. Radar evidence of subglacial liquid water on Mars. *Science*, *361*(6401), pp.490-493.

Osinski, G.R., Tornabene, L.L. and Grieve, R.A., 2011. Impact ejecta emplacement on terrestrial planets. *Earth and Planetary Science Letters*, *310*(3-4), pp.167-181.

Osinski, G.R., Tornabene, L.L., Banerjee, N.R., Cockell, C.S., Flemming, R., Izawa, M.R., McCutcheon, J., Parnell, J., Preston, L.J., Pickersgill, A.E. and Pontefract, A., 2013. Impact-generated hydrothermal systems on Earth and Mars. *Icarus*, *224*(2), pp.347-363.

Owen, T., Biemann, K., Rushneck, D.R., Biller, J.E., Howarth, D.W. and Lafleur, A.L., 1977. The composition of the atmosphere at the surface of Mars. *Journal of Geophysical research*, *82*(28), pp.4635-4639.

Oze, C. and Sharma, M., 2005. Have olivine, will gas: serpentinization and the abiogenic production of methane on Mars. *Geophysical research letters*, *32*(10).

Pace, N.R., 1997. A molecular view of microbial diversity and the biosphere. *Science*, *276*(5313), pp.734-740.

Palle, E., Orell-Miquel, J., Brady, M., Bean, J., Hatzes, A.P., Morello, G., Morales, J.C., Murgas, F., Molaverdikhani, K., Parviainen, H. and Sanz-Forcada, J., 2023. GJ 806 (TOI-4481): A bright nearby multi-planetary system with a transiting hot, low-density super-Earth. *arXiv preprint arXiv:2301.06873*.

Park, J., Bogard, D.D., Nyquist, L.E. and Herzog, G.F., 2014. Issues in dating young rocks from another planet: Martian shergottites. *Geological Society, London, Special Publications*, *378*(1), pp.297-316.

Parkhurst, D.L. and Appelo, C.A.J., 1999. User's guide to PHREEQC (Version 2): A computer program for speciation, batch-reaction, one-dimensional transport, and inverse geochemical calculations. *Water-resources investigations report*, *99*(4259), p.312.

Parkhurst, D.L. and Appelo, C.A.J., 2013. Description of input and examples for PHREEQC version 3—a computer program for speciation, batch-reaction, one-dimensional transport, and inverse geochemical calculations. *US geological survey techniques and methods*, *6*(A43), p.497.

Parnell, J., Boyce, A., Thackrey, S., Muirhead, D., Lindgren, P., Mason, C., Taylor, C., Still, J., Bowden, S., Osinski, G.R. and Lee, P., 2010. Sulfur isotope signatures for rapid colonization of an impact crater by thermophilic microbes. *Geology*, *38*(3), pp.271-274.

Parro, L.M., Jiménez-Díaz, A., Mansilla, F. and Ruiz, J., 2017. Present-day heat flow model of Mars. *Scientific reports*, *7*(1), p.45629.

Pepin, R.O., 1985. Meteorites: evidence of Martian origins. *Nature*, *317*(6037), pp.473-475.

Peretyazhko, T.S., Niles, P.B., Sutter, B., Morris, R.V., Agresti, D.G., Le, L. and Ming, D.W., 2018. Smectite formation in the presence of sulfuric acid: Implications for acidic smectite formation on early Mars. *Geochimica et Cosmochimica Acta*, *220*, pp.248-260.

Petigura, E.A., Howard, A.W. and Marcy, G.W., 2013. Prevalence of Earth-size planets orbiting Sun-like stars. *Proceedings of the National Academy of Sciences*, *110*(48), pp.19273-19278.

Pfalzner, S., Davies, M.B., Gounelle, M., Johansen, A., Münker, C., Lacerda, P., Zwart, S.P., Testi, L., Trieloff, M. and Veras, D., 2015. The formation of the solar system. *Physica Scripta*, *90*(6), p.068001.

Pickersgill, A.E., Christou, E., Mark, D.F., Lee, M.R., Tremblay, M.M., Rasmussen, C., Morgan, J.V., Gulick, S.P.S., Schmieder, M., Bach, W., Osinski, G.R., et al., 2019. Six Million Years of Hydrothermal Activity at Chicxulub?. *Large Meteorite Impacts and Planetary Evolution VI*, *2136*, p.5082.

Pickersgill, A.E., Lee, M.R., Mark, D.F. and Christou, E., 2022. What Do We Know About the Duration of Post-Impact Hydrothermal Activity? *Meteoritics & Planetary Science*, 57.

Pierazzo, E., Vickery, A.M., Melosh, H.J., 1997. A reevaluation of impact melt production. *Icarus 127 (2)*, 408–423.

Pierazzo, E. and Melosh, H.J., 2000. Understanding oblique impacts from experiments, observations, and modeling. *Annual Review of Earth and Planetary Sciences*, *28*(1), pp.141-167.

Pierazzo, E., Artemieva, N.A. and Ivanov, B.A., 2005. Starting conditions for hydrothermal systems underneath Martian craters: Hydrocode modeling. *Large meteorite impacts III*, *384*, pp.443-457.

Plesa, A.C., Grott, M., Tosi, N., Breuer, D., Spohn, T. and Wieczorek, M.A., 2016. How large are present-day heat flux variations across the surface of Mars?. *Journal of Geophysical Research: Planets*, *121*(12), pp.2386-2403.

Podosek, F.A., 1973. Thermal history of the nakhlites by the40Ar-39Ar method. *Earth and Planetary Science Letters*, *19*(2), pp.135-144.

Price, P.B. and Sowers, T., 2004. Temperature dependence of metabolic rates for microbial growth, maintenance, and survival. *Proceedings of the National Academy of Sciences*, *101*(13), pp.4631-4636.

Rahmstorf, S., 2002. Ocean circulation and climate during the past 120,000 years. *Nature*, *419*(6903), pp.207-214.

Ramirez, R.M., Kopparapu, R., Zugger, M.E., Robinson, T.D., Freedman, R. and Kasting, J.F., 2014. Warming early Mars with CO2 and H2. *Nature Geoscience*, *7*(1), pp.59-63.

Ramirez, R.M., Craddock, R.A. and Usui, T., 2020. Climate simulations of early Mars with estimated precipitation, runoff, and erosion rates. *Journal of Geophysical Research: Planets*, *125*(3), p.e2019JE006160.

Rampey, M. and Harvey, R., 2012. Mars Hesperian magmatism as revealed by Syrtis Major and the Circum-Hellas volcanic province. *Earth, Moon, and Planets*, *109*, pp.61-75.

Rathbun, J.A. and Squyres, S.W., 2002. Hydrothermal systems associated with Martian impact craters. *Icarus*, *157*(2), pp.362-372.

Raymond, S.N. and Izidoro, A., 2017. Origin of water in the inner Solar System: Planetesimals scattered inward during Jupiter and Saturn's rapid gas accretion. *Icarus*, *297*, pp.134-148.

Razzell Hollis, J., Abbey, W., Asher, S.A., Bailey, Z., Beegle, L.W., Berger, E., Bhartia, R., Burton, A.S., Bykov, S.V., Cardarelli, E. and Conrad, P.G., 2021, October. First SHERLOC Results from Mars 2020's Green Zone Campaign in Jezero Crater. In *AAS/Division for Planetary Sciences Meeting Abstracts* (Vol. 53, No. 7, pp. 206-07).

Robert, F., Gautier, D. and Dubrulle, B., 2000. The solar system D/H ratio: Observations and theories. *Space Science Reviews*, *92*(1-2), pp.201-224.

Roberts, J.H. and Zhong, S., 2006. Degree-1 convection in the Martian mantle and the origin of the hemispheric dichotomy. *Journal of Geophysical Research: Planets*, *111*(E6).

Robbins, S.J., Di Achille, G. and Hynek, B.M., 2011. The volcanic history of Mars: High-resolution crater-based studies of the calderas of 20 volcanoes. *Icarus*, *211*(2), pp.1179-1203.

Robbins, S.J., Hynek, B.M., Lillis, R.J. and Bottke, W.F., 2013. Large impact crater histories of Mars: The effect of different model crater age techniques. *Icarus*, *225*(1), pp.173-184.

Roush, W., 2020. Extraterrestrials. *MIT Press*.

Rowe, A.R., Chellamuthu, P., Lam, B., Okamoto, A. and Nealson, K.H., 2015. Marine sediments microbes capable of electrode oxidation as a surrogate for lithotrophic insoluble substrate metabolism. *Frontiers in microbiology*, *5*, p.784.

Rubin, A.E., Warren, P.H., Greenwood, J.P., Verish, R.S., Leshin, L.A., Hervig, R.L., Clayton, R.N. and Mayeda, T.K., 2000. Los Angeles: The most differentiated basaltic martian meteorite. *Geology*, *28*(11), pp.1011-1014.

Ruiz, J., 2014. The early heat loss evolution of Mars and their implications for internal and environmental history. *Scientific reports*, *4*(1), pp.1-7.

Ruzicka, A., Grossman, J.N. and Garvie, L., 2014. *The Meteoritical Bulletin, No. 100*, 2014 June.

Ryder, G., 2002. Mass flux in the ancient Earth-Moon system and benign implications for the origin of life on Earth. *Journal of Geophysical Research: Planets*, *107*(E4), pp.6-1.

Sanford, W.E., 2005. A simulation of the hydrothermal response to the Chesapeake Bay bolide impact. *Geofluids*, *5*(3), pp.185-201.

Sasselov, D.D. and Lecar, M., 2000. On the snow line in dusty protoplanetary disks. *The Astrophysical Journal*, *528*(2), p.995.

Sauterey, B., Charnay, B., Affholder, A., Mazevet, S. and Ferrière, R., 2022. Early Mars habitability and global cooling by H2-based methanogens. *Nature Astronomy*, *6*(11), pp.1263-1271.

Scheller, E.L., Hollis, J.R., Cardarelli, E.L., Steele, A., Beegle, L.W., Bhartia, R., Conrad, P., Uckert, K., Sharma, S., Ehlmann, B.L. and Abbey, W.J., 2022. Aqueous alteration processes in Jezero crater, Mars−implications for organic geochemistry. *Science*, p.eabo5204.

Schink, B., 1997. Energetics of syntrophic cooperation in methanogenic degradation. *Microbiology and molecular biology reviews*, *61*(2), pp.262-280.

Schink, B. and Stams, A.J., 2006. Syntrophism among prokaryotes. *The prokaryotes*, *2*, pp.309-335.

Schmidt, R.M. and Housen, K.R., 1987. Some recent advances in the scaling of impact and explosion cratering. *International Journal of Impact Engineering*, *5*(1-4), pp.543-560.

Schmidt, F., Andrieu, F., Costard, F., Kocifaj, M. and Meresescu, A.G., 2017. Formation of recurring slope lineae on Mars by rarefied gas-triggered granular flows. *Nature Geoscience*, *10*(4), pp.270-273.

Schneider, C.A., Rasband, W.S. and Eliceiri, K.W., 2012. NIH Image to ImageJ: 25 years of image analysis. *Nature methods*, *9(7)*, pp.671-675.

Schuerger, A.C., Moores, J.E., Clausen, C.A., Barlow, N.G. and Britt, D.T., 2012. Methane from UV-irradiated carbonaceous chondrites under simulated Martian conditions. *Journal of Geophysical Research: Planets*, *117*(E8).

Schwenzer, S.P., Abramov, O., Allen, C.C., Clifford, S.M., Cockell, C.S., et al., 2012. Puncturing Mars: How impact craters interact with the Martian cryosphere. *Earth and Planetary Science Letters*, *335*, pp.9-17.

Scott, D.H. and Tanaka, K.L., 1986. *Geologic map of the western equatorial region of Mars* (Vol. 1). Geological Survey (US).

Segura, T.L., Toon, O.B., Colaprete, A. and Zahnle, K., 2002. Environmental effects of large impacts on Mars. *Science*, *298*(5600), pp.1977-1980.

Seyfried Jr, W.E., Foustoukos, D.I. and Fu, Q., 2007. Redox evolution and mass transfer during serpentinization: An experimental and theoretical study at 200 °C, 500 bar with implications for ultramafic-hosted hydrothermal systems at Mid-Ocean Ridges. *Geochimica et Cosmochimica Acta*, *71*(15), pp.3872-3886.

Sharp, T.G., Walton, E.L., Hu, J. and Agee, C., 2019. Shock conditions recorded in NWA 8159 martian augite basalt with implications for the impact cratering history on Mars. *Geochimica et Cosmochimica Acta*, *246*, pp.197-212.

Shearer, C.K., Bell, A.S., Herd, C.D., Burger, P.V., Provencio, P., Sharp, Z.D. and Papike, J.J., 2019. The Northwest Africa 8159 (NWA 8159) Martian Meteorite Part 2. Spinel-orthopyroxene intergrowths. A record of fO_2 and crust-basalt interactions. *Geochimica et Cosmochimica Acta*, *258*, pp.242-257.

Shih, C.Y., Nyquist, L.E., Reese, Y. and Wiesmann, H., 1998, March. The chronology of the nakhlite, Lafayette: Rb-Sr and Sm-Nd isotopic ages. In *Lunar and Planetary Science Conference* (No. 1145, p. 1145).

Shoemaker, E.M., 1977. Why study impact craters. In *Impact and explosion cratering: Planetary and terrestrial implications* (pp. 1-10).

Smith, M.R., Laul, J.C., Ma, M.S., Huston, T., Verkouteren, R.M., Lipschutz, M.E. and Schmitt, R.A., 1984. Petrogenesis of the SNC (shergottites, nakhlites, chassignites) meteorites: Implications for their origin from a large dynamic planet, possibly Mars. *Journal of Geophysical Research: Solid Earth*, *89*(S02), pp.B612-B630.

Smith, D.E., Zuber, M.T., Frey, H.V., Garvin, J.B., Head, J.W., Muhleman, D.O., Pettengill, G.H., Phillips, R.J., Solomon, S.C., Zwally, H.J. and Banerdt, W.B., 2001. Mars Orbiter Laser Altimeter: Experiment summary after the first year of global mapping of Mars. *Journal of Geophysical Research: Planets*, *106*(E10), pp.23689-23722.

Soderblom, L.A., Condit, C.D., West, R.A., Herman, B.M. and Kreidler, T.J., 1974. Martian planetwide crater distributions: Implications for geologic history and surface processes. *Icarus*, *22*(3), pp.239-263.

Sokolowska, A., Thomas, N., Wünnemann, K. and Luther, R., 2022. Simulated craters and ejecta on the past Martian water-and ice-rich impact sites (No. EPSC2022-1037). *Copernicus Meetings*.

Solomonidou, A., Coustenis, A., Lopes, R.M., Malaska, M.J., Rodriguez, S., Drossart, P., Elachi, C., Schmitt, B., Philippe, S., Janssen, M., Hirtzig, M., et al., 2018. The spectral nature of Titan's major geomorphological units: constraints on surface composition. *Journal of Geophysical Research: Planets*, *123*(2), pp.489-507.

Song, S.B., Liu, J.F., Yang, D.S., Ni, H.Y., Huang, B.X., Zhang, K. and Mao, X.B., 2019. Pore structure characterization and permeability prediction of coal samples based on SEM images. *Journal of Natural Gas Science and Engineering*, *67*, pp.160-171.

Squyres, S.W., Arvidson, R.E., Ruff, S., Gellert, R., Morris, R.V., Ming, D.W., Crumpler, L., Farmer, J.D., Marais, D.D., Yen, A. and McLennan, S.M., 2008. Detection of silica-rich deposits on Mars. *Science*, *320(5879)*, pp.1063-1067.

Staddon, L.G., Darling, J.R., Dunlop, J. and Stephen, N.R., 2022, March. Northwest Africa (NWA) 13467: A New Augite-Rich Shergottite?. In *53rd Lunar and Planetary Science Conference*, Vol. 2678, p.2212.

Stähler, S.C., Mittelholz, A., Perrin, C., Kawamura, T., Kim, D., Knapmeyer, M., Zenhäusern, G., Clinton, J., Giardini, D., Lognonné, P. and Banerdt, W.B., 2022. Tectonics of Cerberus Fossae unveiled by marsquakes. *Nature Astronomy*, *6(12)*, pp.1376-1386.

Steele, A., Fries, M.D., Amundsen, H.E.F., Mysen, B.O., Fogel, M.L., Schweizer, M. and Boctor, N.Z., 2007. Comprehensive imaging and Raman spectroscopy of carbonate globules from Martian meteorite ALH 84001 and a terrestrial analogue from Svalbard. *Meteoritics & Planetary Science*, *42*(9), pp.1549-1566.

Steele, A., McCubbin, F.M., Fries, M., Kater, L., Boctor, N.Z., Fogel, M.L., Conrad, P.G., Glamoclija, M., Spencer, M., Morrow, A.L. and Hammond, M.R., 2012. A reduced organic carbon component in martian basalts. *Science*, *337*(6091), pp.212-215.

Steele, A., Benning, L.G., Wirth, R., Siljeström, S., Fries, M.D., Hauri, E., Conrad, P.G., Rogers, K., Eigenbrode, J., Schreiber, A. and Needham, A., 2018. Organic synthesis on Mars by electrochemical reduction of CO2. *Science advances*, *4*(10), p.eaat5118.

Steele, A., Benning, L.G., Wirth, R., Schreiber, A., Araki, T., McCubbin, F.M., Fries, M.D., Nittler, L.R., Wang, J., Hallis, L.J., Conrad, P.G., et al., 2022. Organic synthesis associated with serpentinization and carbonation on early Mars. *Science*, *375*(6577), pp.172-177.

Stevens, T.O. and McKinley, J.P., 1995. Lithoautotrophic microbial ecosystems in deep basalt aquifers. *Science*, *270*(5235), pp.450-455.

Stevens, A.H. and Cockell, C.S., 2023. The Water Activity of Mars-relevant Multicomponent Brines: The Changing Influence of Perchlorate on Habitability over Time. *The Planetary Science Journal*, *4*(1), p.6.

Stevenson, D.J. and Lunine, J.I., 1988. Rapid formation of Jupiter by diffusive redistribution of water vapor in the solar nebula. *Icarus*, *75*(1), pp.146-155.

Stewart, S., Davies, E., Duncan, M., Lock, S., Root, S., Townsend, J., Kraus, R., Caracas, R. and Jacobsen, S., 2020, November. The shock physics of giant impacts: Key requirements for the equations of state. In *AIP conference proceedings (Vol. 2272, No. 1)*. AIP Publishing.

Stöffler, D., Ostertag, R., Jammes, C., Pfannschmidt, G., Gupta, P.S., Simon, S.B., Papike, J.J. and Beauchamp, R.H., 1986. Shock metamorphism and petrography of the Shergotty achondrite. *Geochimica et Cosmochimica Acta*, *50*(6), pp.889-903.

Stöffler, D. and Grieve, R.A.F., 2007. Impactites. In *Metamorphic rocks: A classification and glossary of terms, recommendations of the International Union of Geological Sciences*, Cambridge University Press. pp.82-91, 111-125, 126-242.

Stopar, J.D., Taylor, G.J., Velbel, M.A., Norman, M.D., Vicenzi, E.P. and Hallis, L.J., 2013. Element abundances, patterns, and mobility in Nakhlite Miller Range 03346 and implications for aqueous alteration. *Geochimica et Cosmochimica Acta*, *112*, pp.208-225.

Tait, K.T. and Day, J.M., 2018. Chondritic late accretion to Mars and the nature of shergottite reservoirs. *Earth and Planetary Science Letters*, *494*, pp.99-108.

Tanaka, K.L., 1986. The stratigraphy of Mars. *Journal of Geophysical Research: Solid Earth*, *91*(B13), pp.E139-E158.

Tanaka, K.L., Skinner, J.A. and Hare, T.M., 2005. *Geologic map of the northern plains of Mars* (Vol. 2888). US Department of the Interior, US Geological Survey.

Taubner, R.S., Pappenreiter, P., Zwicker, J., Smrzka, D., Pruckner, C., Kolar, P., Bernacchi, S., Seifert, A.H., Krajete, A., Bach, W. and Peckmann, J., 2018. Biological methane production under putative Enceladus-like conditions. *Nature communications*, *9*(1), p.748.

Ten Kate, I.L., 2018. Organic molecules on Mars. *Science*, *360*(6393), pp.1068-1069.

Terentiev, R.A. and Santosh, M., 2017. Post-collisional high-Mg granitoids from the Paleoproterozoic East Sarmatian Orogen (East European Craton): evidence for crust–mantle interaction. *Lithos*, *274*, pp.271-290.

Terentiev, R.A. and Santosh, M., 2020. Baltica (East European Craton) and Atlantica (Amazonian and West African Cratons) in the Proterozoic: The pre-Columbia connection. *Earth-Science Reviews*, *210*, p.103378.

Thorpe, M.T., Bristow, T.F., Rampe, E.B., Tosca, N.J., Grotzinger, J.P., Bennett, K.A., Achilles, C.N., Blake, D.F., Chipera, S.J., Downs, G. and Downs, R.T., 2022. Mars Science Laboratory CheMin data from the Glen Torridon region and the significance of lake-groundwater interactions in interpreting mineralogy and sedimentary history. *Journal of Geophysical Research: Planets*, *127*(11), p.e2021JE007099.

Tijhuis, L., Van Loosdrecht, M.C. and Heijnen, J., 1993. A thermodynamically based correlation for maintenance Gibbs energy requirements in aerobic and anaerobic chemotrophic growth. *Biotechnology and bioengineering*, *42*(4), pp.509-519.

Tomkinson, T., Lee, M.R., Mark, D.F. and Smith, C.L., 2013. Sequestration of Martian CO2 by mineral carbonation. *Nature Communications*, *4*(1), p.2662.

Toner, J.D., Catling, D.C. and Light, B., 2015a. Modeling salt precipitation from brines on Mars: Evaporation versus freezing origin for soil salts. *Icarus*, *250*, pp.451-461.

Toner, J.D., Catling, D.C. and Light, B., 2015b. A revised Pitzer model for low-temperature soluble salt assemblages at the Phoenix site, Mars. *Geochimica et Cosmochimica Acta*, *166*, pp.327-343.

Treiman, A.H. and Drake, M.J., 1983. Origin of lunar meteorite ALHA 81005: Clues from the presence of Terrae clasts and a very low-titanium mare basalt clast. *Geophysical Research Letters*, *10*(9), pp.783-786.

Treiman, A.H., Drake, M.J., Janssens, M.J., Wolf, R. and Ebihara, M., 1986. Core formation in the Earth and shergottite parent body (SPB): Chemical evidence from basalts. *Geochimica et Cosmochimica Acta*, *50*(6), pp.1071-1091.

Treiman, A.H., Barrett, R.A. and Gooding, J.L., 1993. Preterrestrial aqueous alteration of the Lafayette (SNC) meteorite. *Meteoritics*, *28*(1), pp.86-97.

Treiman, A.H., McKay, G.A., Bogard, D.D., Mittlefehldt, D.W., Wang, M.S., Keller, L., Lipschutz, M.E., Lindstrom, M.M. and Garrison, D., 1994. Comparison of the LEW88516 and ALHA77005 martian meteorites: Similar but distinct. *Meteoritics*, *29*(5), pp.581-592.

Treiman, A.H., 1995. A petrographic history of Martian meteorite ALH84001: Two shocks and an ancient age. *Meteoritics*, *30*(3), pp.294-302.

Treiman, A.H., Gleason, J.D. and Bogard, D.D., 2000. The SNC meteorites are from Mars. *Planetary and Space Science*, *48*(12-14), pp.1213-1230.

Treiman, A.H. and Gooding, J.L., 1991. Iddingsite in the Nakhla meteorite: TEM study of mineralogy and texture of pre-terrestrial (Martian?) alterations. *Meteoritics*, *26*, pp.402-402.

Treiman, A.H., 2005. The nakhlite meteorites: Augite-rich igneous rocks from Mars. *Chemie der Erde*, *65*, pp.203-270.

Treiman, A.H., Dyar, M.D., McCanta, M., Noble, S.K. and Pieters, C.M., 2007. Martian Dunite NWA 2737: Petrographic constraints on geological history, shock events, and olivine color. *Journal of Geophysical Research: Planets*, *112*(E4).

Trembath-Reichert, E., Morono, Y., Ijiri, A., Hoshino, T., Dawson, K.S., Inagaki, F. and Orphan, V.J., 2017. Methyl-compound use and slow growth characterize microbial life in 2-km-deep subseafloor coal and shale beds. *Proceedings of the National Academy of Sciences*, *114*(44), pp.E9206-E9215.

Tsiganis, K., Gomes, R., Morbidelli, A. and Levison, H.F., 2005. Origin of the orbital architecture of the giant planets of the Solar System. *Nature*, *435*(7041), pp.459-461.

Tu, L., Johnstone, C.P., Güdel, M. and Lammer, H., 2015. The extreme ultraviolet and X-ray Sun in Time: High-energy evolutionary tracks of a solar-like star. *Astronomy & Astrophysics*, *577*, p.L3.

Tu, V.M., Rampe, E.B., Bristow, T.F., Thorpe, M.T., Clark, J.V., et al., 2021. A review of the phyllosilicates in Gale Crater as detected by the CheMin instrument on the Mars Science Laboratory, Curiosity rover. *Minerals*, *11*(8), p.847.

Udry, A., Howarth, G.H., Herd, C.D.K., Day, J.M.D., Lapen, T.J. and Filiberto, J., 2020. What Martian Meteorites Reveal About the Interior and Surface of Mars. *Journal of Geophysical Research: Planets*, *125(12)*, pp. 1–34.

Vaci, Z., Newsom, H.E., Agee, C.B., Brearley, A.J., Tschauner, O. and Herd, C.D.K., 2016, March. Electron Probe Microanalysis, Micro X-Ray Diffraction, and Deuterium-Hydrogen

Analysis of Hydrous Alteration in Martian Meteorites Northwest Africa 10416 and 8159. In *47th Annual Lunar and Planetary Science Conference* (No. 1903, p. 2538).

Váci, Z. and Agee, C., 2020. Constraints on martian chronology from meteorites. *Geosciences*, *10*(11), p.455.

VanBommel, S.J., Berger, J.A., Gellert, R., et al., 2023. Elemental composition of manganese- and phosphorus-rich nodules in the Knockfarril Hill member, Gale crater, Mars. *Icarus*, *392*, p.115372.

Vicenzi, E.P. and Eiler, J., 1998. Oxygen-isotopic composition and high-resolution secondary ion mass spectrometry imaging of Martian carbonate in Lafayette meteorite. *Meteoritics and Planetary Science*, *33*(S4), pp.A159-A160.

Viviano, C.E., Moersch, J.E. and McSween, H.Y., 2013. Implications for early hydrothermal environments on Mars through the spectral evidence for carbonation and chloritization reactions in the Nili Fossae region. *Journal of Geophysical Research: Planets*, *118*(9), pp.1858-1872.

Viviano, C.E., Murchie, S.L., Daubar, I.J., Morgan, M.F., Seelos, F.P. and Plescia, J.B., 2019. Composition of Amazonian volcanic materials in Tharsis and Elysium, Mars, from MRO/CRISM reflectance spectra. *Icarus*, *328*, pp.274-286.

Wade, J., Dyck, B., Palin, R.M., Moore, J.D. and Smye, A.J., 2017. The divergent fates of primitive hydrospheric water on Earth and Mars. *Nature*, *552*(7685), pp.391-394.

Wadhwa, M. and Lugmair, G.W., 1996. The formation age of carbonates in ALH84001. *Meteoritics and Planetary Science Supplement*, *31*.

Waite, J.H., Glein, C.R., Perryman, R.S., et al., 2017. Cassini finds molecular hydrogen in the Enceladus plume: evidence for hydrothermal processes. *Science*, *356*(6334), pp.155-159.

Walsh, K.J., Morbidelli, A., Raymond, S.N., O'Brien, D.P. and Mandell, A.M., 2011. A low mass for Mars from Jupiter's early gas-driven migration. *Nature*, *475*(7355), pp.206-209.

Warren, J., 2004. Ancient atomists on the plurality of worlds. *The Classical Quarterly*, *54(2)*, pp.354-365.

Way, M.J. and Del Genio, A.D., 2020. Venusian habitable climate scenarios: Modeling Venus through time and applications to slowly rotating Venus-like exoplanets. *Journal of Geophysical Research: Planets*, *125*(5), p.e2019JE006276.

Webster, C.R., Mahaffy, P.R., Flesch, G.J., Niles, P.B., Jones, J.H., Leshin, L.A., Atreya, S.K., Stern, J.C., Christensen, L.E., Owen, T. and Franz, H., 2013. Isotope ratios of H, C, and O in CO2 and H2O of the Martian atmosphere. *Science*, *341*(6143), pp.260-263.

Webster, C.R., Mahaffy, P.R., Atreya, S.K., Flesch, G.J., Mischna, M.A., Meslin, P.Y., Farley, K.A., Conrad, P.G., Christensen, L.E., Pavlov, A.A. and Martín-Torres, J., 2015. Mars methane detection and variability at Gale crater. *Science*, *347*(6220), pp.415-417.

Webster, C.R., Mahaffy, P.R., Atreya, S.K., Moores, J.E., Flesch, G.J., Malespin, C., McKay, C.P., Martinez, G., Smith, C.L., Martin-Torres, J. and Gomez-Elvira, J., 2018. Background levels of methane in Mars' atmosphere show strong seasonal variations. *Science*, *360*(6393), pp.1093-1096.

Werner, S.C., 2008. The early Martian evolution—Constraints from basin formation ages. *Icarus*, *195*(1), pp.45-60.

Werner, S.C., 2009. The global martian volcanic evolutionary history. *Icarus*, *201*(1), pp.44-68.

Werner, S.C., Ody, A. and Poulet, F., 2014. The source crater of martian shergottite meteorites. *Science*, *343*(6177), pp.1343-1346.

Werner, S.C., 2019. In situ calibration of the Martian cratering chronology. *Meteoritics & Planetary Science*, *54*(5), pp.1182-1193.

Westall, F., Hickman-Lewis, K., Hinman, N., Gautret, P., Campbell, K.A., Bréhéret, J.G., Foucher, F., Hubert, A., Sorieul, S., Dass, A.V. and Kee, T.P., 2018. A hydrothermal-sedimentary context for the origin of life. *Astrobiology*, *18*(3), pp.259-293.

Westheimer, F.H., 1987. Why nature chose phosphates. *Science*, *235*(4793), pp.1173-1178.

Whelley, P., Matiella Novak, A., Richardson, J., Bleacher, J., Mach, K. and Smith, R.N., 2021. Stratigraphic evidence for early martian explosive volcanism in Arabia Terra. *Geophysical Research Letters*, *48*(15), p.e2021GL094109.

Wiens, R.C., Becker, R.H. and Pepin, R.O., 1986. The case for a Martian origin of the shergottites, II. Trapped and indigenous gas components in EETA 79001 glass. *Earth and Planetary Science Letters*, *77*(2), pp.149-158.

Wiens, R.C., Maurice, S., Barraclough, B., Saccoccio, M., Barkley, W.C., Bell, J.F., Bender, S., Bernardin, J., Blaney, D., Blank, J. and Bouyé, M., 2012. The ChemCam instrument suite on the Mars Science Laboratory (MSL) rover: Body unit and combined system tests. *Space science reviews*, *170*, pp.167-227.

Wilde, S.A., Valley, J.W., Peck, W.H. and Graham, C.M., 2001. Evidence from detrital zircons for the existence of continental crust and oceans on the Earth 4.4 Gyr ago. *Nature*, *409*(6817), pp.175-178.

Wilhelms, D.E. and Squyres, S.W., 1984. The Martian hemispheric dichotomy may be due to a giant impact. *Nature*, *309*(5964), pp.138-140.

Williams, D.A., Greeley, R., Zuschneid, W., Werner, S.C., Neukum, G., Crown, D.A., Gregg, T.K., Gwinner, K. and Raitala, J., 2007. Hadriaca Patera: insights into its volcanic history from Mars Express high resolution stereo camera. *Journal of Geophysical Research: Planets*, *112*(E10).

Williams, D.A., Greeley, R., Werner, S.C., Michael, G., Crown, D.A., Neukum, G. and Raitala, J., 2008. Tyrrhena Patera: geologic history derived from Mars Express high resolution stereo camera. *Journal of Geophysical Research: Planets*, *113*(E11).

Wittmann, A., Korotev, R.L., Jolliff, B.L., Irving, A.J., Moser, D.E., Barker, I. and Rumble, D., 2015. Petrography and composition of Martian regolith breccia meteorite Northwest Africa 7475. *Meteoritics & Planetary Science*, *50*(2), pp.326-352.

Wolery, T.W. and Jarek, R.L., 2003. Software user's manual. *EQ3/6, version*, *8*, p.376.

Wolery, T.J., 2010. *EQ3/6 A Software Package for Geochemical Modeling* (No. EQ3/6 V. 8.0 a). Lawrence Livermore National Lab.(LLNL), Livermore, CA (United States).

Wordsworth, R., Kalugina, Y., Lokshtanov, S., Vigasin, A., Ehlmann, B., Head, J., Sanders, C. and Wang, H., 2017. Transient reducing greenhouse warming on early Mars. *Geophysical Research Letters*, *44*(2), pp.665-671.

Woo, J.M.Y., Brasser, R., Matsumura, S., Mojzsis, S.J. and Ida, S., 2018. The curious case of Mars' formation. *Astronomy & Astrophysics*, *617*, p.A17.

Woo, J.M.Y., Brasser, R., Grimm, S.L., Timpe, M.L. and Stadel, J., 2022. The terrestrial planet formation paradox inferred from high-resolution N-body simulations. *Icarus*, *371*, p.114692.

Wray, J.J., 2013a. Gale crater: the Mars Science Laboratory/Curiosity rover landing site. *International Journal of Astrobiology*, *12*(1), pp.25-38.

Wray, J.J., Hansen, S.T., Dufek, J., Swayze, G.A., Murchie, S.L., Seelos, F.P., Skok, J.R., Irwin, R.P. and Ghiorso, M.S., 2013b. Prolonged magmatic activity on Mars inferred from the detection of felsic rocks. *Nature Geoscience*, *6*(12), pp.1013-1017.

Yang, J., Cowan, N.B. and Abbot, D.S., 2013. Stabilizing cloud feedback dramatically expands the habitable zone of tidally locked planets. *The Astrophysical Journal Letters*, *771*(2), p.L45.

Yang, J., Abbot, D.S., Koll, D.D., Hu, Y. and Showman, A.P., 2019. Ocean dynamics and the inner edge of the habitable zone for tidally locked terrestrial planets. *The Astrophysical Journal*, *871*(1), p.29.

Ye, C. and Glotch, T.D., 2019. Spectral properties of chloride salt-bearing assemblages: Implications for detection limits of minor phases in chloride-bearing deposits on Mars. *Journal of Geophysical Research: Planets*, *124*(2), pp.209-222.

Ye, C., Legett IV, C., Ito, G. and Glotch, T.D., 2019, December. Modeling Spectra of Transparent Mineral-Bearing Media: Implications for Spectra of Chloride-Bearing Deposits on Mars. In *AGU Fall Meeting Abstracts* (Vol. 2019, pp. P33F-3492).

Yung, Y.L., Chen, P., Nealson, K., Atreya, S., Beckett, P., Blank, J.G., Ehlmann, B., Eiler, J., Etiope, G., Ferry, J.G. and Forget, F., 2018. Methane on Mars and habitability: challenges and responses. *Astrobiology*, *18*(10), pp.1221-1242.

Zahnle, K.J., Lupu, R., Catling, D.C. and Wogan, N., 2020. Creation and evolution of impact-generated reduced atmospheres of early Earth. *The Planetary Science Journal*, *1*(1), p.11.

Zhong, S. and Zuber, M.T., 2001. Degree-1 mantle convection and the crustal dichotomy on Mars. *Earth and Planetary Science Letters*, *189*(1-2), pp.75-84.

APPENDICES

7.1 Research Dissemination: Conference Papers & Publications

[Peer-reviewed / In Review / In Preparation] – In Chronological Order:

1. Christou, E., et al., 2022. A Pessimistic Perspective on the Habitability of Early Mars: Simulations for The Northwest Africa 8159 Environment. *85th Meteoritical Society Meeting, Glasgow, 2022,* LPI No. 2695 (in preparation). Available at: https://www.hou.usra.edu/meetings/metsoc2022/pdf/6486.pdf.

2. Diez Garcia., D. et al. The Hydrothermal System at Cerro do Jarau Crater (accepted in *Annals of the Brazilian Academy of Sciences*, Manuscript ID AABC-2023-0005.R1).

3. Pickersgill, A.E., Lee, M.R., Mark, D.F. and Christou, E., 2022. What Do We Know About the Duration of Post-Impact Hydrothermal Activity? *Meteoritics & Planetary Science,* 57.

4. Daly, L., Lee, M.R., Hallis, L.J., et al., 2021. Solar wind contributions to Earth's oceans. *Nature Astronomy, 5(12),* pp.1275-1285. https://doi.org/10.1038/s41550-021-01487-w.

5. Christou, E., et al., 2021. Fluid Flow in the Martian Subsurface from the Noachian until Present Constrained via Numerical Simulations: Implications for Habitability. NASA / Astrophysics Data System: 2021LPICo2548.2556C (in preparation). *52nd Lunar and Planetary Science Conference, The Woodlands, Texas, USA, March 2021*. Available at: https://www.hou.usra.edu/meetings/lpsc2021/pdf/2556.pdf.

6. Christou, E. et al., 2021. Northwest Africa 8159 Apatite vs. Lafayette Apatite: Effects of Terrestrial Weathering vs. Martian Alteration; NASA / Astrophysics Data System: 2021LPICo2609.6297C / LPI Contribution No. 2609, id.6297 (in preparation). *84th Annual Meeting of The Meteoritical Society, 2021, Chicago, USA.* Available at: https://www.hou.usra.edu/meetings/metsoc2021/pdf/6297.pdf.

7. Pickersgill, A.E., Christou, E. and Lee, M.R., 2021. A Preliminary Simulation of the Hydrothermal System at the Boltysh Impact Structure. LPI Contribution No. 2548, id. 2139. *52nd Lunar and Planetary Science Conference, The Woodlands, Texas, USA, March 2021*. Available at: https://www.hou.usra.edu/meetings/lpsc2021/pdf/2139.pdf.

8. Christou, E., et al., 2021. Resource Identification in Asteroid & Martian Meteorite Samples via Atom Probe Tomography & correlative Nanoscale Analyses (SIMS, TEM, EPMA, SEM); *RawMat Conference, September 2021, Athens, Greece*.

9. Christou, E., et al., 2020. Martian vs. Terrestrial Alteration of Apatite in the Unique Northwest Africa 8159 Meteorite. *51st Lunar and Planetary Science Conference 2020, The Woodlands, Texas, USA, March 2020*. Available at: https://www.hou.usra.edu/meetings/lpsc2020/pdf/1100.pdf.

10. Christou, E., et al., 2020. Martian Alteration vs. Terrestrial Contamination in the Apatite of the Unique Martian Meteorite NWA 8159. *2nd British Planetary Sciences Conference, Oxford, UK, January 2020*.

11. Christou, E., et al., 2019. Unusual Apatite in the Unusual Martian Meteorite Northwest Africa (NWA) 8159. NASA/ Astrophysics Data System: 2019LPICo2157.6283C. LPI Contribution No. 2157, id.6283. *82nd Annual Meeting of The Meteoritical Society, 2019, Sapporo, Japan.* Available at: https://www.hou.usra.edu/meetings/metsoc2019/pdf/6283.pdf.

12. Christou, E., Pickersgill, A.E. and Bach, W., 2019. Controls on the Duration of Impact-Induced Hydrothermal Activity via Numerical Simulations. NASA / Astrophysics Data System: 2019LPICo2136.5037C. LPI Contribution No. 2136, id. 5037; *Large Meteorite Impacts and Planetary Evolution VI, 2019, Brazilia, Brazil*. Available at: https://www.hou.usra.edu/meetings/lmi2019/pdf/5037.pdf.

13. Pickersgill, A. E., Christou, E. et al., 2019. Six Million Years of Hydrothermal Activity at Chicxulub? NASA / Astrophysics Data System: 2019LPICo2136.5082P. LPI Contribution No. 2136, id.5082; *Large Meteorite Impacts and Planetary Evolution VI, 2019, Brazilia, Brazil* (in preparation for *Nature Geoscience*). Available at: https://ui.adsabs.harvard.edu/abs/2019LPICo2136.5082P/abstract.

14. Christou, E. and Bach, W., 2019. Post-Impact Habitability at the Chicxulub Crater. *82nd Annual Meeting of The Meteoritical Society*, 2019, Sapporo, Japan; 82 (2157), 6100.

15. Christou, E., et al., 2019. 2 contributions; [a]: Post-Impact Habitability at the Chicxulub Crater. [b]: Controls on the Duration of Impact-Induced Hydrothermal Activity via Numerical Simulations, *Impacts and their Role in the Evolution of Life, Tällberg, Sweden, 10 - 13 June 2019.*

16. Christou, E., et al., 2019. 3 contributions; [a]: Martian Fluid Compositions: The Habitability of Two Ancient Environments on Mars. [b]: Controls on the Duration of Impact-Induced Hydrothermalism via Numerical Simulations. [c]: Post-Impact Habitability at the Chicxulub Crater. *Scottish Planetary Science Research Network, University of Glasgow, School of Geographical & Earth Sciences, Glasgow, UK, 7-8 May, 2019.*

17. Christou, E. and Bach, W., 2018. Post-Impact Hydrothermal Activity. Thermodynamic Simulations on the Chicxulub Crater & Habitability Assessment. In *European Planetary Science Congress*, 16–21 September 2018, TU Berlin, Berlin, Germany (Vol. 12, pp. EPSC2018-1175).

7.2 HT 3, iSALE & PHREEQC Code Availability

The new version of the HYDROTHERM code (HT 3: including the source Fortran script, the interactive pre-processor and post-processor, and the code's guide), which was used to produce all numerical models for the simulated Martian hydrothermal systems presented in this PhD dissertation, is publicly available and can be downloaded from the following website of the USGS: https://volcanoes.usgs.gov/software/hydrotherm/. The only adjustment needed in the source script to fully reproduce the simulations of this PhD research is to adjust the gravity acceleration parameter of the source code (where needed in Eq. 2.1 – 2.15; as presented in §2.1) to the value of 3,721 m/s², which describes gravitational acceleration on Mars.

The updated version of the PHREEQC code (version 3) which was used to simulate Martian fluid – basalt interactions and the habitability (bioenergetics) of the simulated Martian hydrothermal or hydrous systems is also publicly available and can be downloaded from the following USGS website: https://www.usgs.gov/software/phreeqc-version-3.

The updated version of the iSALE code along with its different components (examples and guidelines for installation) can be accessed here: https://github.com/isale-code.

All parts of the Appendix of this PhD dissertation that are in electronic form (due to the extent and size of datasets) can be accessed here:
https://gla-my.sharepoint.com/personal/e_christou_1_research_gla_ac_uk/_layouts/15/onedrive.aspx?login_hint=e%2Echristou%2E1%40research%2Egla%2Eac%2Euk&id=%2Fpersonal%2Fe%5Fchristou%5F1%5Fresearch%5Fgla%5Fac%5Fuk%2FDocuments%2FE%20Christou%20%5B2023%5D%20PhD%20Thesis%20%5F%20Appendix.

7.3 HT 3 & iSALE Models (§3.1 – 3.2): Thermodynamic Output

All the thermodynamic output – movie files of the constructed HT 3 simulations and exported figures that were presented in §3.1 and §3.2 are available at:
https://gla-my.sharepoint.com/personal/e_christou_1_research_gla_ac_uk/_layouts/15/onedrive.aspx?login_hint=e%2Echristou%2E1%40research%2Egla%2Eac%2Euk&id=%2Fpersonal%2Fe%5Fchristou%5F1%5Fresearch%5Fgla%5Fac%5Fuk%2FDocuments%2FE%20Christou%20%5B2023%5D%20PhD%20Thesis%20%5F%20Appendix%2FHT%203%20Numerical%20Simulations%5FVideos%2Ezip&parent=%2Fpersonal%2Fe%5Fchristou%5F1%5Fresearch%5Fgla%5Fac%5Fuk%2FDocuments%2FE%20Christou%20%5B2023%5D%20PhD%20Thesis%20%5F%20Appendix

For the impact-induced hydrothermal activity models, the figures and simulations presented in §3.1 are included in the ''Higher Permeability'' folders (in Martian Crater_[10, 100, 200] km_ Hydrothermal Flows or in 2x Impacts Noachian) in the above link. A lower permeability scenario was also investigated for each set of simulations, as explained in §3.1. All ''Lower Permeability'' simulations can also be found in the individual folders of each impact-cratering scenario. Additionally, for the 200-km crater, another experimental simulation was performed exploring an almost dry Martian crust (no water-ice deposits on the surface or shallow subsurface). The differences in the lifetime of hydrothermal circulation, as explained in §3.1 can be seen through the mp4 videos included in the ''Martian Crater_200-km_Hydrothermal Flows'' folder. On top of that, experimental models that simulate 1× impact event, or 2×, or 4× simultaneous impact events on the Noachian Martian crust, are found in the ''Martian Cratering_2x Impacts_Noachian'' folder. The models for simultaneous impact-cratering processes on the Martian crust indicate that 2× simultaneous and smaller scale impact-cratering events (D ≈ 5 – 7 km for each crater, and with an in-between distance of 150 km) generate a wider subsurface hydrological system (circa 10× greater volumetric expansion) which durates for a 3 – 5 × greater period, than that in a single larger-scale (D = 10 – 14 km) crater (as analysed in §3.1.4). However, 4× simultaneous impact-cratering processes (with D ≤ 5 km per crater) significantly increase the permeability and porosity of the Martian crust. If permeability and porosity increase above a certain limit, the cooling process is accelerated exponentially. Therefore, although the duration of the 4× wider hydrothermal environment is greater (2-3×)

than that of a single and larger crater, its duration and flux are evidently smaller than that of the hydrothermal system induced after 2× synchronous impact-cratering events. This physical effect was explained in detail through Fig. 4.4 – 4.5 at §4.1.3.2.

Accordingly, a comparison of higher versus lower permeability simulations for each impact-cratering or volcanogenic hydrothermal environment / scenario are also included in the above link. The exported HT 3 simulations – mp4.videos that describe the Martian volcanogenic hydrothermal systems are also organized in individual folders for the different scenarios of hydrothermal or hydrous flows. Furthermore, two extra scenarios are presented therein: Hydrothermal Flows _ Volcanic Plume _ T_{max} = 600 °C; and, Hydrothermal Flows _ Intrusive Veins _ T_{max} = 750 °C (the latter thermodynamic output – dataset was used for the habitability simulations in §3.3.2; Fig. 3.32). The recommended action in order to view the mp4 files of the HT 3 models is to firstly download the zip folder [HT 3 Numerical Simulations_Videos] to your own personal desktop.

The iSALE source code that was used and edited in this research for simulating the formation of impact cratering processes on early Mars, and all modelling results, along with the parameterization (new input) of the Martian basaltic crust can be accessed here: https://gla-my.sharepoint.com/personal/e_christou_1_research_gla_ac_uk/_layouts/15/onedrive.aspx?isAscending=true&id=%2Fpersonal%2Fe%5Fchristou%5F1%5Fresearch%5Fgla%5Fac%5Fuk%2FDocuments%2FE%20Christou%20%5B2023%5D%20PhD%20Thesis%20%5F%20Appendix%2FiSALE%20Simulations%5FCode%20%26%20Results&sortField=Modified&view=0

Please explore and compare the exported videos of the HT 3 and iSALE simulations, through the shared links mentioned previously. If you cannot view the videos of the simulations or access the input code or/and output datasets, it is then recommended that you download the folders or files to your own device to ensure access and smooth processing. Please feel free to contact the author of this PhD dissertation (via email at: e.christou.1@research.gla.ac.uk, or at: e.christou@gla.ac.uk), if you require further assistance with downloading or/and reproducing the numerical simulations of this PhD research.

7.4 PHREEQC Models (§3.3): Habitability Output Datasets

The output of the PHREEQC fluid – basaltic rock interactions (mineral dissolution of the basaltic rock) and habitability simulations for the Martian subsurface are included in the excel sheet: ‘’Martian Habitability_PHREEQC Output_Appendix’’ that can be found and downloaded from:
https://gla-my.sharepoint.com/personal/e_christou_1_research_gla_ac_uk/_layouts/15/onedrive.aspx?login_hint=e%2Echristou%2E1%40research%2Egla%2Eac%2Euk&id=%2Fpersonal%2Fe%5Fchristou%5F1%5Fresearch%5Fgla%5Fac%5Fuk%2FDocuments%2FE%20Christou%20%5B2023%5D%20PhD%20Thesis%20%5F%20Appendix%2FHabitability%20Computations%5FOutput

The results of the PHREEQC simulations are in the form of very extensive tabular datasets, and these could not be included as tables in the appendix of this PhD dissertation. If they were to be included, an additional number of approximately 1000 – 1200 pages would be needed only for the appendix. Therefore, all habitability computations and figures presented in §3.3 derive from the exported and analysed PHREEQC datasets that are included in the aforementioned excel sheet. In particular, the following spreadsheets: ‘’PHREEQC_W-R_I (25 °C – 150 °C)’’, ‘’PHREEQC_W-R_II (150 °C – 70 °C)’’ and ‘’PHREEQC_W-R_III (70 °C – 25 °C)’’ include the thermodynamic (habitable) range and chemical reaction pathways of mineral – fluid interactions under hydrothermal or hydrous conditions. Steps I-III of the geochemical reaction pathways were determined by the HT 3 thermodynamic results, which were imported as boundary conditions for each scenario in the PHREEQC simulations. The thermodynamic boundary conditions and rate limiting steps of the PHREEQC models are included in the following spreadsheets: ‘’HT 3_T-t_Boundary Limits_Loop’’ and ‘’PHREEQC plots’’.

The datasets of these spreadsheets were used to constrain the computed PHREEQC water – mineral reactions under a variety of thermodynamic conditions that do not result in the sterilization of potentially habitable domains in the Martian subsurface (T_{max} = 150 °C; with T = 121 °C, the upper limit for microbial life). The thermodynamic conditions were defined via ‘’HT 3 observatories’’ that acquired thermodynamic data from the simulated Martian

subsurface domains in each scenario (‘’HT 3_T-t_Boundary Limits_Loop’’). The HT 3 code resulted to the identification of potentially habitable niches that formed at any time point during either impact-induced or volcanogenic hydrological activity in the simulated Martian subsurface. Hence, the thermodynamic data of the HT 3 domains were automatically exported and they later served as input – boundary conditions in the PHREEQC geochemical reaction pathways (dissolution of minerals in the basaltic environment by hydrous or hydrothermal flows) and habitability computations. Finally, the ‘’Martian habitability’’ spreadsheet includes the habitability computations for all Martian impact-induced or volcanogenic hydrothermal environments. Thus, all figures and models presented in §3.3 and §4.2 derive from the datasets included in the ‘’Martian habitability’’ spreadsheet.

7.5 SEM-BSE Datasets and ImageJ Processed Results

All the acquired SEM-BSE montage (whole-sample) maps of the examined Martian meteorites NWA 8159 (samples 1 and 2) and Lafayette (sample USNM 1505-5), together with the processed ImageJ datasets and results for the calculated porosity of these Martian rock samples, can be accessed here:

https://gla-my.sharepoint.com/personal/e_christou_1_research_gla_ac_uk/_layouts/15/onedrive.aspx?isAscending=true&id=%2Fpersonal%2Fe%5Fchristou%5F1%5Fresearch%5Fgla%5Fac%5Fuk%2FDocuments%2FE%20Christou%20%5B2023%5D%20PhD%20Thesis%20%5F%20Appendix%2FSEM%2DBSE%20Imaging%20%26%20ImageJ%20Results&sortField=Modified&view=0

The End _

Comet 2022 E3 [ZTF]: 01/02/2023_04:54_orbital period: 50 Kyr [JPL, NASA, ESA]